ISSN 2367-7570

Workshop
"Solar Influences on the Magnetosphere, Ionosphere and Atmosphere"

Book of Proceedings

Thirteenth Workshop
September, 2021

Organized by:

Space Research and Technologies Institute
Bulgarian Academy of Sciences

Scientific Organizing Committee

Editors: **Katya Georgieva, Boian Kirov, Dimitar Danov**

DOI: 10.31401/WS.2021.proc

CONTENT

Sun and Solar Activity

Preface

The Thirteenth Workshop "Solar Influences on the Magnetosphere, Ionosphere and Atmosphere" was held from September 13 to 17, 2021 in Primorsko, Bulgaria. 62 scientists from 14 countries participated in the workshop. 39 papers are included in these Proceedings. The Scientific Organizing Committee and the Editors of the Proceedings thank all the participants in the Workshop and contributors to the Proceedings.

Analyse of ionospheric and Geomagnetic Pre -earthquake Anomalies

Adibekyan M.V.

Ministry of Emergency Situations of the Republic of Armenia Territorial Survey for Seismic Protection State Non-Commercial Organization
e-mail: adibekyan@yahoo.com

Abstract

Aiming at earthquake precursors apportionment the earthquake preparation displays of VARDENIS (Armenia, 29.04.2008, M=3.7) BORISAKHO (Georgia, 09.06.08, M =4.1), NAKHITCEVAN (Azerbaijan, 02.09.2008, M=5.1), earthquakes in time-series have been studied using the geomagnetic and ionosphere tools. Aiming at earthquake forecasting the anomaly in the ionosphere plasma is investigated by a radio-astronomical method. There were received some results, allowing to make out the difference of seismogenic anomalies of ionosphere between the longer anomalies connected to magnetic activity of ionosphere by the method of vertical reconnaissance of ionosphere.

Introduction

It is known, that the geophysical environment, including seismically active zones, is made up of solid, liquid and gaseous phases. It is known as well that in the zone of two phases separation a Zone of Separated Changes (ZSC) is forming, or as they are called in physical chemistry, double ionic (electric) layers. Depending on their structure, each of the ZSC of geophysical environment is characterized by capacity, inductivity and resistance (see [1]).

The results obtained earlier allow to make out the difference between activity of ionosphere, by the method of vertical reconnaissance of ionosphere.

Radio astronomical monitoring method makes possible, along with immediate detection of electromagnetic emission from the Earth's depth in the selected frequency band, to observe other types of lithospheric impact on the atmosphere, such as aerosol, electrostatic, acoustical/gravitational, etc. Those sources ultimately create anomalies at different altitudes of the atmosphere, high affect the propagating radio astronomical signal. Radio astronomical monitoring method has the following clear advantages over the active sensing methods: 1) Cosmic radio sources (Galactic background, discrete radio stars, etc.) are used instead of man-made radiation sources, often powerful, which are able to affect the observed layers of atmosphere; 2) Cosmic radio sources generate noise-like signals, which makes possible observation of the same source at several wavelengths (this is increasing the informative ness of monitoring); 3) Since the signals from the stellar radio sources pass through all layers of the atmosphere, their informative ness is high; 4) The radio astronomical instruments are highly sensitive and able to detect the smallest changes in the state of the atmosphere; 5) The method allows monitoring of solar activity by direct measurement of solar radiation density in the receiver waveband; 6) The cosmic source's power in the radio-frequencies range (over 10 MHz) is stable and known with high accuracy, while stability of the receiver system is provided by a controlled noise power source. This configuration allows reception of signals from point cosmic radio sources Swan and Cassiopeia-A, with nearly the same amplitudes of interference lobes. Time interval between these sources by the local meridian is 3 hours and 30 min.

The method and technique of research

A new Methodology has been elaborated that provides possibility to estimate the current Seismic hazard (its intensity, location and time) with a sufficiently big probability. The elaborated methodology was used for analysis of data received in the process of perpendicular ionosphere from "Swan- A" and "Cassiopeia - A" point radio sources by radio astronomy methods. The time – series of geomagnetic field tension of T full vector.

Aiming at the earthquake forecasting the anomaly formations in the ionospheric plasma are investigated by a radio-astronomical method. For considering the geomagnetic field, the high accuracy proton magnetometers, which are measuring the T inductivity of geomagnetic field each 5 minutes are used for measuring the geomagnetic field. There have been used the time – series for Shooshi and Saravand ionospheric stations and Aruch and Bavra geomagnetic stations [2].

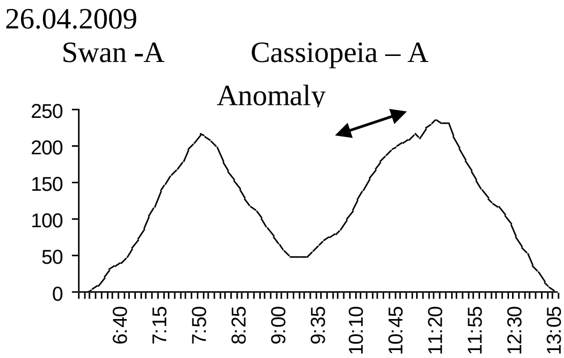

Fig.1. The time – series of the ionosphere field (Saravand station) obtained by Radio astronomical method for the VARDENIS (Armenia, 29.04.2008, M=3.7) earthquake.

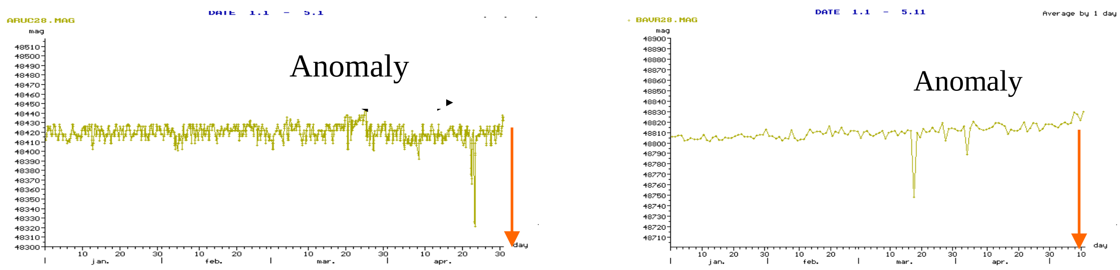

Fig.2. The time – series of the geomagnetic field (Aruch, Bavra stations) for the VARDENIS (Armenia, 29.04.2008, M=3.7) earthquake.

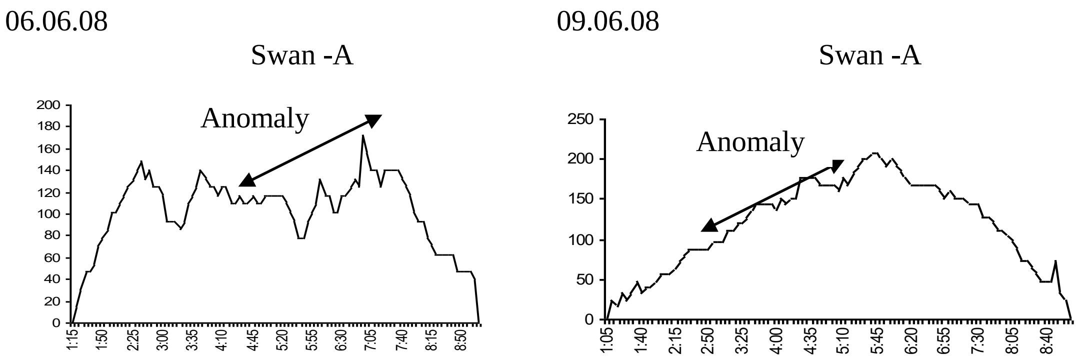

Fig.3. The time – series of the ionosphere field (Shooshi station) obtained by Radio astronomical method for BORISAKHO (Georgia, 09.06.08, M =4.1) the earthquake.

27.08.08

Swan -A Cassiopeia – A

Anomaly

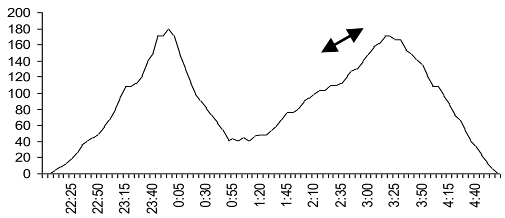

Fig.4. The time – series of the ionosphere field (Saravand station) obtained by Radio astronomic method for the NAKHITCEVAN (Azerbaijan, 02.09.2008, M=5.1) earthquake.

Results

The results of the retrospective analysis of ionosphere observation data before NAKHITCEVAN (Azerbaijan, 02.09.2008, M=5.1), VARDENIS (Armenia, 29.04.2008, M=3.7) BORISAKHO (Georgia, 09.06.08, M =4.1), revealed the following basic types of anomaly (Figure. 15):

1. Blinking of ionosphere active radio-source Swan – A on the frequency of 74 MHz.
2. Anomaly of above – mentioned precursors is coming out up to 40 days before earthquake.

Conclusion

The results of analysis by used methods show that the anomalies generally appear on 1- 40 days before the earthquake.

References

Badalyan M., Petrosyan. H., Adibekyan M.V. (2001) Peculiarities of Magnetic Precursors of Earthquakes on the Territory of Armenia.Journal of Georgian Geophysical Society.Physics of SolidEarth, vol.5, Tbilisi, p.37-43, 2001.

Balassanian S. (1990), Dynamic Geo-electricity. Novosibirsk, "NAUKA", Siberian Department, pp.232.

Flares in Low State in KR Aurigae

Boeva[1] S., Zamanov[1] R., Koleva[2] K., Dechev[1] M.,

[1] Institute of Astronomy and NAO Rozhen, BAS, Sofia, Bulgaria
[2] Space Research and Technology Institute, BAS, Sofia, Bulgaria
E-mail: sboeva@astro.bas.bg

Abstract

We present examples of light curves observed during the last low state of the cataclysmic variable KR Aur, containing flares with amplitudes up to 2 magnitudes. We calculate the energy of these flares and compare with the energies of similar events in the Sun, single eruptive stars and cataclysmic variables.

The relatively high energy of the flares (10^{33} – 10^{35} erg) in *UBV* bands can be interpreted as evidence of their accretion origin.

Introduction

KR Aur is a novalike cataclysmic variable (CV). It is member of VY Scl class and occasionally drops to low state with 6 mag down from its normal brightness. Long-term light curve from 1980 to 2021 is presented on Fig.1.

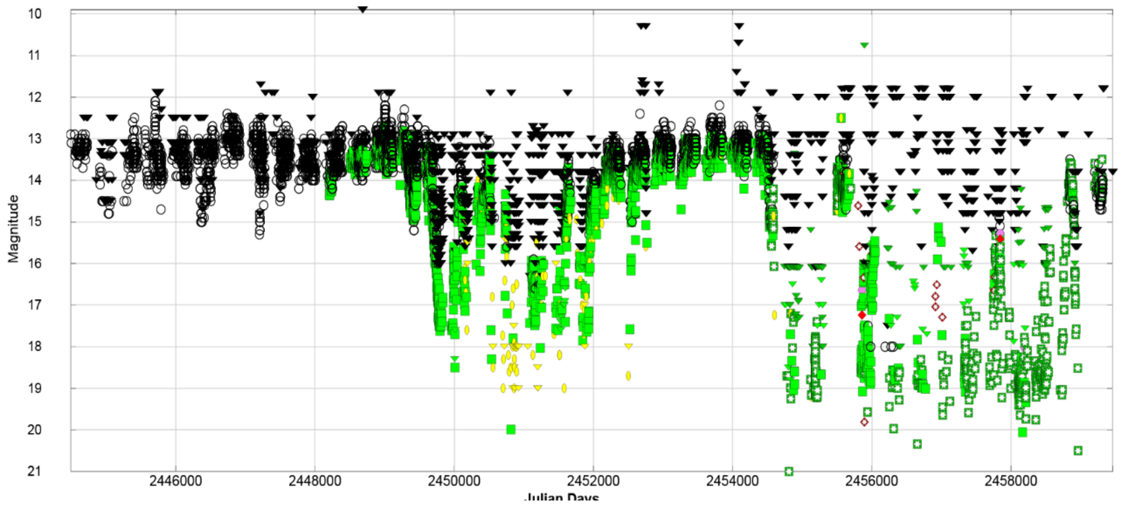

Fig.1. Long-term light curve from 1980 to 2021 from AAVSO data. The two low states of KR Aur in 1994-2001 and 2008-2020 are clearly visible.

The system consists of a white dwarf with mass 0.94 $M_\odot$ and a red dwarf with mass 0.37 $M_\odot$ [Rodríguez-Gil et al. 2020]. In high photometric state the brightness of system is dominated by the accretion disk. In low state the disk is weak or lacking due to reduced mass transfer rate from the secondary component. The solar type magnetic cycles of the secondary can be the reason for such a behavior [Bianchini 1990]. It is possible, the system to be detached for some time. Nevertheless, we rarely observe flares with high amplitude during the low state 2008-2020. Flaring activity in the light curve and in the spectra due to episodic accretion was reported by Rodríguez-Gil et al. (2020).

The spectral type of the secondary is M4-5V. Such low mass stars have relatively strong magnetic fields and can produce flares with energy $10^3 - 10^4$ times greater than observed on the Sun ($10^{28} - 10^{32}$ erg) [Paudel et al. 2021]. Flares emit significant energy from X-ray, UV, optical, infrared to radio wavelengths.

Results and discussion

We use observations, obtained with the 2 m and the 50/70 cm Schmidt telescopes at NAO Rozhen and 1.4 m telescope at AS Vidojevica during the latest minimum of KR Aur [Boeva et al. 2012, 2021]. Only a part of the low-state observations contain flare activity in KR Aur. Light curves with duration 3-6 hours in one (17.02.2018) and 3 bands (20.01.2009; 26.02.2009; 23.02.2017) are selected and plotted on Fig. 2.

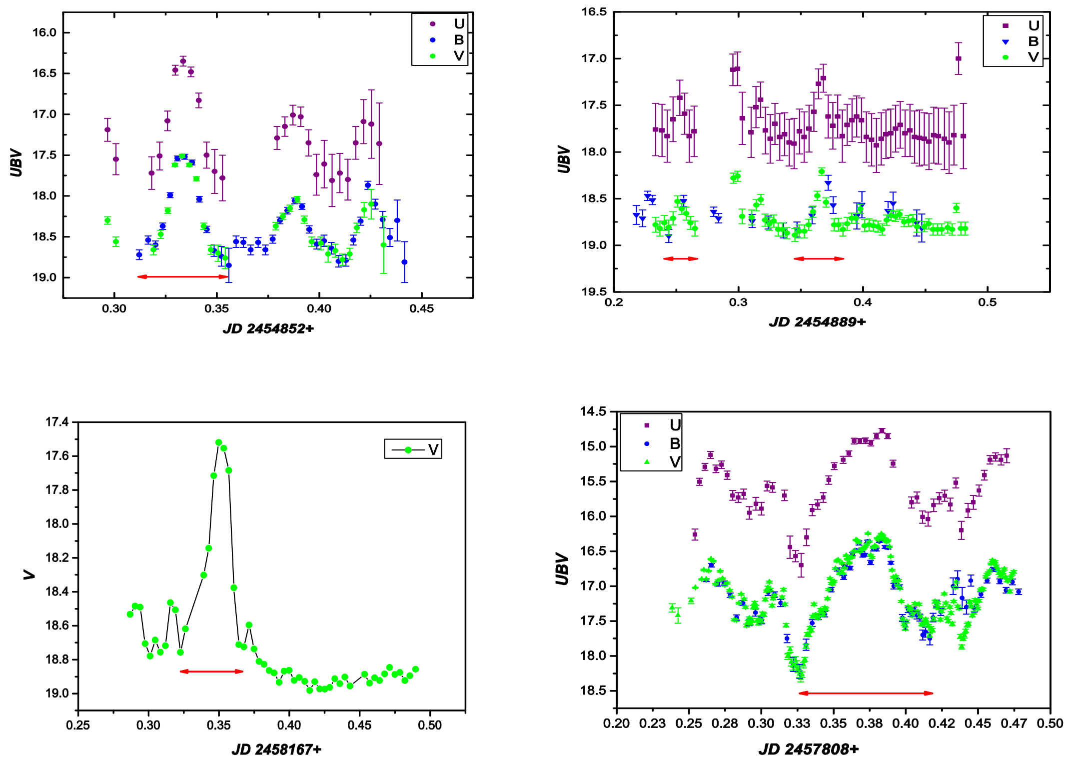

Fig.2 Light curves of KR Aur in low state. Flares used for calculation are marked with red arrows. The arrow's length correspond to the flare duration.

In low states for some CVs flares were reported: with durations 15 – 90 min with amplitudes up to 0.6 mag for AM Her [Kafka et al. 2005], with durations ~ 30 min and amplitudes up to 2 mag for MV Lyr [Scaringi et al. 2017]. Our observations show even larger amplitudes. The brightest flare observed on 23.02.2017 in *UBV* bands has amplitude ~2 magnitudes (2.08 mag in *V*) and duration more than 2 hours. Similar flare was reported by Shakhovskoy et al. (1993) in low state of AM Her (duration ~ 20 min, $\Delta V = 2.14$ mag).

We calculate the energy of the flares for different filters using the relation:

$$E = 4\pi d^2 F_\lambda \Delta\lambda \Delta t$$

where d is the distance (we used d=500 pc), F_λ is the flux, $\Delta\lambda$ is filter's equivalent width and Δt is duration on the flare.

In Table 1 we present our results. The values of ***E*** are larger for blue and UV bands in comparison to the visible band (V band). The weaker flares with amplitude ~ 0.3 mag show energy ~ 10^{33} erg and the strongest flare reaches 10^{35} erg.

Date	A [mag]	Δt [min]	E_U [x 10^{33} erg]	E_B [x 10^{33}erg]	E_V [x 10^{33}erg]	E_U/E_B	E_U/E_V
20.1.2009	1.25-1.50	70	38.67	25.35	12.45	1.53	3.11
26.2.2009	0.30-0.40	30	3.08	2.17	0.98	1.42	3.15
26.2.2009	0.60	45	5.10	4.61	2.26	1.11	2.25
23.2.2017	1.50-2.00	120	482.79	466.70	135.22	1.03	3.57
17.2.2018	1.30	65			10.64		

Tabl.1 Date of observations, amplitude, duration and calculated absolutely and relative energy of the flares in UBV bands.

The total energy of the flare is few times more than the energy in *U* or *B* band. For single M dwarfs (flare stars) observed simultaneously in different bands Gershberg & Shakhovskaya (1983) derived relation:

$$E_U = 1.2\ E_B = 1.8\ E_V.$$

For the total optical radiation they give:

$$E_{opt} = 3.5\ E_U = 4.2\ E_B.$$

In the case of KR Aur average values are:

$$E_U = 1.3\ E_B = 3.0\ E_V.$$

The coefficients are larger and depend on the flare. Probably it is due to the different temperatures of the flares.

Woods et al. (2004) obtained that only ~ 20 % of the flare's energy was emitted at UV and X-ray bands and assumed that the main part of the energy was emitted at optical wavelengths. If we use the approximation for the total energy:

$$E \approx 5\ E_U,$$

the energy of the flares is from 10^{34} erg for weak to 10^{36} erg for the strongest flare. These values are close to the energy of the most powerful flares in other systems (~ 10^{36} – 10^{37} erg) [Schmitt et al. 2019].

Contrary to the normal flares in active single stars, the shape of the flares in KR Aur is almost symmetrical or with slower rising than declining. Relatively high energy even for weak flares can be explaine with accretion of blobs on the white dwarf. Therefore our data support the claim of an accretion origin of the flare events proposed by Rodríguez-Gil et al. (2020).

Coronal mass ejections (CME's) in the Sun contribute 15-20 % of the mass loss rate. CME's in secondaries in CVs can provide blobs and episodic mass transfer, which can produce such flares.

Conclusions

Our observations in low state show flares in KR Aur with duration 30-120 min and amplitudes 0.3 – 2.0 mag in *UBV* bands.

The calculated energy of the flares is 10^{33} - 10^{35} erg. The energy in U is on average 1.3 times more than E_B and 3.0 times more than E_V. The total energy of the largest flare is estimated to be close to the strongest flares in other systems.

The shapes and energies of the flares support the claim of an accretion origin of the observed flare events. Coronal mass ejections from secondary star can be the reason for these events.

Acknowledgements

This work is partialy supported by the grant KP-06-28/2 „Binary stars with compact object“ (Bulgarian National Science Fund). K.K. acknowledge the support of Bulgarian Science Fund under grand № КП-06-Н44/2 27.11.2020

References

Bianchini, A. (1990). Solar-Type Cycles in Close Binary Systems, AJ, v.99, p.1941.

Boeva, S., Bachev, R., Antov, A., Tsvetkova, S., Stoyanov, K. A. (2012), Low State of KR Aurigae (2008 - 2010), PASRB, vol. 11, pp. 369-373.

Boeva, S., Latev, G., Zamanov, R., Tsvetkova, S. Nikolov, P. , Petrov, B., Spassov, B. , Cvetković, Z., Stoyanov, K., Damljanović, G. (2021). Optical flickering of KR Aur in different states, The Golden Age of Cataclysmic Variables and Related Objects V. 2-7 September 2019. Palermo, Italy, Proceedings of Science**,** 368, 028.

Gershberg, R. E., Shakhovskaia, N. I. (1983). Characteristics of activity energetics of the UV cet-type flare stars, Ap&SS, Vol.95, I.2, pp.235-253.

Kafka, S., Robertson, J., Honeycutt, R. K., Howell, S. B. (2005). Low-State Flaring Events in AM Herculis, AJ, Vol. 129, I. 5, pp. 2411-2419.

Paudel, Rishi R. , Barclay, Thomas , Schlieder, Joshua E. , Quintana, Elisa V. , Gilbert, Emily A. , Vega, Laura D. , Youngblood, Allison , Silverstein, Michele , Osten, Rachel A. , Tucker, Michael A. , Huber, Daniel , Do, Aaron , Hamaguchi, Kenji , Mullan, D. J. , Gizis, John E. , Monsue, Teresa A. , Colón, Knicole D. , Boyd, Patricia T. , Davenport, James R. A. , Walkowicz, Lucianne (2021). Simultaneous Multiwavelength Flare Observations of EV Lacertae, arXiv:2108.04753.

Rodríguez-Gil, P. , Shahbaz, T. , Torres, M. A. P. , Gänsicke, B. T., Izquierdo, P. , Toloza, O. , Álvarez-Hernández, A. , Steeghs, D., van Spaandonk, L. , Koester, D. , Rodríguez, D. (2020). When the disc's away, the stars will play: dynamical masses in the nova-like variable KR Aur with a pinch of accretion, MNRAS, Vol. 494, I. 1, pp.425-441.

Scaringi S., Maccarone T. J., D’Angelo C., Knigge C., Groot P. J. (2017). Magnetically gated accretion in an accreting ‘non-magnetic’ white dwarf, Nature, Vol.552, I.7684, pp. 210-213.

Schmitt, J. H. M. M. , Ioannidis, P. search by orcid , Robrade, J. , Czesla, S. , Schneider, P. C. (2019). Superflares on AB Doradus observed with TESS, A&A, Vol. 628, id.A79, 9 pp.

Shakhovskoy N. M., Alexeev I. Y., Andronov I. L., Kolesnikov S. V. (1993). Unprecedented Flare at Red Secondary Components of AM Herculis, Annals of the Israel Physical Society, Vol. 10, p. 237.

Woods, T.N., Eparvier, F.G., Fontenla, J., Harder, J., Kopp, G., McClintock, W. E., Rottman, G., Smiley, B., Snow, M. (2004). Solar irradiance variability during the October 2003 solar storm period, Geophys. Res. Lett., vol.31, i.10, L10802.

First flare M 1.9 AR 10365: comparing results real-scale time MHD modeling and observational data

BorisenkoA.V.[1], PodgornyI.M.[2], PodgornyA.I.[1]

[1]Lebedev Physical Institute of the RAS, Moscow, Russia
[2]Institute of Astronomy of the RAS, Moscow, Russia
E-mail: sunw77@mail.ru

Abstract

As shown the first results of MHD modeling in real scale of time above the active region (AR) 10365, the maximum current density appeared before the first flare M 1.9 (05/26/2003 05:34) in the neighborhood of an X-type singular line of magnetic field with superimposed diverging magnetic flux at heights of about 18,000 km (in lower corona). Ground based (NobeyamaNoRH 17 Ghzradioheliographic data) and space (SOHO) data also confirm finding of flare source M 1.9 (GOES class) at heights of solar corona. Since the configuration (singular X-type line) – supposed flare source is clearly visible in coronal ultraviolet lines of iron Fe IX / X, Fe XII, Fe XV (SOHO / EIT 171A, 195A, 284A), authors suggest possible formation of current sheets at heights from lower corona up to heights more above 18000 km (radioheliographic data NoRH 17 Ghz). The first results of MHD modeling in real scale of time showed high precision with compare observed data (in particular to form X-type magnetic configuration of first preflare source over multi flare AR 10365).

Introduction

As know, solar flares are the most powerful phenomena of solar activity. Flares always occur above active regions, where local magnetic fields of several thousand Gauss are much stronger than the surrounding these active regions of solar mean magnetic field (about of several Gauss). This permit to conclude that the energy released at the flare should first be accumulate in the magnetic field. It is very possible that nature of small scale micro and nano flares are similar, because it is difficult to propose for them another mechanism of slow accumulation and then fast release of magnetic energy. The forecast of solar flares and the appearance of solar cosmic rays (SCR) and other solar flare manifestations is an important scientific and technical task. This idea of the accumulation of solar-flare energy in the magnetic field of a current sheet was suggested by the famous Soviet physicist and astrophysicist Sergei Ivanovich Syrovatskii (1925–1979) (Syrovatskii, 1966). The flare model, the main model based on the current sheet, have some features of the pinch-based flare model proposed early other famous researchers. In fact, a current sheet is an analog of a pinch, which can be produced in the solar corona plasmaas a result of the accumulation of small perturbations that propagate from the solar surface. Therefore, S.I. Syrovatskii introduced the term "pinch current sheet". There are also other theories that describe flare scenarios with the use of models of force-free magnetic fields. However, it is not completely clear, for example, how very small perturbations of the photospheric magnetic field, which occur before flares, canlead to the accumulation of magnetic energy in twisted magnetic-line tubes (ropes) high above the photosphere. The magnetic tubes obtained in the force-free approximation are unstable and rapidly disintegrate. Difficult to imagine how energy can accumulate long time in such magnetic structures for a flare. In 1988, Igor Maksimovich Podgorny (1925–2018) suggested an electrodynamic model of a solar flare (Fig. 1) [*Podgorny and Podgorny*, 2012]. Based on that model, the evolution of the current sheet was numerically simulated for the first time [*PodgornyandPodgorny*, 2003]. The numerical solution of a set of three-dimensional magnetohydrodynamic (MHD) equations with dissipative terms for compressible plasma with anisotropic thermal conductivity was implemented in the Fortran program PERESVET.This program realized absolutely implicit finite-difference schemeconservative relative to magnetic flux, which was specially developed to accelerate calculations [*Podgorny and Podgorny*, 2004, 2018].

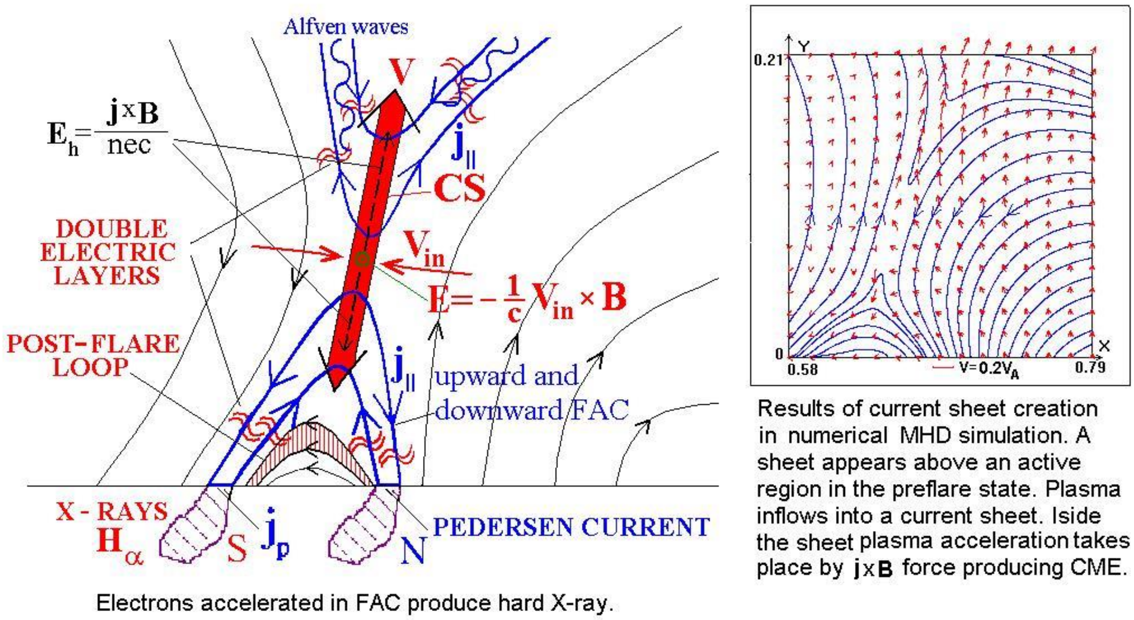

Fig. 1. Electrodynamic model of a solar flare by I.M. Podgorny based on Interkosmos-Bulgaria-1300 satellite measurements.

The current sheet is formed in the neighborhood of an X-type singular line of the magnetic field, due to field deformation by plasma flow caused by **j**×**B** force. Due to essential resistivity of thin current sheet, the freezing-in condition in it is violated, and in the geometry of X-type configuration it appears impression, that magnetic lines moves to the sheet, reconnected in the sheet, and then moves from the sheet with plasma outflow. Therefore, the process in the sheet as called as "magnetic reconnection". During quasi-stationary evolution of the sheet the plasma density drops with time in the sheet and near it due to fast outflow from the sheet under the action of strong magnetic tension (**j**×**B**) force. When due to such strong outflow the plasma density near the sheet becomes less than the threshold value and so the plasma near the sheet cannot stabilize the instability. During the instability the balance between the plasma pressure plasma in the sheet and magnetic pressure is violated so the current sheet shrink fast under the action of plasma pressure. Therefor fast magnetic dissipation occurs with flare energy release [*Podgorny 1989; Podgorny and Podgorny, 2012*].

To obtain the correct development of physical processes in time, it is necessary to carry out MHD simulation in the real scale time. MHDsimulationin corona above the AR allows us to find the appearance of current sheets in the solar atmosphere which are sources of magnetic energy of flares.In view of the appearance of solar flares high in the corona, as well as the impossibility of obtaining from observations the configuration of the magnetic field in the corona, in order to study the mechanism of flares and their prognosis, MHD simulation in the corona above the AR is necessary [*Podgorny and Podgorny, 2012*].In the conditions of complicated configuration of magnetic field in the solar corona the appeared current sheets can be found using specially developed graphical system of search basing of the founding of local current density maxima [*Podgorny et al., 2013, 2017; 2018*].In spite of using specially developed methods, calculations are performed rather slow, and MHD simulation above the real active region using ordinary computer is possible only in strongly reduced (in 10^4 times) time scale [*Podgorny and Podgorny, 2013, 2017, 2018*]. MHD simulation in real scale of time become possible using parallel computing on Nvidia GPUs using CUDA technology [*Borisenko e tal*., 2020]. Modernizing of algorithm with using possibilities of modern hardware and software permit accelerate of computations more few hundred speed up times.MHD simulation in strongly reduced time scale showed the appearance of numerical instability near thephotospheric boundary due to unnaturally fast magnetic field increase on the photosphere [*Podgorny et al., 2013, 2017*].For MHD simulations in the real scale of time, numerical instabilities unexpectedly appear at the photospheric and non-photospheric boundaries of the computational domain, which have time to develop over a long calculation interval. These instabilities were stabilized thanks to specially developed methods [*Podgorny et al., 2021*].

In the general case, a magnetic field near the X-type singular line can be superimposed on a "mirror cell" -type field, diverging along the singular line (see [Podgorny et al., 2021] for details). If the X-type field dominates the diverging field, the result is a deformed X-type field, in which the magnetic lines are hyperbolic. In this case, each magnetic line lies in one of four sectors, into which two intersecting planes divide the space. If a diverging magnetic field dominates, then the magnetic lines are parabolic and the space does not share sectors with magnetic lines. But, as shown by MHD simulation, even in this case, a sufficiently powerful current sheet can also appear in the vicinity of the singular line, since the X-type magnetic field is also present in the superposition of fields.

Active Region 10365: observational data and results MHD modelling

AR 10365was interesting because from May 26 - June 3, 2003, was produced 49 flares were observed (C M and X GOES class). After several flares was produced coronal emission mass (CME), as well as the acceleration of SCR, which were dangerous for people and equipment in the near-Earth space, Earth polar latitudes.

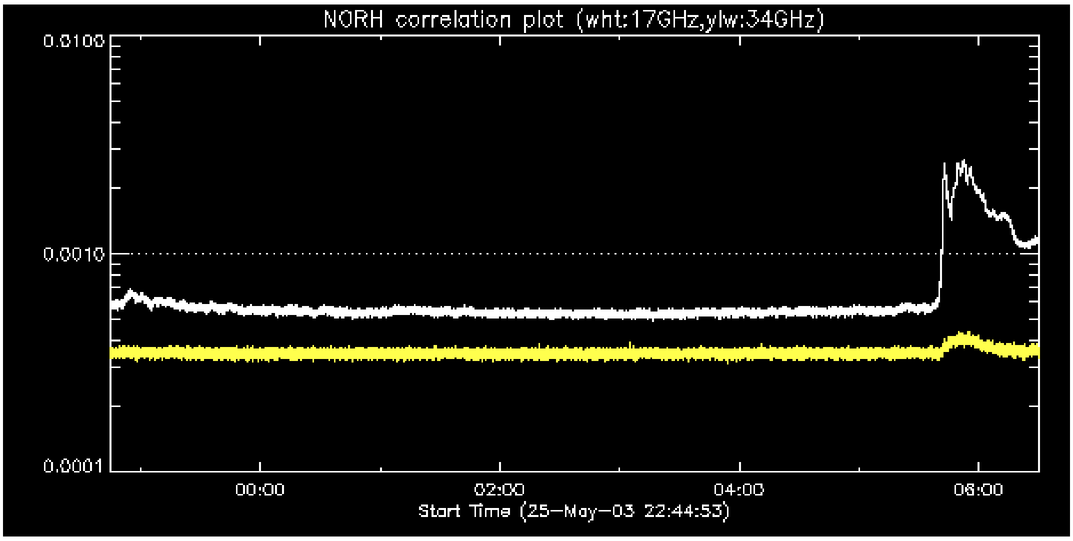

Fig. 2. NoRH 17 ghz plot (25-26 May2003) (from NobeyamaRadioHeliograph Team)

First flare M 1.9 (05/26/2003 05:34) was detected different ground-based and space instruments. For example on Fig. 2 shows a white curve (NoRH 17 GHz) at 05: 34 at the nearest time, a sharp signal amplification is observed, until this moment a quit background was observed.

In Fig. 3 shows the projections of magnetic lines on the central plane perpendicular to the photosphere and parallel to the solar equator, magnetic lines in three-dimensional space and their projections onto the picture plane (perpendicular to the line of sight). The positions of the current density maxima are indicated by green dots. In the vicinity of point 1 (the 115th

maximum of the current density, all the maxima are numbered in decreasing order), an X-type field configuration appeared (Fig. 4). In the vicinity of point 2 (the 5th maximum of the current density, which is the maximal near the position of the flare) a divergent field is superimposed on the X-type configuration (Fig. 5).

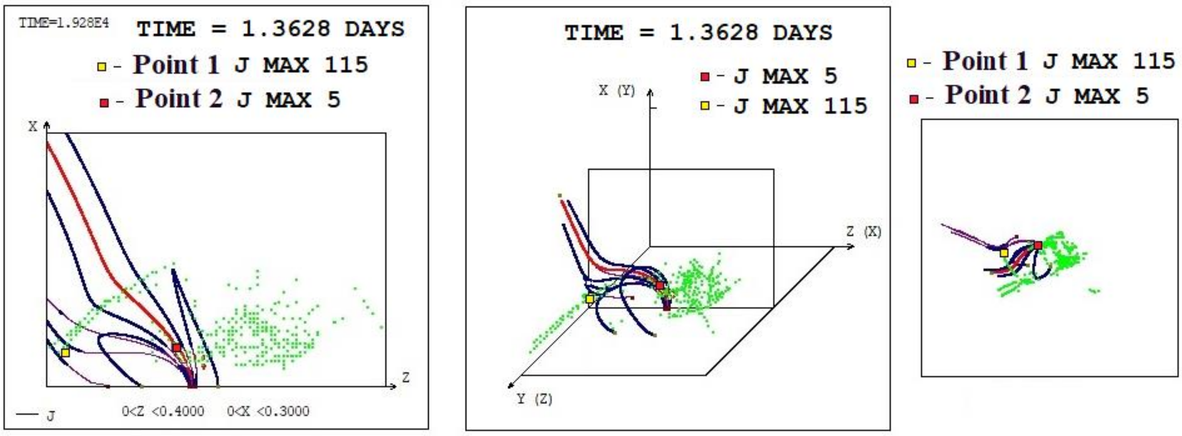

Fig. 3. The magnetic field configuration and the maximums of the current density in the computational domain at the time of the first flare of M 1.9 in AR 10365(1.3628 days after beginning of simulation).

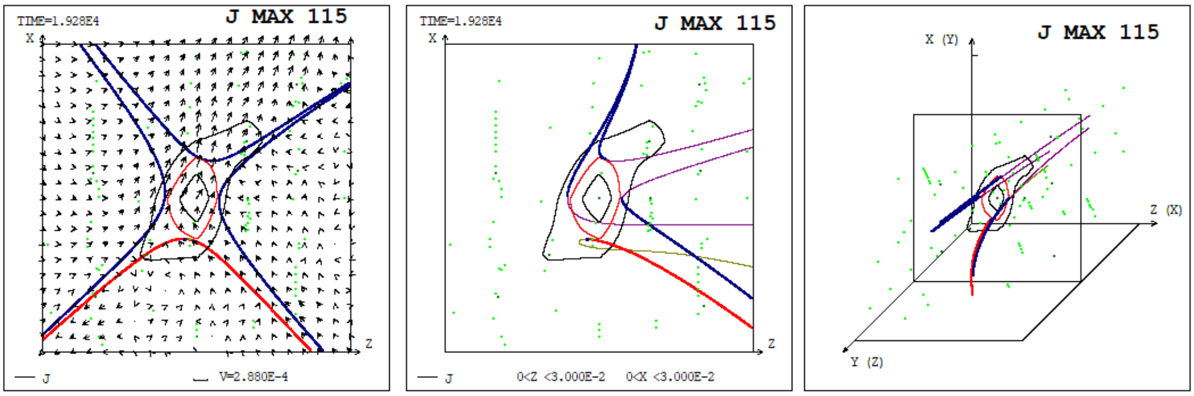

Fig. 4. Plane magnetic lines (tangent to the projections of the magnetic field vectors on the plane of the configuration of the current sheet) with the velocity vectors, the projections of the magnetic lines on the plane of the configuration (which is perpendicular to the magnetic field vector at the point of maximum current density, in which the current sheet is most distinctly pronounced) and three-dimensional magnetic lines in the vicinity of point 1 (115th maximum of the current density).

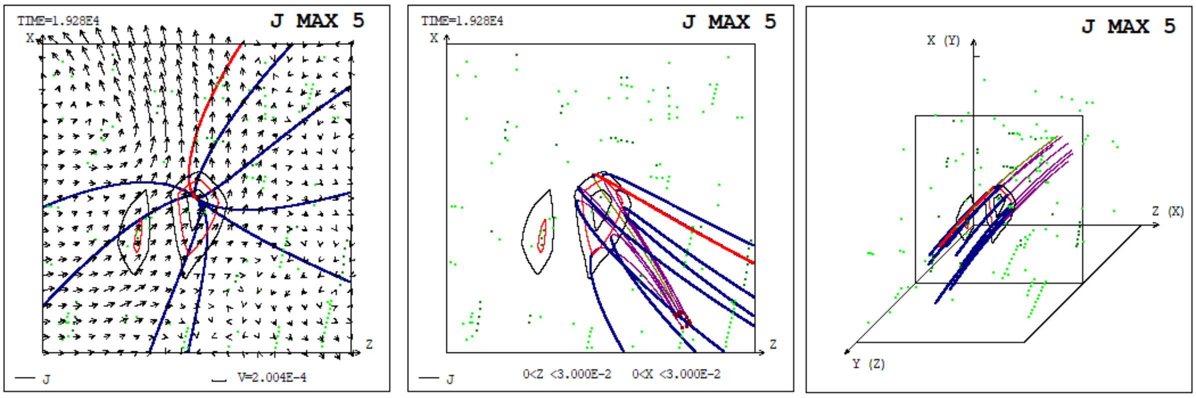

Fig. 5. Magnetic field configuration in the vicinity of point 2 (5thmaximumof current density).

On Fig. 6 show the AR 10365 for greater clarity at the same zoom scale (approximately 0.6" sec/pixel) for different instruments (SOHO/MDI images, SOHO/EIT 171A, Nobeyama radioheliograph NoRH 17 Ghz) at close moments (more precisely, moments 4.5 hours before the start of the first flare M 1.9 26.05.2003 05: 34). Additionally, Po and Bo angles were corrected to more precision overlaid the Nobeyama radioheliograph ground-based data and SOHO data. On Fig. 6a showed superimposed bright loop from the NoRH 17 Ghz image coincides with points 1 and 2 with high precision. Bright emission areas on NoRH 17 Ghz wave show presence of strong magnetic fields. The green points showed are the current density maximums.

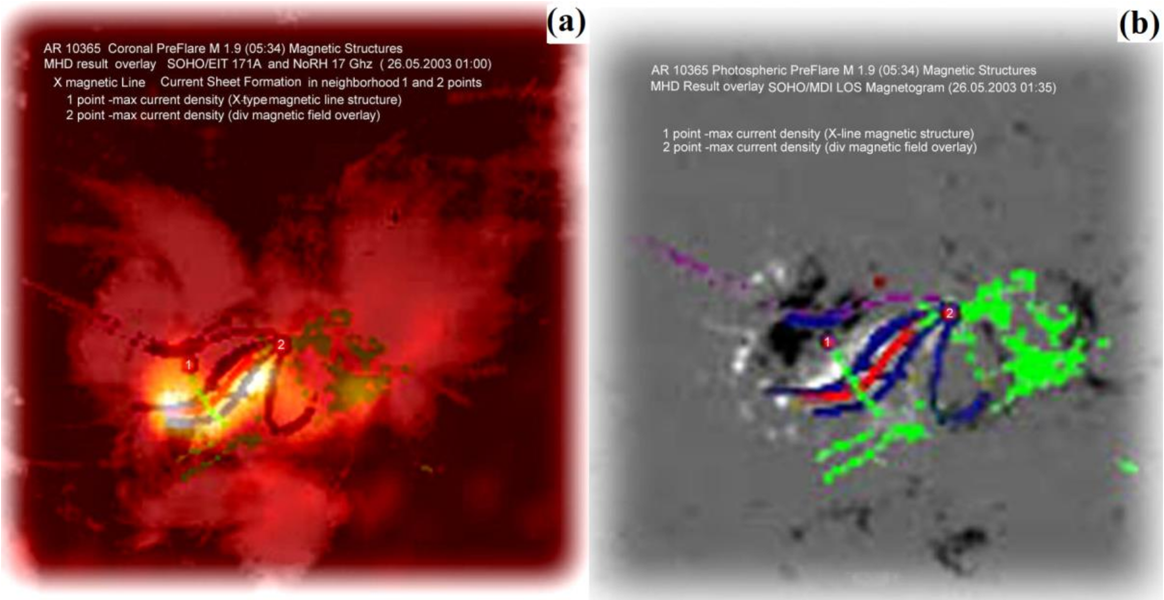

Fig. 6. AR 10365 coronal magnetic structures (a) and AR 10365 photospheric magnetic structures (b) before flare M 1.9 (26.05.2003 05:34) with superimposed MHD simulation results.

Point 1 above the left negative magnetic field region (Fig. 6b, SOHO/MDI Magnetogram black areas), point 2 is located above the right in the positive magnetic field region (SOHO/MDI Magnetogram white areas). After 4.5 hours, at the place under the top of the loop, Nobeyama will show a bright flare emission (starting of the first flare M 1.9 26.05.2003 05:34) exactly at the place where the intersection occursthe current density maximums (green dotted curve line) from point 1 and the open divergent magnetic flux from point 2.

Conclusion

From results of MHD modeling received the height of the current sheet formation in the neighborhood of a singular X-type line about 18,000 km. This is 'pre-flare events' clear viewed take place from the lower corona ahd higher (SOHO/EIT 171A Fe IX/X ionisation temperature ~ 800 000 -1,300,000 K, Nobeyama radioheliograph 17 Ghz).

Thus, similar pre-flare magnetic structures (X-type line or more complex configurations with superimposed divergent magnetic field) in the neighborhood of a current sheet occurs (who may longenergy accumulation 'energy budget' for a flare) are characteristic of many multi-flare AR on the Sun.

Since the image of the MHD results coincides well with the structures from superimposed images of different tools, we can conclude that the high precision of the MHD modeling performed in real scale of time is occur maybe for future flare forecasts.Thus, solar flare mechanism, based on the accumulation of energy in current sheet (in the neighborhood of X-type singular magnetic line), proposed by S.I.Syrovatskii and other known-well researchers was confirmed for first flare AR 10365 the obtained results of MHD modeling inreal scale of time.

Acknowledgments

The authors are grateful to the many scientific teams for the scientific public data provided, as well as to the many professional cloud service specialists, which made it relatively easy for us to configurate rented remote computers for GPU computing.

References

Borisenko A.V, Podgorny I. M. Podgorny A.I. (2020). Magnetohydrodynamic Simulation of Preflare Situations in the Solar Corona with the Use of Parallel Computing. Geomagnetism and Aeronomy, 60, 1101-1113.

Borisenko A.V., Podgorny I.M., Podgorny A.I. (2020). Using of Parallel Computing on GPUs for MHD Modeling of Solar Flare Behavior in Real Time Scale. 12-th Workshop "Solar Influences on the Magnetosphere, Ionosphere and Atmosphere", Primorsko, Bulgaria, September, 2020. 81 - 86.

Podgorny, A.I. and Podgorny, I.M., MHD simulations ofcurrent-sheet formation over a bipolar active region, Astron. Rep., 2003, vol. 47, no. 8, pp. 694–700.

Podgorny A.I., Podgorny I.M. (2004) MHD Simulation of Phenomena in the Solar Corona by Using an Absolutely Implicit Scheme. Computational Mathematics and Mathematical Physics. 44, 1784-1806.

Podgorny A.I., I.M. Podgorny I.M. (2008) Formation of Several Current Sheets Preceding a Series of Flares above the Active RegionAR 0365. Astronomy Reports. 52, 666–675.

Podgorny A.I, I. M. Podgorny I.M.(2012).Magnetohydrodynamic Simulation of a Solar Flare: 1. Current Sheet in the Corona. Geomagnetism and Aeronomy, 52, 150-161.

Podgorny A.I., Podgorny I.M. (2013) MHD Simulation of Solar Flare Current Sheet Position and Comparison with X-ray Observations in active region NOAA 10365. Sun and Geosphere. 8(2), 71-76.

Podgorny A.I., Podgorny I.M., MeshalkinaN.S. (2017) Magnetic field configuration in corona and X-ray sources for the flare from May 27, 2003 at 02:53. Sun and Geosphere. 12, 85-92.

Podgorny A.I., Podgorny I.M., Meshalkina N. S. (2018) Current sheets in corona and X-ray sources for flares above the active region 10365. Journal of Atmospheric and Solar-Terrestrial Physics. 180, 16-25.

Podgorny A.I., Podgorny I.M., Borisenko A.V. (2020). Study of the Solar Flare Mechanism by MHD Simulation in the Corona Above the Active Region in Real Time Scale.Proc. 12-th Workshop "Solar Influences on the Magnetosphere, Ionosphere and Atmosphere", Primorsko, Bulgaria, September, 2020. 93 - 98.

Podgorny A.I., Podgorny I.M., Borisenko A.V., Meshalkina N.S. (2021). MHD simulation of a flare situation in real scale of time above AR 10365: development of a technique, choice of parameters, the appearance of field singularities at flare sites. Proc. 13-th Workshop "Solar Influences on the Magnetosphere, Ionosphere and Atmosphere", Primorsko, Bulgaria, September, 2021. This Issue.

Simultaneous Observations of Solar Radio Bursts with Ukrainian Radiotelescopes and by Parker Solar Probe During Its Encounter

Bubnov I.N.[1,2], *Stanislavsky L.A.*[1] *and Yerin S.N.*[1,2]

[1] Institute of Radio Astronomy NASU, Kharkiv, Ukraine
[2] V.N. Karazin Kharkiv National University, Ukraine

E-mail: bubnov.igor.n@gmail.com

Abstract.

The analysis of solar radio bursts observed by the Parker Solar Probe (PSP) and their interpretation are of great interest. In the encounter phase the space-based instrument has the time resolution about 7 sec in the frequency range of 10 kHz – 19 MHz However, this is not enough to recognize a fine structure of solar bursts, especially in high frequencies. It is useful for understanding intrinsic properties of emission mechanism in the solar corona. The problem can be overcome (partially or completely) by simultaneous ground-based observations using more advanced antennas and receivers. In this context the Ukrainian radiotelescopes are very useful, because they record solar radio emission at extremely low frequencies, near the ionospheric cutoff. We detect directly the radio events, observed by the PSP, having the frequency range that intersects with the frequency band of our instruments. This allows ones to discover solar phenomena in the corona reliably and confidently.

Introduction

Solar radio bursts are currently observed below 8 MHz by spacecraft devices above the terrestrial ionosphere [see, for example, *Bougeret et al.*, 2008; *Gopalswamy*, 2016 and references therein]. The success of such measurements is due to a number of reasons. Often the solar bursts of II, III and IV types are very intensive and sufficiently long in time. However, many ground-based observations manifest that the diversity of solar radio bursts at low frequencies is much more, and they varies in flux and frequency-time features [*Alissandrakis*, 2020], demonstrate a fine structure. Unfortunately, the spacecraft capabilities do not give such high resolution in time and frequency as ground-based instruments. Besides, the sensitivity of low-frequency spacecraft antennas is not high yet because of their simple design [*Stanislavsky et al.*, 2009]. Therefore, coordinated observations of solar bursts with ground- and space-based instruments are so preferable for better understanding the generation mechanisms leading to the variety of solar bursts, during different solar activity events. New missions open extended possibilities for space-based observations together with ground-based instruments. One of them is the Parker Space Probe (PSP).

The aim of this work is to consider a specific limiting feature of the PSP in radio observations of solar bursts and the role of ground-based radio telescopes with high time-frequency resolution in overcoming them. It should be pointed out that the Ukrainian radio telescopes (such as UTR-2, GURT, URAN) have been participated in the ground-based support of many space missions (STEREO, Wind/WAVES, Cassini, Juno) [*Konovalenko et al.*, 2016]. Their contribution was successful and informative. The PSP mission possesses new interesting advantages allowing us to improve this collaboration and our experience in the study of solar radio emission at low frequencies.

Observations and facilities

a) PSP spacecraft and its radio instruments

The PSP spacecraft are going to make 26 orbits around the Sun. Using repeated gravity assists at Venus, the probe will incrementally decrease its orbital perihelion to achieve a final altitude (above the surface) of approximately 8.5 solar radii. On June 7, 2020 it was in perihelion 5. Direct radio measurements on PSP are performed with the FIELDS instrument [*Bale et al.*, 2016]. As sensors of radio emission, it uses four whip antennas (called V1-V4) mounted near the edge of the PSP heat shield, and each of them is 2 meters long. Radio observations are processed by the dual-channel receiver. Low Frequency Receiver (or briefly LFR) covers the bandwidth of 10.5 kHz – 1.7 MHz, and another (High Frequency Receiver or HFR) is designed for the bandwidth of 1.3 MHz – 19.2 MHz [*Pulupa et al.*, 2017]. If the spacecraft flies closer to the Sun than 0.25 au, all its instruments operate continuously at a high-rate recording mode. This case is an encounter phase. There is also a cruise phase, when the distance of PSP from the Sun is larger than 0.25 au, and the data-recording rate becomes low. During the encounter phase, LFR and HFR record raw data at a cadence of one spectrum per ~7 seconds, whereas in another phase the data-recording cadence is noticeably less, one spectrum per ~56 seconds.

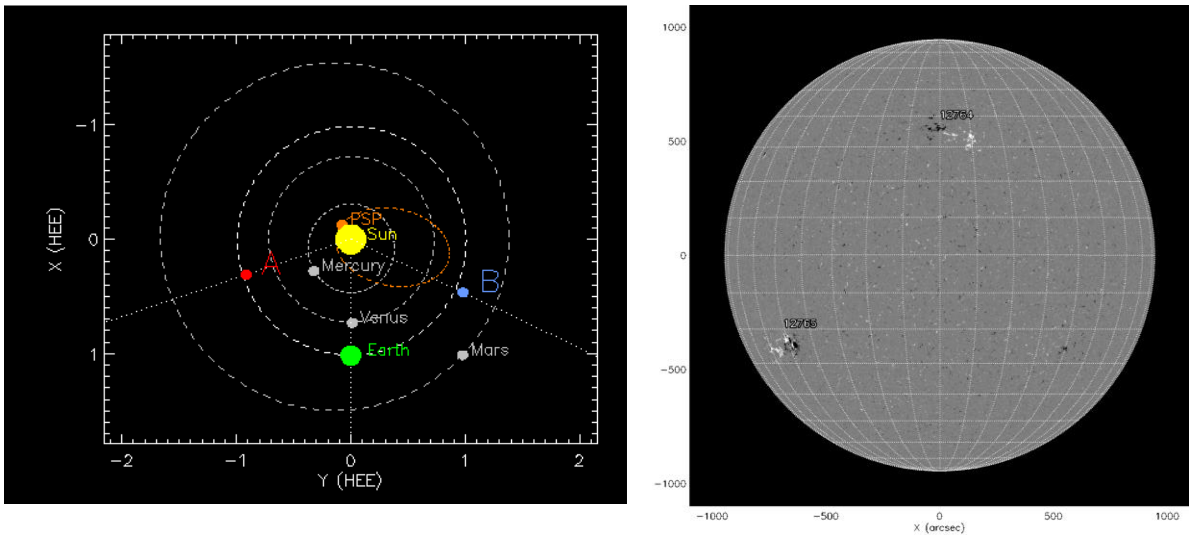

Fig.1. Positions of planets, spacecrafts STEREO A and B, as well as the PSP orbit (orange dotted line) and its position on June 5, 2020 (left picture). The right picture represents the solar SDO HMI magnetogram with active regions in that day.

b) Ground-based radio telescopes

The Giant Ukrainian Radio Telescope (GURT) is a new instrument designed to empower the UTR-2 in terms of spatial dimensions and frequency range and located nearby the latter [*Konovalenko et al.*, 2016]. One array section of the GURT consists of 25 cross-dipoles, five in each column and row. It just was used for the observations on June 5, 2020. The distance between the crossed dipole antenna elements is 3.75 m, and the suspension height is 1.6 m. The subarray design provides a wide frequency coverage from 8 to 80 MHz, high sensitivity (the galactic background level exceeds their self-noise by more than 7 dB), and high radio-frequency interference immunity due to high dynamic range of the dipole amplifier (input IP3 is 30 dBm). The effective area at the central frequency, confirmed by computer simulations and direct measurements, is about 350 m^2. The apparent advantages of the GURT over the UTR-2 are the ability to measure full polarization characteristics of the received radio waves and to track the source down to the altitude of a few arc degrees above the horizon. The GURT subarray is inferior to each UTR-2 section in sensitivity in the same frequency range, but the former has more than two times wider frequency band for observations. The spectrum records of solar radio emission were obtained by using the receiver ADR (short abbreviation for advanced digital receiver) which is a standard device of the radio telescope GURT [*Konovalenko et al.*, 2016]. Based on the technique, the frequency and time resolutions were about 4.8 kHz and 100 ms, respectively, in each channel.

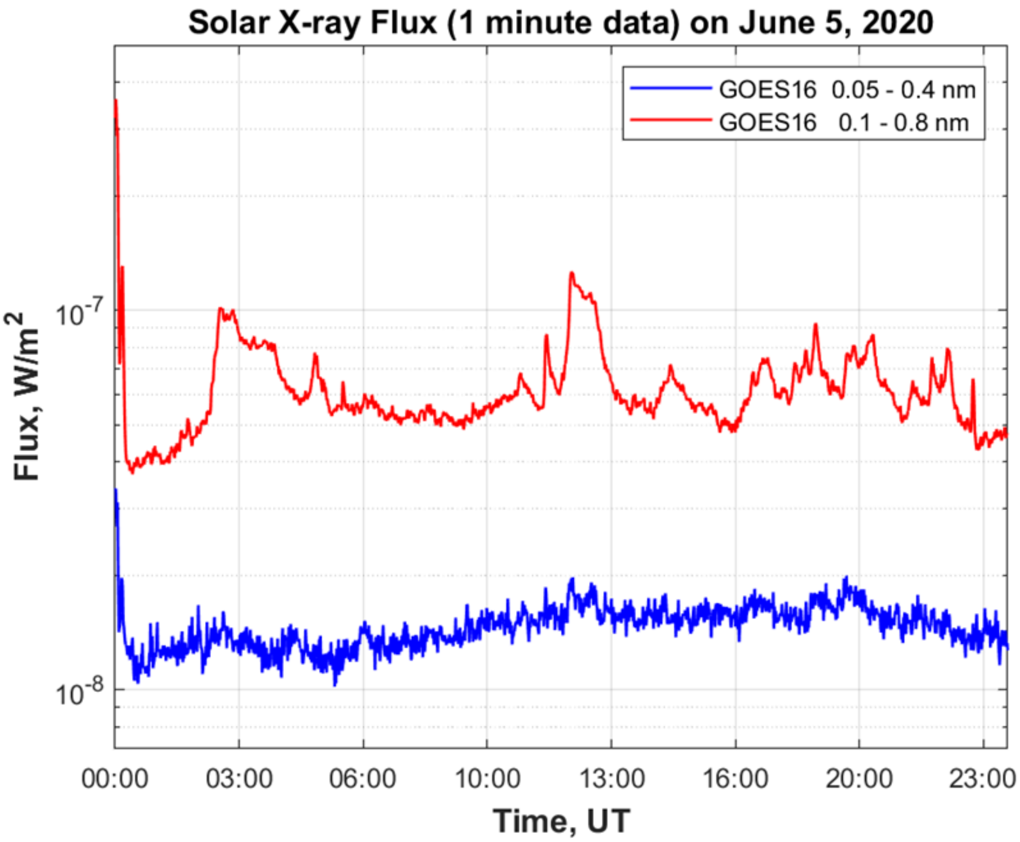

Fig.2. Solar X-ray data from GOES-16 covering 0.05-0.4 nm and 0.1-0.8 nm integrated passbands on June 5, 2020. Solar activity was weak.

c) Solar events and their observations

In the summer of 2020 the Sun was in a deep minimum. After the flare of the M class on May 29, 2020 the solar radio bursts were detected in early June 2020. This was the first noticeable manifestation of solar activity, starting from October 2017, when several X-class flares of September 2017 were observed. The activity was connected with a new active area, named NOAA AR12765, appeared on the limb from the eastern side of the Sun on June 3, 2020. The evolution of the active region started with a single spot, which became a small bipolar region on June 5, 2020 (Fig. 1). In the following days the region remained bipolar, but decaying, after 10 June it became unipolar until it vanished completely, moving to the far side of the Sun. The AR 12764 was only unipolar and non-active. Fig. 2 demonstrates the solar X-ray data from the satellite GOES-16. Often bipolar magnetic fields on the Sun are responsible for the type U solar radio bursts [*Reid and Ratcliffe*, 2014]. Such a radio burst was recorded with the GURT on June 5, 2020 [*Stanislavsky et al.*, 2021]. Solar observations on June 5, 2020 were also available with space-based observatories: Wind/WAVES, STEREO-A and PSP. They together observed the Sun and its activity from different points of view (Fig.1). On June 5, 2020, the PSP was near perihelion, at the distance of ~0.15 au from the Sun. This case just corresponds to the encounter phase. For the PSP spacecraft the AR 12765 was behind the solar limb with respect to the central meridian of the Sun. The STEREO-A, Wind/WAVES and ground-based observers can "see" directly the active region on the solar photosphere. The spectrogram from the PSP observations is shown in Fig. 3, whereas Fig. 4 shows the GURT U-type burst record.

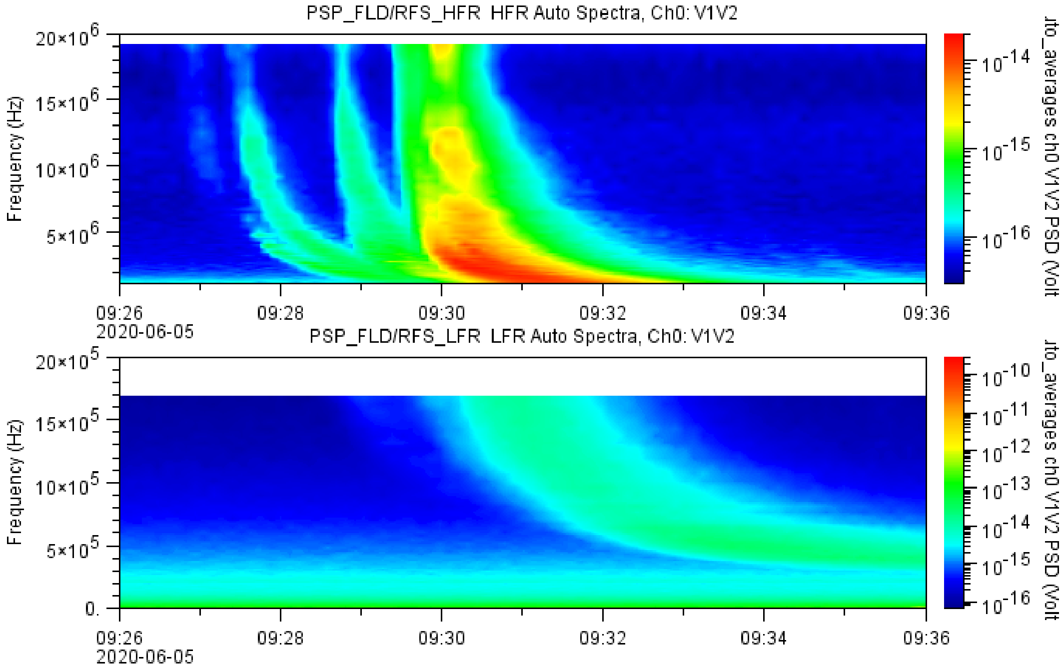

Fig.3. PSP radio spectra on June 5, 2020: the top picture was obtained with HFR, whereas the bottom picture manifests the LFR spectrum.

Data analysis and results

The most numerous among the solar bursts are bursts of type III [*Reid and Ratcliffe*, 2014], observed during both high and low solar activity and caused by high velocity electron beams. The electron beams move through open magnetic field lines, generating plasma waves which are scattered on ions, transforming into radio emission. That is why their frequency drift rate is so high. Typically, the type III bursts manifest a monotonic shape in dynamic spectra, going from high to low frequencies, showing the motion of beams to Earth. Nevertheless, the closed magnetic fields on the Sun can change this motion direction of beams, exhibiting the effect in dynamic spectra. Their overall spectral signature resembles the letters J and U, and the bursts are therefore called the type J and the type U, respectively [*Reid and Kontar*, 2017].

On June 5, 2020 we observed the U-type burst associated with type III solar radio bursts. This event was detected by many ground- and space-based radio instruments. These include such as the Nançay Decametric Array (NDA) in France, e-Callisto network stations, STEREO

A, Wind/WAVES and our radio telescopes [see *Stanislavsky et al*., 2021]. This means that the

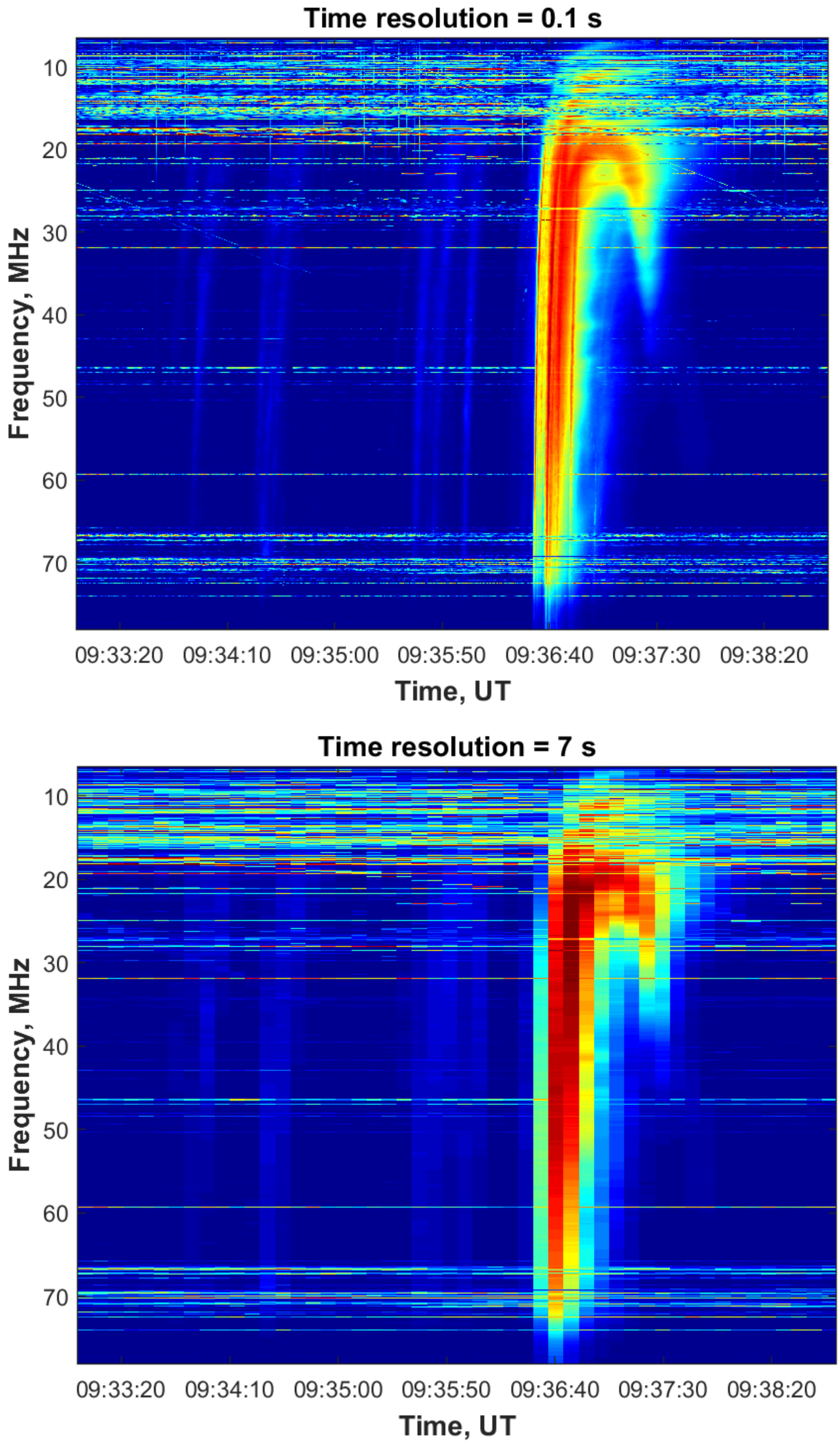

Fig.4. GURT spectra on June 5, 2020 with two different time resolutions: the top picture has original resolution (100 ms), whereas the bottom picture shows what the spectrum would look like with a resolution of 7 seconds typical for PSP radio measurements in the encounter phase.

observed U+III bursts had the solar origin and cannot be caused by ionospheric disturbances and/or equipment malfunctions. According to the radio observations by the PSP (Fig. 3), the event contains four bursts following each other. The most power burst was last. It is just related to the U-type solar burst mentioned above. Notice, the PSP received signals of solar bursts about 7 minutes earlier than the ground-based radio telescopes as the former was located about 6.7 times closer to the Sun. If we compare them with records obtained with the GURT (Fig. 4), the first, second and third bursts, shown in Fig. 3, are nothing but groups of type III solar bursts rather than separate bursts, as it may seem. This effect is explained by the PSP time resolution in ~ 7 sec. Therefore, very close bursts merge into one. As an example, Fig. 4 demonstrates two GURT spectra, the first of which has the original resolution, whereas another is rougher.

Conclusions

Based on this study we can notice following points:

1. The radio measurements with the PSP in the frequency range 8 – 19.2 MHz have so low temporal resolution that they cannot compete with observations of the ground-based radio telescopes such as the UTR-2 or the GURT.
2. Nevertheless, the PSP records manifest that the type III solar bursts were interplanetary.
3. Analyzing the solar bursts with the PSP measurements, the ground-based radio telescope records with high frequency-time resolution will come in handy.

Acknowledgment

The authors acknowledge a support of Grant 0120U101334 from the National Academy of Sciences of Ukraine and the GOES, STEREO and SDO teams for developing and operating the instrument as well as for their open data policy. The FIELDS experiment on the Parker Solar Probe spacecraft was designed and developed under NASA contract NNN06AA01C.

References

Alissandrakis, C.E. (2020). Structure of the solar atmosphere: a radio perspective, Front. Astron. Space Sci., 7, id.74, 10.3389/fspas.2020.574460, 2020.

Bale, S.D., Goetz, K., et al. (2016). The FIELDS instrument suite for solar probe plus–Measuring the coronal plasma and magnetic field, plasma waves and turbulence, and radio signatures of solar transients, Space Sci. Rev., 204, 49-82, 10.1007/s11214-016-0244-5, 2016.

Bougeret, J.L., Goetz, K., et al.: (2008). S/WAVES: The radio and plasma wave investigation on the STEREO mission, Space Sci. Rev., 136, 487-528, 10.1007/s11214-007-9298-8, 2008.

Gopalswamy, N. (2016). Low-frequency radio bursts and space weather, URSI Asia-Pacific Radio Science Conference, 471-474, 10.1109/URSIAP-RASC.2016.7601368, 2016.

Konovalenko, A., Sodin, L., et al. (2016). The modern radio astronomy network in Ukraine: UTR-2, URAN and GURT, Exp. Astron., 42, 11-48, 10.1007/s10686-016-9498-x, 2016.

Pulupa, M., Bale, S., et al. (2017). The Solar Probe Plus Radio Frequency Spectrometer: Measurement requirements, analog design, and digital signal processing, J. Geophys. Res., 122, 2836-2854, 10.1002/2016JA023345, 2017.

Reid, H.A.S., Kontar, E.P. (2017). Imaging spectroscopy of type U and J solar radio bursts with LOFAR, Astron. Astrophys., 606, A141, 10.1051/0004-6361/201730701, 2017.

Reid, H.A.S., Ratcliffe, H. (2014). A review of solar type III radio bursts, Res. Astron. Astrophys., 14, 773, 10.1088/1674-4527/14/7/003, 2014.

Stanislavsky, A.A., Konovalenko, A.A., et al. (2009). Antenna performance analysis for decameter solar radio observations, Astron. Nachr., 330, 691-697, 10.1002/asna.200911226, 2009.

Stanislavsky, L.A., Bubnov, I.N., et al. (2021). The first detection of the solar U+III association with an antenna prototype for the future lunar observatory, Res. Astron. Astrophys., 21, id. 187, 10.1088/1674-4527/21/8/187, 2021.

On the Correlation between EUV Solar Radiation Proxies and their Long-Term Association

Elias A.G.[1,2], de Haro Barbas B.F.[1,2], Medina F.D.[1,2], and Zossi B.S.[1,2]

[1] Laboratorio de Ionosfera, Atmosfera Neutra y Magnetosfera (LIANM), Facultad de Ciencias Exactas y Tecnologia (FACET), Universidad Nacional de Tucuman (UNT), Argentina
[2]INFINOA (CONICET-UNT), Argentina
E-mail: aelias@herrera.unt.edu.ar

Abstract.

EUV solar radiation proxies, in particular monthly mean Mg II, Lyman α flux, F10.7 and Rz, are analyzed during the period 1979-2020. Their variability is compared through a correlation analysis. When the whole period is considered, the linear correlation is greater than 0.95 between each pair of solar proxies if monthly or 12-month running mean series are used. But, when short sub-periods are correlated this value decreases markedly during maximum and minimum solar activity levels. This result may be due to the random noise part of each series as we show it through a "statistical experiment". Their hysteresis along a solar activity cycle is also reproduced as part of this analysis.

Introduction

The main variation in monthly mean solar activity proxies is that related to the quasi-decadal solar cycle. In particular, in the case of EUV solar radiation proxies, the correlation between them is greater than 0.95 at this time scale, even though in general each index is originated in a different region of the Sun. In addition, their variation along the quasi-decadal cycle in percentage terms is also different.

Based on a work by *Bruevich et al.* [2014], in the present work we analyze the correlation between four EUV solar radiation proxies for sub-periods in order to go through the different phases of the solar cycle. With a simple "statistical experiment" we reproduce some results linked to this correlations analysis, and also to the hysteresis effect which is characteristic of all pairs of the solar indices showing differences during the rising and declining phases of solar cycles [*Bruevich et al.*, 2016].

Data

Four solar activity proxy were considered:

(1) MgII core-to-wing ratio (MgII), which corresponds to the ratio of the h and k lines of the solar MgII emission at 280 nm to the background solar continuum near 280 nm, and serves as a proxy for UV and EUV spectral solar irradiance variability. We used the composite MgII, which combines data from different satellites. It is also called Bremen composite MgII index, available from the University of Bremen [*Viereck et al.*, 2010; *Snow et al.*, 2014].

(2) Lyman α flux (Fα) (in W/m^2 units), which corresponds to the full disk integrated solar irradiance over 121-122 nm, and is dominated by the solar HI 121.6 nm emission. We used the composite Fα, which combines multiple instruments and models, available from the Laboratory for Atmospheric and Space Physics (LASP, University of Colorado) Interactive Solar Irradiance Data Center (LISIRD) [*Machol et al.*, 2019].

(3) F10.7 (in sfu=10^{-22}Ws/m^2), which corresponds to the radio emission from the Sun at a wavelength of 10.7 cm (2800 MHz), and is measured at the Earth's surface at the Penticton Radio Observatory in British Columbia, Canada.

(4) The sunspot number (Rz), from the revised Rz data base obtained from SILSO (Sunspot Index and Long-term Solar Observations), Royal Observatory of Belgium, Brussels.

In the case of MgII and Fα monthly means were estimated from their daily data base, while F10.7 and Rz monthly values were directly obtained from their data source. The period January 1979-December 2020 is considered.

Regarding their source from the Sun, they are: the photosphere for Rz, higher in the chromosphere for Mg II, the transition region to the corona for Fα, and higher chromosphere and corona for F10.7

An additional characteristic which differs among these solar EUV proxies is their sensitivity along the quasi-decadal solar cycle. In fact, in terms of percentage variation, estimated as the amplitude of the decadal cycle relative to the mean value considering a whole cycle, it is, from highest to lowest: ~250% for Rz, ~120% for F10.7, ~45% for Fα, and 10% for MgII.

Correlation analysis

For the correlation analysis we have analyzed the monthly series and also the 12-month running means, that is the low-pass filtered version where intra-annual variability is filtered out. In both cases an almost ideal linear association is noticed when the whole period is considered, with a correlation coefficient above 0.95 in all the cases considering all six pairs between our four indices. It could be said, at least statistically, that they have a common forcing, which we also assume is the same as for the EUV solar radiation.

Based on the work by *Bruevich et al.* [2014] we analyzed this correlation for shorter periods in order to detect its variation along the solar cycle. In Fig. 1, the running correlation using a 3-year window for each of the six pairs of solar EUV proxies can be seen, considering monthly mean series (left panel), and the 12-month running means (right panel). The correlation clearly decreases for maximum and minimum periods, which are indicated in the figure by dotted and dashed vertical lines respectively.

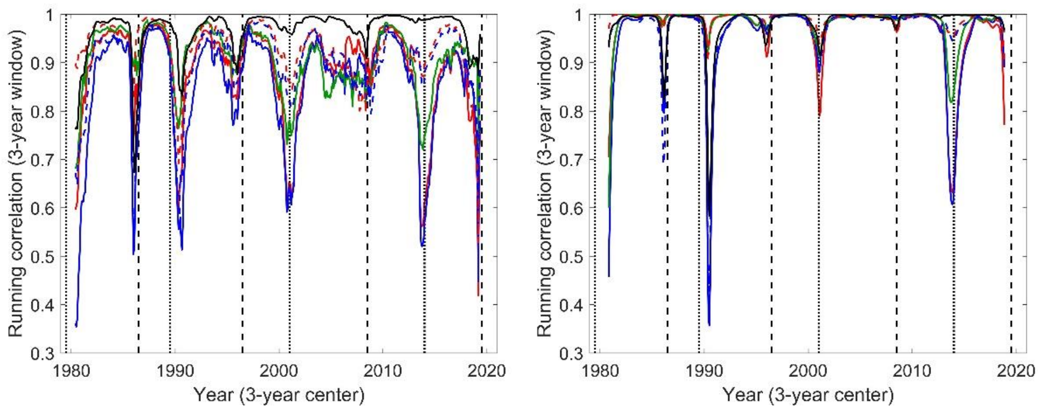

Fig.1. Running correlation (3-year window) between Rz&MgII (red solid), Rz&Fα (blue solid), Rz&F10.7 (green solid), F10.7&MgII (red dashed), F10.7&Fα (blue dashed), and MgII&Fα (black solid), considering monthly means (left panel) and 12-month running means (right panel). Note: solar maxima indicated by vertical dotted and solar minima by vertical dashed lines.

Statistical experiment

In order to analyze the running correlations between each pair of EUV proxies from a pure statistical point of view, we considered two artificial time series, Y_1 and Y_2. They were generated as the sum of a cosine function of 11-year periodicity to simulate the quasi-decadal variation, which we assume common to all of them, and a random noise to simulate the inter-annual variation, which we assume different for each series, that is:

$$Y_1 = 40\times\cos(2\pi t/11) + \varepsilon_1$$
$$Y_2 = 80\times\cos(2\pi t/11) + \varepsilon_2$$

where t is time running from January 1979 to December 2020, with monthly resolution.

Both series share then the same cosine function, with the same phase and only different amplitudes (40 and 80 units respectively), but distinct and unrelated random noises, ε_1 and ε_2, as indicated schematically in Fig. 2.

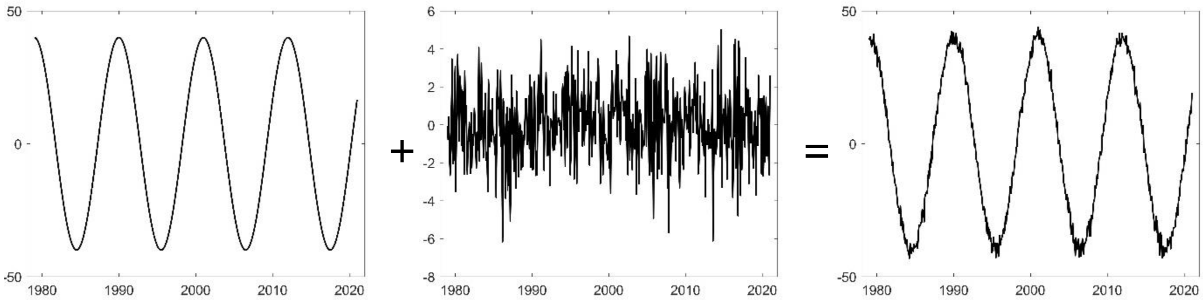

Fig.2. Schematic representation of an artificial series generated to simulate an EUV proxy (right panel), that results from the sum of cos(2πt/11) (left panel) (with 40 units amplitude) and a random noise (middle panel).

Fig. 3 shows the running correlation with a 3-year window between Y_1 and Y_2, where again vertical dotted lines indicate maxima periods, that correspond to the cosine crests in this case, and dashed lines indicate minima periods, that corresponds to the cosine valleys.

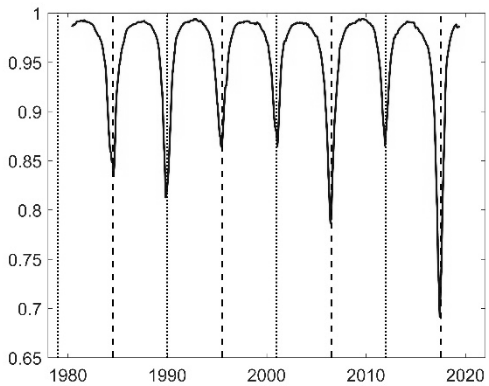

Fig.3. Running correlation (3-year window) between Y_1 and Y_2. Note: crest of cosine component indicated by vertical dotted and valley cosine component by vertical dashed lines.

The same time pattern of the 3-year running correlation behavior between "real" EUV solar proxies, seen in Fig.1, can be noticed in Fig. 3; that is a systematic correlation decrease during maxima and minima periods only, when monthly or 12-month running mean series as well are considered.

We made an additional analysis considering the same artificial series, which consist in their dispersion diagram along a quasi-decadal cycle. Fig. 4 shows Y_1 vs. Y_2, considering their 12-month running means, for a complete cycle, where a hysteresis can be clearly noticed. In fact, the dots in the plot are joined consecutively in time. The hysteresis size increases with the increase of the random noise amplitude relative to the cosine wave amplitude. If pure monthly series are considered, without any smoothing, the hysteresis pattern is completely blurred out.

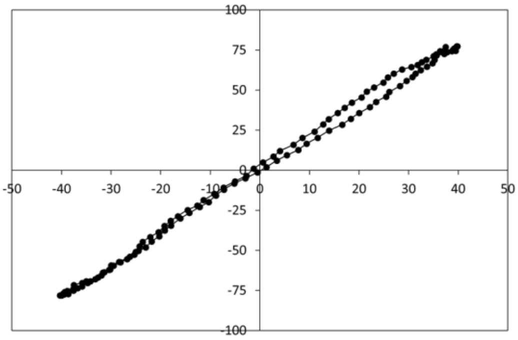

Fig.4. Y_1 vs. Y_2 (12-month running means) along an 11-year cycle.

Discussion and conclusions

The correlation between solar EUV proxies, considering sub-periods approximately spanning a solar minimum or solar maximum period, clearly decreases during maxima and minima, as already shown by *Bruevich et al.* [2014] and in this work in Fig. 1. A reason for this could be purely statistical, as demonstrated in our analysis considering artificial time series. This is due to during minima and maxima periods, the "true" EUV, given by the 11-year cosine cycle, varies too little (first derivatives are zero at these points) and the only variation left is the noise, which is random and consequently unrelated to anything.

Regarding the hysteresis effect [*Bruevich et al.*, 2016], this special pattern can be obtained also considering the dispersion diagram of an 11-year cycle of the 12-month running mean artificial series. This hysteresis disappears if only the cosine terms are considered and it is blurred out if the un-smoothed Y_1 and Y_2 series are used. So, this effect can be also obtained, as in the case of the running correlations, as a statistical by-product, without any physical association or process going on, but due solely to random noise which may always be present in any time series which is the result of measurements, as is the case of EUV proxies, and whose smoothing can generate a hysteresis effect.

Definitely, however, the statistical analysis presented in this work does not rule out a physical underlying mechanism for the correlation decrease during maxima and minima, and for the hysteresis behavior. In fact, in this last the case, for example, the hysteresis is also seen in ionospheric parameters when plotted against solar activity proxies with a convincing physical explanation through the geomagnetic activity effect, which, on average, is higher during the descending than during the ascending phase [*Ozguc et al.*, 2008; *Elias*, 2014].

References

Bruevich, E.A., Bruevich, V.V., and Yakunina, G.V. (2014). Changed Relation between Solar 10.7-cm Radio Flux and some Activity Indices which describe the Radiation at Different Altitudes of Atmosphere during Cycles 21–23. J. Astrophys. Astr., 35, 1-15.

Bruevich, E.A., Kazachevskaya, T.V., Katyushina, V.V., Nusinov, A.A., and Yakunina, G.V. (2016). Hysteresis of Indices of Solar and Ionospheric Activity during 11-year Cycles. Geomagnetism and Aeronomy, 56, 1075-1081.

Elias, A.G. (2014) Filtering ionosphere parameters to detect trends linked to anthropogenic effects. Earth, Planets and Space, 66, 113.

Machol, J., Snow, M., Woodraska, D., Woods, T., Viereck, R., and Coddington, O. (2019). An improved lyman-alpha composite. Earth and Space Science, 6, 2263– 2272.

Ozguc, A., Atac, T., Pektas, R. (2008) Examination of the solar cycle variation offoF2 for cycles 22 and 23. J. Atmos. Solar Terr. Phys., 70, 268–276.

Snow, M., Weber, M. Machol, J., Viereck, R., and E. Richard (2014). Comparison of Magnesium II core-to-wing ratio observations during solar minimum 23/24. J. Space Weather Space Clim., 4, A04.

Viereck, R. A., Snow, M., DeLand, M.T., Weber, M., Puga, L., and Bouwer, D. (2010). Trends in solar UV and EUV irradiance: An update to the MgII Index and a comparison of proxies and data to evaluate trends of the last 11-year solar cycle, Abstract GC21B-0877 presented at 2010 Fall Meeting, AGU, San Francisco, CA, 13-17 Dec.

Relationship between the Intensity of the SCR Proton Flux and the Parameters of Type II Radio Bursts in the 25-180 MHz Range

Isaeva E.A.

Institute of Radio Astronomy of NAS of Ukraine, URAN-4 observatory
E-mail: isaeva-ln@ukr.net

Abstract

The relationship between the intensity of the SCR proton flux and various parameters of type II radio bursts in the 25-180 MHz range has been investigated. The sample under study contains 112 proton events registered for the period from 24-11-2000 to 20-12-2014 years. For the analysis, we used the original records on the fluxes of protons with proton energies > 1-100 MeV from the GOES series spacecraft, as well as the original records of the dynamic spectra of solar radio emission in the 25-180 MHz range according to data from the solar radio spectrograph (SRS). Comparative analysis showed that there is a fairly strong relationship between the intensity of the SCR proton flux and the drift velocity and the relative distance between the harmonics of type II radio bursts.

Introduction

Earlier, in works (Tsap and Isaeva, 2011, 2012, 2013), some issues were considered regarding the relationship between the SCR proton flux and the parameters of type II radio bursts. In the course of studies of the relationship between the frequency drift velocity of meter-decameter type II bursts and the intensity of the proton flux I_p of different energies, two families of events were discovered. This implies the generation of shock waves both in the flare energy release region and in a moving coronal mass ejection (CME) (Isaeva and Tsap, 2011). In works (Isaeva and Tsap, 2011; Tsap and Isaeva, 2012, 2013), the results of studying the efficiency of SCR acceleration by coronal and interplanetary shock waves are presented, as well as arguments in favor of a two-stage proton acceleration process (Tsap and Isaeva, 2012).

A comparative analysis showed that the acceleration of protons by coronal shock waves is more efficient than by interplanetary shock waves, and that the main acceleration of protons occurs in the flare region and additional acceleration at the fronts of shock waves. Study of the fine spectral structure of meter-decameter type II radio bursts showed that there is a fairly strong relationship between the proton flux and the average relative distance $b_i = (f_{i,2}-f_{i,1})/f_{i,1}$ between the 1-st and 2-nd harmonics over time the duration of a type II burst t_i, where the correlation coefficient r between the investigated quantities is ≈ 0.70, while the relationship between the mean drift velocity $V_{i,mII}$ and the proton flux intensity I_p turned out to be weak, where the correlation coefficient r between the proton flux and the drift velocity does not exceed 0.40 (Tsap and Isaeva, 2013). The presence of a low correlation between the proton flux intensity I_p and the frequency drift velocity $V_{i,mII}$ can be associated with a number of reasons, firstly, in (Tsap and Isaeva, 2013), the average drift velocities were used during the duration of a type II burst, and - second, to approximate the harmonics of a type II burst, a model was used that did not give a sufficiently accurate approximation.

Later, in paper (Isaeva, Tsap, 2017), a new regression model (1) was proposed to approximate the harmonics of type II bursts, where $f_{i,j}$ is the frequency of the maximum of a type II burst at a given harmonic at a given time t_i, i- is the reference number, j - harmonic number, a_j and b_j - linear regression coefficients.

$$\log_{10} f_{i,j} = a_j \cdot \sqrt{t_i} + b_j \qquad (1)$$

This model makes it possible to fairly accurately estimate the frequency drift rate for 95% of type II bursts in the 25-180 MHz range, for which the correlation coefficient r between the observed and calculated frequency values is $r >= 0.98$. The zero-point time reference for all events corresponded to the beginning of the first harmonic at a frequency of 180 MHz. More accurate detailed studies of the fine structure of type II radio bursts were carried out using the new model (1). It was shown that all type II bursts associated with proton events are characterized by a monotonic decrease in the relative distance between burst harmonics to a minimum value with a subsequent increase (Isaeva, 2019; Tsap, Isaeva, Kopylova, 2020).

This paper presents the results of studying the relationship between the intensity of the SCR proton flux I_p and the parameters of type II radio bursts in the 25-180 MHz range using a new regression model (1). The sample under study contains 112 type II bursts associated with proton events for the period from 24-11-2000 to 20-12-2014 years. For the analysis, we used the original records of the proton flux intensity I_p from the GOES devices with an energy $E_p >$ 1-100 MeV (https://satdat.ngdc.noaa.gov/sem/goes/data/avg/), as well as the original records of dynamic spectra in 25-180 MHz band with SRS (Solar Radio Spectrograph) (http://www.ngdc.noaa.gov/stp/space-weather/solar-data/solar-features/solar-radio/rstn-spectral/).

Investigation of the dynamics of the relationship between the intensity of the flux of SCR protons I_p with the drift velocity $V_{i,mII}$ and the relative distance b_i between the harmonics of type II bursts in the range 25-180 MHz over time t_i

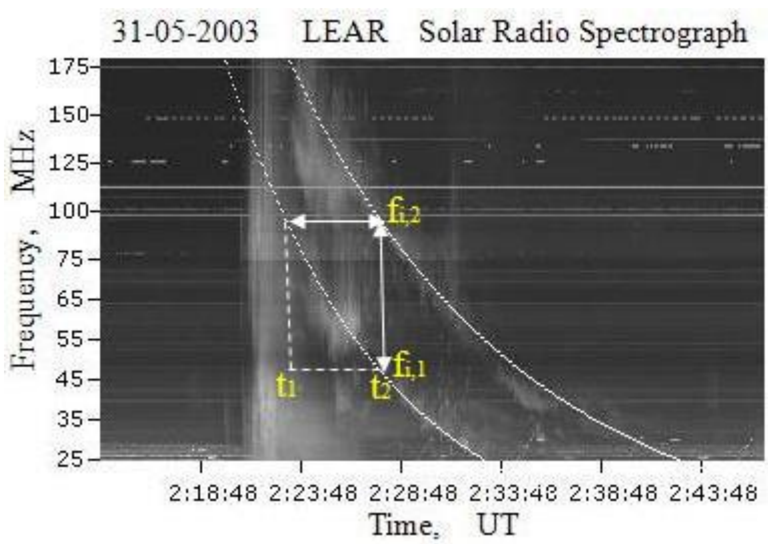

Fig. 1. Methodology for determining the drift velocity $V_{i,mII}$ and the relative distance b_i

The relationship between the intensity of the SCR proton flux I_p and the drift velocity $V_{i,mII}$ and the relative distance b_i over time t_i in the range 25-180 MHz is investigated. For all investigated proton events, the drift velocities $V_{i,mII}$, and b_i were calculated with a 10 MHz step in the 10–180 MHz range using formulas (2) and (3), respectively,

$$V_{i,mII} = \frac{f_{i,2} - f_{i,1}}{t_2 - t_1} \quad (2)$$

$$b_i = \frac{f_{i,2} - f_{i,1}}{f_{i,1}} \quad (3),$$

where $f_{i,1}$ and $f_{i,2}$ are frequencies at the 1-st and 2-nd harmonics at a given time t_2, which were determined from formula (1). In fig. 1 shows a technique for calculating the drift velocity $V_{i,mII}$ and the relative distance b_i. In fig. 1 that the frequency difference between the harmonics at time t_2 is equal to the frequency difference at the 1-st harmonic in the time interval t_2 - t_1. Therefore, the drift velocity $V_{i,mII}$ is related to the relative distance b_i by relation (4).

$$\boldsymbol{V_{i,mII}} = \frac{\boldsymbol{b_i \cdot f_{i,1}}}{\boldsymbol{t_2 - t_1}} \qquad (4)$$

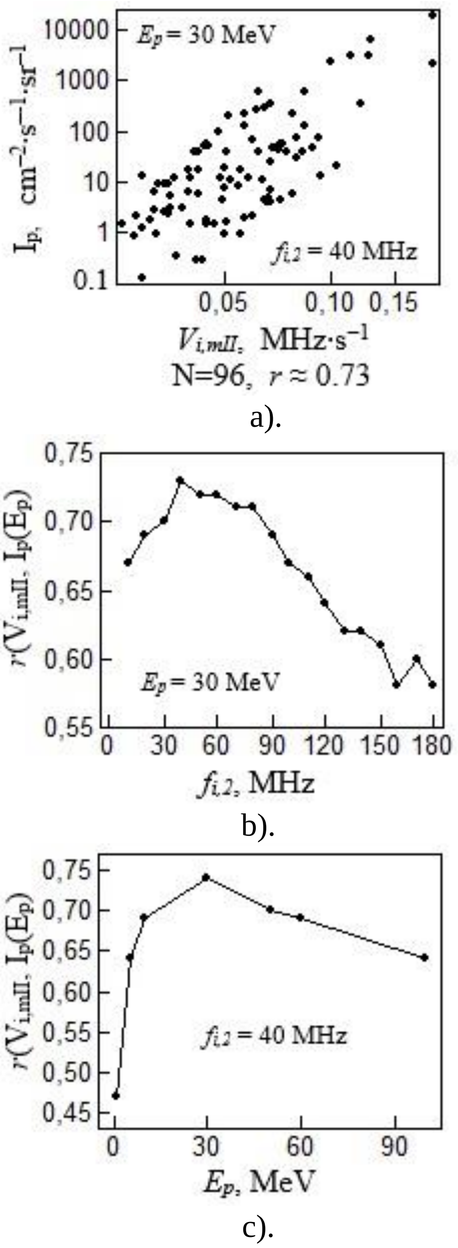

Fig. 2. Relationship between the drift velocity $V_{i,mII}$ and the intensity of the SCR proton flux I_p.

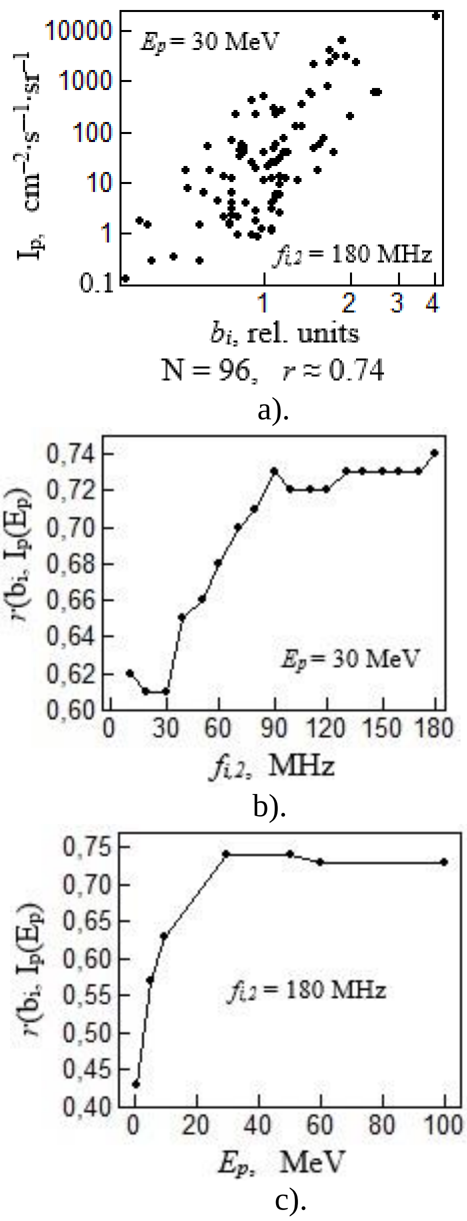

Fig. 3. Relationship between the relative distance b_i and the intensity of the SCR proton flux I_p.

Detailed studies have shown that the relationship between the intensity of the SCR proton flux I_p and the parameters of type II bursts $V_{i,mII}$, and b_i largely depends on the frequency range in which the studies were carried out. In fig. 2 a) and 3 a) show the relationship between the intensity of the flux of protons with energy E_p > 30 MeV and the drift velocity $V_{i,mII}$ and b_i, calculated using formulas (2) and (3) at the frequency $f_{i,2}$, at which the maximum correlation I_p is observed with a drift velocity $V_{i,mII}$ ($f_{i,2}$ = 40 MHz) and a relative distance b_i ($f_{i,2}$ = 180 MHz). In fig. 2 a) and 3 a) N is the number of events, r is the correlation coefficient between the studied parameters. In fig. 2 b) and 3 b) show the dependence of the correlation coefficient r between the proton flux intensity I_p and the parameters $V_{i,mII}$, and b_i on the frequency $f_{i,2}$. Comparative analysis showed that the strongest relationship between the proton flux intensity I_p and the drift velocity $V_{i,mII}$ is observed at the frequency $f_{i,2}$ in the range 30-80 MHz, and with the relative distance b_i at the frequency $f_{i,2}$ in the range 90-180 MHz (see Fig. 2 b) and 3 b)). The relationship between the intensity of the proton flux I_p and the parameters $V_{i,mII}$, and b_i, depending on the proton energy E_p, was also investigated. In fig. 2c) and 3c) show the dependence of the correlation coefficient r between the proton flux intensity I_p and the parameters $V_{i,mII}$, and b_i on the proton energy E_p. Comparative analysis showed that the strongest relationship between I_p and the parameters $V_{i,mII}$, and b_i is observed for protons with energies E_p > 30 MeV (see Fig. 2 c) and 3 c)).

Conclusions

1. It is shown that the relationship between the intensity of the SCR proton flux I_p and the drift velocity $V_{i,mII}$ and the relative distance b_i between the harmonics of type II radio bursts changes over time.
2. The strongest relationship between the proton flux intensity I_p and the frequency Drift $V_{i,mII}$ is observed in the range 30-90 MHz, and with the relative distance b_i in range 90-180 MHz.

References

Isaeva E.A. and Tsap Yu.T. The Origin of Solar Energetic Particles and Type II Meter Radio Burst // Bulleten of the Crimean Astrophysical Observatory. 2011.V.107. P.78-83.

Isaeva E.A., Tsap Yu.T. Microwave Emission of Solar Flares: Coronal Mass Ejections and Shock Waves // Odessa Astronomical Publications. 2017. V.30.

Isaeva E.A. Relationship of the Proton Flux Intensity with Relative Distance Between Harmonics of Type II Radio Bursts in the Range 25-180 MHz // Odessa Astronomical Publications. 2019. V.32.

Tsap Yu.T., Isaeva E.A. Solar Radio Bursts and Acceleration of Solar Energy Particles // Bulletin of the Crimean Astrophysical Observatory, 2012, Vol. 108, pp. 52–57.

Tsap Yu.T., Isaeva E.A. To-Stage Accelaration of Solar Cosmic Rays // Geomagnetism and Aeronomy. 2012. V.52. № 7. P.921-925.

Tsap Yu.T., Isaeva E.A. Acceleration of Solar Cosmic Rays and the Fine Spectral Structure of Type II Radio Bursts // Cosmic Research. 2013.V.51. № 2. P.108-113.

Tsap Yu.T., Isaeva E.A. and Kopylova Yu.G. On the Evolution of Bands in the Dynamic Spectra of Solar Type II Radio Bursts // Astronomy Letters. 2020. V.46. № 2. P.144–148.

Statistical Characteristics of Radio Source Scintillations at Decameter Wavelengths

Kalinichenko[1]M.M., Kuhai[1,2]N.V., Konovalenko[1]O.O., Romanchuk[1]O.I., Brazhenko[3]A.I., Ivantishin[4]O.L., Stasiuk[1]T.A.

[1] Institute of Radio Astronomy of NASU, Kharkiv, Ukraine;
[2] Oleksandr Dovzhenko Hlukhiv National Pedagogical University, Hlukhiv, Ukraine;
[3] Gravimetrical observatory of Geophysical institute of NASU, Poltava, Ukraine;
[4] Institute of physics and mechanics of NASU, Lviv, Ukraine;
E-mail: m.m.kalinichenko.space@gmail.com

Abstract.

This article shows the results of determination of some statistical characteristics (break frequency and exponent of power spectrum and cross - correlation coefficient between signals at two frequencies) of the interplanetary and ionospheric radio stars scintillations in the frequency range 20 to 30 MHz. These statistical characteristics have been obtained by processing synchronous scintillation data from two radio telescopes UTR-2 and URAN-2 belonging to Ukrainian low frequency system URAN (operating frequency range of the radio telescopes is 8 to 32 MHz, decameter wavelengths). The data processing with record statistics for decameter wavelengths has shown that mentioned above statistical characteristics are essentially different for interplanetary and ionospheric scintillations. The results obtained in the article can be used at decameter wavelengths for: improving techniques used for obtaining the interplanetary and ionospheric plasma parameters, separation of the interplanetary and ionospheric scintillations, estimation of their effects on low frequency radio astronomical observations.

Introduction

When conducting low frequency radio astronomical observations from Earth’s surface, the main source of errors and an important interfering factor is the influence of irregularities in the interplanetary and ionospheric plasma. To estimate these effects, it is necessary to know scintillation characteristics on the specified media with sufficient statistics. Also, the better we know scintillation characteristics the more sophisticated technique can be created and used for data processing and obtaining the parameters of the interplanetary and ionospheric plasmas. The statistical characteristics of the interplanetary scintillations are well known at high frequencies (higher or about 100 MHz) [see e.g. *Cohen et al.*, 1966; *Salpete*r, 1966; *Shishov and Shishova*, 1979; *Fallows et al.*, 2008 and others] at least in the weak scattering case. This cannot be said about the decameter range of radio waves. There is a small set of works made in the last century based on episodic observations [Bovkoon and Zhock, 1981a, Bovkoon and Zhock, 1981b]. Among other things, this is due to the relative complexity of scintillation observations in the discussed frequency range when the operating frequencies are close to the critical frequency of Earth’s ionosphere and when there exist a relatively large level of human made interference. The ionospheric scintillation characteristics are better known [see e.g. *Crane*, 1972, *Rashkovsky*, 2004] although there are some debatable issues here too [*Fallows e*t *al.*, 2016]. The purpose of this work was to estimate break frequency and exponent of power spectrum as well as cross - correlation coefficient between signals at two frequencies for the interplanetary and ionospheric scintillations in the operating frequency range 20 to 30 MHz with record statistics for decameter range.

Observations

Since 2001, we have regularly carried out scintillation observations [*Kalinichenko*, 2009; *Kalinichenko et al.* 2019; *Kalinichenko et al.*, 2021] with URAN radio telescope system containing 5 radio telescopes including the largest in the world decameter radio telescope UTR-2 [Konovalenko et al., 2016] (Fig. 1). Ukrainian low frequency radio telescopes are situated throughout the Ukraine (UTR-2 – Grakove, URAN-1 – Zmiiv, URAN-2 – Poltava, URAN-3 – Lviv, URAN-4 – Odesa). The operating frequency range of the radio telescopes is 8 to 32 MHz (decameter range).

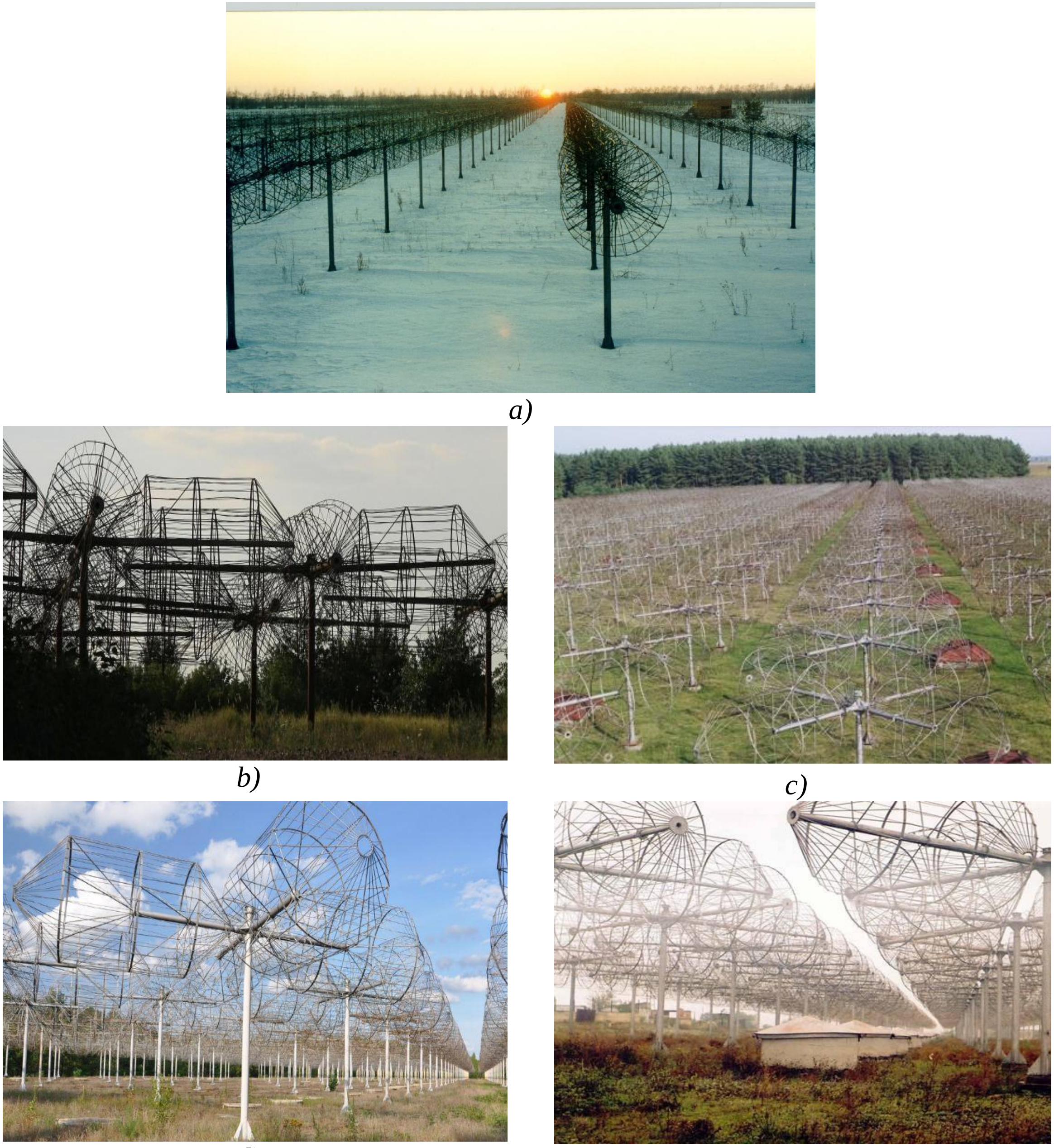

a)

b) *c)*

d) *e)*

Fig.1. Outward appearances of Ukrainian decameter radio telescopes: a) - UTR-2, b) - URAN-1, c) - URAN-2, d) - URAN-3, e) - URAN-4).

Fig. 2 shows an example of the registration of scintillations by using radio telescopes UTR-2 and URAN-2. These are so-called dynamic spectra (intensity on plane time vs frequency).

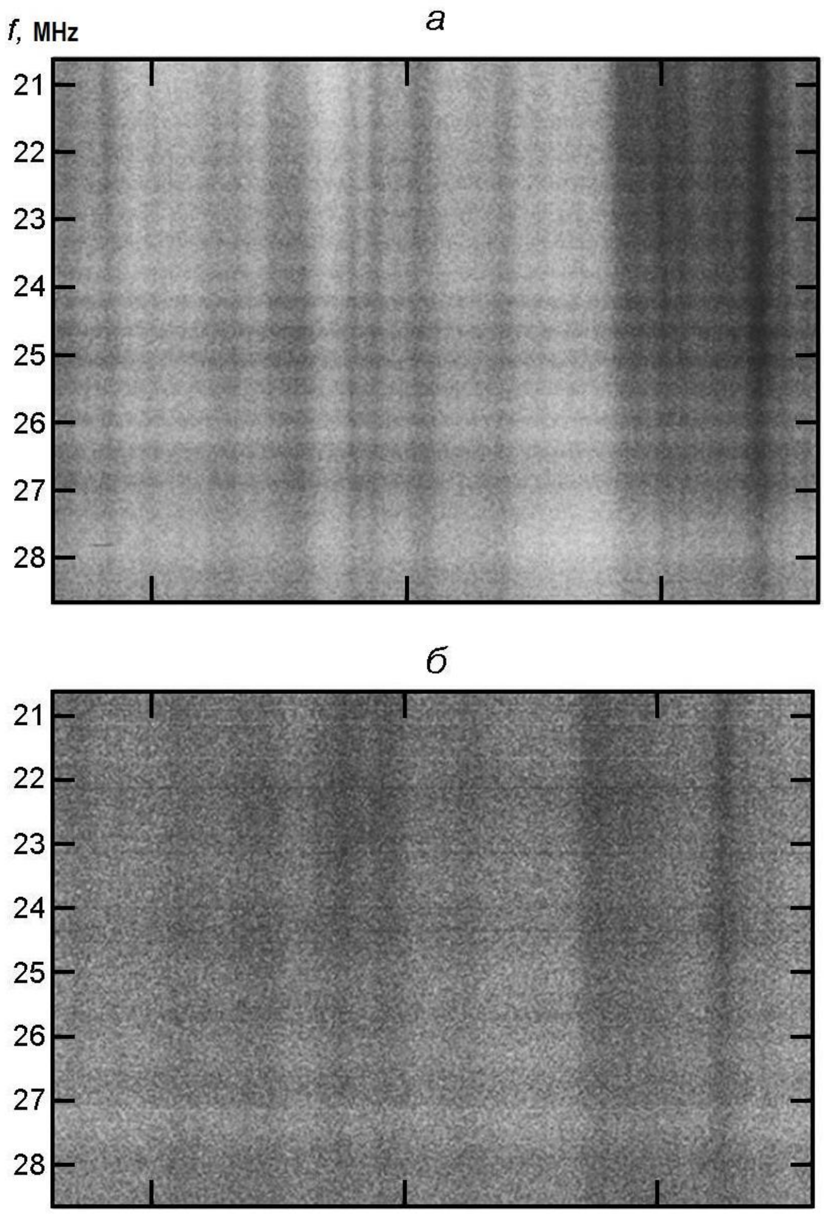

Fig.2. Dynamic spectra of scintillations registered by using the radio telescopes UTR-2 (a) and URAN-2 (b).

Data processing

To achieve our goal, we have analyzed scintillation data from the radio telescope UTR-2 and the radio telescope URAN-2 obtained synchronously since 2015, for 5 years, in the same month, in November. The observations session lasted as usually for 7 days. We have analyzed scintillations among many others of three sources. One of them is the radio galaxy Virgo A and two others are the supernova remnants Cassiopeia A and Crab Nebula. These are the most powerful radio sources at decameter wavelengths in the sky. Cassiopeia A and Virgo A scintillate only on the irregularities of Earth’s ionosphere while Crab Nebula shows the interplanetary scintillations too. So we could obtain statistical characteristics both of the interplanetary and ionospheric scintillations.

Data processing consists in estimation of power spectrum $P(\nu)$ (1) and the cross-correlation coefficient between signals at two frequencies selected at the edges of the range 20 to 30 MHz (2):

$$P(\nu) = |F(\nu)|^2 / T, \tag{1}$$

where $F(\nu)$ is Fourier transform of $I(t)$ process, ν is the fluctuation frequency, T is the duration of time series.

$$R(\tau) = \int_{-T}^{T} I_1(t) I_2(t+\tau) dt \tag{2}$$

Fig. 3 shows daily averaged values for two important parameters of scintillations spectrum: break frequency (Fig. 3a) and exponent of spectrum (spectral index) (Fig. 3b). The red histograms correspond to the ionospheric scintillations and blue histograms are the interplanetary scintillations.

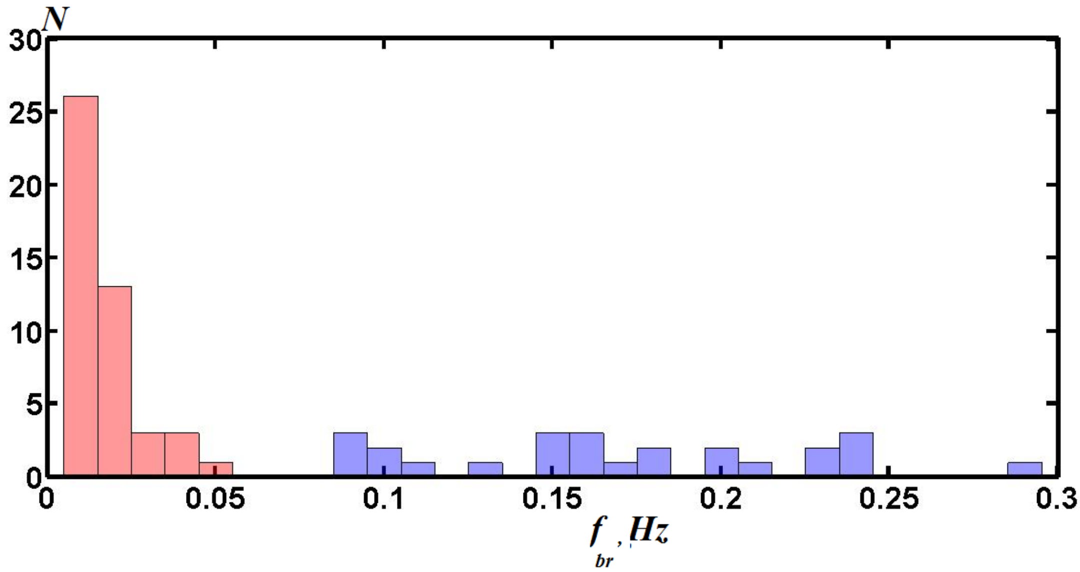

a)

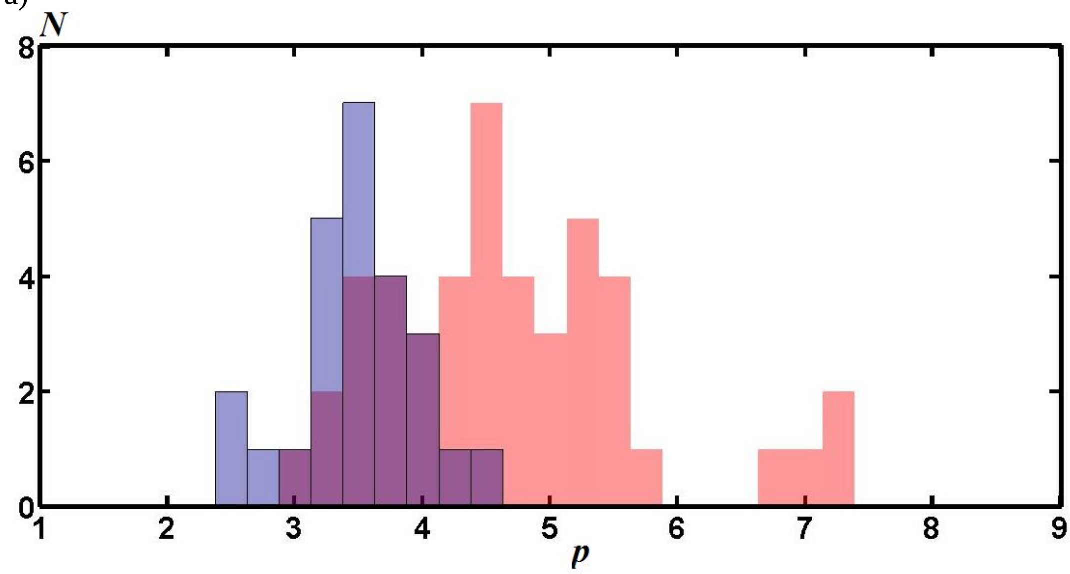

b)

Fig.3. The break frequency (a) and exponent of power spectrum (b) for interplanetary (blue) and ionospheric (red) scintillations .

It is well seen that the mean values of break frequency are essentially different for the interplanetary and ionospheric scintillations (0.16 and 0.01 Hz correspondingly). There is an appreciable difference in exponent of power spectrum (3,5 and more than 4) for the interplanetary and ionospheric scintillations. These results are consistent with those obtained earlier at decameter wavelengths in the articles [Bovkoon and Zhock, 1981a] and [Bovkoon and Zhock, 1981b] based on episodic observations with low statistics. Our results also demonstrate all possible values for break frequency and exponent of power spectrum. The difference between power spectra of the interplanetary and ionospheric scintillations is used for spectral separation of these types of scintillations. And in general, the different fluctuation frequencies are frequently the most obvious criterion for existence of one or the other type of scintillations in low frequency radio astronomical data.

Fig. 4 shows cross - correlation coefficient between signals at two frequencies (which were selected at the edges of the range 20 to 30 MHz). The frequency spacing is 8 MHz. The red histogram corresponds to the ionospheric scintillations while the blue histogram is the interplanetary scintillations. It is well seen that the interplanetary scintillations are well correlated for mentioned above frequency spacing while ionospheric ones not. These results are also consistent with those obtained in earlier work at higher frequencies [*Fallows et al.*, 2014, *McKay-Bukovski et al*., 2015].

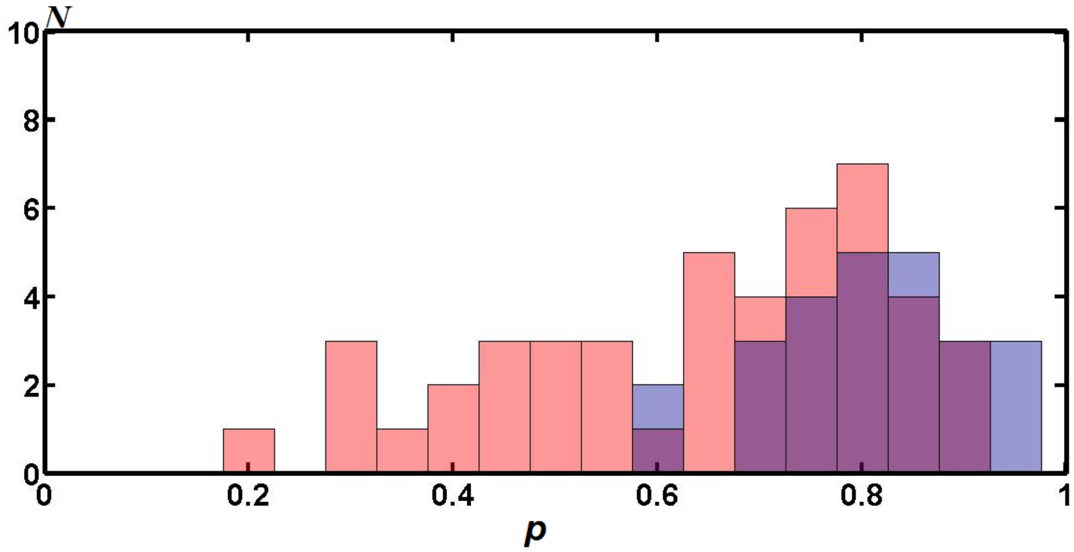

Fig.4. The cross - correlation coefficient between signals at two frequencies selected at the edges of the range 20 to 30 MHz. The red histogram corresponds to the interplanetary scintillations and the blue histogram is the interplanetary ones.

Conclusions

Obtained results can be used for: improving techniques used for estimation of the interplanetary and ionospheric plasma parameters, separation the interplanetary and ionospheric scintillations, estimation of the interfering influence of the interplanetary and ionospheric plasma on radio astronomy experiments of a wide range of targets, analysis of the interplanetary scintillations at other frequencies.

Acknowledgment

This study was supported by Target Complex Program of NAS of Ukraine for Scientific Space Studies for 2018-2022 (projects "Ground-based support by UTR-2-URAN-GURT low-frequency radio telescope system of international and Ukrainian space missions" and “Creation of low-frequency radio astronomical elements and systems for the study of objects in the Universe from the surface of the Moon”) and the project "Instrumental and information connection of radio telescopes UTR-2, URAN, GURT to world networks of low-frequency radio astronomy".

References

Bovkoon, V.P., Zhouck, I.N. (1981a). Scintillations of cosmic radio sources in the decameter waveband. Part I. Spectra of scintillations due to ionospheric and interplanetary plasma fluctuations and the possibility of their separation. Astrophysics ans space science, 79, 165 – 180, 1981.

Bovkoon, V.P., Zhouck, I.N. (1981b). Observations of compact source scintillations in the Crab Nebula and CAS A in the decameter range. Dopovidi Akademii Nauk Ukrains'koj RSR. Seriya A, Fiziko-Tekhnichni ta Matematichni Nauki, 7 ,54-57, 1981 (in Russian).

McKay-Bukovski, D., Vierien, J., Virtanen, I.I., Fallows, R., Postila, M. Ulich, T., Wueknitz, O., Brentjens, Ebbendorf, N., Enell, C-F., Gerbers,M., Grit, T., Gruppen, P., Kero, A., Linatti, T., Lehtinen, M., Meulman, H., Norden, M., Orispaa, M., Raita, T., de Reijer, J-P., Roininen, L., Schoenmakers, A., Stuurwold, K., Turunen, E. (2015). Kaira: The Kilpisjarvi atmospheric imaging receiver array – system overview and first results, IEEE Transactions an Geoscience and remote sensing, 53, 3, 1440-1451, 2015.

Crane, R.K. (1972) Ionospheric scintillation. Proceedings of the IEEE, 65, 2, 180 – 199, 1972.

Cohen, M.H., Gundermann, E.J., Hardebeck, H.E., Harris, D.E., Sharp, L.E. (1966). Interplanetary scintillations. II. Observations. Astronomical journal, 71, 449 – 466, 1966.

Fallows, R.A., Breen, A.R., Dorrian, G.D. (2008). Developments in the use of EISCAT for interplanetary scintillation, Ann Geophys. 26, 2229‑2236, 2008

Fallows, R.A., Coles, W.A., McKay-Bukowski, D., Vierinen, J., Virtanen, I.I., Postila, M., Ulich, Th., Enell, C-F., Kero, A., Linatti, T., Lehtinen, M., Orispaa, M., Raita, T., Roininen, L., Turunen, E., Brentjens, M., Ebbendorf, N., Gerbers, M., Grit., T., Gruppen, P., Meulman, H., Norden, M.J., de Reijer, J-P., Schoenmakers Stuurwold, K. (2014). Broadband meter-wavelength observations of ionospheric scintillation. Journal of Geophysical Research, 119, 12, 10-544, 2014.

Fallows, R.A., Bisi, M.M., Forte, B., Ulich, Th., Konovalenko, A.A., Mann, G., Vocks, C. (2016). Separating nightside interplanetary and ionospheric scintillation with LOFAR. The Astrophysical Journal Letters, 828, 1, 1-6, 2016.

Kalinichenko, N.N. (2009). A search for compact decametric radio sources in supernova remnants using the interplanetary scintillation technique. Astrophysics and Space Science, 319, 2-4, 131-138, 2009.

Kalinichenko, N. N., Olyak, M. R., Konovalenko, A. A., Brazhenko, A. I., Kuhai, N. V., Romanchuk, A. I. (2019). Large-scale structure of solar wind beyond the Earth's orbit: reconstruction using the data of two-site measurements of interplanetary scintillations in the decameter radio range. Kinematics and Physics of Celestial Bodies, 35, 1, 17-27, 2019.

Kalinichenko, M. M., Kuhai, N. V., Konovalenko, O. O., Brazhenko, A. I., Bubnov, I. M., Yerin, S. M., Rucker, H. O., Zarka, P., Lecacheux, A., Ivantyshyn, O. L., Lytvynenko, O. O., Romanchuk, O. I., Frantsuzenko, A. V. (2021). Investigations of cosmic sources radioemission scintillations due to interplanetary plasma irregularities at the Institute of Radio Astronomy, Nas Ukraine, Radio physics and radio astronomy, 26, 2, 148-164, 2021.

Konovalenko, A., Sodin, L., Zakharenko, V., Zarka, Ph, Ulyanov, O., Sidorchuk, M., Stepkin S., Tokarsky P., Melnik, V., Kalinichenko, N., Stanislavsky, A., Koliadin, V., Shepelev, V., Dorovskyy, V, Ryabov, V., Koval, A., Bubnov, I., Yerin, S., Gridin, A., Kulishenko, V., Reznichenko, A., Bortsov, V., Lisachenko, V., Reznik, A., Kvasov, G., Mukha, D., Litvinenko, G., Khristenko, A., Shevchenko, V., Shevchenko, V., Belov, A., Rudavin, E., Vasylieva, I., Miroshnichenko, A., Vasilenko, N., Olyak, M., Mylostna, K., Skoryk, A., Shevtsova, A., Plakhov, M., Kravtsov, I., Volvach, Ya., Lytvinenko, O., Shevchuk, N., Zhouk, I., Bovkun, V., Antonov, A., Vavriv, D., Vinogradov, V., Kozhin, R., Kravtsov, A., Bulakh, E., Kuzin, A., Vasilyev, A., Brazhenko, A., Vashchishin, R., Pylaev, O., Koshovyy, V., Lozinsky, A., Ivantyshin, O., Rucker, H., Panchenko, M., Fischer, G., Lecacheux, A., Denis, L., Coffre, A., Grieβmeier, J-M, Tagger, M., Girard, J., Charrier, D., Briand, C., Mann, G. (2106), The modern radio astronomy network in Ukraine: UTR-2, URAN and GURT. Experimental astronomy, 42, 1, 11- 48, 2016.

Rashkovsky, S.L. (2004). Study of decameter-wavelength ionospheric scintillations by astronomical methods using the URAN-1 radiotelescope. Radiophysics and Quantum Electronics, 47, 9, 631-645, 2004.

Salpeter, E.E. (1966). Interplanetary scintillations. I. Theory. Astrophysical journal, 71, 433 – 448, 1966.

Shishov, V.I., Shishova, T.D. (1979). Influence of source sizes on the spectra of interplanetary scintillations. Observations. Soviet Astronomy, 23, 3, 345-350, 1979.

Properties of Filament Eruption and Associated Flare Ribbons on 2021 May 9

Koleva K.[1], Devi P.[3], Duchlev P.[2], Dechev M.[2], Chandra R.[3], Simić[4] Z.

[1]Space Research and Technology Institute, Bulgarian Academy of Sciences
[2]Institute of Astronomy and NAO, Bulgarian Academy of Sciences
[3]Department of Physics, DSB Campus, Kumaun University, Nainital - 263 002, India
c) [4]Astronomical Observatory Belgrade
E-mail: kkoleva@space.bas.bg

Abstract
We present the first results from the investigation of a filament eruption and associated flare ribbon, occurring in the southern solar hemisphere on 2021 May 9. Before the eruption, the filament was located in a plage region close to the disk center and laid along the S-shaped polarity inversion line. The filament began to rise slowly at 09:30 UT and at 10:00 UT it erupted, which was accompanied by spreading ribbons at its base. During the eruption two flare ribbons slowly separated. During the ribbons evolution, hot post-flare loops appeared at 11:00 UT and later, at 11:55 UT they formed PFL arcade.

Using the high resolution multi-wavelength data from the Atmospheric Imaging Assembly onboard the Solar Dynamics Observatory we study the kinematics and morphology evolution of the eruption and flare ribbons. The event was also registered by STEREO-Ahead Observatory, which allows us to explore the event kinematics and evolution from two different points of view.

The filament evolution before the eruption was traced by H-alpha data from the Global Oscillation Network Group. The photospheric magnetic field configuration was analyzed with the Helioseismic Magnetic Imager (HMI) onboard the SDO.

Introduction

Eruptive prominences (EPs) (or filaments if observed on the solar disk) are large-scale phenomena occurring in the solar atmosphere. They are frequently associated and physically related to coronal mass ejections (CMEs) and flares (Tandberg-Hanssen, 1995; Munro et al., 1979; Chandra et al., 2017). Such close relationship between EPs and the other eruptive solar occurrences (Lin et al, 2003; Priest and Forbes, 2002) suggests that the three eruptive events are different manifestations of a same huge physical process, whose energy source is the free energy stored in coronal magnetic fields (Forbes, 2000). Various studies indicate that prominences can erupt in many different ways depending on their magnetic environment (e.g. Joshi and Srivastava, 2011 for reviews). One of the most favorable for eruption magnetic configuration is that, associated with S-shaped sigmoids (Gosain et al, 2009, Green et al, 2018). Sigmoids are S-shaped coronal emission structures seen in soft X-ray and EUV observations. They form along a polarity inversion lines and are best observed near the disk center.

The filament eruptions are usually associated with two ribbon flare (Benz, 2017, Chandra et al, 2009, Krucker et al, 2011 and references cited therein). The flare ribbons are formed opposite site of polarity inversion line and they are separated as the time progresses. These flares ribbons are connected by post flare loops during the decay phase of flares. The separation, formation of flare ribbons and post flare loops appearance can be explain by the CSHKP model (Carmichael (1964), Sturrock (1966), Hirayama (1974), and Kopp and Pneuman (1976)). For the trigger of the eruption another sets of models are proposed by several authors. Among these models, the tether cutting (Moore and Sterling, 2006), magnetic breakout (Antiochos et al, 1999), kink (Török and Klein, 2005) and torus instability (Kliem and Török, 2006) models are important and can explain the various eruptive solar events.

In this work we present the study of a sigmoid filament eruption that occurred on 09 May 2021, close to the disk center. The used data are introduced in Section 2. Morphology and events timing are presented in Section 3. The kinematics is described in Sections 4. Finally the summary is given in Section 5.

2. Observations

In the present work we used high spatial and temporal resolution data in Extreme Ultraviolet (EUV) channels from the Atmospheric Imaging Assembly (AIA; Lemen et al., 2012) on board the Solar Dynamics Observatory (SDO, Pesnell et al., 2012). The filament eruption kinematics and morphology were studied by data in He II 304 Å channel of AIA/SDO. For tracing the PFL and PFL arcade we used also data in Fe IX 171 Å and in FeXIV 211 Å channels of AIA/SDO.

H-alpha images from the Kanzelhöhe Solar Observatory (KSO; Otruba & Pötzi, 2003) were used to investigate the location and chromosphere nature of filament eruption.

To study the event kinematics from another viewpoint we used observations in 304 Å (He II) channel from the Extreme Ultraviolet Imager (EUVI) onboard the STEREO Ahead (A) spacecraft (Wuelser at al, 2004).

The pixel and temporal resolution of AIA data sets are 0.65 arcsec and 12 sec respectively. For the STEREO-A data the pixel resolution is 1.6 arcsec and the cadence is 10 min. All the data is processed and analyzed by the solar software.

3. Morphology and events timing

On 2021 May 09, we have observed the FE, occurring in the southern solar hemisphere. This filament appeared next to a plage region close to the disk center. It was situated along the S-shaped magnetic polarity inversion line (PIL) and represented a sigmoid filament. The eruption was clearly traceable with aid by spreading ribbons at its base. The FE was also observed by EUVI instrument onboard the STEREO A observatory. The event morphology in different pass-bands is shown in Figure 1. In panel (a) is shown the filament at 08:44 UT in quiet state, as observed in H-alpha line by KSO. Figure 1 (d) represent the HMI magnetogram, showing the line-of sigh photospheric magnetic fields at 08:45 UT. The filament channel is traced by red dotted line. It is obvious that the filament **laid along a** S-shaped PIL.

Initially from 08:00 UT to 09:30 UT a pre-eruptive changes of the 304 Å intensity flux in the western filament vicinity was observed. The eruption started at 09:30 UT when the filament slow rising began. The slow rise phase lasted until 10:00 UT. After that time the FE entered in its fast-rising phase, when the dark filament FR, accompanied with filament flux rope rotation, escaped from the solar surface with increasing speed up to ~140 km/s. The acceleration phase lasted until 11:00 UT, when was the end of eruption. In Figure 1 (b) the FE in AIA field of view (FOV) is shown at 10:35 UT, when the eruption was in progress.

Between 10:03 and 11:00 UT along the two sides of the filament channel the flare ribbons were observed to develop. After 11:05 UT a hot post-flare loops formed above the filament channel, which subsequently, at 11:55 UT developed to the PFL arcade. These events were well observed in hotter AIA channels, such as 171 Å (Fig.1c) and 211 Å (Fig.1 f).

The eruption observed by a different view point from EUVI in 304 Å is shown in panel (e) of the Figure.

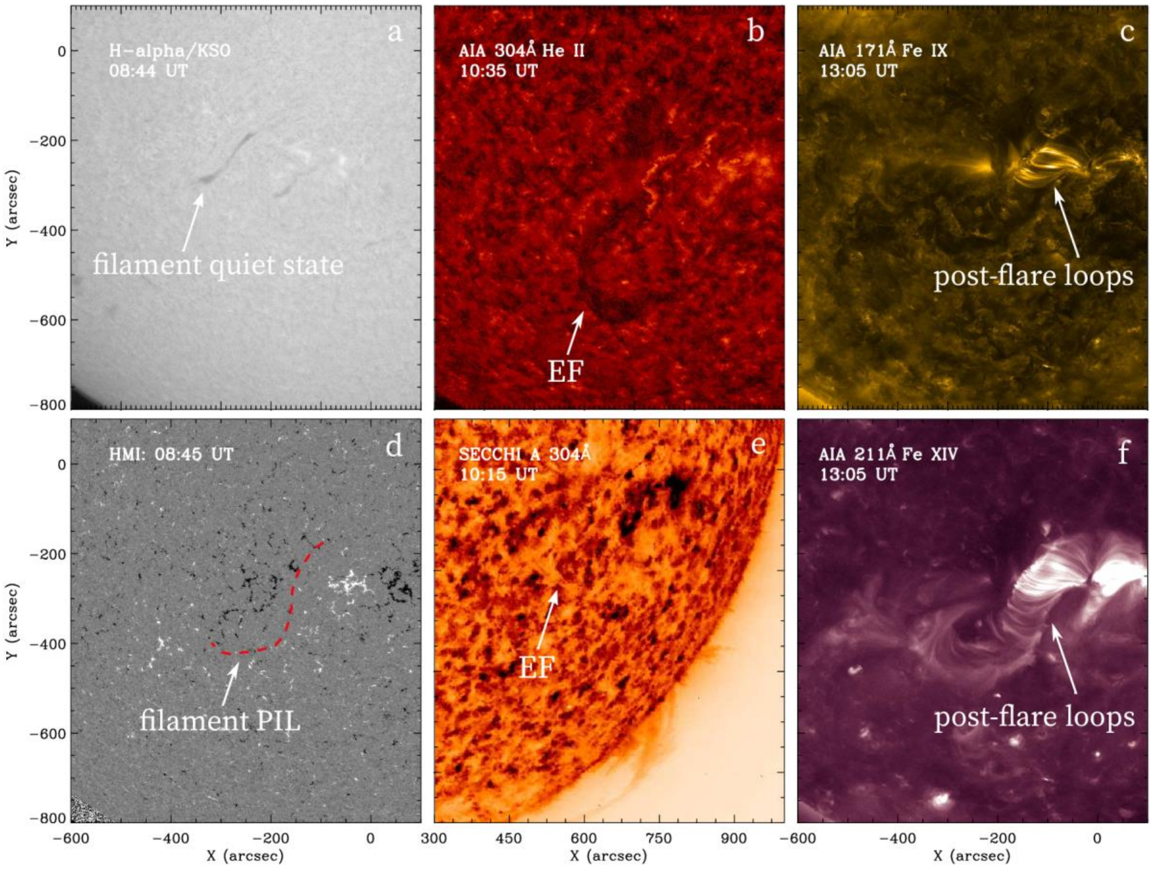

Figure 1: (a) Image of the event in H-alpha, showing the filament in quiet state before the eruption. (b) the EF observed in AIA 304 Å and (c) in AIA 171 Å. (d) HMI magnetogram with over-plotted the filament PIL position (red dotted line). (e) Filament eruption observed by EUVI/STEREO A in 304 Å (in reversed colour table). (f) image in the AIA 211 channels, showing the post-flare loops.

In the H-alpha image before the eruption, we could see the filament sinistral barbs (Figure 1a). The sinistral barbs indicate the positive twist of the filament. The shape of the filament is also the 'S' shape, which also indicate the positive twist (Gosain et al 2009), since the filament is located in the southern hemisphere. According to hemispheric rule of helicity, the southern solar hemisphere is dominated by the the positive helicity (Pevtsov et al., 1995). Therefore, the filament follows the hemispheric rule of helicity. Further, looking at the orientation of the post flare loops, we infer again the positive helicity (see Figure 1f). Therefore, there is good agreement between the helicity sign of filament and the post flare loops. Such a consistency was also reported in previous observations (for example see Chandra et al, 2009).

4. Eruption Kinematics

4.1 AIA/SDO FOV

To explore the eruption kinematics in the AIA FOV we used the slice-time plot. For our purposes we have selected the artificial slice (S1) shown in Figure 2 (a). The direction of the slice was selected according to the direction of filament material ejection. The results of this analysis as a time-distance plots are shown in Figure 2 (b).

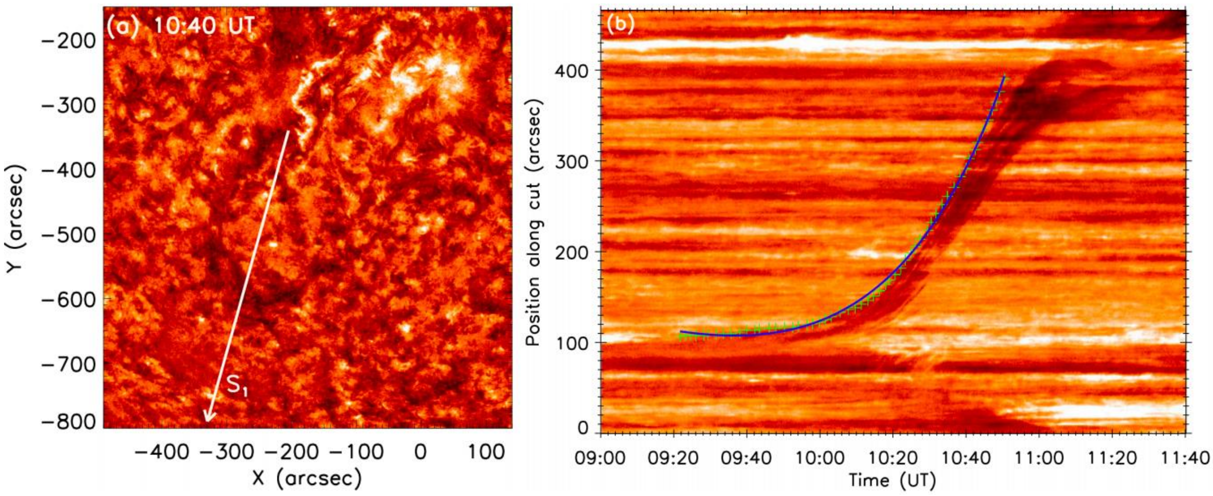

Figure 2: (a) Location of the slice selected for the height-time plot of the filament eruption and the filament material flow. (b) The height-distance plot along the slits S1.

Filament stared to erupt around 09:30 UT, when the filament material began to ascend slowly in southeast direction. The eruption clearly showed two eruptive phases. The slow-rise phase lasted between 09:30 UT and 09:58 UT. The fast-rise phase of FE began after that time. The eruption fast-rise phase start time (09:58 UT on 09 May 2021) was calculated using the fitting function applied to the data points in time-distance plot. The fitting and the formula to find the exact eruption start time is taken from Cheng et al., 2020 and Chandra et al, 2021.
The eruption speed in the fast-rise phase varied from ~ 20 km/s to 140 km/s. The calculated maximum acceleration in this time period was 70 m/s^2. The filament was visible up to heights approximately 360 Mm, when after 11:00 UT the filament material left the AIA FOV.

4.2 EUVI/STEREO A FOV

The eruption was observed also by STEREO Ahead spacecraft. For analyzing the event kinematics, we used data in 304 *Å c*hannel from EUVI instrument. The position of the selected slice and the resulting time-distance plot are shown in Figure 3 (a) and (b), respectively. In EUVI FOV the eruption again showed two phases. For calculate the eruption speed we fitted the time-distance plot with two linear fits. The slow-rise motion of the filament was observed after 09:00 UT. The average estimated velocity for this phase is about 9 km/s. That phase lasted until 09:55 UT. After that time the filament material continued to rise rapidly with an average speed of about 42 km/s. The two eruption phases are very clear and easily distinguishable by its velocities. In STEREO FOV the filament material reach heights about 320 Mm.

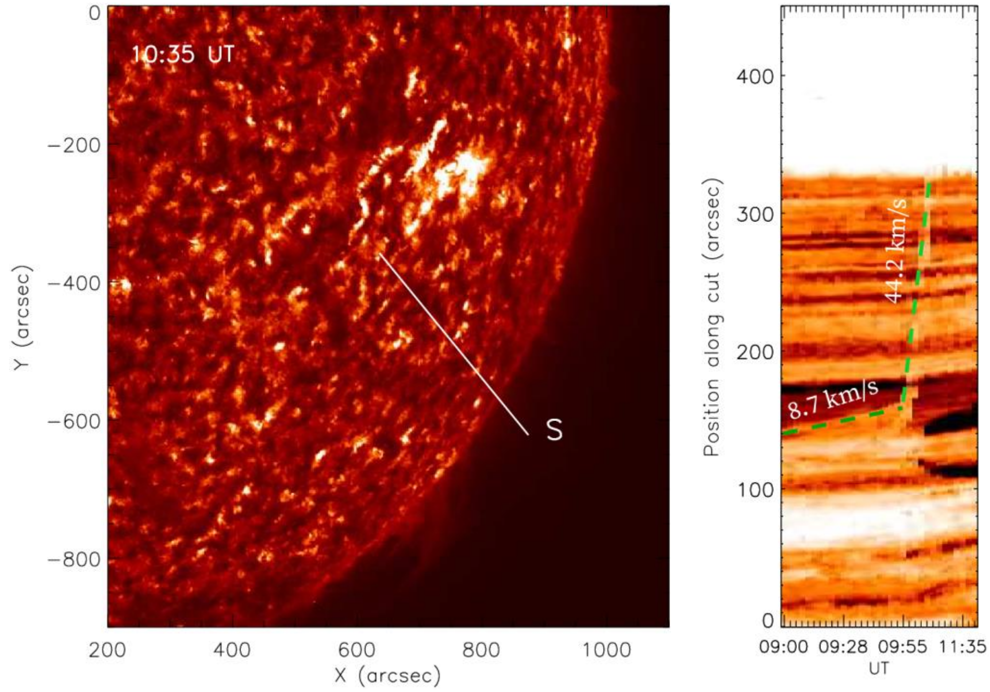

Figure 3: (a) Location of time slice selected for the FE eruption direction in EUVI/STEREO A FOV; (b) Corresponding time-distance plot in reversed colour table.

5. Summary

We have studied the eruption of a quiet filament, observed in the southern solar hemisphere on 2021 May 09. *The eruption was accompanied by spreading ribbons at its base. The filament represented a* S-shaped sigmoids. Sigmoids are highly sheared and twisted loops that form along the polarity inversion lines and are best observed close to the disk centre. It has been widely accepted that the magnetic field configuration associated with a sigmoid tends to erupt with a high probability (Canfield et al. 1999).

We analyzed the morphology and kinematics of FE from two different points of view using multi-wavelength data. The eruption kinematics clearly shows two distinct phases. The first one was the phase of filament slow rising and the second phase was characterized with fast filament upwards motion. During the last phase the filament material reach velocity up to 140 km/s. The results obtained from two different FOV, these of SDO and STEREO A observatory, are similar.

The twist sign inferred from the filament chirality, shape and the orientation of post flare loops indicate the positive twist in the active region and consistence with hemispheric helicity rule. Therefore, our study shows the same twist sign in the chromosphere (visible in H-alpha) and in transition region (visible in AIA 211 *Å*), which confirm the helicity conservation characteristic.

In future we plan to expand this work, analyzing the spreading ribbons and post-eruptive arcade behaviors in detail.

Acknowledgments

The AIA data used here is the courtesy of SDO (NASA) and AIA consortium. The authors thank the STEREO/SECCHI consortium for providing the data. Hα data were provided by the Kanzelhöhe Observatory, University of Graz, Austria. The work is supported by the Bulgarian Science Fund under Indo–Bulgarian bilateral project INT/BLG/P-11/2019 (KP-06-

India/14 19 -Dec-2019) and partially supported by the Bulgarian Science Fund under grand **№ КП-06-Н44/2 27.11.2020.** Financial support from the Bulgarian Academy of Sciences (Bilateral grant agreement between BAS and Serbia) is gratefully acknowledged by M.D. and Z.S.

References

Antiochos, Spiro K., DeVore, C. Richard: 1999, Magnetic Helicity in Space and Laboratory Plasmas: Geophysical Monograph 111. Edited by Michael R. Brown, Richard C. Canfield and Alexei A. Pevtsov. Published by the American Geophysical Union, Washington, DC USA, 1999, p.187

Benz, Arnold O.:2017, Living Reviews in Sol. Phys., Volume 14, Issue 1, p. 2

Canfield, Richard C., Hudson, Hugh S., McKenzie, David E.: 1999, Geophysical Research Letters, Volume 26, Issue 6, p. 627

Carmichael, H.: 1964, The Physics of Solar Flares, Proceedings of the AAS-NASA Symposium held 28-30 October, 1963 at the Goddard Space Flight Center, Greenbelt, MD. Edited by Wilmot N. Hess. Washington, DC: National Aeronautics and Space Administration, Science and Technical Information Division, 1964., p.451

Chandra, R., Schmieder, B., Aulanier, G., Malherbe, J. M.: 2009, Sol. Phys., 258, Issue 1, p.53

Chandra, R., Filippov, B., Joshi, R., & Schmieder, B. 2017, Sol. Phys., 292, p. 81

Chandra, R., Dèmolunn, P., Devi, P., Joshi, R., Schmieder, B.: 2021, Submitted to ApJ.

Cheng, X., Zhang, J., Kliem, B., Török, T., Xing, C., Zhou, Z.J., Inhester, B., Ding, M.D.: 2020, Astrophys. J. 894(2), p. 85

Hirayama, T.: 1974, SoPhys, 34, Issue 2, p.323

Forbes, T. G.: 2000, JGR, 105, Issue A10, p. 23153

Gosain, S., Schmieder, B., Venkatakrishnan, P., Chandra, R., Artzner, G.: 2009, Sol. Phys., 259, Issue 1-2, p. 13

Green, Lucie M.; Török, Tibor; Vršnak, Bojan; Manchester, Ward; Veronig, Astrid: 2018, SSRs, 214, Issue 1, p. 46

Joshi, Anand D.; Srivastava, Nandita: 2011, ApJ, 730,104

Kliem, B., Török, T : 2006, Physical Review Letters, vol. 96, Issue 25, p. 255002

Kopp, R. A., Pneuman, G. W. : 1976, Sol. Phys., 50, p. 85

Krucker, Säm, Hudson, H. S., Jeffrey, N. L. S., Battaglia, M., Kontar, E. P., Benz, A. O., Csillaghy, A., Lin, R. P.: 2011, ApJ, 739, Issue 2, p. 96

Lemen, J. R., Title, A. M., Akin, D. J., et al.: 2012, Sol. Phys., 275, p.17

Lin, J., Soon, W., Baliunas, S. L.: 2003, New Astronomy Reviews, 47, Issue 2, p. 53

Moore, Ronald L., Sterling, A. C.: 2006, American Astronomical Society, SPD meeting, Bulletin of the American Astronomical Society, Vol. 38, p.247

Munro, R. H., Gosling, J. T., Hildner, E., et al. 1979, Sol. Phys., 61, p. 201

Otruba, W., Pötzi, W.: 2003, Hvar Obs. Bull. **27**, 189

Pevtsov, Alexei A., Canfield, Richard C., Metcalf, Thomas R.: 1995, Astrophysical Journal Letters, 440, p.L109

Pesnell, W. D., Thompson, B. J., & Chamberlin, P. C. 2012, Sol. Phys., 275, p. 3

Priest, E. R., Forbes, T. G.: 2002, The Astronomy and Astrophysics Review, 10, Issue 4, p. 313

Sturrock, P. A.: 1966, Nature, Volume 211, Issue 5050, p. 695

Tandberg-Hanssen, E., ed. 1995, Astrophysics and Space Science Library, 199, The nature of solar prominences

Török, T.,Kliem, B.: 2005, Astrophysical Journal, 630, p. L97

Wuelser, J., Lemen, J.R., Tarbell,T.D., et al.: 2004, in SPIE Conf. 5171, ed. S. Fineschi, & M. A. Gummin, p. 111

Predictions for SC25, 26 and SC27 Magnitudes in Relation to the Long-Term Solar Activity Changes

Komitov B.P.
Institute of Astronomy and NAO, BAS, Sofia, Bulgaria
komitovboris97@gmail.com

Abstract

In this work the results about the near-maximal amplitudes of present (SC25) as well as the next two Schwabe- Wolf's sunspot cycles SC26 and SC27 are discussed. For this aim two data series has been used: They are the mean monthly sunspot numbers (the new SILSO_version 2) for the epoch Jan. 1818- Jul.2021 and the complemented "historical" Schove's series (214 BC - 2009AD). It has been found on the base of mean monthly data analysis for the first 20 months after the starts (minima) of sunspot cycles that the SC25 near-maximal amplitude should expect to be 149±39, which corresponds to 99±26 as a classical Wolf's number. On the other hand, by using of kinematic model based on time series analysis (T-R periodogram algorithm) the corresponding near maximal Wolf's number of SC25 is in range 75±38. Taken into account that the near-maximal amplitude of SC24 in 2014 AD is ~82 it could to conclude that a violation of the amplitude Gnevishev-Ohl-Kopecky's rule for the even-odd sunspot cycles pair SC24-SC25 is possible. It has been found by using of auto-regression models of sunspot cycles amplitudes in Schove's series that the magnitude of the next SC26 should be expect in range of 90-95 as Wolf's (Ri) number. There is also prediction for a very shallow sunspot minimum between SC26 and SC27 in 2038-2040AD

Introduction

The long term solar activity predictions are significantly more complicate than the related only for the current or next sunspot Schwabe-Wolf’s cycle. The reason for this one relates to the circumstance that instrumental space climate data series are relative short, while the forecasts for two or more SC requires information, which includes at least few or more centuries. That’s why events like grand solar minima or maxima should be taken into account in such forecasts. On the other hand, the theoretical or mixed solar activity models, based on the modern solar dynamo theory are focused mainly on the quasi 11 (Schwabe-Wolf) a 20-22 yr (Hale) cycles and generally the explanation and forecasting of such events like the grand solar minima is problematic for the most of them. That’s why for the aims of long time solar activity and space climate prediction needs to use no only instrumentally indexes data series, but also of indirect historical data series such as the Schove’s series [*Schove*, 1955, 1983], “Chinese” giant naked eye visible sunspots [*Witmann and Xu*, 1987], “cosmogenic” radioisotopes (14C, 10Be) [*Stuiver and Quay*, 1980; *Damon and Sonett*, 1991; *Reimer et al*, 2013; Bard et al, 1997, *Usoskin*, 2013]. It has been shown that the using of statistical methods as factor type regressions and autoregressions [*Komitov*, 2007] or kinematic models [*Komitov and Kaftan*, 2003] is very successful. In this study results about the forecasting of the present 25^{th} in Zurich series Schwabe-Wolf’s sunspot cycle (SC25) magnitude, as well as for the next two (SC26 and SC27) are shown.

Data and methods

a) Data

The study is based on two types of data series. The first one is the instrumental sunspot Zurich series of the mean monthly sunspot number since January 1750. The both versions of these data has been used – the “classical” Wolf number, presented by the International sunspot number (*Ri* or *SN_v1*) for the epoch January 1750- December 2014 and the new sunspot data series, suggested by Clette and Lefevre few years ago [*Clette and Lefevre,* 2016]. The last one is used for the epoch January 1750- March 2021.

The second data series is by "historical" type. It is the so called "Schove's series", suggested by Derek Schove in 1955 and improved by him in 1983 [*Schove*, 1955, 1983]. It contains the macro- characteristics of the sunspot cycles since 642 BC. These parameters are the calendar years of minima and maxima as well as the cycle magnitude in 9-level scale. The last one is calibrated to the near –maxima annual sunspot *Ri* index data for each cycle between 1750 and 1948 AD in the primary version of this data set [*Schove* 1955] and slightly improved after that in 1980th [*Schove*, 1983]. The Schove's series has been constructed on the base of ancient and medieval messages about aurora, giant sunspots, annual tree ring widths data, extreme natural (environmental) events like very cold winters or very dry and warm summers, floods, earthquakes etc. After 1750 AD the Schove's series continues in the instrumental Zurich series.

It is necessary to note that before 219 BC the macro- parameters are established only for separate sunspot cycles. There is also a second calendar interval between 196 and 284 AD where the sunspot cycles data are not complete - the calendar years of sunspot cycles extremes has been established, but the magnitudes are unknown. After 284 AD the Schove's series is complete.

b) Regression models, based on "Waldmeier's rule"

It has been established in an other our previous study [*Komitov et al*., 2011] that the so called "Waldmeier's rule" (the sunspot cycles magnitudes are higher when the corresponding upward sunspot solar cycle phase is faster and shorter) is well expressed even if only the first 1.5-2 years are taken into account. It helps for a relative certain estimation for the mean annual near maximal *Ri* value (magnitude, Ri_{max}) on an earlier stage of the current sunspot cycle. It has been found for the first 18 months after the sunspot minima the following regression relationship between the mean monthly *Ri* change ($\alpha = dRi/dt$) after minimum and Ri_{max} :

$$Ri_{\max} = 2.44\alpha + 69.7 \pm 27 \tag{1}$$

This relationship is by using of monthly Ri values for the last 17 to this moment sunspot cycles, i.e SC7-SC23 (1818 – 2010 AD). The corresponding correlation coefficient of this relationship is r=+0.69.

It has been found by instrumental data for the first 18 months of SC24 that the corresponding value of α is 0.91. It follows by (1) that Ri_{max} for SC24 should be 72±27. The real Ri_{max} value of SC24 in 2014 AD is 82. Thus it could consider the prediction of SC24 magnitude as successful.

About six months later a new similar analysis has been provided, but this time on base of the first 24 months after minima for the same sunspot cycles (SC7 to SC23) [*Komitov and Kaftan,* 2011] . The regression function was significantly improved. In this case has been found a relationship:

$$Ri_{\max} = 23.63\alpha + 46.9 \pm 17 \tag{2}$$

with r = +0.91 and Snedecor- Fishers *F*- parameter equal to 5.34, which is around the critical value of last one for 99% confidence ($F_{99} \approx 5.2$) , while for 95% it is 3.24. The corresponding predicted SC24 magnitude in this case is Ri_{max} = 90±17.

It has been also found for the 24-months case that the regression model could even more slightly improved if the monthly *Ri* value for the sunspot minimum (*Rm*) as a second factor is used [*Komitov and Kaftan,* 2011]. In this case

$$Ri_{\max} = 23.63\alpha + 1.94Rm + 41.6 \pm 16 \tag{3}$$

The corresponding coefficient of multiple correlation in this case is R=0.92 with F= 5,97. The predicted SC24 magnitude is Ri_{max} =86±16.

Thus all these three regression models, which has been applied to SC24 magnitude prediction indicate their successful fitness to current sunspot cycle forecasting during the earlier stage of its upward phase. To the present moment (~19 months after the sunspot minimum between SC24 and SC25) a one- factor regression model of type (1) or (2) could uses for prediction of SC25 magnitude. In the present study the whole instrumental data series of monthly sunspot numbers *Ri* since January 1750 and up to December 2014 is used. The results are presented and discussed in the section "Results and analysis" of the paper.

c) Autoregression models, based on Schove's series

In 2007 author found in Schove's series a regression relationship between the sunspot cycles with even numbered according to Zurich series standard with numbers 2n and 2n+2 [*Komitov*, 2007]. The founded relationship has been extracted on base of whole epoch between 296 and 2000 AD plus the calendar interval 219BC – 196AD, where the sunspot cycles macro-characteristics data are complete. The obtained auto-regression function is

$$\Delta Ri_{max(2n,2n+2)} = 98.5 - 1.06Ri_{max(2n)} \pm 29 \quad (4)$$

The quantity $\Delta Ri_{max(2n,2n+2)}$ presents the magnitude difference between even numbered cycles 2n and 2n+2nd . The correlation coefficient is r=-0.71 and F=2.04, while the critical "threshold" for 99% confidence of last one is $F_{99} = 1.59$.

The above mentioned formula (5) for prediction of SC24 magnitude has been used. The magnitude of SC22 ($Ri_{max(SC22)}$ =157) is taken as a predictor. It has been found by this way that $\Delta Ri_{max(SC22,SC24)}$ = -68 and the SC24 magnitude should be 89±29. As the real value $Ri_{max(SC24)}$ = 82 it need to conclude that the prediction, based of regression formula is very succesfull.

The second obtained auto-regression model, based on Schove's series is of two-factor type [*Komitov*, 2007]:

$$\Delta Ri_{max(2n,2n+2)}=69 - 1.16Ri_{max(2n)}+0.4Ri_{max(2n+1)} \pm 27 \quad (5)$$

As a second factor in this model is the odd numbered 2n+1st sunspot cycle magnitude. The characteristics of this model are slightly better as (4): the coefficient of multiple correlation is *R*=0.78 and *F*= 2.45. It has been found by using of formula (5) a predicted SC24 magnitude $Ri_{max(SC24)}$ = 92± 27.

The both above signed SC24 magnitude predicted values indicate for the good applicability of the auto-regression formulas (4) and (5) for prediction of even numbered sunspot cycles magnitudes. In this study it relates to SC26. The passed SC24 magnitude as well as the predicted by SC25 magnitude on base of Waldmeier's rule regression models are used as predictors.

(d) Kinematic models, based on T-R periodogram algorithm

The T-R periodogram algorithm (TRPA) has been suggested by the author in 1980th as an alternative method on the place of discrete Fourier analysis for detecting and statistical estimation of cycles in time series. The advanced features of this method are generally two: the independence of obtained results from the time series length and the possibility for much better study of low frequency oscillations as the Fourier method, including also such ones which corresponding periods are comparable or even slightly longer as the studied time series ("hyper-cycles"). The T-R periodogram algorithm and its using for time series kinematic models composition have been already in details described in few previous papers [see *Komitov*, 2021 and cites therein].

In the present study two kinematic models have been build – the first one on base of the mean monthly old *Ri* index for the epoch January 1750 to December 2014 and the second one is based on the new sunspot index *SN_v2*. The both models are extrapolated and compared until 2080 AD. The magnitudes of SC25, SC26 and SC27 have been predicted on the base of the extrapolations.

Results and analysis

The predicted SC25, SC26 and SC27 magnitudes, obtained by using of the above mentioned prediction models are shown on Table 1. The first column contains the sunspot cycles numbers in Zurich series, while in the next three ones the corresponding predicted values of the sunspot cycles, calculated by one of the above described statistical models are presented. The used formula (1 to 5) a signed as "Type (1-5)". The real SC24 magnitude in 2014 is also shown for comparison in column 5.

By comparison of the presented results it could conclude that: 1. the magnitudes of SC25 and SC26 are similar to the SC24 one; 2 Most probably SC25 and SC26 magnitudes should be arround 80-100 as *Ri*-index (the "classical" old sunspot counting system) or 120-150 in *SN_v2* (the new system). It corresponds to sunspot cycles of moderate sunspot cycles unlike SC17-SC23, which magnitudes are in order of 1.5-2 times higher. This prediction supports the thesis for the beginning of a new grand solar minimum in 21st century.

Some authors suggestthat this grand minimum should be of centurial type as the Gleissberg minimum (1898-1924AD), while according to other ones it should be of Dalton-type [*Abdussamatov*, 2004; *Javaraiah*, 2017] or even of Maunder-type [*Zharkova et al*., 2015]. By authors opinion the new grand solar minimum is of Dalton-type due to the circumstance that it is related to the downward and near minimum phase of quasi 200 yr deVries- Suess solar cycle [see *Komitov*, 2021 and cites therein]. An additional indicator for such suggestion is the fact of Gnevishev-Ohl-Kopecky's rule violation (G-O-K) [*Gnevishev and Ohl*, 1948; *Kopecky*, 1950] for the even-odd pair cycles SC22-SC23. As it has been shown by author and Bonev [*Komitov and Bonev*, 2001] the strong G-O-K violations are precursors namely of Dalton-type grand solar minima.

As it is shown in Fig.1 the new grand Dalton-type minimum should expect to be more continuous as its eponym (the Dalton minimum from 1793/98 to 1833AD) and it will be ended at ~2080 AD (i.e. after SC29 or SC30). The calculated on the base of Waldmeier's rule regression model (Type 1) indicates that SC25 should be slightly higher as SC24, i.e. G-O-K should be valid for the even-odd pair SC24-SC25. This supports also be the auto-regression models on the base of Schove's series (see in Table 1, column 3). On the other hand, the kinematic models (Table 1 and Fig.1) predict a well expressed G-O-K for the sunspots cycles pair SC26-SC27. As it is shown on Fig.1 there a local maximum of sunspot cycles magnitudes near to SC27 or SC28 is predicted. It follows by new downward tendency between SC28 and SC30 and new G-O-K violation for the pair SC28-SC29.

SC\Method	Waldmeier's rule regression for Ri_{max} Type(1); Type(2); Type(3)	Schove's series auto-regression Type(4); Type(5)	TRPA kinematic model Ri_{max} ; (SN_v2_{max})	Real magnitude Ri_{max}
24	72±27; 90±17; 86±16	89±29; 92±27	78±26; (122±38)	82
25	99±26; - ; -	-; -	58±26; (97±38)	-
26	-;-;-	96±29; 94±27**	79±26; (142±38)	-
27	-;-;-	-;-	113±26; (164±38)	-

Table 1. The predicted and real values of SC24 –SC27 magnitudes

(** - by using of predicted SC25 magnitude on the base of 'Waldmeier's rule')

Very interesting situation is predicted by the both kinematic models for the minimum between SC 26 and SC27 around 2038 AD. This minimum should be very shallow and SC26 seems to be very closely pressed to the more powerful SC27. Such scenario is possible in the case if a significant mixing of the convective zone fluxes of the both sunspot cycles occurs during and even before this minimum. Thus a significant part of observed during the SC26 sunspot activity downward phase could belong to the next SC27 if the magnetic polarity of active regions will be taken into account. That's why the "pure" SC26 sunspot activity could be significantly weaker as the predicted or observed one.

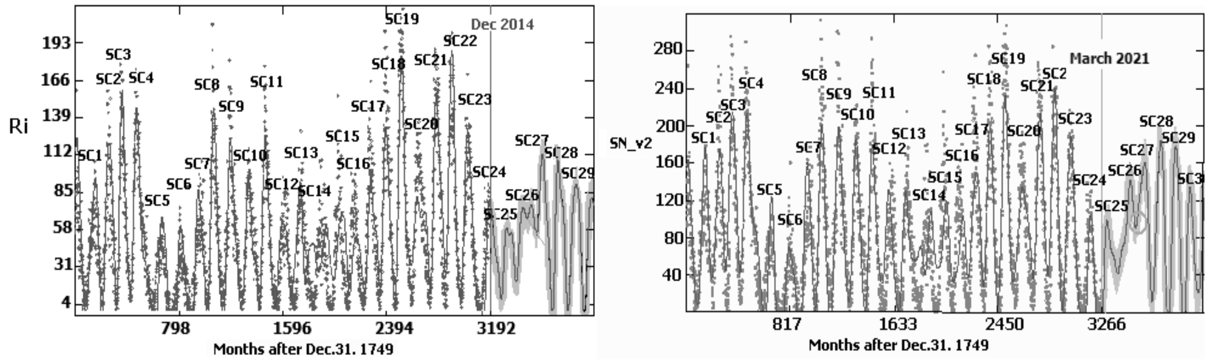

Fig.1 Kinematic model of Zurich sunspot series (old version (left panel): Jan. 1749-Dec.2014) on the base of T-R periodogramm analysis and its extrapolation up to SC30 maximum (~2080 AD); the new version (right panel): Jan. 1750-March.2021

References

Abdussamatov, H.I., 2004, About the long term coordinated variations of the activity, radius, total irradiance of the Sun and the Earth's climate, paper presented at the International Astronomical Union symposium, No.223

Bard E., Raisbeck G., Yiou F. and Jouzel J., 1997, Solar modulation of cosmogenic nuclide production over the last millennium: comparison between 14C and 10Be records, Earth and Planet. Sci. Lett., v150, 453 –462

Clette, F., Lefèvre, L., 2016, The New Sunspot Number: assembling all corrections, Solar Physics, 291, DOI: 10.1007/s11207-016-1014-y.

Damon,P. E. And Sonett,C.P., 1991, in The Sun in Time, ed.Sonett.,C.P.,Giampapa,M.S

Gnevishev. M., Ohl A., 1948, 22yr cycle in solar activity (in Russian), Astron.J,, 38, 18-22

Javaraiah, J., , 2017, " Will Solar Cycles 25 and 26 Be Weaker than Cycle 24?", Solar Physics, Volume 292, Issue 11, article id.172, 13

Komitov B. , 1997, The Schove's series. Centural and Supercentural variations of the solar activity. Relationships between adjacent 11-year cycles, Bulg.Geoph.J,23,74 –82

Komitov B. and Bonev B., 2001 Amplitude Variations of the 11-year Solat Cycle and the Current Maximum 23, Astrophys. J. Lett v.554,L119-L122, 2001 June 10

Komitov B. and Kaftan V., 2003 Solar Activity Variations for the Last Millenia. Will the Next Long-Period Solar Minimum be Formed?, International Journal of Geomagnetism and Aeronomy,v.43,No5,2003, 553-561

Komitov, B., Duchlev, P., Stoychev, K., Dechev, M Koleva, K. , 2011, Determination of the sunspot minimum epoch between the cycles No 23 and 24 and prediction of the cycle No 24 magnitude on the base of the 'Waldmeier's Rule '. Bulg. Astron J., 16, 45-49

Komitov B., 2021, The European Beech Annual Tree Ring Widths Time Series, Solar-Climatic Relationships and Solar Dynamo Regime Changes, Atmosphere 12(7), 829

Kopecky, M., 1950, Cycle de 22 ans de l'activit´e solaire, B. Astron. Institute of Czechoslovakia,, 2, 14–16

Reimer P.J +29 coauthors, 2013, INTCAL13 AND MARINE13 RADIOCARBON AGE CALIBRATION CURVES 0–50,000 YEARS CAL BP, RADIOCARBON, Vol 55, Nr 4,, p 1869–188

Schove, D. J. 1955, The Sunspot Cycle 649 BC to AD 2000, J. Geophys. Res., 60, 127

Schove D.J. ,1983, Sunspot Cycles (Stroudsburg: Hutchinson Ross, Pennsylvania.)

Stuiver M. and Quay P.D., 1980, Changes in Atmospheric Carbon -14 Attributed to a Variable Sun ,Science, v207,No 44, 26

Usoskin I.G., 2013, A History of Solar Activity over Millennia: ArXiv-0810.3972v3

Wittman A. D and Xu Z.D., 1987, A catalogue of sunspot observations from 165 BC to AD 1684, Astron. Astrophys., Supl.Ser.70, 83-94

Zharkova V.V., Sheperd S.J., Popova E., Zharkov S.I., Heartbeat of the Sun from Principal Component Analysis and prediction of solar activity on a millennium timescale, Nature, Sci Reports, open access, 2015, 5:15689; doi: 10.1038/srp15689

Temporal Analysis of the GCR Flux Obtained from the Liulin-MO Instrument in Orbit around Mars

Krastev[1] K., Semkova[1] J., Koleva[1] R., Benghin[2] V., Drobyshev[2] S.

[1]Space Research and Technology Institute, Bulgarian Academy of Sciences
[2] Institute of Biomedical Problems of Russian Academy of Sciences

Abstract.

In this article we present the results of measurements of the radiation environment obtained from the Liulin-MO instrument on ExoMars Trace Gas Orbiter (TGO) in orbit around Mars for the last three years. Special attention is paid to two interesting events that occur with a rapid change in the flux of cosmic rays, measured by the instrument. The possible connection between these two events and the increased solar activity for the respective time intervals, characterized by the manifestation of coronal mass ejections and solar flares, is shown.

Introduction

The radiation field in interplanetary space is complex, composed of galactic cosmic rays (GCR) and solar energetic particles (SEP). The GCR - charged particles that originate from sources beyond the Solar System - represent a continuous radiation source. The variations of the GCR flux is determined mainly by its interaction with interplanetary magnetic field (IMF). The interplanetary magnetic field is formed by the solar wind (solar plasma flow), which carries away the frozen magnetic fields (regular and random) into the interplanetary space. The depth of the modulation of this interaction depends on several factors - the size and direction of the regular component, the size of the random component of the magnetic field, i.e. from its disturbance, from the speed of the solar wind, etc. (Toptygin., 1985). All these events are in one way or another related to the cycles of solar activity.

The dosimetric telescope Liulin-MO for measuring the radiation environment onboard the ExoMars TGO (Semkova et al, 2018) is a module of the Fine Resolution Epithermal Neutron Detector (FREND), (Mitrofanov et al. 2018). The parameters that Liulin-MO measures are energy deposition spectra, particle flux and dose rate in 2 perpendicular direction. TGO was inserted into Mars science orbit (circular orbit with about 400 km altitude, 74^0 inclination, ~ 2 hours orbit period) on 9 April 2018. On 16 April 2018 Liulin-MO was switched on and since then operates almost continuously (Semkova et al, 2021). The relatively short period of our data obtained in Mars orbit (three years) allows us to trace only part of the 11-year variation of galactic cosmic rays, but it allows us to observe short term variations in the charged particles flux, caused by large-scale disturbances of the solar wind (Forbush effect). There are two main types of solar wind disturbances: recurrent and sporadic (Belov., 2008). Recurrent Forbush decreases are caused by high speed solar wind streams flowing from coronal holes. Non-recurrent Forbush effects are associated with coronal mass ejections (CME) that pass into an interplanetary cloud (ICME).

Observations

The data for the entire period during which the Liulin –MO instrument is in scientific orbit around Mars are shown in Figure 1.

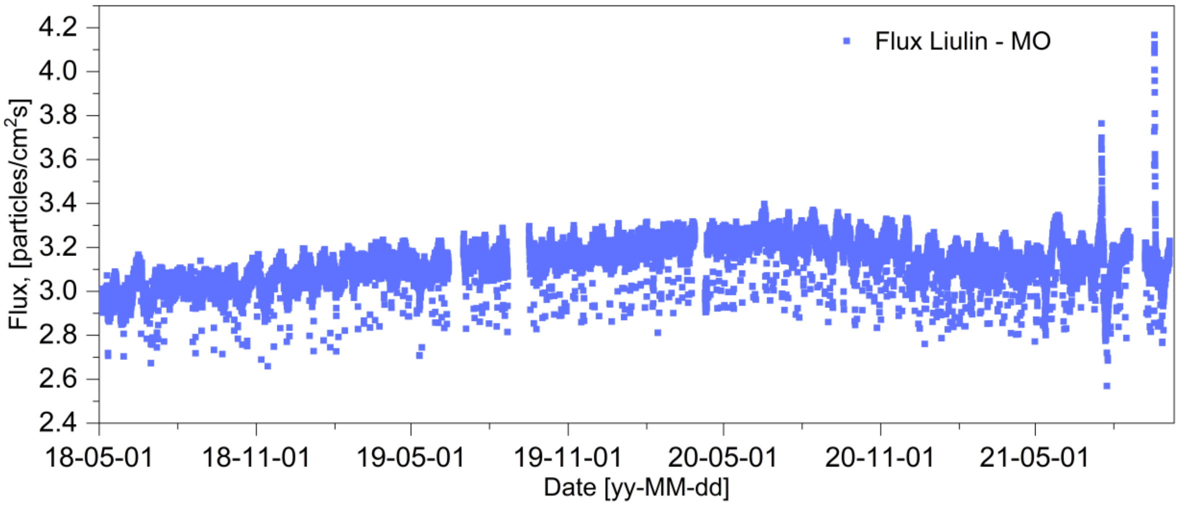

Figure 1. Data for the period 1 May 2018 to 30 September 2021, measured by the Liulin-MO instrument.

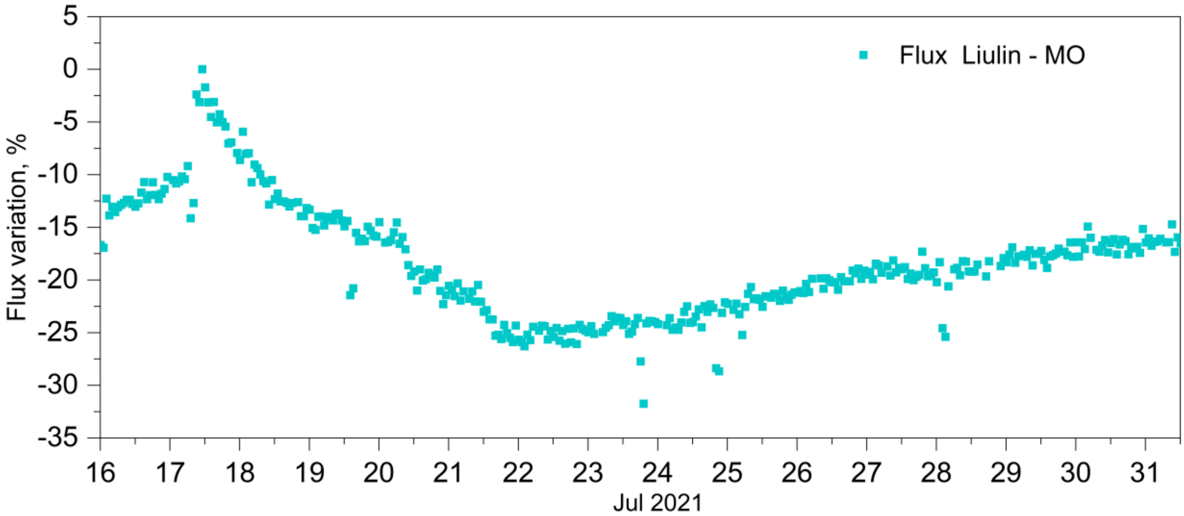

Figure 2. The July, 2021 event.

The two events of 17 July and 17 September 2021 stand out clearly. The event of July 17 is expressed in an initial increase in the charged particle flux followed by a decrease of about four days (see Figure 2). This event has a typical time profile of an Forbush effect caused by coronal mass ejection. First the instrument is hit by the accelerated by the wave front to high energies solar material - SEP, forming the pick in the particle flux. After several days to Mars arrive the dense solar plasma which causes the Forbush depression. Unlike the July event, the september event lacked a Forbusch decrease. The time profiles of the two spikes are identical. Initially for about 5-7 hours there is an increase in the flux and then within 30 hours it reaches the initial values.

Analysis

Figure 2 shows that the Forbusch decrease was most likely caused by several CMEs separated in time. In the interval 13-17 July, several CMEs were registered. As an illustration, three events from the CACTus/LASCO database are shown, which we can relate to our measurements (see Figure 3, 4, 5). The SPE preceding Forbusch effect was most likely caused by CME from 17.07.

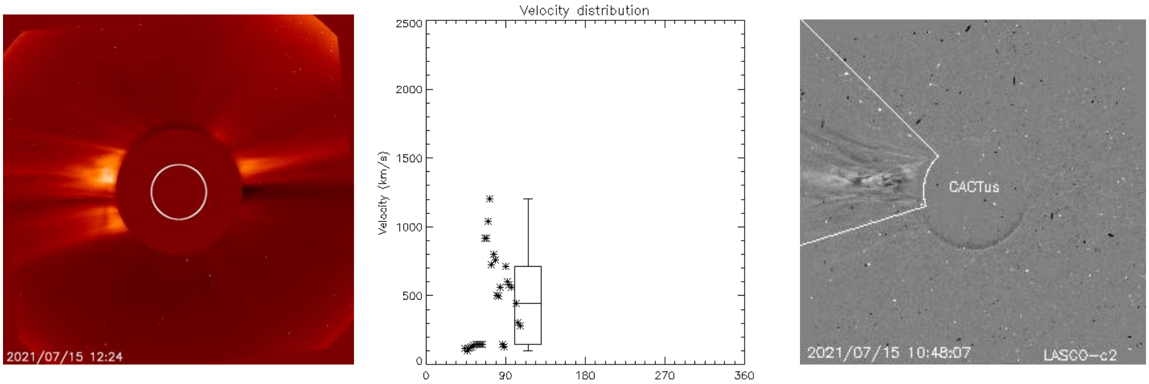

Figure 3. The CME (0035) from July 15, 2021 and its velocity distribution.

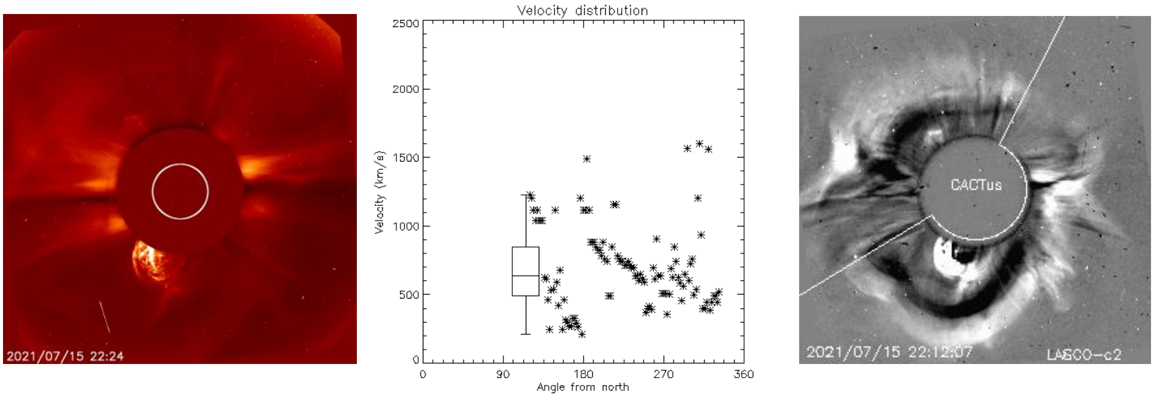

Figure 4. The CME (0036) from July 15, 2021, and its velocity distribution.

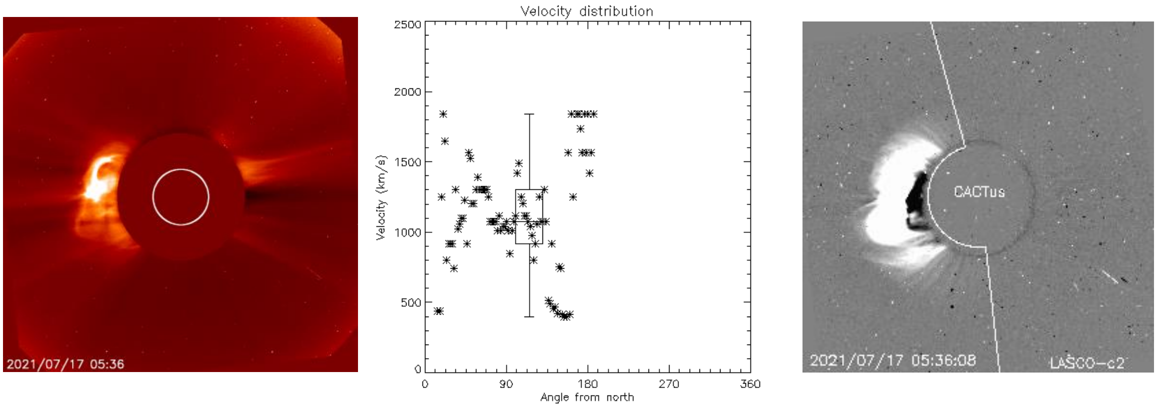

Figure 5. The CME from July 17, 2021 and its velocity distribution.

It is now widely agreed that SEPs come from two different sources with different acceleration mechanisms working: the flares themselves release impulsive events while the coronal mass ejection (CME) shocks produce gradual events. It is not excluded that the event we observe on September 17 (Figure 6) is the so-called hybrid event (Papaioannou at al, 2016). The solar flare that we associate with the increase in the CR flux is shown in Figure 7.

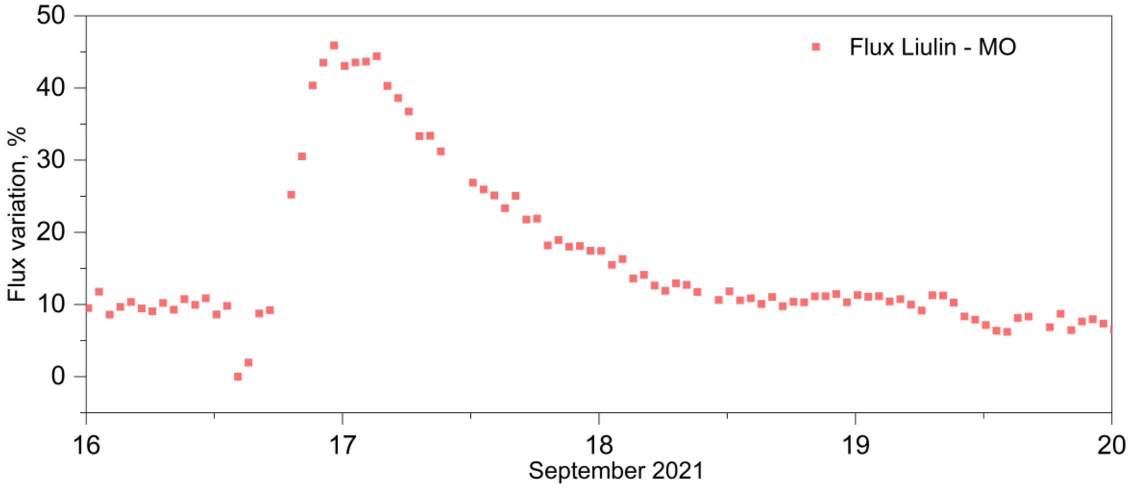

Figure 6. The event from 17 September, 2021 - rapid increase in the flux of cosmic rays.

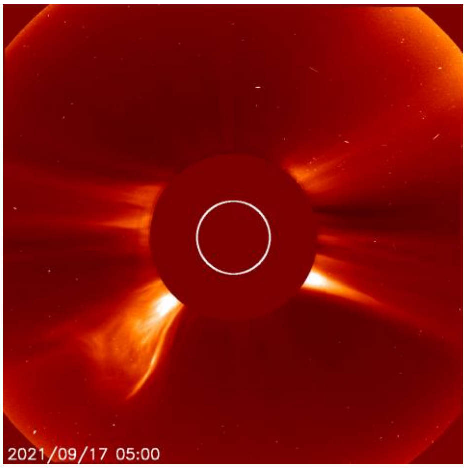

Figure 7. Solar flare associated with the event from 17 september, 2021.

Conclusions

The registration of the two discussed events allows us to trace the propagation in the interplanetary space of sporadic magnetic fields caused by phenomena such as CME and solar flares. This work is in progress. Comparison of the Liulin-MO measurements with the measurements of fluxes of the charged particles by the neutron detectors of FREND instrument, as well as comparison with the parameters of the magnetic field and solar wind in Mars orbit for the discussed events are planned.

Acknowledgements

The CME Catalog used in this work is generated and maintained at CACTus/LASC0 CME database: https://wwwbis.sidc.be/cactus/catalog.php. The work in Bulgaria is supported by Project No 129 (Grant KP-06 Russia 24) for bilateral projects of the National Science Fund of Bulgaria and Russian Foundation for Basic Research and by Contract No 4000133961/21/NL/SC funded by the Government of Bulgaria through an ESA Contract under the Plan for European Cooperating States.

References

Belov, A.V. (2008) Forbush effects and their connection with solar, interplanetary and geomagnetic phenomena, Proceedings of the International Astronomical Union 4(S257):439 – 450, 2008.

Mitrofanov I., A. Malakhov, B. Bakhtin, D. Golovin, A. Kozyrev, M. Litvak, M. Mokrousov, A. Sanin, V. Tretyakov, A. Vostrukhin, A. Anikin, L.M. Zelenyi, J. Semkova, S. Malchev, B. Tomov, Y. Matviichuk, P. Dimitrov, R. Koleva, T. Dachev, K. Krastev, V. Shvetsov, G. Timoshenko, Y. Bobrovnitsky, T. Tomilina, V. Benghin, V. Shurshakov, 2018. Fine Resolution Epithermal Neutron Detector (FREND) onboard the ExoMars Trace Gas Orbiter, Space Science Reviews, August 2018, 214:86, https://doi.org/10.1007/s11214-018-0522-5.

Semkova, J., R. Koleva, V. Benghin, T. Dachev, Yu. Matviichuk, B. Tomov, K. Krastev, St. Maltchev,P. Dimitrov, I. Mitrofanov, A. Maklahov, D. Golovin, M. Mokrousov, A. Sanin, M. Litvak, A. Kozyrev, V. Tretyakov, S. Nikiforov, A. Vostrukhin, F. Fedosov, N. Grebennikova, L. Zelenyi, V. Shurshakov, S. Drobyshev, 2018. Charged particles radiation measurements with Liulin-MO dosimeter of FREND instrument aboard ExoMars Trace Gas Orbiter during the transit and in high elliptic Mars orbit, Icarus, Vol. 303, Pp 53-66, https://doi.org/10.1016/j.icarus.2017.12.034

Semkova, J., R. Koleva, V. Benghin, T. Dachev, Yu. Matviichuk, B. Tomov, K. Krastev, St. Maltchev, P. Dimitrov, I. Mitrofanov, A. Maklahov, D. Golovin, M. Mokrousov, A. Sanin, M. Litvak, A. Kozyrev, S. Nikiforov, D. Lisov, A. Anikin, V. Shurshakov, S. Drobyshev, 2021. "Results from radiation environment measurements aboard ExoMars Trace Gas Orbiter in Mars science orbit in May 2018 - December 2019", Icarus, June 2021, 114264, https://doi.org/10.1016/j.icarus.2020.114264

Papaioannou, A., Sandberg, I., Anastasiadis, A., Kouloumvakos, A., Georgoulis, M., Tziotziou, K., Tsiropoula, G., Jiggens, P., Hilgers, A. (2016) Solar flares, coronal mass ejections and solar energetic particle event characteristics, Space Weather and Space Climate 6(A42), 2016.

Toptygin, I. N. (1985) Cosmic Rays in Interplanetary Magnetic Fields, Springer Netherlands, Geophysics and Astrophysics Monographs 27, 1985, 375 p.

Solar wind stream structure by IPS observations at decameter wavelengths

Kuhai[1,2] N.V., Kalinichenko[1] M.M., Konovalenko[1] O.O., Olyak[1] M.R., Brazhenko[3] A.I.

[1] Institute of Radio Astronomy of NASU, Kharkiv, Ukraine;
2 Oleksandr Dovzhenko Hlukhiv National Pedagogical University, Hlukhiv, Ukraine;
[3] Gravimetrical observatory of Geophysical institute of NASU, Poltava, Ukraine;
E-mail: nkuhai@gmail.com

Abstract.

This work is to demonstrate the potential of the solar wind streams investigations by using interplanetary scintillation observations with the decameter radio telescopes UTR-2 and URAN-2 (Ukraine). The paper includes the description of the techniques used for observations, registration, data processing and analysis. The examples of registrations of corotating flows and streams associated with ICME are shown. Statistics of velocity and spectral index of the interplanetary turbulence for slow and fast solar wind streams is also given.

Introduction

The solar wind observed anywhere in the heliosphere is a collection of streams with different parameters. In this collection of streams, two types of solar wind streams can be distinguished according to their velocity: slow streams with the velocity of around 350 km/s and fast streams with the velocity of around 750 km/s [*Lang*, 1996]. The slow streams are associated with bright coronal streamers, whereas coronal holes and coronal mass ejections (CMEs) are associated with the fast streams. The fast streams have a significant impact on space weather in the heliosphere in general and near the Earth in particular. Therefore, the development of effective methods for detecting solar wind streams, studying their parameters, dynamics and laws to which they obey is of particular interest. Spacecraft measurements allow us to find solar wind streams and obtain their parameters with high accuracy *in situ* [see e.g. *Paularena et al.*, 1997]. There is another possibility to find and investigate solar wind streams. Radiation from compact cosmic radio sources is scattered by density irregularities in the interplanetary plasma. Observations of the intensity fluctuations (interplanetary scintillations or IPS [*Hewish, et al.*, 1964]) caused by this scattering also enable us to detect solar wind streams and study their characteristics [*Coles*,1996; *Gosling and Pizzo*,1999]. The accuracy of the second method is lower than the first one, but it gives us possibility to study solar wind streams anywhere in the heliosphere including the high heliolatitudes where such studies are very rare. Investigations of the solar wind and its stream structure by using IPS techniques are actively made at frequencies of few hundred megahertz [see e.g. *Dennison and Hewish*, 1967; *Kojima et al.*, 1982; *Bourgois et al.*, 1985; *Fallows et al.*, 2008]. In recent years, such work has been actively carried out at decameter radio waves [*Falkovich*, 2010; *Kalinichenko et al.*, 2019]. Decameter radio waves allow conclusions to be made on the solar wind stream parameters both at small and large elongations. The last ones correspond to the solar wind beyond Earth's orbit where high frequencies are only weakly scattered by the rarefied interplanetary plasma.
The aim of this work is to demonstrate the potential of the investigations of the solar wind streams by using interplanetary scintillation observations at decameter radio waves.

Radiotelescopes.

Ukraine has a radio astronomical system URAN which includes the largest in the world decameter radio telescope UTR-2 (that is situated near East Ukrainian city Kharkiv) and four smaller radio telescopes belonging to the different institutions of National Academy of Sciences of Ukraine: URAN-1 (near Zmiiv), URAN-2 (near Poltava), URAN-3 (near Lviv) and URAN-4 (near Odesa), [*Konovalenko et al.*, 2016], Fig.1. The distances between some radio telescopes of URAN system are the next: UTR-2 - URAN-2 is 153 km, UTR-2 - URAN-3 is 946 km and URAN-2 - URAN-3 is 810 km. The operational frequency range of the Ukrainian low frequency radio telescopes is 8 to 32 MHz, decameter radio waves. These are large antenna arrays consisting of hundreds of antenna elements.

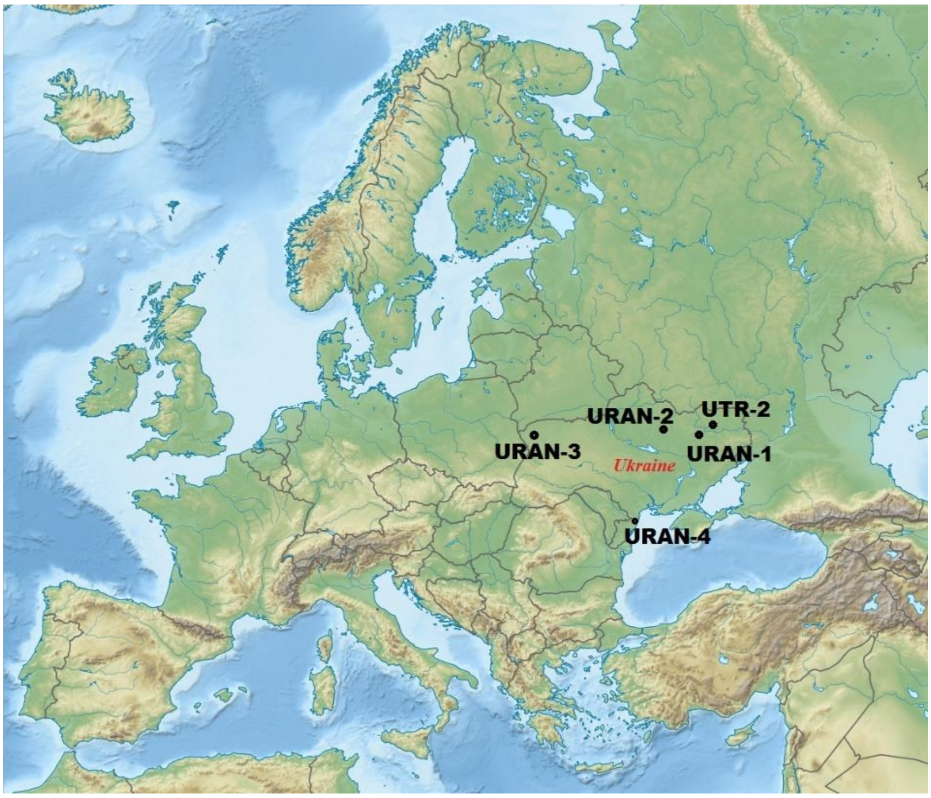

Fig.1. A map of the locations of UTR-2 and URAN radio telescopes throughout Ukraine

Observations

Since 2011, IPS observations have been regularly carried out synchronously with the radio telescopes UTR-2 and URAN-2. If the task requires it, other radio telescopes of URAN system are periodically connected to work. IPS observations are carried out monthly. An ordinary observational session usually lasts for 7 days (1 weak). The list of the observed sources includes several dozen of compact radio sources with small angular size at decameter radio waves (equal or less than 5 arc seconds). These are powerful pulsars and quasars. The radio sources with larger angular size are used for ionosphere monitoring. These are a super nova remnant Cassiopeia A, a radio galaxy Virgo A and others.

Data processing

Records are obtained by using digital spectrum analyzers with parameters: instant band of analysis is 33 MHz (sampling frequency is 66 MHz); the number of channels is 8192; the time and frequency resolutions are 0.5 ms and 4 kHz, respectively; the ADC resolution is 16 bit. The use of the high linearity wideband receivers and records from several radio telescopes allow us to apply a special technique for selecting data, which are not corrupted by Earth's ionosphere and interferences, and to achieve sensitivity that is close to maximal [*Kalinichenko*, 2013]. Fig.2a shows an example of IPS records obtained synchronously with the radio telescopes UTR-2 and URAN-2.

The solar wind stream structure is obtained by fitting the model theoretical characteristics to the experimental ones. Power spectrum (Fig.2b) and dispersion dependence which is obtained from spatial cross-correlation function (Fig. 2c) are usually used as such characteristics. We consider spectrum and cross-correlation function as a sum of contribution from each stream. The model equations are obtained by using Feinman path integral technique [*Frehlich*, 1987]. Among other things, the applied technique uses the fact that power spectra and dispersion dependences depend on stream parameters in different ways [*Olyak*, 2013]. For corotating streams these technique gives good results and allows us to estimate the width of the solar wind stream.

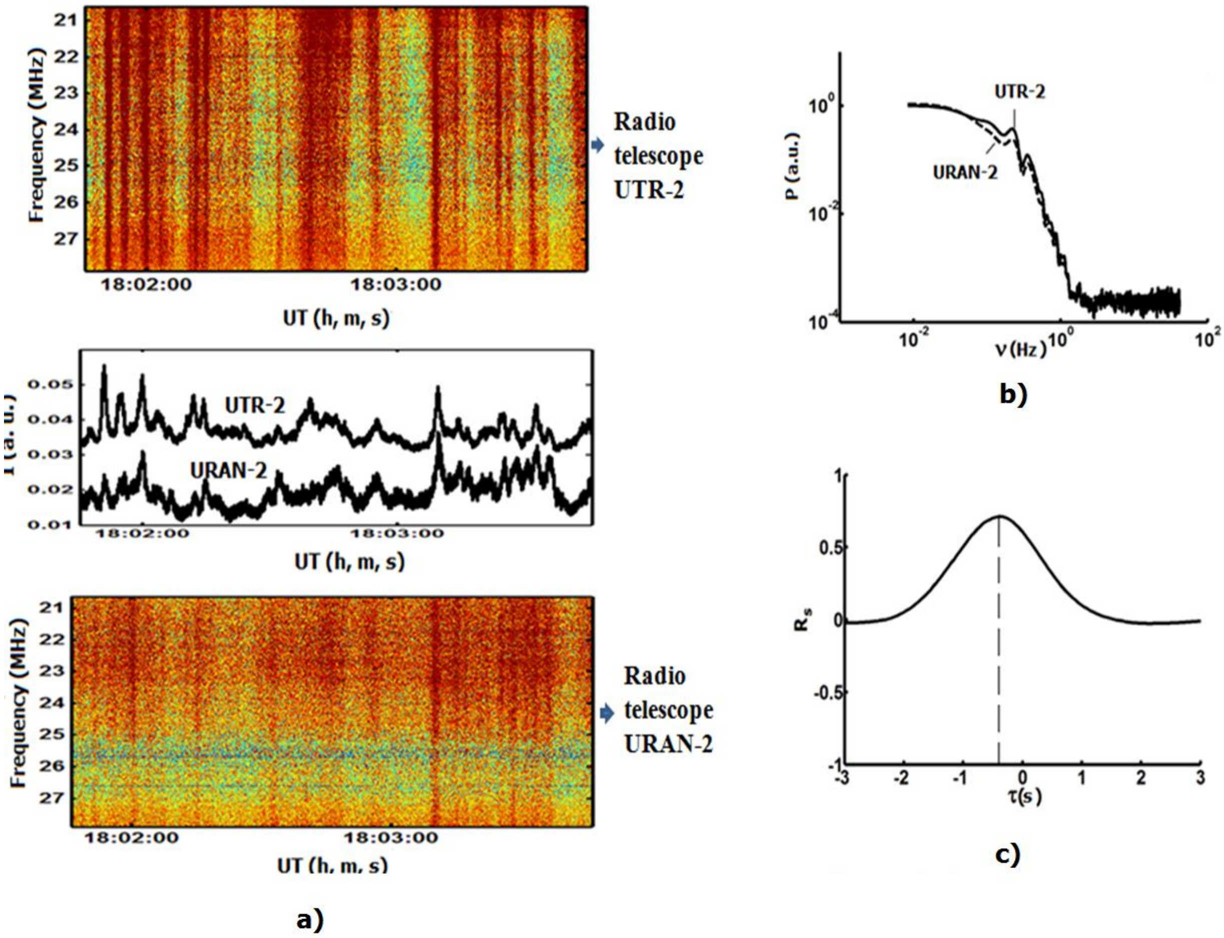

Fig.2. . a) an example of IPS records obtained synchronously with the radio telescopes UTR-2 and URAN-2;b) synchronous power spectra, c) spatial cross-correlation function

Corotating streams

Fig.3 shows an example of the reconstructed stream structure of the solar wind for 3 successive days (January 12, 13 and 14, 2016) obtained by processing UTR-2 - URAN-2 IPS data. The different streams are marked by the different colors, the higher velocity, the deeper red color is used). The data was obtained during observations of Crab Nebula which contains the compact source with angular size about 2 arc seconds. The compact radio source in Crab Nebula is associated with a pulsar J0534+2200. It is seen that on the first day, January 12, only one powerful flow (marked A) is detected on the line of sight to the radio source. The next day, January 13, the stream A becomes weaker and it becomes possible to see the stream B, which is situated ahead of the stream A. The next day, January 14, the streams A and B are pushed by the next stream C. The solar wind speed, which was estimated by using the method of interplanetary scintillations, agreed with the speed measured onboard the Solar and Heliospheric Observatory (SOHO), Wind, and other spacecrafts near the Earth. What is the nature of the solar wind streams detected with the interplanetary scintillation method? These can be both streams in the ordinary sense and the large-scale structures within one stream.

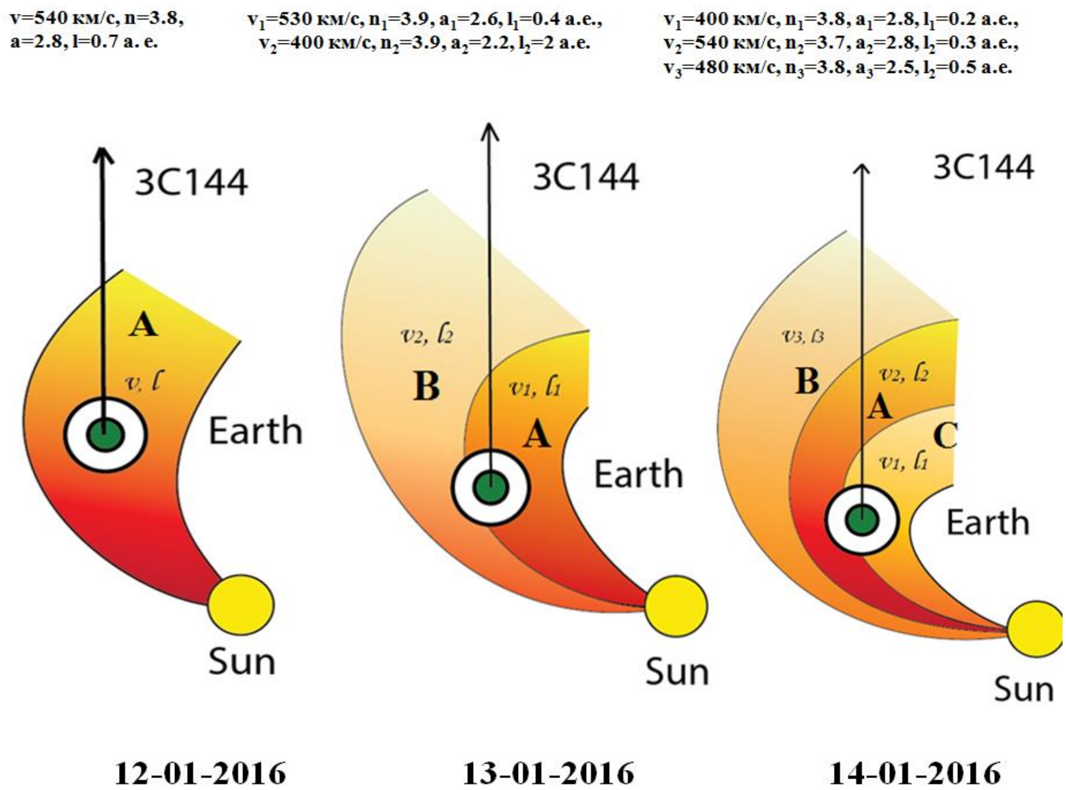

Fig.3. The reconstructed stream structure of the solar wind for 3 successive days (January 12, 13 and 14, 2016). The estimated parameters of the streams A, B and C are marked at the top of Figure too.

Interplanetary coronal mass ejection

Interplanetary coronal mass ejection (ICME) reveals itself in IPS data at decameter wavelengths as a sharp increase of scintillation level (Fig.4a,b). Since the plasma density in ICME is many times higher than in the undisturbed solar wind (Fig. 4c), ICME makes the main contribution to the observed interplanetary scintillations. And since the ICME dimension in the radial direction is a fraction of an astronomical unit, it is logical to model ICME by a phase screen model. Fig.4d shows an example of ICME movement in the interplanetary plasma reconstructed by using IPS observations made with the radio telescopes UTR-2 and URAN-2. It should be emphasized that it is important to trace the ICME throughout the heliosphere including region beyond the Earth's orbit. Why are ICME observations beyond Earth's orbit important? As ICMEs continue slowing at the distances of several astronomical units from the Sun, the investigations of ICME dynamic beyond Earth's orbit will allow us to construct a reliable model of ICME propagation in the heliosphere. Such model for instance makes possible a precise prediction of the arrival time of ICME at the Earth that is the key problem in the space weather science. Decameter radio waves are very useful for such investigations.

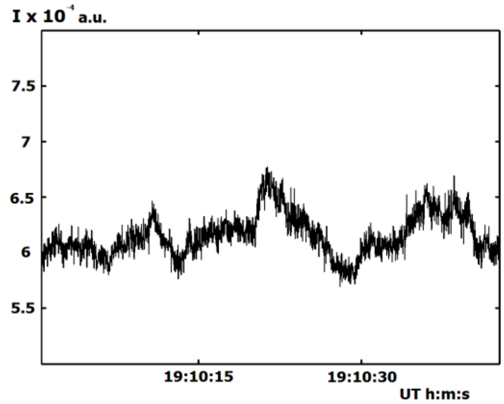

a)

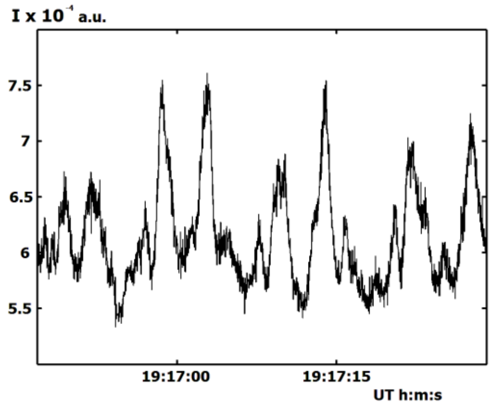

b)

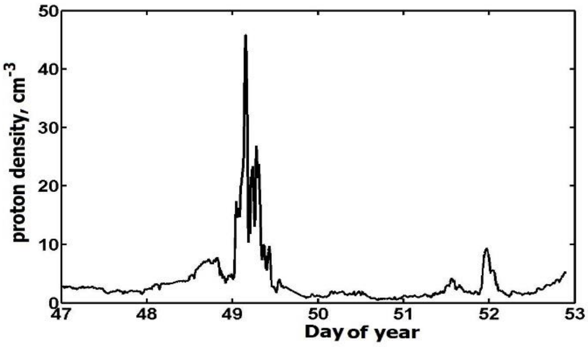

c)

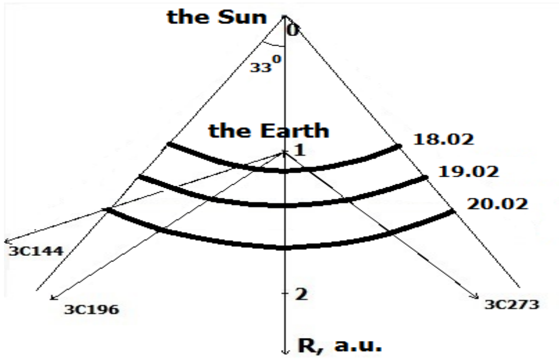

d)

Fig.4. Interplanetary scintillations: a) before and b) during ICME passing across the line of sight to the radio source. Proton density including ICME measured by "Wind" spacecraft - c). The position of ICME in the interplanetary medium obtained by IPS data - d)

Statistics of stream parameters

Large enough volume of experimental data allows us to obtain the statistics of the solar wind stream parameters. Histograms for velocity and spectral index of the interplanetary turbulence are shown in Fig.5.

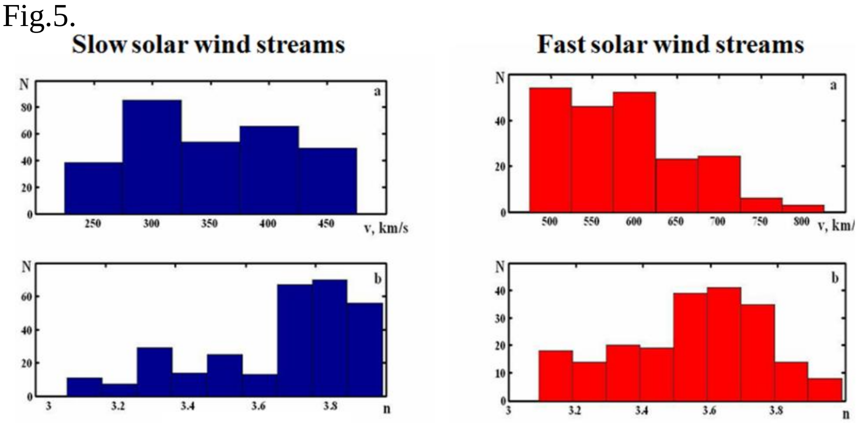

Fig.5.Statistics of parameters of slow and fast solar wind streams: v - velocity, n - spectral index of the interplanetary turbulence.

Conclusions

The results discussed in this work are important for studies of solar wind streams in the interplanetary plasma, including those related to space weather prediction problems. Studies at decameter radio waves can be an additional aid to the investigations of the solar wind streams, which are already being carried out by using IPS technique at higher frequencies and other methods, in particular, *in situ* using spacecraft measurements.

Acknowledgment

This study was supported by Target Complex Program of NAS of Ukraine for Scientific Space Studies for 2018-2022 (projects "Ground-based support by UTR-2-URAN-GURT low-frequency radio telescope system of international and Ukrainian space missions" and “Creation of low-frequency radio astronomical elements and systems for the study of objects in the Universe from the surface of the Moon”) and the project "Instrumental and information connection of radio telescopes UTR-2, URAN, GURT to world networks of low-frequency radio astronomy".

References

Bourgois, G., Coles, W.A., Daigne, G., Silen, J.Turunen, T., Williams, P.J. (1985). Measurements of the solar wind velocity with EISCAT, Astron. Astrophys., 144, 452‑462, 1985.

Coles, W. A. (1996), A bimodal model of the solar wind speed, Astrophysics and Space Science, 243,1, 87–96, 1996.

Dennison, P.A., Hewish, A. (1967). The solar wind outside the plane of the ecliptic, Nature, 213, 343-346, 1967.

Falkovich, I.S., Konovalenko, A.A., Kalinichenko,N.N., Olyak,M.R., Gridin,A.A., Bubnov,I.N., Brazhenko,A.I., Lecacheux, A., Rucker, H. (2010), Dispersion Analysis of Interplanetary Scintillations at Decameter Wavelengths: First Results., Radio Physics and Radio Astronomy, 1, 1, 3-9,2010.

Fallows, R.A., Breen, A.R., Dorrian, G.D. (2008). Developments in the use of EISCAT for interplanetary scintillation, Ann Geophys. 26, 2229‑2236, 2008.

Gosling, J.T., Pizzo, V.J.(1999). Formation and evolution of corotating interaction regions and their dimension structure. Space Science Reviews, 89, 21-52, 1999.

Frehlich, R.G., (1987). Space-time fourth moment of waves propagating in random media, Radio Science 358, 481-492, 1987.

Hewish, A., Scott, P.F., Wills, D. (1964), Interplanetary Scintillation of Small Diameter Radio Sources, Nature, 203, 4951, 1214-1217, 1964.

Kojima, K., Ishida, Y., Maruyama, K., Kakinuma, T., (1982). An observation system of interplanetary scintillation at UHF, Proc. Res. Inst. Atmos. Nagoya Univ., 29, 61,1982.

Kalinichenko, N. N., Falkovich, I. S., Konovalenko, O. O., Brazhenko, A. I. (2013). Separation of Interplanetary and Ionospheric Scintillations of Cosmic Sources at Decameter Wavelengths, Radio Physics and Radio Astronomy, 18, 3, 210-219, 2013.

Kalinichenko, N.N., Olyak, M.R., Konovalenko, A.A., Brazhenko, A.I., Kuhai, N.V., Romanchuk, A.I. (2019). Large-scale structure of solar wind beyond the Earth’s orbit: reconstruction using the data of two-site measurements of interplanetary scintillations in the decameter radio range. Kinematics and Physics of Celestial Bodies, 35, 1, 17–27, 2019.

Konovalenko, A., Sodin, L., Zakharenko, V., Zarka, Ph, Ulyanov, O., Sidorchuk, M., Stepkin S., Tokarsky P., Melnik, V., Kalinichenko, N., Stanislavsky, A., Koliadin, V., Shepelev, V., Dorovskyy, V, Ryabov, V., Koval, A., Bubnov, I., Yerin, S., Gridin, A., Kulishenko, V., Reznichenko, A., Bortsov, V., Lisachenko, V., Reznik, A., Kvasov, G., Mukha, D., Litvinenko, G., Khristenko, A., Shevchenko, V., Shevchenko, V., Belov, A., Rudavin, E., Vasylieva, I., Miroshnichenko, A., Vasilenko, N., Olyak, M., Mylostna, K., Skoryk, A., Shevtsova, A., Plakhov, M., Kravtsov, I., Volvach, Ya., Lytvinenko, O., Shevchuk, N., Zhouk, I., Bovkun, V., Antonov, A., Vavriv, D., Vinogradov, V., Kozhin, R., Kravtsov, A., Bulakh, E., Kuzin, A., Vasilyev, A., Brazhenko, A., Vashchishin, R., Pylaev, O., Koshovyy, V., Lozinsky, A., Ivantyshin, O., Rucker, H., Panchenko, M., Fischer, G., Lecacheux, A., Denis, L., Coffre, A., Grieβmeier, J-M, Tagger, M., Girard, J., Charrier, D., Briand, C., Mann, G. The modern radio astronomy network in Ukraine: UTR-2, URAN and GURT. (2016). Experimental astronomy, 42, 1, 11- 48, 2016.

Lang, K.R. (1996), Unsolved Mysteries of the Sun, Sky and Telescope, 92, 2, 38, 1996.

Olyak, M.R., (2013). The dispersion analysis of drift velocity in the study of solar wind flows,” J. Atmos. Sol.-Terr. Phys. 102, 185‑191, 2013.

Paularena, K.I., Richardson, J.D., Lazarus, A.J., Zastenker, G.N., P.A.Dalin, P.A. (1997). IMP 8, WIND and INTERBALL observations of the solar wind. 22, 7–8, 1997, 629-637, 1997.

Interferometer Observations of Type II and Type IV Bursts at 20 and 25 MHz in May 2014

Melnik V.N.[1], Shepelev V.A.[1], Dorovskyy V.V.[1], Brazhenko[2]

[1] Institute of Radio Astronomy, Kharkiv, Ukraine
[2] Institute of Geophysics, Gravimetrical Observatory, Poltava, Ukraine
e-mail: melnik@rian.kharkov.ua

Abstract.

We discuss results of interferometer observations of Type II and Type IV bursts by the radio telescope UTR-2 on 29 May 2014. Type IV burst was initiated by coronal mass ejection (CME) which moved behind the eastern limb with longitude -110° - -120°. The source of Type IV burst was situated at the distance of 30` at both frequencies 20 and 25 MHz and practically coincided with location with CME core. But their sizes were different at these frequencies, approximately 27` and 35` - 40` at 25 and 20 MHz correspondingly. Type II bursts were consisted of sub-bursts for which their sizes and distances were measured. Sub-bursts have sizes from 10` to 28` and were situated at distances from 20` to 45`.

Introduction

Most papers, which discussed sizes and places of sources of different bursts types at low frequencies, were published in 60-80th of the preceding century (Erickson, 1963, Malitson, and Erickson, 1966, Gergely, and Kundu, 1974, 1975, Nelson, and Robinson, 1975, Abranin, et al., 1976,1980, Chen, and Shawhan, 1978, Dulk et al., 1980). At present some papers considered interferometer observations of Type III bursts (Morosan et al., 2014; Melnik et al., 2017; Mann et al., 2018) and herring-born structures of Type II bursts.

Type II bursts are rare phenomenon so their sizes and distances were measured rarely. According to Nelson and Robinson (1975) Type II sources had sizes mainly from 5' to 20' at 40 MHz and their distances at this frequency were changed from 2Rs to 3.2Rs. Chen and Shawhan (1978) obtained 40' for Type II sizes at 26.4 MHz. Recently Dorovskyy et al. (2018) reported sizes and distances of sources of Type II herring-born sub-bursts at frequencies 20-30 MHz. Average sizes were about 15' with smallest ones about 10'. Distances were from 1.5 Rs to 2Rs (Dorovskyy et al., 2018).

Interferometer observations of decameter Type IV bursts were not frequent also. Gergely and Kundu (1975) observed four Type IV bursts at frequencies 20-60 MHz in 1971 with the radio telescope in Clark Lake and obtained their sizes and positions. They remarked that bursts appeared at high frequencies firstly and after that their radio emissions were registered at lower frequencies. All Type IV sources moved outward the Sun from the distances 1.5-1.9 Rs to 2.5-3.5 Rs. At some distances this movement was deceased. Sizes at low frequencies were larger than those at higher frequencies and were as large as 1.4-1.9 Rs. Chen and Shawhan (1978) measured sizes of Type IV sources also and they found that those sizes were not larger than 30' (1.9 Rs) at 26.4 MHz.

In this paper we consider results of interferometer observations of Type II, and Type IV bursts with the UTR-2 radio telescope, which were carried out in observational campaign May-June 2014.

Observations

Observations in May-June 2014 campaign were conducted at UTR-2 radio telescope (Kharkiv, Ukraine), which worked in an interferometer regime, and at URAN-2 (Poltava, Ukraine) radio telescope, which worked in an usual spectrometric regime. As the saying was in (Melnik et al., 2017, 2018b) sections of east-west and north-south arms of UTR-2 radio telescope (Fig.1) were used in the interferometer regime of observations. This allowed forming interferometer bases 225, 450 and 675 m in the east-west direction and 225, 450, 675, 900, 1125, and 1350 m in the north-south direction. On 27-30 May only the east-west arm was used.

The dynamic spectrum of solar radio emission from 8:44 to 11:25 UT on 29 May 2014 is shown in Fig.2. We see that there was a group of powerful Type III bursts with maximum fluxes of $10^3 s.f.u.$ from 8:45 to 8:55 UT. Polarization of these bursts were not large, only 10%. Frequency drift rates of Type III bursts were about 3 MHz/s. These bursts were generated by active region NOAA 2079, which was situated behind east limb with the longitude angle -110° - -120° (Fig.3a). A flare in this region began at 8:42 UT and ended at 9:12 UT (http://www.helioviewer.org/). Its maximum was at 8:57 UT. So the group of Type III bursts was apparently initiated by this flare. This flare was a cause of CME also, whose mass was $6.2\cdot10^{15} g$ and velocity of 398 km/s. We connect the Type IV burst observed in frequency band of 16-60 MHz (Fig.2) with this CME. The maximum duration of Type IV burst was about 2 hours at 33 MHz. The duration was shorter at lower frequencies. This Type IV burst was weak, its maximum flux was about $10 s.f.u.$ and polarization was up to 40%.

Type II bursts (Fig.2) were imposed on the Type IV burst. There were four of them. They had different drift rates and frequency bands. Type II burst (1) (Fig.2) was registered in the frequency band 17-22 MHz from 9:06 to 9:10 UT. Its drift rate, duration, flux and polarization were 60 kHz/s, 40 s, $50 s.f.u.$ and 20% correspondingly. Other Type II bursts were weaker with fluxes not higher than $10 s.f.u.$ Their polarizations were not higher than 10%. Drift rates were 60, 20 and 20 kHz/s for 2, 3 and 4 Type II bursts (Fig.2) correspondingly. The whole durations of these bursts were more than 2 minutes. All four Type II bursts consisted of sub-bursts with durations of 2-20 s.

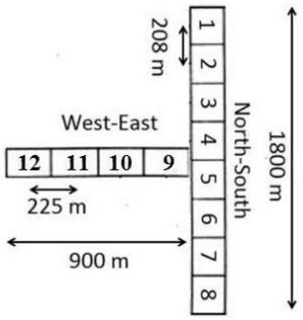

Fig.1. Scheme of the radio telescope UTR-2, which consists of 8 North-South sections and 4 West-East sections.

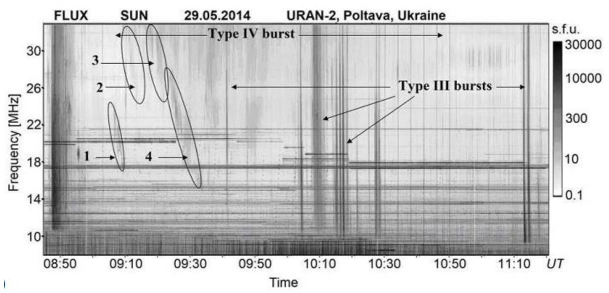

Fig.2. Dynamic spectrum of solar radio emission from 8:43 to 11:23 UT on 29 May 2014 according to URAN-2.

Type II bursts

The first burst (1) (Type II burst) was registered from 9:06 to 9:10 UT in the frequency band 17-22 MHz (Fig.2). We observed it in the interferometer regime at 20 MHz. This burst had fine structure as separate clouds. There were four such sub-bursts with durations 4, 3, 6 and 5 s at 20 MHz. The total duration of Type II burst was 30 s and this is smaller than durations of standard decameter Type II bursts at this frequency (Melnik, et al., 2005). Fluxes of sub-bursts were not high - $17 s.f.u., 108 s.f.u., 38 s.f.u.$ and $19 s.f.u.$ Polarizations of these bursts were not high also, about 1-3%. As a whole Type II burst had frequency drift rate approximately 60 kHz/s. Sizes were following 10`, 20`, 27` and 24` and they were at distances 25`, 28`, 28` and 30` correspondingly. This time the front of CME was situated at this distance too. So we conclude that the burst (1) was generated by the shock ahead of CME.

Next Type II burst (burst 2) (Fig.2) observed from 9:10 to 9:13 UT at 25 MHz. This burst consisted of three sub-bursts with fluxes of $1.3 s.f.u.$, $1.9 s.f.u.$, $3.9 s.f.u.$ Polarizations of sub-bursts were practically zero. Frequency drift rate of this Type II burst the same as for burst 1, about 60 MHz/s. According to interferometer observations sizes of sub-bursts were 15`, 13` and 15`. Distances for all sub-bursts were the same and equaled 35`($2.2 \cdot R_S$).

At times 9:19 - 9:21 and 9:21 - 9:26 UT there were two Type II bursts (3 and 4 bursts) at 25 MHz (Fig.2). At the first period of time different separate sub-bursts had fluxes up to $10 s.f.u.$ Sizes of all sub-bursts were in the range 13`-18` and they were at 30` ($1.9 \cdot R_S$) from the center of the Sun. At the second interval (9:21 - 9:26 UT) fluxes of sub-bursts were $10-30 s.f.u.$ They were a little larger, with sizes up to 20` and they placed at distances about 40`- 45` ($2.5-2.8 \cdot R_S$). Approximately, at this distance at 9:21 - 9:26 UT the CME nose is situated. Thus, we conclude that burst (4) was generated by nose shock and 3 burst was generated by flank shock. As a whole both bursts (3) and (4) drifted with drift rate of 20 kHz/s.

Type IV burst

Type IV burst was observed from 9:10 to 10:50 UT at 33 MHz. Profiles of flux and polarization are shown in the Fig.3. Its maximum flux is about $10 s.f.u.$ and maximum polarization is 40%.We see that flux maximum achieved at about 9:40 UT and polarization maximum was at 10:15 UT, more than half hour latter. Type II bursts were against Type IV burst and we cannot recognize drift of Type IV front. But we can say definitely that Type IV burst continued from 9:18 to 10:25 UT and from 9:19 to 9:25 UT at 25 and 20 MHz correspondingly. Fig.4 shows sizes and places of Type IV burst at 20 and 25 MHz

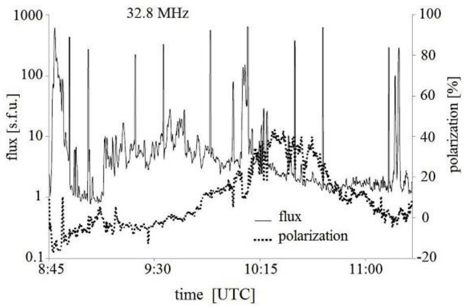

Fig.3. Flux (solid line) and polarization (dotted line) of Type IV burst at 32.8 MHz according to URAN-2 radio telescope.

according to our interferometer observations. We see that centers of Type IV radio emission at both frequencies were situated at the same distances, about 30`, and only at the end of burst at 25 MHz the center of radio emission became closer to the Sun (Fig.4a). Type IV size at 25 MHz was about 27` and it decreased to 20` to the end of the burst. At frequency of 20 MHz, the size was about 37` all time of its existence. Sizes of Type IV burst at 20 and 25 MHz against CME at 9:48 UT are shown in Figure 5. We see that at this time Type IV source coincides with CME on position and size. Later the source of Type IV burst does not move, but CME continues to move with velocity of about 400km/s and we conclude that this Type IV burst is a stationary one.

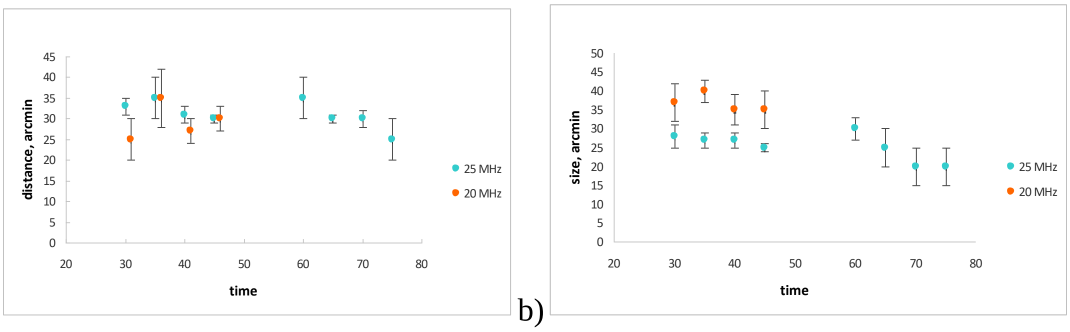

Fig.4. Positions (a) and sizes (b) of Type IV source at 20 and 25 MHz.

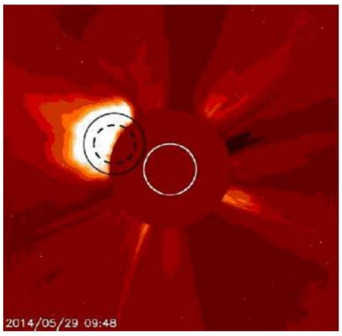

Fig.5. CME at 9:48 UT and source of Type IV burst at frequency of 20 and 25 MHz this time.

Discussion

All discussed Type II bursts have fine structure in the form of sub-bursts that is standard phenomenon for decameter Type II bursts (Melnik et al. 2005). Sub-bursts sizes change from 10` to 30`. Their positions show that they were governed by flank shock. Their brightness temperatures $10^7 K$-$10^9 K$ are close to those of Type III bursts (Melnik et al., 2017). Supposing that frequency drift rate is described by equation ($df / dt = f / 2 \cdot dn / ndr \cdot v$) we find that velocity is higher than CME velocity and correspondingly shock velocity. In our opinion this high velocity is velocity of shock region, which generates radio emission registered by radio telescope but it is not the same shock region. Such situation was already marked in the paper (Dorovskyy et al., 2018) and can present some sort of arc eye effect. As a whole Type II burst had drift rate about 60 kHz/s that give linear velocity about 2000 km/s in Newkirk model [Newkirk, 1961]. This radio emission escaped the distance of $1.9R_S$. The region, which is responsible for Type IV radio emission against CME, is shown in the Fig.5. We see that the CME core can be source of this radio emission. But if in the case of moving Type IV bursts this core moves, in our case the CME core does not move and it situated at the distance of 30`. So we can conclude that this is a stationary Type IV burst. Centers of radio emission at both frequencies 20 and 25 MHz are the same. At the same time sizes at these frequencies are different, 27` and 37` at 25 and 20 MHz correspondingly. We can conclude that moving CME after time 11:00 UT is shock which was initiated by CME core at first stage of movement. The CME core had energy enough to reach the distance 30` and after that core stopped. Such behavior was marked also by Gergely, and Kundu (1974). Kundu and Gergely observed movement of CME to distances 3.5 Rs and after that movement deceased. Our Type IV burst began to go out at first at low frequencies and latter at higher frequencies. Size to the end of the radio emission at 25 MHz decreased to 20` and its brightness temperature at this frequency was $3.2 \cdot 10^7 K$. At the beginning the brightness temperatures of Type IV burst were $3.5 \cdot 10^7 K$ and $1.8 \cdot 10^7 K$ at 25 and 20 MHz correspondingly. The range of radio emission frequency of Type IV burst is not very high, only from 18 to 45 MHz. If we suppose that mechanism of radio emission is plasma one (Melnik et al., 2018) and radio emission is fundamental then we can consider that the highest frequency, 45 MHz, escapes the center of CME core and the lowest frequency, 19 MHz, is radiated at periphery of the core. It means that densities in the center and at the periphery are $n_c = 2.5 \cdot 10^7 cm^{-3}$ and $n_{19} = 4.9 \cdot 10^6 cm^{-3}$ correspondingly. From the equation $n(r) = n_c \exp(-\alpha r)$ (Melnik et al., 2018) we derive that $\alpha = 1.45 / R_{\odot}$ having in mind that at $R_{20} = 18'$ core density is equaled to $n_{20} = 4.9 \cdot 10^6 cm^{-3}$ and at the radius $R_{25} = 13'$ the core density is $n_{25} = 7.7 \cdot 10^6 cm^{-3}$ and in the center of the core density is $n_c = 2.5 \cdot 10^7 cm^{-3}$ (it corresponds to plasma frequency of 47 MHz). The mass of the CME core is $2.9 \cdot 10^{16} g$. This value is higher than the mass from the SOHO catalogue (https://cdaw.gsfc.nasa.gov/CME_list/). If we suppose that radio emission was generated at the second harmonic then mass of the CME core equals $6 \cdot 10^{15} g$ which is closed to (https://cdaw.gsfc.nasa.gov/CME_list/). So we conclude that in this case the radio emission of the CME core occurred at the second harmonic.

References

Abranin, E.P., Bazelian, L.L., Goncharov, N.I., Zaitsev, V.V., Zinichev, V.A., Rapoport, V.O., Tsybko, I.G.(1976) Angular sizes of sources of solar radio bursts in the decameter Range, Soviet Astron. 19, 602, 1976.

Abranin, E.P., Bazelian, L.L., Goncharov, N.I., Zaitsev, V.V., Zinichev, V.A., Rapoport. V.O., Tsybko, I.G. (1980), Positions of Solar Storm Burst Sources by Observations with a Heliograph Based on the UTR-2 Antenna at 25 MHz. Solar Phys. 66, 393, 1980.

Chen, H.S.-L., Shawhan, S.D. (1978), Structure and evolution of solar radio bursts at 26.4 MHz. Solar Phys. 57, 205, 1978.

Dorovskyy, V., Melnik, V., Konovalenko, A., Brazhenko, A., Rucker, H. (2018), Spatial properties of the complex decameter type II burst observed on 31 May 2013. Sun and Geosphere 13, 25.

Dulk, G.A., Gary, D. E., Suzuki, S. (1980), The position and polarization of Type V solar bursts, Astron. Astrophys. 88, 203, 1980.

Erickson, W.C. (1963) High-Resolution Studies of Type III Solar Emission at 11.4-MeterWavelength. J. Geophys. Res. 68, 3169, 1963.

Gergely, T.E., Kundu, M.R. (1974) Decameter Type IV Bursts Associated with Coronal Transients. Solar Phys. 34, 433, 1974.

Gergely, T.E., Kundu, M.R. (1975) Decameter Storm Radiation Solar Phys. 41, 163, 1975.

Malitson, H.H., Erickson, W.C. (1966) Observations of Type III and Type IV Solar Radio Bursts at 26.3 Mc/s. Astrophys. J. 144, 337, 1966.

Mann, G., Breitling, F., Vocks, C., Aurass, H., Steinmetz, M., Strassmeier, K.G., Bisi, M.M., Fallows, R.A., Gallagher, P., Kerdraon, A., Mackinnon, A., Magdalenic, J., Rucker, H., Anderson, J., Asgekar, A., Avruch, I.M., Bell, M.E., Bentum, M.J., Bernardi, G., Best, P., Birzan, L., Bonafede, A., Broderick, J.W., Br • uggen, M., Butcher, H.R., Ciardi, B., Corstanje, A., de Gasperin, F., de Geus, E., Deller, A., Duscha, S., Eisloffel, J., Engels, D., Falcke, H., Fender, R., Ferrari, C., Frieswijk, W., Garrett, M.A., Grie_meier, J., Gunst, A.W., van Haarlem, M., Hassall, T.E., Heald, G., Hessels, J.W.T., Hoeft, M., Horandel, J., Horneffer, A., Juette, E., Karastergiou, A., Klijn, W.F.A., Kondratiev, V.I., Kramer, M., Kuniyoshi, M., Kuper, G., Maat, P., Marko, S., McFadden, R., McKay-Bukowski, D., McKean, J.P., Mulcahy, D.D., Munk, H., Nelles, A., Norden, M.J., Orru, E., Paas, H., Pandey-Pommier, M., Pandey, V.N., Pizzo, R., Polatidis, A.G., Rafferty, D., Reich, W., Rottgering, H., Scaife, A.M.M., Schwarz, D.J., Serylak, M., Sluman, J., Smirnov, O., Stappers, B.W., Tagger, M., Tang, Y., Tasse, C., ter Veen, S., Thoudam, S., Toribio, M.C., Vermeulen, R., van Weeren, R.J., Wise, M.W., Wucknitz, O., Yatawatta, S., Zarka, P., Zensus, J.A.: (2018) Tracking of an electron beam through the solar corona with LOFAR. Astron. Astrophys. 611, A57, 2018.

Mel'Nik, V.N., Konovalenko, A.A., Abranin, E.P., Dorovskyy, V.V., Stanislavsky, A.A., Rucker, H.O., Lecacheux, A. (2005), Solar sporadic radio emission in the decametre waveband. Astronomical and Astrophysical Transactions 24, 391, 2005.

Melnik, V.N., Brazhenko, A.I., Konovalenko, A.A., Dorovskyy, V.V., Rucker, H.O., Panchenko, M., Frantsuzenko, A.V., Shevchuk, M.V. (2018a) Decameter Type IV Burst Associated with a Behind-the-limb CME Observed on 7 November 2013. Solar Phys. 293, 53, 2018.

Melnik, V.N., Shepelev, V.A., Poedts, S., Dorovskyy, V.V., Brazhenko, A.I., Rucker, H.O.(2018b), Interferometric Observations of the Quiet Sun at 20 and 25 MHz in May 2014, Solar Phys. 293, 97, 2018.

Melnik, V., Shepelev, V., Brazhenko, A., Dorovskyy, V., Rucker, H., Stefaan, S. (2017) Interferometer Observations of Solar Type III Bursts by the Radio Telescope UTR-2. Sun and Geosphere 12, 105, 2017.

Morosan, D.E., Gallagher, P.T., Zucca, P., Fallows, R., Carley, E.P., Mann, G., Bisi, M.M., Kerdraon, A., Konovalenko, A.A., MacKinnon, A.L., Rucker, H.O., Thid_e, B., Magdalenic, J., Vocks, C., Reid, H., Anderson, J., Asgekar, A., Avruch, I.M., Bentum, M.J., Bernardi, G., Best, P., Bonafede, A., Bregman, J., Breitling, F., Broderick, J., Br • uggen, M., Butcher, H.R., Ciardi, B., Conway, J.E., de Gasperin, F., de Geus, E., Deller, A., Duscha, S., Eisloffel, J., Engels, D., Falcke, H., Ferrari, C., Frieswijk, W., Garrett, M.A., Grie_meier, J., Gunst, A.W., Hassall, T.E., Hessels, J.W.T., Hoeft, M., H • orandel, J., Horner, A., Iacobelli, M., Juette, E., Karastergiou, A., Kondratiev, V.I., Kramer, M., Kuniyoshi, M., Kuper, G., Maat,P.,Markoff, S., McKean, J.P., Mulcahy, D.D., Munk, H., Nelles, A., Norden, M.J., Orru, E., Paas, H., Pandey-Pommier, M., Pandey, V.N., Pietka, G., Pizzo, R., Polatidis, A.G., Reich, W., Rottgering, H., Scaife, A.M.M., Schwarz, D., Serylak, M., Smirnov, O., Stappers, B.W., Stewart, A., Tagger, M., Tang, Y., Tasse, C., Thoudam, S., Toribio, C., Vermeulen, R., van Weeren, R.J., Wucknitz, O., Yatawatta, S., Zarka, P. (2014), LOFAR tied-array imaging of Type III solar radio bursts. Astron. Astrophys. 568, A67, 2014.

Nelson, G.J., Robinson, R.D. (1975), Multi-Frequency Heliograph Observations of Type II Bursts, Proceedings of the Astronomical Society of Australia 2, 370, 1975.

Newkirk, J. Gordon (1961), The Solar Corona in Active Regions and the Thermal Origin of the Slowly Varying Component of Solar Radio Radiation. Astrophys. J. 133, 983, 1961.

Thompson, A.R., Moran, J.M., Swenson, G.W. Jr. (2001), Interferometry and Synthesis in Radio Astronomy, 2nd Ed., John Wiley and Sons, New York, 2001.

Preliminary Results of Statistical Study on the Solar Cycle 24: Active Regions vs. Coronal Mass Ejections

Nakeva Y. [1], Tsvetkov Ts. [2], Petrov N. [2], Shirov, G. [2]

[1] Aix-Marseille University, Department of Physics, France
[2] Institute of Astronomy and National Astronomical Observatory,
Bulgarian Academy of Sciences, Sofia, Bulgaria
E-mail: tstsvetkov@astro.bas.bg

Abstract

To better understand the relation between different solar activity phenomena we summarized the active regions (ARs) data of NOAA Space Weather Prediction Center and coronal mass ejections (CMEs) SOHO/LASCO observations for the period of solar cycle 24 (December 2008 – December 2019). The initial sample consists of 1736 ARs and 16108 CMEs.

We present our first results of statistical analyses on the occurrence of different active processes during the last solar cycle.

Introduction

According to the SILSO Database of Royal Observatory of Belgium[1] in December 2019 began the solar cycle (SC) 25 that is expected to reach its maximum in July 2025, with peak of 115 sunspots [*Yan et al.*, 2021]. This makes the present moment appropriate for summarizing and analyzing the data about the previous solar cycle 24. It started with solar minimum in December 2008 and peaked in April 2014 with sunspot number of 116.4 (based on the 13-month smoothed monthly sunspot number time series[1]). That makes cycle 24 the fourth weakest solar cycle in history after cycles 5, 6 and 14 with maximum sunspot number of 82, 81.2 and 107.1, respectively. It lasted exactly 11 years, which puts it in the middle of the ranking of solar cycles' duration – 12 cycles lasted longer and 11 others ended before the eleventh year after their beginning. The longest one ever recorded (SC4, 1784-1798) continued 13 years and 7 months, while the shortest one – only 9 years (SC2, 1766-1775).

Coronal mass ejections (CMEs) are large structures of plasma and magnetic fields that are expelled from the Sun into the heliosphere [*Webb and Howard*, 2012]. Each CME can carry a mass of up to 10^{13} kg and release up to 10^{25} J of energy from the Sun into the heliosphere [*Guo et al.*, 2007]. As progenitor of the most powerful and extreme space weather events, they are of interest for technological reasons. They are considered as active solar events and therefore the frequency of their occurrence depends on the solar cycle progression. The peak of CMEs is usually 6-12 months after the maximum of the solar cycle [*Raychaudhuri*, 2005; *Robbrecht et al.*, 2009]. Near solar minimum appear about 0.5 CMEs per day, while near maximum the number increases up to 6 per day [*Yashiro et al.*, 2004]. Near the minimum of solar activity, they are observed at lower latitudes and tend to migrate to higher latitudes with cycle progression. Their latitude distribution is more similar to the distribution of helmet streamers than to the Maunder's butterfly diagram.

It is believed that CMEs often originate from active regions (ARs) [*Wang and Zhang*, 2008] – complex structures that unite various solar activity events that take place in different layers of solar atmosphere. As areas of magnetic flux concentration they appear as bright regions at latitudes between -30° and +30° [*Priest*, 2014].

According to a study of 32 CMEs, 84% are associated with ARs [*Subramanian and Dere*, 2001]. Other researchers link almost all CME events associated with flares (stronger than class C3.0) with ARs [*Yashiro et al.*, 2005]. More detailed analysis of 224 CMEs, observed between

[1] http://sidc.oma.be/silso/cyclesminmax

1997 and 1998, found that about 63% of the CMEs are AR-related, about 53% of the ARs produced at least one CME, and about 14% of ARs generated 3 or more CMEs during one transit across the visible disk [*Chen et al.*, 2011].

We present a new statistical study on the active regions and coronal mass ejections detected during the solar cycle 24. Our sample consists of 1736 ARs and 16108 CMEs observed between December 2008 and December 2019. These are preliminary results of larger research on different types of solar activity events of SC24.

Data selection

a) Active regions

We adopt the list of detected ARs during the SC24 given by the NOAA Space Weather Prediction Center[2]. The AR 11018 that appeared on 2009 May 23 is the first one observed at latitude higher than 30° since December 2008. Therefore, we assume it as the first AR from the SC24 and use it as a starting point in our analyses.

The latest AR included in our report is the NOAA 12754 that appeared on 2019 December 25. One year after the beginning of the SC25 ARs with latitudes lower than 30° are occasionally observed after that, but they are not part of the current study because of the uncertainty about their affiliation to the SC24.

The explored sample consists of 1736 ARs. We tracked the changes in their position and configuration for each day they were detected, which makes overall 12108 different records in our sample.

b) Coronal mass ejections

We use LASCO coronagraphs data and the SOHO LASCO CME CATALOG [*Yashiro et al.*, 2004] to determine whether there was a CME associated with an AR. Since the CME location information is defined by central position angle (CPA), we convert the AR heliographic coordinates to two-dimensional CPA and require that the difference between the CPAs of the AR and the CME to be not more than 20° taking into account the irregular forms and sizes of both events and the projection effects [*Munro et al.*, 1979].

For the observed period between December 2008 and December 2019 a total of 16108 CMEs were detected by LASCO coronagraphs.

Association rates

The yearly mean total number of events, presented on Figure 1, confirms the well-known fact that both ARs and CME events follow the SC variation. The frequency of their occurrence increases around the solar maximum. The peak at their activity was observed in 2014 (coinciding with the solar maximum of SC24 in April 2014) when 6.79 CMEs and 0.85 ARs per day are detected on average. Their weakest activity was registered in 2018 with mean of 1.3 CMEs and 0.1 ARs per day. The values for CMEs are higher than reported by other researchers, but still close to the ones considered as typical [*Yashiro et al.*, 2004].

[2] https://www.swpc.noaa.gov/products/solar-region-summary

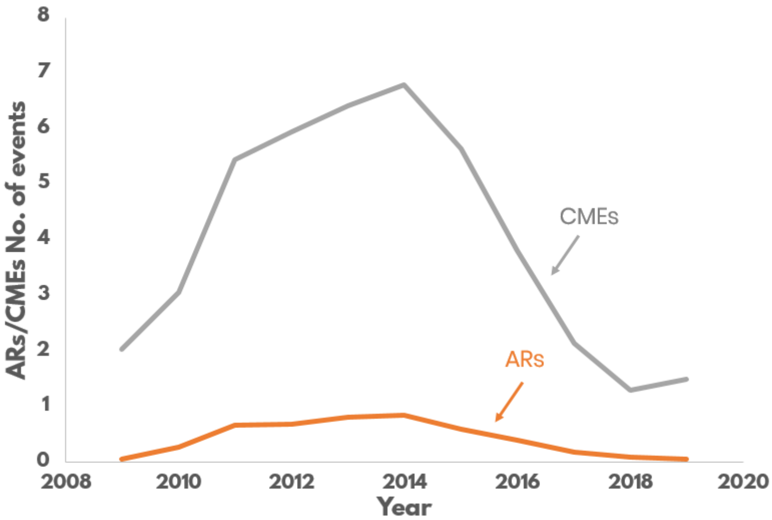

Fig.1. Yearly mean total number (total daily number of events/365) of ARs/CME events during the SC24.

A bit more complex is the comparison between the number of days with lack of activity per year (Figure 2). The least number of days without CMEs were registered in 2015 – 0 and for a period of 3 years around the maximum of SC24 (2013-2015) there were only 4 CME-less days. This coincides with the expectation that the peak of activity of CMEs might be registered 6-12 months after the solar maximum [*Raychaudhuri*, 2005; *Robbrecht et al.*, 2009]. At the same time, in 2018 the days without mass ejections were 92 (most for the explored period). ARs were observed least frequently in 2019 – in 339 days no ARs were detected, while in 2014 that happened in only 155 days. As the sunspots are largely accepted as the most representative active structure for the solar cycle progression, all days between 2012 and 2015 were completely spotless except for one day in 2014.

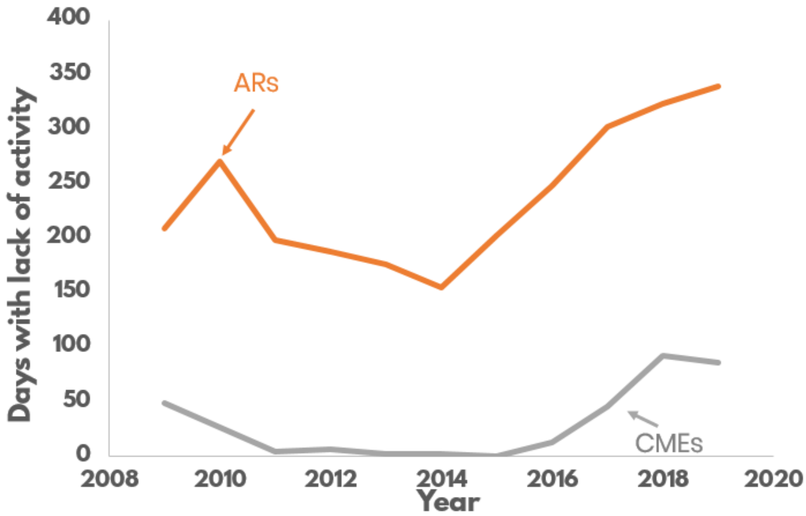

a) *Fig.2. Days with lack of observed ARs/CMEs per year during the SC24.*

Finally, the comparison between the number of observed CMEs and ARs (Table 1) shows that more than 31% of 16108 CMEs cannot be associated with an AR, but about 90% of ARs produce CMEs. The number of CMEs linked with AR source (about 68%) coincides well with previously reported results – 63% [*Chen et al.*, 2011] and is close to the value of 84% estimated by *Subramanian and Dere* [2001] despite the number of events included in the different studies is dramatically distinct (224 and 32, respectively vs. more than 16000). The reverse case shows closer values as we report about 10% ARs that do not generate any CME and that 73% of all 1736 ARs are CME-rich (produced more than 2 CMEs), which is exactly 81% of the ARs that are source of at least one ejection event. Other study estimated the CME-less ARs as 47% and 14% of CME-rich ARs [*Chen et al.*, 2011].

Table 1. Relationship between the ARs and CMEs observed during SC24.

<table>
<tr><td colspan="2" rowspan="2"></td><th colspan="4">CMEs</th></tr>
<tr><th colspan="2">Number</th><th colspan="2">%</th></tr>
<tr><th colspan="2">AR-related</th><td colspan="2">10984</td><td colspan="2">68.2</td></tr>
<tr><th colspan="2">Non-AR-related</th><td colspan="2">5124</td><td colspan="2">31.8</td></tr>
<tr><th colspan="2">Total</th><td colspan="2">16108</td><td colspan="2"></td></tr>
<tr><td colspan="2"></td><th>-less</th><th>-productive</th><th>-rich (≥3)</th><th>Total</th></tr>
<tr><th rowspan="2">ARs</th><th>Number</th><td>169</td><td>1567</td><td>1269</td><td>1736</td></tr>
<tr><th>%</th><td>9.7</td><td>90.3</td><td>73.1</td><td rowspan="2"></td></tr>
<tr><td colspan="4"></td><td>81.0</td></tr>
</table>

Conclusions

We investigate the link between ARs and CMEs observed during the solar cycle 24 (December 2008 – December 2019) and found the following dependencies:

1. The frequency of occurrence of both events increases around the solar maximum (April 2014) – 6.79 CMEs and 0.85 ARs per day are detected on average.
2. Least days without any registered event were registered in 2015 (for CMEs – 0) and in 2014 (for ARs – 155).
3. More than 68% of explored CMEs are related with an AR.
4. Only less than 10% of all ARs are CME-less.
5. 1269/1736 (73.1%) ARs are CME-rich, which is 81% of the ARs that produced at least one CME.

Acknowledgment

This work is supported by the National Science Fund of Bulgaria with contract No. KP-06-M38/3 and the Bulgarian Ministry of Education and Science under the National Research Programme "Young scientists and postdoctoral students" approved by DCM #577/17.08.2018.

References

Chen, C., Wang, Y., Shen, C., Ye, P., Zhang, J., Wang, S. (2011). Statistical study of coronal mass ejection source locations: 2. Role of active regions in CME production, J. Geophys. Res. 116, A12108.

Guo, J., Zhang, H. Q., Chumak, O. V. (2007). Magnetic properties of flare-CME productive active regions and CME speed, A&A 462, 1121–1126.

Munro, R. H., Gosling, J. T., Hildner, E., MacQueen, R. M., Poland, A. I., Ross, C. L. (1979) The association of coronal mass ejection transients with other forms of solar activity, Sol. Phys. 61, 201-2015.

Priest, E. (2014). Magnetohydrodynamics of the Sun, Cambridge University Press.

Raychaudhuri, P. (2005). Variability of Coronal Mass Ejections, in Coronal and Stellar Mass Ejections, Beijing, China, September 13 – 17, 2004, (Eds.) Dere, K., Wang, J., Yan, Y., vol. 226 of IAU Symposia, pp. 211–212.

Robbrecht, E., Berghmans, D., Van der Linden, R.A.M. (2009). Automated LASCO CME Catalog for Solar Cycle 23: Are CMEs Scale Invariant?, ApJ 691, 1222–1234.

Subramanian, P., & Dere, K. P. (2001). Source Regions of Coronal Mass Ejections, ApJ 561, 372.

Wang, Y., Zhang, J. (2008). A statistical study of solar active regions that produce extremely fast coronal mass ejections, ApJ 680:1516-1522.

Webb, D., Howard, T. (2012). Coronal Mass Ejections: Observations, Living Rev. Solar Phys. 9, 3.

Yan, Y., Stenning, D. C., Kashyap, V. L., Yu, Y. (2021). Forecasting Solar Cycle 25 with a Principled Bayesian Two-stage Statistical Model, Res. Notes AAS 5 192.

Yashiro, S., Gopalswamy, N., Michalek, G., St Cyr, O.C., Plunkett, S.P., Rich, N.B. and Howard, R.A. (2004). A catalog of white light coronal mass ejections observed by the SOHO spacecraft, J. Geophys. Res. 109, 7105.

Yashiro, S., Gopalswamy, N., Akiyama, S., Michalek, G., & Howard, R. A. (2005). Visibility of coronal mass ejections as a function of flare location and intensity, J. Geophys. Res. 110, No. A12S05.

Medium-Term Oscillations of the Solar Activity

Obridko V.N.[1,5], Sokoloff D.D.[1,2,4], Pipin V.V.[3], Shibalova A.S.[1,2,4]

[1]IZMIRAN, Troitsk, Moscow
[2]Physical Faculty, Lomonosov State University, Moscow
[3]Institute of Solar-Terrestrial Physics, Russian Academy of Sciences, Irkutsk
[4]Moscow Center for Fundamental and Applied Mathematics, Moscow
[5]Central Astronomical Observatory of the Russian Academy of Sciences at Pulkovo, St. Petersburg, Russia

Abstract.

Besides the well-known 11-year cycle, longer and shorter characteristic periods can be isolated in variations of the parameters of helio-geophysical activity. In geomagnetic variations, one can also isolate oscillations with characteristic periods of 5-6 years (QSO) and 2-3 years (QBO). Periods of ~36 and ~60 years were revealed in geomagnetic activity variations and a ~60-year periodicity, in correlation between the pressure in the lower atmosphere and the solar activity.We have considered 5-6-year periodicities observed in variations of the sunspot numbers and the intensity of the dipole component of the solar magnetic field. Comparison with different magnetic dynamo models allowed us to conjecture the origin of these oscillations. As a result of the study, we conclude that the 5-6-year activity variations are related to the processes of nonlinear saturation of the dynamo in the solar interior. Quasi-biennial oscillations are actually separate pulses related little to each other. Therefore, the methods of the spectral analysis do not reveal them over large time intervals. They are a direct product of local fields, are generated in near-surface layers, and are reliably recorded only in the epochs of high solar activity.

Introduction

The main cycle of activity with the magnetic-field sign variations taken into account is ~20 years. Accordingly, the SSN variations determined by the energy of the magnetic field (i.e., its square intensity) have a half period (about 10 years). These cycles are determined by a large-scale dynamo process. The equations describing the dynamo process have eigenvalues, which determine this main cycle.

As concerns other periodicities found in the solar cycle, the situation is much more complicated. The difficulty is that the wavelet analysis of sunspot data [Frick et al., 1996] does not recognize 7-year (and 2-year) fluctuations. [Obridko et al., 2006] tried to overcome this difficulty by considering the presence of a subcritical dynamo with a period of about 7 years between the modes. This regime corresponds to a strong toroidal field emerging from the lower part of the convection zone.

In this brief review, we will focus on secondary variations. These are short-term (1-4 years) quasi-biennial oscillations (QBO), medium-term (4-8 years) quasi-sexennial oscillations (QSO), and long-term variations (over 50 years). The origin of these variations is not completely clear. They are apparently associated with the turbulent decay of large-scale magnetic structures, nonlinearity of the dynamo process, and fluctuations of parameters. We do not intend to provide here a comprehensive review of the data available. Rather we are going to outline some possibilities and difficulties of explaining the generation of such variations on the Sun.

A special note (which is appropriate at a geophysical conference) is that many variation periods of the solar activity were first established in variations of geophysical parameters. In this sense, the Earth turns out to be in itself an observational instrument for studying solar activity.

Quasi-biennial oscillations (QBO)

Quasi-biennial oscillations are known almost as widely as the 11-year cycle. Some authors considered them even a more fundamental phenomenon than the 11-year cycle [*Ivanov-Kholodny et al*., 2006*; Ivanov-Kholodny and Chertoprud*, 2009]. There is a vast bibliography devoted to QBO. We will focus here only on a few milestones in the history of the QBO studies.

Quasi-biennial oscillations were first reported by *Reed* [1960] as 26-month oscillations in the system of tropical atmospheric winds. All works published during seven years after that concerned QBO only in the Earth's atmosphere (references can be found in [*Maeda*, 1967]). It was Maeda who first, in 1967, drew attention to the fact that QBOs were also observed in cosmic rays But, there is still no certainty that QBOs on the Sun and Earth are directly related [*Baldwin et al.*, 2001*; Petrick et al.*, 2012].

The next important step was taken in the works by Karin Labitzke and Van Loon [*Labitzke*, 1987; van *Loon and Labitzke*, 1988*; Labitzke and van Loon*, 1989]. They showed that there was a relationship between the polar stratospheric temperature in the northern winter and the solar cycle in the winters when equatorial 50 mb winds were blowing from the west: the fewer sunspots in such winters, the lower the temperature.

Only in the early 1990-ies is was suggested that similar quasi-biennial oscillations could also occur in the Sun [*Djurovic and Pâquet*, 1990*; Hoeksema*, 1991*; Obridko and Gaziev,* 1992].

In 1995, Elena Benevolenskaya published a very important work, which is sometimes mistakenly referred to as the first work on solar QBOs [*Benevolenskaya*, 1995]. In fact, the importance of this work is that she proposed interpretation of QBO as a manifestation of a double dynamo cycle. Later, *Benevolenskaya* [1998] formulated the concept of two spatially separated dynamos - at the base of the convection zone and immediately below the surface.

So, what do we know about QBO today?

Quasi-biennial oscillations are actually separate impulses poorly related to each other. They are a directly produced by local fields in the near-surface layers and are reliably recorded only during the periods of high solar activity.

Figure 1 shows by way of example the squared magnetic field on the photosphere surface averaged over a Carrington rotation as a function of time. One can see that the pulses do not form a quasi-periodic process; individual pulses are not phase-related. The spectral methods do not detect them over large time intervals because of the chaotic nature of the phase shifts.

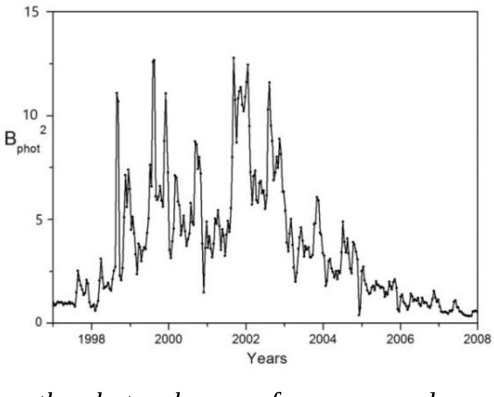

Fig.1. Squared magnetic field on the photosphere surface averaged over a Carrington rotation as a function of time.

To understand the origin of quasi-biennial oscillations, it is important to find out what scale of the large-scale field they are associated with. Such an analysis was performed in [*Obridko and Gaziev,* 1992; *Shelting and Obridko,* 2001; *Obridko and Shelting*, 2003; *Obridko et al.*, 2006]. It turned out that QBOs are associated with structures that are even with respect to the equator. The amplitude of fluctuations in the range of the periods of 1.5-2.5 years was identified on the synoptic maps using the wavelet analysis [*Obridko et al.*, 2006] (see Figure 2).

The magnetic field pattern on the latitude-time diagram looks like a set of bands running from the equator to the poles. The width of the bands is approximately 2 years. The bands drift towards the poles. The duration of the drift of each band is also several years. One can clearly see enhancements in the vicinity of the solar maxima and weakening as the solar activity decreases.

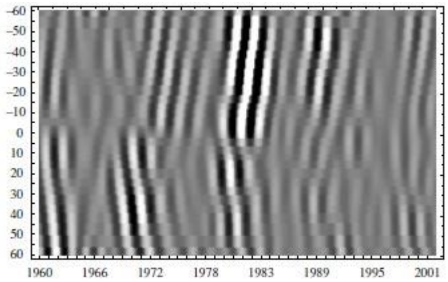

Fig. 2. Synoptic diagram of the amplitude of the magnetic field component even with respect to the equator.

When expanding the photospheric magnetic field into Legendre polynomials, we naturally see the even harmonics in the QBO spectrum best of all. There is also another particularity: the QBO are revealed mainly in the relatively low-order harmonics with l=2 and l=4. This is visible on the wavelet diagram (Fig. 6). In addition, one can clearly see these oscillations intensify at the cycle maxima (Figs.2 and 3). Since the 1980-ies, they have been gradually weakening in accordance with the general trend of decreasing solar activity.

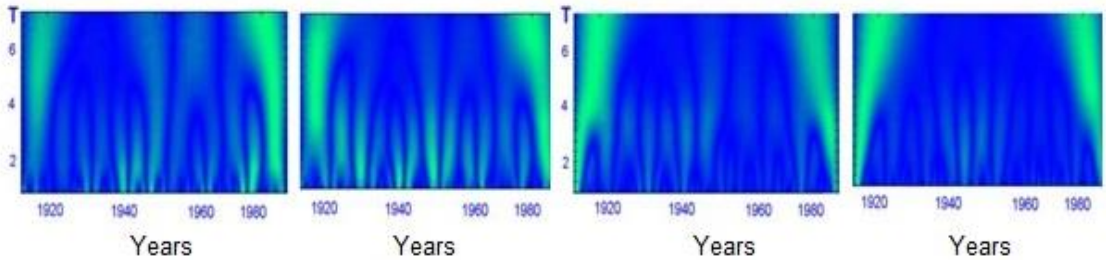

Fig.3. Wavelet diagram of the photospheric magnetic field in the range of 2-6 years. Shown are the harmonics with l=2,4,6,8.

Quasi-sexennial oscillations (QSO)

The analysis of the global magnetic field carried out in these papers, revealed the existence of quasi-sexennial oscillations, i.e., variations with a period of about half an 11-year cycle.

A smoothed butterfly diagram for the spectral band of 5.5-7.5 yr is shown in the Fig. 4 [*Obridko et al.*, 2006]. Note that the stripes that represent amplitude oscillations in this band are anti-symmetric relative to the equator, i.e., they form an odd system.

The existence of QSO was confirmed in a number of subsequent publications. Gavryuseva [2006] isolated this period in the differential rotation of the photospheric magnetic field and Den et al. [2020], in the rotation of the corona. Le Mouël, Lopes, and Courtillot [2019] analyzed the periodicities of sunspots, polar plumes, aa and Dst geomagnetic indices and showed that only the periods of 22, 11, and 5.5 years were present in all realizations.

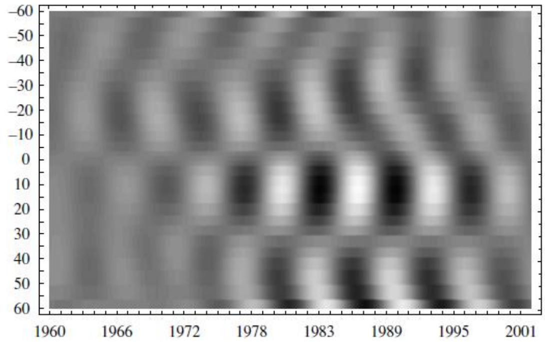

Fig. 4. Smoothed butterfly diagram for a spectral band (5.5-7.5 yr).

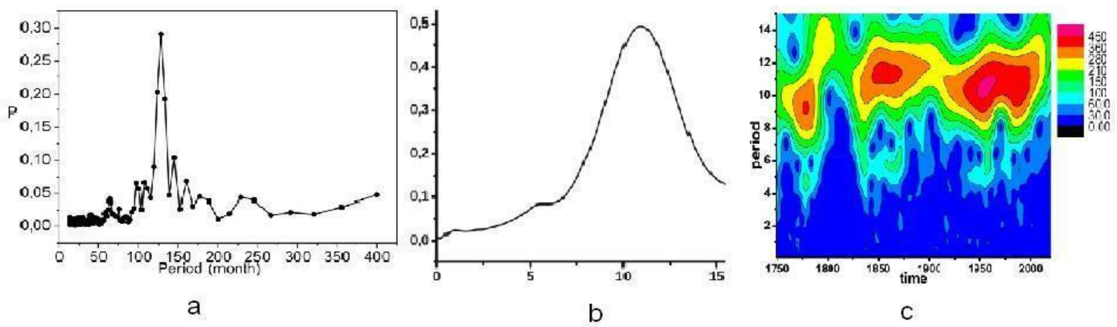

Fig. 5. (*a) Fourier spectrum for the monthly mean sunspot data for the time interval 1749–2019. P is the amplitudes of the Fourier harmonics normalized to the sum of their moduli. The harmonic of the maximal amplitude corresponds to the 25th harmonic, i.e. 126 months. The spectral resolution in the calculated spectrum is about five months. (b) Integral wavelet spectra for sunspot data. (c) The wavelet plane for the real part of the modulus of the sunspot wavelet coefficients (color version online).*

Figure 5 is a result of the spectral analysis of sunspot numbers (SSN) for the period from 1750 to 2021. Fig. 5a illustrates the spectral Fourier analysis. One can readily see QSO, while QBO are virtually absent. Figs. 5b and 5c illustrate the results of the wavelet transform. Here, the QSO are clearly visible, too. Besides that, one can see that oscillations in the range of 5-7 years disappear completely in the epochs of the Dalton and Gnevyshev secular minima, as well as at the present time.

Gleissberg cycle (80-60 years)

This variation was first isolated by Gleissberg in 1944 [*Gleissberg*, 1944, 1965]. The studies of the Gleissberg cycle have revealed variation periods of 55, 65, 58, 78.8, 83, 87, 95, 104, 130, and 150 years [*Kuklin*, 1976; *Silverman*, 1992; *Feynman and Fougere*, 1984; *Ogurtsov et al.*, 2002; *McCracken et al*., 2013; *Usoskin*, 2017]. Most likely, the resulting cycles have no strict periodicity. It is assumed that they are rather variations with a changing period that ranges from 50 to 160 years [*Ogurtsov* et al., 2002].

Because of a significant duration of this cycle, its study requires long series of data. Unfortunately, reliable series of direct solar observations of such duration are not available. Therefore, all studies dealing with the analysis of the Gleissberg cycle usually rely on geophysical data as mentioned above in the Introduction. *Ptitsyna and Demina* [2020] performed a reconstruction based on the statistics of polar lights at mid latitudes with allowance for the screening effect of the Earth's magnetic moment for 700 years (1000-1700). In [*Ptitsyna and Demina*, 2021], they used this 700-year series, as well as the reconstruction based on the content of radiocarbon 14C in tree rings for ~11350 years [Solanki et al., 2004]. The analysis has shown that the Gleissberg cycle consists of three components with the periods of 130-100, 100-80, and 60 years.

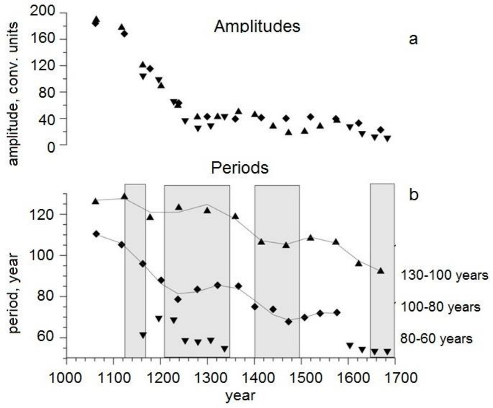

Fig.6. Variations in the amplitude and period of the Gleissberg cycle in 1000-1700. Symbols show the experimental values; the solid line is approximation by the sum of sinusoids. The grey areas correspond to the Oort, Wolf, Spörer, and Maunder Minima. (The figure was borrowed from [Ptitsyna and Demina, 2021], courtesy of the authors).

It should be noted that, like the QBO and QSO, the components of the Gleissberg cycle weaken and somewhat decrease in the epochs of the Grand Minima. The components with a period from 36 to 60 years are described on the basis of geophysical data in [Veretenenko and Ogurtsov, 2014; Veretenenko et al., 2020]. Quasi-periodic fluctuations with these periods are known to exist in geomagnetic activity. An approximately 60-year periodicity was discovered in the evolution of correlations between the pressure in the lower atmosphere and characteristics of solar activity. Similar periods are observed in the cyclonic activity.

2D dynamo model

Now, compare the results of the spectral analysis based on observational data with the data derived from the mean-field dynamo model. A preliminary analysis shows that QSO in the axial dipole can be reproduced in terms of different mean-field dynamo models, e.g. the 1D models proposed in [*Moss and Brandenburg*, 1991; *Moss et al.*, 2008] and the recent 2D model by *Pipin and Kosovichev* [2020]. We have found that the presence of the non-linear dynamo saturation effect is sufficient for the emergence of QSO, both in the parameters of the toroidal magnetic field and in the axial dipole. For our study, we need the parameters of both the axisymmetric and non-axisymmetric large-scale magnetic fields. For this reason, we use the simplified version of the non-axisymmetric dynamo model. The model simulates the dynamo process in a thin layer deep in the convection zone. The effect of magnetic buoyancy seeds the bipolar active region at a random position within the large-scale toroidal magnetic field. This effect accounts for the escape of magnetic energy from the dynamo region, as well. Magnetic buoyancy [*Kitchatinov and Pipin*, 1993] occurs at an arbitrary longitude, at a random time (correlation time of about 0.01 of the dynamo period), and in a randomly selected hemisphere [*Pipin and Kosovichev*, 2018].

To clarify the nature of QSO periodicity, we have followed the evolution of the magnetic field starting with a tiny seed magnetic field [*Sokoloff et al.*, 2020]. It is found out that the 11-year periodicity starts at the very beginning of the magnetic field evolution. Quasi-sexennial oscillations gain considerable power when the dynamo cycle becomes stationary as the magnetic energy reaches the nonlinear saturation state. This means that QSO can be considered a non-linear effect. Note that the non-linear saturation in the model is due to the magnetic buoyancy effect. The time evolution of the axial and equatorial dipoles is discussed. The latter looks like noise, while the time evolution of the axial dipole seems to be almost sinusoidal. Also, we have found out that the maximum power of the axial dipole QSO is observed at the rise and decline of the axial dipole cycle. This result of the dynamo-model agrees qualitatively with our observational findings. The integral wavelet spectra for the axial and equatorial dipole in our dynamo model are shown in Fig.7. However the QBO in model calculations are not pronounced, although they are seen in the observation data.

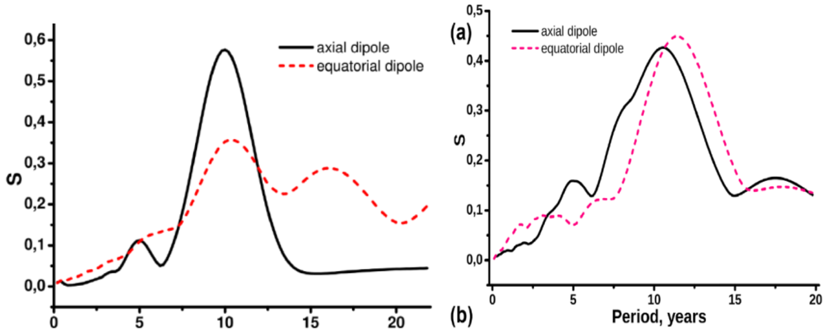

Fig. 7. Dynamo model: the integral wavelet spectra for the axial and equatorial dipole (left – model; right – observed.)

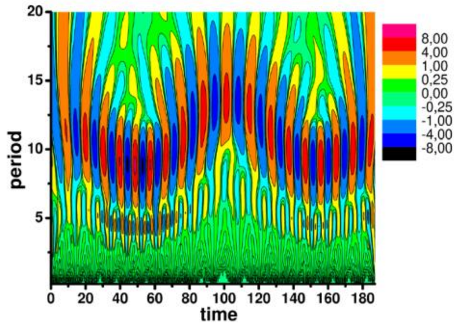

Fig. 8. 2D wavelet spectra for the model with a variable α effect.

Variations in the period of the axial dipole cycle and QSO in the dynamo model output are shown in Fig. 8. We see that a shift of the cycle period results in a corresponding shift of the QSO period.

The model shows that the period of the dipole cycle increases to about 15 years during the grand minimum. The corresponding QSO almost disappear during this period. The model shows similar behavior of the long-term evolution of QSO in the mean flux density of the toroidal magnetic field. Bearing in mind our mechanism for QSO, we suggest that the analysis of longer observational time series of the axial dipole may reveal saturation of the QSO power in the case of strong variations in the axial dipole cycle.

The dynamo model suggests that QSO reflect the nonlinear shape of the cycles of the activity parameters. The model results are reproduced for different types of nonlinearity.

Acknowledgements

The authors are grateful to the WSO teams for a free access to their data. V.Obridko, D.Sokoloff, and A.Shibalova thank RFBR for the support with grants nos. 20-02-00150, and 19-52-53045. The authors appreciate the financial support of the Ministry of Science and

Higher Education of the Russian Federation: VVP subsidy no. 075-GZ/C3569/278; DDS and AAS agreement No. 075-15-2019-1621.No. 20-02-00150, 19-52-53045, as well as DDS and AAS support by BASIS fundation number 18-1-1-77-3.

References

Baldwin M.P., Gray L.J., Dunkerton T.J., Hamilton K., Haynes P.H., Randel W.J., Holton J.R., Alexander M.J., Hirota I., Horinouchi T., Jones D.B.A., Kinnersley J.S., Marquardt C., Sato K., Takahashi M. (2001). The quasi-biennial oscillation, Rev. Geophys., 39, 179. doi:10.1029/1999RG000073.

Bazilevskaya G., Broomhall A.-M., Elsworth Y., Nakariakov V.M. (2014). A Combined Analysis of the Observational Aspects of the Quasi-Biennial Oscillation in Solar Magnetic Activity Space Sci Rev., 186, 35.

Benevolenskaya E.E. (1995). Double Magnetic Cycle of Solar Activity, Solar Phys., 161, Issue 1, 1.

Benevolenskaya E.E. (1998). A model of the double magnetic cycle of the sun. Astrophys. J. Lett., 509, 49. doi:10.1086/311755.

Djurovic D., Pâque, P. (1990). A Publ. Dep. Astron., Univ. Beogr., No. 18, 5.

Feynman J., Fougere P.F. (1984). Eighty-eight year periodicity in solar– terrestrial phenomena confirmed. J. Geophys. Res., 89, 3023–3027.

Gleissberg W. (1944). Evidence for a long solar cycle. The Observatory, 65, 282, 123-125.

Gleissberg W. (1965). The eighty-year solar cycle in auroral frequency numbers. J. Br. Astron. Assoc., 75, 227– 231.

Hoeksema J.T. (1991). J.Geomagn.Geoelecticity, 43, 59.

Ivanov-Kholodny G.S., Mogilevsky E.I., Chertoprud V.Ye. (2006). Fractal dimension of changes in the solar magnetic field energy and quasi-biennial solar activity variations, Geomagn. Aeron., 46, 2, 139-145.

Ivanov-Kholodny G.S., Chertoprud V.E. (2009). Quasi-biennial variations of the total solar flux: Their manifestation in variations of the stratospheric wind and the Earth's rotation velocity, Geomagn. Aeron., 49, 8, 1283-1284.

Kitchatinov L.L., Pipin V.V. (1993). Mean-field buoyancy, A&A, 274, 647.

Kuklin G.V. (1976). Cyclical and secular variations of solar activity. Basic Mechanisms of Solar Activity, ed. V. Bumba and J. Kleczek, Boston, Mass., D. Reidel, 147–190.

Labitzke K., Loon van H. (1989). Associations between the 11-year solar cycle, the QBO and the atmosphere. Part III: Aspects of the association. J.Clim., 2, 554.

Labitzke K. (1987). Sunspots, the QBO, and the stratospheric temperature in the north-pole region, Geophys. Res. Let., 14, 535.

Le Mouël J.L., Lopes F., Courtillot V. (2019). J. Geophys. Res. Space Phys., 124, 8, 6403.

Loon van H., Labitzke K. (1988). Associations between the 11-year solar cycle, the QBO and the atmosphere. Part III: Surface and 700 mb in the Northern hemisphere in winter. J.Clim., 1, 905.

Maeda K. (1967). Quasi-Biennial Cycles in Cosmic Ray Intensity Journal of Atmospheric Sciences, 24, 3, 320.

McCracken K.G., Beer J., Steinhilber F., Abreu J. (2013). A phenomenological study of the cosmic ray variations over the past 9400 years, and their implications regarding solar activity and the solar dynamo. Solar Phys., 286, 2, 609-627.

Obridko V.N., Gaziev G.: 1992, Some comments to the problem of extended cycles in large scale magnetic fields. The solar cycle. Proc. of the National Solar Observatory, Sacramento Peak 12 Summer Workshop, ed. K.L.Harvey, v. 27, p. 410.

Obridko V.N., Shelting B.D. (2003). Meridional drift of large-scale magnetic fields in the Sun, Astron. Zh., 80, 364; 2003, Astronomy Reports, 47, 4, 333 (engl.).

Obridko V.N., Sokoloff D.D., Kuzanyan K.M., Shelting B.D., Zakharov V.G. (2006). Solar cycle according to mean magnetic field data, Monthly Notices of the Royal Astronomical Societies, 365, 827.

Ogurtsov M. G, Nagovitsyn Yu.A. , Kocharov GE, Jungner H. (2002). Long-period cycles of the Sun's activity recorded in direct solar data and proxies. Solar Phys., 211, 371-394. doi: https://doi.org/10.1023/A:1022411209257. 2002.

Pipin V.V., Kosovichev A.G. (2018). Does Nonaxisymmetric Dynamo Operate in the Sun? ApJ., 867, 145.

Pipin V.V., Kosovichev A.G. (2020). Torsional Oscillations in Dynamo Models with Fluctuations and Potential for Helioseismic Predictions of the Solar Cycles, ApJ,. 900, 1, id.26.

Petrick C., Matthes K., Dobslaw H., Thomas M. (2012). Impact of the solar cycle and the QBO on the atmosphere and the ocean, J. Geophys. Res., Atmos., 117, 17111, doi:10.1029/2011JD017390.

Ptitsyna N.G. and Demina I.M. (2021). Solar-Activity Cycles Reconstructed from Statistics on Polar Lights with Allowance for the Contribution of the Main Magnetic Field of the Earth in 1000–2000. Geomagn. Aeron., 61, 3, 312–324. doi: 10.1134/S0016793221020122.

Ptitsyna N.G. and Demina I.M. (2021). Geomagn. Astron., in press.

Reed R.J. (1960). The circulation of the stratosphere. Paper presented at the 40th Anniversary Meeting of the Amer. Meteorol. Soc.

Shelting B.D., Obridko V.N. (2001). Quasi-biennial oscillations of the solar global magnetic field, Astron. and Astrophys. Tr., 20, 491.

Silverman S.M. (1992). Secular variation of the aurora for the past 500 years. Rev. Geophys., 30, 4. 333–351.

Sokoloff D.D., Shibalova A.S., Obridko V.N., Pipin V.V. (2020). Shape of solar cycles and mid-term solar activity oscillations, MNRAS, 497, 4376.

Solanki S.K., Usoskin I.G., Kromer B., Schüssler M., Beer J. (2004). Unusual activity of the Sun during recent decades compared to the previous 11,000 years. Nature, 431, 1084-1087. doi : 10.1038 / nature02995 ..

Usoskin I.G. (2017). A history of solar activity over millennia. Living Rev. Sol. Phys., 14, 3, 1-94. doi:10.1007/s41116-017-0006-9. 2017.

Veretenenko S., Ogurtsov, M. (2014). Stratospheric polar vortex as a possible reason for temporal variations of solar activity and galactic cosmic ray effects on the lower atmosphere circulation Advances in Space Research, 54, 12, 2467.

Veretenenko S., Ogurtsov, Obridko V. (2020). Long-term variability in occurrence frequencies of magnetic storms with sudden and gradual commencements Journal of Atmospheric and Solar-Terrestrial Physics, 205, article id. 105295.

Temporal Variation of Solar Flare Index for the Last Solar Cycle (Cycle 24)

Ozguc[1]A., Kilcik[2]A.

[1]Kandilli Observatory and Earthquake Research Institute, Bogazici University, 34684, Istanbul, Turkey

[2]Department of Space Science and Technologies, Akdeniz University Faculty of Science, 07058, Antalya, Turkey

Abstract: In this study we compared selected some monthly and yearly mean solar activity indices with hemispheric and total Hidrogen-alpha Flare Index (FI) during the last solar cycle (Cycle 24). First we plot the temporal variations of 11 step running average smoothed data sets. Then the cross correlation analyses were performed between FI and other solar indices. Finally, we performed hysteresis analysis by using the yearly mean data sets. We found following results; 1) In general FI data sets show higher correlations with F10.7 compared to other parameters. 2) Total FI shows higher correlation with all other parameters compared to the hemispheric FI data. 3) All data sets show some amount of time delay with FI data sets except F10.7 which does not show any time delay. 4) Hysteresis behavior generally appears during the ascending and descending phases of the cycle.

Introduction

Solar activity variations display themselves in electromagnetic radiation from radio frequencies of a few kHz to powerful gamma rays and also in particle flux. Images of the Sun show that solar flares are one of the most powerful and explosive of all forms of solar activity. Many studies in the solar terrestrial field classified solar flares as one of the most important solar events affecting the Earth as coronal mass ejections (CMEs). The long-term evolution of solar activity, on time scales of the solar cycle and beyond, has been studied from different perspectives using a variety of short and long-term solar activity indicators (Barbieri, and Mahmot, 2004; Knaack, Stenflo, et al, 2005). Kleczek (1952) introduced the quantity Q = i t to quantify the daily flare activity over a 24-h period. He assumed that this relationship roughly gave the total energy emitted by the flare and named it 'flare index' (FI). In this relation, i denotes the intensity scale of importance of a flare in Hα and t denotes the duration of the flare in minutes. Calculated values are available for general use in our observatory website (https://astronomi.boun.edu.tr/flare-index). Some reviews of flare activity using the flare index are given for each day from 1936 to 2001 by Kleczek [1952], Knoska and Petrasek [1984], and Ataç and Özgüç [1998, 2001]. In this paper the results of the determination of the flare index during the solar cycle 24 are presented. Its relation with other solar activity indices is described. Comparison with the similar solar indices of the flare index is examined.

Data and Methods

We compared the amplitudes of cycle 24 by using similar activity indices which are produced at different layers in the solar atmosphere and by different processes. Each of them reflects different physical conditions in the solar atmosphere. The indices to be selected are as follows:

(1) The mean solar magnetic field (MMF): Stanford University, The Wilcox Solar Observatory's measurement of the net magnetic field intensity in microteslas summed over the disk. Such integrated light measurements have been made daily since May 1975 [Scherrer *et al.*, 1977] (*http://wso.stanford.edu/*).

(2) The relative sunspot number (RSN). This is an index of the activity of the entire visible disk of the Sun calculated by the Sunspot Index Data Center (https://wwwbis.sidc.be/silso/datafiles)

(3) Composite record of the Sun's total irradiance (IR) is compiled from measurements made by five independent space-based radiometers since 1978. We used EMPIRE daily reconstruction data set. (*http://www2.mps.mpg.de/projects/sun-climate/data.html /*).

(4) Coronal index (CI) introduced by Rybansky (1975) represents the total irradiance of the green corona emitted from the Sun's visible hemisphere (http://www.suh.sk/online-data).

(5) The Mg II index was first proposed by Heath and Schlesinger (1986). According to Cebula and DeLand (1998), the Mg II index is defined as the ratio between the core emission and the solar continuum intensity in the wings. This index is a dimensionless quantity measuring mid-UV solar activity. We used GOME-2A Mg II Index version. http://www.iup.uni-bremen.de/UVSAT/datasets/mgii

(6) solar radio flux (F10.7) is derived from the daily measurements of the integrated emission from the solar disc at 10.7 cm wavelength, which have been made by the National Research Council (NRC) of Canada since 1947. The flux values are expressed in solar flux units (1 s.f.u.=10^{-22} $Wm^{-2}Hz^{-1}$) and originate in the chromosphere and corona. (http://www2.mps.mpg.de/projects/sun-climate/data.html)

Analysis and Results

To investigate the possible relationship between hemispheric/total solar FI and other data sets used in this study the temporal variation, the cross correlation and the hysteresis analysis were performed. In Figure 1 we presented the temporal variation plots of all data sets used in this study for the whole Solar Cycle 24 (from 2009 to 2020). To remove the short term fluctuation and reveal the long term variations an 11 step running average smoothing method were applied. From this figure we obtained the following results; 1) North and south hemisphere FI data show different temporal behavior that the north hemisphere FI data access to its maximum around 2012 while the south hemisphere data reach its maximum around 2015 like all other solar indices used in this study. 2) All data sets used in this study have a double peak structure that this structure was not so remarkable in south hemisphere FI, CI and TSI data sets. 3) The second peaks dominated in all data sets except north hemisphere FI data.

The cross-correlation analyses have been performed between hemispheric/total FI and the other studied parameters in order to find the highest correlation with delay times. The cross-correlation function is derived up to a time lag of ±48 months, with a step of one month. Calculated correlation coefficients between the FI and other solar activity indicators (CI, F10.7, RSN, Mg II, TSI, and MMF) are shown in Figure 2, and calculated correlation coefficients for the most probable time lags and their Fisher's test errors at a 95 % significance level are presented in Table 1.

From Figure 2 and Table 1 we access the following results: i) North and South hemisphere FI data sets show the same amount of correlations with all other data sets used in this study, ii) the highest correlations exist between total FI and other parameters in all cases without any exception, iii) all data sets show their maximum correlation with FI data sets by some amount

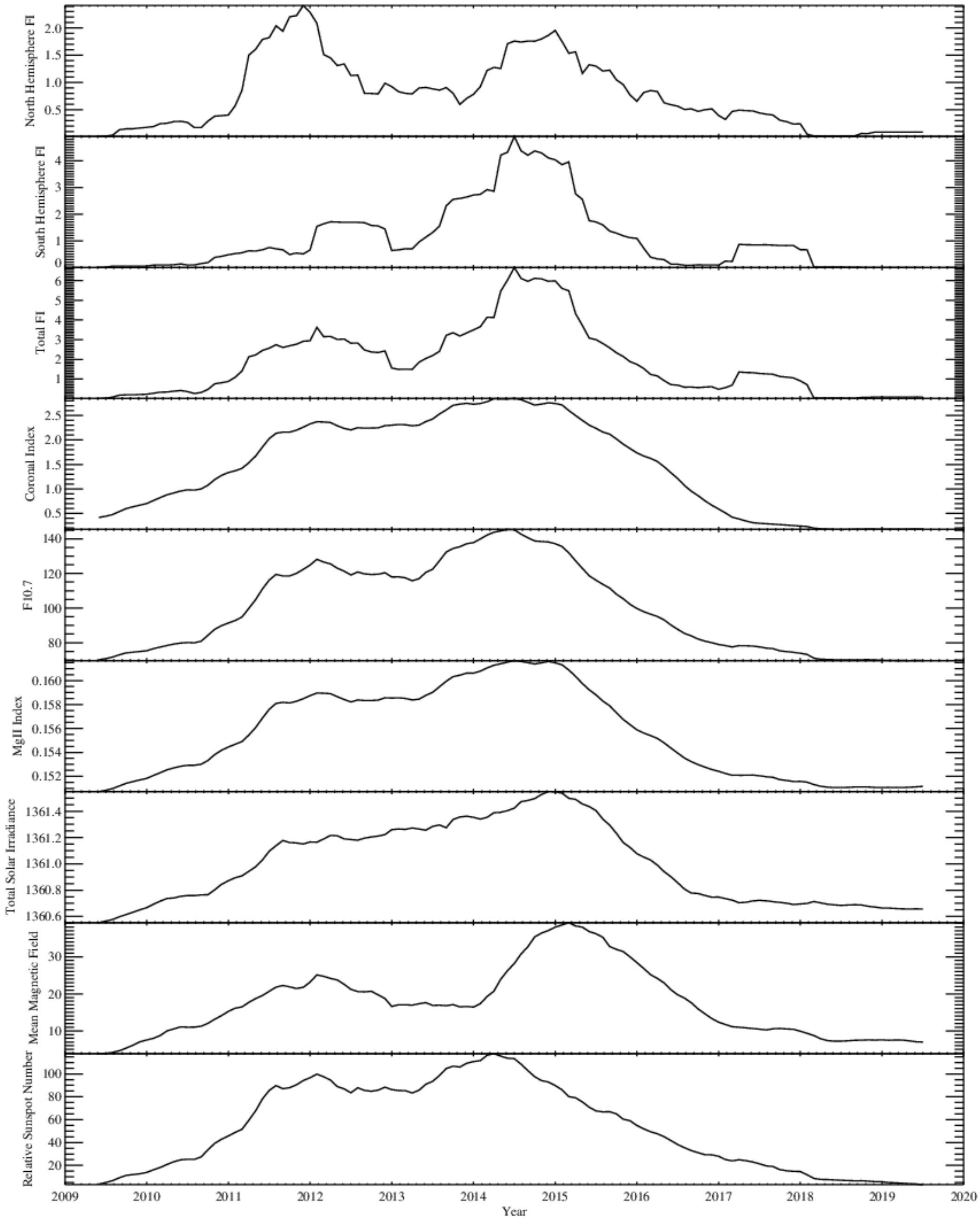

Figure 1. The temporal variation of all data sets used in this study during the Solar Cycle 24 (2009-2020).

of time delay except F10.7 data. It has the highest correlation coefficient and zero time delay in all cases.

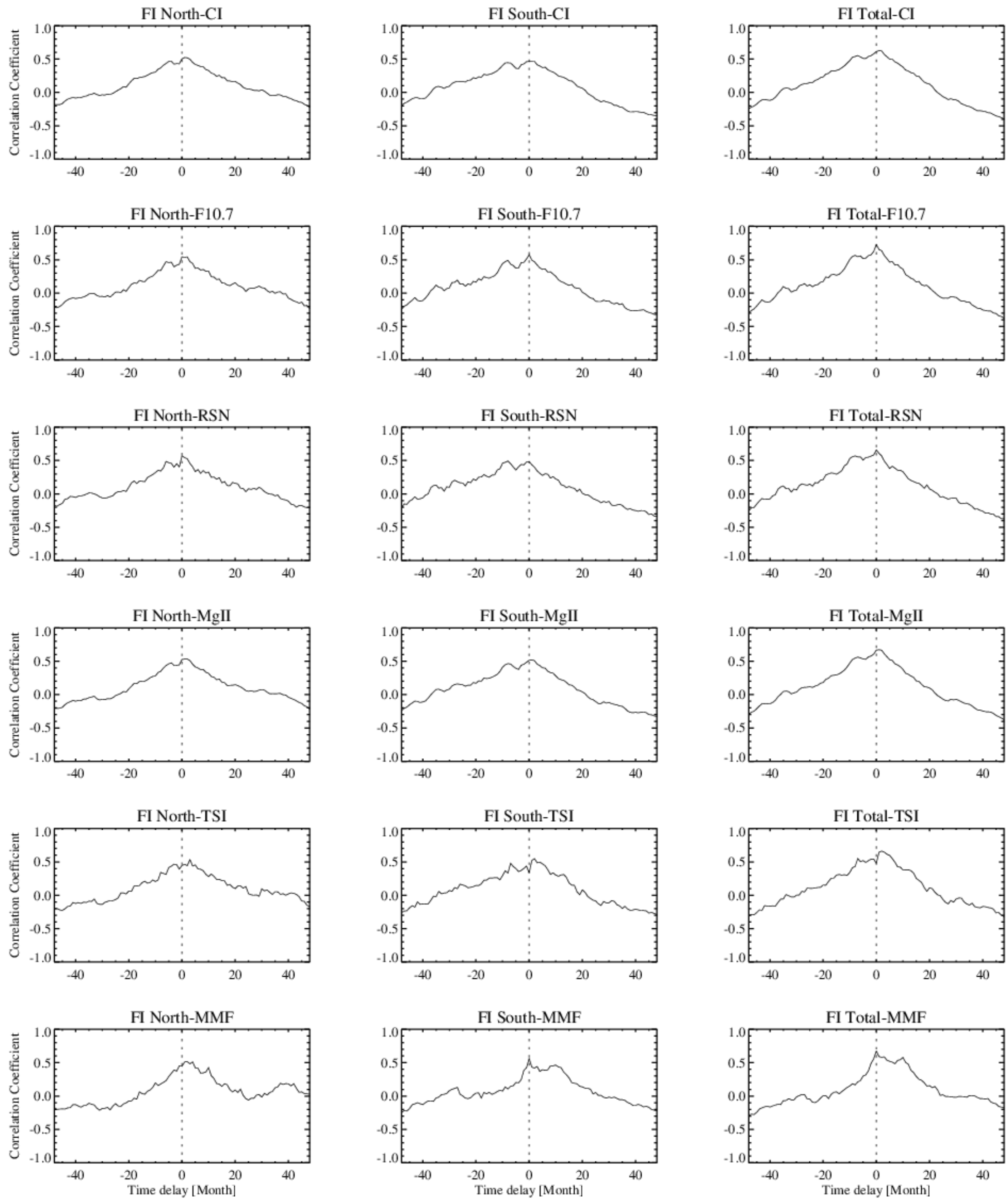

Figure 2. Cross correlation analysis results of hemispheric/total FI data and other solar activity indices used in this study.

Figure 3 shows a clear example of anticlockwise (e.g. the descending path follows an upper track) hysteresis between FI and two indices (MMF and TSI), during solar cycle 24. The hysteresis pattern is not the same for all the indicators, but with some difference in the widths: MMF, RSN and TSI depict broad loops, while the others depict narrow hysteresis loops.

Other Properties of Solar Cycle 24

One of the interesting features of this cycle is the clear appearance of the double maximum. Two peaks are seen during the maximum phase separated by 1–2 years from Figure 1, which shows the time plot of the 11-month moving average of all activity indices. However, most other authors believe that it is better using 13-month moving average for cyclic behavior studies. Because of the limited time interval which we studied, 13-month moving average

Table 1. Cross correlation analysis results for the hemispheric/total FI and other solar activity indices used in this study.

	FI North	Time Delay [Month]	FI South	Time Delay [Month]	FI Total	Time Delay [Month]
Coronal Index (CI)	0.52±0.14	1	0.47±0.15	1	0.63±0.12	1
10.7 cm solar radio flux (F10.7)	0.54±0.13	0	0.58±0.13	0	0.73±0.10	0
Relative sunspot number (RSN)	0.57±0.13	0	0.49±0.15	8	0.66±0.11	0
Magnesium II index (MgII)	0.53±0.14	2	0.52±0.14	1	0.67±0.11	1
Total solar irradiance (TSI)	0.54±0.13	3	0.55±0.13	2	0.66±0.11	2
Mean magnetic field (MMF)	0.52±0.14	2	0.56±0.13	0	0.68±0.11	0

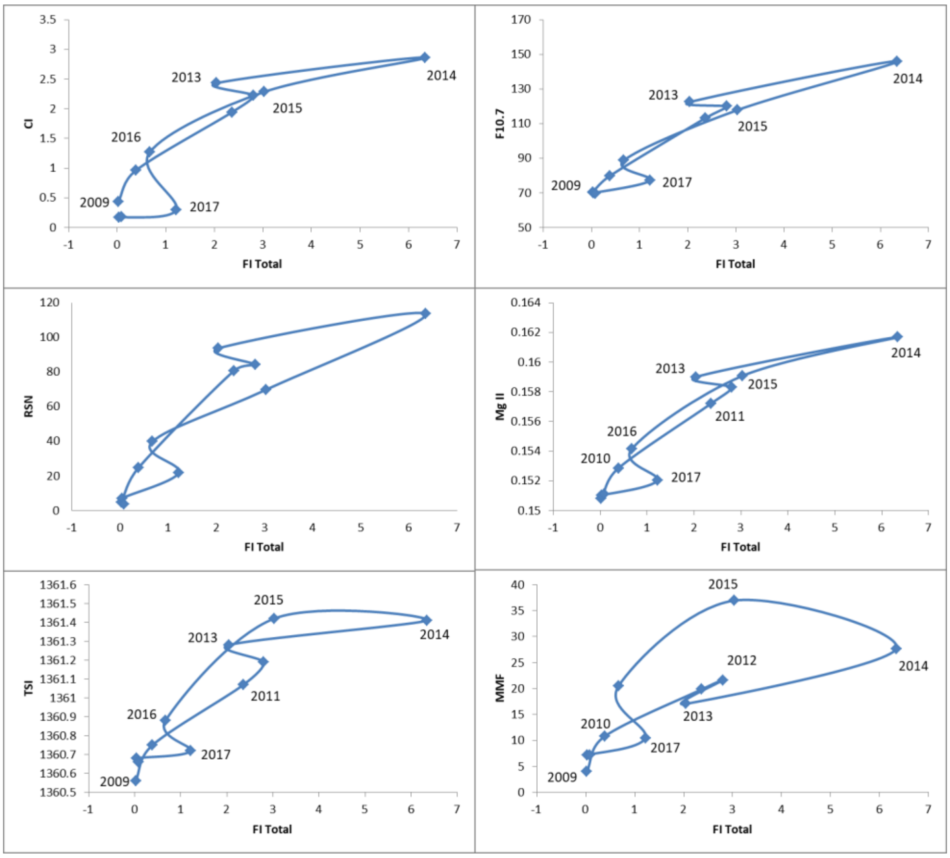

Figure 3. Hysteresis behavior of total FI and other parameters used in this study.

procedure can cause to disappear some properties of activity variations. The existence of a complex structure of the maximum phase of the 11-year solar cycle was recognized in 1960s by Gnevyshev (1963, 1967). He suggested that 'the 11-year cycle does not contain one but two waves of activity with different physical properties'. Thus, it was decided to call this time interval of the solar activity maximum phase in which the dip or valley periods were seen as Gnevyshev gap (GG) after the Russian astronomer who initiated this concept (Storini et al., 2003). Until 2011 there has been no clear understanding of the GG's nature. Kilcik et al (2011) and Kilcik and Ozguc (2014) brought a clear description about this nature; they analyzed sunspot groups in two categories as large (D, E and F) and small (A, B, C, and H) classes and found that the large classes sunspot groups reach to their maximum about two years later than the small ones. They suggest that two different dynamo mechanisms responsible from this behavior and as a result of these different dynamo processes the double-peaked structures appear during the solar maximum.

North–South Asymmetry of the Flare Index during Solar Cycle 24

It has been known for a long time that the occurrence of different features on the northern and southern hemispheres of the solar disk is not uniform, and that more features occur in one or the other part of the disk in different time intervals. This phenomenon is called the north–south (N–S) asymmetry. Many authors have used different features of solar activity to study N–S asymmetry. As shown in Figure 1 the temporal variation of the solar FI for the north and south hemispheres show remarkable differences. This different behavior is also seen in the results of correlation analysis that different hemispheric FI data show different amount of correlation and delay with other solar activity indicators.

Discussion

We have studied the final results of the FI and some other indices of the solar activity for cycle 24 from January 1, 2009 to December 31, 2020. We examined in the FI data the N–S asymmetry and the relations with other activity indices. The solar cycle 24 with its weak magnetic activity throughout its progression merits all this detailed studies which was done with different indices. Recent research of the long-term solar variability shows that our epoch is at the onset of an upcoming minimum of the 100-year Gleissberg cycle (Bonev et al., 2004). So, it can be expected that the ongoing cycle may be magnetically weaker than the solar cycle 24.

References

Ataç, T. and Özgüç, A.: (1998). Flare index of solar cycle 221998, Solar Phys. 180, 397.

Ataç, T. . and Özgüç, A. (2001), Flare index during the rising face of solar cycle 23, Solar Phys. 198, 399.2001.

Ataç , T., Özgüç, A., Rybak J.i. 2005, Overview of the flare index during the maximum phase of the solar cycle 23. Adv. Space Res. 35, 400–405

Barbieri, L.P. and Mahmot, R.E. 2004, October–November 2003's space weather and operations lessons learned, Space Weather **2**, S09002.

Bonev, B.P., Penev, K.M., Sello, S. 2004, Long-term solar variability and the solar cycle in the 21st century. Astrophys. J. 605, L81–L84.

Gnevyshev, M. N. 1963, Soviet Astron. 7, 311.

Gnevyshev, M. N. 1967, Solar Phys. 1, 107.

Kilcik, A., Yurchyshyn, V.B., Abramenko, V., Goode, P.R., Ozguc, A., Rozelot, J.P., and Cao, W. 2011, Time distribution of large and small sunspot groups over four solar cycles. Astrophys. J., 731:30 (8pp).

Kilcik, A., and Ozguc, A. 2014, One Possible Reason for Double-Peaked Maxima in Solar Cycles: Is a Second Maximum of Solar Cycle 24 Expected? Solar Phys. 289, 1379-1386.

Kleczek, J. 1952, Calculation of flare index. *Publ. Centr. Inst. Astron.* No. 22, Prague. 1952

Knoska, S. and Petrasek, J. 1984, Flare index calculations, Contrib. Astron. Obs. Skalnat´e Pleso 12, 165.

Heath, D.F., and Schlesinger, B.M. 1986, The 280 nm doublet as a monitor of changes in solar ultraviolet irradiance, *J. Geophys. Res. 91*, 8672-8682.

Scherrer, H. P.,Wilcox, M. J., Svalgaard, L., Duvall, L. T., Dittmer, H. P., and Gustafson, E. K. 1977, The mean magnetic field of the Sun: Observations at Stanford, Solar Phys. 54, 353, 1977.

Storini, M., Bazilevskaya, G. A., Fl¨uckiger, E. O., Krainev, M. B., Makhmutov, V. S., and Sladkova, A. I.: 2003, The GNEVYSHEV gap: A review for space weather, Adv. Space Res. 31, 895.

MHD Simulation of a Flare Situation in Real Scale of Time Above AR 10365: Development of a Technique, Choice of Parameters, The Appearance of Field Singularities at Flare Sites

Podgorny A.I.[1], Podgorny I.M.[2], Borisenko A.V.[1], Meshalkina N.S.[3]

[1]Lebedev Physical Institute RAS, Moscow, Russia
[2]Institute of Astronomy RAS, Moscow, Russia
[4]Institute of Solar-Terrestrial Physics SB RAS, Russia
E-mail: podgorny@lebedev.ru

Abstract. The mechanism of release of the magnetic energy of the current sheet formed in vicinity of singular X-type magnetic field line explains the observed primordial release of solar flare energy in corona. The observed manifestations of the flare are explained by the electrodynamic model of a solar flare proposed by I.M. Podgorny. The study of the flare mechanism is impossible without performing MHD simulations above a real AR, MHD simulation in the solar corona in real time can only be carried out thanks to parallel calculations using CUDA technology. To select the conditions for the numerical solution of MHD equations under which various viscosities. Mainly, the configuration of the magnetic field at the maxima of the current density is the configuration of the X-type singular line, which is strongly distorted by superimposed diverging magnetic field.

Introduction.

The mechanism of S.I. Syrovatskii [*Syrovatskii 1966*], accor ding to which, during a solar flare, the magnetic energy of the current sheet formed in the vicinity of the X-type singular line of the solar corona magnetic field is released, explains the observed primordial energy release of the flare above the active region (AR) at an altitude of ~ 1/40 - 1/20 of the solar radius. The primordial release of energy high in the corona is evidenced by observations of thermal X-ray emission from flares on the limb [*Lin et al., 2003*], the invariability of the magnetic field during flares on the solar surface [*Podgorny et al., 2015*], changes in the corona temperature at the flare site according to observations of ultraviolet radiation of highly ionized iron ions [*Podgorny and Podgorny 2018*] and other observations. The flare release of the energy of the current sheet causes the observed manifestations of the flare, which are explained by the electrodynamic model of the flare proposed by I.M. Podgorny [*Podgorny et al., 2010*]. According to this model the hard X-ray beam radiation on the surface of the sun during a flare is explained by the deceleration in the lower dense layers of the solar atmosphere of electron fluxes accelerated in field aligned currents caused by the Hall electric field in the current sheet. The model was developed based on the results of observations and numerical MHD simulation and uses analogies with the electrodynamic substorm model proposed earlier by the author on the basis of Intercosmos-Bulgaria-1300 satellite data [*Podgorny et al*., 1988].

The results of the studies lead to the conclusion that the study of the flare mechanism is impossible without carrying out MHD simulations above a real AR, in which the magnetic fields observed in the photosphere are taken as boundary conditions, and the calculation begins several days before the appearance of flares. When setting the problem, no assumptions were done about the flare mechanism.

Method for the numerical solution of MHD equations

In order for the finite-difference scheme approximating the system of MHD equations to remain stable for the maximum possible time step, which is necessary to increase the calculation speed, an absolutely implicit upwind finite-difference scheme, conservative with respect to the magnetic flux, was developed. The scheme is solved by the iteration method.

To obtain the correct development of physical processes in time, it is necessary to carry out MHD simulation in the real scale time. Despite the use of specially developed methods, the calculations are slow. **There is a need to use parallel computing.** The time of calculation of evolution of the field and plasma in the solar corona above the active region is determined by:

1) The size of the time step (at which the scheme remains stable)
2) The number of iterations
3) The time of calculation of one iteration

Choice of parameters of MHD equations. Stabilization of instabilities arising near the boundary

Due to the difficulties in matching the solution in the computational domain with the values specified at the boundary, a calculation in the real scale time can lead to the development of a strong instability that has time to develop during a long time interval, both near the photosphere and non-photospheric boundaries. The strongest instabilities arise at low viscosities The problem of stabilization of instabilities arising at the boundaries of the computational domain was almost completely solved [*Podgorny at al., 2020*], for which artificial limitation of the rate of plasma inflow into the computational domain through the non-photospheric boundary, the setting of artificial viscosity near the non-photospheric boundary, and other stabilization methods were used. The viscosities were set in accordance with the principle of limited modeling [*I.M. Podgorny 1978*], according to which much larger or much smaller units, dimensionless parameters remain much larger or smaller than units when simulated without their exact preservation.

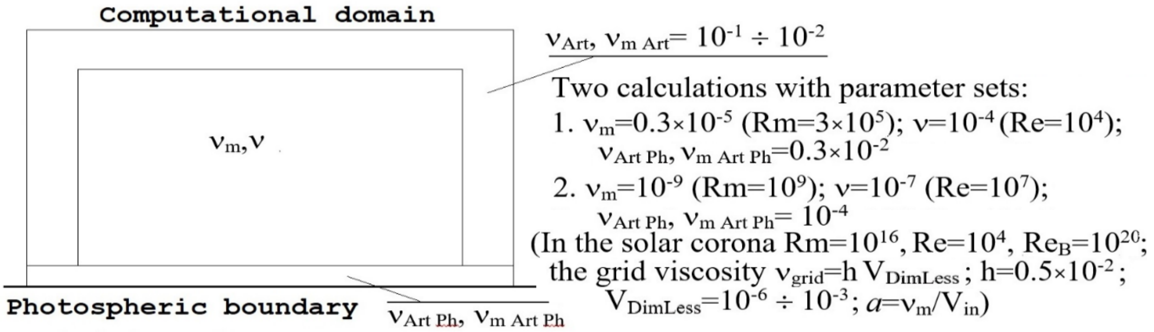

Fig. 1. Viscosity and artificial viscosity for two calculation variants.

For the active region AR 10365, two calculations were carried out for two sets of parameters corresponding to relatively high and low viscosities within three days (see Fig. 1.). In both calculations near the non-photospheric boundary, to stabilize the numerical instability, sufficiently large artificial viscosities were taken, their dimensionless values (inverse to the Reynolds numbers) are $\nu_{Art}=\nu_{m\ Art}=10^{-1}\div10^{-2}$.

In the first variant, the viscosities were taken equal to $\nu_m=0.3\times10^{-5}$ ($Rm=3\times10^5$); $\nu=10^{-4}$ ($Re=10^4$), the artificial viscosity near the boundary was taken relatively high $\nu_{Art\ Ph}$, $\nu_{m\ Art\ Ph}=0.3\times10^{-2}$. With these parameters, due to the suppression of the perturbation propagating from the photosphere by the artificial viscosity, a sufficiently intense accumulation of the flare energy does not occur in the region; therefore, a calculation with the second set of parameters with significantly lower viscosities was required. The calculation results with these parameters are given in [*Podgorny et al. 2020*].

In the second variant of the calculation, a set of parameters was selected $\nu_m=10^{-9}$ ($Rm=10^9$); $\nu=10^{-7}$ ($Re=10^7$); $\nu_{Art\ Ph}$, $\nu_{m\ Art\ Ph}= 10^{-4}$, the simulation results with these parameters are presented in the next chapter. If instabilities did not arise at the boundary, then, proceeding only from the need to obtain a stable solution inside the region, it is possible to make the following estimate of the computation time of one day of evolution in the solar corona above the active region. The time step from the Courant condition $\tau_K=h/(V_{MV}+V_{MA})$ in the calculations is $\tau_K = 10^{-8} \div 10^{-7}$ days. To estimate the computation time with a step τ_K : the computation time of one iteration on graphics cards using the CUDA technology is 2×10^{-2} sec, for 5 iterations the computation time of one step is 0.1 sec, so that (day ~ 10^5 sec) the computation time of one day of evolution in the solar corona is 10 - 100 days.

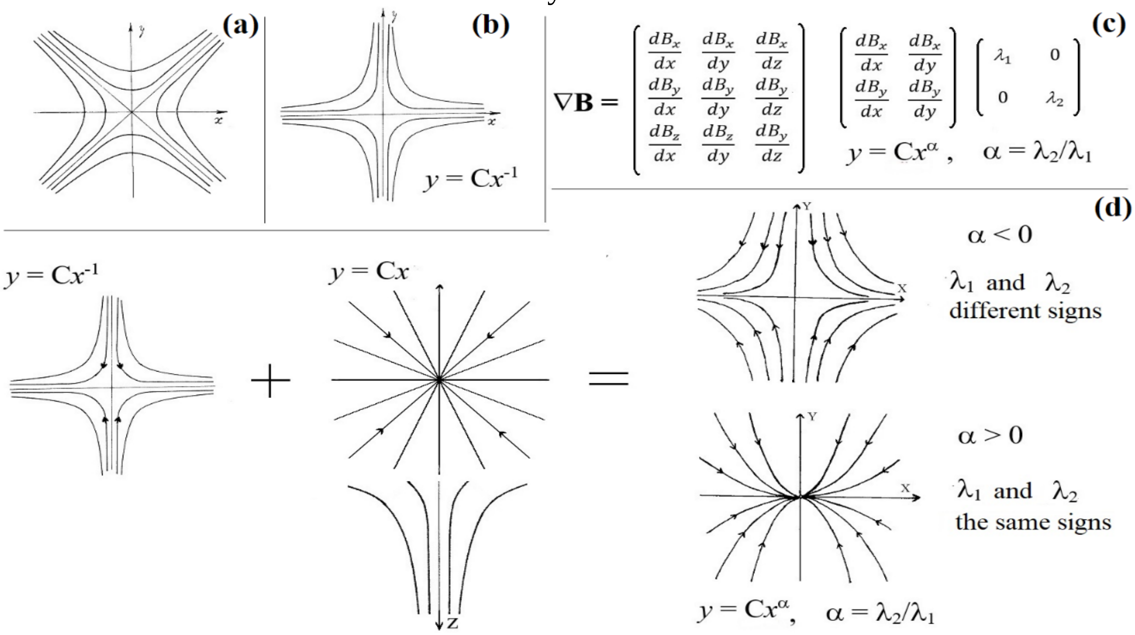

Fig. 2. Superposition of X-type magnetic field and diverging magnetic field.

At low viscosities, strong disturbances arise in some places of the computational domain. These disturbances are propagating towards the boundary. The perturbations are so strong that, despite setting a large artificial viscosity near the boundary, they cause numerical instability. For this set of parameters to stabilize the instabilities, it is also necessary to decrease the step (less than 10^{-8} days) and increase the number of iterations (in the calculations, their number reached 60 and more). As a result, the calculation time is greatly increased, reaching several months.

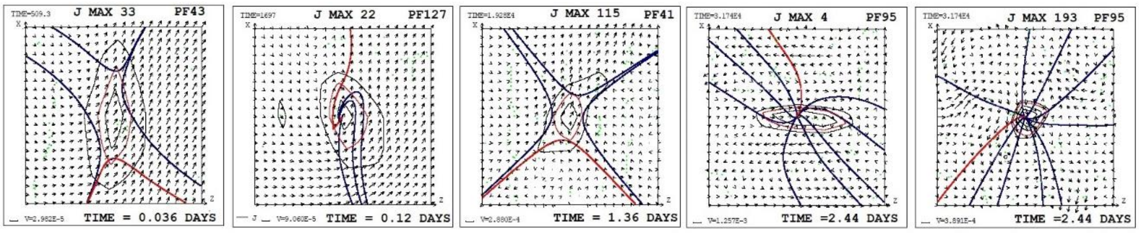

Fig. 3. Examples of superposition of X-type and diverging magnetic field obtained from MHD simulation.

MHD simulation results. Flare M1.4 27.05.2003 at 2:43

MHD simulation above AR 10365 showed the appearance of special lines in which a diverging magnetic field is superimposed on the configuration of the X-type magnetic field (Fig. 2, 3). The diverging magnetic field can be large, it can dominate the X-type field, fundamentally distorting its configuration However, even in this case, the presence of the X-type configuration leads to the accumulation of perturbations with the formation of a current sheet, in the magnetic field of which the flare energy is accumulated. In this case, even with a significant dominant diverging magnetic field, a sufficiently powerful current sheet may appear (Fig. 3, J Max 4), leading to the appearance of not only a weak flare, but also a flare of medium power.

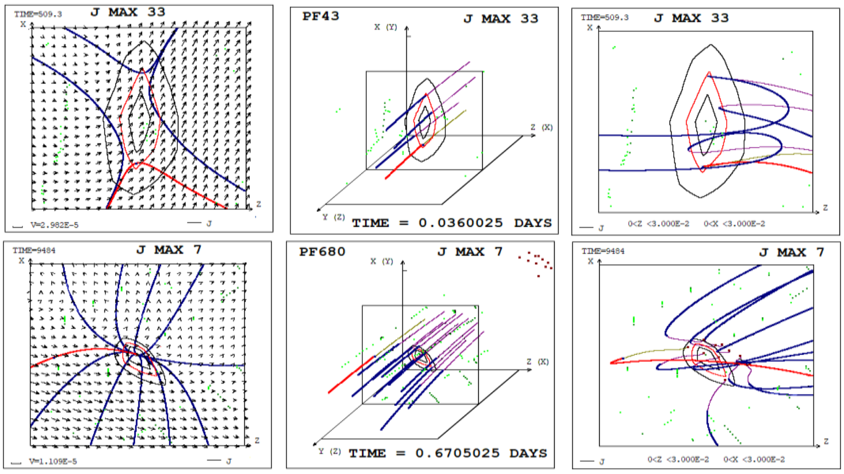

Fig. 4. Field configurations near singular lines. Flat magnetic lines, three-dimensional configurations, projections of field lines on the plane of configuration.

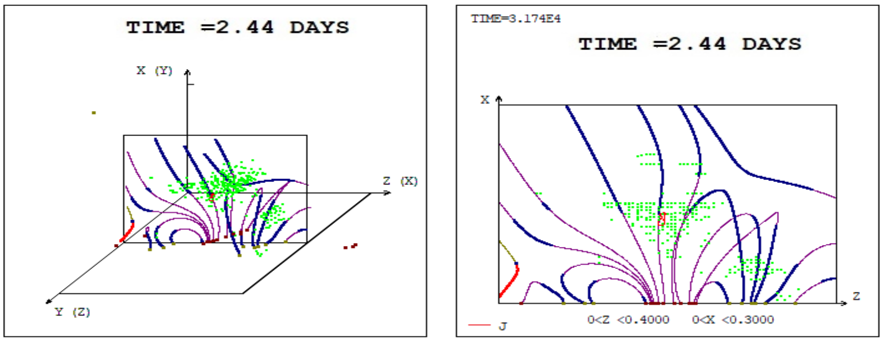

Fig. 5. Three-dimensional configuration of the magnetic field in the computational domain and the projection of the magnetic lines on the central plane.

When the X-type field and the diverging field are superimposed (Fig. 2d), the magnetic lines of the resulting field have the form $y = Cx^{\alpha}$, where $\alpha = \lambda_2/\lambda_1$, λ_1 and λ_2 are the eigenvalues of the matrix ($\nabla\mathbf{B}$) [*Podgorny 1989*]. If the X-type field dominates, then the magnetic lines have the form of hyperbolas ($\alpha < 0$, λ_1 and λ_2 have different signs). If the diverging field dominates, then the magnetic lines have the shape of parabolas ($\alpha > 0$, λ_1 and λ_2 of the same sign). Most often, the three-dimensional configuration of the magnetic field in the vicinity of the singular line is complex (examples are shown in Fig. 4), from this configuration it is impossible to determine that the line is singular. Therefore, a specially developed system for finding points through which singular line pass is required [*Podgorny et al., 2013a,b, 2017*].

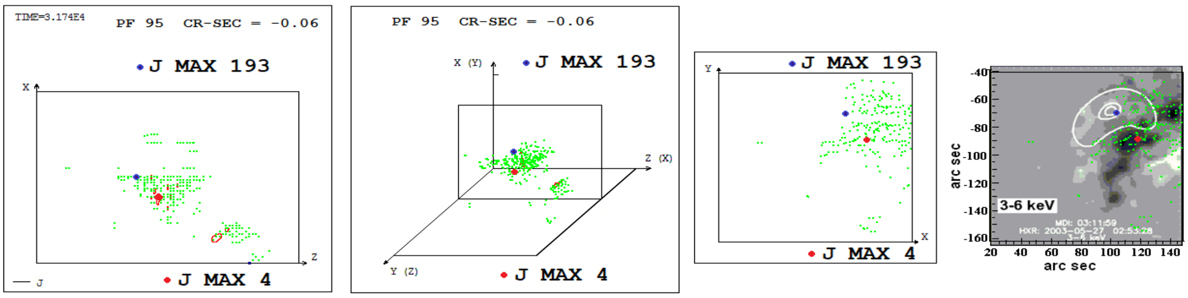

Fig. Flare-M1_4-2. The location of the current density maxima in the region, their projections onto the central plane, the picture plane (perpendicular to the line of sight), and the distribution in the picture plane of soft X-ray emission of 3-6 keV, received by the RHESSI spacecraft during the M 1.4 flare on May 27, 2003 (http://rhessidatacenter.ssl.berkeley.edu).

In Fig. 5. shows the configuration of the magnetic field in the computational domain of corona at the time of the M 1.4 flare on May 27, 2003 at 2:43 am, which corresponds to 2.44 days from the beginning of the calculation. The current density maxima found by the graphical search system through which singular magnetic field lines can pass are indicated by green dots in Figures 5, 6. The positions of the current density maxima in the region are shown, their projections onto the central plane, which passes through the central point of the computational region and is located perpendicular to the photosphere and parallel to the solar equator. Fig. 6 shows the location of many of the current density maxima in the picture plane close to the thermal X-ray source. The 193rd maximum of the current density is located in the central region of the source (all the maxima are numbered in decreasing order). The 4th maximum near the source of thermal X-ray radiation has the most powerful current sheet. The field configurations near the 193rd and 4th current density maxima (Fig. 7) show the dominance of the diverging magnetic field over the X-type field. MHD simulation showed the coincidence of the positions of some current density maxima with the position of the source of the flare thermal X-ray radiation; the maximum of the current density with a sufficiently powerful current sheet is located at a distance of ~ 10" from the source. In the future, it will be necessary to try to more accurately select the parameters for a more precise calculation.

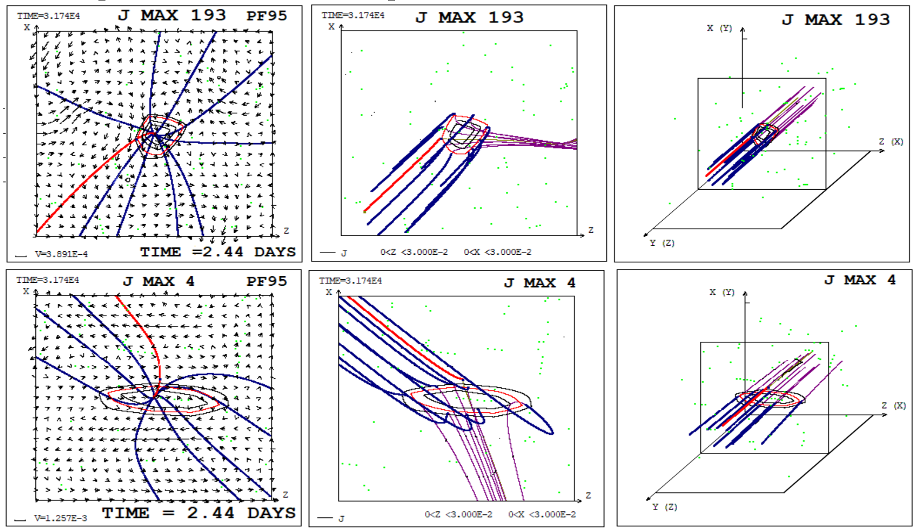

Fig. 7. Magnetic field configurations near the193rd and 4th current density maxima.

Conclusion.

To understand the physical processes causing the flare situation, simulation in the real scale of time is necessary, and the calculation should begin several days before the flare, when the magnetic energy of the flare has not yet been accumulated in the corona.

1. A technique has been developed for the numerical solution of MHD equations in the solar corona in real scale of time, which is impossible without the use of parallel computations. Boundary conditions are taken from observations.

1.1 In order to reduce the calculation time, an absolutely implicit upwind finite-difference scheme was developed, which is conservative with respect to the magnetic flux in order to maximize the spatial step at which the scheme remains stable.

1.2 Methods for stabilizing instabilities near boundaries have been developed. Mainly, this is an application of artificial viscosity near the boundary, both magnetic and ordinary, as well as other methods of stabilization.

2. The simulation performed above AR 10365 showed the formation of local maxima of the current density on singular lines of the magnetic field.

2.1. Some current density maxima did not appear on singular X-type magnetic field lines.

2.2 In addition, a large number of current density maxima arise in places where the configuration of the X-type singular line is significantly distorted by the diverging magnetic field superimposed on it. Apparently, in the places of current density maxima with such a configuration, the appearance of low-power flares is possible.

2.3. Comparison of the calculation results with observations showed the appearance of current density maxima at the flare sites with a field configuration strongly distorted by the superimposed diverging magnetic field. Perhaps for this reason, solar flares over AR 10365 on May 26 and 27, 2003 were not very large.

References

Lin R.P., Krucker S., Hurford G.J. et al. (2003) RHESSI observations of particles acceleration and energy release in an intense gamma-ray line flare. Astrophys. J., 595, L69-L76.

Podgorny I.M. (1978) Simulation Studies of Space. Fundamentals of Cosmic Physics. 1. №1. 1 - 72.

Podgorny I.M., Dubinin E.M., Israilevich P.L., Nicolaeva N.S. (1988) Large-scale structure of the electric field and field-aligned currents in the auroral oval from the Intercosmos-Bulgaria satellite data. GRL. 15, 1538-1540.

Podgorny A.I. (1989) Solar Physics. On the possibility of the solar flare energy accumulation in the vicinity of a singular line. 123, 285 – 308.

Podgorny A.I., Podgorny I.M. (2004) MHD Simulation of Phenomena in the Solar Corona by Using an Absolutely Implicit Scheme. Computational Mathematics and Mathematical Physics. 44, 1784-1806.

Podgorny A.I., I.M. Podgorny I.M. (2008) Formation of Several Current Sheets Preceding a Series of Flares above the Active Region AR 0365. Astronomy Reports. 52, 666–675.

Podgorny I.M., Balabin Yu.V., Vashenuk E.M., Podgorny A.I. (2010) The generation of hard X-rays and relativistic protons observed during solar flares. Astronomy Reports. 54, 645–656.

Podgorny A.I., Podgorny I.M. (2013a) MHD Simulation of Solar Flare Current Sheet Position and Comparison with X-ray Observations in active region NOAA 10365. Sun and Geosphere. 8(2), 71-76.

Podgorny A.I., Podgorny I.M. (2013b) Positions of X-ray emission sources of solar flare obtained by MHD simulation. Phys. of Auroral Phenomena, Apatity, Proc. 36, 117-120

Podgorny A.I., Podgorny I.M., Meshalkina N.S., (2015) Dynamics of Magnetic Fields of Active Regions in Pre-flare States and during Solar Flares. Astronomy Reports. 59, 795–805.

Podgorny A.I., Podgorny I.M., Meshalkina N.S., (2017) Magnetic field configuration in corona and X-ray sources for the flare from May 27, 2003 at 02:53, Sun and Geosphere, 12/2, 85 - 92,

Podgorny I.M., A.I. Podgorny A.I. (2018) Diagnostic of a Solar Flare via Analyses of Emission in Spectral Lines of Highly Ionized Iron. Astronomy Reports. 62, 696-704.

Podgorny A.I., Podgorny I.M., Borisenko A.V. (2020). Study of the solar flare mechanism by MHD simulation in the corona above the active region in real time scale. Proc. 12-th Workshop "Solar Influences on the Magnetosphere, Ionosphere and Atmosphere", Primorsko, Bulgaria, June, 2020, 93-98.

Syrovatskii, S.I. (1966) Dynamic Dissipation of Energy in the Vicinity of the Magnetic Field Neutral Line. Zh. Eksp. Teor. Fiz. 50, 1133–1147.

Determination of the Solar Rotation Elements and Period from Ruđer Bošković's Sunspot Observations in 1777

Roša, D.[1], Hržina, D.[1], Husak, M.[2], Brajša, R.[3], Špoljarić, D.[3], Skokić, I.[3], Maričić, D.[1], Šterc, F.[1], Romštajn, I.[1]

[1] Zagreb Astronomical Observatory, Zagreb, Croatia
[2] Trakošćanska 20, 42000 Varaždin, Croatia, https://orcid.org/0000-0002-2814-5119
[3] Geodetski fakultet Sveučilišta u Zagrebu, Opservatorij Hvar, Fra Andrije Kačića Miošića 26, 10000 Zagreb, Croatia
E-mail: drosa@zvjezdarnica.hr

Keywords:
Ruđer Bošković, sunspot observations, solar rotation elements, solar rotation period

Abstract

This paper focuses on the observations of sunspots made by Ruđer Bošković in 1777. We derived the expressions needed to calculate the elements of the Sun's rotation and period from observations. We used modern ephemeris data in the processing of the observation results. Obtained results are very similar to Bošković's original calculations. In addition to historical significance, they also provide scientifically valuable data on the Sun's differential rotation, which plays a significant role in generating and maintaining solar magnetic activity.

Introduction

Ruđer Bošković (1711 - 1787) was one of the most famous Croatian scientists. He was a Jesuit priest and had broad interests and achievements in mathematics, science, civil engineering, philosophy, as well as in poetry and diplomacy (James, 2004). His main research field was astronomy (Špoljarić and Kren, 2016; Špoljarić and Solarić, 2016). Among other things, Bošković developed several methods for the determination of the solar rotation elements and the rotational period of the Sun and applied the methods to his own sunspot observations made in 1777 in Noslon near Sens, 120 km south from Paris (Husak et al., 2021a; Husak et al., 2021b). He was there as a guest of the cardinal Paul d'Albert de Luynes (1703–1788), an amateur astronomer.

Bošković's historical observations are significant because they provide additional data about the solar differential rotation. Many observations show that the solar rotation changes in time (Brajša et al., 1997; Brajša et al., 2006; Wöhl et al., 2010). These changes are in correlation with the solar activity cycle (Jurdana-Šepić et al., 2011; Ruždjak et al., 2017).

Bošković observed sunspots using the telescope with optical micrometre and pendulum for time measurement. In this way it is possible to determine (relatively accurate) the positions of the sunspots on the solar disk. Knowing the coordinates of the centre of the solar disk (e.g. from an astronomical almanac) it is possible to determine the (celestial) equatorial coordinates (declination and right ascension) of the observed sunspot.

As an example, Figure 1 shows a drawing of the solar disk and the position of one sunspot. The line WE passing through the centre of the solar disk is parallel to the plane of the celestial equator. The angular distance of the sunspot from the direction WE corresponds to the difference between the declination of the sunspot (δ_f) and the declination (δ_S) of the centre of the solar disk. The right ascension of the sunspot (α_f) is equal to:

$$\alpha_{\mathrm{f}} = \alpha_{\mathrm{S}} + \frac{d}{\cos\alpha_{\mathrm{f}}}, \ (1)$$

where d is the angular distance of the sunspot from the arc NS which is perpendicular to WE and which passes through the centre of the solar disk and α_S is right ascension of the centre of the solar disk.

From the quantities α and δ, we can easily calculate topocentric ecliptic coordinates of the sunspot (topocentric ecliptic latitude β'_f and topocentric ecliptic longitude λ'_f) according to the well-known transformation formulas between the equatorial and ecliptic coordinate systems:

$$\begin{aligned} \sin\beta'_{\mathrm{f}} &= \cos\varepsilon\sin\delta_{\mathrm{f}} - \sin\varepsilon\cos\delta_{\mathrm{f}}\sin\alpha_{\mathrm{f}} \\ \cos\beta'_{\mathrm{f}}\cos\lambda'_{\mathrm{f}} &= \cos\delta_{\mathrm{f}}\cos\alpha_{\mathrm{f}} \\ \cos\beta'_{\mathrm{f}}\sin\lambda'_{\mathrm{f}} &= \sin\varepsilon\sin\delta_{\mathrm{f}} + \cos\varepsilon\cos\delta_{\mathrm{f}}\sin\alpha_{\mathrm{f}} \end{aligned} \quad , \ (2\text{ a, b, c})$$

where ε is the obliquity of the ecliptic.

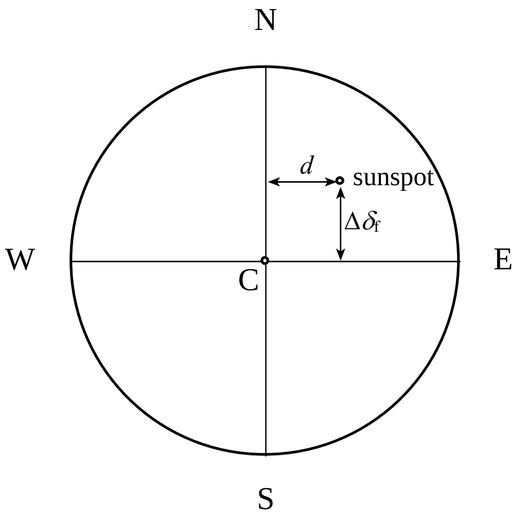

Fig. 1: drawing of a solar disk with the position of a single spot. Line WE *is parallel to the plane of the equator and is easily determined from observations.*

Expressions needed to find the elements of the Sun's rotation and period from observations

By the following procedure one can determine the elements of the Sun's rotation and the period from observations. Another approach can be found for e.g. in Waldmeier, 1941. With the known obliquity of the ecliptic ε at the observation times t and from the expression (2) we can calculate the apparent topocentric ecliptic coordinates of the sunspot (λ'_f, β'_f). The apparent angular and rectangular topocentric coordinates of the Sun ((λ'_S, β'_S) and (x_S, y_S, z_S)) as well as the current distance to the Sun can be determined using some of the publicly available ephemeris. Due to the small apparent angular distance of the sunspot from the centre of the Sun (σ) following expression can be used:

$$\sigma = 2\arcsin\sqrt{\sin^2\frac{\beta'_{\mathrm{f}} - \beta'_{\mathrm{S}}}{2} + \cos\beta'_{\mathrm{f}}\cos\beta'_{\mathrm{S}}\sin^2\frac{\lambda'_{\mathrm{f}} - \lambda'_{\mathrm{S}}}{2}}, \ (3)$$

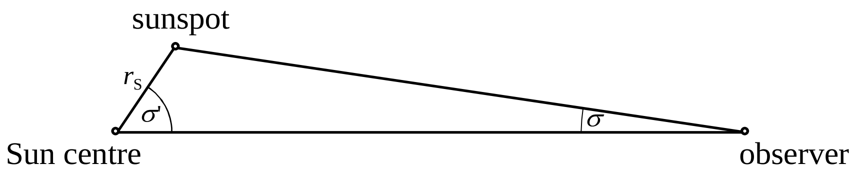

Fig. 2: with known distance between observer and the Sun ($d_{\text{observer-S}}$), apparent angular distance between centre of the Sun and sunspot (σ) and Solar radius (r_S), angle (σ') can be determined, as well as heliocentric coordinates of sunspot.

The heliocentric angular distance between the sunspot and observer is equal to (Fig. 2):

$$\sigma' = 180° - \sigma - \arcsin\left(\frac{d_{\text{observer-S}}}{r_S}\cdot\sin\sigma\right), \ (4)$$

where $d_{\text{observer-S}}$ is the topocentric distance to the Sun's centre, and r_S is the radius of the Sun.

The topocentric distance to the sunspot ($d_{\text{f-S}}$) is:

$$d_{\text{f-S}} = r_S \frac{\sin\sigma'}{\sin\sigma}, \ (5)$$

The heliocentric rectangular ecliptic coordinates of the sunspot (x_f, y_f, z_f) are:

$$\begin{aligned} x_f &= d_{\text{f-S}} \cos\lambda'_f \cos\beta'_f - x_S \\ y_f &= d_{\text{f-S}} \sin\lambda'_f \cos\beta'_f - y_S \\ z_f &= d_{\text{f-S}} \sin\beta'_f - z_S \end{aligned}, \ (6\text{ a, b, c})$$

and finally heliocentric ecliptic coordinates of the sunspot (instead of λ_f, β_f in the following text we will use notation λ, β):

$$\begin{aligned} \beta &= \arcsin\frac{z_f}{r_S} \\ \lambda &= \arctan\frac{x_f}{y_f} \end{aligned}, \ (7\text{ a, b})$$

In this procedure we use value of the obliquity of the ecliptic for the instant of time of each observation, i.e. the same that was used during individual transformation of the equatorial coordinates to the ecliptic.

Figure 3 shows the heliocentric celestial sphere. X denotes the position of a sunspot that has coordinates (λ, β) in the celestial heliocentric ecliptic system and coordinates (l, b) in the heliographic system (b is the heliographic latitude, l is arc NX ', where N is the ascending node of the solar equator). Point P_0 is the north ecliptic pole, and point P_S is the north pole of the Sun's rotational axis.

The direction of the solar axis in space can be unambiguously determined by two elements: inclination (i) - the angle between the ecliptic plane and the solar equatorial plane and ecliptic longitude (Ω) of the ascending node of the solar equator - the angle, in the ecliptic plane, between the equinox direction and the direction where the solar equator intersects (N on Fig. 1) the ecliptic from the South, i.e. in the sense of rotation.

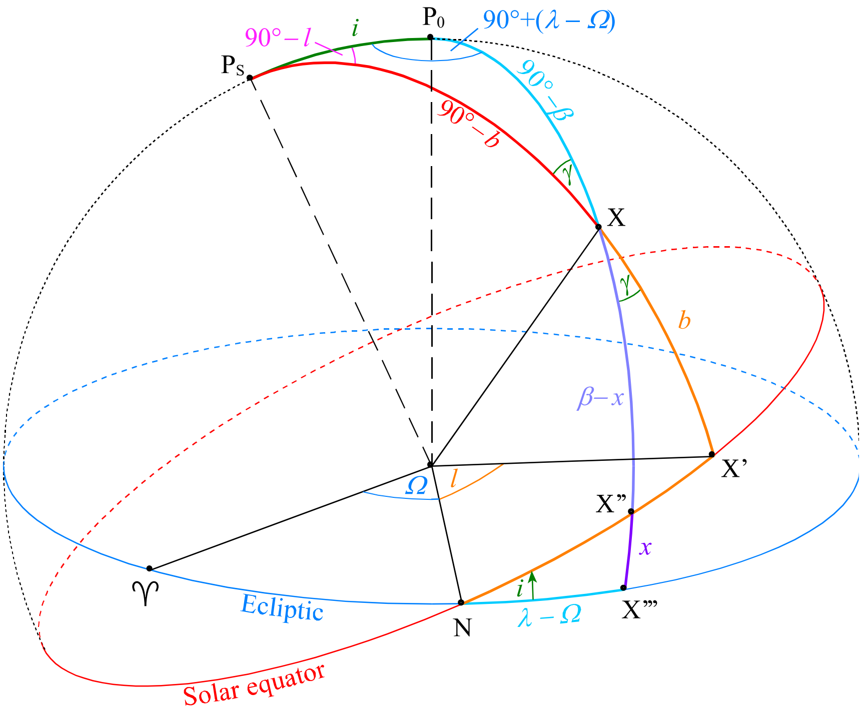

Fig. 3: coordinates of sunspot X *on heliocentric celestial sphere in celestial ecliptic system and heliographic system*

By applying the basic formulas of spherical trigonometry to a spherical triangle $P_S X P_0$, we have:

$$\cos i = \cos(90°-b)\cos(90°-\beta)+\sin(90°-b)\sin(90°-\beta)\cos\gamma\ , (8)$$

from which we find the expression:

$$\cos\gamma = \frac{\cos i - \sin b \sin\beta}{\cos b\cos\beta}\ . (9)$$

From the triangle XX'X" we have:

$$\cos\gamma = \tan b\cot(\beta - x) = \tan b\frac{1+\tan\beta\tan x}{\tan\beta - \tan x} \quad (10)$$

and from the triangle NX"X'" we find:

$$\begin{array}{l} \sin(\lambda-\Omega) = \tan x\cot i \\ \Rightarrow \tan x = \sin(\lambda-\Omega)\tan i = \sin\lambda\cos\Omega\tan i - \cos\lambda\sin\Omega\tan i \end{array}\ . (11)$$

By eliminating the angle γ from equations (9) and (10) we can get the expression:

$$\frac{\sin b}{\cos i}\left(\frac{1}{\sin\beta\cos\beta}\right)+\frac{\tan x}{\sin\beta}=\frac{1}{\cos\beta} \quad (12)$$

and by substituting $\tan x$ according to expression (11), we finally find:

$$X + Y\cos\beta\sin\lambda - Z\cos\beta\cos\lambda = \sin\beta\ , (13)$$

where the $X = \sin b/\cos i$, $Y = \cos\Omega\tan i$ and $Z = \sin\Omega\tan i$ are unknown quantities.

Expression (13) for processing measurements originates from Delambre, (1814). Equation (13) contains three unknowns. So it is necessary to have at least three equations to determine *X*, *Y* and *Z*. In other words, we need to have at least three observations of a sunspot to get one value of *b*, *Ω* and *i*. Of course, we neglect the already small meridional motions of the sunspot, that is, we assume that *b* is a constant for a particular sunspot. After we determine *X*, *Y*, *Z* we easily calculate *b*, *Ω*, *i* with the following expressions:

$$\begin{aligned} b &= \arcsin\left(X \cos i\right) \\ \Omega &= \arctan\left(\frac{Z}{Y}\right) \\ i &= \arctan\left(\sqrt{Y^2+Z^2}\right) \end{aligned} \quad . \text{ (14 a, b, c)}$$

If we have more than three observations, we can calculate the error of quantity *Ω* and *i* (Stark and Wöhl, 1981).

To calculate the sidereal velocity of the Sun's rotation (and sidereal period of rotation), it is sufficient to determine the change in the quantity *l* in time. It is possible to derive different formulas for calculating the quantity *l*, but the most suitable is the one in which *l* is the argument of the tangent function. From a spherical triangle P_SP_0X (Fig. 3) we find:

$$\begin{aligned} \cos b \cos l &= \cos\beta \cos\left(\lambda-\Omega\right) \\ \cos b \sin l &= \sin\beta \sin i + \cos\beta \cos i \sin\left(\lambda-\Omega\right) \end{aligned} \quad . \text{ (15 a, b)}$$

If we substitute the cos*b* from the first formula into the second, we have:

$$\tan l = \frac{\sin i \tan\beta}{\cos\left(\lambda-\Omega\right)} + \cos i \tan\left(\lambda-\Omega\right) \quad . \text{ (16)}$$

From the sidereal period, we can calculate the synodic period by taking into account the details of the Earth's motion (Roša et al., 1995; Skokić et al., 2014).

Processing of Bošković's measurements

The individual observation times t_x (for first and second contacts of the solar disk, and for the sunspot) recorded in Bošković's work (Boscovich, 1785) have been measured as the time that elapsed from the moment when Sun was in upper culmination in Sens, France. Therefore, the right ascension is directly given by measured time. Distance in declination from northern edge of the Sun was measured by use of micrometer. The instant of measurement time can be expressed as $t_{xUT1} = t_{s\ kulmUT1} + t_x$. There where 6 days of observations (between 12 and 19 September 1777) of the same sunspot with set of 5 measurements each day of observation. Let the observation time *t* be the arithmetic mean of the first t_{1UT1} and the last moment of observation t_{nUT1}. Also, $\Delta\alpha_f$ and $\Delta\delta_f$ are the mean distances from the centre of the solar disc in right ascension and declination respectably for a given set of measurements. Then the coordinates of the sunspot at the moment of observation (*t*) are the difference between the apparent topocentric equatorial coordinates of the Sun (α_S; δ_S) and the observed angular distances of the sunspot from the centre of the solar disc in right ascension and declination respectively ($\Delta\alpha_f$, $\Delta\delta_f$). Heliocentric ecliptic coordinates of the sunspot (λ, β) are then obtained by using expressions (2 a, b, c), (3), (4), (5), (6 a, b, c) and (7 a, b). By a combination of coordinates obtained from three observations and solving system of three equations (13) we calculate *b*, *Ω*, *i* using expressions (14 a, b, c) for each triplet of observations. Mean values of b = 26.43°, Ω = 65.61°, i = 7.88° are used for calculation of *l* (expression 16) for each of 6 sets of measurements. Result for sidereal period at mean latitude b = 26.43° using least square method is P = (26.696 ± 0.044) days (ω = (13.485 ± 0.022) °/day) which corresponds to mean value of the synodic period of P = (28.780 ± 0.047) days (ω = 12.508 ± 0.020 °/day). In calculation of the sidereal period from synodic we used mean angular heliocentric velocity of the Earth (0,9765°/day) during period between 12 and 19 September 1777. Bošković's results for sidereal period is 26.77 days and it is close to our result.

Conclusions

This paper presents an analysis of a part of Bošković's observations of sunspots with a presented mathematical approach and with the use of modern ephemeris parameters. The obtained values for the solar rotation parameters and the rotation period are close to Bošković's results, which indicates the accuracy of Bošković's methods. Furthermore, we plan to extend the processing to all of Bošković's observations and compare them with the results of other historical and modern measurements.

Acknowledgements

R. Brajša and I. Skokić acknowledge the support by the Croatian Science Foundation under the project 7549 "Millimeter and submillimeter observations of the solar chromosphere with ALMA".

References

Boscovich, R. J. (1785): *Opuscule II: Sur les éléments de la rotation du soleil sur son axe déterminés par l'observation de ses taches.* in: Opera pertinentia as opticam, et astronomiam. Maxima ex parte nova, & omnia hucusque inedita, In quinque Tomos distributa Ludovico XVI. Galliarum Regi Potentissimo Dicata. Tomus quintus, Bassani, 75-178. (in French)

Brajša, R., Ruždjak, D. and Wöhl, H. (2006): Temporal variations of the solar rotation determined by sunspot groups. Solar Physics, 237, 365-382

Brajša, R., Ruždjak, V., Vršnak, B., Pohjolainen, S., Urpo, S., Schroll, A. and Wöhl, H. (1997): On the possible changes of the solar differential rotation during the activity cycle determined using microwave low brightness-temperature regions and H-alpha filaments as tracers. Solar Physics, 171, 1-34.

Delambre (1814): Astronomie Theorique, Paris

Husak, M.; Brajša, R.; Špoljarić, D. (2021a): On the Determination of the Solar Rotation Elements i, Ω and Period using Sunspot Observations by Ruđer Bošković in 1777, Rudarsko-geološko-naftni zbornik (The Mining-Geology-Petroleum Engineering Bulletin), 77-98

Husak, M.; Brajša, R.; Špoljarić, D. (2021b): Solar Rotation Eelements i, Ω And Period Determined using Sunspot observation by Ruđer Bošković in 1777, Central European Astrophysical Bulletin (2021) 45:1, 1–7.

James, I. (2004). Remarkable Physicists, Cambridge University Press, Cambridge

Jurdana-Šepić, R., Brajša, R., Wöhl, H., Hanslmeier, A., Poljančić, I., Svalgaard, L. and Gissot, S. F. (2011): A relationship between the solar rotation and activity in the period 1998–2006 analysed by tracing small bright coronal structures in SOHO-EIT images. Astronomy and Astrophysics, 534, A17, 1-6

Roša, D.; Brajša, R.; Vršnak, B.; Wöhl, H. (1995): The relation between the synodic and sidereal rotation period of the Sun, Solar Physics, 159, 393–398

Ruždjak, D., Brajša, R., Sudar, D., Skokić, I. and Poljančić Beljan, I. (2017): A Relationship Between the Solar Rotation and Activity Analysed by Tracing Sunspot Groups. Solar physics, 292, 179, 1-11

Skokić, I.; Brajša, R.; Roša, D.; Hržina, D.; Wöhl, H. (2014): Validity of the Relations Between the Synodic and Sidereal Rotation Velocities of the Sun, Solar Physics, 289, 1471-1476

Špoljarić, D. and Kren, T. (2016): Ruđer Bošković and Astronomy. In: Lapaine, M. (ed.): Ruđer Bošković and Geosciences. Faculty of Geodesy, University of Zagreb, Zagreb

Špoljarić, D. and Solarić, N. (2016): Bošković, Perfector and Inventor of Geodetic, Astronomic and Optical Instruments. In: Lapaine, M. (ed.): Ruđer Bošković and Geosciences. Faculty of Geodesy, University of Zagreb, Zagreb

Stark, D. and Wöhl, H. (1981): On the Solar Rotation Elements as Determined from Sunspot Observations. Astronomy and Astrophysics, 93, 241-244

Waldmeier, M. (1941): Ergebnisse und Probleme der Sonnonforschung, Leipzig

Wöhl, H., Brajša, R., Hanslmeier, A. and Gissot, S. F. (2010): A precise measurement of the solar differential rotation by tracing small bright coronal structures in SOHO-EIT images. Astronomy and Astrophysics, 520, A29, 1-11

Solar Gravitational Moments: What Are They and What Do They Do? A Short Comprehensive Review.

Rozelot J.P.[1], *Kosovichev A.G.*[2],
[1] Universit´e de la Cˆote d’Azur, Grasse, France
[2] New Jersey Institute of Technology, USA
e-mail: jean-pierre.rozelot@univ-cotedazur.fr

Abstract.

Among all the fundamental solar parameters, mass, diameter, surface gravity, temperature, luminosity..., all well inventoried since several years in reference books, multi-gravitational moments are not yet well documented. Several theoretical estimates have been proposed through different approaches, mainly theory of Figure, helioseismology. We will show their own merits. Exact values of multipolar gravitational moments are important as they are at the crossroads of solar physics, solar astrometry, celestial mechanics, and General Relativity. Their temporal variations are still often neglected; they are yet an essential aspect for constraining solar-cycle modeling or solar-evolution theories. They induced planet-planet inclinations in multi-transiting systems gravitating in the neighboring of a star. This paper emphasizes some key issues to understand the role of these parameters.

1. Introduction.

Up-to-now, key solar parameters as found in books devoted to astronomy are: its diameter (or angular size), mass, absolute magnitude, spectral classification, metallicity, rotation, and sometimes some others such as cycle, modes…, but never the gravitational multipolar moments. Why? Essentially due to (i) their faint order of magnitude (10-7 or less) and (ii) because they are notoriously difficult to measure directly. Detecting a so faint value is at the cutting edge of the current available techniques, even through space dedicated missions. However, they are of fundamental interest, being at the crossroad of celestial mechanics, solar physics, solar astrometry and General Relativity. Their accurate determinations, both theoretically and from observations lead to a better knowledge of the internal properties of our star, down to the core. Extending the issue to stars, by their external influences, gravitational multipolar moments constrain planet-planet inclinations in multi-transiting systems gravitating in the neighboring of the rotating body -a forward thinking issue.

2. What are the gravitational moments?

They are the embodiment of the gravity field induced by the mass of the body, remembering that the gravity field is the sum of the gravitational potential, due to the mass of the body and its centrifugal potential, due to its rotation. And so, they give information on how the distribution of mass and velocity rates act inside the body (the Sun) to finally render the *outer visible shape non spherical*. In other words, determining the gravitational moments is the same as to know the exact equilibrium figure of the body in rotation. From this point of view, such a problem was tackled by many physicists since the XVIII century. Let us quote for instance:

- Maclaurin (1742), Clairaut (1743): in the case of a uniform ellipsoid;
- Jacobi (1834): in the case of spheroids. Study of the stability made by Riemann (1860);
- Bruns (1878): introduced the concept of Figure of a body;
- Radau (1885), Darwin (1889), Wavre (1932), Molodensky (1945), Moritz (1990) and many others provided additional refinements, whilst
- Milne (1923), then Chandrasekhar (1965, 1966) addressed the case of a non-uniform density from the surface down to the center.

Thus, the equilibrium surface of a body in rotation is distorted under the non-uniform distribution of mass and the non-uniform velocity rate, and the question is: how to quantify the departures to sphericity, i.e., how to determine the *shape coefficients*, called also *asphericities coefficients.*

3. **Short analysis**

Any surfaces can be described by their distance $s(r, q)$ to the center of the body, for each co-latitude q, developed in the form of Legendre polynomials $P_2(cosq)$, $P_4(cosq)$, $P_6(cosq)$, (…) in such a way

$$s(r,\theta) = r\left[1 + s_2(r)P_2(cos\theta) + s_4(r)P_4(cos\theta) + s_6(r)P_6(cos\theta) + (...)\right]$$

that where s_2(r), s_4(r), s_6(r), (...) are functions to be determined, according to the velocity *w* and the density profile *r(r).*

Some basic definitions:

1. Oblateness.

f $= (R_{eq}\text{-}R_{pol})/R_{eq}$ or **Dr** $= (R_{eq}\text{-}R_{pol})$

Best sphere passing through R_{eq} and R_{pol} $\quad R_{\odot} = \sqrt[3]{R_{eq}^2 \times R_{pol}}$

- Numerical application: R_{eq} = 695509.9835 km and R_{pol} = 695504.0331 km

So that: $R_{\odot}$ = 695508.0000 km (astrometric accuracy!, but needed)

$$f = 8.56 \times 10^{-6}$$

2. Geodetic parameter: $q = (w^2 R_{\odot}^3)/GM$

q is a small quantity and thus permits expansion in power series. For the Sun, $q \approx 2.05\ 10^{-5}$

Note that it is straightforward to see (by writing $r(\theta=0°) - r(\theta=90°)$) that *Dr* (in the general case of a fluid in rotation) is a linear function of the asphericities terms:

$Dr = -(3/2)s_2 - (5/8)s_4 - (21/16)s_6 - (...)s_n$.

General case:

The external gravitational potential $F(r) = -GM/r + (\ldots) + O(1/r^n)$ can be expanded in form of Legendre polynomials:

$F(r, q, l) = -GM/r$ [1 + coefficient * Polynomial expansion $P_{(n,m)}(q)$], where $n = 0, 1, 2, 3 \ldots$, is called the degree and $m = 0, 1, \ldots n$, is called the order of the function under consideration.

$$\Phi(r,\theta,\lambda) = -\frac{GM}{r}\underbrace{\left[1 - \sum_{n=1}^{\infty}\sum_{m=0}^{\infty}\left(\frac{R_{eq}}{r}\right)^n \left[C_{nm}cos(m\lambda) + S_{nm}sin(m\lambda)\right]P_{nm}(cos\theta)\right]}_{\text{Gravitational potential}} + \Phi[\omega^2(\theta), r^2]$$

Total Potential ϕ is called the **Gravity field**

Asphericities

Potential of the centrifugal force

θ: latitude, λ : longitude

0 ≤ order m ≤ degree n ≤ L

The coefficients C_{nm} are called the **tesseral** coefficients.

For the Sun (or stars), for which an axially symmetric distribution of the rotating matter can be assumed (not for the Earth), $S_{nm} = 0, m = 0,$ so that

$$\Phi \ (r,\theta,\lambda) = -\frac{GM}{r}\left[1 - \sum_{n=2}^{\infty}\left(\frac{R_{eq}}{r}\right)^{n}\left[C_{n0}P_{n0}\left(cos\theta\right)\right]\right] \quad \Phi$$

C_{n0} are the **zonal coefficients**.

C_{20} (namely zonal harmonic of degree 2 order 0) is the dynamical flattening of the body, called **quadrupole moment**, more simply denoted by $\boldsymbol{J_2}$, but by convention $C_{20} = -J_2$. In the same way, $C_{40} = -J_4$ is called the octupole moment, $C_{40} = -J_6$ is the hexadecapole moment, and so forth. They have a **physical meaning:** they told us how much the matter deviates from a "perfect" sphere (Figure 1).

The development in power series gives the following results:

$$c_{2,0} = -J_2 = -\left[s_2 + \frac{q}{3} + \frac{11}{7}s_2^2 + \frac{q}{7}s_2 - \frac{223}{196}s_2^3 - \frac{61}{196}qs_2^2 - \frac{27}{28}s_4s_2 - \frac{19}{84}qs_4\right]$$

$$c_{4,0} = -J_4 = -\left[s_4 + \frac{36}{35}s_2^2 + \frac{6}{7}qs_2 + \frac{594}{245}s_3^2 + \frac{54}{245}qs_2^2\right]$$

$$c_{6,0} = -J_6 = -\left[s_6 + \frac{120}{77}qs_2^2 + \frac{30}{11}s_4s_2 + \frac{25}{33}qs_4 + \frac{90}{77}s_3^2\right]$$

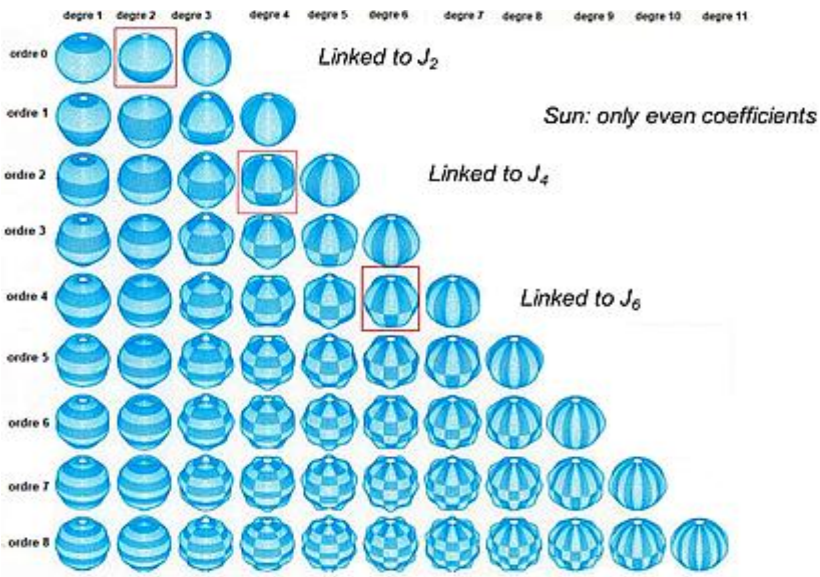

Figure 1. Overview of the Laplace spherical harmonics showing the surface distortions of a rotating fluid body in the general case. The solar case is surrounded by a square. After R. Biancale, 2006 personal communication).

Results:

Taking a solar differential law as found by Javaraiah (2020),

$w = A + B\sin^2(q)$; $A = 14.503$ deg/day; $B = -2.43$ deg/day , it comes, at $q = 45°$

$J_2 \approx 2.54\ 10^{-7}$, $J_4 \approx -1.46\ 10^{-10}$, $J_6 \approx 5.31\ 10^{-16}$ (…) .

Note that J_n are of the order of q^n *(q: geodetic parameter)*. It is also assumed that q is independent of q. To overcome this difficulty, Dicke (1974) suggested to do computations at the inflexion point of the limb shape curvature. This is justified as it can be seen that the excess of the radius vector over that of the true ellipsoid is obtained at the colatitude for which the change occurs in the external contour shape, i.e. when the radial rotation gradient $\partial\omega/\partial r$ changes in sign. Indeed $\partial\omega/\partial r$ is < 0 at the equator up to $\theta \approx (40 - 55)^\circ$ and is positive thereafter[1].

4. **What can be done with J_n?**

4.1. Accurate astrometry

- **Planetary Ephemerides** are developed on the basis of numerical integration of the motion of the planets and the Moon fitted to the most accurate available observations. High precision planetary ephemerides are made independently by three main institutes. (1) The Institute of Applied Astronomy (IAA–RAS) in Saint-Petersburg (Russia), which developed the Ephemerides of Planets and the Moon (EPM), created in the 1970's. (2) The Jet Propulsion Laboratory (JPL, Pasadena, Ca, USA) which created the "Development Ephemerides (DE)" remaining since a long time the basis of the Astronomical Almanac and (3) the "Institut de Mécanique Céleste et de Calcul des Ephémérides" (IMCCE-Paris, F) which developed since the early 80's, analytical solutions for the planetary motion called Intégration Numérique Planétaire de l'Observatoire de Paris (INPOP). As a sub-product of the data fitting of the analytical solutions with observations, is the determination of J_2. Table 1 gives the results, for which the ponderated mean is (2.17 ± 0.6) 10^{-7} on good agreement with the estimation of Pireaux and Rozelot (2003): (2.0 ± 0.4) 10^{-7}.

Name of the ephemeris & Institute	Quadrupole moment (in 10^{-7})	Author & Reference
DE405 JPL (USA)	1.9 ± 0.3	Standish 1998
EPM2004 IAA (Russia)	1.9 ± 0.3	Pitjeva 2005; Pitjeva 2013
INPOP06 IMCCE (F)	1.95 ± 0.55	Fienga 2011
EPM2008 IAA (Russia)	1.92 ± 0.30	Pitjeva 2014a
INPOP08 IMCCE (F)	1.82 ± 0.47	Fienga 2011
DE423 JPL (USA)	1.80	Folkner 2015
INPOP10e IMCCE (F)	1.8 ± 0.25	Verma 2014
EPM2011 IAA (Russia)	2.0 ± 0.2	Pitjeva 2014a
DE430 JPL (USA)	2.1 ± 0.7	Folkner 2015
EPM2013 IAA (Russia)	2.22 ± 0.23	Pitjeva 2014a
INPOP13a IMCCE (F)	2.40 ± 0.20	Verma 2014
INPOP13c IMCCE (F)	2.3 ± 0.25	Fienga 2015
MESSENGER JPL (USA)	2.26 ± 0.09	Park 2017

Table 1: Estimates of the solar quadrupole moment J_2, with their uncertainties, deduced from the Ephemerides. JPL: NASA Jet Propulsion Laboratory in Pasadena (USA). IAA: Institute of Applied Astronomy in Saint Petersburg (Russia). IMCCE: Institut de M´ecanique C´eleste et de Calcul des Eph´em´erides in Paris (F). INPOP13c is an upgraded version of INPOP13a,

[1] The order of magnitude of this outwardgradient is 5.7 10^{16} m^{-1} s^{-1} at the equator.

fitted to LLR (Laser Lunar Ranging) observations, including new observations of Mars and Venus deduced from MEX, Mars Odyssey and VEX tracking data.

4.2. Accurate astrometry

1.2. The perihelion precession of planetary orbits is linked to J_2 and J_4:

$$\dot{\omega}_{J_2} = \frac{3}{2}\frac{nJ_2}{(1-e^2)^2}\left(\frac{R}{a}\right)^2\left(1-\frac{3}{2}\sin^2 i\right)$$

$$\dot{\omega}_{J_4} = -\frac{15}{16}nJ_4\left(\frac{R}{a}\right)^4\left[\frac{3}{(1-e^2)^3}+7\frac{(1+(3/2)e^2)}{(1-e^2)^4}\right]\times\left(\frac{7}{4}\sin^4 i - 2\sin^2 i + \frac{2}{5}\right)$$

where $n = \sqrt{GM/a^3}$ is the Keplerian mean motion, R, the Sun's mean equatorial radius, i the angle between the planet's orbit and the Sun's equator.
For instance, Venus' perihelion precession induced by the solar quadrupole mass moment amounts to +0.0026 arcs.y^{-1}, and by the octupole mass moment 4.8 10-9 arcs.y^{-1}.
An analytical development has been made by Xu et al. (2011):

- perihelion precession of Mercury's orbit: $\Delta\omega = 2.95694\times10^5\ J_2$, which is 0.0591 (arcs/yr),
- perihelion precession of Venus's orbit: $\Delta\omega = 6.28801\times10^4\ J_2$, which is 0.01258 (arcs/yr),
- perihelion precession of Mars's orbit: $\Delta\omega = 2.95694\times10^3\ J_2$, which is 0.0013 (arcs/yr).

4.3. Application to stars

Dynamical influence of stellar oblateness may be approximated using the leading order quadrupole terms, neglecting those of order O(f_2). In the case of an exoplanet of mass mp orbiting around its host star of radius r∗ and mass M∗, the disturbing part of the stellar potential is:

$$D = \frac{GM_*m_p}{2a_p}\left(\frac{R_*}{a_p}\right)^2 J_2\left(\frac{3}{2}sin^2 i_p - 1\right)$$

where a_p is the distance of the planet from its host and i_p its inclination orbit.

Ex: Precession rates of planets orbiting the rapidly-rotating main-sequence stars WASP- 33, Kepler-13A and HAT-P-7 reveal associated values of J_2 stars of the order of $\mathbf{10^{-4}}$**.**

5. Conclusion

We emphasized here the need to better determined the solar mutipolar gravitational moments. The solar limb's tiny departure from perfect circularity, i.e. the asphericity, is sensitive to the Sun's otherwise invisible interior conditions[2] allowing us to learn empirically about flows and motions there that would otherwise only be guessed from theoretical considerations. There is

[2] Isaak (1999) called this peering inside the Sun from its surface "an open window on the solar interior".

still work to be done, for instance, are the multipolar moments temporal dependent? At last, the solar gravitational moments knowledge can be applied to stars and their planets, highlighting the dynamical influence of stellar oblateness.

References

Bruns, H., "Die Figur der Erde", Pub. K¨onigl. Preuss. Geodid¨at Inst., Berlin (1878).
Chandrasekhar, S., The Equilibrium and the Stability of the Riemann Ellipsoids. I, Astrophys. Jour., 142, 890-921 (1965).
Chandrasekhar, S., The Equilibrium and the Stability of the Riemann Ellipsoids. II, Astrophys. Jour., 145, 842–877 (1966).
Clairaut, A.C., "Thorie de la Figure de la Terre", in Principes de l'Hydrostatique, Durand ed., Paris (1743).
Darwin, G.H., The theory of the figure of the Earth carried to the second order, Monthly Not. Roy. Astro. Soc., 60, 82–124, (1899).
Dicke, R.H., The Oblateness of the Sun and Relativity, Science, 184, Issue 4135, 419–429 (1974).
Fienga, A., Laskar, J., Kuchynka, P., Manche, H., Desvignes, G., Gastineau, M., Cognard, I., Theureau, G., The INPOP10a planetary ephemeris and its applications in fundamental physics. Celest. Mech. Dyn. Astr. 111, 363–385 (2011).
Fienga, A., Laskar, J., Exertier, P., Manche, H., Gastineau, M., Numerical esti- mation of the sensitivity of INPOP planetary ephemerides to general relativity parameters. Celest. Mech. Dyn. Astr. 123, 325–349, (2015).
Folkner, W.M., Williams, J.G., Boggs, D.H., Park, R.S., Kuchynka, P., IPN Progress Report 42-196 February 15, 2014. The Planetary and Lunar Ephemerides DE430 and DE431 (2014).
Isaak, G.R., Solar core rotation, in European Meeting on Solar Physics, 12-18 September 1999, Florence (I), ESA SP–448 (1999).
Jacobi, C. G. J., De usu legitimo formulae summatoriae Maclaurinianae, Journal fu¨r die Reine und Angewandte Mathematik, Volume 1834: Issue 12, 263-281 (1834).
Javaraiah, J.. Long-Term Variations in Solar Differential Rotation and Sunspot Activity, II: Differential Rotation Around the Maxima and Minima of Solar Cycles 12 – 2. Sol. Phys., 295, 170 (2020).
Maclaurin, C., in Thomson, W. & Tait, P. G., Treatise on Natural Philosophy, Cambridge University Press, Part II, Art. 772 (1742).
Modolenvsky, M.S., Geodezika i Kartografiya, 5, 11 (1988).
Moritz, H., "The Figure of the Earth", Wichmann ed. Paris (1980).
Park, R.S., Folkner, W.M., Konopliv, A.S., Williams, J.G., Smith, D.E., Zuber, M.T., Precession of Mercurys Perihelion from Ranging to the MESSENGER spacecraft. Astronom. Jour. 153 (3), 121 (2017).
Pireaux, S., Rozelot, J.P., Solar quadrupole moment and purely relativistic gravitation contributions to Mercury's perihelion advance, Astrophys. Space Sci. 284, 1159–1194 (2003).
Pitjeva, E.V., Relativistic effects and solar oblateness from radar observations of planets and spacecraft, Astron. Lett. 31 (5), 340–349 (2005).
Pitjeva, E.V., Updated IAA RAS Planetary Ephemerides-EPM2011 and their use in scientic research. Solar System Research, Vol. 47, No. 5, pp. 386402. Original Russian Text published in Astronomicheskii Vestnik, 2013, Vol. 47, No. 5, pp. 419–435 (2013).
Pitjeva, E.V., Pitjev, N.P., Development of planetary ephemerides EPM and their applications, Celest. Mech. Dyn. Astr. 119 (3), 237–256 (2014).
Radau, R., "Remarques sur la Th´eorie de la Figure de la Terre", Bull. Astron., 2, 157 (1885).
Riemann, B., Abb. d. K¨onigl. Gessel, der Wis. d. Gottingen, 9, 3–36 (1860).
Standish, M., JPL Interoffice Memoradum, IOM 312.F - 98-048, August 26, 1998, 18pp. (1998).
Verma, A.K., Fienga, A., Laskar, J., Manche, H., Gastineau, M., Use of MES- SENGER radioscience data to improve planetary Ephemeris and to test general relativity. Astron. Astrophys. 561, A115 (2014).
Wavre, R., "Figures plan´etaires et g´eod´esie", Gauthiers–Villars ed., Paris (1932).
Xu, Y., Xu Y., Yang Y., Zhang Q., Xu G., Solar oblateness and Mercury's perihelion precession, Monthly Notices Roy. Soc., 415, 3335–33 (2011).

Determination of the CME Core Parameters by Means of the Associated Spikes

Shevchuk M., Melnik V., Dorovskyy V., Konovalenko A.

Institute of Radio Astronomy, Kharkov, Ukraine,
E-mail: mykola.shevchuk@rian.kharkov.ua

Abstract

The paper presents the analysis of the event observed on August 22, 2015 with UTR-2 and NDA radio telescopes. The main attention is paid to the study of the Type IV burst and spikes which were observed against its background. We assume that the emissions of Type IV burst and spikes escape from the CME core. Thus using the duration of spikes we reconstruct the profiles of the temperature and the magnetic field from the core center to its periphery.

Introduction

Simultaneous occurrence of Type IV bursts and spikes on the dynamic spectrum are rare events, especially when spikes are the fine structure of a Type IV burst [*Messerotti et al.*, 1985, *Nonino et al.*, 1986]. According to [*Ninino et al.*, 1986] in 120 Type IV bursts observed between 1972 and 1984 there were only 15 time intervals with spikes. The authors concluded that about 20% of all Type IV bursts might contain spikes as the intrinsic fine structure. In the meter wavelengths band the average duration of such spikes were about 100 ms with relative frequency width $\Delta f / f \approx 0.02$ [*Malville et al.*, 1967, *Bernold*, 1979, *Nonino et al.*, 1986, *Bouratzis et al.*, 2014, 2016]. Malville [*Malville et al.*, 1967] and Messerotti [*Messerotti et al.*, 1985] found that the spikes polarization degree varied from 0 to 100% and the sign of polarization coincided with that of the associated Type IV burst. Comparing the spikes parameters given in the literature we may conclude that spikes associated with Type III bursts and Type IV bursts practically do not differ from each other. It is in particular follows from the paper [*Bouratzis et al.*, 2016] who compared the parameters of different spikes in different frequency bands.

In this work, for the first time, we used spikes as a kind of “diagnostic tool” for remote determination of the temperature and the magnetic field in the CME core.

Observations

The analyzed event was observed on August 22, 2015 in the frequency band 8-80 MHz with the radio telescopes UTR-2 and NDA. This day the active region AR2403 exhibited enhanced activity resulted in 15 flares of C and M classes (https://tesis.lebedev.ru/). The AR was located near the center of the solar disk with the coordinates S14E09. In meter and decameter wavelengths bands this activity manifested itself in the form of Type II, Type III and IIIb, Type IV bursts and spikes.

Based on the observational data we concluded that the observed radio bursts were associated with the M1.2 flare started at 6.39 UT. The flare onset time coincides with the beginning of radio bursts observed with the UTR-2 radio telescope (Figure 1a). First Type III bursts appeared on the dynamic spectrum at 6:47 UT. They were followed by the Type II bursts that lasted from 6:53 till 7:30 UT. The Type IV burst itself was registered by the UTR-2 radio telescope between 7:34 and 9:44 UT while NDA radio telescope observed this burst from 8:00 till 9:45 UT (Figure 1b) (https://realtime.obs-nancay.fr/#). Judging from the dynamic spectrum it was a moving Type IV burst with the leading edge drifting from 73 MHz to 16 MHz with the drift rate of about 5 MHz/s. The spikes appeared against the Type IV burst background approximately at 8:23 UT and lasted until the end of the Type IV burst and further. However, the spikes observed against the Type IV background were bounded in the frequency by the

Type IV burst borders while spikes observed after the Type IV burst end were observed in the whole frequency band from 8 to 32 MHz.

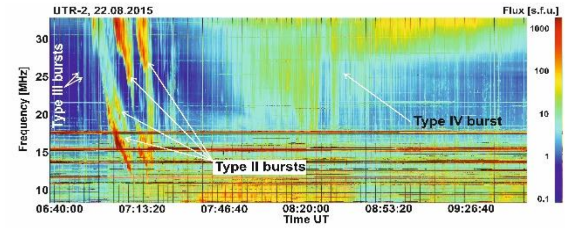

a)

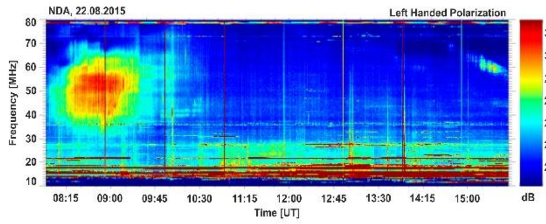

b)

Fig. 1 The event observed on August 22, 2015 with UTR-2 (a) and NDA (b) radio telescopes.

Analysis of the spikes parameters

For the analysis we chose spikes whose parameters could be reliably measured. It should be noted that their parameters were measured manually. More than 230 spikes against the Type IV burst background were processed. Statistical analysis shows that average duration and bandwidth of the spikes equal 1.2 s and 50 kHz respectively.

The dependences of average durations and bandwidths on frequency are presented on the Figure 2. Figure 2a shows that durations of spikes do not reveal regular dependence on frequency and lie within 1-1.5 s interval except a few cases. At the same time their bandwidth is proportional to frequency $\Delta f \approx Af$ (Figure 2b). The proportion coefficient A equals 1.7×10^{-3}. The same dependencies with slightly different A were also obtained in [*Melnik et al.*, 2014] and [*Shevchuk et al.*, 2016].

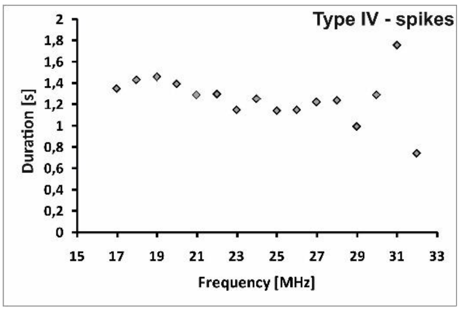

a)

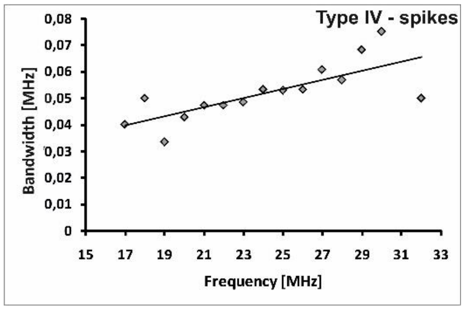

b)

Fig. 2 The dependencies of spikes average durations(a) and bandwidth (b) on frequency.

Determination of the CME parameters

The first determined parameter was density distribution across the CME core, which in turn allowed to estimate the CME mass. Since this CME moved toward Earth we couldn't obtain the exact size of its core. Nevertheless in the recent papers by [*Melnik et al.*, 2018, 2020] the sizes of two CMEs were determined as $1R_s$ and $2R_s$ respectively (R_s is the solar radius). Thus we determined the density distributions and masses for these two sizes. Similarly to [*Melnik et al.*, 2018] we assumed that the radio emission at the highest frequency $\approx 73MHz$ (Figures 1b) was radiated from the center of the core, while the lowest frequency emission $\approx 16MHz$ originated from the peripheral area (Figures 1a). Thus in the frames of plasma emission mechanism and supposing that the emission radiates at the first harmonic the densities at the center and borders of the CME core equal $n_c \approx 6.6\times10^7 cm^{-3}$ and $n_p \approx 3.2\times10^6 cm^{-3}$ respectively. If the density across the core follows the exponential law as [*Melnik et al.*, 2018]:

$$n(r) = n_c \exp(-\alpha r),$$

then we obtain $\alpha \approx 6/R_s$ for the core size of $1R_s$, and $\alpha \approx 3/R_s$ for the core size of $2R_s$. For both cases the peripheral density - $n_p \approx 3.2\times10^6 cm^{-3}$. Obtained values allow us to estimate the CME mass as:

$$M_{CME} \approx 4\pi \int_0^r m_p n(r) r^2 dr \, .$$

The CME masses were approximately $10^{15} g$ and $10^{16} g$ for the core radiuses of $r = 0.5R_s$ and $r = 1R_s$ respectively. These values agree well with the data provided by SOHO/LASCO CME Catalog (https://cdaw.gsfc.nasa.gov/CME_list/) - $\approx 1.5 \times 10^{15} g$.

Another parameter is the CME core temperature and in particular its distribution across it. Similarly to [*Shevchuk et al.*, 2016] we estimated the temperature by the spikes decay time (τ_d). The dependence of τ_d on frequency is shown in Figure 3. Unlike the total durations of spikes their decay times decrease with frequency as $\tau_d \sim f^{-0.5}$.

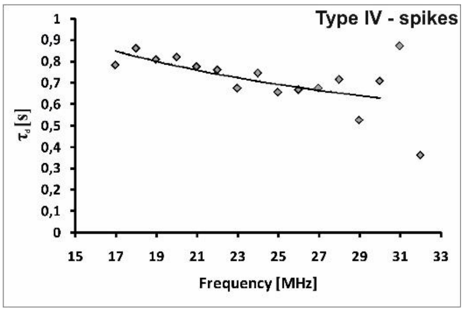

Fig. 3 . The dependence of the average decay times of spikes on frequency.

Based on the obtained observational dependency we got the relation for the temperature distribution on frequency:

$$T \approx 1.9 \times 10^4 f \, .$$

Figure 4 shows the obtained dependence for our particular case. This dependence essentially differs from the earlier obtained one by [*Shevchuk et al.*, 2016] for the storm of spikes observed before Type IV burst ($T \sim f^{2/3}$). The obtained temperature varied from 1.3 MK in the core center to 0.3 MK at its periphery.

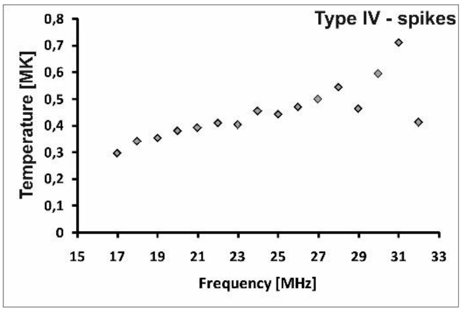

Fig. 4 The dependence of the temperature on frequency for the plasma inside the CME core.

Using the obtained dependence *T(f)* and following [*Melnik et al.*, 2018] we found the magnetic field distribution across the CME core. The gas-kinetic pressure $p = nkT$ (k is the Boltzmann constant) of the core should be compensated by the magnetic pressure $p = B^2/8\pi$. From the equality of these two pressures and obtained dependency *T(f)* we got an expression for the magnetic field:

$$B \approx 9 \times 10^{-4} f^{3/2} \, .$$

The obtained dependence is illustrated by Figure 5. One can see that the magnetic field decreases from $0.5G$ at the core center to $5\times10^{-2}G$ at its periphery. This result agrees well with the magnetic field value obtained in [*Melnik et al.*, 2018].

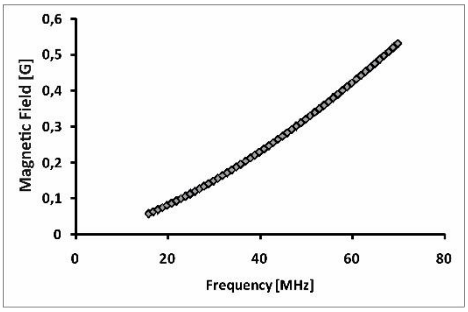

Fig. 5 The dependence of the magnetic field in the CME core.

Conclusion

In this article we analyzed the spikes observed against the Type IV burst background on August 22, 2015. It was shown that in this particular case the duration of spikes did not depend on the frequency, while their bandwidth revealed linear increase with frequency. Using spikes as a kind of "thermometer" we determined the temperature inside the CME core which appeared to change from 0.3 MK at the CME core periphery to 1.3 MK at its center. Also using the obtained dependence *T(f)* we got the value of the magnetic field and its profile across the CME core ($B \sim f^{3/2}$). The magnetic field varied from $5\times10^{-2}G$ at the core borders to $0.5G$ at its center.

Acknowledgements

The research was supported by the National Academy of Sciences of Ukraine in the framework of projects Spectr-3 (0117U000245) and Horizont (0120U100234).

References

McKim Malville J., Aller H. D., Jensen C. J. (1967). Spike bursts during the Type IV event of February 5, 1965, Astrophysical Journal, 147, p.711, 1967.

Messerotti, M., Nonino, M., Zlobec, P. (1985). Polarization and brightness temperature of 'spike' bursts related to metric Type IV solar radio events, Società Astronomica Italiana, Memorie (ISSN 0037-8720), 56, p. 795, 1985.

Bernold, T. (1980). A catalogue of fine structures in type IV solar radio bursts, Astronomy and Astrophysics, 42, p. 43, 1980.

Nonino, M., Abrami, A., Comari, M., Messerotti, M., Zlobec, P. (1986). The characteristics of type IV-associated spikes at metric wavelengths, Solar Physics, 104, p.111, 1986.

Melnik, V. N., Shevchuk, N. V., Konovalenko, A. A., Rucker, H. O., Dorovskyy, V. V., Poedts, S., Lecacheux, A. (2014). Solar Decameter Spikes, Solar Physics, 289, p.1701, 2014.

Bouratzis, C., Hillaris, A., Alissandrakis, C. E., Preka-Papadema, P., Moussas, X., Caroubalos, C., Tsitsipis, P., Kontogeorgos, A. (2015). Fine Structure of Metric Type IV Radio Bursts Observed with the ARTEMIS-IV Radio-Spectrograph: Association with Flares and Coronal Mass Ejections, Solar Physics, 290, p. 219, 2015.

Bouratzis, C., Hillaris, A., Alissandrakis, C. E., Preka-Papadema, P., Moussas, X., Caroubalos, C., Tsitsipis, P., Kontogeorgos, A. (2016). High resolution observations with Artemis-IV and the NRH. I. Type IV associated narrow-band bursts, Astronomy and Astrophysics, 586, p. 11, 2016.

Shevchuk, N. V., Melnik, V. N., Poedts, S., Dorovskyy, V. V., Magdalenic, J., Konovalenko, A. A., Brazhenko, A. I., Briand, C., Frantsuzenko, A. V., Rucker, H. O., Zarka, P. (2016). The Storm of Decameter Spikes During the Event of 14 June 2012, Solar Physics, 291, p. 211, 2016.

Melnik, V. N., Brazhenko, A. I., Konovalenko, A. A., Dorovskyy, V. V., Rucker, H. O., Panchenko, M., Frantsuzenko, A. V., Shevchuk, M. V. (2018). Decameter Type IV Burst Associated with a Behind-the-limb CME Observed on 7 November 2013, Solar Physics, 293, p. 10, 2018.

Melnik, V. N., Rucker, H. O., Brazhenko, A. I., Panchenko, M., Konovalenko, A. A., Frantsuzenko, A. V., Dorovskyy, V. V., Shevchuk, M. V. (2020). Radio Signature of a Distant behind-the-limb CME on 2017 September 6, The Astrophysical Journal, 905, p. 5, 2020.

On the Magnetosphere Stand-Off Distance at the Timescale of Geomagnetic Storms

Sima A.R, Dobrica V., Demetrescu C.

"Sabba S. Stefanescu" Institute of Geodynamics of the Romanian Academy, 19–21, Jean-Louis Calderon St., 020032 Bucharest, Romania
E-mail: alexandra.sima@geodin.ro

Abstract

The magnetosphere shape and dimensions are a result of the equilibrium between the magnetic pressure of the geomagnetic field and the dynamic pressure of the solar wind in which the Earth and its magnetosphere are embedded. Our previous studies [Dobrica et al., 2012, Stefan et al., 2013] concerned the long term evolution (the last ~ 150 and, respectively, 300 years) of the stand-off distance, i.e. the sub-solar distance to the magnetopause, commeasured in Earth's radii (R_E). In the present article we tackle the stand-off distance evolution at much shorter time scale, i.e., during 21 moderate and intense geomagnetic storms (Dst<-100 nT) occurred in the solar cycle 24 (2008-2020). While the long-term evolution of the stand-off distance shows variations between 11.6 and 9.5 R_E, during geomagnetic storms it shows variations of 6-12 R_E. An attempt is done to use the superposed epoch analysis in comparing various storms.

Key words: solar activity, solar wind, geomagnetic storms, superposed epoch analysis

Introduction

Generally, the sub-solar distance to the magnetopause (the so-called stand-off distance) results from the equilibrium between the magnetic pressure of the geomagnetic field and the dynamic pressure of the solar wind in which the Earth and its magnetosphere are embedded. At long-term timescale (the last ~150 years) this parameter was evaluated by [Dobrica et al. 2012, Stefan et al., 2013] reconstructed the stand-off distance evolution in the last 300 years. In the present paper we tackle the stand-off distance evolution at the much shorter time scale of geomagnetic storms, looking at 21 moderate and intense geomagnetic storms (Dst<-100 nT) that occurred in the solar cycle 24 which are presented in Table 1.

Two of this 21 geomagnetic storms are excluded from our analysis (August 2011, July 2012) because of no data availability.

Geomagnetic storms are a part of the geomagnetic activity, which is the result of the interaction of the solar wind (SW) and the heliospheric magnetic field with the magnetosphere and ionosphere. Most of intense geomagnetic storms (Dst <-100 nT) are generally caused by coronal mass ejections (CMEs). These involve the expulsion from the solar corona of huge quantities of solar magnetized plasma at high speeds into interplanetary (IP) space. CMEs observed in interplanetary space are also known as interplanetary coronal mass ejections (ICMEs) and are responsible for many major disturbances to the Earth's space environment [Kamide and Chian, 2007]. In general, ICMEs are detected by a number of characteristics measured by the satellite placed in the Lagrange point L1 in space: sudden increase in SW speed, increase in magnetic field, rotation of the magnetic field, decrease in electron density and temperature etc.

Data and method

1-minute data for the interplanetary and solar wind parameters (B, Bx, By, Bz, the heliospheric magnetic field, V, the solar wind speed, P, the solar wind dynamic pressure) available at https://omniweb.gsfc.nasa.gov/form/omni_min.html and data for geomagnetic indices designed to proxy the evolution of magnetospheric ring current and of auroral electrojets (Dst and SymH, and, respectively, AE) available at http://wdc.kugi.kyoto-u.ac.jp/wdc/Sec3.html, as well as data related to the coefficients of the IGRF-13 main field model (g_1^0, g_1^1, h_1^1), available at https://www.ngdc.noaa.gov/IAGA/vmod/igrf.html, have been used in this study.

Variation of interplanetary and geomagnetic parameters during March 2015, June 2015, and September 2017 geomagnetic storms, chosen as examples, is displayed in Fig. 1.

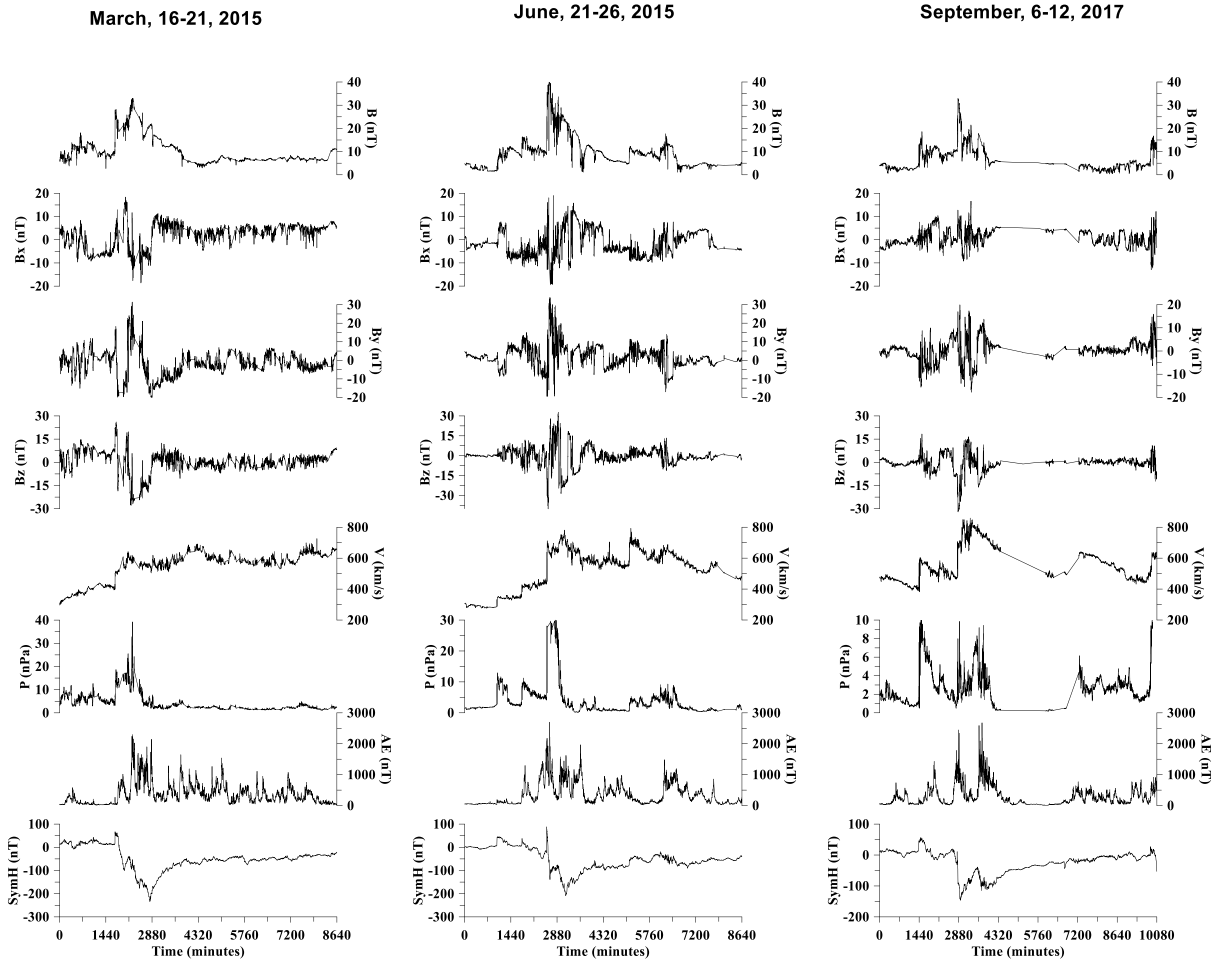

Fig. 1 – Variation of geomagnetic and interplanetary parameters during March 2015, June 2015, September 2017 geomagnetic storms

In order to determine the stand-off distance, we used the expression given by Schield [1996]:

$$L = \left(\frac{k^2 M^2}{2\mu_0 P}\right)^{\frac{1}{6}}, \qquad (1)$$

where M is the Earth's magnetic moment, P is the dynamic pressure of the solar wind, μ_0 is the permeability of the vacuum, and k is a given constant.

Though the magnetic moment of the Earth is time-dependent at long-term timescale [Demetrescu and Dobrica, 2020], we consider it constant during the short-time span (hours, days) of geomagnetic storms. The magnetic moment of the dipole was calculated by the formula: $M = \left(\frac{4\pi R_E^3}{\mu_0}\right)\sqrt{(g_1^0)^2 + (g_1^1)^2 + (h_1^1)^2}$ where: R_E – Earth radius (6370km), μ_0 = $4\boldsymbol{\pi}$*10-7 is the permeability of vacuum, and g_1^0, g_1^1, h_1^1 are the first order coefficients of a spherical harmonic model of the main field [Chapman and Bartels, 1940]. As regards the latter, the IGRF13 model [Alken et al., 2021] was chosen.

The evolution of the magnetic moment during the solar cycle 24 is presented in Fig. 2.

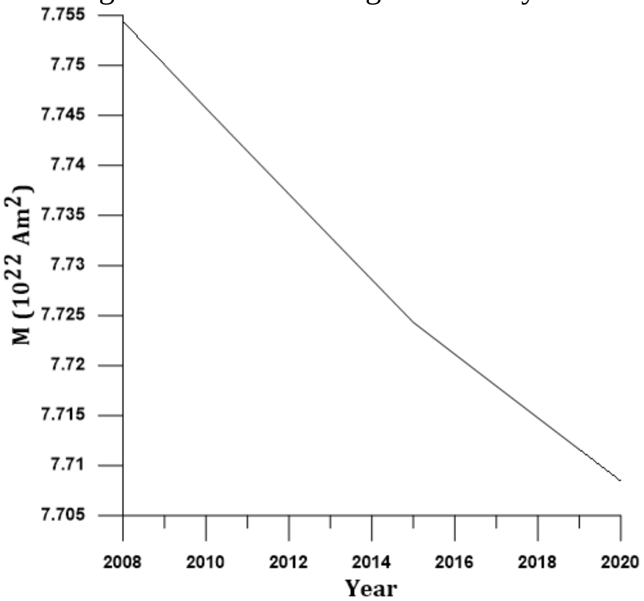

Fig. 2 Intensity of geomagnetic dipole during 2008-2020 (SC 24)

Further, the behavior of this relationship, at the timescale of the solar cycle 24 geomagnetic storms, was treated using a superposed epoch analysis, separately for single and multiple steps storms. The superposed epoch method of analysis was originally proposed by Chree, [1912].

Results

The evolution of the solar wind pressure and the magnetopause stand-off distance during the three geomagnetic storms, chosen as examples, are presented in Fig. 3.

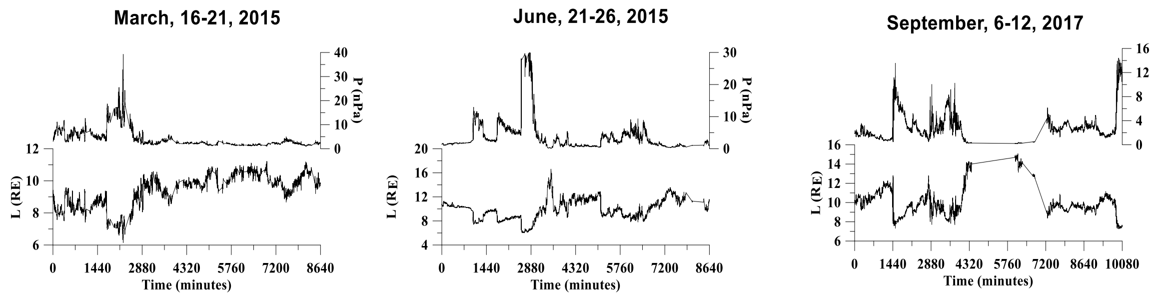

Fig. 3 – Evolution of solar wind pressure P, magnetopause stand-off distance L, in case of March 2015, June 2015, September 2017 geomagnetic storms

The correlation plots between the magnetopause stand-off distance and the solar wind pressure for the three geomagnetic storms are given in Fig. 4.

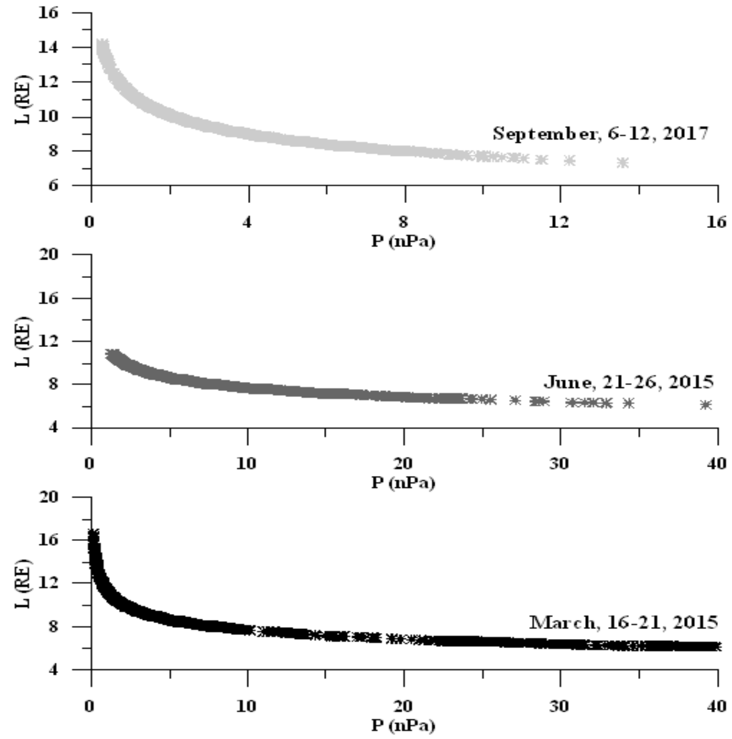

Fig. 4 – Correlation plots between the stand-off distance and the solar wind pressure for the three geomagnetic storms

The results of the superposed epoch analysis are shown in Fig. 5 for simple storms. The upper panel illustrates the evolution of the solar wind dynamic pressure, the middle panel the evolution of the SymH index, and the lower one the evolution of the magnetopause stand-off distance during the selected geomagnetic storms. We superimposed the evolution of the geomagnetic index SYM-H for the 13 selected one-step storms, referring the time of the minimum value of the index as zero time. The minimum value of SYM-H varies between – 234 nT and - 117 nT. At the maximum of the geomagnetic storm (minimum SymH values), L shows values between 6 R_E and 12 R_E. In Fig.5 L curves are standardized against the value at the time of the minimum SymH.

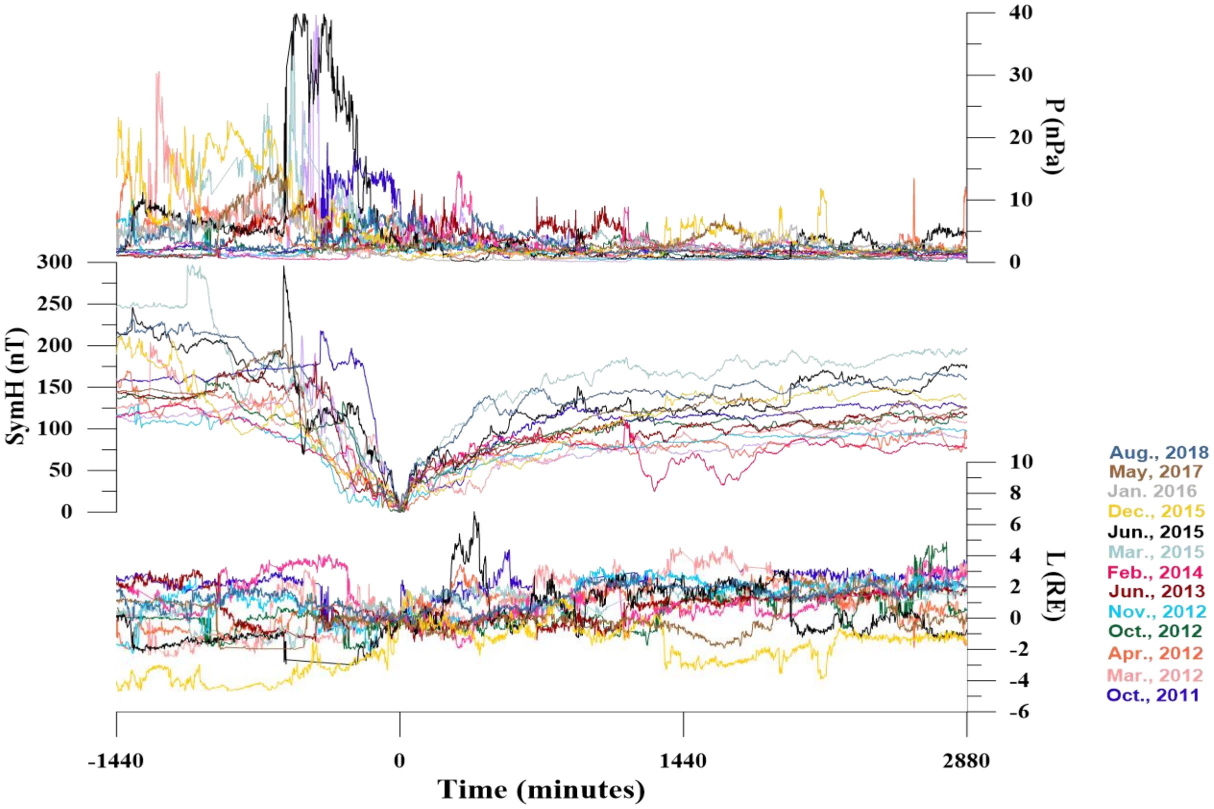

Fig. 5 – Superposed epoch analysis in case of 13 simple geomagnetic storms. The initial time is the time when SymH reached the minimum value.

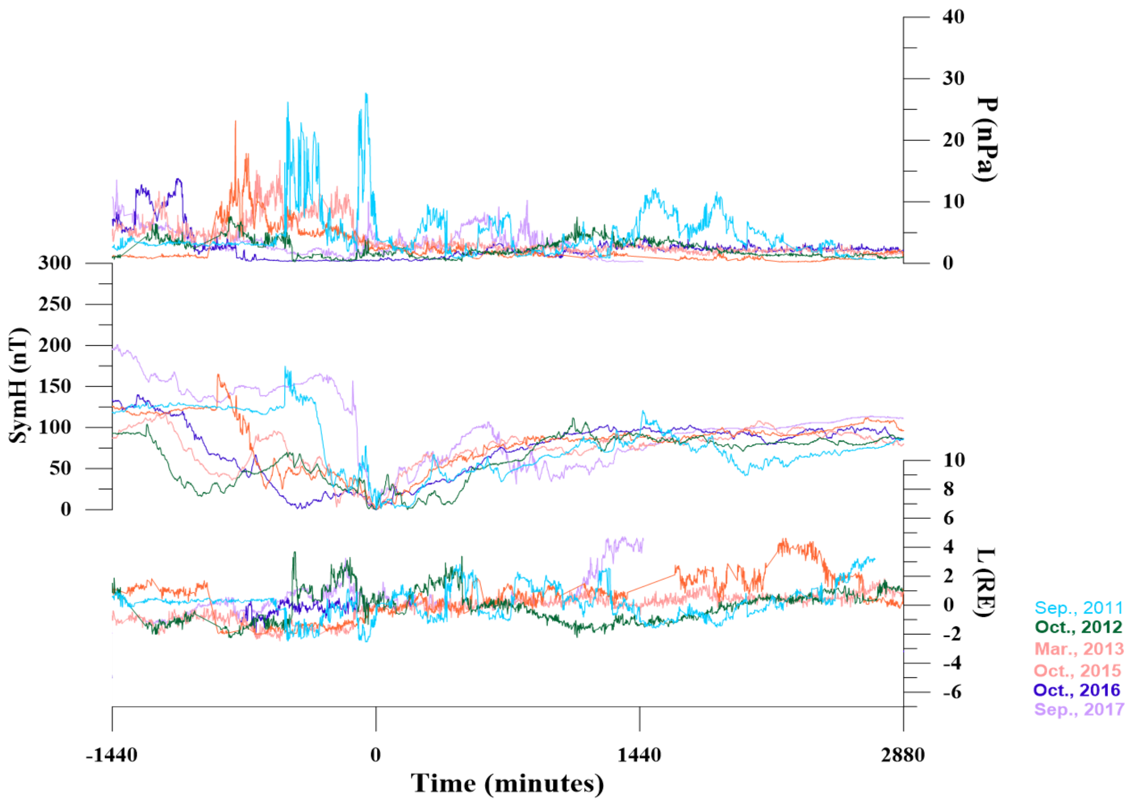

Fig. 6 - Superposed epoch analysis in case of 6 complex geomagnetic storms. The initial time is the time when the SymH reached the minimum value.

The results of the superposed epoch analysis for complex geomagnetic storms (storms with two or more steps morphology) are shown in Fig. 6. Data are organized as in Fig.5. The time of the SymH minimum values was taken as origin, no matter the number of steps of the storm. No particular regularity is observed.

The variation of the magnetosphere stand-off distance during the main phase of the geomagnetic storm has amplitudes between 2 R_E and 6 R_E.

Concluding remarks

The magnetosphere stand-off distances were calculated for moderate and intense geomagnetic storms in solar cycle 24. A similar evolution of the analyzed storms is noted.

An attempt to use the superposed epoch analysis in comparing various storms is done. The main results are: (1) the minimum stand-off distance varies between 6 and 12 R_E, (2) in the case of some storms (e. g. September 2012, August 2011) the stand-off distance can reach values as high as 6-7 R_E, depending on the conditions in the solar wind (very low SW dynamic pressure). The stand-off magnetopause distance variations are much larger than long-term ones are considered [Dobrica at al., 2012, Stefan et al., 2013].

The low values of L indicate times when there is an increased space weather hazard to technical networks (power networks and/or hydrocarbon pipes networks) at the Earth's surface. This subject will be approached in a separate paper.

Table 1 – Geomagnetic storms (SC 24)

Year	Date	Dst (nT)	SymH (nT)
2011	Aug, 06	-115	-126
2011	Sep, 26	-118	-113
2011	Oct, 25	-147	-160
2012	March, 09	-145	-150
2012	Apr, 24	-120	-125
2012	July, 15	-139	-123
2012	Oct, 01	-122	-138
2012	Oct, 09	-107	-116
2012	Nov, 14	-108	-118
2013	March, 17	-132	-132
2013	June, 01	-124	-137
2014	Feb, 19	-119	-127
2015	March, 17	-223	-234
2015	June, 23	-204	-208
2015	Oct, 07	-124	-124
2015	Dec, 20	-155	-170
2016	Jan, 01	-110	-117
2016	Oct, 13	-104	-114
2017	May, 28	-125	-142
2017	Sep, 8	-124	-146
2018	Aug, 26	-174	-206

References

Alken, P., Thebault, E., Beggan, C.D., et al. (2021), International Geomagnetic Reference Field: the thirteenth generation. Earth, Planets and Space, 73-49, doi: 10.1186/s40623-020-01288-x.

Chree, C., (1912), Some phenomena of sunspots and of terrestrial magnetism at Kew observatory. Philosophical Transactions A 212, 75

Chapman, S., Bartels, J., (1940), Geomagnetism. Oxford University Press, 1049 p.

Demetrescu, C., Dobrica, V., (2020), The geomagnetic dipole evolution in the last 400 years. Sub-centennial oscillations, in Chitea F. (Ed.), Geoscience for Society, Education, and Environment." Edited by Publishing Haus of the Romanian Academy.

Dobrica, V., Demetrescu, C., Maris, G., (2012), Solar Wind Dynamic Pressure and Magnetopause Stand-Off Distance. Sun and Geosphere, 7(1), 45-48.

Kamide, Y., Chian, A., (2007), Handbook of the Solar-Terrestrial Environment., Berlin, Heidelberg, Springer, 1, 128 p., doi: 10.1007/b104478.

Schield, M.A., (1996), Pressure balance between solar wind and magnetosphere. Journal of Geophysical Research, 5, 74.

Stefan, C., Dobrica, V., Demetrescu, C., (2013), On the evolution of geomagnetic activity in the last 300 years. Implications regarding solar wind dynamic pressure and magnetopause standoff distance. Sun and Geosphere, 8(1), 7-10.

Continuous Component of Solar Activity Spectrum and Solar Dynamo

Sokoloff D.D.

Moscow State University and IZMIRAN, Moscow, Russia
E-mail: sokoloff.dd@gmail.com.

Abstract.

Temporal spectrum of solar activity consists of a continuous part as well as eigenfrequency which correspond to the famous 11-year cycle. Nature of continuous elements of activity spectrum can be connected with nonlinear dynamo effects however an explanation in the framework of the linear mean-field dynamo approach seems to be possible as well. A scenario of the later explanation is suggested.

Introduction

Solar 11-year activity cycle is the most pronounced feature of solar activity. Solar dynamo is believed to be the physical mechanism underlying this activity cycle. More specifically, the cycle is connected with excitation of an eigen solution in mean-field solar dynamo equations. The imaginary part of corresponding eigen value gives the cycle length while the real part of the eigen value corresponds to the growth rate of the large scale magnetic field. Of course, this grows is saturated by various nonlinear effects and can not be observed directly.

The problem is that the 11-year cycle is far to be the only detail containing in solar activity spectrum. Various oscillations from about 1 year up to centuries have been reported as (quasi) biannual oscillations, mid-term oscillations, Gleissberg cycle etc. These oscillations seem to be substantially less regular rather the 11-year cycle. [*Frick et al., 2020*] consider them as continuous elements of solar activity spectrum.

Interpretation of the oscillations under discussion as continuous elements of solar activity spectrum requires a physical explanation for the elements. The point is that continuous spectrum is something different from eigensolution and the traditional explanation for dynamo action has to be somehow modified.

A most straightforward idea here is to claim that the continuous part of the spectrum arises as a nonlinear saturation of the excited eigensolution similarly to the continuous spectrum in turbulence or convection. This explanation suggested by [*Obridko et al., 2020*] exploits the same idea as famous Kolmogorov scenario for turbulent spectra. The only difference is that Kolmogorov considers multiplications of wave vectors while here one have to consider multiplication of frequencies from that one of 11-yers cycle up to frequencies which corresponds to events with duration of about 1 month.

This straightforward idea look reasonable indeed for many elements of continuous spectrum known however not covers however all known possibilities here. Indeed, stars without pronounced activity cycles which could be identified with excited eigensolution are possible and V833 Tau seems to be an instructive example here [*Stepanov et al., 2020*]. One more point is that the timescales longer rather 11-year cycle (say, Gleissberg cycle) are difficult for this explanation.

It looks attractive to suggest a mechanism for continuous spectrum generation just in the linear mean-field dynamo equations. It is just the aim of this paper.

Bohr-Sommerfeld conditions for spherical dynamos and continuous activity spectrum.

The explanation under discussion departs from the classical Landau scenario for transition to turbulence. Landau believed that enlarging intensity of fluid motion drivers one excites more and more eigenfrequencies in linearized version of governing equations for fluid motion. Due to various nonlinearities and instabilities each spectral line corresponding to an eigenfrequency has a finite width. If the density of spectral lines is high enough taken together they could be considered as a continuous spectrum. Each eigensolution arising can be obtained in the framework of a short-wavelength approximation from distribution of drivers of motion and boundary conditions similar to the Bohr-Sommerfeld conditions in quantum mechanics. The scenario is underlying by expectation that spectral problems for various equations of mathematical physics are more or less similar to that one for Schroedinger equation in quantum mechanics.

Indeed, mean-field dynamo equations for a spherical shell are formally similar to the Schroedinger equation [*Kuzanyan and Sokoloff, 1996*]. The point however is that this similarity is not perfect and dynamo equations do demonstrate some specific features. In particular, [*Galitsky and Sokoloff, 200?*] obtained the Bohr-Sommerfeld conditions for dynamo equations to learn that they can be satisfied for the leading growing solution while the value responsible for dynamo drivers distribution looks similar to a deep potential well and one could be expect excitation of many eigensotution.

Physical meaning of the Bohr-Sommerfeld condition is that the wave travelling inside the potential well reflects properly at the borders of the well what allows for the wave to exist unlimited times. Dealing with a problem where the Bohr-Sommerfeld conditions can not be properly satisfied for many possible eigenvalues, one can expect that corresponding magnetic oscillation survives for a limited time only and looks like (quasy)biannual, mid-term and other solar activity oscillations apart from the much more stable 11-year cycle/

Scenario suggested here requires a confirmation (or rejection) from the spectral theory of linear differential operators and is an open problem of functional analysis. Corresponding discussion is obviously out of the scope of this very paper.

Financial support from the BASIS Foundation under grant 21-1-1-4-1 is acknowledged.

Conclusions

1. Temporal spectrum of solar activity consists of a continuous part as well as eigenfrequency which correspond to the famous 11-year cycle.
2. Nature of continuous elements of activity spectrum can be connected with nonlinear dynamo effects however an explanation in the framework of the linear mean-field dynamo approach seems to be possible as well.
3. A scenario of the later explanation is suggested.

References

Frick, P., Sokoloff, D., et al. (2020). Spectral characteristic of mid-term quasi-periodicities in sunspot data, MNRAS, 491, 4, 5572-5578, 2020.

Galitsky V.M., Sokoloff, D.D. (1998). The spectrum of the Parker equations, Astronomy Reports, 42, 1, 127 - 133, 1998.

Kuzanyan, K.M., Sokoloff, D.D. (1995). A dynamo wave in an inhomogeneous medium, Geophysical and Astrophysicakl Fluid Dynamics, 81,1, 113 – 129 (1995) .

Stepanov, R., Bondar', N.I., et al. (2020). Wavelet analysis of the long-term activity of V833 Tau, MNRAS, 495, 4, 3788-3794 (2020).

Properties of Solar Activity Phenomena Detected during 2020 December 14 Total Solar Eclipse

Tsvetkov Ts., Petrov N., Shirov G.

Institute of Astronomy and National Astronomical Observatory,
Bulgarian Academy of Sciences, Sofia, Bulgaria
E-mail: tstsvetkov@astro.bas.bg

Abstract

During the total solar eclipse on 2020 December 14 a coronal mass ejection has been detected above a prominence on the eastern solar limb. Two active regions at the base and a streamer higher in the corona completed the diversity of activity phenomena on the Sun at that time.

Unfortunately, the expedition that our team planned to Argentina to observe the total solar eclipse failed and we had to use SDO/AIA and SOHO/LASCO data to analyze the parameters of the observed processes and trace the connection between the various manifestations of solar activity.

Introduction

Even in present days the total solar eclipses (TSEs) are still a significant opportunity for detailed explorations of solar corona and the dynamic events taking place in it, because of the ability they provide to capture the different parts of the corona simultaneously. The latest total eclipse was observed on 2020 December 14 from territories in South America. Our team planned an expedition to Argentina [*Tsvetkov et al.*, 2020] that was cancelled because of the international travel restrictions. Nevertheless, the eclipse that happened in a moment of a relatively active Sun, offered a rare opportunity to observe a coronal mass ejection (CME) during the totality.

CMEs originate in regions with closed magnetic field in the lower corona and erupt into the open-field regions of interplanetary space. Both space- and ground-based coronagraphs have been contributing to the study of CMEs with their continuous height coverage. Still they cannot effectively cover the distance range of 1.3 to 2.2 solar radii [*Boe et al.*, 2021] and 74% of CMEs undergo most dramatic acceleration below 1.5 solar radii [*Bein et al.*, 2011].

Other observers successfully captured the phenomenon [*Abramson*, 2021; *Boe et al.*, 2021]. Similar observations are also reported during previous eclipses [*Druckmüller et al.*, 2017; *Filippov et al.*, 2020; *Hanaoka et al.*, 2014; *Koutchmy et al.*, 2002].

Although we could not collect our own data, we use space-based observations from the day of the TSE to investigate the solar activity on the SE solar limb, partially or fully linked with the registered CME, in order to expand our knowledge about the relations between different active processes in the corona.

Space-based observations

The observations of space-based telescopes, shown on Figure 1, reveal part of the detected solar activity phenomena during the eclipse. Taken at 17:30 UT before the end of the full eclipse, the data from SOHO coronagraphs capture a “double-bubble” CME [*Boe et al.*, 2021], while AIA/SDO 304 Å observations demonstrate two active regions (ARs) and one of the two prominences on the south-eastern (SE) limb.

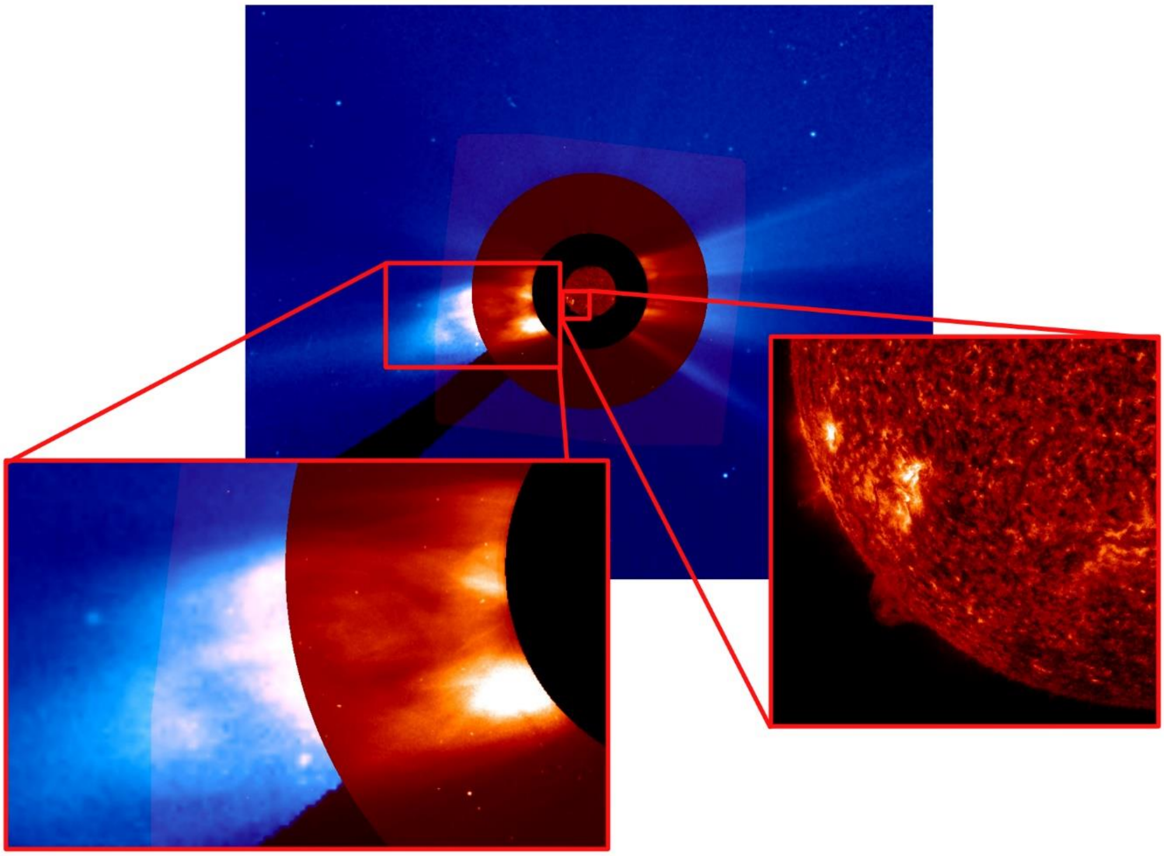

Fig. 1. Combined observations of LASCO/SOHO coronagraphs C2 and C3 with AIA/SDO 304 Å during the total solar eclipse (2020-12-14 17:30 UT).

Properties of the detected solar activity phenomena

a) Timeline of the events

The solar activity included in the current study covers only the phenomena registered at the SE quarter of the Sun on the day of the TSE – between 00:00 and 23:59 UT on 2020 December 14. The timing of the explored events is summarized on Figure 2. The base of the timeline is divided into two-hour intervals, its upper half shows the moments of onset of the eruptive events, while the length of the bars in the lower half demonstrate the duration of each phenomenon.

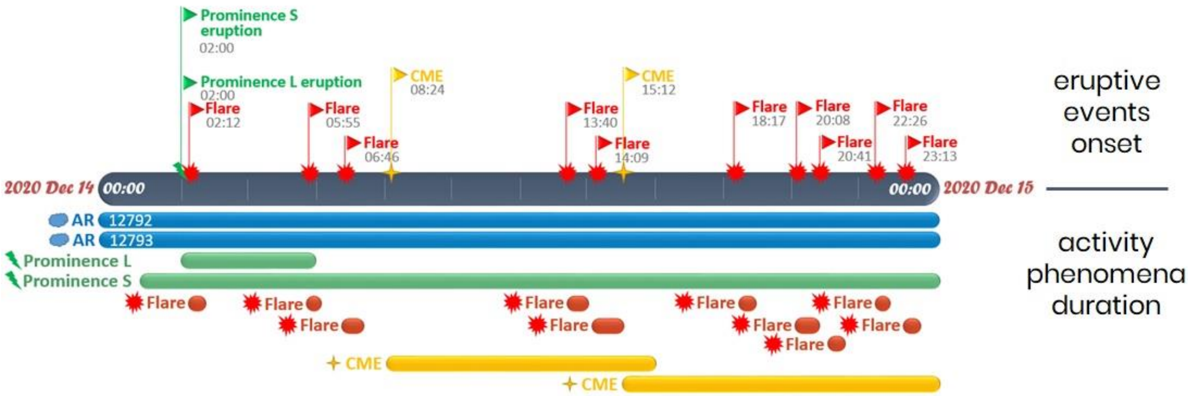

Fig. 2. Timeline of the events observed at the day of the TSE connected with the activity at the SE part of the Sun.

b) Active regions

Two ARs visible on the HMI/SDO magnetograms take place near the SE limb (Figure 3). The AR 12792 is better developed in the day of the TSE and it is the one clearly connected with the observed spectacular CME (hereby stated as CME2).

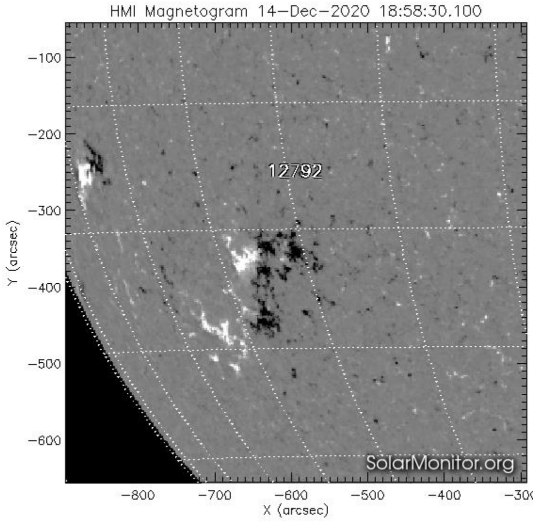

Fig.3. HMI/SDO magnetograms on the day of the eclipse showing the two ARs 12792 and 12793.

Information about the days of emergence, disappearance of the ARs and their properties in the day of the eclipse is presented in Table 1.

Table 1. Details for the two observed ARs according to the NOAA Space Weather Prediction Center.

NOAA	12792	12793
Emergence	13/12/2020	14/12/2020*
Disappearance	25/12/2020	27/12/2020
Position**	S22E52	S16E??
Hale Class**	Beta	Alpha
No. of sunspots**	4	-

**AR12793 is visible on the magnetograms from Dec 14, but receives officially NOAA No. the next day.*
***On the day of the eclipse (the information about AR12793 latitude is not given for that day).*

c) Prominences and their environment

Two prominences are visible on the SE limb on the day of the eclipse (Figure 4a). The first one (conditionally called "small") emerged before midnight on 2020 Dec 14 and remained a stable inhomogeneous structure even after the eclipse except for the time slot 2:00-9:00 when it erupted.

The other one ("large" prominence) appeared with its symmetric and less dense body, which made it difficult to observe to erupt at about 2:00 reaching higher altitudes (h_{max}) despite the relatively similar developed velocities (v_{max} & v_{avg}).

We tracked the position of the highest point of every prominence to build the height-time profiles of the two eruptions (Figure 5). The eruption of the large prominence is shorter and

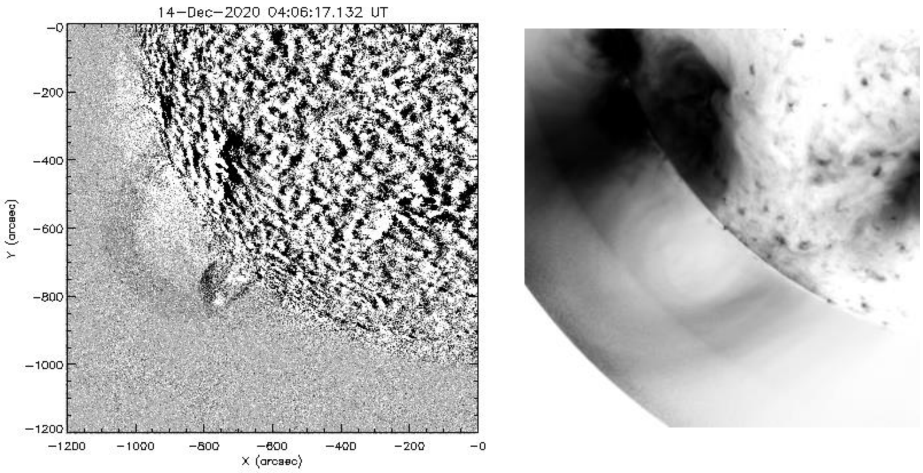

(a) (b)

Fig.4. AIA/SDO 304 Å image difference reveals the structure of the two prominences (a) while their environment is better displayed on AIA/SDO 211 Å data (b).

does not go through an activation phase. As soon as the prominence becomes visible in AIA 304 Å field of view, it starts rising, reaching almost 240 000 km for less than 3 hours while the smaller prominence reaches 150 000 km for more than 5.5 hours, but finally the eruption turns out to be confined and the prominence material starts falling back down to the Sun. More details are presented in Table 2.

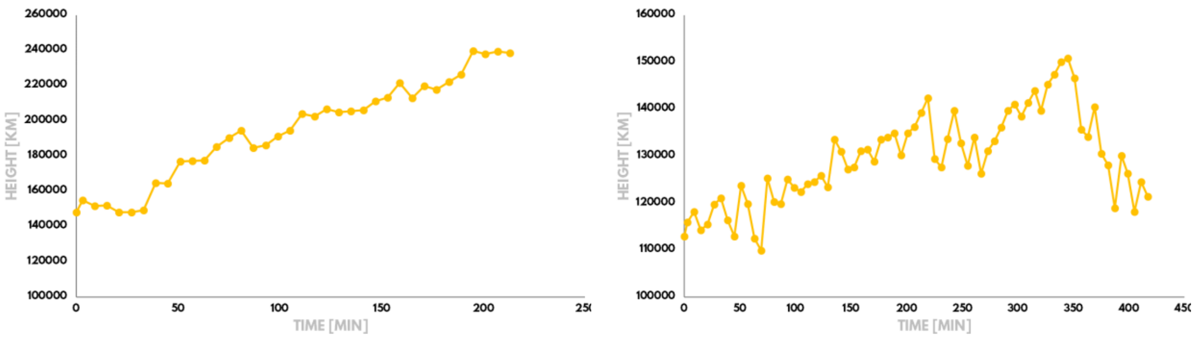

(a) (b)

Fig.5. Height-time profiles of the eruptions of the large prominence (a) and the small prominence (b).

Table 2. Properties of the explored prominences.

	Large	Small
Visibility [UT]	02-06	00-24
Eruption [UT]	02-06	02-09
Limb	SE	SE
Symmetry	S	A
h_{max} | h_{avg} [10^3 km]	239.5 | 193.7	150.8 | 129.4
v_{max} | v_{avg} [km s^{-1}]	43.2 | 12.7	42.8 | 11.9

At 6:00 UT on the day of the eclipse, a relatively stable equatorial streamer feature that had persisted for several hours is visible [*Boe et al.*, 2021]. Around 13:30 UT, a slow moving front on the northern part of the streamer (near the equator), continues to propagate for a few hours until it is enveloped by the fast CME seen during the eclipse, starting at 15:12 UT. Given its

location, speed and timing, this feature is likely to be the same, or part of the same overall structure, as a slowly erupting arch of the large prominence visible on the 211 Å data a few hours before (Figure 4b).

e) Coronal mass ejections

The two CMEs observed on 2020 Dec 14 could be linked with the active regions discussed above. The second CME that happens in the afternoon of 2020 December 14 (approximately and hour before the totality) is undoubtedly faster and more powerful (Table 3). It reaches almost 20 solar radii height and develops more than 10 times the speed of CME1 while the first CME doesn’t even enter the C3 coronagraph FOV. The CME speeds and heights are in agreement with the evaluations of other authors [*Boe et al.*, 2021].

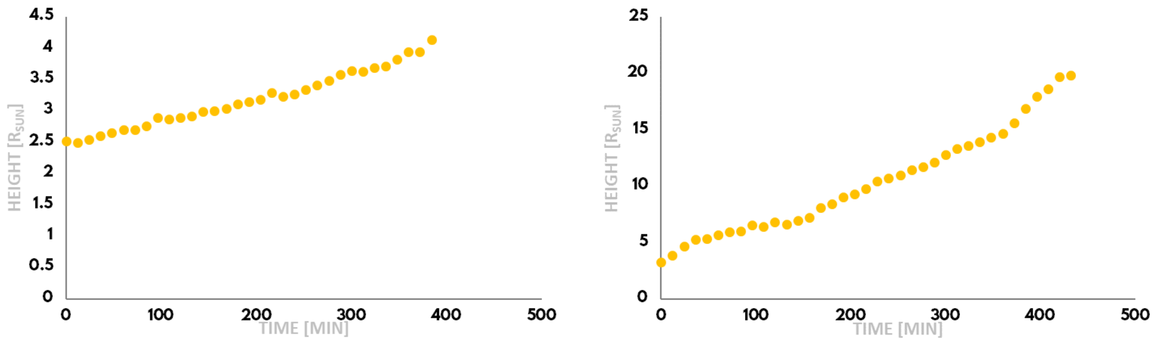

(a) (b)

Fig.6. Height-time profiles of CME1 (a) and CME2 (b).

Table 3. Temporal, spatial and kinematic properties of the explored CMEs. The information for the onset, position angle, angular width and linear speed is taken from SOHO/LASCO CME Catalog [Yashiro et al., 2004].

	1	2
Time [UT]	08:24:05	15:12:10
Central Position Angle [deg]	121	121
Angular Width [deg]	80	88
v [km s^{-1}]	41	437
h_{max} [R_{sun}]	4.14	19.87
h_{avg} [R_{sun}]	3.19	10.42

d) Flares

The two ARs observed on the SE limb on the day of the eclipse demonstrated relatively high flare-productivity – 10 flares are registered by the GOES soft X-ray flare listings (Table 4). Special attention attracts the C4.0 class flare reported at 14:09 during the activation of CME2. The association obtained by GOES flare listing with AR12792 and the given coordinates (S22E48) coincide with the location and timing of the erupting AR that is also linked with CME2.

Table 4. Characteristics of the flares from the SE quarter of the Sun on the day of the TSE as given by the GOES soft X-ray flare listings.

Start [UT]	Peak [UT]	End [UT]	Class	AR
02:12	02:20	02:26	B1.3	12792
05:55	05:59	06:04	B1.4	12793
06:46	06:57	07:03	B1.1	12792
13:40	13:49	13:59	B1.4	12792
14:09	14:37	14:56	C4.0	12792
18:17	18:24	18:32	B2.2	12793
20:08	20:16	20:38	B2.4	12793
20:41	20:44	20:56	B3.5	12793
22:26	22:33	22:37	B2.0	12793
23:13	23:21	23:30	B1.7	12793

Conclusions

The present study summarizes the data from various sources for solar activity observed on the day of the latter total solar eclipse (2020 December 14) on the southeastern limb. Comparison between the spatial and temporal characteristics of various solar activity events in combination with data from different instruments on different wavelengths shows the relations between the active processes in solar atmosphere.

Our measurements and analyses expand the knowledge for different manifestations of solar activity and the connection between them especially when combined with the data of observers that successfully monitored the corona during the eclipse.

Acknowledgment

This work is supported by the National Science Fund of Bulgaria with contracts No.: KP-06-H28/4 and KP-06-M38/3.

References

Abramson, G. (2021). Serendipitous observation of a coronal mass ejection during the total solar eclipse of 14 December 2020, Pap. Phys., vol. 13, art. 130004.

Bein, B. M., Berkebile-Stoiser, S., Veronig A. M., Temmer, M., Muhr, N., Kienreich, I., Utz, D., Vršnak, B. (2011). Impulsive Acceleration of Coronal Mass Ejections. I. Statistics and Coronal Mass Ejection Source Region Characteristics, ApJ 738, 191.

Boe, B., Yamashiro, B., Druckmuller, M., Habbal, S. (2021). The Double-Bubble CME of the 2020 December 14 Total Solar Eclipse, ApJ 914 (2), L39.

Druckmüller, M., Habbal, S., Alzate, N., Emmanouilidis, C. (2017). Tethered Prominence-CME Systems Captured during the 2012 November 13 and 2013 November 3 Total Solar Eclipses, ApJL 851, L41.

Filippov, B., Koutchmy, S., Lefaudeux, N. (2020). Solar Total Eclipse of 21 August 2017: Study of the Inner Corona Dynamical Events Leading to a CME, Sol. Phys. 295**,** 24.

Hanaoka, Y., Nakazawa, J., Ohgoe, O., Sakai, Y., Shiota, K. (2014). Coronal Mass Ejections Observed at the Total Solar Eclipse on 13 November 2012. Sol. Phys. 289(7), 2587–2599.

Koutchmy, S., Baudin, F., Bocchialini, K., Daniel, J.-Y., Delaboudinière, J.-P., Golub, L., Lamy, P., Adjabshirizadeh, A. (2004). The August 11th, 1999 CME, A&A 420, 709-718.

Tsvetkov, Ts., Petrov, N., Miteva, R., Ivanov, E., Popov, V. (2020). Bulgarian Expedition for the Total Solar Eclipse on 2020 December 14, Proc. 12-th Workshop “Solar Influences on the Magnetosphere, Ionosphere and Atmosphere”, p. 40.

Yashiro, S., Gopalswamy, N., Michalek, G., Cyr, St., Plunkett, S. P., Rich, N. B., Howard, R. A. (2004). A catalog of white light coronal mass ejections observed by the SOHO spacecraft, J. Geo

Decrease in Solar Wind Parameters after a Minimum of 22-23 Solar Cycles

Yermolaev Yu.I., Lodkina I.G., Khokhlachev A.A., Yermolaev M.Yu.

Space Research Institute RAS, Moscow, Russia
E-mail: yermol@iki.rssi.ru

Abstract.

On the basis of the OMNI database data, the behavior of solar wind plasma and magnetic field parameters of 21-24 solar cycles (1976-2019) is studied. In the analysis, the data are selected according to the types of large-scale solar wind phenomena in the site http://www.iki.rssi.ru/pub/omni [*Yermolaev et al.*, 2009] and phases of solar cycles. The analysis showed that during the minimum of 22-23 solar cycles, the parameter values decreased by 20-40% in different types of solar wind and continued to be low during the 23 and 24 cycles [*Yermolaev et al.*, 2021]. The effect of this decrease in solar wind parameters on space weather is discussed.

Introduction

One of the aims of solar, interplanetary and solar-terrestrial physics is the experimental investigation of long-term variations in solar wind (SW) parameters. Variations in the interplanetary parameters with scales ~1 year are an important characteristic of solar activity and the basis for a long-term space weather forecast [*Dmitriev et al.*, 2009; *Yermolaev et al.*, 2012; 2021; *Gopalswamy et al.*, 2015]. Changes in the parameters can be associated both with a change in the number of different large-scale types of SW and with variations in the values of these parameters at different phases of the solar cycle (SC) and during the transition from one cycle to another. Therefore, in this work, we average the data selected by the types of large-scale SW phenomena and phases of solar cycles 21-24, and study their changes in the period 1976-2019.

Data and Methods

In this work, we use two sources of information: (1) Hourly data of OMNI base parameters for 1976-2019 (https://spdf.gsfc.nasa.gov/pub/data/omni/low_res_omni, *King and Papitashvili*, 2005), and (2) Intervals of different types of SW of the catalog of large-scale phenomena (http://www.iki.rssi.ru/pub/omni, *Yermolaev et al.*, 2009), created on the basis of the OMNI database. The data were divided into intervals of SC phases, as shown in Table. 1.

Table 1. *Averaging intervals over phases of the solar cycle*

№ interval	№ Cycle	Phase of cycle	Years
1	21	minimum phase	1976
2		rising phase	1977,1978
3		maximum phase	1979-1981
4		declining phase	1982-1984
5		minimum phase	1985-1987
6	22	rising phase	1988
7		maximum phase	1989-1991
8		declining phase	1992-1994
9		minimum phase	1995-1997
10	23	rising phase	1998-1999
11		maximum phase	2000-2002
12		declining phase	2003-2005
13		minimum phase	2006-2009
14	24	rising phase	2010,2011
15		maximum phase	2012-2014
16		declining phase	2015-2016
17		minimum phase	2017-2019

Results

Figs 1-6 present time profiles of parameters of solar wind plasma and interplanetary magnetic field (IMF) averaged over phases of solar cycles (Table 1): minimum – black circles, rising phase – blue triangles, maximum – purple squares, declining phase – green inverted triangles, without selection with phases – red open squares. The data for magnetic clouds are widely scattered in all figures due to the small number of events. The largest scatter is observed for the proton temperature T, and since it has a lognormal distribution [Dmitriev et al., 2009], we averaged the logT value.

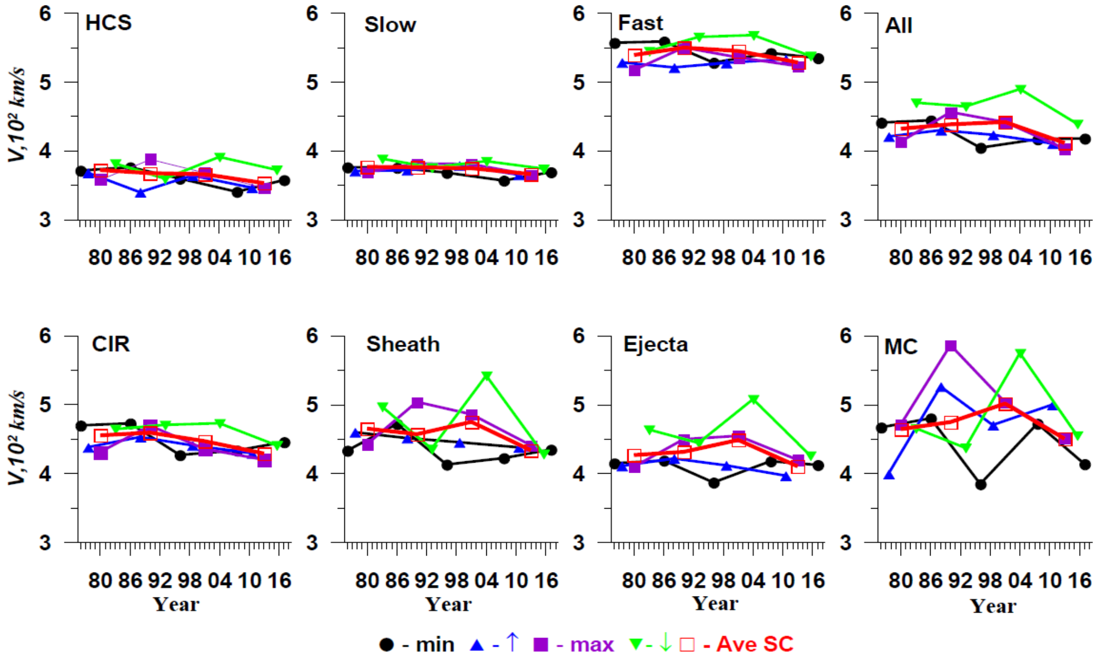

Fig.1. Time profiles of bulk velocity V in 7 different types of SW (heliospheric current sheet – HCS, Slow and Fast streams, CIR, Sheath, Ejecta and MC) and without SW type selection (All)

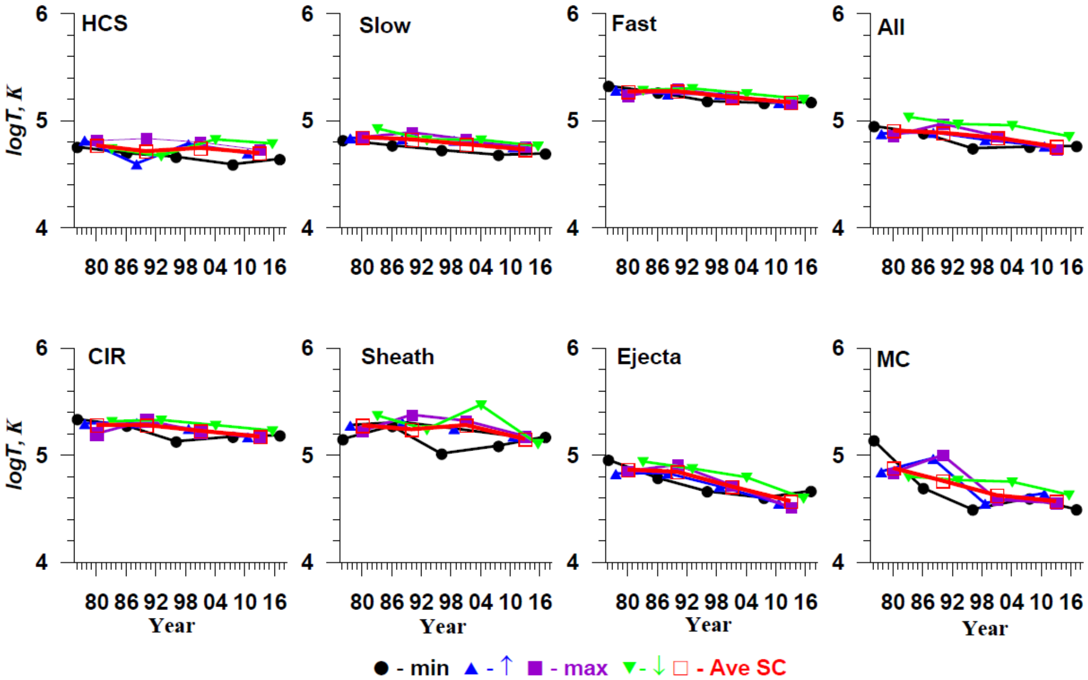

Fig.2. Time profiles of logarithm of proton temperature T

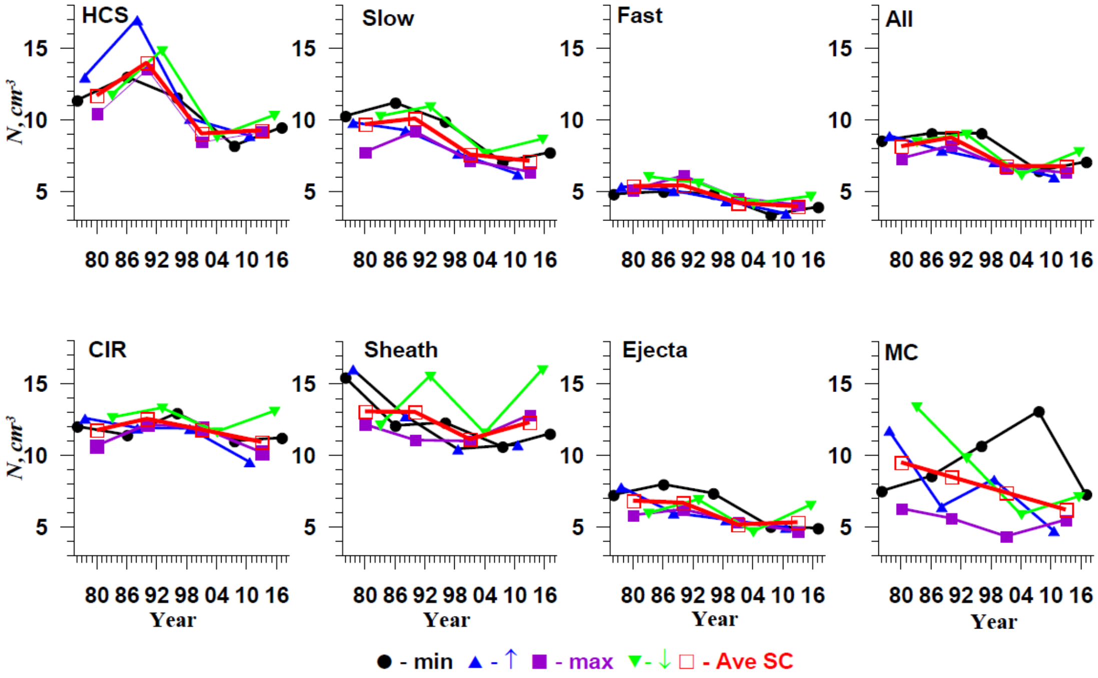

Fig.3. Time profiles of density N

The speed (V) and temperature (log T) depend little on the phase of cycle, but show a weak decreasing trend with an increase in the SC number. Density changes in a similar way, but shows a higher dependence on phase (higher in minimum phase) and a sharper drop in the middle of the interval. The parameters calculated on the basis of V, T and N change in a similar way with more obvious decreases at ~1995 (not shown here).

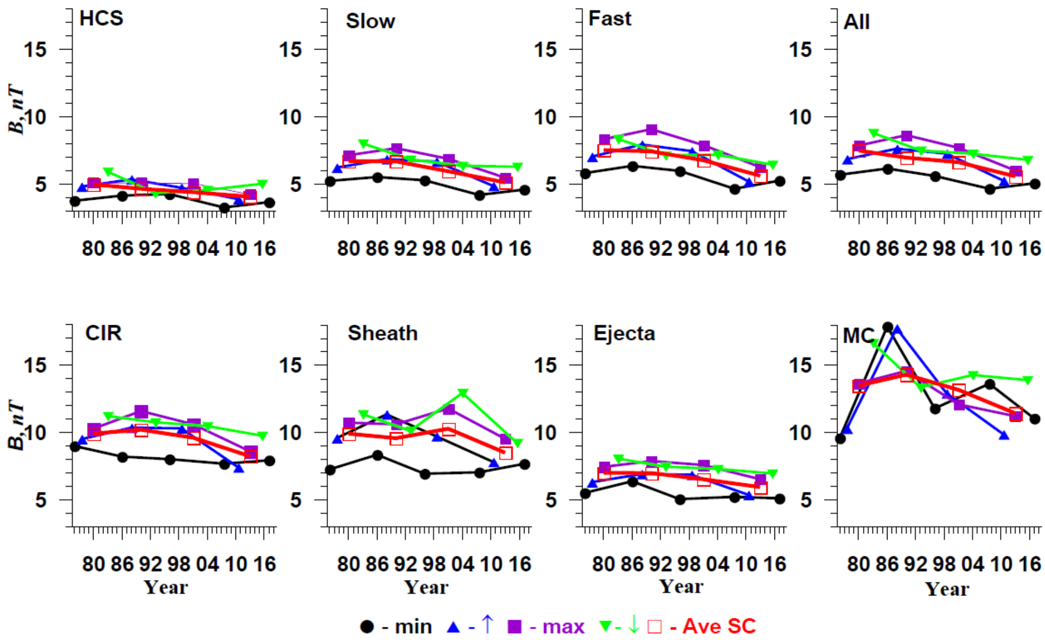

Fig.4. Time profiles of magnitude of IMF B

Magnitude of IMF B depends rather strongly on the SC phase (lower in minimum phase) and clearly decreases near the minimum of 22-23 cycles.

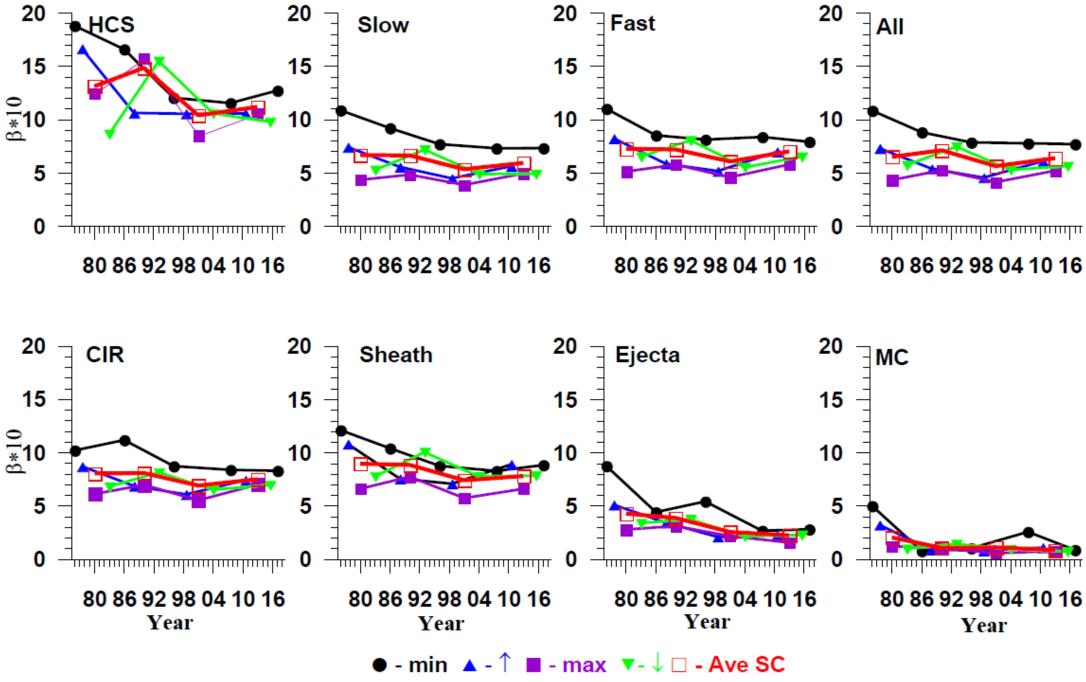

Fig.5. Time profiles of proton β-parameter

Despite the fact that the β-parameter is the ratio of thermal to magnetic pressures, which have decreasing trends over time, the β-parameter has a clear dependence on the SC phase and clearly decreases near the minimum of 22-23 cycles.

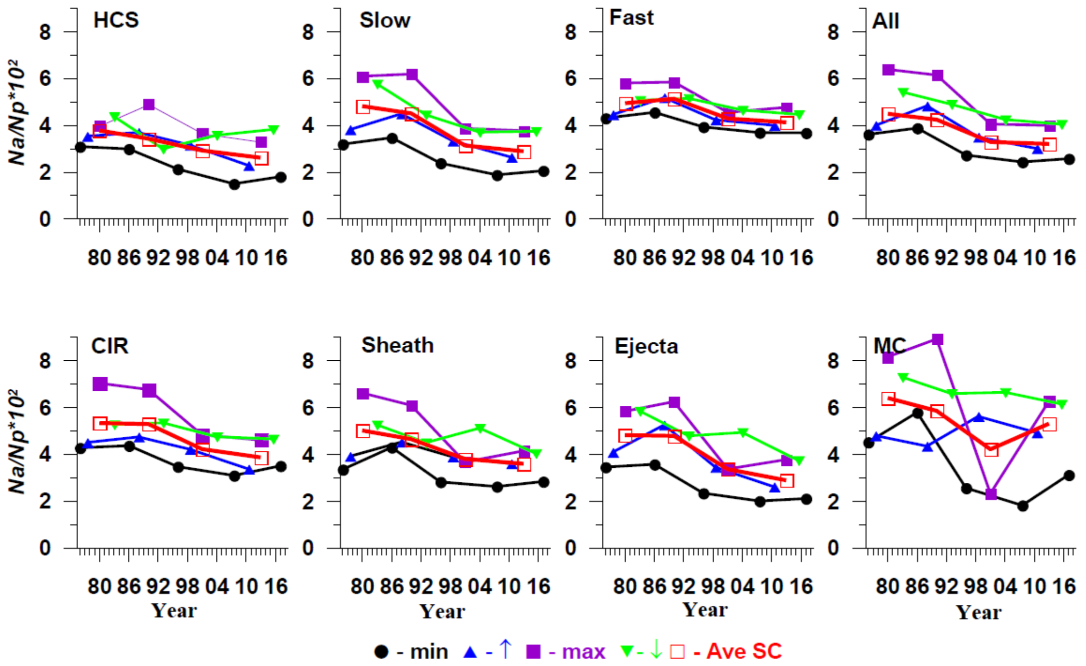

Fig.1. Time profiles of helium abundance Nα/Np

Helium abundance Nα/Np depends rather strongly on the SC phase (lower in minimum phase) and clearly decreases near the minimum of 22-23 cycles.

Discussion and Conclusions

Thus, we examined the behavior of interplanetary plasma and IMF parameters over 21-24 solar cycles on the basis of OMNI database (https://spdf.gsfc.nasa.gov/pub/data/omni) [*King and Papitashvili*, 2005]. We selected the intervals in accordance with various types of solar wind using the catalog of large-scale solar wind types for 1976-2019 (http://www.iki.rssi.ru/pub/omni, [*Yermolaev et al.*, 2009]) and in accordance with the phases of the solar cycles, and averaged the parameters at selected intervals. As a result of this analysis, the following important conclusion can be drawn. In addition to the well-known fact that in 23-24 solar cycles the number of disturbed types of solar wind (ICME and related Sheath types) sharply decreased, at the end of the 20th century and the beginning of the 21st century there is a noticeable drop (by 20-40%) in the values of the parameters plasma and magnetic field in various types of solar wind and the low level of parameters persists or continues to decrease in 23-24 cycles [*Yermolaev et al.*, 2021].

It should be noted that the above results on the decrease in parameters in 23-24 cycles were obtained for different physical quantities measured by various methods and different instruments on various spacecraft included in the OMNI database. This greatly reduces the likelihood that this decline is associated with some methodological effects and increases the reliability of the results and conclusions.

Such a drop in the solar wind parameters in 23-24 cycles is apparently associated with a decrease in solar activity and results in a noticeable decrease in space weather factors.

References

Dmitriev, A. V., Suvorova, A. V., Veselovsky, I. S. (2009). Statistical characteristics of the heliospheric plasma and magnetic field at the earth's orbit during four solar cycles 20-23, in HANDBOOK ON SOLAR WIND: EFFECTS, DYNAMICS AND INTERACTIONS. — Nova Science Publishers, Inc New York

Gopalswamy, N., Tsurutani, B. & Yan, Y. (2015). Short-term variability of the Sun-Earth system: an overview of progress made during the CAWSES-II period. Prog. in Earth and Planet. Sci. 2, 13. https://doi.org/10.1186/s40645-015-0043-8

King, J. H., & Papitashvili, N. E. (2005). Solar wind spatial scales in and comparisons of hourly wind and ACE plasma and magnetic field data. Journal of Geophysical Research, 110, A02209. https://doi.org/10.1029/2004JA010649

Yermolaev, Yu. I., N. S. Nikolaeva, I. G. Lodkina, and M. Yu. Yermolaev (2009), Catalog of Large-Scale Solar Wind Phenomena during 1976-2000, Cosmic Research, , Vol. 47, No. 2, pp. 81-94.

Yermolaev, Yu. I., Nikolaeva, N.S., Lodkina, I.G., Yermolaev, M. Yu. (2012). Geoeffectiveness and efficiency of CIR, sheath, and ICME in generation of magnetic storms. Journal of Geophysical Research: Space Physics,117, https://doi.org/10.1029/2011JA017139

Yermolaev, Yu. I., Lodkina, I. G., Khokhlachev, A. A. et al., (2021), Drop of solar wind at the end of the 20th century, J. Geophys. Res. Space Physics, DOI: 10.1029/2021JA029618

Probing the Double Dynamo Model with Solar-Terrestrial Activity in the Past Millennia

Zharkova V.V.[1,2], Popova E.[2], Shepherd S. [3], Zharkov S.I.[2,4]*

[1]Northumbria University, Department of MPEE, Newcastle upon Tyne, UK
[2] ZVS Research Enterprise Ltd., London, UK
[3]PRIMAL Research Group, Sorbonne University, Paris, France
[4]University of Hull, Department of Physics and Mathematics, Kingston upon Hull, HU6 7RX, UK *valentina.zharkova@northumbria.ac.uk

Abstract
Using a summary curve of two eigen vectors of solar magnetic field oscillations derived with Principal Components Analysis (PCA) from synoptic maps for solar cycles 21-24 we extrapolate solar activity backwards three millennia showing 9 grand cycles of 350-400 years. The summary curve shows a remarkable resemblance to the past sunspot and terrestrial activity: grand minima - Maunder Minimum (1645-1715AD), Wolf minimum (1280-1350 AD), Oort minimum (1010-1050 AD) and Homer minimum (800-900 BC) and grand maxima - modern warm period (1990-2015), medieval warm period (900-1200 AD), Roman warm period (400-10 BC) and others. We verify the extrapolated activity curve by pre-telescope observations of large sunspots, by maximum of the terrestrial temperature and extremely intense terrestrial auroras seen in 14-16 centuries and observed and simulated butterfly diagram for the Maunder Minimum (MM). We confirm the occurrence of upcoming Modern grand minimum in 2020-2055 and show it will have higher solar activity and shorter duration compared to MM. We argue that Sporer minimum (1450-1550) derived from the increased abundances of isotopes ^{14}C and ^{10}Be is likely produced by a strong increase of the terrestrial background radiation caused by galactic cosmic rays of powerful supernovae.

Introduction

Cycles of magnetic activity are associated with the action of a mean solar dynamo mechanism called '$\alpha - \Omega$ dynamo (Parker 1955) assuming that the action of the solar dynamo occurs in a single spherical shell, where twisting of the magnetic field lines (α-effect) and the magnetic field line stretching and wrapping around different parts of the Sun, owing to its differential rotation (Ω-effect), are acting together (Brandenburg & Subramanian 2005; Jones et al. 2010). As a result, the magnetic flux tubes (toroidal magnetic field) seen as sunspots are produced from the solar background magnetic field (SBMF) (poloidal magnetic field) during 11 years of solar cycle by a joint action of differential rotation and radial shear, while the conversion of toroidal magnetic field into poloidal field is governed by the convection in a rotating body of the Sun.

Our understanding of solar activity is tested by the accuracy of its prediction. The latter became very difficult to derive from the observed sunspot numbers and to fit sufficiently close into a few future 11 year cycles or even into a single cycle until it is well progressed (Pesnell, 2008). Consistent disagreement in a large number of models between the measured sunspot numbers and the predicted ones for cycle 24 is likely to confirm that the appearance of sunspots on the surface during a solar cycle is governed by the action of some physical processes of solar dynamo, which are not yet considered in the models.

In order to reduce dimensionality of these processes in the observational data, Principal Component Analysis (PCA) was applied (Zharkova et al, 2012) to the low-resolution full disk magnetograms captured by Wilcox Solar Observatory in cycles 21-23. This approach revealed a set of more than 8 independent components (ICs) of temporal variations of solar background magnetic field (SBMF), which seem to appear in pairs. The two principal components (PCs) (reflecting strongest waves of solar magnetic oscillations) have the highest eigen values covering about 39% of the data by variance (Zharkova et al, 2012), or 67% of the data by standard deviation.

The main pair of PCs is shown (Zharkova et al, 2015) to be associated with the two magnetic waves attributed to the poloidal magnetic field describing a double dynamo action in two different layers of the solar interior with dipolar magnetic sources in each layer. These waves are found originating in the opposite hemispheres and travelling with an increasing phase shift to the Northern hemisphere in odd cycles and the Southern hemisphere in even cycles (Shepherd et al, 2014, Zharkova et al, 2015). The maximum (or double maximum for the double waves with a larger phase shift) of solar activity for a given cycle coincides with the time when each of the waves approaches a maximum amplitude and the hemisphere where it happens becomes the most active one. This can naturally account for the north-south asymmetry of solar activity often reported in many cycles.

At every phase of an 11 solar cycle, these two magnetic waves of poloidal field can be converted by electromotive force to a toroidal magnetic field associated with sunspots (Parker, 1955). The existence of two waves in the poloidal (and toroidal) magnetic fields instead of a single one for each of them, used in the most prediction models, and the presence of a variable phase difference between the waves can naturally explain the difficulties in predicting sunspot activity with a single dynamo wave on a scale longer than one solar cycle (Karak & Nandy 2012). We showed that the sunspot activity (average sunspot numbers) is associated with the modulus summary curve (Zharkova et al, 2015), which is not a single wave as often assumed but a superposition, at least, of two waves, the PCs, used for production of the summary curve, from which one takes a modulus.

Recently, these solar activity prediction results about the modern GSM in cycles 25-27 were confirmed by the other researchers (Kitiashvili 2020; Obridko et al. 2021), who were using the same WSO synoptic magnetic field data and compared the spectra of the zonal harmonics of the SBMF and 3D solar dynamo models. Furthermore, Velasco Herrera et al. (2021) applied the machine learning (ML) algorithm to the averaged sunspot numbers taken from the International Sunspot Number (SSN) from the World Data Center Sunspot Index and Long-term Solar Observations reporting the modern Grand Solar Minimum to occur in cycles 25-27, exactly as reported by Zharkova et al. (2015).

In the current paper we show that the application of the appropriate statistical method used to reproducing the highly oscillating function of solar activity (Zharkova et al, 2015) by a set of periodic functions cosines allows us to extrapolate the solar magnetic field rather accurately backward three thousand years. We also highlight the essential differences of the solar activity curve reconstructed by us in the current paper from the recent long-term reconstruction of solar activity based on the terrestrial carbon 14 and beryllium 10 isotope dating and using a linear regression method for their extrapolation (Usoskin et al. 2002, 2004; Solanki & Krivova 2011). Moreover, we show below that Spoerer minimum derived by this reconstruction is likely to be an artefact of the terrestrial and Galactic activity caused by supernovae and not associated with solar activity.

Restoration of double dynamo waves for the past three millennia

As in our previous papers (Zharkova et al, 2015, 2020) we tested the original magnetic field data from full disk magnetograms for the past 3 solar cycles (21-23) with Principal Component Analysis and derived the eigen values and eigen vectors of solar oscillations. These came in pairs, with the highest eigen values of variance considered as the two principal components (PCs) associated with the dipole magnetic sources in both layers. These waves can be closely reproduced by the simulated waves derived from the two-layer dynamo model with meridional circulation (Zharkova et al, 2015) similar to the two cells reported from the helioseismic observations (Zhao et al, 2013)

There are rather stable magnitudes of the eigen values of these two dynamo waves for each and every solar cycle considered proving that the parameters of own oscillations of the Sun are maintained the same over a large period of time (millennia). This is re-assuring a very good health of the Sun's dynamo machine. The variations of the dynamo wave parameters occur owing to different conditions in these two layers where the waves are generated leading to their close but not equal frequencies. These variations are shown to cause the beating effect of these two waves, which produces a number of grand cycles and grand minima occurring every 350-400 years shown in the past millennium (see Fig.3 in Zharkova et al, 2015).

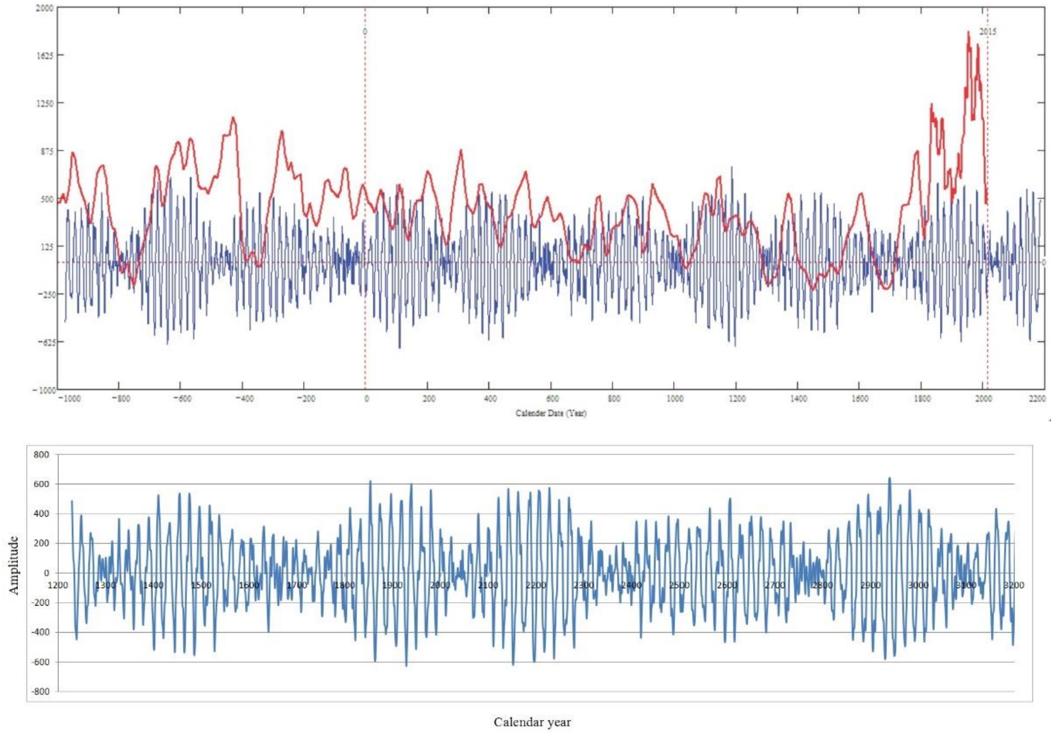

Figure 1. *Top plot: solar activity prediction backwards 3000 years with a summary curve (blue line) of the two principal components (PCs) of solar background magnetic field (SBMF) (Zharkova rt al, 2015) derived from the full disk synoptic maps of Wilcox Solar Observatory for cycles 21-23 versus the reconstruction by Solanki et al. (2004) (red line) by merging the sunspot curve (17-21 centuries) and carbon dating curve (before the 17 century). The bottom plot: the summary curve of two PCs calculated for 1200-3200 years (Zharkova et al., 2015)*

In the current paper we extend this extrapolation 3000 years backwards to 1000 BC as shown in Fig.1 (top plot, blue curve). For comparison, we have overplotted the curve of the solar activity reconstructed by Solanki et al 13, 15-17 from the average sunspot numbers observed before the 17 century and from the isotope $\Delta^{14}C$ and ^{10}Be abundances in earlier years (9-16 centuries) (top plot, red curve).

It can be noted that our summary curve extended by 3000 years backward (up to 1000 BC) in Fig. 1 is rather different from the curve reconstructed by Usoskin and Solanki et al (Solanki et al. 2004; Usoskin et al. 2004; Solanki & Krivova 2011). We believe, these differences are caused by the inaccuracies of reconstruction of a periodic function of solar activity by a linear regression analysis used by these authors, which is, in fact, only applicable to the normal data (with Gaussian distribution).

Whilst our reconstruction summary curve uses a Hamiltonian regression analysis with periodic cosine functions for reproduction of the oscillatory curve of solar activity (see Methods section). The curve reveals a remarkable resemblance to the sunspot and terrestrial activity reported in the past years showing accurately: the recent grand minimum (Maunder Minimum) (1645-1715), the other grand minima: Wolf minimum (1300-1350), Oort minimum (1000-1050), Homer minimum (800-900 BC); also the Medieval Warm Period (900-1200), the Roman Warm Period (400-150 BC) and so on. These minima and maxima in the past millennia reveal the presence in solar activity of a grand cycle with a duration of about 350-400 years with the next grand cycle minimum (we call it a Modern minimum) approaching in 2020-2053 (Zharkova et al, 2015, Zharkova, 2020).

The long-term 'grand' cycle was previously considered as a 300-400 year cycle superimposed on the 22 year cycle using the observations of aurorae, periods of grape harvests etc. (Kingsmill 1906; Wagner et al. 2001). These periods are close to the period of a grand cycle (350-400 years) reported by Zharkova et al, 2015 as plotted in Fig.1 (bottom plot) and extended to further 3 millennia in Fig.1 (top plot).

It turns out that longer grand cycles have a larger number of regular 22 year cycles inside the envelope of a grand cycle but their amplitudes are lower than in shorter grand cycles. This means that there are significant modulations of the magnetic wave frequencies generated in the two layers: a deeper layer close to the bottom of the Solar Convective Zone (SCZ) and shallow layer close to the solar surface for these different grand cycles and their individual solar cycles, whose physical conditions define the frequencies and amplitudes of dynamo waves generated in these layers. The larger the difference between these frequencies the smaller the number of regular 22 years cycles and the higher their amplitudes.

In addition to the grand cycle of 350-400 years, by combining the curves in Fig.1 (top plot, blue curve) and the curve used for the prediction for the next 1000 years in Fig. 3 of Zharkova et al (2015) reproduced in Fig. 1 (bottom plot), one can also note a larger *super-grand cycle* of about 2000-2100 years (Hallstatt's cycle), which is often reported in the spectral analysis of solar and planetary activity (Steinhilber et al, 2009, 2012; Zharkova et al., 2019). This super-grand cycle can be distinguished by comparing the five grand cycles in Fig. 1 (bottom plot) (years 1001-3000 AD) with the next 5 grand cycles restored for 1000 BC-1000 AD) (top plot), which clearly show the same repeating patterns for every 5 grand cycles (Zharkova et al, 2019).

There are the other 3 pairs of the significant independent magnetic field components (Zharkova et al, 2012), which are associated with quadruple magnetic sources in these layers, which can further modify the individual variations of 22 year cycles within each grand cycle (Zharkova et al, 2022). Although, quadruple waves (covered by smaller variance) have much smaller amplitudes, they are expected to modify solar activity to reproduce intermediate minima similar to Dalton's minimum (Popova et al, 2018).

However, there is another minimum, Spoerer's one (1450-1550), which is also not present in our summary curve (the blue curve) plotted in Fig.1, which shows during the same period of time a maximum of the grand cycle. In this case even the inclusion of quadruple components is unlikely to account for the major solar minimum, like Spoerer one, which has the properties of a grand minimum but in the absolutely wrong time. We discuss the discrepancy of Spoerer minimum in one of the sections below.

Verification of the solar activity from PCA with historic observations

Let us first check the evidences from the solar-terrestrial environment in the previous grand cycle in 14-16 century and the presence of the grand maximum when Spoerer minimum occurred plotted in Fig.2 as the summary curve.

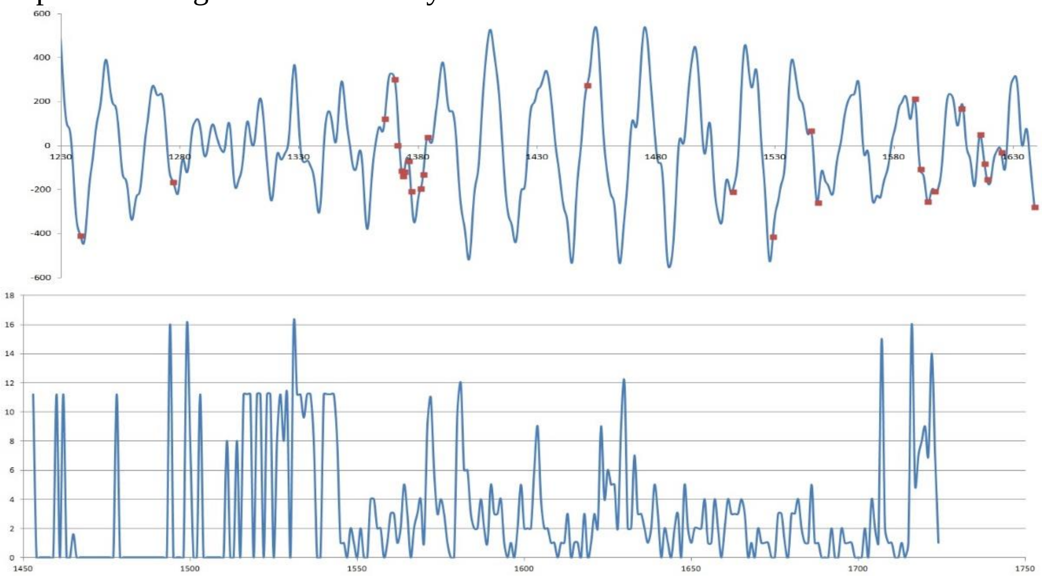

Figure 2. *Top plot: verification of the summary curve (blue line) with large sunspots (red dots) derived from the pre-telescope visual observations for the time of Sporer minimum. Bottom plot: distributions of terrestrial auroras over the period of Spoerer minimum revealing the strongest auroras ever observed. The auroras are widely observed all over the central Europe and often reached Mediterranian countries.*

The first verification comes from the pre-telescope observations of large sunspots observed (when possible) with the naked eye by Chinese and Japanese astronomers in the 13-16 centuries (Williams 1873; Wittmann 1978; Wittmann & Xu 1987) presented in Fig. 2, top plot. It can be seen that in the times when the large sunspots were observed they fit extremely well the individual solar cycles predicted by our summary curve in the 13-14 centuries prior to the alleged Spoerer minimum. It can be also seen that the pre-telescope observations of large sunspots in the 14-15 centuries done by Chinese astronomers (Wittmann 1978; Wittmann & Xu 1987) were rather patchy in the 14-15 centuries. They did not show any signs of a minimum of solar activity during the two cycles before and after 1380, which fit rather closely our predictions of the summary curve for these cycles.

Then during 1450-1550 (the alleged Spoerer minimum) there were also two large sunspots observed with a naked eye (see Fig.2, top plot), while during the next large solar minimum in the 17th century, Maunder Minimum, there were no large sunspots reported at all by any researchers even with telescopes, and the sunspot numbers were very small. This makes Spoerer minimum with two large sunspots a bit peculiar minimum, and we discuss its further in the sections below.

The second verification occurs from the reconstruction of the terrestrial temperature in Northern hemisphere compiled from 6 different sources as reported by Usoskin et al. (2005) (see Fig.2, bottom plot). It clearly shows that the temperature variations between 1450-1600 have a clear maximum and not the minimum as one could expect if the solar activity had the Sporer minimum. For example, for Maunder Minimum the terrestrial temperature goes through a well defined minimum seen clearly in the same Fig.2, bottom plot) from Usoskin et al. (2005).

The third verification comes from very strong auroras a reported in 14-16 centuries over ll over the skies of the whole Europe including Germany, Poland, Switzerland and even Portugal with other Mediterrenian countries (Schlamminger 1990; Schroder & Treder 1999). For this particular grand cycle in Fig.2 (bottom plot) we present the intensities of auroras during the period of Spoerer minimum. Similar to the terrestrial temperatures above, strong auroras coincide with the *maxima* of solar activity and not with its minima and, especially, not with the prolonged minimum as Spoerer’s one is assumed to be. It is clear that the intensities of these unusual auroras in 14-16 centuries significantly exceed the intensities of the auroras ever observed on Earth in the past 500 years s (Schlamminger 1990; Schroder & Treder 1999) and, definitely, they do not have lower intensities expected for a deep solar minimum.

The butterfly diagrams for Maunder and Modern grand minima

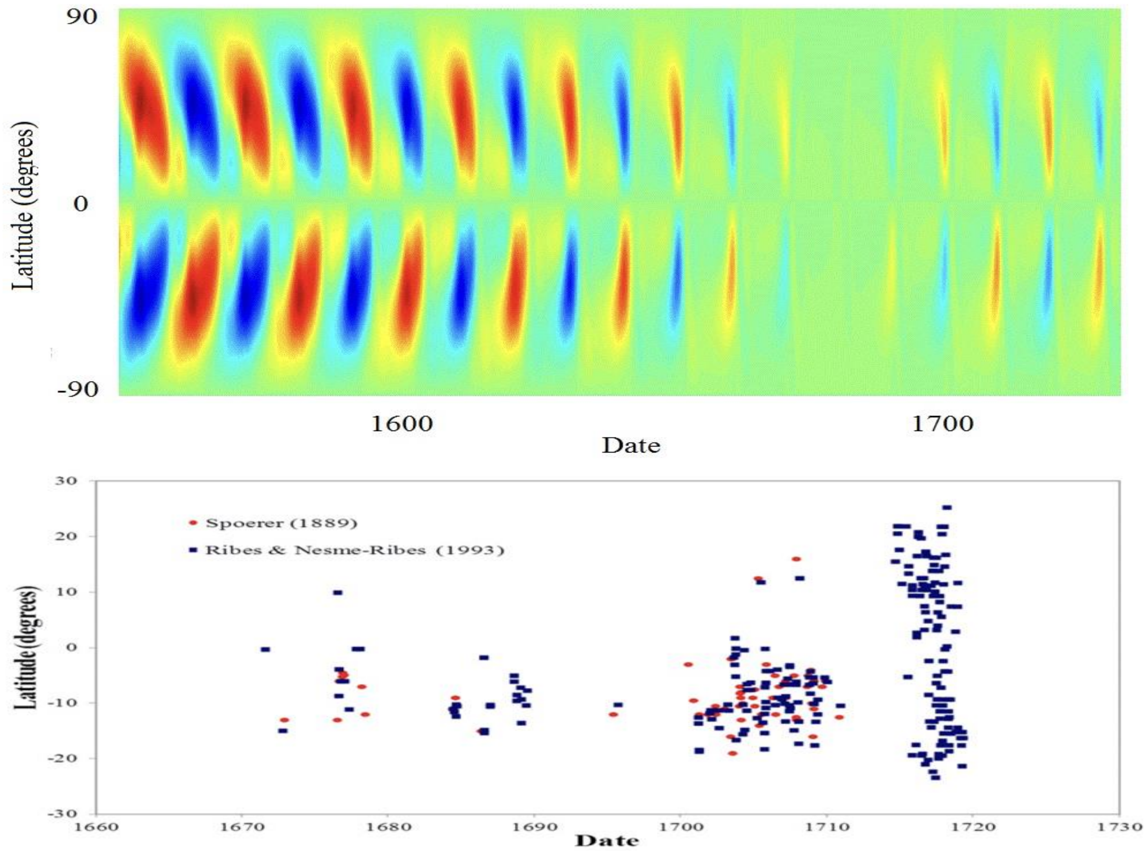

Figure 3. *Top plot: The butterfly diagram derived from the reported observations of sunspots for the Maunder minimum in the 17th century. Bottom plot: the simulated butterfly diagram using the same model for the parameters of magnetic field derived from PCA as shown in Fig. 1*.

The fourth independent verification of our reconstruction of solar activity in Fig. 1 comes from a comparison of the observed butterfly diagrams for the past Maunder minimum from 17th century (Eddy 1976, 1983) plotted in Fig.3 (top plot) with the theoretical butterfly diagram in Fig.3 (bottom plot). The theoretical butterfly diagram is derived from the two principal components of solar toroidal magnetic field, generated by the double solar dynamo with dipole sources in two different layers with meridional circulation (Zharkova et al, 2015). It can be seen that the simulated butterfly diagrams for the Maunder minimum occurred between the two grand cycles plotted in Fig.3 show a reasonable ’face fit’ to the observed one in terms of their emergence timing and latitudes. For example, the observations show that the sunspots emerge in narrow strips of the times about 1690, 1705 and 1718 followed by the gaps between them without any sunspots (Eddy 1976, 1983). These gaps are also shown in the simulated diagram in the bottom plot with the largest gap clearly occurring between 1690 and 1705, similarly to the one shown in the observations (top plot).

In order to understand what kind of sunspot activity one can expect in the forthcoming grand minimum, we also simulate the butterfly diagrams for this modern grand solar minimum started in 2020 as plotted in Fig.4 (bottom plot) and for the period of 2000 years (1200-3200) with the five grand cycles from Zharkova et al, 2015) plotted in Fig.4 (top plot). It is evident from Fig.1 that the upcoming Modern minimum in the 21st century (2020-2055) is expected to last only for 3 standard 11 year cycles (25-27) and, thus, to be much shorter compared to the Maunder Minimum in the 17 century. There are also more sunspots expected to appear in the individual strips of the butterfly diagram, compared to the previous grand minimum, with the number of spotless gaps between the burst of sunspot activity to be the same as in the Maunder minimum (see Fig.4 (bottom plot)). The next extended grand minimum resembling Maunder minimum is expected after the next grand cycle in 2060-2420 (see Fig.1, bottom plot). This trend

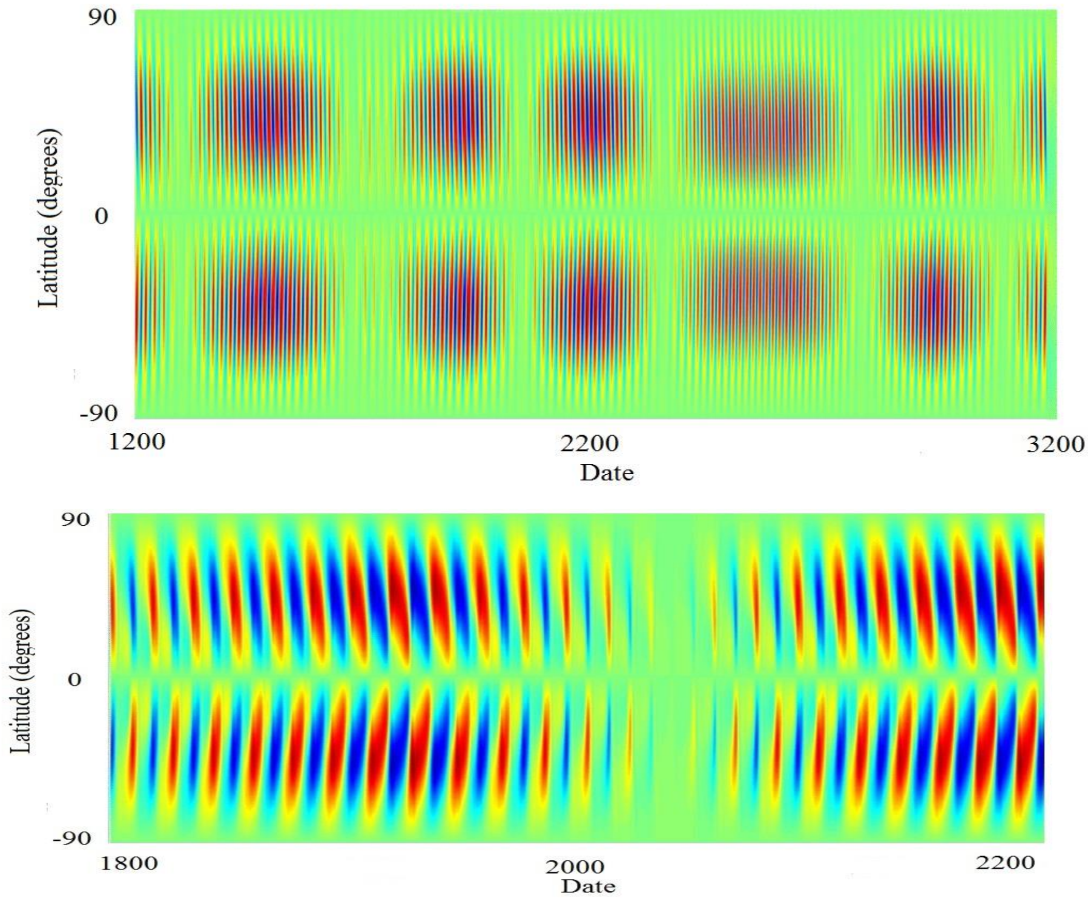

Figure 4. *The butterfly diagrams calculated for the dynamo model in the solar interior with two cells as derived from HMI/SDO observations by Zhao et al, 2013 having the opposite meridional circulation (Zharkova et al, 2015) for the period of 1200 to 3200 years (top plot) and for the upcoming Modern grand minimum in 2020-2055 (bottom plot).*

is confirmed by the numbers of spotless days observed for the current cycle 25 which is in the ascending phase until 2024 (see https://wwwbis.sidc.be/silso/spotless).

Solar activity during Spoerer minimum and possible effects of supernovae

One can note that Spoerer's minimum (1450–1550) indicated by Eddy (1976, 1983) is not present in our summary curve plotted in Fig. 1, as pointed out by Usoskin and Koval'stov (2015) showing a maximum of the solar grand cycle during the same period of time. Moreover, after investigating the method of the time dating with $\Delta^{14}C$ isotope (Libby 1946; Arnold & Libby 1949) and considering the terrestrial and extra-terrestrial conditions reported in the literature (Williams 1873; Wittmann 1978; Schroder & Treder 1999), we are puzzled with a question about the validity of assigning the abundances of $\Delta^{14}C$ and ^{10}Be to the minimum of solar activity in the period of the alleged Spoerer minimum. If one assumes that, indeed, it was a long Spoerer minimum in solar activity in the 14-16 centuries, as suggested by the Holocene curve derived from restoration of the carbon 14 isotope abundances (Eddy 1976; Usoskin et al. 2004; Solanki & Krivova 2011), then this minimum is in a very strong contradiction not only to our prediction in Fig. 1 but also to the other proxies of solar activity discussed in the section above, like large sunspots (Fig.2, top plot), strongest auroras ever observed on the Earth (Fig.2, bottom plot) and cosmic ray intensity in that period (McCracken & Beer 2007).

Keeping in mind that, normally, a) strong auroras coincide with the maxima of solar activity and not with its minima, and b) in the telescope era such strong auroras, as they were seen in the 14-16 centuries, were never observed, it is logical to assume that in that period there was/were some other source/sources, which increased *a flow of relativistic particles causing the auroras*. The Sun could not provide such the increase as its grand cycle for these centuries was not much different from the previous and the next grand cycles (which we are experiencing now) as shown in Fig. 1. Furthermore, there was an area increases recorded in Antarctic while the Arctic ice reveals the signs of area decreases as it should be during a normal solar activity that can be explained by the very southern location of the supernova Vela Junior not affecting the northern hemisphere. In addition, the terrestrial temperature in the period of Spoerer minimum had, in fact, a maximum and not minimum as expected during large solar minima (Zharkova et al, 2018).

We reckon that Spoerer minimum is, in fact, an artefact of the reconstruction techniques used (Usoskin (Solanki et al. 2004; Usoskin et al. 2004), where a linear regression analysis developed for data with normal distribution (Good & Hardin, 2009) was applied to the strongly oscillating function describing the variations of sunspot numbers in the past 400 years contrary to our method using special periodic functions to account for these oscillations. One of the examples of fitting incorrectly the oscillating function with a linear regression approach is shown by Akasofu (2010) (see their Fig. 9), when explaining the modern era recovery of the Earth from the little ice period and the incorrect use of a linear part of the temperature variations for the extremely incorrect prediction of the terrestrial temperature growth in the next century.

Possible uncertainties in the carbon dating approach

By default, the accuracy of the carbon dating method is dependent on the knowledge of the background radiation at the evaluation periods as indicated by Libby (Arnold & Libby 1949). Normally, the calculations of carbon dating produce dates in radiocarbon years: i.e. dates that represent the age the sample would be if the $^{14}C/^{12}C$ ratio had been constant historically (Taylor & Bar-Yusef 2014).

Libby's original exchange reservoir hypothesis assumed that the $^{14}C/^{12}C$ ratio in the exchange reservoir is constant all over the world and gives an error about 80 years.

Then later Libby had pointed out as early as 1955 the possibility that this assumption was incorrect, it was not until discrepancies began to accumulate between the measured ages and the known historical dates for artefacts that it became clear that a correction would need to be applied to radiocarbon ages to obtain calendar dates (Aitken 1990; Taylor & Bar-Yusef 2014).

Any addition of carbon to a sample of a different age will cause the measured date to be inaccurate. Contamination with modern carbon causes a sample to appear to be younger than it really is: the effect is greater for older samples while contamination with old carbon, with no remaining ^{14}C, causes an error in the other direction independent of age – a sample contaminated with 1% old carbon will appear to be about 80 years older than it really is, regardless of the date of the sample (Aitken 1990).

There are several causes of variation in the ratio across the reservoir, which can significantly increase the errors (see, e.g., Damon and Sonett, 1991): variations of the cosmic-ray flux on a geological timescale due to the changing galactic background (e.g., a nearby supernova explosion or crossing the dense galactic arm); secular-to-millennial variations are caused by the slowly-changing geomagnetic field or by solar magnetic activity; mixing of atmospheric carbon with the surface waters, 'marina effects' or water running from aged rocks and volcanic eruption and even differences in atmospheric circulation in hemispheres. While the variations of the terrestrial magnetic field and solar activity were actively considered in the past (Usoskin et al, 2004, Solanki and Krivova, 2011) the contributions of some other effects including the effects of supernovae were somehow overlooked. Possible implications of supernovae on the terrestrial events and carbon dating prior and during the Spoerer minimum is discussed in the section below.

Near-Earth supernova effects on the terrestrial conditions in the 13-15 centuries

The strong increase of the cosmic rays in 14-15 centuries was already reported by McCracken and Beer (2007). Here we suggest that this increase was caused by supernovas, which are considered the major source of galactic cosmic rays as suggested by Walter Baade and Fritz Zwicky.[?] The streams of galactic cosmic rays caused by the supernovae are likely to increase very dramatically the backround cosmic ray intensity in the solar system and the Earth (Baade & Zwicky 1934; Ruderman 1974; Atri & Melott 2014; Thomas et al. 2016) that, in turn, can significantly affect an accuracy of the time dating with carbon 14 isotope during this period as pointed by a few authors (Bowman 1995) including Libby (1946) who introduced this method.

Also a near-Earth supernova can produce noticeable effects on terrestrial biosphere by destroying to large extent its ozone layer (Gehrels et al. 2003; Becker Tjus et al. 2016) if it occurred as far as 700-3000 light-years away depending upon the type and energy of the supernova. Gamma rays from a supernova would induce a chemical reaction in the upper atmosphere converting molecular nitrogen into nitrogen oxides, depleting the ozone layer enough to expose the surface to harmful solar radiation. This has been proposed as the cause of the Ordovician–Silurian extinction, which resulted in the death of nearly 60% of the oceanic life on Earth (Melott et al. 2004). It was noted that the traces of past supernovae might be detectable on Earth in the form of metal isotope signatures in rock strata as iron-60 enrichment was later reported in deep-sea rock of the Pacific Ocean (Knie et al. 2004). Then later the elevated levels of nitrate ions were found in Antarctic ice (Motizuki et al. 2010, which coincided with the 1006 and 1054 supernovae of our Galaxy. Gamma rays from these supernovae could have boosted levels of nitrogen oxides, which became trapped in the ice (Motizuki et al. 2010).

In Fig. 5 we overplotted on the summary curve all the supernovae occurred in the past 2000 years (top plot) and made a close-up plot of the supernovae occurred prior and after the alleged Sporer minimum shown in bottom plot. The remnant of a mysterious supernova Vela Junior, which became a neutron star, was found in 1998 (Iyudin et al. 1998) when gamma ray emissions from the decay of 44Ti nuclei were discovered. The remnant is located in the southern sky in the constellation Vela inside the much older Vela Supernova Remnant. The distance to this object is argued to be only 650-700 light-years away. Also it's radiation and particles reached the Earth comparatively recently, perhaps within the last 800 years, at about 1250-1290.

This supernova was located at 46 degrees south that may have been too far south for the observers in the Northern hemisphere to notice it, especially if it obtained peak brightness during the northern summer. At this declination, the supernova would be invisible above about 45 degrees north, making it invisible to the majority of Europe. And this is the supernova, which could be the major reason of a long streak of epidemics in the Earth, including China, in 14-15 centuries leading to decline in number of solar observers reporting large sunspots in the pre-telescope era.

This location of supernova Vela Junior can explain the paradoxal contradiction occurred in the SN reconstructions based upon the Greenland data (Usoskin et al. 2004). Contrary to the Antarctic ice data (the solid curve named An), the ^{10}Be data from Greenland exhibits the very pronounced maxima in 1500 and in 1560 when it was supposed to be Spoerer minimum. Also it is clearly seen that during the Maunder Minimum, or after 1650, the both An and Gr curves become rather consistent showing the minimum of solar activity (Usoskin et al. 2004).

We suggest that the cosmic rays from another supernova, Tycho's supernova (Brahe & Kepler 1602), combined with the effect of Kepler's supernova (Kepler 1609; Kepler et al. 1627) occurred just 32 years later changed the terrestrial background to very high magnitudes of carbon 14 isotope that led to the occurrence of Spoerer minimum, which is, in fact, not related to solar activity at all. This suggestion is proved by the fact Tycho Brahe's supernova remnant is still the most intense γ-ray source in the night sky (Lu et al. 2011) meaning that 500 years ago the stream of cosmic rays from this supernova was enormous as reported before and caused the most powerful terrestrial auroras ever observed.

Hence, the links of supernovae with the solar activity curve derived for the 14-16 century from the carbon dating (Usoskin et al. 2002; Solanki et al. 2004)can be summarised as follows.

1. High abundances of $\Delta^{14}C$ time-dated to 14-16 centuries leading to assumption of the Spoerer solar minimum can be created prior this time because of the occurrence in the 13 century of supernova observed in the Southern hemisphere with the Imaging Compton Telescope (COMPTEL) at the distance of only 700 light years (Iyudin et al. 1998).

2. The most intense supernova observed by Tycho Brahe (Brahe & Kepler 1602) in 1572 in our galaxy at the distance of 3200 light years that was after the Spoerer minimum and whose radiation could contaminate the samples with carbon 14 used for dating of earlier events.

3. There was also other supernova observed in 1604 by Kepler (the last supernova in our galaxy) (Kepler 1609)(see Fig.5 and a few other supernovas from our galaxy in the 12-18 centuries).

Many of these supernovae originated from the Milky Way's galaxy core proving that the galactic core was very active in the pre- and early telescopic era, providing the most extensive streams of cosmic rays during the supernova formation preceding or coinciding with Spoerer minimum derived in $\Delta^{14}C$ on the Earth. Tycho Brahe's and Kepler's supernovae could change significantly the background radiation of the Earth, contaminate the samples used for the carbon dating and lead, in turn, to errors in carbon 14 dating, if this background is not taken into account.

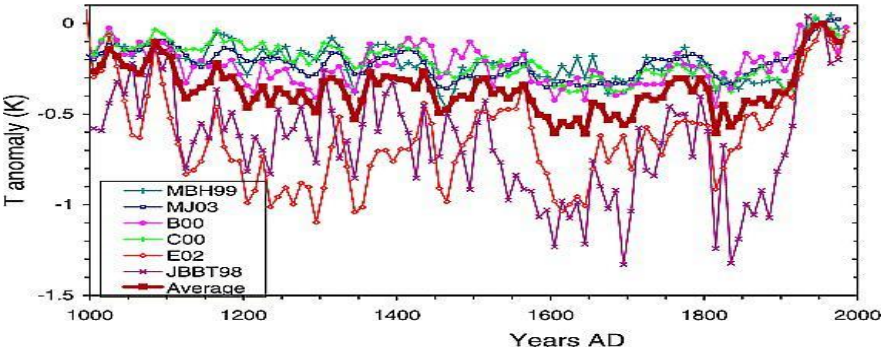

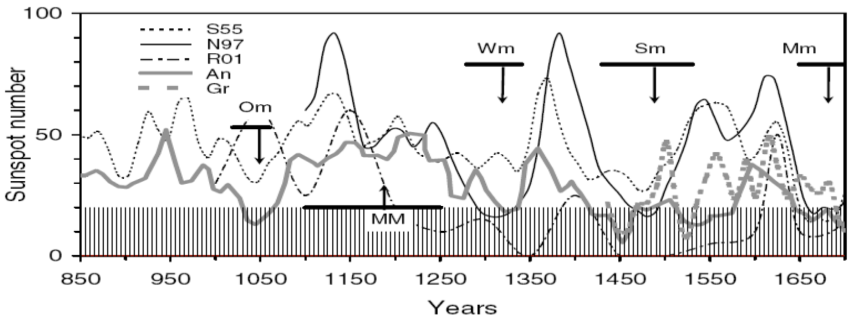

Figure 5. *Top plot: the terrestrial temperature variations derived by Usoskin et al. (2005)· Bottom plot: The sunspot plots versus ice variation in Greenland (Gr) and Antarctic (An) from Usoskin et al. 2004.*

Conclusions

In this paper we reproduce the summary curve for the last 3000 years and showing it's remarkable resemblance to the sunspot and terrestrial activity reported in the past millennia including the significant grand minima: Maunder Minimum (1645-1715), Wolf minimum (1200), Oort minimum (1010-1050), Homer minimum (800-900 BC) and so on. We verify the extrapolated summary curve of the principal components of the solar background magnetic field, as a new solar activity curve, by the available pre-telescope observations of large sunspots, by the intense terrestrial auroras seen in 14-16 centuries and by simulated and observed butterfly diagrams for the Maunder Minimum.

We confirm the prediction of the modern grand minimum in 2020-2053 (Zharkova et al, 2015, Zharkova 2020), which already started in cycle 25 to have the sunspot activity reduced with a further decrease of solar magnetic field and sunspot numbers in cycles 26 and 27.

We argue that Spoerer minimum (1460-1550) derived from the isotope Δ^{14}C time dating technique is likely produced by a strong increase of the terrestrial background radiation caused by the galactic cosmic rays of powerful supernovae. The supernova Vela Junior occurred in ~1280 close to the Earth (<700 light-years) could strongly affect its atmosphere leading to a long time of epidemics recorded in the Northern hemisphere, in general, and in China, in particular. These epidemics of diseases in the 15-16 century's China combined with Mongolian invasion and expansion of the Great Chinese Wall, eliminated the pool of people trained to observe sunspots until the 17 century.

In addition, the supernovae observed by Tycho Brahe and Kepler brought very powerful cosmic rays, which, in turn, affected the Earth atmosphere and surface creating a very strong nuclei background much different from the standard one accepted in the carbon dating. This increased background intensity can definitely introduce the time-dating error of a few hundred years providing a plausible explanation why Spoerer minimum did not exist in the solar magnetic field summary curve in the 15-16 centuries derived with the principal component analysis and symbolic regression classification of solar magnetic field, which reveals in Fig. 1 only a normal maximum of the grand cycle.

Given the number of grand solar minima and grand solar maxima correctly fit, combined with the other means of verification discussed above, we can confidently reinforce our previous findings (Zharkova et al, 2015) that the solar activity is produced by two magnetic waves, or PCs, as derived from the full disk magnetograms in cycles 21-24, which are proven to be generated by a double solar dynamo in inner and outer layers of the solar interior. This finding also emphasizes the fact that the solar activity has a very well-maintained periodicity of its dynamo waves maintained over three millennia that reflects a good health of the solar dynamo of the Sun.

References

Ackermann, M., Ajello, M., Allafort, A., et al. 2013, Science, 339, 807
Aitken, M. J. 1990, Science-based Dating in Archaeology (London: Longman), 404
Arnold, J. R. & Libby, W. F. 1949, Science, 110, 678
Baade, W. & Zwicky, F. 1934, Proceedings of the National Academy of Science, 20, 259
Becker Tjus, J., Eichmann, B., Kroll, M., & Nierstenhöfer, N. 2016, Astroparticle Physics, 81, 1
Bowman, S. 1995, 64
Brahe, T. & Kepler, J. 1602, Tychonis Brahe Astronomiae instauratae progymnasmata : quorum haec prima pars de restitutione motuum SOLIS et lunae stellarumque inerrantium tractat, et praeterea de admiranda nova stella anno 1572 exorta luculenter agit. (Typis inchoata Vraniburgi Daniae, absoluta Pragae Bohemiae : [s.n.])
Brandenburg, A. & Subramanian, K. 2005, Phys. Rep., 417, 1
Damon, P. E. & Sonett, C. P. 1991, in The Sun in Time, ed. C. P. Sonett, M. S. Giampapa, & M. S. Matthews, 360–388
Eddy, J. A. 1976, Science, 192, 1189
Eddy, J. A. 1983, Sol. Phys., 89, 195
Iyudin, A. F., Schönfelder, V., Bennett, K., et al. 1998, Nature, 396, 142
Jones, C. A., Thompson, M. J., & Tobias, S. M. 2010, Space Sci. Rev. , 152, 591
Karak, B. B. & Nandy, D. 2012, Astrophys. J. Lett., 761, L13
Kepler, J. 1609, Astronomia nova. (Pragae)
Kepler, J., Brahe, T., & Eckebrecht, P. 1627, Tabvlae Rudolphinae, qvibvs astronomicae scientiae, temporum longinquitate collapsae restauratio continetur
Kingsmill, T. W. 1906, Nature, 73, 413
Knie, K., Korschinek, G., Faestermann, T., et al. 2004, Physical Review Letters, 93, 171103
Libby, W. F. 1946, Physical Review, 69, 671
Libby, W. F. 1963, J. of Geophys. Res., 68, 2933
Lu, F. J., Wang, Q. D., Ge, M. Y., et al. 2011, Astrophys. J. , 732, 11
McCracken, K. G. & Beer, J. 2007, Journal of Geophysical Research (Space Physics), 112, A10101
Melott, A. L., Lieberman, B. S., Laird, C. M., et al. 2004, International Journal of Astrobiology, 3, 55
Motizuki, Y., Naka, Y., & Takahashi, K. 2010, Highlights of Astronomy, 15, 630
Motizuki, Y., Takahashi, K., Makishima, K., et al. 2009, ArXiv e-prints
Obridko, V. & Nagovitsyn, Y. 2014, in COSPAR Meeting, Vol. 40, 40th COSPAR Scientific Assembly
Parker, E. N. 1955, Astrophys. J. , 122, 293
Pesnell, W. D. 2008, Sol. Phys., 252, 209
Popova, E., Zharkova, V., & Zharkov, S. 2013, Annales Geophysicae, 31, 2023
Popova, E., Zharkova, V., Zharkov, S. & Shepherd S.J., 2018, JASTP, 176, 61
Reischauer, O., Fairbank, J. K., & Craig, A. M. 1960, 64
Scafetta, N. 2014, Astrophysics and Space Science, 354, 275
Schlamminger, L. 1990, Mon. Notices of RAS, 247, 67
Schove, D. J. 1948, Popular Astronomy, 56, 247
Schroder, W. & Treder, H. J. 1999, Geofisica Internecional, 39, 197
Sekido, Y., Masuda, T., Yoshida, S., & Wada, M. 1951, Physical Review, 83, 658
Shepherd, S. J., Zharkov, S. I., & Zharkova, V. V. 2014, Astrophys. J. , 795, 46
Solanki, S. K. & Krivova, N. A. 2011, Science, 334, 916

Solanki, S. K., Usoskin, I. G., Kromer, B., Schu ̈ssler, M., & Beer, J. 2004, Nature, 431, 1084

Taylor, R. E. & Bar-Yusef, O. 2014, Radiocarbon Dating: Archaeological Perspective (Routledge), 404

Usoskin, I. & Kovaltsov, G. 2015, ArXiv e-prints

Usoskin, I. G. 2013, Living Reviews in Solar Physics, 10

Wagner, G., Beer, J., Masarik, J., et al. 2001, Geophys. Res. Lett., 28, 303 Williams, J. 1873, Mon. Notices of RAS, 33, 370

Wittmann, A. 1978, Astron. and Astrophys., 66, 93

Zhao, J., Bogart, R. S., Kosovichev, A. G., Duvall, Jr., T. L., & Hartlep, T. 2013, Astrophys. J. Lett., 774, L29

Zharkova, V. V., Shepherd, S. J., & Zharkov, S. I. 2012, Mon. Notices of RAS, 424, 2943

Zharkova, V. V., Shepherd, S. J., Popova, E., & Zharkov, S. I. 2015, Nature Scientific Reports, 5, 15689

Zharkova, V. V., Shepherd, S. J., Popova, E., & Zharkov, S. I., 2018, JASTP, 176, 72

Zharkova, V. V., Shepherd, S. J., Popova, E., & Zharkov, S. I. 2019, Nature Scientific Reports, 9, 9197

Zharkova, V.V., 2020, Temperature, 7:3, 217-222, DOI: 10.1080/23328940.2020.1796243,

Zharkova, V.V., 2021, chapter in the book Solar System Planets and Exoplanets, DOI:

Characteristics of the Midlatitude Effects of Different Substorms

Guineva V[1], *Werner R.*[1], *Atanassov A.*[1], *Bojilova R.*[2], *Raykova L.*[1], *Valev D.*[1]

[1]Space Research and Technology Institute (SRTI), Bulgarian Academy of Sciences, Stara Zagora Department, Bulgaria
[2]National Institute of Geophysics, Geodesy and Geography (NIGGG), Bulgarian Academy of Sciences, Sofia, Bulgaria
E-mail: v_guineva@yahoo.com

Abstract.

Depending on the interplanetary conditions and the solar wind transients, different substorms can develop. By one classification they can be divided in ”usual“, ”expanded“ and ”polar“. The ”usual“ substorms begin and develop at auroral latitudes (~60°- ~ 71° GMLat). When the substorm onset is at auroral latitudes, but the substorm propagates to higher latitudes (>~70° GMLat), the substorm is ”expanded“. And in the case, when the substorm originates and develops at latitudes above ~70° GMLat, without expansion to South, it is ranked among the ”polar“ ones. The substorm effect at midlatitudes consists of the appearance of peaks in the X component of the magnetic field at ground, called midlatitude positive bays (MPB). A number of characteristics as conversion latitude of the magnetic bay sign, amplitude and duration of the MPB, horizontal power of the magnetic field etc., can be attributed to the midlatitude effects of substorms.

The characteristics of the midlatitude effects have been determined by data of the Bulgarian midlatitude station Panagjurishte (PAG) (~37° GMLat, ~97° GMLon) for 3 substorms: a polar substorm at 18:45 UT on 06.01.2013, a usual substorm at 22:30 UT on 31.01.2013 and an expanded substorm at 18:42 UT on 02.02.2013. The differences between the MPB characteristics for these different types of substorms have been analyzed.

Introduction

Substorms are a typical phenomenon in the auroral latitudes (~ 60°- ~ 71° MLAT) [*Akasofu*, 1964]. The magnetic substorms display at auroral latitudes represents negative bays in the X-component of the surface magnetic field. Depending on the solar wind and Interplanetary Magnetic Field (IMF) conditions, substorms can extend to both: very high latitudes (>70° MLAT) (e.g. [*Pudovkin* and *Troshichev*, 1972; *Nielsen et al.*, 1988; *Despirak et al.* 2008]) and middle (~ 50° MLAT) latitudes [*Feldstein and Starkov*, 1967]. Furthermore, magnetic substorms produce positive bays in the X-component of the ground-based magnetic field (midlatitude positive bays, MPB). Nowadays, the commonly adopted opinion of this phenomenon is, that the positive bays are associated with a current system, the substorm current wedge (SCW) [*McPherron et al*. 1973a].

It has to be stressed that substorms, occurred during different conditions in the solar wind can differ considerably from each other (e.g., [*Tanskanen et al*., 2002; *Guineva et al.*, 2016; *Guineva et al.*, 2018]). By reason of this, diverse categories of substorms have been introduced: “limited” and “extended” [*Lui et al*., 1976], “localized” and “normal” [*McPherron et al*. 1973b], “substorms on the contracted oval” and “normal” [*Kamide et al*., 1975], "polar" and "classical" or “usual” [*Kleimenova et al*., 2012], “high latitude” and “normal” [*Despirak et al.* 2008], “expanded” and “polar” [*Despirak et al.* 2018]. Therefore, the development of positive bays at midlatitudes during substorms should also have some various characteristics, according to the different conditions.

The goal of this work is to study the peculiarities of the midlatitude positive bays (MPB) at the Bulgarian midlatitude station Panagjurishte (PAG) (~37° GMLat, ~97° GMLon), associated with different types of substorms. Three isolated substorms were chosen, a polar substorm at 18:45 UT on 06.01.2013, a usual substorm at 22:30 UT on 31.01.2013 and an expanded substorm at 18:42 UT on 02.02.2013.

Data

To identify the substorms and to follow their development, data from the magnetometer networks IMAGE, INTERMAGNET and SuperMAG have been used. The interplanetary conditions have been verified by means of the OMNI data base and the solar wind large-scale phenomena catalog (http://www.iki.rssi.ru/omni/).

Interplanetary and geomagnetic conditions

Three cases of isolated substorms were selected. The interplanetary and geomagnetic conditions during the substorms are presented in Fig.1. From up to down the following quantities are drawn: the magnitude of the IMF vector, the IMF Bz component, the X component of the velocity Vx, the proton density PD, the temperature T, the dynamic pressure P, and the AL and SYM/H indices. The boundaries of the structures in the solar wind are marked by rectangles. The red vertical lines indicate the substorm onsets.

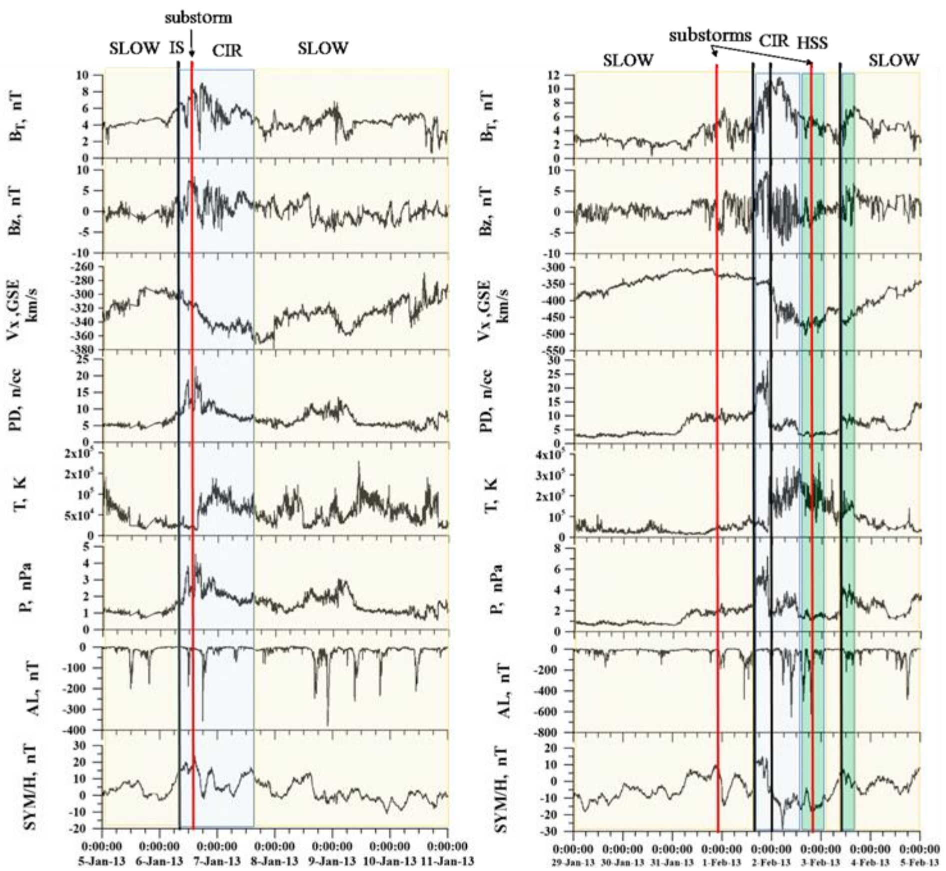

Fig.1. Interplanetary and geomagnetic conditions concerning the three examined substorms: on 06 January 2013 (left panel, time interval from 05 to 11 January 2013) and on 31 January and 02 February 2013 (right panel, time interval from 29 January to 05 February 2013).

The first substorm, on 06.01.2013, occurred during CIR in the solar wind on the background of a slow solar wind, Vx was about -310 km/s, Bz fell down from positive to negative values, jumps in PD, P and T were registered, AL was about -200 nT (Fig.1, left panel). The second substorm, on 31.01.2013 (Fig.1. right panel), happened during a slow stream in the solar wind, Vx was ~-330 km/s, a drop in Bz of ~7 nT to negative values was observed, AL=~-200 nT. These substorms developed under quiet conditions. The third substorm originated in more disturbed conditions, during a high-speed stream (HSS) in the solar wind, Vx=~-460 km/s, AL=~-600 nT. All three substorms developed in non-storm conditions.

Substorms development and midlatitude display

Substorm at 18:45 UT on 06.01.2013

The substorm development at auroral latitudes and its appearance at PAG station are given in Fig.2. This substorm can be classified as polar. The first negative disturbances in X are observed at BJN (71.45° GMLat) and development to South is not seen (left upper panel of Fig.2). This substorm is weak, which is typical for polar substorms, and its effect at PAG station is feebly seen. The horizontal power reached just about 25 nT^2.

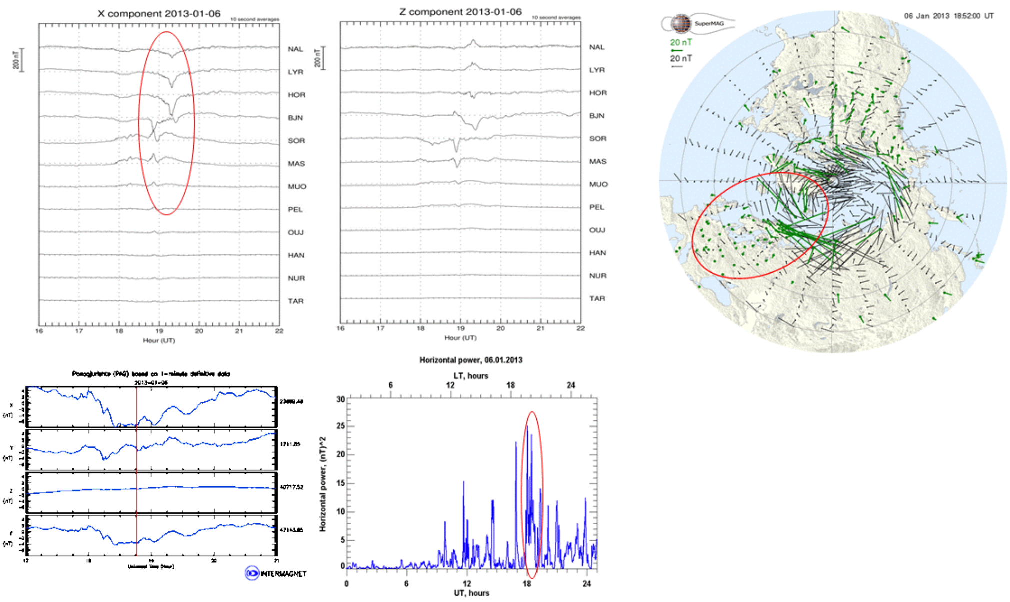

Fig.2. The substorm on 06.01.2013. Upper panels – magnetic field X (to the left) and Z (in the middle) components by the IMAGE NAL-TAR chain and magnetic field vectors by SuperMAG at the time of the MPB maximum (to the right). The substorm is indicated by red ellipse in the left panel and the substorm region is marked by a red ellipse in the right panel. Left bottom panel – the magnetic field at PAG station by INTERMAGNET. The MPB onset is marked by a red vertical line. Right bottom panel – the computed horizontal power of the magnetic field for the PAG station. The peak, associated with the substorm, is shown by a red ellipse.

Substorm at 22:30 UT on 31.01.2013

This substorm is presented in Fig.3. This is a usual substorm, which developed at auroral latitudes (~60°- ~ 71° GMLat), without higher latitudes (above ~70°GMLat) expansion (Fig.3, left upper panel). This is a weak substorm, as the one on 06.01.2013, but its display at PAG is better expressed (e.g. the horizontal power of the magnetic field reached ~34 nT^2 and the positive bay is much better manifested).

Substorm at 18:42 UT on 02.02.2013

The substorm on 02.02.2013 is presented in Fig.4. This is an expanded substorm, it began at auroral latitudes and the magnetic disturbances reached NAL (75.25°GMLat) (upper left and middle panels of Fig.4). Its effect at PAG is clearly expressed. The horizontal power of the magnetic field reached ~400 nT^2, the positive bay is higher and well seen.

Results

For the considered substorms, the sign conversion latitude, and some positive bays characteristics at PAG have been determined. The X-bay sign conversion latitude was determined by data of the magnetometer networks IMAGE, SuperMAG and

INTERMAGNET in the longitudinal band 90° - 104° GMLon, which is round the longitude of the Bulgarian station Panagjurishte (~97° GMLon). This boundary can be estimated by the map of the magnetic field vectors (upper right panels in Fig.2, Fig.3 and Fig.4). The MPB onset, MPB maximum, MPB amplitude and MPB end at PAG have been determined by the processed X-component of the magnetic field, after the subtraction of the main field and the mean field caused by solar quiet day variations [*Guineva et al*., 2021].

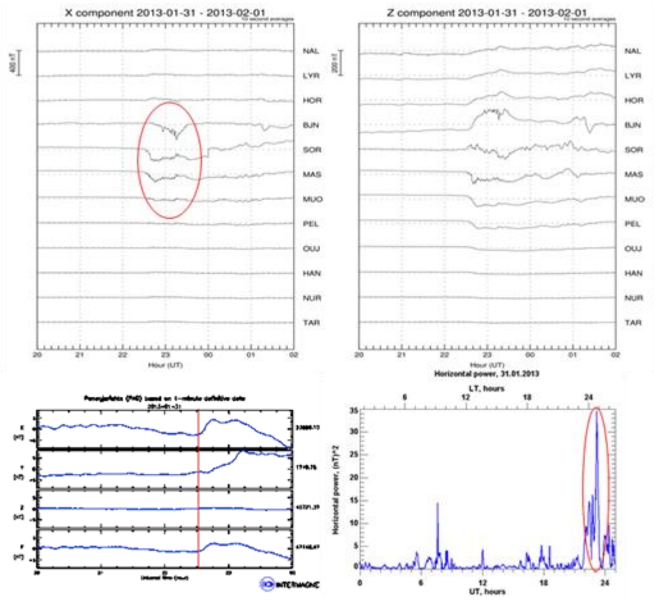

Fig.3. The substorms on 31.01.2013. The presented quantities and symbols are the same as for the substorm on 06.01.2013.

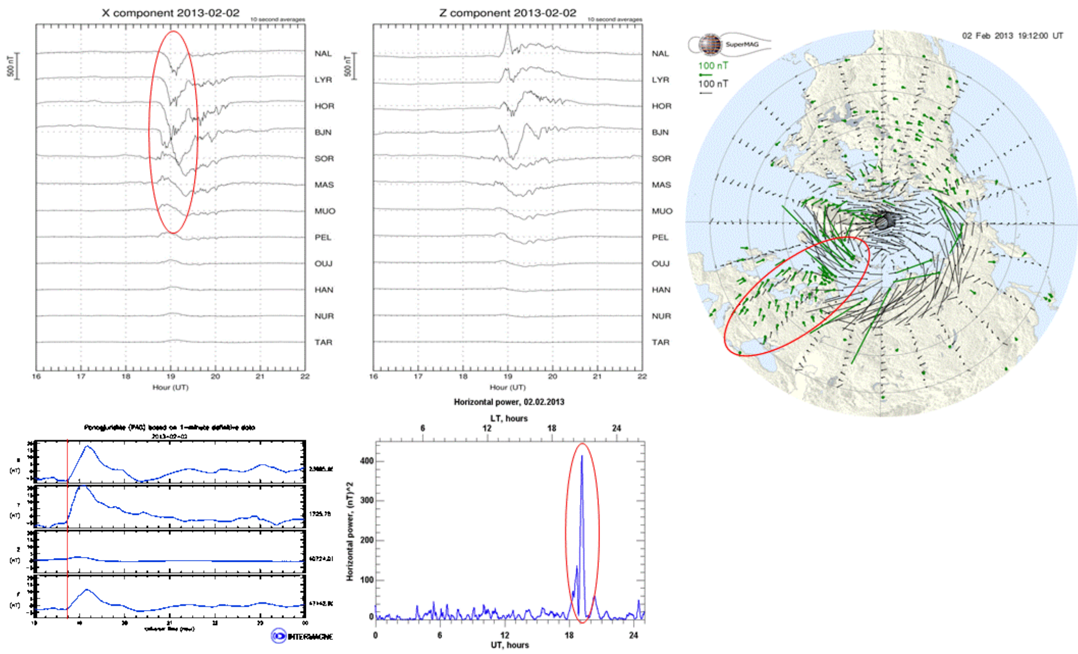

Fig.4. The substorms on 02.02.2013. The presented quantities and symbols are the same as for the substorm on 06.01.2013.

The results for the examined substorms are summarized in Table 1.

Table 1. Parameters of the midlatitude positive bays (MPB), determined at the Panagjurishte station (PAG), associated with the considered substorms. From up to down: bay sign conversion latitude, MPB onset time, MPB maximum time, MPB amplitude, MPB end time.

Parameter/date	6.01.2013	31.01.2013	02.02.2013
Conv. lat., deg.	69	61	65
MPB onset, UT	18:45	22:30	18:42
MPB max, UT	18:51	22:47	19:10
MPB ampl., nT	3	7.5	24.4
MPB end, UT	19:03	00:01	19:45

Summary

Three isolated substorms of different type have been examined, namely a polar substorm, at 18:45 UT on 06.01.2013, a usual substorm, at 22:30 UT on 31.01.2013, and an expanded substorm at 18:42 UT on 02.02.2013. It was found out, that:

- The conversion latitude is the highest for the polar substorm, and lowest for the usual one.
- The midlatitude positive bay amplitude is very small for the polar substorm, higher for the usual substorm, and greatest for the expanded substorm. The same result is obtained for the horizontal power of the magnetic field.

The effect of the weak polar and usual substorms can be detected at PAG station (~37° GMLat), but it is negligible.

These results should be verified by a wide investigation, based on a number of different types of substorms, occurred during long time intervals, and during various interplanetary conditions.

Acknowledgements. The authors are grateful to the creators of the databases OMNI (http://omniweb.gsfc.nasa.gov), IMAGE (http://space.fmi.fi/image/), INTERMAGNET (http://intermagnet.org/), SuperMAG (http://supermag.jhuapl.edu/), and the solar wind large-scale phenomena catalog (http://www.iki.rssi.ru/omni/) for the opportunity to use them in this work.

This study was supported by the National Science Fund of Bulgaria (NSFB) (project number КП-06-Русия/15) and by the RFBR (project number 20-55-18003Болг_а).

References

Akasofu, S.-I. (1964) The development of the auroral substorm, Planet. Space Sci., 12, No 4, 273–282.

Despirak, I. V., A. A. Lyubchich, H. K. Biernat, A. G. Yahnin (2008) Poleward expansion of the westward electrojet depending on the solar wind and IMF parameters, Geomagn. Aeronomy. 48, No 3, 284–292.

Despirak I. V., A. A. Lubchich, N. G. Kleimenova (2018) High-latitude substorm dependence on space weather conditions in solar cycle 23 and 24 (SC23 and SC24), J. Atmos. Sol. Terr. Phys., 177, 54-62.

Feldstein, Y. L., G. V. Starkov (1967) Dynamics of auroral belt and geomagnetic disturbances, Planet. Space Sci., 15, No 2, 209–229.

Guineva V., I. Despirak, B. Kozelov (2016) Substorms observations during two geomagnetically active periods in March 2012 and March 2015, Sun and Geosphere, 11, No 2, 125-130.

Guineva V., I. V. Despirak, R. Werner (2018) Observations of substorm auroras by MAIN cameras system in Apatity during two winter seasons: 2014/2015 and 2015/2016, Journal of Atmospheric and Solar-Terrestrial Physics, 177, 63-72.

Guineva, V., R. Werner, A. Atanassov, R.Bojilova, L. Raykova, D. Valev, I. Despirak, N. Kleimenova (2021) Construction of a catalog of the magnetic variations by data of the Bulgarian station Panagjurishte, Proc. of the 17th International Scientific Conference "Space, Ecology, Safety" SES2021, in press

Kamide, Y., S.-I. Akasofu, S. E. Deforest, J. L. Kisabeth (1975) Weak and intense substorms, Planet. Space Sci., 23, No 4, 579-584.

Kleimenova, N. G., E. E. Antonova, O. V. Kozyreva, L. M. Malysheva, T. A. Kornilova, I. A. Kornilov (2012) Wave structure of magnetic substorms at high latitudes, Geomagn. Aeronomy, 52, No 6, 746–754.

Lui, A. T. Y., S.-I. Akasofu, E. W. Hones, Jr., S. J. Bame, C. E. McIlwain (1976) Observation of the plasma sheet during a contracted oval substorm in a prolonged quiet period, Substorms in space: The correlation between ground and satellite observations of the magnetic field, J. Geophys. Res., 81, No 7, 1415–1419.

McPherron, R. L., C. T. Russell, M. Aubry (1973a) Satellite studies of magnetospheric substorms on August 15, 1968, 9: phenomenological model for substorms, J. Geophys. Res., 78, No 16, 3131–3149.

McPherron, R. L., C. T. Russell, M. G. Kivelson, P. J. Coleman, Jr. (1973b) Substorms in space: The correlation between ground and satellite observations of the magnetic field, Radio Science, 8, No 11, 1059-1076.

Nielsen, E., J. Bamber, Z.-S. Chen, A. Brekke, A. Egeland et al. (1988) Substorm expansion into the polar cap, Ann. Geophys. 6, No 5, 559-572.

Pudovkin M. I., O. A. Troshichev (1972) On the types of current patterns of weak geomagnetic disturbances at the polar caps, Planet. Space Sci., 20, 1773-1779.

Tanskanen E., T. I. Pulkkinen, H. E. J. Koskinen, J. A. Slavin (2002) Substorm energy budget during low and high solar activity:1997 and 1999 compared, J. Geophys. Res., 107, No A6, SMP 15-1 – SMP 15-11.

Polar Substorm, Svalbard Auroras and Mid-Latitude Positive Magnetic Bays: Case Study

Kleimenova N.G.[1], *Despirak I.V.* [2], *Malysheva L.M.*[1], *Gromova L.I.*[3], *Lubchich A.A.* [2]

[1]Schmidt Institute Physics of the Earth RAS, Moscow, Russia
[2] Polar geophysical Institute, Apatity, Russia
[3]IZMIRAN, Moscow, Russia
e-mail: kleimen@ifz.ru

Abstract

The high-latitude magnetic substorms known as "polar substorms" or "substorms on a contracted oval" have been studied basing on the analysis of the data from the Scandinavian IMAGE magnetometer chain and the visible auroras observed by the Svalbard all-sky-cameras in the 2010-2011 winter. In addition, there was a study of the relationship between the polar substorm occurrence and the localized intensification of the Field Aligned Currents (FACs) near the poleward edge of auroral oval, inferred by the AMPERE data (cancellation of the 66 simultaneous commercial satellites with magnetometer measurements). We also compared the polar substorms recorded at Svalbard with the magnetic data from the mid-latitude stations located at the same meridian, e.g., Borok (BOX) and Kiev (KIV). We found that all polar substorms under consideration were accompanied by the well-defined mid-latitude positive magnetic bays with the amplitudes of ~ 15-40 nT in the X-component of the geomagnetic field. These positive magnetic bays are usually interpreted as the evidence of the substorm West Travelling Surge (WTS) development due to the dipolarization process. Thus, it allows us to conclude that the source of polar substorms is located on closed magnetic field lines. The analysis of two events of the selected polar substorms is presented.

Introduction

Bay-like magnetic disturbances observed at high latitudes above 70° MLAT in the absence of disturbances at the lower auroral latitudes, are called the "*substorms on a contracted oval*" [*Lui et al*., 1976] or the "*polar substorms*" [*Kleimenova et al*., 2012]. It was found [*Despirak et al.*, 2019] that polar substorm are typically observed under slow solar wind. The statistics [*Kleimenova et al.*, 2012] showed that polar substorms are observed mainly in the pre-midnight sector. Similar to the classical substorms, the polar substorms are accompanied by Pi2 geomagnetic pulsations and auroral breakups. Polar substorms are poorly studied because the observation data at such high latitudes are not included in the estimation of the geomagnetic indexes. Moreover, the mid-latitude effects of polar substorms have not yet been investigated.

The aim of our work is to study the relationship of polar substorm with visible auroras observed at Svalbard and with the high-latitude distribution of the Field Aligned Currents (FAC) inferred by AMPERE satellite system. We also compared the polar substorm occurrence with simultaneous magnetic mid-latitude observations at the same meridian area.

Instrumentation

Our study is based on: (i) ground-based magnetic data of the Scandinavian IMAGE magnetometer chain (http://space.fmi.fi/image/) with the time resolution of 10 s [*Tanskanen*, 2009]; in addition to the magnetogram, we used data of the ionospheric equivalent currents [*Amm and Viljanen*, 1999]; the all-sky cameras (ASC) at Ny Alesund station (76.6° MLAT) was used for imaging auroral borealis covering a circular area with a diameter of about 600 km at 110 km altitude; (ii) the global network of the stations INTERMAGNET (http://www.intermagnet.org), (iii) the AMPERE data, based on the ionospheric magnetic measurements on 66 low-altitude globally distributed Iridium communication satellites (http://ampere.jhuapl.edu/products/plots), (iiii) OMNI database of the Interplanetary Magnetic field (IMF) data of the 1-min resolution (http://omniweb.gsfc.nasa.gov).

Observation results and discussion

First at all we selected all events of the visible aurora occurrence obtained by the Svalbard Ny Alesund (76.6° MLAT) all-sky-camera (ASC) in the 2010-2011 winter, because this record is possible only under certain meteorological conditions. It was found that all considered aurora events were accompanied by polar substorms. Two substorm events are presented below: 29 December 2010 (Fig.1) and 12 February 2011 (Fig. 2).

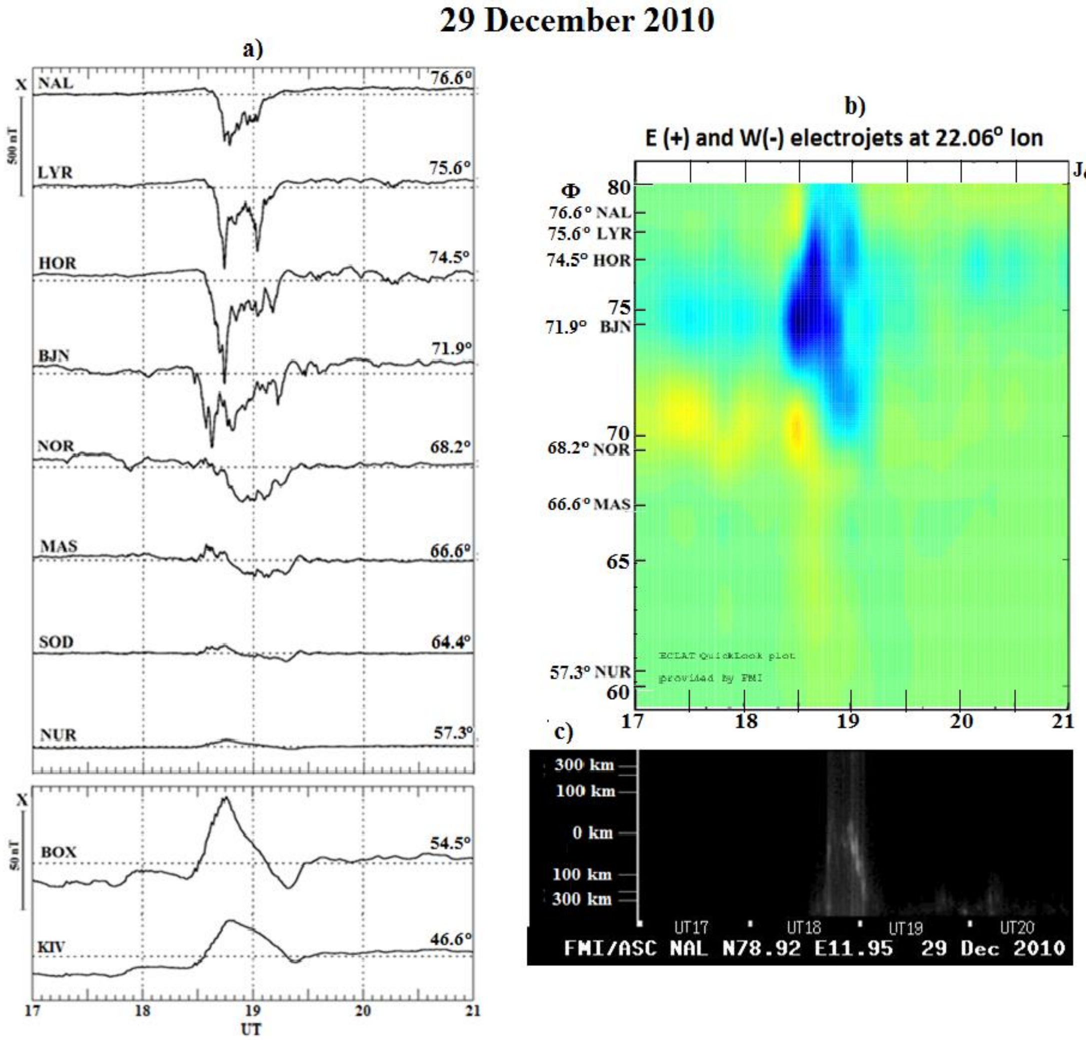

Fig.1. Here are shown: (a)- the magnetograms from selected high-latitude IMAGE stations and from two mid-latitude INTERMAGNET stations; (b)- the correspondent equivalent currents distribution; (c) aurora keogram from the Ny Alesund all-sky-camera.

The magnetograms from the selected stations IMAGE (Fig. 1a) demonstrate the polar substorm at ~18.30-19.15 UT, recorded only at the highest latitudes. The plot of the Ionospheric equivalent currents (Fig. 1b) confirms the presence of the westward electrojet enhancement at the latitudes higher 70° MLAT in the same time interval at the same time. The keogram from Svalbard cameras shows the visible aurora development at the same time and in the same area.

We compared this polar substorm occurrence with the INTERMAGNET magnetic observations at the mid-latitude stations Borok (BOX, 54.5° MLAT) and Kiev (KIV, 46.6° MLAT) located at the IMAGE meridian. It was found that at this time, there were the positive mid-latitude magnetic bay observed with the amplitude of ~40 nT at BOX and of ~25 nT at KIV.

The second polar substorm event is shown in Fig. 2.

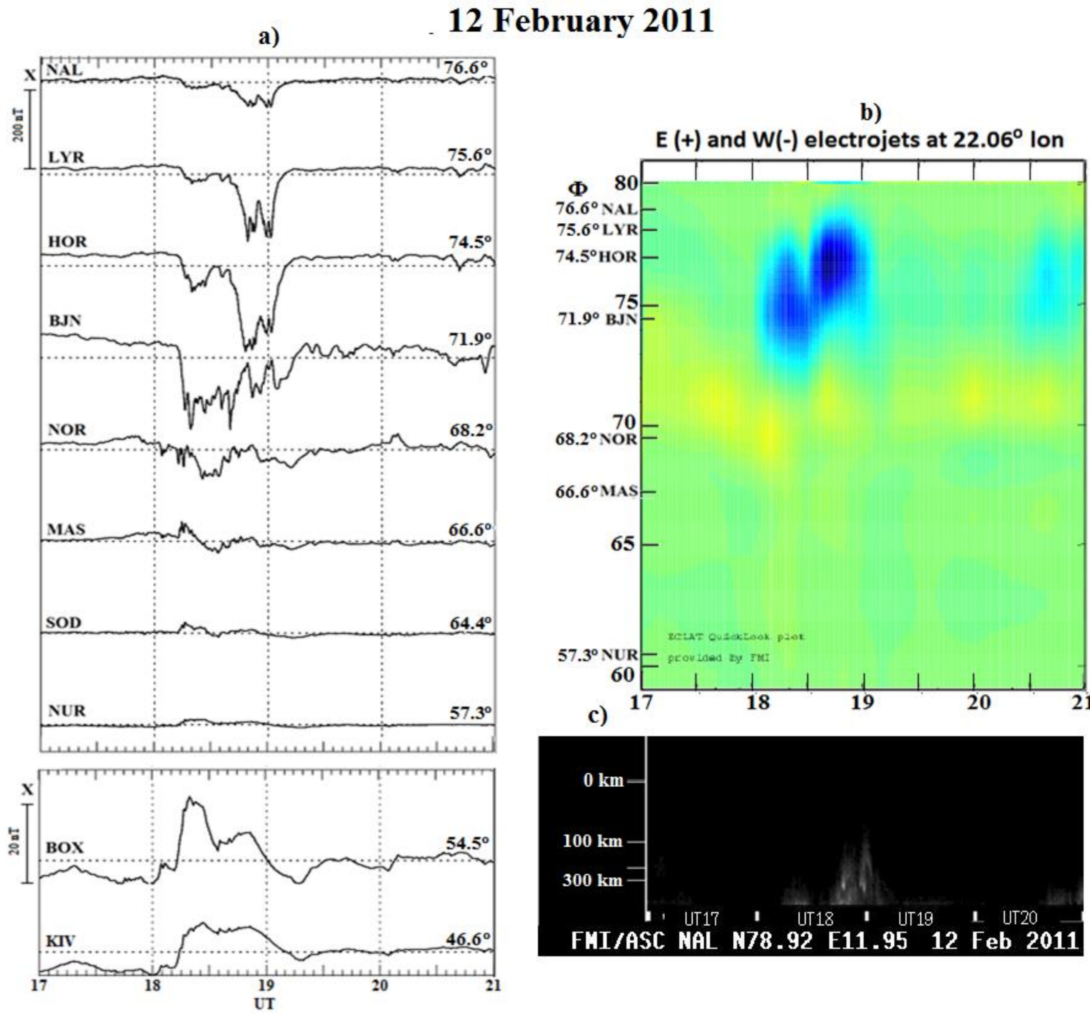

• *Fig.2. The same as in Fig. 1 for the second event.*

• As in the previous event, the magnetograms from the selected stations IMAGE (Fig. 2a) demonstrate the polar substorm development at ~18.15-19.15 UT, recorded at the highest latitudes. The plot of the Ionospheric equivalent currents presents the westward electrojet enhancement at the latitudes higher 70° GMAG in the time interval of ~ 18-19 UT. The keogram from Svalbard camera shows the visible aurora development at the same time and in the same area.

• As in previous event, we compared this polar substorm occurrence with the INTERMAGNET magnetic observations at the mid-latitude stations Borok and Kiev and found that at this time, there were the positive mid-latitude magnetic bays observed with amplitude of ~20 nT at BOX and of ~10 nT at KIV.

The next step was to study the relationship between polar substorm and the Field Aligned Current distribution inferred from the AMPERE data, based on the ionospheric magnetic measurements on 66 low-altitude globally distributed Iridium communication satellites. These results for two considered events are shown in Fig. 3*a* and 3*b*.

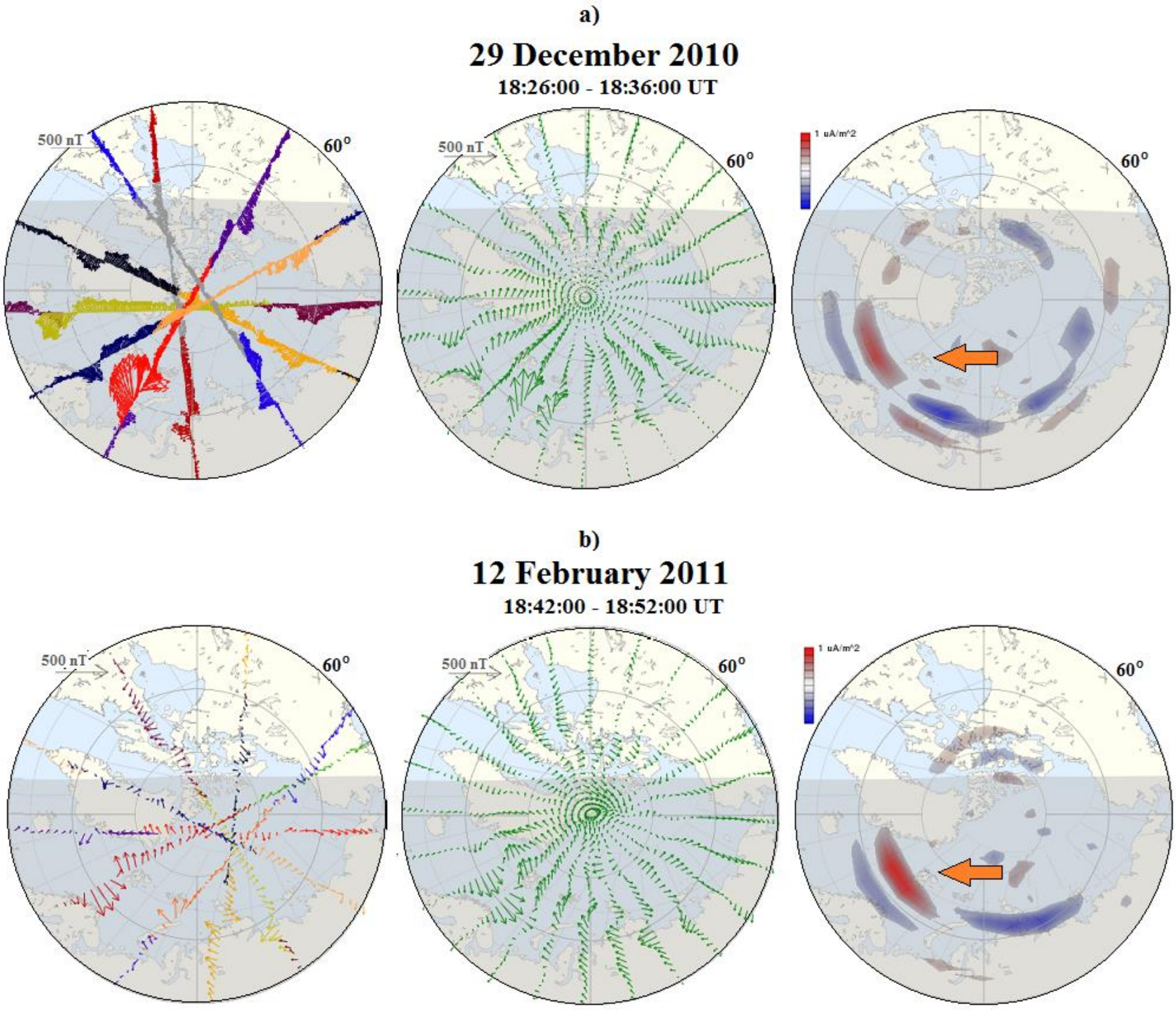

Fig.3. Maps of the distribution of magnetic vectors in the ionosphere (on the left), its spherical harmonic analysis (in the center}, Field Aligned Currents (on the right) inferred from the AMPERE system. Upward FACs are shown in red and downward FAC in blue. The red arrows show the Svalbard location.

It is seen that both considered polar substorms were accompanied by the localized enhancement of the upward Field Aligned Currents in the vicinity of the poleward boundary of the auroral oval. This indicates the increasing of the soft electron precipitation into the lower ionosphere, causing the aurora as well as electrojet progress, i.e., polar substorms occur.

We found (Fig. 4) that the both events were recorded under quiet magnetic conditions: (Kp ~ 0-1), the slow solar wind velocity (Vsw ~ 360 km/s) and low dynamic pressure (Psw ~ 08-1.2 nPa), the IMF Bz values changed from near zero to +1 nT. Under such conditions, the auroral oval should be constructed. The polar substorm were accompanied by a small enhancement of the PC-index indicating a moderate solar wind energy input into the magnetosphere.

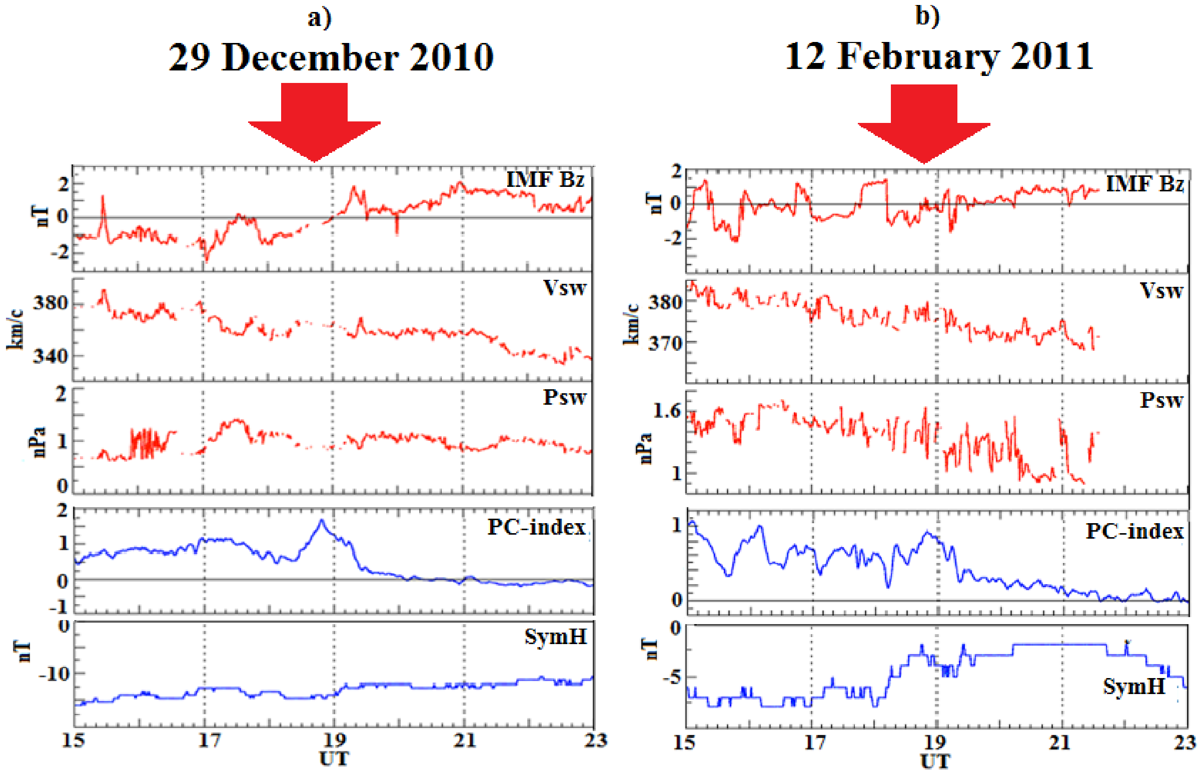

Fig. 4. OMNI data during the studied polar substorms

Later on, we identified 120 events of the polar substorms, based on the analysis of the IMAGE data from 10 winter seasons (November-February, 2010-2020). The most of these events have been recorded during the local late evening (at 21-23 MLT, i.e., 18-20 UT), only 30 events were observed near or immediately after midnight.

These events were compared with the simultaneous magnetic observations at mid-latitude INTERMAGNET stations Borok (BOX) and Kiev (KIV) located along the IMAGE meridian. It was found that 85% of the considered polar substorms were accompanied by positive mid-latitude magnetic bays. The most of the non-effective polar substorms were recorded near or after local magnetic midnight (at ~00-02 MLT, i.e., 21-23 UT).

In many papers, e.g., [*McPherron and Chu*, 2018; *Stepanov et al*., 2021], the mid-latitude positive magnetic bays, associated with "classical" sustorms, are interpreted as the effects of the appearance of the dipolarization process and the substorm West Travelling Surge (WTS) formation. The analysis of the satellites and ground data performed in [*Safargaleev et al.*, 2020] fit to the near-tail current disruption scenario as a possible source of the dipolarization and WTS, associated with polar substorm onset.

Conclusion

1. It was found that all visible aurora enhancement, recorded by the Svalbard Ny Alesund (76.6° MLAT) all-sky-camera (ASC) in the 2010-2011 winter, have been accompanied by polar substorms observed at the IMAGE stations at the latitudes higher ~70° MLAT. At the same spatial area, there were located the amplified Field Aligned Current inferred from the AMPERE data, based on the ionospheric magnetic measurements on 66 low-altitude globally distributed Iridium communication satellites.

2. We have analyzed the 120 events of polar substorm recorded by ground-based IMAGE magnetometer network in 2010-2017 in vicinity of the auroral oval poleward boundary, in the association with the simultaneous mid-latitude INTERMAGNET station data. It was found that the polar substorms as the "classical" ones are typically accompanied by the mid-latitude positive magnetic bays being an indicator of the night-side magnetic field dipolarization causing the energy injection into the inner magnetosphere. Thus, we could conclude that the polar substorm have the similar generation mechanism as the "classical" substorms, and the source of polar substorms is located on closed magnetic field lines of the inner magnetosphere, not in the distant magnetotail.

Aknowledgment

The work of N.G. Kleimenova, I.V. Despirak and A.A. Lubchich carried out within the framework of the RFBR grant No. 20-55-18003_Bulg_a; work by L.I. Gromova executed within the framework of the state assignment IZMIRAN; the work of L.M. Malysheva was carried out within the framework of the state assignment of the IPE RAS

References

Amm O., Viljanen A. (1999). Ionospheric disturbance magnetic field continuation from the ground to the ionosphere using spherical elementary current system, Earth, Plane. Space, 51, 431-440. https://doi.org/10.1186/BF03352247

Despirak I.V., Lyubchich A.A., Kleimenova N.G. (2019). Solar wind streams of different types and high-latitude substorms, Geomagnetism and Aeronomy., 59, 1, 3-9. https://doi.org/10.1134/S0016793219010055

Kleimenova N.G.. Kozyreva O.V, Malysheva L.M., Antonova E.E., Kornilova T.A., Kornilov I.A. (2012). Wave structure of magnetic substorms at polar latitudes, Geomagnetism and Aeronomy, 52, 746-754.

Lui A.T.Y., Akasofu S.-I., Hones E.W., Jr., Bame S.J., McIlwain C.E. (1976). Observation of the plasma sheet during a contracted oval substorm in the prolonged quiet period, J. Geophys. Res., 81, 7, 1415–1419. https://doi.org/10.1029/JA081i007p01415

McPherron R.L., Chu X. (2018). The midlatitude positive bay index and the statistics of substorm occurrence. J. Geophys. Res., 81, 7, 1415–1419. https://doi.org/10.1002/2017JA024766

Safargaleev V.V, Kozlovsky A.E., Mitrofanov V.M. (2020). Polar substorm on 7 Decmber 2015: preonset phenomena and features of auroral breakup, Ann. Geophys., 38, 4, 901–918. https://doi.org/10.5194/angeo-38-901-2020

Stepanov N.A., Sergeev V.A., Shukhtina M.A., Ogawa Y., Chu X., Rogov D.D. (2021). Ionospheric electron density and conductance changes in the auroral zone during substorms, J. Geophys. Res.: Space physics, 126, 7. https://doi.org/10.1029/2021JA029572.

Tanskanen E.F. (2009). A comprehensive high-throughput analysis of substorms observed by IMAGE magnetometer network: Years 1993-2003 examined, J. Geophys. Res., 114. A05204. https://doi.org/10.1029/2008JA013682

Impact of Space Weather on Ionospheric Scintillation

Shepeliev V.[1], Lytvynenko O.[2]

[1]Institute of Radio Astronomy NAS, Kharkiv, Ukraine
[2]Observatory URAN-4, Institute of Radio Astronomy NAS, Odesa, Ukraine
E-mail: shep@rian.kharkov.ua

Abstract.
Amplitude and phase fluctuations of a field of an incident electromagnetic wave arise when the radiation passes through a plasma layer with electron density inhomogeneities. This phenomenon is found in interstellar medium, interplanetary plasma and in the Earth's ionosphere when radio astronomy observations are carried out. Such amplitude and phase scintillation significantly impact on radio astronomy studies at low frequencies and should be taken into account during the observations and data reduction. Ionospheric scintillation affects an accuracy of radio astronomy observations the most severely. On the other hand, observational data distorted by the scintillation provide information on parameters of the scattering medium itself. We observed powerful radio sources with the URAN decameter interferometer network to study a temporal and spatial variation of the ionospheric scintillation in order to determine their relationship with terrestrial phenomena and space weather. We found, that an increase of the ionospheric scintillation measured by the UTR-2 radio telescope coincide with disturbances in the solar wind detected by space laboratories in Earth's orbit and with the URAN interferometers

Introduction
The Sun, as the most powerful source of energy in the solar system, has a decisive effect on many processes in near-earth space and on the Earth. This influence occurs both through electromagnetic radiation in various wavelength ranges and through flux of solar wind particles and coronal mass ejections. At present, within a framework of solar-terrestrial relations, various aspects of this influence are widely studied - from various physical phenomena in the interplanetary medium, magnetosphere and atmosphere of the Earth to the effect on wildlife and technical systems. The influence of the solar activity on radio communication is well known, from the longest wavlengths which do not pass beyond the ionosphere to the shortest ones used in satellite broadcasting and navigation. Radio astronomy observations are also a subject of this influence. Signals from radio sources, received by ground-based radio telescopes, pass through the space plasma and the Earth's ionosphere. Various physical phenomena in this medium lead to absorption of radio emission, scattering, phase and amplitude fluctuations of the received signals, refraction, a dispersion delay, and a polarization plane rotation. All these effects are developed the stronger, the lower frequency of radiation. The influence of the sporadic activity of the Sun often leads to a rather rapid change in parameters of the signal propagation medium, that must be taken into account when radio astronomy studies are planing and conducting.
In the Institute of Radio Astronomy of the NAS of Ukraine, cosmic radio sources are being studied using the world largest UTR-2 radio telescope and smaller URAN instruments, that operate according to various observational programs both independently and as a part of an interferometer network with the maximum resolving power of the order of an arc second [Konovalenko A. et al. 2016]. These studies are carried out in the decameter range, i.e. at the longest wavelengths applicable for the observations from the Earth's surface, which significantly interact with the plasma. Of the mentioned above plasma phenomena, the scattering of radio waves by inhomogeneities of an electron density of the ionized medium

affects the radio astronomical observations at decameter waves the most significantly. It leads to scintillations effect i.e. fluctuations in an amplitude and phase of the received signals.

Scintillation modes in the space plasma

On the way to the observer, radio waves from space radio sources pass through the inhomogeneous plasma of the interstellar medium, the solar wind, and the ionosphere, which have significantly different properties. The interstellar medium is very rarefied, but it has a huge extent and the scintillations at the decameter waves are in the strong scattering regime. In this mode, the emission of a radio source is spread in an angle of scattering, that is the interstellar scintillation leads to an increase in the angular size of a point source proportional to density and extent of the turbulent medium. In particular, the observed angular size of extragalactic radio sources depends on a proximity of a line of sight to the Galaxy plane and can be approximated by the empirical relation [Shishov et al., 2001]:

$$\theta_s \cong 20(10\lambda)^{2.2}(\sin b)^{-0.6},$$

where b is a galactic latitude, λ is in meters, and θ_s is in microseconds of arc. At the frequency of 25 MHz even for $b = 90°$ this expression gives an estimate $\theta_s \approx 0{,}75''$ i.e. of the order of maximum angular resolution of the URAN interferometer network and therefore the scattering must be taken into account on the lines of sight close to the galaxy plane when determining an image of a radio source.

The interplanetary medium is significantly less extended but denser then the interstellar one. Scattering in it depends on the proximity of the line of sight to the Sun. At small elongations scattering can be strong up to the decimeter wavelengths [Anantharamaiah et al., 1989], and at the decameter wavelengths strong scintillation and distortion of a source image is observed up to elongations 90°. This effect limits the period of interferometer observations of compact radio sources in this range to night time. At larger elongations, scintillation is weak and, due to the high speed of the solar wind, a scintillation period is of the order of one second. In this case, the amplitude flickers are well averaged and have weak effect on an accuracy of source flux measurements. However, phase fluctuations at an interferometer output expand a signal spectrum and can limit coherent integration time and so a sensitivity of the instrument. In addition, unlike the interstellar medium, the turbulence in the interplanetary plasma is affected by the space weather and does not remain constant over time. For example, when a coronal mass ejection propagates through the interplanetary medium, the interplanetary scintillation index increases significantly [Kalinichenko et al., 2013, Glyantsev et al., 2015]. Such an increase in turbulence of the interplanetary medium lasting up to several days caused by the sporadic solar activity also increases the signal bandwidth at the correlator output, that limits a possibility of interferometer observations with high sensitivity [Shepeliev et al., 2020]. An account of solar activity events must be used for a short-term forecast when determining the strategy of highly sensitive observations.

The third layer of the plasma on the path of radio waves to a radio telescope is the Earth's ionosphere – the least extended but most dense medium. This layer introduces the greatest distortion in the received signal at the decameter wavelengths. The scintillation on ionospheric irregularities is often high in amplitude, and its period is comparable to the transit time of the source through a radio telescope pattern. It makes difficult to obtain a reliable estimate of the received signal power. Therefore, a prediction of the scintillation level raising, and hence an analysis of its causes, is important for the decameter radio astronomy. The level of ionospheric scintillation depends on the time of day and season. Observations with the URAN and the UTR-2 showe that the average level of the ionospheric scintillation is quite high in the summer time. Therefore, for the observations at the decameter wavelengths, winter time is mainly used, when the scintillation index in nighttime observations is in the range of 0.1–0.5 both in the period of minimum and maximum of the solar activity. This value makes it possible to obtain sufficiently high-quality radio astronomy data. However, sometimes there are periods of several days with an ionospheric scintillation index *SI* ~ 1, when it is practically impossible to obtain reliable data.

Data reduction and results

To investigate the causes of such events, we used archived data of cosmic radio sources observations with the URAN interferometers. These data have been processed to obtain the ionospheric scintillation indexes. There are no long periods of continuous observations in this data set. As a rule, one session of the interferometer observations lasts one week and is repeated a month later. We selected the sessions during which there was a sharp increase in the scintillation index relative to its ordinary level. In this work, we study possible connection of such events with the space weather. Therefore, for the selected sessions, the level of solar wind turbulence was also determined by the method proposed in [Shepeliev et al., 2020]. In that work, it was shown that a width of a spectrum of ionospheric scintillations at the output of the URAN interferometer, measured in observations of extended radio sources, does not exceed 0.1 Hz. Consequently, for a compact radio source flickering both on the ionospheric irregularities and on the interplanetary ones, it is possible to filter a part of the spectrum larger than this value, which is determined only by the interplanetary scintillations. It was shown that an increase in the energy of the high-frequency part of the spectrum correlates with an increase in the turbulence of the interplanetary medium during abrupt changes in the solar wind parameters measured in the Earth's orbit and associated with manifestations of a sporadic solar activity. In this work, we used the compact source in the Crab Nebula, which was observed in every session, as a probe for determining the level of the solar wind turbulence. The part of the spectrum of the interferometric signal of the same source lower than 0.1 Hz can serve as an indicator of the ionospheric turbulence level. However, this part also contains low-frequency components of the interplanetary scintillations spectrum. For this reason, to determine the ionospheric scintillation index, we used the observational data of extended radio galaxies, the angular size of which is greater than a critical value for the interplanetary scintillations.

Fig.1 represents the data obtained in the session on October 24–31, 2011. The black dots show the change in the day average of the ionospheric scintillation index (SI) of two extended radio galaxies 3C55 and 3C47. The red dots show the power of interplanetary scintillations (PIS) - the energy of the high-frequency part of the scintillation spectrum of the compact source in the Crab Nebula.

It should be noted that on October 24, 2011, the Advanced Composition Explorer (ACE) satellite detected a sharp jump in the density and temperature of the near-Earth plasma, as well as a change in the solar wind speed from 350 to 500 km/s. The position of this event is marked with a green arrow in Fig.1. This event was also accompanied by a change in Dst geomagnetic index with the delay of 1.5 days, (low panel of Fig. 1) Interestingly, that according to the observation by Geostationary Operational Environmental Satellite (GOES), more than a day before the changes in plasma parameters at 10:25 UT 22.10.2011 there was a significant increase in X-ray emission and proton flux from the Sun, which indicates a powerful sporadic solar activity. In the Solar and Heliospheric Observatory (SOHO) coronagraph images, this time corresponds to a coronal ejection with a mass of $1.2 \cdot 10^{16}$ g and an energy of $6.2 \cdot 10^{30}$ erg of a halo type, i.e. directed towards the Earth, shown in Fig.2.

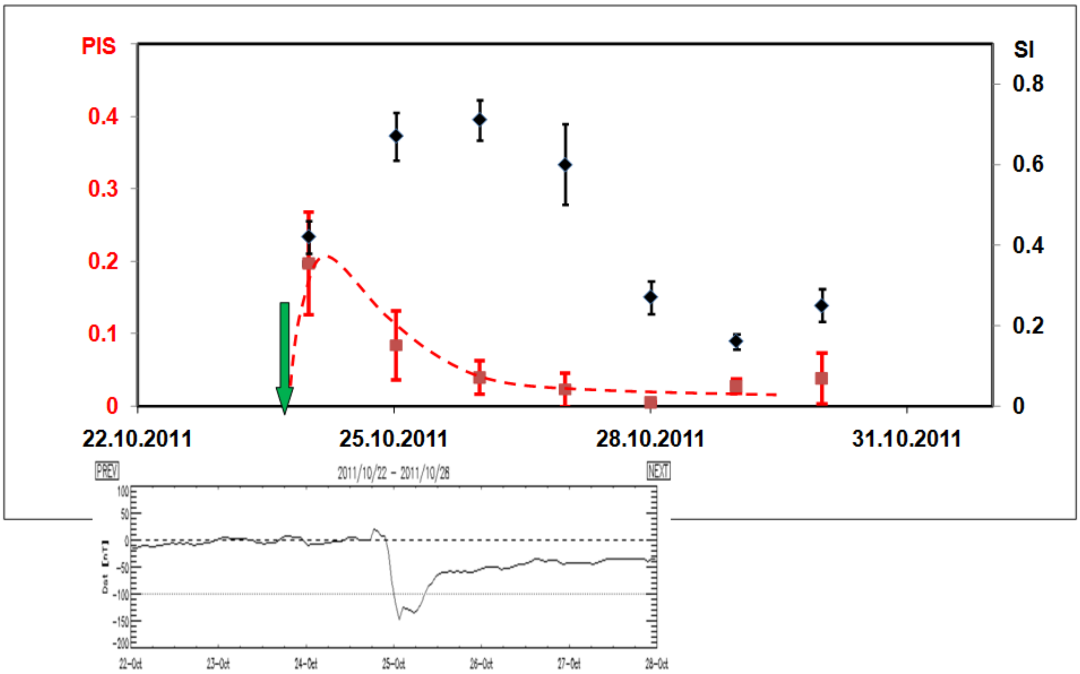

Fig.1. *Ionospheric scintillation index (SI, black points), power of interplanetary scintillation (PI, red points) and Dst geomagnetic index from World Data Center for Geomagnetism, Kyoto*

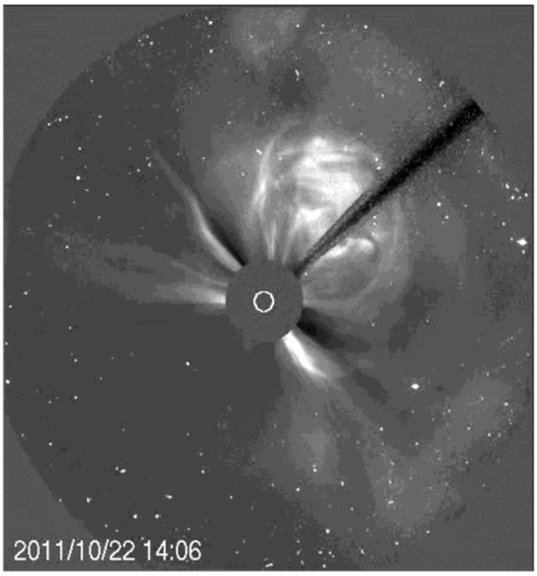

Fig.2. *Coronal mass ejection recorded by SOHO C3 coronagraph 10/22/2011*

Thus, a chain of successive events can be traced: a solar flare, a coronal mass ejection, a near-Earth shock wave, which caused an increase in interplanetary plasma turbulence, a magnetic storm, and an increase in the ionospheric scintillation index (ionospheric turbulence). This chain of events gives a hope for the possibility of a short-term forecast of a sharp deterioration in conditions of radio astronomy observations at the decameter wavelengths. However, in other cases of an increase in the ionospheric scintillation index, no previous powerful events on the Sun were found. So in the session on February 15–21, 2010, the increase in the ionospheric scintillation index was noted, which was accompanied by the increase in the turbulence of the interplanetary medium (Fig. 3). Here, the interplanetary scintillation were also determined from observations of the compact source in the Crab Nebula, and the day-averaged ionospheric scintillation indices were obtained from observational data of the extended radio galaxies 3C288, 3C350, and 3C351.

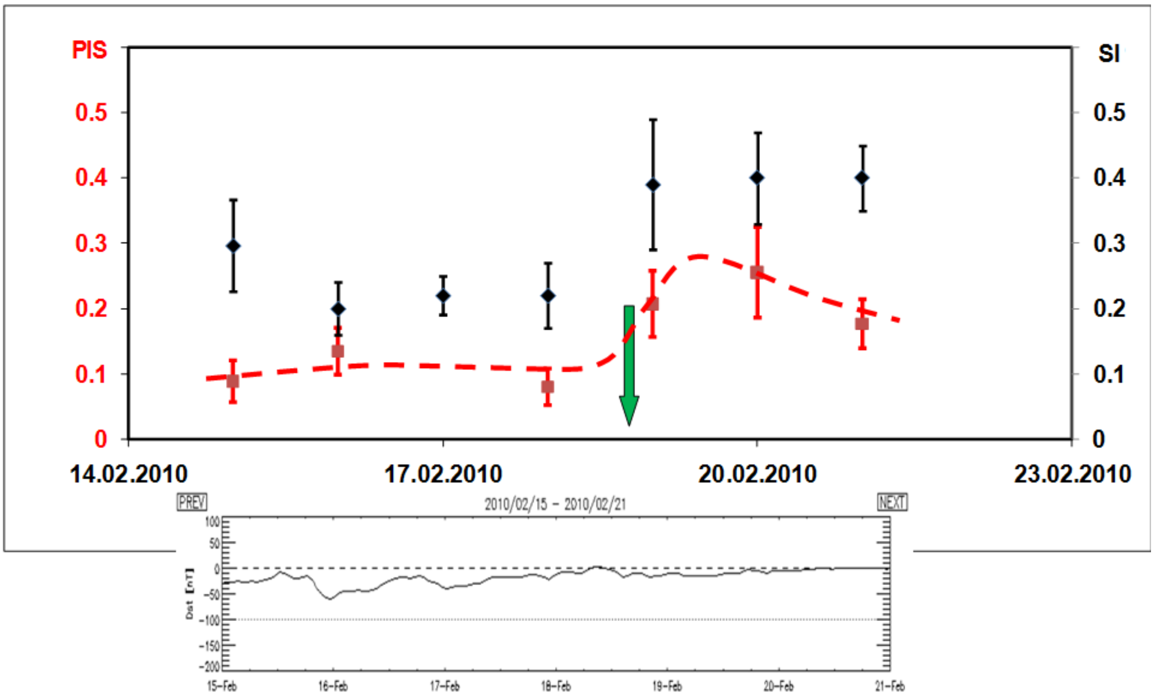

Fig.3. Ionosphere scintillation index (SI, black points), power of interplanetary scintillation (PI, red points) and Dst geomagnetic index from World Data Center for Geomagnetism, Kyoto

The presence of disturbances in the near-Earth solar wind is confirmed by the ACE data. However, in this case, the changes in the parameters of the near-Earth plasma were much less strong and fast, the solar wind speed, for example, changed from 400 to 450 km/s. Time of these disturbances is shown by arrow in Fig.3. There was no change in the geomagnetic index (low panel Fig. 3) and in the previous few days, there was no increase in the proton flux, and only small fluctuations in the intensity of the X-ray radiation were noted. Also, no significant coronal mass ejection was detected. It is possible that such complex of disturbances in the near-Earth plasma and solar activity can be associated with coronal holes and high-speed solar wind streams.

Conclusions

1. The processing of the archived data of radio sources observations with the UTR-2 radio telescope and the URAN interferometers was carried out. The data reduction made it possible to determine the magnitude of ionospheric and interplanetary scintillation separately.
2. A connection has been found between disturbances in the near-Earth interplanetary medium and the turbulence of the ionosphere.
3. The data obtained on the causes of the deterioration of the "radio astronomical weather" can be used for forecasting disturbances and planning the observations at the decameter wavelengths.

References

Anantharamaiah, K. R., Cornwell, T. J., and Narayan, R. (1989). Synthesis imaging of spatially coherent objects, in Synthesis Imaging in Radio Astronomy, 1989, 6, 415–430.

Glyantsev, A. V., Tyul'bashev, S. A. et al. (2015). Interplanetary-scintillation observations of coronal mass ejections near the maximum of the 24th solar-activity cycle, Astron. Rep. 2015, 59, 1, 40–45.

Kalinichenko, N. N., Konovalenko, A. A., et al. (2013). 2011 February 15 CME in the Interplanetary Medium by Observations of Radio Source Scintillations at the Decameter Wavelengths, Radio Phys. Rradio Astron., 2013, 18, 4, 301–308. (in Russian).

Konovalenko A., Sodin L. . et al. (2016). The modern radio astronomy network in Ukraine: UTR-2, URAN and GURT. *Exp. Astron.* 2016. 42, 1, 11–48.

Shepeliev, V., Lytvynenko, O. et al. (2020). Influence of the solar wind on interferometric observations at the decameter wavelengths, Radio phys. radio astron., 2020, 25(2) 87-99. (in Russian).

Shishov, V. I. (2001). Turbulent interstellar plasma and ultrahigh angular resolution in radio astronomy, Astronomy Reports, 2001, 45, 195–202.

The Relationship between Solar Activity and Geomagnetic Activity Indices in the Last Four Solar Cycles

Tirnakci M., Kilcik A.

Department of Space Science and Technologies, Akdeniz University Faculty of Science, 07058, Antalya, Turkey

Abstract

In this study, Lyman-alpha solar spectral irradiance (SSI) compared with geomagnetic Ap, Dst and PC index time series for the time period of 1975-2020. All data sets used in this study are taken from OMNIWeb. To compare Lyman-alpha SSI and geomagnetic indices cross correlation and Morlet wavelet analysis methods were used. In results of our analysis we found following results: i) Selected geomagnetic activity indices weakly correlated with Lyman-alpha SSI index. ii) The Lyman-alpha SSI is ahead of all geomagnetic activity indices except Dst index. iii) All indices used in this study show 11 year solar cycle and 27 day solar rotation periodicities.

Introduction

The sun is the largest radiation source continually affecting near space environment with a flow of charged particles, known as the solar wind, originating from its outer layer. Although the sun is a quiet star compared to other stars, many active structures are observed with detail due to its nearness to earth. When the temporal variations of these structures are investigated, it can be evaluated that the sun is a quasiperiodic star. All time and location dependent changes observed on the sun can be defined as solar activity. The best known indicators of solar activity are sunspots and solar flares.

There are several periodic variations of solar activity. The most well-known of these variations are the 27-day solar rotation and the 11-year sunspot cycle. The longest-running and most common dataset used to study the solar cycle is sunspot numbers. Since about 1610, sunspots have been systematically observed by using telescopes. The other datasets used are sunspot area, 10.7 cm solar radio flux (F10.7), Lyman-alpha SSI, solar flare index (FI), and coronal mass ejections (CMEs), etc. Generally, all solar activity indicators are strongly correlated with each other (Hathaway et al., 2002).

Geomagnetic storm is defined as irregularities in the Earth's total magnetic field. These irregularities are also show differences with time and location. Various indices are used to measure these irregularities such as AE index, K index, Dst index, PC index. The relationship between geomagnetic indices depends on the evolution of solar activity and there are strong losses in the correlation between geomagnetic activity indices during the declining phases of the 20th and 23rd solar cycles. Geomagnetic activity indices also have a certain level of correlation both with each other and with solar activity (Verbanac et al., 2011).

The most important feature of the aa time series is its double-peak structure (Gonzalez et al., 1990). The first peak of this double structure is caused by coronal mass ejections associated with solar activity, while the second peak is caused by the high speed streams originate from coronal holes located at the polar regions of the sun (Gonzalez et al., 1990).

Russell and Mulligan (1995) obtained a significant correlation between the aa index and the solar polar magnetic field for the time period of 1868 to 2006. The highest correlation between monthly solar activity and geomagnetic indices were observed between solar wind and Ap index (r = 0.76) and Dst index (r = 0.52) with zero-time delay (Kilcik et al.,2017). In addition, Mursula and Zeiger (2000) found1.3 years periodicity between solar wind and Ap indices in even cycles, while they found 1.5-1.7 years periodicity in odd cycles. Although the relationship between the solar activity and geomagnetic activity indices has been extensively studied, a detailed explanationof their nature has not yet been clearly given (Echer et al., 2004; Verbanac et al., 2011).

In this study, a time series analysis was performed using data obtained for the last four solar cycles (1975 – 2020). We describe data and methods used in Section 2, analysis and results are given in Section 3, finally the discussion and conclusions are given in Section 4.

Data and Methods

a) Data

In this study we used Lyman-alpha SSI index as solar activity index and Dst, Ap and PC(N) indices were used as geomagnetic activity indices.

The Lyman-alpha line is hydrogen's strongest emission line at 121,567 nm and it describe the full disc integrated solar irradiance over 121-122 nm wavelength interval. The composite Lyman-alpha SSI data used in this study was taken as daily form from OMNIWeb.

Figure 1 shows the temporal variation of sunspot number and Lyman-alpha SSI index. Considering the sunspots number as a very good index of solar activity, it is clearly seen from the figure that the Lyman-alpha SSI index also represents the solar activity quite well.

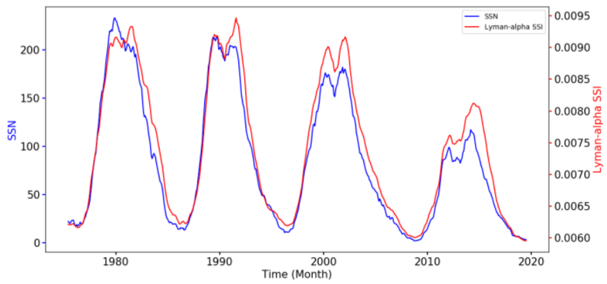

Fig.1. Comparison of SSN and Lyman-alpha SSI

The F10.7 radio flux is a commonly used index of solar activity (Tapping, 2013). Barth et al. (1990) found a high correlation between the Lyman-alpha SSI index and F10.7 radio flux in the ascending and descending phases of the sunspot cycle over a 200-day or longer time period. Based on their results and the temporal variation between the sunspots number and the Lyman-alpha SSI index (Figure 1), the Lyman-alpha SSI index was used as an index of solar activity in this study.

Dst (Disturbing Storm Time) index it allows to investigate the symmetrical axis situation of magnetospheric currents, especially ring currents. This index, which is directly relevant to geomagnetic activity, is also known as the vertical component of the magnetic field. Data from four observatories are used to derive the Dst index. Because of good data quality these observatories were chosen sufficiently far from the auroral and equatorial electrojet regions. Irregularities observed in the Dst index have a negative sign and -50 nT≤Dst< -30 nT are called small storm, -100nT≤Dst< -50nT are called moderate storm, -200 nT≤ Dst< 100 nT are called intense storm and values less than -250 nT are called big storms (Gonzalez et al., 1999).

The K index is used to measure changes in the horizontal component of the magnetic field. However, on the grounds that K index is not directly related to geomagnetic activity. Thus, produce an activity-related index was required. Therefore, first, the Kp index was derived from the mean standardized K-index of 13 geomagnetic observatories located between ± 44 and 60 degrees geomagnetic latitudes. This planetary index is designed to measure the magnetic effect of solar particle radiation. The 3-hourly ap index is derived from the Kp index by using following table (Table 1). Then, the daily Ap index value is obtained by averaging the eight values of ap for each day.

Table1. Derivation table of the ap index from Kp index given by J. Bartels (https://www.ngdc.noaa.gov/stp/GEOMAG/kp_ap.html

Kp = 0o	0+	1-	1o	1+	2-	2o	2+	3-	3o	3+	4-	4o	4+
ap = 0	2	3	4	5	6	7	9	12	15	18	22	27	32
Kp = 5-	5o	5+	6-	6o	6+	7-	7o	7+	8-	8o	8+	9-	9o
ap = 39	48	56	67	80	94	111	132	154	179	207	236	300	400

PC index, it is an index improved to predict the instantaneous state of global magnetic activity and to easily calculate it from ground based measurements. Basically to calculate this index, the concept of convection in the near polar region controlled by solar wind parameters is considered. Quiet periods of ionospheric conductivity are selected for each day of the year from Thule (PC- North) and Vostok (PC-South) to exclude the daily and seasonal variation of ionospheric conductivity produced by the solar ultraviolet radiation (Troshichev et al.,2006). In the statistics made as a result of the agglomerated data, it shows that the PC index is a good index for magnetospheric parameters such as auroral electrojets, ionospheric electric field in the near polar region, etc.

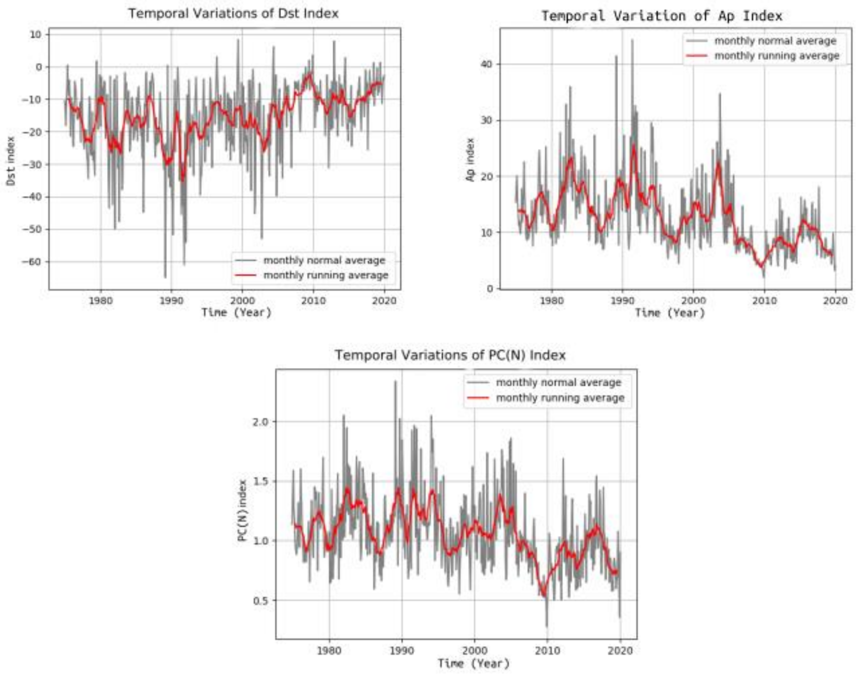

Figure2. Temporal variations of geomagnetic Dst, Ap and PC(N) indices.

b) Methods

All data sets used in this study were taken as daily form from OMNIWeb for 1975-2020 time intervals. Then monthly data sets were produced. In order to eliminate the small fluctuations in these monthly data, the data sets smoothed with 12-step running average smoothing method. Then, the cross-correlation analysis method was applied to obtain the highest correlation coefficients with possible time delay between the Lyman-alpha SSI index and geomagnetic activity indices used in this study.

Morlet wavelet analysis method was applied to determine the possible periodicities with their occurrence time. This technique is becoming a valuable method to analyze localized variations of power within a given time series (Torrence and Compo, 1998). It has been widely used in the literature for different kind of time series such as astronomical (Kilcik et al., 2020), geophysical (Torrence and Compo, 1998), etc. In this study, Lyman-alpha SSI index and Ap, Dst and PC(N) geomagnetic activity indices analyzed and the scalograms were obtained to address the presence of the detected periodicities. We have used “Morlet” mother function considering a “red noise” background (Torrence and Compo, 1998). The edge effects is represented by the cone of influence (COI) plotted with a black line in the figures shown below. On the other hand, the periods detected above the 95% confidence level inside the COI are shown by black contours in these figures.

Analysis and Results

Figure 3 plots the cross correlation analysis results between solar and geomagnetic activity indices used in this study. The detailed results of the correlation analysis are given in Table 2.

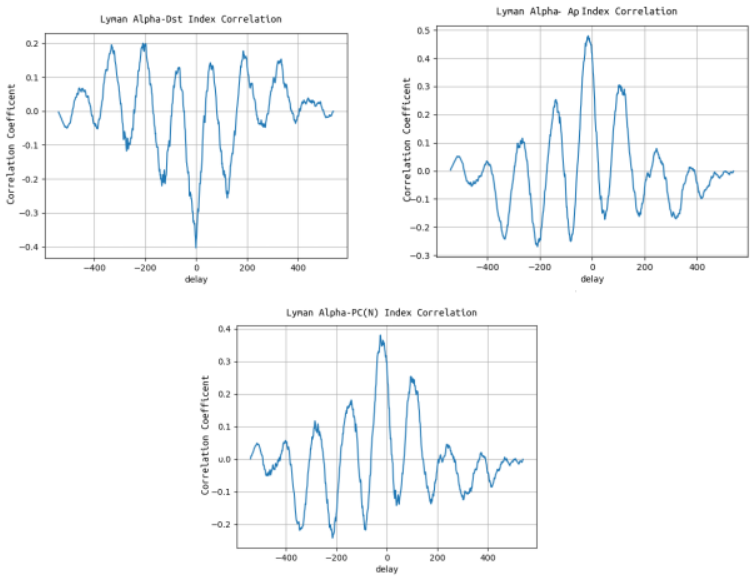

Figure3. Dst, Ap and PC(N) index cross-correlation results with Lyman-alpha SSI

Table2. Cross-correlation coefficients and their corresponding time delays

	Lyman-alpha SSI-Dst	Lyman-alpha SSI-Ap	Lyman-alphaSSI-PC(N)
Cross Correlation Coefficient	-0.40±0.04	0.42±0.04	0.30±0.04
Time Delay (Month)	0	14	25

As shown in Figure 3 and Table 2, geomagnetic Ap index and Dst index show the same level of correlation with Lyman-alpha SSI index. The Ap index correlation looks a bit higher than the Dst correlation but it has 14-month time delay compared to Dst and this time delay does not any meaning. Thus we may suggest that the Dst index better describe the Lyman-alpha SSI index. The lowest correlation and largest time delay obtained between PC(N) and Lyman-alpha SSI index.

Figure 4 shows the period analysis results of solar and geomagnetic activity indices used in this study.

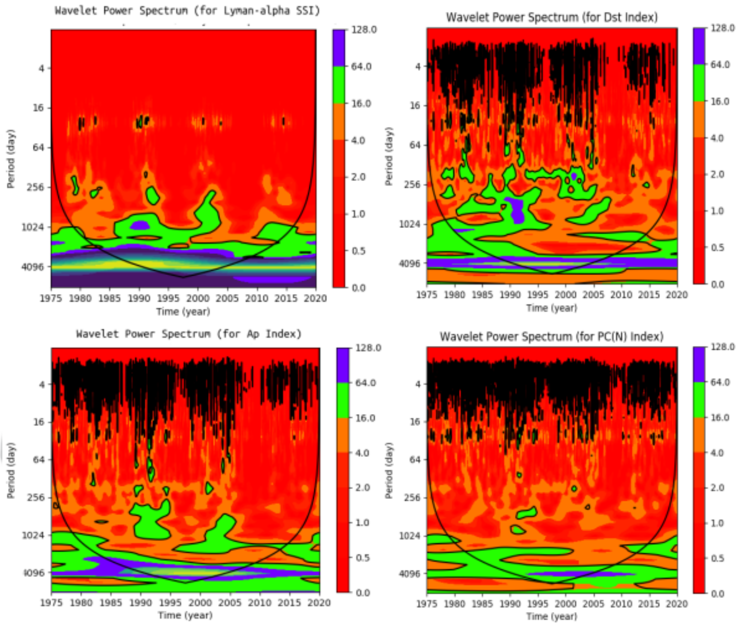

Figure 4. The Morlet wavelet analysis results for the used data sets.

As shown in Figure 4, about 11 years solar cycle periodicity clearly seen in the Morlet wavelet scalograms of all data sets for the investigated time period (from 1975 to 2020) except PC(N) index that it only seen between 1993-2013 time interval. 27 days solar rotation periodicity is also clearly seen in the wavelet scalogram of all data sets especially during the maximum phases of solar cycles. A 1024 days periodicity is seen in all data sets used in this study without any exception and it appears around the maximum phases. The one another meaningful period in the wavelet spectrum are about 1800 days for the PC(N) index and it seen around 1975-2000 and 2010-2020 time intervals. About 500 days periodicity is appear in all geomagnetic activity indices; it only seen during the maximum phases of solar cycles 22 and 23. A 256 days periodicity appear in all data sets except PC(N) index. It is clearly seen especially during the maximum phases of cycles 22 and 23.

Discussion and Conclusions

In this study, we investigated the correlation and periodicity relationship between solar (Lyman-alpha SSI and geomagnetic activity indices (Ap, Dst and PC(N)) for the 1975 – 2020 time periods. Our main findings are as follows;

1. Selected geomagnetic activity indices weakly correlated with Lyman-alpha SSI index,
2. The Lyman-alpha SSI index is ahead of all geomagnetic activity indices exceptDst index.
3. All indices used in this study show about 11 year solar cycle and 27 day solar rotation periodicities.

Kilcik et al. (2017) obtained remarkable correlations between the geomagnetic Ap and Dst indices and different categories of sunspot counts. As shown in Figure 1sunspot number and Lyman-alpha SSI index are well correlated. Thus, we may expect that the Lyman-alpha SSI index show some level of correlation with geomagnetic indices used in this study. As expected, we found that the Lyman-alpha SSI index and geomagnetic activity indices are weakly correlated (r =-040, r=0.42 and r=0.30) with Ap, Dst and PC(N), respectively. Verbanac et al. (2011) found that the Dst index has zero time lag and Ap index has 1-2 year time lag with used solar activity indices. Here, we confirm their results with Lyman-alpha SSI index. Kilpua et al (2014) analyzed Dst, Auroral Elektrojets (AE) and interplanetary magnetic field (IMF) between

1995-1999 and 2006-2012 and showed that there is very low geomagnetic activity during the solar cycle 24. Here, we also confirm their results as shown in Figure 2.

Mursula and Zieger (2000) found about 1.3 year periodicity for solar wind speed, geomagnetic activity indices and auroras. They conclude that this periodicity related to the evolution of coronal holes. In our study, we found about 500-day periodicity for all used geomagnetic activity indices which cover recent solar cycles. Thus we confirm their results and further suggest that this periodicity may be the general characteristics of geomagnetic activity.

Solar activity time series generally show a double/multiple peak structure during the maximum phase of cycles. The visible gap between peaks is called as the 'Gneyvshev Gap' (Bazilevskaya et al., 2006). Verbanac et al. (2010) suggested that the time delay between F10.7 and Dst index is less than one year and it is due to the Gnevyshev gap. They concluded that the response of Ap and Dst indices to solar activity are different; while Dst index is affected by coronal mass ejections, Ap index is more sensitive to high speed streams (HSS). We also found different time delays for different geomagnetic indices and confirm above results with recent data.

References

Barth, C. A.,Tobiska, W. K.,Rottman, G. J., White, O. R. (1990). Comparison of 10.7 cm radio flux with SME solar Lyman alpha flux,Geophys. Res. Lett., 17(5), 571–574.

Bazilevskaya, G.A., Makhmutova, V.S., Sladkova, A.I. (2006). Gnevyshev gap effects in solar energetic particle activity, Adv. Space Res. 38, 484.

Echer, E., Gonzalez,W. D., Gonzalez, A. L. C., Prestes, V., Vieira,L. E. A., Dal Lago, A., Guarnieri, F. L., Schuch, N. J. (2004). Long-term correlation between solar and geomagnetic activity, J. Atmos. Sol. Terr. Phys., 66, 1019-1025

Gonzalez, W. D., Tsurutani, B. T., Clúe de Gonzalez,A. L. (1999). Interplanetary origin of geomagnetic storms, Space Sci. Rev., 88, 529–562.

Gonzalez, W., Gonzalez, A. Tsurutani, B. (1990). Dual-peak cycle distribution of intense geomagnetic storms. Planetary Space Science, 38, 181–187.

Hathaway, D. H.,Wilson, R. M., Reichmann, E. J.(2002). Group Sunspot Numbers: Sunspot Cycle Characteristics, Sol. Phys. 211, 357 – 370.

Kilcik, A., Chowdhury, P., Sarp, V., Yurchyshyn, V., Donmez, B., Rozelot, J. P., Ozguc, A. (2020). Temporal and Periodic Variation of the MCMESI for the Last Two Solar Cycles; Comparison with the Number of Different Class X-ray Solar Flares, Sol. Phys., 295, 1-17.

Kilcik A., Yiğit E.,Yurchyshyn V. ,Ozguc A. ,RozelotJ.P. (2017). Solar and Geomagnetic Activity Relation for the Last two Solar Cycles, Sun and Geosphere, 12, 31-39.

Kilpua, E. K. J., Luhmann, J. G., Jian, L. K., Russell, C.T. Li, Y.(2014). Why have geomagnetic storms been so weak during the recent solar minimum and the rising phase of cycle 24? J. Atmos. Sol. Terr. Phys., 107, 12.

Mursula K., Zieger, B. (2000). The 1.3-Year Variation in Solar Wind Speed and Geomagnetic Activity, Adv. Space Res. 25,1939.

Russell, C.T., Mulligan, T.(1995). The 22-year Variation of Geomagnetic Activity: Implications for the Polar Magnetic Field of the Sun," Geophys. Res. Lett., 22, 3287.

Tapping, K. F. (2013). The 10.7 cm solar radio flux (F10.7), Space Weather,11,394–406.

Troshichev, O. A., Janzhura, A., Stauning, P. (2006). Unified PCN and PCS indices: Method of calculation, physical sense and dependence on the IMF azimuthal and northward components. J. Geophys. Res., 111,A05208.

Torrence, C., Compo, G.P. (1998). A Practical Guide to Wavelet Analysis, Bulletin of the American Meteorological Society, 79,61-78.

Verbanac, G., Vršnak, B., Temmer, M., Korte, M., Mandea, M. (2010). Four decades of geomagnetic and solar activity: 1960 – 2001, J. Atmos. Solar-Terr. Phys.72, 607 –616.

Verbanac, G., Mandea, M., Vršnak, B., Sentic, S. (2011). Evolution of Solar and Geomagnetic Activity Indices, and Their Relationship: 1960 – 2001, Sol. Phys., 271, 183–195.

Calculation of the Horizontal Power Perturbations of the Earth Surface Magnetic Field

Werner R.[1]*, Guineva V.*[1]*, Atanassov A.*[1]*, Bojilova R.*[2]*, Raykova L* [1]*, Valev D.*[1]*, Lubchich A.*[3]*, Despirak I.*[3]

[1]Space Research and Technology Institute (SRTI), Bulgarian Academy of Sciences, Stara Zagora Department, Bulgaria
[2]National Institute of Geophysics, Geodesy and Geography (NIGGG), Bulgarian Academy of Sciences, Sofia, Bulgaria
[3]Polar Geophysical Institute, Apatity, Russia
E-mail: rolwer52@yahoo.co.uk

Abstract.

The substorm effect at midlatitudes is expressed by a rise and decay of the X-component of the surface magnetic field, called midlatitude positive bay (MBP). McPherron has introduced a new geomagnetic index based on the calculation of the horizontal power perturbations of the Earth surface magnetic field. In this work, a developed processing tool to determine the horizontal power of the magnetic field is presented. A main element in these calculations is the estimation of the main field by smoothed spline fits to the midnight field using 25 consecutive daily observations centred over the day in consideration. The estimated field was removed from the measurements. We used the Grubs test for detection of days with strong magnetic disturbances. Excluding the disturbed days from further calculations, the mean solar quiet day variations (Sq) were determined by averaging the field components and were subtracted from the magnetic field observations of the central day. The resulting X and Y horizontal components were high pass filtered to suppress periods longer than 3 hours. Thus, adopting the McPherron s algorithm we have calculated the horizontal power for the Panagjurishte station (PAG). In the algorithm we have incorporated procedures for gape and peak detection and removing. The MPB index is defined as the average of the horizontal power of a multitude of stations and monitors the intensity in the substorm disturbances.

Introduction

During substorms large amounts of energy accumulated in the magnetosphere tail is released into the ionosphere and the inner magnetosphere. A lot of phenomena are generated, among which, disturbances in the surface magnetic field. During substorm expansions a typical systematic pattern of the surface magnetic field is observed. At auroral latitudes negative bays are observed in the X-component and at midlatitudes - positive bays.

To characterize storms, several indices were developed, as the disturbance storm time index (Dst) and as a measure of the substorm intensity AL and AU indexes, and their difference AE - the auroral electrojet index, for example.

McPherron and Chu (2017) have introduced a new index to describe the substorm activity at midlatitudes, the midlatitude positive bay index (MPB). We have worked out a program to calculate the horizontal power of the surface magnetic field, mainly based on the algorithm of McPherron and Chu. To compare our results with the ones, published by McPherron and Chu in Space Science Revue (2017), we have used the same data. We have applied our program for one of the European stations, the Panagjurishte station. European stations were not considered by McPherron.

Data used

In the description of the algorithm McPherron and Chu illustrate the calculation steps by data from the International Real-time Magnetic Observatory Network (Intermagnet) [Data Download (intermagnet.org)] for the American station Honolulu (HON) (21.32°N 158.0°W, 21.65°GMLat, Elevation: 4 meters) Hawai (centered over the substorm day 2/3.03.2.2008). We used the same data, and for comparison – data from the Bulgarian station Panagjurishte (PAG) (42.5°N, 24.2°E, 556 m altitude; ~37° GMLat, ~ 97° GMLon) including the time interval from 08.02 up to 04.03.2017 (centered over the substorm day 20.2.2017). In the original data files, the one-minute mean data for the magnetic field components X, Y, Z and the total field intensity are given in nT related to UT.

The magnetic field data for 25 successive days centred at the day under consideration were processed. This time interval length is sufficient to estimate and remove the main magnetic field and the mean field for quiet solar conditions (McPherron and Chu, 2017). From the daily data time series were constructed, consisting of 36000 one minute sampled data points for every magnetic component. A general view of these series of the magnetic field X-component for the Honolulu and the Panagjurishte stations is given in Fig.1.

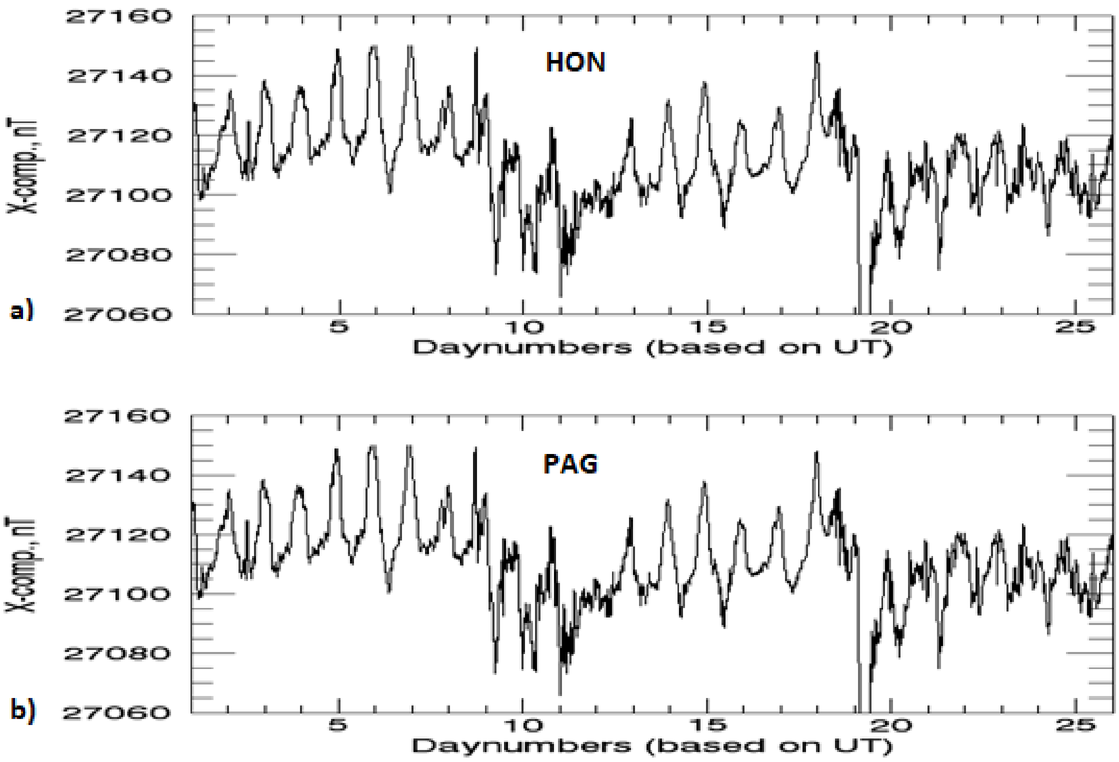

Fig. 1. X-component of the magnetic surface field of 25 sucessive days (20.02 - 15.03.2008 for the Honolulu station and 08.02 - 15.03.2017 for the Panagjurishte station as given in the Intermagnet data base.

The daily solar variations in the Honolulu data are more pronounced in comparison with the variations in the Pangjurishte series. The Panagjurishte data are much noisier and sharp peaks (spikes) are clearly visible. This series is interrupted by data gaps of different length. The longest gap in the considered here time interval is in the day 16 (23.02.2017), shown by a horizontal plateau. The plateau arises by repeating of the last measured value within the gap.

Preprocessing

The preprocessing of the observed magnetic data includes procedures for peak detection, for removal of data gaps and for detection and removal of days with very high magnetic disturbances (called for shortness "disturbed days"). Data gaps and peaks are usually randomly distributed and are not concentrated within an only day. Because the data are given for UT, the time series are converted to local time (LT) by data shift, corresponding to the geographical longitude. In LT it is very easy to determine the midnight points. Around this points the magnetic field is assumed as quiet.

a) Data gaps removal

Data gaps have mostly technical reasons as electrical power outage or required maintenance. If no data was registered, then the value 99999 was written in the original data file. In the gaps the values of an additional series are set to a constant much greater than the magnetic variances and so they are well graphically presentable. The interval borders of the data gapes are then easy to find by means of the first differences. The no data values were replaced by the result of the linear interpolation between the last and first measurements outside of the no data interval. In the special case when no data were measured at the beginning or end of the 25 days series, the no data were replaced by the nearest observations. In the studied here time interval five gaps were identified. One example is shown in Fig.2.

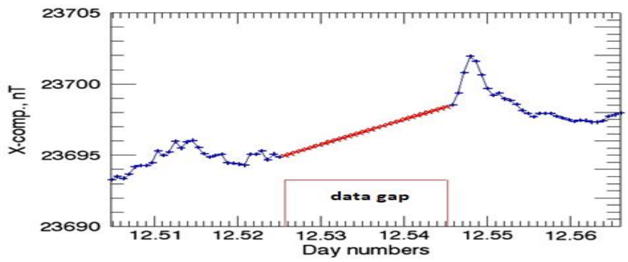

Fig.2. The figure demonstrates the procedure for the gap removal. One gap, observed on the day 13 (20.02.2017) of the time interval is marked by the bar plot. The original data are presented by plusses, connected with/by lines, and the interpolated data are shown by asterisks, connected by a line as well. The sequence of days begins with number one for 08.02.2017.

b) Peak detection and removal

Under a peak here a sudden increase or decrease of the magnetic component intensity was understood. Such type of peaks are often referred spikes. The reason of spikes can be running engines of cars passing through the station periphery. The sudden change can be characterised by the absolute value of the first derivation greater than a given threshold. The peak borders at

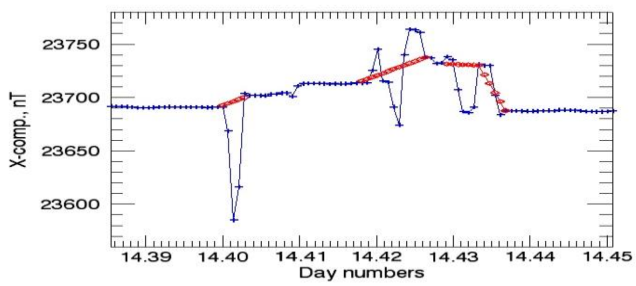

Fig.3. The figure demonstrates how the peak removal is working. The original data are shown by blue plusses connected by a blue line. The interpolated data are drawn by red diamonds, connected also by a red line. In the left side near the day number of 14.40 (22.02.2017) a single peak, detected and removed, is presented. In the right side a sequence of peaks was found and removed by linear interpolation. The sequence of days is the same as in Fig.2.

the peak base were determined by the first undercut of mean standard deviation of the first derivation at left and right of the peak. The values between the peak borders were replaced in the same manner as for the gap removal, by linear interpolation. The peak detection and removal is organized in program loops, where in every loop the peak with the maximal first derivation is removed. The detection stops when the first derivations do not exceed a given threshold. An example of detection and removal of a single peak and of a sequence of peaks is presented in Fig. 3.

Data processing

The calculation of the MPB follows in general the algorithm developed by McPherron and Chu (2017). At first, to eliminate the main magnetic field and the slow changes due to the ring current and partial ring current a base line was constructed by a smoothed spline interpolation through the midnight points (at 24 LT) (see Fig.4). The resulting spline was subtracted from the time series. The remaining series were splitted again in daily sequences but with three additional hours at the beginning and at the end of every day. (For the PAG station data this allows later the easy conversion again to UT). The time segments with the length of 30 hours hereinafter are called extended days.

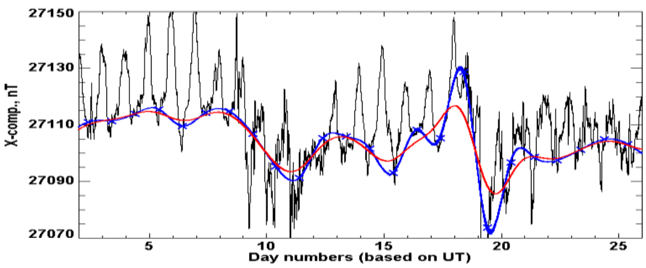

Fig.4. X-component series for 25 days of the HON station, centered on 03 February 2008. The midnight points (24 LT) are marked by blue" x" sign. The computed spline through the midnight points is drawn by a continuous blue line, the smoothed spline by a red line. The result is very close to the one of McPherron. (Compare Fig. 5a in McPherron and Chu.)

After the time series split from the original 25 days (in UT), 23 extended days (in LT) remain. To calculate the mean Solar quiet day variations (Sq), extended days with strong magnetic disturbances have to be removed. A disturbed day can be set by its high standard deviation. The standard deviations are calculated for all 23 extended days. The results are considered as random quantities. By the Lilliefors test (Lilliefors, 1967) was verified, that they are approximately normally distributed. We have determined outliers, meaning disturbed days, applying the Grubbs test, using the one side significance level of 0.12 (Grubbs and Beck, 1972). The procedure is convergent and in average up to two, three or four disturbed extended days were found. These days were excluded in further calculations. From the remaining days Sq is determined by averaging of the daily variations of the field components (superposed epoch analysis) like in the procedure applied in the Chu's algorithm of the MBP calculation (Chu,2015). High frequency variations in Sq were smoothed using running mean. Tests to calculate Sq with the help of Principal component analysis (PCA) as in the McPherron and Chu (2017) computations were also performed. This procedure is much complicated and slower. Much more, the result is very close to the one obtained by a simple averaging and smoothing.

Analogous to the McPherron's method the X and Y components with removed Sq effects were filtered by a high pass filter to suppress the low frequencies longer than three hours and to keep the high frequency changes (see Fig. 5).

The horizontal power of the magnetic perturbations obtained by the sum of the processed squared X and Y magnetic components is shown in Fig. 6.

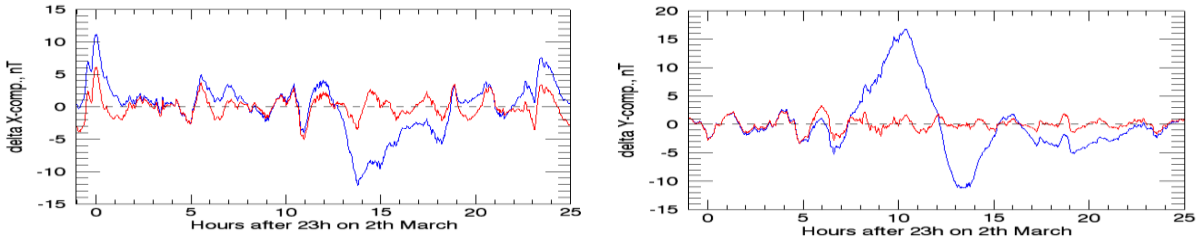

Fig.5 the resulting X (left panel) and Y (right panel) magnetic components for extended day on 2 March 2008 for the Honolulu station are presented. The blue lines represent the Sq removed components and the result after high pass filtering is show as red lines. The time on the x-axis represents the universal time (UT) in hours.

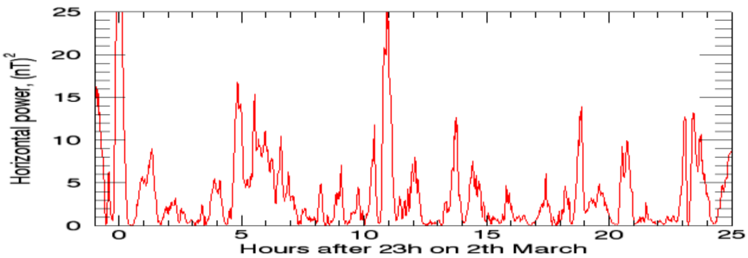

Fig. 6 Obtained horizontal power perturbations in the magnetic field on 2.03.2008 at the Honolulu station. The time is given as station time (LT).

The calculated horizontal power for the HON station for the substorm day 2.03 .2008 has the same structure as the original, published by McPherron and Chu in 2017 (compare with Fig. 10 c in McPherron and Chu (2017), but some power differences are evident.

The algorithm was adopted to calculate the power perturbations also for European stations. One example for the Panagjurishgte station for the substorm day 20.02. 2017 is shown in Fig. 7. Between 16 UT and 19 UT strong perturbations in the X and Y-components (Fig. 7 a) and b)) are observed which are responsible for the strong power perturbations of more than 400nT. A careful analysis is necessary to clarify if the magnetic field perturbations are caused by one or more individual successive and probably overlapping in time substorms. The considered here substorm was studied in more detail in Guineva et al. (2021). The substorm onset was determined to be about 18:40h. This is in very good agreement with the location of the first minimum before the power maximum. The maximum about 18:20 UT rises due to the comparatively high negative values in both X and Y components.

Summary and conclusions

A program to calculate power perturbations in the geomagnetic field was developed based in general on the algorithm of McPherron and Chu with some new elements. In difference to eliminate days with strong disturbed magnetic field components, and gap and peak detection and removal are implemented in the pre-processing procedure. To remove the main field and the magnetic mean Solar quiet day variations, a window of 23 days centered over the considered day is used, but secular variations have not been determined. To obtain the mean field under quiet solar conditions after the subtraction of the main field components low pass filtered superposed epoch means of the components are applied. By the developed program very like structures in the calculated power perturbations for the substorm day 2.03.2008, as the original, published by McPherron and Chu in 2017, are obtained. This demonstrate that the power perturbations determined by the developed program can be reliable.

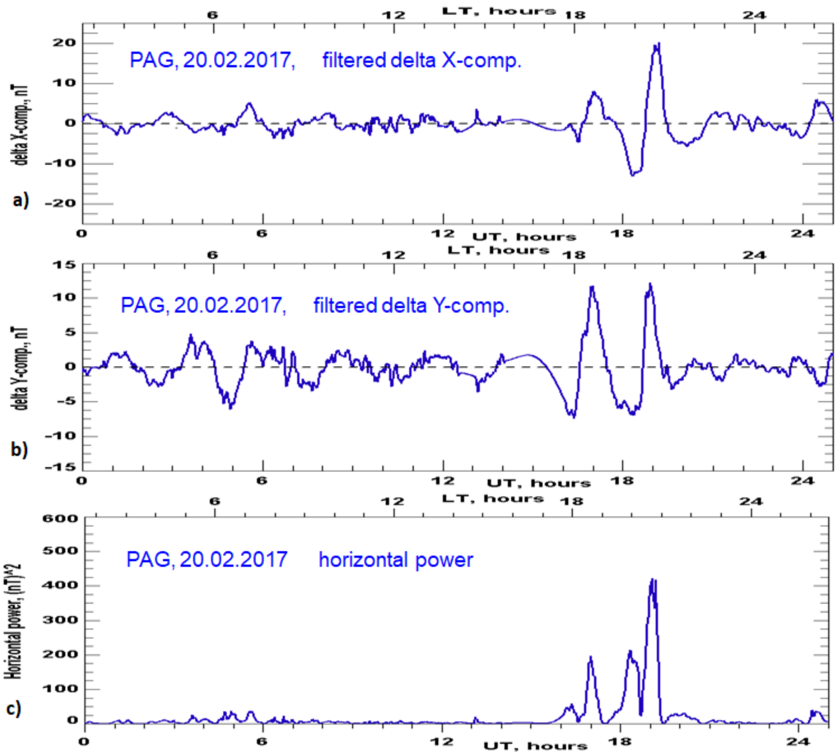

Fig. 7. The obtained results for the substorm day 20.02.2017 for the Panagjurishte station. Between 16 UT and 19 UT strong perturbations in the X and Y-components are observed (Fig. 7 a) and b), which are responsible for the strong power perturbations of more than 400nT

Acknowledgements

The authors are grateful to the creators of the database International Real-time Magnetic Observatory Network (Intermagnet). We thank the experts from Panagjurishte observatory (NIGGG-BAS) for providing data and support for their processing.

This study was supported by the National Science Fund of Bulgaria (NSFB) (project number КП-06-Русия/15) and by the RFBR (project number 20-55-18003Болг_a); the work of I.V. Despirak and A.A. Lubchich was carried out within the framework of the RFBR grant No. 20-55-18003_Bulg_a.

References

Chu X., Configuration and generation of substorm current wedge, Los Angeles: University of California Los Angeles, 2015.

Guineva V., I. Despirak, R. Werner, R. Bojilova, L. Raykova, Mid-latitude effects of “expanded” geomagnetic substorms: a case study, presented at the XII International Conference “Solar-terrestrial relations and physics of earthquakes precursors”, Paratunka, Kamchatsky kray, Russia, September 27 – October 01, 2021, in press

Grubbs F.E., G. Beck, Technometrics, 14, 847-857, 1972.

Lilliefors H.W., Journal of the American Statistical Association, 62, 399-402, 1967.

McPherron, R.L., X. Chu, The midlatitude positive bay and the MPB indexof substorm activity, Space Sci. Rev., 206(1–4), 91–122, 2017.

A New Approach for Forecasting the Main Ionospheric Parameters over Bulgaria

Bojilova R., Mukhtarov P.

National Institute of Geophysics, Geodesy and Geography, Bulgarian Academy of Sciences,
Acad. G. Bonchev St, Bl. 3, 1113 Sofia, Bulgaria
E-mail: rbojilova@geophys.bas.bg

Abstract.

In order to build up a new reliable approach for forecasting the short-term variability of the main ionospheric parameters (foF2 and MUF3000) over Bulgaria the following two conditions have to be fulfilled: (i) a detailed study of the main physical processes defining the observed short-term ionospheric variability over the considered mid-latitude aria, and (ii) the use of an appropriate mathematical apparatus enabling the observed relationships to be described correctly. The results of the regression and correlation analysis of ionospheric characteristics demonstrating how the external factors, as short-term solar anomalies and geomagnetic activity, affect the ionosphere over Bulgaria. The obtained results are used for justifying the functional dependence choice incorporated in the established empirical model for short-term forecast of foF2 and MUF3000 for the territory of our country, taking into account the variations in Kp and F10.7 indices. The proposed model is based on the data from the ionosonde station Sofia for the period of 1995-2014 and is designed to make prediction of the radio wave propagation up to three days ahead if the ionospheric reflection occurs over the territory of Bulgaria. The practical application of this model consists of its ability to predict the basic parameters of a particular radio path at a given distance determined by the user.

Introduction

The ionosphere is an extremely interesting one for scientists because of its scientific and practical significance. Ionization is the process by which neutral atoms break down into negatively charged free electrons and positively charged ions. Ions are the ones that give their name to the ionosphere, but much lighter and freer moving electrons are responsible for HF radio propagation. The A1 method used by the ionosondes allows the measurement of the virtual height of the reflection signal at a given frequency of the emitter. The obtained ionograms provide information about the main parameters of the ionosphere, such as the two values foF2 and MUF3000, which allow determining the operating frequencies of radio communication at a given distance of the radio path from the user. The variations of the Earth's geomagnetic field, are just one manifestation of a complex geophysical phenomenon of cosmic origin. The influence of the solar wind on the Earth's atmosphere is the change in the electron concentration of the ionosphere. These variations, called "ionospheric storms," are essential for long-range radio communications and satellite navigation systems. The study and modeling of the electron density anomalies under the influence of the solar wind are of practical importance for these communications and navigation [*Bojilova and Mukhtarov*, 2020].

This work presents the newest empirical model for forecasting the ionospheric critical frequencies, developed in the section "Physics of the ionosphere" at the National Institute of Geophysics, Geodesy and Geography - Bulgarian Academy of Sciences.

Data

The geomagnetic activity, described by the planetary Kp-index, and solar activity, described by F10.7 is provided from: https://omniweb.gsfc.nasa.gov/. The foF2 and MUF3000 values are derived from the ionosonde station Sofia - SQ143 (42.4°N, 23.2°E) that belongs to the National Institute of Geophysics, Geodesy and Geography, Bulgarian Academy of Sciences for the period of 1995-2014.

In order to create a working empirical model with sufficient accuracy for practice, it is necessary to find the relationships between the predicted quantities and the factors that determine them. For this purpose it is necessary to use correlation analysis, on the basis of which conclusions can be made about the existence of a causal relationship [*Kutiev et al.*,1999*; Muhtarov et al.*, 1998]. If such a connection between the quantities is established, a regression analysis is performed, the results of which can also determine the type of the required dependence between the predicted quantities and the input parameters. The results of the correlation analysis performed by [*Bojilova*, 2019] show that there is a correlation as it is different in different months. It turns out that in general the reaction of the ionosphere from geomagnetic activity is negative except for the months of December and January. The need to separate day and night conditions of the response to critical frequencies is also substantiated. The result of the group regressions is that the relationship between foF2 and the short-term variations in solar activity represented by F10.7 is close to the linear one, but a second-degree polynomial is accepted in the model [*Bojilova and Mukhtarov*, 2020a]. The obtained results of the regression analysis reveal that during the winter months the response is weaker than that in the summer and equinoxes. The dependencies between both ionospheric characteristics and the geomagnetic activity turn out to be substantially nonlinear, requiring a third-degree polynomial approximation [*Bojilova and Mukhtarov*, 2020b].

Model functions

The main dependences of the relative deviation (formally denoted by Φ) of the critical frequencies of the day time, solar and geomagnetic activity can be represented as:

$$\Phi = \Phi_{UT}(UT)\Phi_{sol}(F10.7_{rel})\Phi_g(K_{pi}) \tag{1}$$

Each of the three unknown functions is assumed to be continuous, so it can be represented by the partial sum of its decomposition in order. Obviously, the periodic dependence on the diurnal time is represented by its Fourier decomposition, and the aperiodic dependences on the solar and geomagnetic activity are presented by Taylor decomposition. The study of the functional dependence of the relative deviations from the geomagnetic activity shows that it is expedient to use a third degree polynomial, which means that the partial sum of the Taylor order can be limited to the third degree. The dependence on solar activity turned out to be close to the linear one, but a second degree polynomial will be accepted [*Mukhtarov and Bojilova*, 2017; *Bojilova and Mukhtarov*, 2020b].

Under these assumptions, the three functions take the following form:

$$\begin{aligned}\Phi_{UT} &= a_0 + a_1\cos\left(\frac{2\pi}{24}UT\right) + a_2\sin\left(\frac{2\pi}{24}UT\right) + \\ &\quad a_3\cos\left(\frac{2\pi}{12}UT\right) + a_4\sin\left(\frac{2\pi}{12}UT\right)\end{aligned} \tag{2}$$

$$\Phi_s = b_0 + b_1 F10.7_{rel}(t-t_s) + b_2 F10.7^2_{rel}(t-t_s) \tag{3}$$

$$\begin{aligned}\Phi_g &= c_0 + c_1 K_{piT1}(t) + c_2 K^2_{piT1}(t) + c_3 K^3_{piT1}(t) + \\ &\quad c_4 K_{piT2}(t-t_{g2}) + c_5 K^2_{piT2}(t-t_{g2}) + c_6 K^3_{piT2}(t-t_{g2})\end{aligned} \tag{4}$$

In accordance with the study of the global ionosphere response [*Mukhtarov et al*., 2013], it is assumed that there are two types of ionosphere responses to geomagnetic disturbances with two different time constants denoted by T1 and T2, respectively. Two additional time delays have been introduced. The delay t_s reflect the delay of variations in the electron concentration with variations in solar activity. The delay tg2 reflects the additional delay of the negative reactions of the electron concentration during geomagnetic disturbances, related to the time required to transport the heated air from polar to mid latitudes.

The model is described by a total of 193 constants, which are different for rfoF2 and rMUF3000 and for each calendar month of the year. Separately calculated the constants of the model for day and night conditions. They are determined by the method of least squares, which minimizes the standard deviation of the model values from the data.

Results

In order to demonstrate the results of the created empirical model in the conditions of geomagnetic disturbances, examples from the real-time forecasting simulation of some selected storms at different levels of solar activity as well as for different seasons are presented. For this purpose, each figure shows the course of the index Kp (green), the measured values from Sofia station, marked in red for both critical frequencies (left panel shows foF2, right MUF3000) and model values plotted in blue and for both parameters. For the considered time interval of each individual storm, the respective ME and RMSE errors for the two critical ones are calculated and presented in tables in order to illustrate the comparative analysis between the generated empirical model and the data obtained from the ionospheric station Sofia.

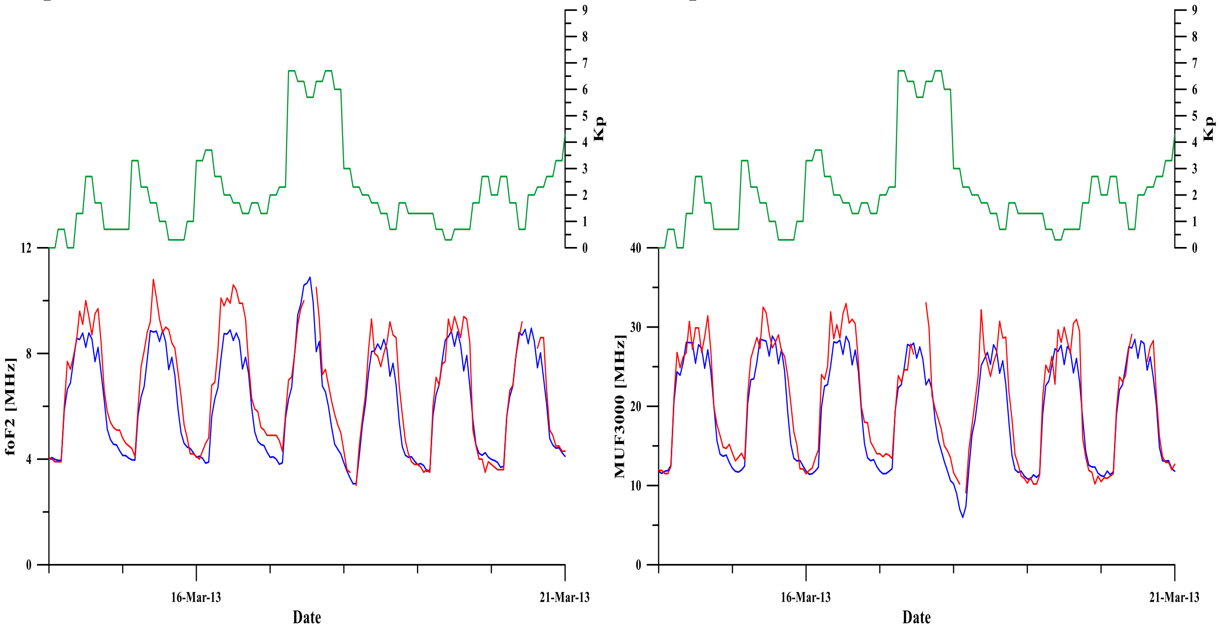

Fig.1. Comparison between the predicted foF2 by the model (left lower panel; line in blue) and MUF3000 (right lower panel; line in blue) with the same quantities received from Sofia station again for foF2 (left lower panel; line in red) and MUF3000 lower right panel; red line) during the geomagnetic storm of 17.03.2013, represented by Kp (upper panel; green line)

Fig. 1 shows an example of a geomagnetic storm in the spring season that occurred on March 17, 2013 with a maximum Kp index of 7. The shown storm has a sudden onset and duration of about one day, the initial phase being at night. The reaction of the critical frequencies (foF2 left lower panel and MUF3000 right lower panel of Fig. 1) is positive in daytime conditions, and the next night on 18.03, after the storm subsides, the response turns negative, which can be seen in the station data (red line) and the values obtained from the model (blue line). Due to the fact that the storm is clearly separated from the previous and next quiet periods, the presence of a positive reaction with a small delay relative to the maximum of Kp and a negative response with a significant delay, again relative to the same index, can be seen.

If we consider only the two disturbed days, March 16 and 17, 2013, foF2 shows that the model very well describes the positive reaction during the day of the storm and the negative one on the night of March 16/17, while with MUF3000 the model underestimated the positive reaction and overestimated the negative one. During the rest of the quiet days, it can be seen that on average both the day and night model values are slightly lower than the measured ones. The mean error (ME) and the root mean square error (RMSE) for the both critical frequencies are presented in the table below:

ME_{foF2}	***- 0.55*** *MHz*	$RMSE_{foF2}$	***0.87*** *MHz*
$ME_{MUF3000}$	***-1.53*** *MHz*	$RMSE_{MUF3000}$	***2.69*** *MHz*

Table 1. The mean error and the root mean square error for both critical frequencies for the period March 14-20, 2013

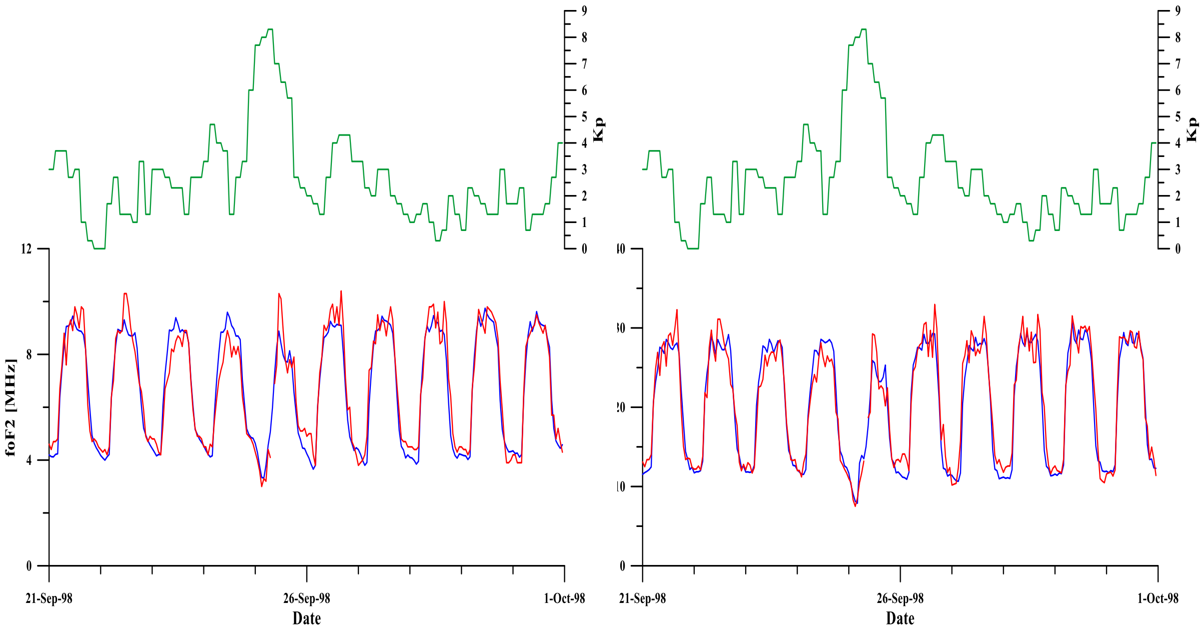

Fig. 2. Comparison between the predicted foF2 by the model (left lower panel; line in blue) and MUF3000 (right lower panel; line in blue) with the same quantities received from Sofia station again for foF2 (left lower panel; line in red) and MUF3000 lower right panel; red line) during the geomagnetic storm on September 24-25, 1998, represented by Kp (upper panel; green line)

Fig. 2 shows a geomagnetic storm with a maximum Kp index of almost 9 and a duration of about one day in the autumnal equinox. The geomagnetic storm has a sudden onset. The increase in Kp values on 25 September (upper left and right panel; green line) was initially accompanied by a weak negative reaction in the critical frequencies of the ionosphere in the early hours of 25 September, followed by a weak positive reaction (more pronounced in foF2; lower left panel; red line) shortly before reaching the maximum of the Kp index. Characteristic of this typically autumn storm is the relatively weak response to critical frequencies. Confirmation of the good similarity between model and data is shown in Table 2, containing the mean and root mean square error for the two critical frequencies for the period 21-30 September 1998. And in this example we have a good match between data and model, with minor average (systematic) errors for both parameters, as well as completely satisfactory for the practical application of the model values of RMSE (Table 2).

ME_{foF2}	***-0.08** MHz*	*$RMSE_{foF2}$*	***0.57** MHz*
$ME_{MUF3000}$	***- 0.26** MHz*	*$RMSE_{MUF3000}$*	***1.90** MHz*

Table 2. The mean error and the root mean square error for both critical frequencies for the period September 21-30, 1998

Fig. 3 shows three examples of storms occurring in typical winter conditions. The time interval shown (from 16 to 25 January) includes two separate storms, studied in detail by [*Bojilova and Mukhtarov*, 2019]. The first storm (January 17-19) has a very smooth onset and a significant duration of more than two days, and the index of geomagnetic activity Kp in this period is between 6 and 8. The second storm (the night hours of 21 to the night of January 22) has a sudden onset and it is brief with a duration of one day, with a maximum value of Kp of about 8 (upper left and right panel; green line). The model did not evaluate the positive responses of the critical frequencies (foF2 left bottom panel; blue line and MUF3000 right bottom panel; blue line) in daytime conditions (from 17 and 18 January), but successfully represented the negative reaction on 19 January (attenuation of storm) at both critical frequencies. In the second storm presented in Fig. 3 (January 21-22) we have a good match of the model data (lower left and right panel; blue line) with the measured ones (lower left and right panel; red line) for both critical frequencies: foF2 (left lower panel) and MUF3000 right bottom panel).

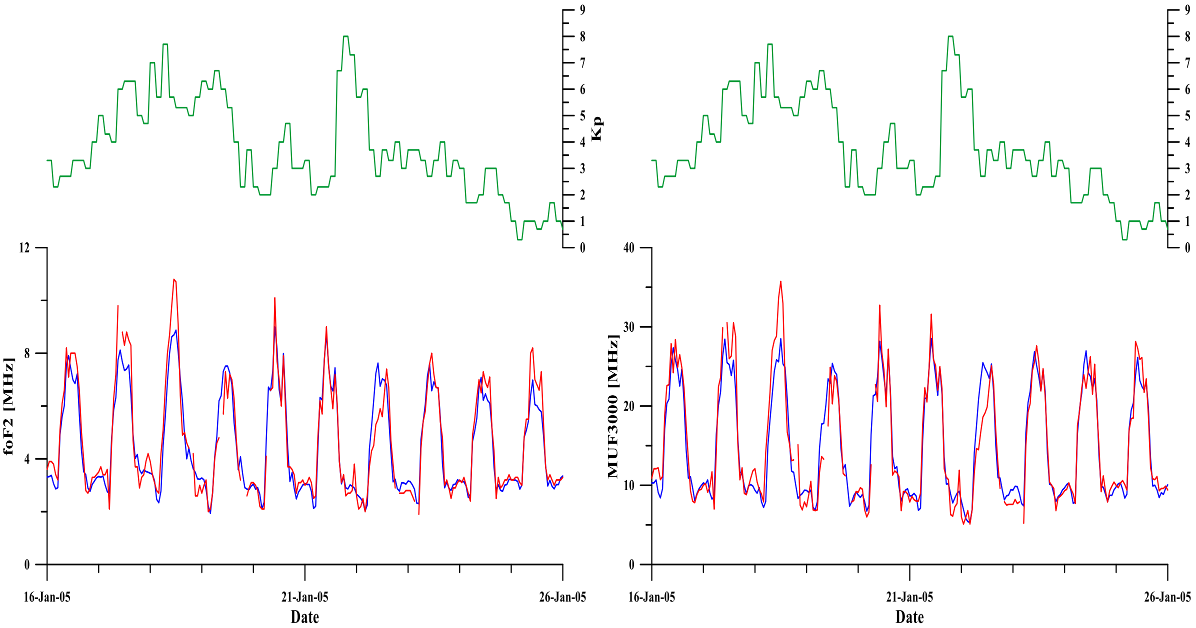

Fig. 3. Analogous to previous figures, but for two geomagnetic events in January 2005.

ME_{foF2}	***-0.12** MHz*	*$RMSE_{foF2}$*	***0.67** MHz*
ME_{MUF300}	***-0.20** MHz*	*$RMSE_{MUF3000}$*	***2.31** MHz*

Table 3. The mean error and the root mean square error for both critical frequencies for the period September 16-25, 2005

Table 3 shows the mean error and the root mean square error, again in order to show whether the model performed well or not and as can be seen the results are sufficiently satisfactory for the purposes of radio forecasting.

Conclusions

The model for short-term prediction of the ionospheric critical frequencies foF2 and MUF3000 presented in this study is designed for automatic and in real-time preparation of forecasts for the propagation of radio waves over Bulgaria to be used in the implementation of radio communication through ionospheric reflection. The model is based on measured values of the critical frequencies for a 15-days period before the current day and on forecasts of solar and geomagnetic activity indices.

Forecasts of solar and geomagnetic activity are available online from Space Weather Prediction Center, National Oceanic and Atmospheric Administration (https://www.swpc.noaa.gov/) [*Gadzhev*, 2020; *Gadzhev et al.*, 2015]. The presented model is developed on the basis of data from vertical sounding of the ionosphere over Bulgaria for the period 1995-2014. The errors obtained in the examples above allow calculating with sufficient accuracy a specific radio path for the territory of Bulgaria [*Bojilova and Mukhtarov*, 2020].

Acknowledgment

This work was partially supported by the Bulgarian Ministry of Education and Science under the National Research Programme “Young scientists and postdoctoral students” approved by DCM № 577 / 17.08.2018 and by project № КП-06-Н44/2 from 27.11.2020.

References

Bojilova, R., & Mukhtarov, P. (2020). LOCAL TIME DEPEDENCE OF THE IONOSPHERIC RESPONSE TO GEOMAGNETIC DISTURBANCES OVER BULGARIA. International Multidisciplinary Scientific GeoConference: SGEM, 20(1.2), 615-622, DOI:10.5593/sgem2020/1.2/s05.078, 2020.

Kutiev, I., Muhtarov, P., Cander, L. R., & Levy, M. F. (1999). Short-term prediction of ionospheric parameters based on auto-correlation analysis. Annals of Geophysics, 42(1), 1999.

Muhtarov, P., Cander, L., Levy, M., & Kutiev, I. (1998, March). Application of the geomagnetically correlated statistical model to short-term forecast of foF2. In 2nd COST 251 Workshop, European Cooperation in the field of Science and Technological Research (COST), Side, Turkey, pp. 30-31, 1998.

Bojilova, R. (2019). Influence of geomagnetic activity on electron concentration of the ionosphere. In 10th Congress of the Balkan Geophysical Society .Vol. 2019, No. 1, pp. 1-5, DOI:10.3997/2214-4609.201902636, 2019.

Bojilova, R., & Mukhtarov, P. (2020)a. Relationship between short-term variations of solar activity and critical frequencies of the ionosphere represented by FoF2 and MUF3000. COMPTES RENDUS DE L ACADEMIE BULGARE DES SCIENCES, 73(10), 1416 – 1424, 2020.

Bojilova, R., & Mukhtarov, P. (2020)b. Relationship between the Critical Frequencies of the Ionosphere over Bulgaria and Geomagnetic Activity. COMPTES RENDUS DE L ACADEMIE BULGARE DES SCIENCES, 73(8), 1113-1122, DOI: 10.7546/CRABS.2020.08.10, 2020.

Mukhtarov, P., & Bojilova, R. (2017). Influence of solar and geomagnetic activity on the ionosphere over Bulgaria. Comptes rendus de l'Académie bulgare des Sciences, 70(9), 1289-1297, 2017.

Mukhtarov, P., Andonov, B., & Pancheva, D. (2013). Global empirical model of TEC response to geomagnetic activity. Journal of Geophysical Research: Space Physics, 118(10), 6666-6685, 2013.

Bojilova, R., & Mukhtarov, P. (2019). Response of the electron density profiles to geomagnetic disturbances in January 2005. Studia Geophysica et Geodaetica, 63(3), 436-454, DOI: 10.1007/s11200-019-0510-6 2019.

Gadzhev, G. (2020). The Seasonal Recurrence of Air Quality Index for the Period 2008–2019 Over the Territory of Sofia City. In International conference on Environmental protection and disaster RISKs (pp. 161-170). Springer, Cham, 2020.

Gadzhev, G., Ganev, K., & Miloshev, N. (2015). Numerical study of the atmospheric composition climate of Bulgaria-Validation of the computer simulation results. International Journal of Environment and Pollution, 57(3-4), 189-201, 2015.

Bojilova, R., & Mukhtarov, P. (2020). Forecasting the Propagation of HF Radio Waves Over Bulgaria. In International conference on Environmental protection and disaster RISKs (pp. 309-324). Springer, Cham, DOI: 10.1007/978-3-030-70190-1_21, 2020.

“Obstanovka” experiment on determining spacecraft surface charging aboard the International Space Station

Kirov B.[1], Georgieva K.[1], Asenovski S.[1], Shepelev, V. [2], Litvinenko, O.[2]

[1] Space Research and Technology Institute, Bulgarian Academy of Sciences, Sofia, Bulgaria
e-mail: bkirov@space.bas.bg
[2] Institute of Radio Astronomy NASU, Ukraine

Abstract

First data from the measurements of the surface charging and potential of the International Space Station (ISS) is presented. The data is a result of the 'Obstanovka' scientific experiment and hardware currently operating aboard ISS since 19 April 2013. The initial results show the ISS surface potential varies in the range ~ (10-25) V.

Introduction

In the last decades the Langmuir probe is one of the classical instruments for plasma diagnostics [1] and among the first space-borne instruments. Langmuir probes have been successfully used aboard a number of rockets and satellites for in situ measurements of thermal plasma parameters in the terrestrial ionosphere [2], at other planets [3] and comets [4-5]– e.g. in satellite mission such as Tiros, Explorer, Alouette, ISIS, DMSP, Atmosphere Explorer, Interkosmos, Dynamics Explorer, Kosmos, Interball, Demeter, Astrid, Freja, Kyushu, CHAMP, CRRES, SCATHA, KOREASAT and many other, including several stratosphere rocket launches of the Vertical series, and planetary exploration missions such as Viking (Mars), Cassini (Saturn), Pioneer Venus (Venus), VEGA (Venus and the Comet Halley), etc.

The objective of this work is to describe the plasma wave complex (PWC) “Obstanovka” (“Situation”) experiment carried out aboard the International Space Station (ISS) and, in particular, the operation and the results from the Langmure Probe (LP) device designed to characterize the surface charging and potential of ISS. The hardware was brought in operation aboard ISS on April 19, 2013, after 6 hours of extra vehicular activity (EVA) of a team of the ISS crew.

The ISS surface charging characterization

The specific research goals of 'Obstanovka' were defined as follows:

-Study the plasma wave processes established in the outer environment of ISS in result of its interaction with the ionosphere;

-Determination of the sources for disturbance of the plasma flux and the electromagnetic field around ISS;

-Geophysics study pf the plasma wave processes related to the solar- Earth megnetosphere-ionosphere-atmosphere and litosphere interactions;

-Ecology control of the low frequency anthropogenic electromagnetic radiation [2];

-Study of the disturbances in the surrounding ISS plasma and electromagnetic field in result of the activity of the electron and ion gun aboard ISS, and the mechanism of propagation of artificial electromagnetic waves;

- Study of the space weather environment in the equatorial and mid-Earth altitudes and in the sub-aurorial ionosphere.

Theory

In general, any conductive body placed in plasma environment can be used as an LP. One needs to apply potential across the LP and measure the probe current. The achieved specific IV is used to determine the plasma parameters.

In it, section (1) represents the ion saturation regime, in which the probe current is entirely due to plasma charging due to ions (all electrons are repelled by the probe negative potential). In regime (2), the less negative probe potential allows the most energetic electrons to overcome the probe potential barrier and to generate exponentially increasing electron current, in addition to the background ion current. In region (3), the probe positive potential (relative to the plasma) accelerates the electrons and repels the ions, thus the probe current is entirely made of electrons.

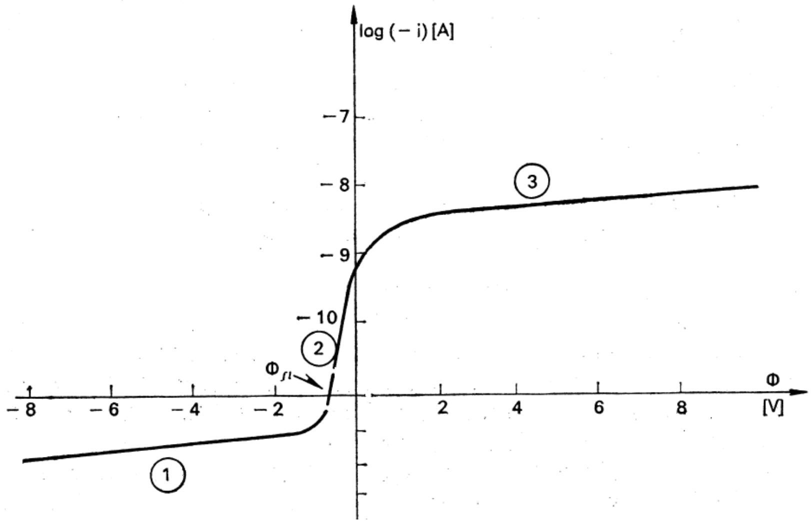

a) Fig.1. Typical IV of a Langmuir probe at Te = 20000 K, Ni=Ne=108 m-3, Mi=16 a.m.u.

The LP current in region (1) is described by Equation 1, where I_i is the net ion current from the different ion species (1-j), φ is the potential applied to the probe with respect to the plasma, *a* and *b* are physical coefficients:

$$I_i = \sum_{j=1}^{n} (\alpha_j \varphi + b_j)^{\frac{1}{2}} \tag{1}$$

Typically, the space environment plasma prevails of two types of ions, and the concentration of the other ion types can be neglected since it is at least an order of magnitude lower. In this case, n=2 and a good approximation of (1) is expressed as:

$$\mathrm{I_i} = (\alpha\varphi + b)^{\frac{1}{2}} \tag{2}$$

Using Eq.2, and the experimental IV data, one could extract the coefficients ***a*** and ***b***. Knowing the two, one could identify the plasma total ion concentration Ni and the effective ion mass Mi:

$$N_i = \frac{\pi}{Aew}\sqrt{\frac{2be - akT}{2e}} \tag{3}$$

$$M_i = \frac{2be - akT}{2e} \tag{4}$$

From region (2) of the IV, one could determine the electron temperature $T_e = \frac{e}{k}\left(\frac{d\ln I_e}{d \quad U}\right)^{-1}$ [6]. In the above equations, I_i is ion current, A is the probe area, N_j, q_j, T_j, m_j are the concentraton, the charge, the temperature and the mass of the j-th type of ions in the plasma; *w* is the plasma velocity, φ is the probe potential, *e*- the electron charge, and *k*- *the Boltzmann's* constant.

Nevertheless, despite the challenges posed by various factors and uncertainties, it is important to note that most processes exhibit a high degree of nonlinearity [7-10], making their behavior difficult to predict and analyze using traditional linear models.

"Obstanovka" Hardware

The PWC hardware of 'Obstanovka' consists of several modules, combined in three blocks. Two of them are placed in open space location outside of ISS and the third block (BSTM) is located inside the station. The following physical parameters are being measured by the system: - electron and ion temperatures Te and Ti; electron and ion concentrations Ne, Ni; DC and AC electrostatic and magnetic fields and currents; plasma and ISS potentials; electron spectra in the range 0.01-10keV; spectra of the VLF electromagnetic waves. To study the plasma discharge effects in space, PWC includes as well a separate discharge generator.

There are two cylindrical LP probe setups (LP-1,2), see Figure 2.

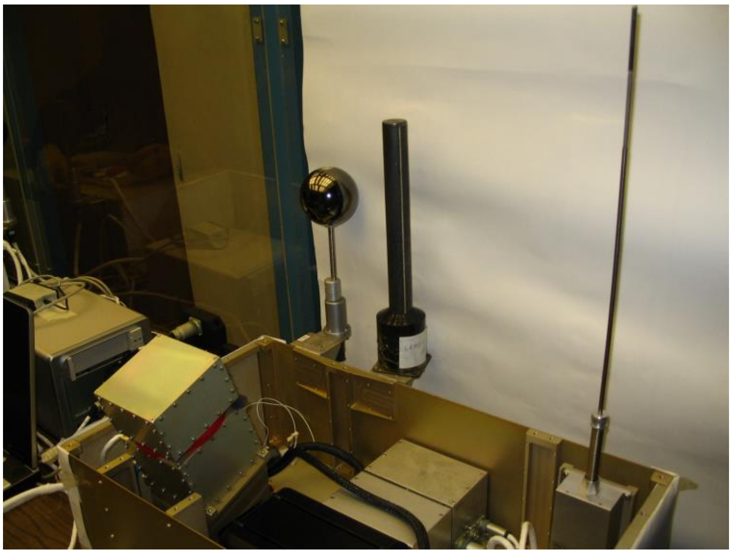

b) Figure 2: View of one of the the cylindrical LP modules

LP1 and LP2 are used to characterize

- the thermal plasma parameters in two locations outside ISS;
- plasma electron temperature Te in the range 1000-6000 Kelvin;
- electron and ion concentration Ne, Ni in the range 1.109 – 1.1013 m^{-3};
- the ISS potential Up, (referenced to the surrounding plasma, in the range ±100 V;
- fast fluctuations in the plasma concentration.

Figure 3 Further Illustrates the position of the PWC on the body of ISS and the location of LP1 and LP2 in a cross-section.

The complete hardware setup of PWC "Obstanovka" is shown in Table 1. Several research teams from the UK, Poland, Russia, Ukraine, Hungary, Sweden and Bulgaria partnered in the full PWC implementation.

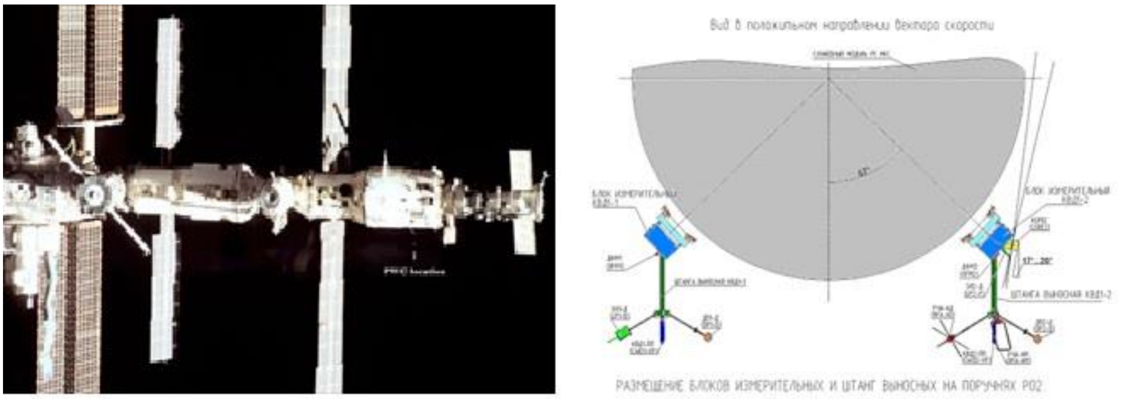

a) b)

Fig. 3 (a) location of the PWC modules placed on the outer surface of ISS; (b) cross section of the position of LP1 and LP2 on the body of ISS, in the direction of the positive ISS speed vector.

Table 1: Full hardware module list of the PWC setup

Device	Research Organization
C	LC ISR
Magnetometer – DFM-1	IKI
Magnetometer – DFM-2	LC ISR
,	SRTI-BAS
D	SRTI-BAS
Plasma discharge simulator – SPP	SKB
eV – 10KeV) CORES	Sussex University
Radio frequency Analyzer – RFA (Scorpion)	SISP; SRC
Signal Analyser – SAS3	SRG, BLE
D A	KFKI RMKI; Sheffield University
Telemetry information storage module – BSTM (inside ISS)	KFKI RMKI; Sheffield University
Ground segment equipment – GSE	KFKI RMKI; SRC

Results and discussion

The system generates a lot of real-time data, which is being stored on a hard drive aboard ISS, and which is to be send back to Earth when the ISS crew completes its mission. Only limited amount of data is sent through the regular ISS telemetry channels.

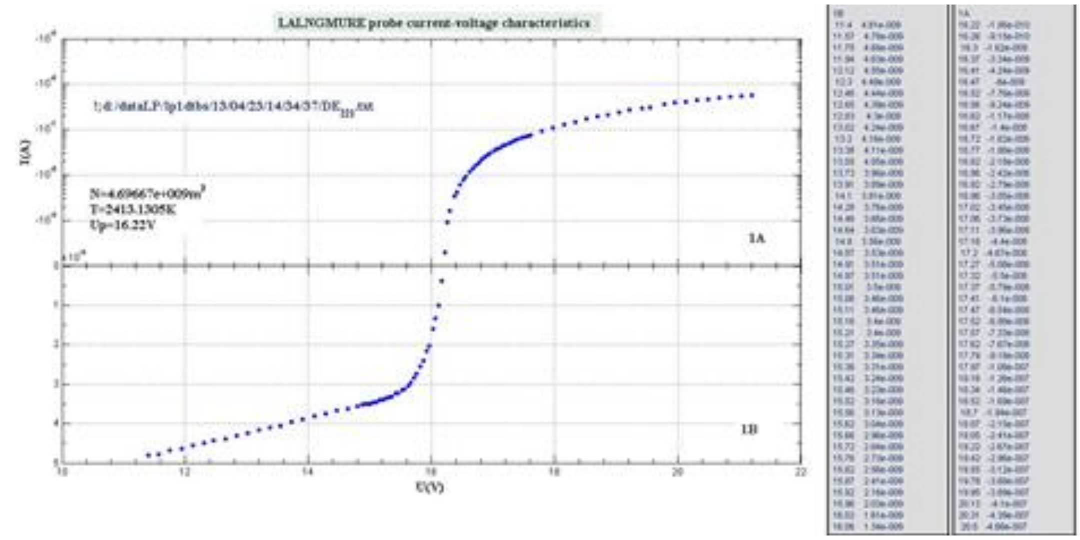

Fig. 4 Experimental IV of the Langmuir probe providing data to characterize the plasma surrounding ISS

Figure 4 shows typical Volt-Ampere curves from one of the Langmuir probes placed in the plasma surrounding the ISS. From the plot, the following preliminary plasma parameters are identified: plasma electron concentration N=4.69667 10-9 [m-3], the electron temperature T=2413.1305 K, ISS surface potential Up=16.22V. Figure 5 Further shows the evolution of the extracted plasma parameters in a typical 20 minutes' measurement session. An interesting observation is that the ISS surface potential Up never drops below 10V. This is not quite yet understood and needs further investigation. It is further needed to study and understand the mechanism of charging large spacecraft such as the ISS.

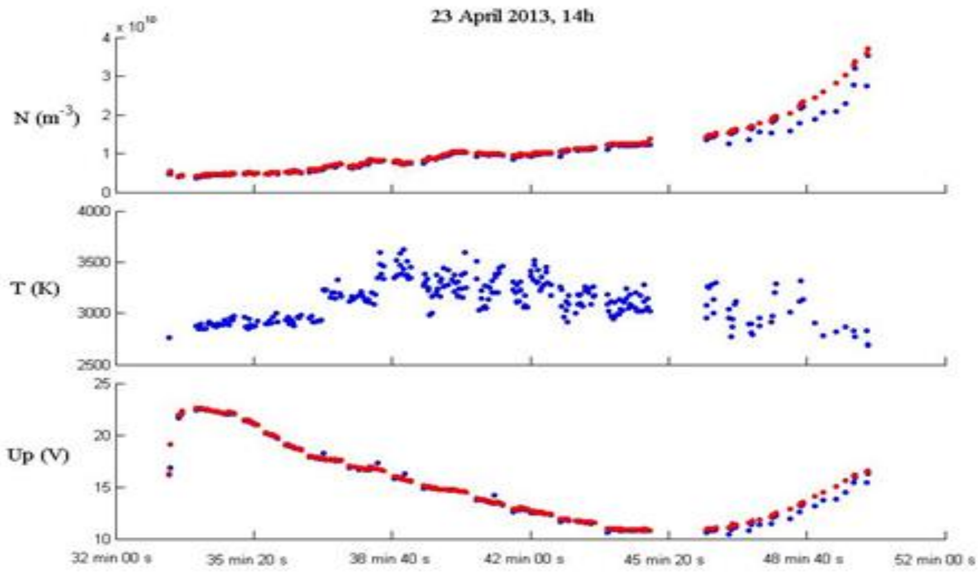

Fig. 5 Evolution of the extracted plasma parameters in time

Conclusions

First results from the ongoing "Obstanovka" ("Situation") experiment aboard the ISS are presented. The Plasma Wave Complex is shown to be fully operational and providing scientific data about the parameters of the plasma surrounding the ISS in flight. The specially developed Langmuir probes allow to extract the charging and the potential of the ISS surface (relative to the surrounding plasma). Further understanding of the charging mechanism of large spacecraft such as ISS is needed.

Acknowledgment

This work effort is partially supported by the Air Force Office of Scientific Research, Air Force Material Command, USAF under grant number FA8655-08-1-3006 and the Bulgarian National Science Fund, under grant number КП-06-Н44/2.

References

[1] Mott-Smith H.M., Langmuir I. The Theory of Collectors in Gaseous Discharges. Phys. Rev., 28, 727, 1926.
[2] Klimov S.I., Agafonov Yu.N., Skalsky A.A., Rodin V.G. The electromagnetic clean sub-satellite SPELIS for studies on plasma-wave phenomena caused by operations of the electrodynamics tethered systems (EDTS) in space plasmas. Proceedings of the Fourth International Conference on Tethers in Space. Smithsonian Institution, Washington, D.C., 10-14 April, p.1643-1652, 1995.
[3] Bogges R.L., Brace L.H., Spencer N.W. Langmuir probe measurements in the ionosphere. J. Geophys. Res., 64, 1627, 1959.
[4] Krehbiel J.P Brace L.H., Theis R.F., et al. Pioneer Venus Orbiter Electron Temperature Probe. J. Geophys. Res. GE-18, 1980, 49-54
[5] Grard R., Laakso H., Pedersen A., Trotignon J.G., Mikhailov Y. Observations of the plasma environment of Comet Halley during the VEGA flybys Annales Geophysicae 7, 1989, 141-149.
[6] Brace L.H. Langmuir Probe Measurements in the Ionosphere. In: Pfaff, R.F., Borovsky, J.E., Young, D.T. (Eds.), Measurement Techniques in Space Plasmas -- Particles: Geophysical Monograph 102. AGU, Washington, DC USA, pp. 23-35, 1998.
[7] Damgov V., Trenchev P. Phenomenon of "Quantized" Oscillation Excitation. In: Abdullaev, F., Bang, O., Sørensen, M.P. (eds) Nonlinearity and Disorder: Theory and Applications. NATO Science Series, Springer, Dordrecht, 2001, v.45, pp. 397-409, ISBN: 978-1-4020-0192-5, DOI:doi.org/10.1007/978-94-010-0542-5_33
[8] Damgov V., Trenchev P. Class of kick-excited self-adaptive dynamical systems: Quantized oscillation excitations. Chaos, Solitons and Fractals, 2003, 17, 1, pp. 11-40, ISSN: 0960-0779, DOI: https://doi.org/10.1016/S0960-0779(02)00445-9
[9] Damgov V., Trenchev P., Sheiretsky K. "Oscillator-wave" model: properties and heuristic instances. Chaos, Solitons and Fractals, 2003, 17, 1, pp. 41-60 ISSN: 0960-0779, DOI: https://doi.org/10.1016/S0960-0779(02)00446-0, 41-60
[10] Damgov, V., Trenchev, P. "Oscillator-Wave" Model: Multiple Attractors and Strong Stability. In: Abdullaev, F.K., Konotop, V.V. (eds) Nonlinear Waves: Classical and Quantum Aspects. NATO Science Series II: Mathematics, Physics and Chemistry, Springer, Dordrecht, 2004, v. 153, pp. 163 – 171, ISBN: 978-1-4020-2190-9, DOI: https://doi.org/10.1007/1-4020-2190-9_15

Prediction and Measurement of the Space Radiation Altitudinal Profile during the Flight of the Virgin Galactic SpaceShipTwo

Dachev T.[1], Dimitrov P.[1], Tomov B.[1], Matviichuk Y.[1], Semkova J.[1], Koleva R.[1], Jordanova M.[1], Bankov N.[1], Mitev M.[1], Carlucci P.[2], Cairo F.[2], Kostadinov I.[3] Paciucci L.[4]

[1]Space Research and Technology Institute BAS, Sofia, Bulgaria, E-mail: tdachev@bas.bg

[2]National Research Council of Italy, Institute of Atmospheric Sciences and Climate (CNR-ISAC), Rome, Italy, E-mail: francesco.cairo@artov.isac.cnr.it

[3]Proambiente CNR Technopole, Bologna Italy, E-mail: i.kostadinov@isac.cnr.it

[4]National Research Council of Italy, Engineering, ICT and Technologies for Energy and Transportation Department (CNR-DIITET), Rome, Italy E-mail: lucia.paciucci@cnr.it

Abstract

The paper presents the design of the Portable Dosimeter-Spectrometer (PDS) Liulin-CNR-VG, which is expected to measure the space radiation altitudinal profile during the flight of the Virgin Galactic SpaceShipTwo in the fall of 2021 (https://www.space.com/virgin-galactic-announces-unity-23-spaceflight-crew). The PDS size is 66x56x26 mm and weighs 0.092 kg. The PDS should measure the following parameters: the flux of the charged particles in the range from 0.1 to 20,000 particles per square centimeter in 1 second; the absorbed dose in the range from 0.3 nGy to 1.56 mGy; the dose rate in the range from 0.04 µGy/hour to 0.18 Gy/hour. The altitude profile during the flight of Virgin Galactic SpaceShipTwo up to the 37.2 km altitude is expected to be similar to the profile measured with no shielded Liulin battery operated unit during the June 8, 2005 certification flight of the NASA Deep Space Test Bed balloon flight at Ft. Sumner, New Mexico, USA. During the ascending part of the flight, up to 13.7 km, the dose rate will rise from 0.058-µGy/hour up to 2.4 µGy/hour. The Pfotzer maximum is not expected to be well observed in the ascending part of the SpaceShipTwo flight. Above the maximum, at about 110 km altitude, the dose will fall down to 0.7 µGy/hour. During the re-entry, the SpaceShipTwo will observe the Pfotzer maximum of an expected dose rate of 3.4 µGy/hour. In the glide to land part of the flight, the dose rate will decrease back to 0.058-µGy/hour. The predicted values for the hourly dose rate of 1.83 µSv/hour and accumulated dose of 2.5 µSv reveals that there is no any radiation risk for the crew and astronauts flying at the VG SpaceShipTwo.

Introduction

The era of suborbital touristic flights up to 100-110 km altitude is already open by the missions of Virgin Galactic first crewed spaceflights on 11 July and Blue Origin on July 20 2021. It is rather difficult to say exactly where the atmosphere ends and space starts. A widely accepted definition uses what is called the Karman line (*https://astronomy.com/news/2021/03/the-krmn-line-where-does-space-begin*), which is at 100 km above the sea level as the boundary for space. According to NASA and the U.S. military, space starts at 80 km above the sea level. Richard Branson and his crew in the Virgin Space Ship Unity flew to an altitude of 86 km, whereas Jeff Bezos and other passengers in Blue Origin flew up to 107 km.

Liulin-CNR-VG is part of a Bulgarian - Italian research project "Portable Dosimeter-Spectrometer Liulin-CNR-VG". The project partners are Space Research and Technology Institute of the Bulgarian Academy of Sciences (SRTI-BAS) and the National Research Council of Italy, Department of Engineering, ICT and Technologies for Energy and Transport.

The design of the portable dosimeter-spectrometer Liulin-CNR-VG is not a new one. Since 1989, SRTI-BAS, in international cooperation with scientists from Russia, Germany, Japan, Czech Republic, Italy, Norway, USA and India flew in space with seventeen similar devices [*Dachev et al.*, 2015, 2017, 2020].

The ionizing radiation data obtained by the Liulin type instruments are part of the "Unified web-based database with Liulin-type instruments", available online, free of charge at the following URL: http://esa-pro.space.bas.bg/database. The instrument data are stored along with the orbital parameters of the satellites. The User Manual of the database is available online at http://esa-pro.space.bas.bg/manual. In the future, all parameters obtained with the Liulin-CNR-VG instrument will be added to the database.

Payload Technical Description

The external view of the portable dosimeter-spectrometer (PDS) is presented on Fig. 1. It is situated in an Extruded Aluminum Enclosure with a size 66x56x26 mm. The weight of the PDS is 0.092 kg.

The Portable dosimeter-spectrometer Liulin-CNR-VG measures the following parameters: the flux of the charged particles with an ionizing capacity above 1 MeV/mm in silicon, with a sensitive area of 2 cm^2, an energy resolution of 100 keV in the range from 0.1 to 20000 particles or quanta per square cm per sec.; absorbed dose in the range from 0.3 nGy to 1.56 mGy; dose rate in the range from 0.04 µGy/hour to 0.18 Gy/hour; energy deposited in the detector from 0.08 to 20.3 MeV. The measurement error is no more than ± 20%.

Fig. 1.

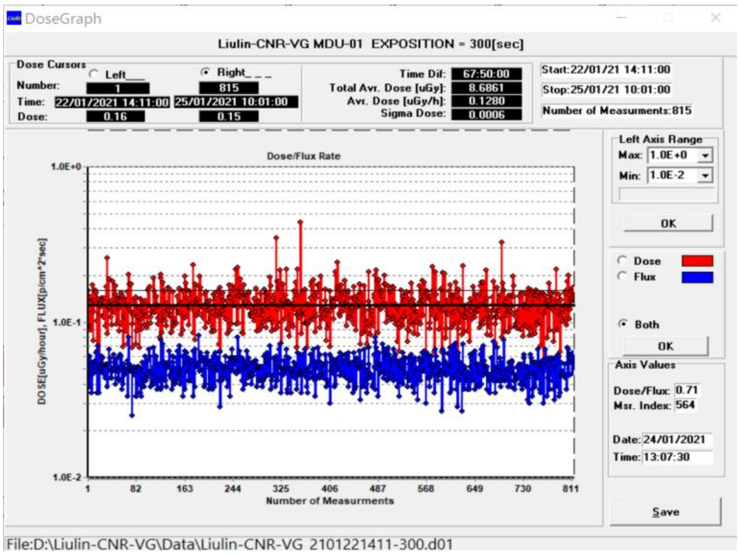

Fig. 2.

Fig. 1. External view of the portable dosimeter-spectrometer; Fig. 2. Example of the long-term measurements of the natural background radiation with Liulin-CNR-VG PDS.

Below the upper panel of the PDS are mounted the ON/OFF switch, the red status LED and the USB mini female connector. Below the panel are situated the two rechargeable cylindrical AAA size Lithium Ion cells 10440 of Portable Power Corp.

Under the 0.5 mm thick bottom panel of the PDS is situated the 2 cm^2 Hamamatsu PIN diode detector. In addition, there is a technological shielding of 0.07-mm copper and 0.2-mm plastic material. They all provide a total shielding of 0.25 g cm^{-2}. The calculated required kinetic energies of normally falling particles to the detector are 0.67 and 12.5 MeV for electrons and protons, respectively (https://www.nist.gov/pml/stopping-power-range-tables-electrons-protons-and-helium-ions). This indicates that only protons and electrons with energies higher than the values listed above can cross the PDS shielding materials and reach the surface of the detector.

The Liulin-CNR-VG PDS is a Liulin type deposited energy spectrometer (DES) [*Dachev et al.*, 2015]. It uses one silicon detector to measure the deposited energy and the number of particles or quanta that allows calculating the dose rate and the flux.

The spectrometer-dosimeter contains one silicon-PIN diode of Hamamatsu S2744-08 (2 square cm area and 0.3 mm thickness), 1 ultra-low noise charge-sensitive preamplifier of AMPTEK A225F, 2 microcontrollers and 64 MB flash memory. After passing a charge-sensitive preamplifier, the signal is digitized by a 12-bit fast analog to digital (A/D) converter. The doses (deposited energies) are determined by a pulse height analysis technique and then passed to a discriminator.

According to AMPTEK A225F specifications the pulse amplitudes, A[V] are proportional by a factor of 240 mV/MeV to the energy loss in the detector and respectively to the dose. The amplitude of each signal from the income particles and quanta are transformed into digital signals that are sorted into 256 channels by a multichannel analyzer. For every exposure interval, a single 256 channels energy deposition spectrum is collected. The energy channel number 256 accumulates all pulses with amplitudes exceeding the maximal level of the spectrometer of 20.83 MeV.

Liulin-CNR-VG PDS is already constructed and manufactured. It is ready for the flight of the Virgin Galactic SpaceShipTwo. Fig. 2 presents example of the long-term measurements of the natural background radiation with Liulin-CNR-VG PDS. The start of the measurements was on January 22, 2021 at 14:11:00 hour. The end was on January 25, 2021 at 10:01:00. Eight hundred and fifteen measurements of the dose rate (red lines) and flux (blue lines) are presented. The exposition is 300 seconds. It is seen that the total dose for all measurements (67 hours and 50 minutes) is 8.6861 μGy. The average dose rate is 0.1280 μGy/hour. This value is normal for the SRT-BAS laboratory. Similar values were observed in the last 20 years. The sigma of the dose is 0.0006. A high-energy deposition in the 256th channel is registered. It is depicted close to the center of Fig. 2.

Expected Dose Rates during the Flight of Virgin Galactic SpaceShipTwo

Goals of the study

The following objectives of the study are foreseen: Assessment of the human exposure to radiation into the cabin of SpaceShipTwo; Data collection for space weather modelling; Scientific publications; Optimization and proposal for new on-board equipment, useful for human exposure monitoring and standardization of the procedures to guarantee high safety levels. Project partners consider using Liulin-CNR-VG PDS in other experiments.

Expected flight times and altitudes

The following approximate flight times and altitudes can be expected during a typical flight of SpaceShipTwo: The two mated vehicles climb to an altitude of approximately 45,000 feet (13.7) km for 60 minutes; Boost: ~60 seconds up to 110 km; Coast (microgravity) at 110 km: 3 minutes; Re-entry: ~2-3 minutes back to 15.24 km; Glide to Land: ~15 minutes.

Altitude profile of the galactic cosmic radiation

Dachev in 2013 studied experimentally the altitude profile of the galactic cosmic radiation, which is the main, always-existing component of the radiation environment between the ground and the Moon orbit. Fig. 3 visualizes this profile. The altitude profile during the flight of SpaceShipTwo is expected to be similar in the range from ground up to 110 km altitude.

Overview of the radiation profiles data, obtained during three balloon flights

There are three experiments on balloons with participation of battery operated Liulin type instruments:

The first balloon flight, with one Liulin battery operated mobile dosimetry unit (MDU) [*Spurny et al.*, 2000], was launched from Gap-Tallard aerodrome, France (44.46°N, 6.03°E) during a technological flight of CNES balloon program at 07:58 UTC on 14 June 2000. The effective cutoff rigidity at the coordinates of the Gap-Tallard aerodrome at 29 km altitude was calculated by SPENVIS, Magnetocosmics model (http://www.spenvis.oma.be/) and was found to be equal to 5.18 GV. The measured maximal dose rate was 2.74-μGy/hour. The conditions are solar activity maximum. The Pfotzer maximum [*Regener, E. & G. Pfotzer*, 1935] was found at about 18.5 km altitude.

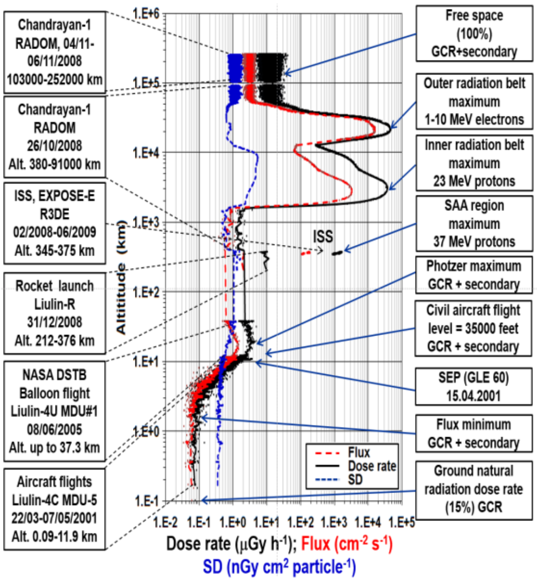

Fig. 3.

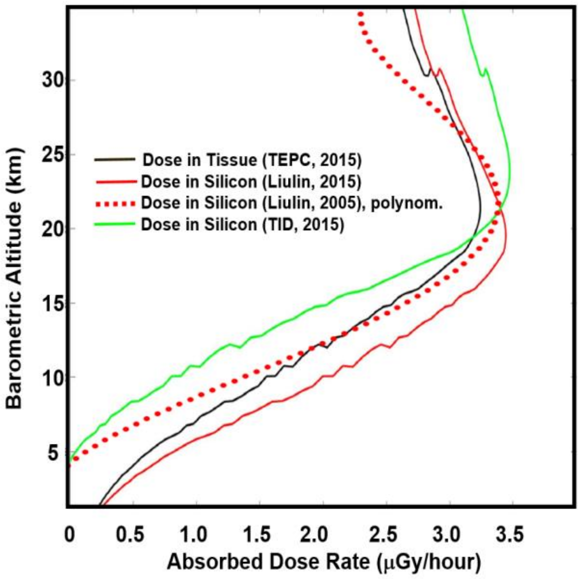

Fig. 4.

Fig. 3. Variations of the absorbed dose rate, flux and specific dose for the altitudinal range from 0.1 to 250,000 km.

Fig. 4. Altitude profiles of the absorbed dose rates measured in tissue (TEPC) and in silicon (Liulin and TID) during the ascent phase of the RaD-X balloon flight using the Fourier transform filtering: TEPC (black line), Liulin (red line), and TID (green line).The dashed red line presents the profile, obtained with the non-shielded Liulin MDU during the second balloon flight in June 2005.

The second balloon flight, with three MDUs, was performed during the June 8, 2005 certification flight of the NASA Deep Space Test Bed (DSTB) balloon at Ft. Sumner 104.24°W, 34.47°N, New Mexico, USA with an effective cutoff rigidity Rc=4.08 GV [*Benton*, 2005]; [*Adams et al.*, 2007]. Data in Fig. 4 present the altitude profile between 12.5 and 37 km altitude obtained from the no shielded MDU. One of the other three MDUs was below 5 g/cm^2 shielding. The last one was below a carousel with a variable shielding. The measured maximal dose rate in the Pfotzer maximum, with the no shielded Liulin, was 3.5-μGy h^{-1}. The other 2 devices showed a bit higher dose rates and accumulated doses because of the higher amount of secondary particles generated in the shielding.

The coordinates of the VG Spaceport America are 106.95W 32.98°N. As SpaceShipTwo will take off and land after almost a vertical flight up to 110 km, the difference in the coordinates between the Spaceport America and Ft. Sumner of 2-3 degrees is neglectable for the space radiation profile. That is why we may consider that the data obtained during this balloon flight are relevant to be extrapolated to the expected radiation profile up to ~37.2 km (122,000 feet) altitude.

The predicted F10.7 radio flux value in the fall of 2021 and the first half of 2022, when the flight is expected, is between 77 and 89 s.f.u. These values are close to the F10.7 radio flux value during the balloon flight in June 2005 of 94 s.f.u. This is another reason to consider 2005 data relevant to the expected measurements in 2021-2022.

The third balloon flight was the NASA high-altitude RaD-X mission [*Mertens et al*, 2016]. It was performed again from Ft. Sumner on 25 of September 2015. Four radiation dosimeters were on the board of RaD-X: a Far West HAWK tissue equivalent proportional counter (TEPC version 3) (https://www.fwt.com/detector/fw-ad1ds.htm), a Teledyne dosimeter (UDOS001), a Liulin dosimeter (MDU 6SA1) and a RaySure dosimeter (version 3b).

Fig. 4 in this paper represents Fig. 10 of [*Mertens et al.* 2016]. Three altitude profiles from the flight in 2015 are depicted. The Liulin-6SA1 profile is with a red line. It is seen that the Liulin-6SA1 profile is very similar to TEPC and TID profiles, which confirms the Liulin instruments quality of measurements. The three profiles from TEPC, TID and Liulin-6SA1 seen in Fig. 4 do have almost linear rise in the range from ground up to 15-16 km altitude.

The polynomial presentation (4th order) (Fig. 4 red dashed line) is used to illustrate Liulin doses obtained during the flight in 2005. As expected, the Liulin profiles in 2005 and 2015 are very similar. The latter again backs up the decision Liulin 2005 data to be used in the predicted dose rate profile during the flight of Virgin Galactic SpaceShipTwo.

Predicted dose rates during the flight of Virgin Galactic SpaceShipTwo in the fall of 2021

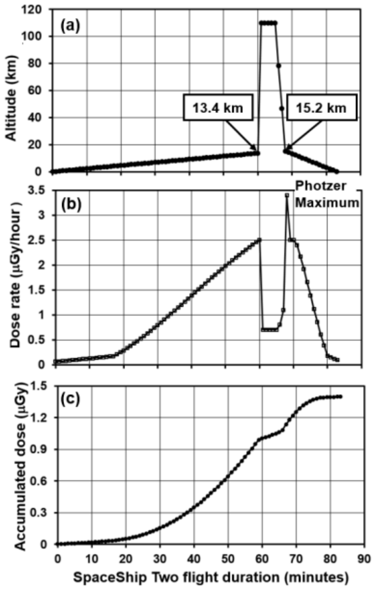

Fig. 5.

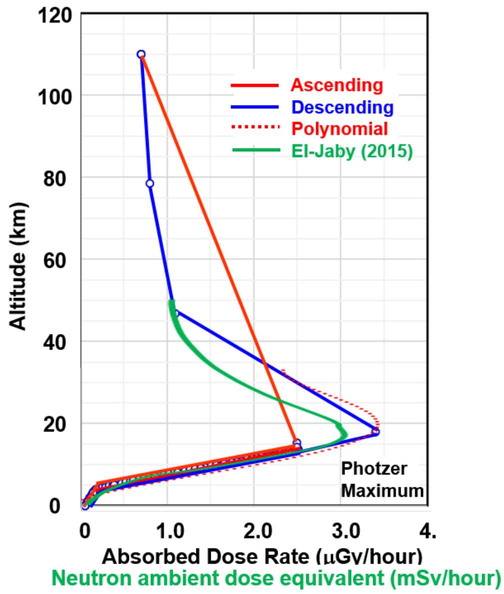

Fig. 6.

Fig. 5. Predictions: Fig. 5a SpaceShipTwo altitude during the flight; Fig. 5b Hourly absorbed dose rates; Fig 5c Accumulated absorbed dose rate.

Fig. 6. Predicted altitudinal profile of the absorbed dose rate during the flight.

Fig. 5a presents the time profile of the altitude of SpaceShipTwo during the flight with 1-minute resolution up to altitude of 110 km. The data shown in section ***Expected flight times and altitudes*** is used. Fig. 5b shows the predicted hourly-absorbed dose rates during the flight. Polynomial data of order of four from the second balloon flight in 2005 (Fig. 4), was used for the altitudes above 3.9 km. Other dose rate profiles were predicted by linear rise equations. The similarity of the data is explained with similarity of the solar activity in 2005 and 2015. Similar moderate solar activity is expected during the VG flights in 2021-2022 (https://www.swpc.noaa.gov/products/solar-cycle-progression).

During the first part of the flight, the dose rate rises from 0.058-µGy/hour up to 2.5 µGy/hour. The Pfotzer maximum with a dose rate of 3.4 µGy/hour is not expected to be seen in the ascending part of the flight because of the very fast crossing through it. Above the maximum, the dose falls down to 0.8 µGy/hour and slowly decreases up to 110 km altitude in a similarity of the [*El-Jaby, and Richardson,* 2015] profile (green line). The dose rate does not change during the 4 minutes of microgravity. It starts to increase during the re-entry, going through the Pfotzer maximum. In the "glide to land" part of the flight, the dose rate decreases back to 0.058-µGy/hour.

Fig. 6 presents the same data with 1-minute time resolution as in Fig. 5b but in dependence of the altitude. The doses during the ascending part of the orbit are presented with red points and line, while the descending part with blue line. The polynomial presentation of the Liulin data in 2005 is shown with red dashed line.

As illustrated in Fig. 5c, the increase of the accumulated dose rate alters in μGy from zero to 1.4 μGy. The equivalent dose during the flight is calculated to be about 2.5 μSv for 82 minutes (1.83 μSv/hour) because the mean quality factor is about 1.8 for a subsonic flight (1.4x1.8=2.5 μSv). Having in mind that a passenger, flying from London to New York at a height of 11 km, will receive for about 7 hours a dose of 32 μSv (4.6 μSv/hour), the equivalent of a panoramic dental X-ray scan https://www.radioactivity.eu.com/site/pages/Radioactivity_in_Flight.htm. The calculated by us accumulated dose of 2.5 μSv is about 13 times less. The predicted values for the hourly dose rate of 1.83 μSv/hour and accumulated dose of 2.5 μSv reveals that there is no any radiation risk for the crew and astronauts flying at the VG SpaceShipTwo.

Conclusions

The paper presents the design of the Portable Dosimeter-Spectrometer Liulin-CNR-VG. The latter will measure the space radiation altitudinal profile during the flight of the Virgin Galactic SpaceShipTwo in the fall of 2021.

It is very important and interesting to obtain the dose rates between 37 and 110 km altitude as this region is rather poorly studied.

The data obtained will be beneficial for the space tourism, the newly developing segment of the aviation industry that seeks to give tourists the ability to become astronauts and experience space travel for leisure or business purposes.

References

Adams, J.H., Adcock, L., Apple, J., Christl, M., Cleveand, W., Cox, M., Dietz, K., Ferguson, C., Fountain, W., Ghita, B., Kuznetsov, E., Milton, M., Myers, J., O'Brien, S., Seaquist, J., Smith, E.A., Smith, G., Warden, L., Watts, J., (2007). Deep space test bed for radiation studies. Nuclear Instruments and Methods in Physics Research Section A: Accelerators, Spectrometers, Detectors and Associated Equipment 579 (21), 522–525 1.

Benton, E., (2005). Deep Space ICCHIBAN: An International Comparison of Space Radiation Dosimeters aboard the NASA Deep Space Test Bed. 10thWorkshop for Radiation Monitoring on ISS, Chiba, Japan, 7-9 September 2005. Available online at: (https://wrmiss.org/workshops/tenth/pdf/08_benton.pdf).

Dachev, T. P., Semkova, J. V., Tomov, B. T., Matviichuk, Y. N., Dimitrov, P. G., Koleva, R. T.,…Kubancak, I. N. (2015). Overview of the Liulin type instruments for space radiation measurement and their scientific results. Life Sciences and Space Research, 4, 92–114. https://doi.org/10.1016/j.lssr.2015.01.005.

Dachev, T.P., Bankov, N.G., Tomov, B.T., Matviichuk, Y.N., Dimitrov, P.G., Häder, D.-P, Horneck, G., (2017). Overview of the ISS radiation environment observed during the ESA EXPOSE-R2 mission in 2014–2016. Space Weather, **15**, 1475–1489. https://doi.org/10.1002/2016SW001580.

Dachev, T.P., Tomov, B.T., Matviichuk, Y.N., Dimitrov, P.G., Semkova, J.V., Koleva, R.T., Jordanova, M.M., Bankov, N.G., Shurshakov, V.A. and Benghin, V.V., (2020). Solar modulation of the GCR flux and dose rate, observed in space between 1991 and 2019. Life Sciences in Space Research, 26, 114-124, 2020. https://doi.org/10.1016/j.lssr.2020.06.002.

Dachev, T.P., (2013). Profile of the ionizing radiation exposure between the Earth surface and free space, Journal of Atmospheric and Solar-Terrestrial Physics, 102, 148–156. http://dx.doi.org/10.1016/j.jastp.2013.05.015.

El-Jaby, S. and Richardson, R.B., (2015). Monte Carlo simulations of the secondary neutron ambient and effective dose equivalent rates from surface to suborbital altitudes and low Earth orbit, Life sciences in space research, 6, pp.1-9.

Mertens, C.J., et al. (2016). Cosmic radiation dose measurements from the RaD-X flight campaign, Space Weather, 14, 874–898.

Regener, E. & Pfotzer G. (1935), Vertical Intensity of Cosmic Rays by Threefold Coincidences in the Stratosphere, Nature 136, 718-719, 1935.

Spurny, F., Dachev T., Tomov B., Matviichuk Yu., Dimitrov Pl., Fujitaka K., Uchihori Y., Kitamura H., (2000). Dosimetry Measurements during a Balloon and Aircraft Flights, Proceedings of 7th STIL-BAS conference, 169-172, Sofia, November, 2000.

Atlantic Multidecadal Oscillation Driven by Solar Harmonics

Chapanov Ya.

Climate, Atmosphere and Water Research Institute, Bulgarian Academy of Sciences
E-mail: yavor.chapanov@gmail.com

Abstract.

The oscillations of climatic parameters of North Atlantic Ocean play important role in various events in North America and Europe. Several climatic indices are associated with these oscillations. The long terms of Atlantic temperature anomalies are presented by Atlantic Multidecadal Oscillation. Its time series is analyzed by means of the Method of Partial Fourier Oscillations. The cycles of AMO in narrow frequency bands are compared with corresponding oscillations of Total Solar Irradiance (TSI). Very good agreement exists between interannual and decadal cycles of AMO and TSI.

Introduction

The aim of this work is to determine influence of solar harmonics on Atlantic Sea Surface Temperature (SST). The Atlantic Multidecadal Oscillation (AMO), also known as Atlantic Multidecadal Variability (AMV), is the variability of the sea surface temperature (SST) of the North Atlantic Ocean on the timescale of several decades. The AMO is correlated to air temperatures and rainfall over much of the Northern Hemisphere, in particular in the summer climate in North America and Europe (Ghosh et al., 2016; Zampieri et al., 2017). Rainfall patterns are affected in North Eastern Brazilian and African Sahel. It is also associated with changes in the frequency of North American droughts and is reflected in the frequency of severe Atlantic hurricane activity (Trenberth et al., 2005). Climate models suggest that a warm phase of the AMO strengthens the summer rainfall over India and Sahel and the North Atlantic tropical cyclone activity (Zhang and Delworth, 2006).

The solar activity affects all Earth system and excites their periodic variations with the essential solar frequencies and their harmonics. Solar irradiance is Earth’s primary energy input. It establishes the thermal and dynamical structure of the terrestrial environment and is the primary external cause of terrestrial variability. The specification of solar irradiance over multiple centuries is requisite input for numerical simulations of climate variability prior to the industrial epoch that provide a baseline against which to evaluate contemporary anthropogenic influences.

One of the main reason of Sea Surface Temperature (SST) variation is the direct influence of TSI on the ocean. The common analyze and comparison of TSI and AMO oscillations in different narrow frequency bands may significantly improve our knowledge of solar-terrestrial influences and contribute to more precise climatic models and forecasts.

Data and Methods

a) AMO and TSI time series

Wang et al. (2017) reconstructed Summer (during May to September) Atlantic Multidecadal Variability (AMV) time series by applying the principal component regression method to 46 annually-resolved terrestrial proxy records from the North Atlantic region (Fig.1). The internal variability component of Atlantic Multidecadal Variability (i.e., Atlantic Multidecadal Oscillation; AMO) was estimated by empirically removing externally-forced variations at multidecadal (> 30 years) timescales. Data are reported as sea surface temperature anomalies with respect to 1856-1973. Fig.1 demonstrates map of data sources of AMO variations for the last 1200 years, according (Wang et al., 2017). The reconstructed time series of AMO variations are shown in Fig. 2. Lean (2018) creates TSI time series for the period 850-2010 (Fig. 2).

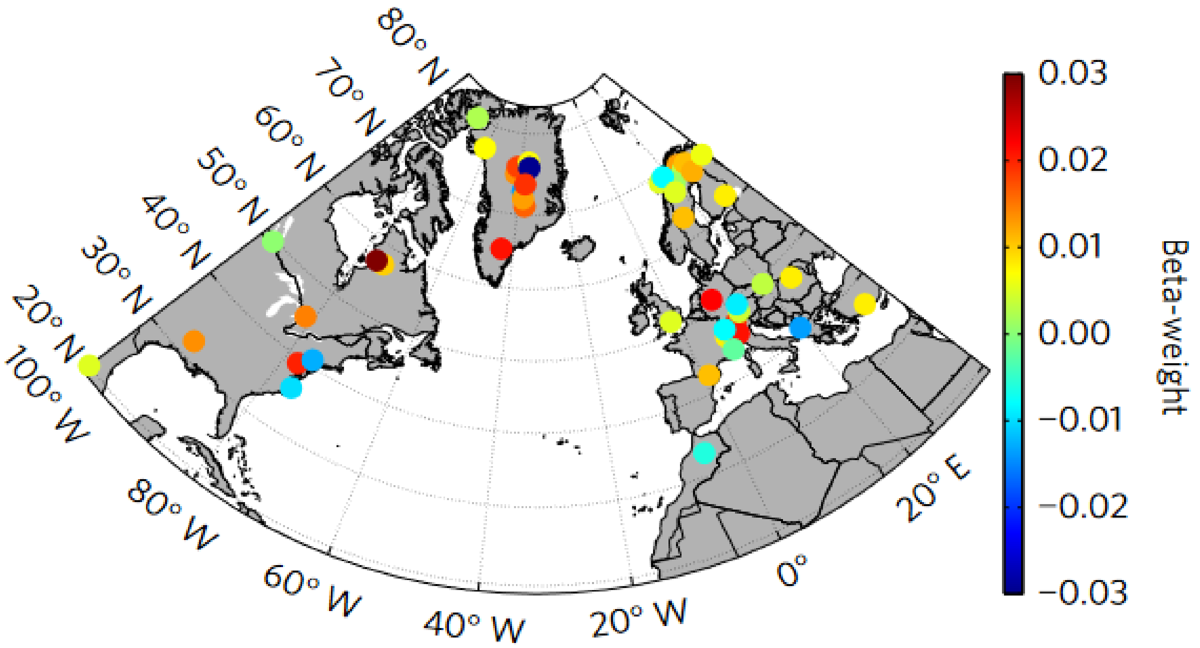

Fig.1. Region 20N-80N; 100W-35E of AMO data determination, according Wang et al. (2017).

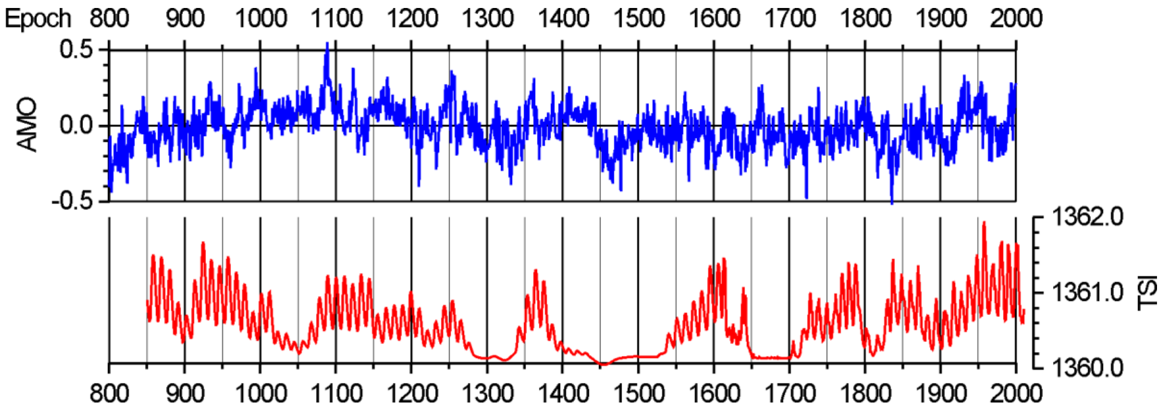

Fig.2. AMO time series (top, blue line) and TSI time series (bottom, red line).

b) Partial Fourier Approximation

The AMO periodic variations, whose cycles are identical with the solar cycles, are determined by the Method of Partial Fourier Approximation (PFA). The time series of oscillations from a given frequency band are calculated as a superposition of two neighbor Fourier harmonics, whose coefficients are estimated by the Least Squares (LS) Method. The details of this method are described in (Chapanov et al., 2015). Shortly, the Partial Fourier approximation $F(t)$ of discrete data is given by

$$F(t) = f_0 + f_1(t-t_0) + \sum_{k=1}^{n} a_k \sin k \frac{2\pi}{P_0}(t-t_0) + b_k \cos k \frac{2\pi}{P_0}(t-t_0), \quad (1)$$

where P_0 is the period of the first harmonic, t_0 - the mean epoch of observations, f_0, f_1, a_k and b_k are unknown coefficients and n is the number of harmonics of the partial sum, which covers all oscillations with periods between P_0/n and P_0. The application of the LS estimation of Fourier coefficients needs at least $2n+2$ observations, so the number of harmonics n is chosen significantly smaller than the number N of sampled data f_i. The small number of harmonics n yields to LS estimation of the coefficient errors. This estimation is important difference with the classical Fourier approximation. The other difference is the possibility of arbitrary choice of the period of first harmonic P_0, instead of the observational time span, so the estimated frequencies may cover the desired set of real oscillations. This method allows a flexible and easy separation of harmonic oscillations into different frequency bands by the formula

$$B(t) = \sum_{k=m_1}^{m_2} a_k \sin k \frac{2\pi}{P_0}(t - t_0) + b_k \cos k \frac{2\pi}{P_0}(t - t_0), \quad (2)$$

where the desired frequencies ω_k are limited by the bandwidth

$$\frac{2\pi m_1}{P_0} \leq \omega_k \leq \frac{2\pi m_2}{P_0}, \quad (3)$$

After estimating the Fourier coefficients, it is possible to identify a narrow frequency band presenting significant amplitude, and defining a given cycle. Then this cycle can be reconstructed in time domain as the partial sum limited to the corresponding frequency bandwidth. Doing this for terrestrial and solar time series, we shall identify their common cycles.

The used time series of AMO and TSI long-term variations cover 1161-year overlapped time interval for the period 850.0 – 2011.0. The PFA performs estimation of 150 harmonics with the accuracy better than 0.006 for AMO and 5 mW/m^2 for TSI coefficients.

Results

a) FFT spectra

The AMO and TSI spectra are determined by the Fast Fourier Transform (FFT). Their spectra have common centennial oscillations with periods 80-200 years and some decadal cycles, whose periodicity lays above 30 years (Fig. 3).

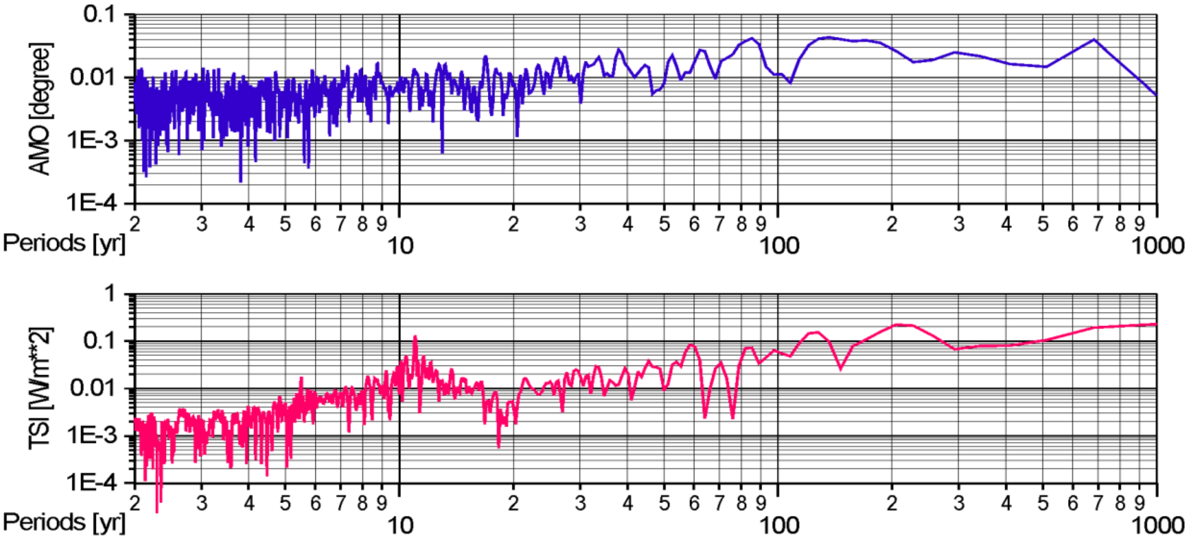

Fig.3. FFT spectra of AMO and TSI time series.

b) Solar influence on centennial AMO cycles

The solar influences on centennial AMO oscillations are presented in 3 bands, whose periodicity is between 116 and 233 years (Figs. 4-6). The TSI and AMO variations with periods between 193.2 and 232.8 years are shown in Fig. 4. The agreement between time series with these oscillation is excellent with a high correlation between them for the time interval 1100-2010. Before 1100 these oscillations are out of phase. Next partial correlation between TSI and AMO cycles are detected for periodicity 144.9-165.6 years for time interval 900-1600 (Fig. 5). Only common cycles with periods 115.9-128.8 years cover the whole 1100-year time interval 900-2000 (Fig. 6).

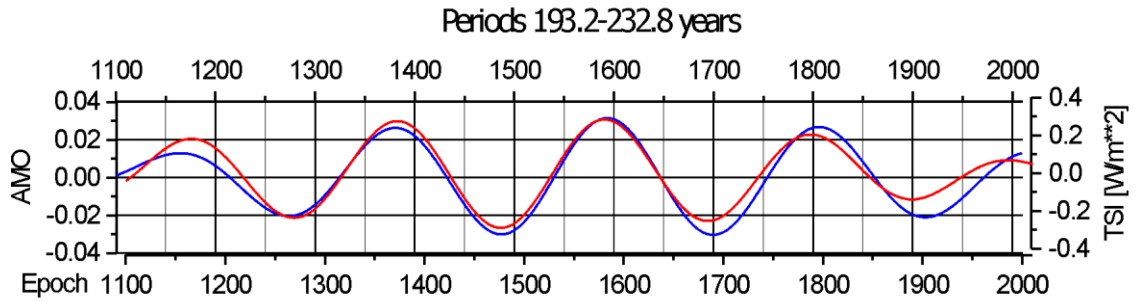

Fig.4. Centennial AMO (blue line) and TSI (red line) cycles with periods 193.2-232.8 years.

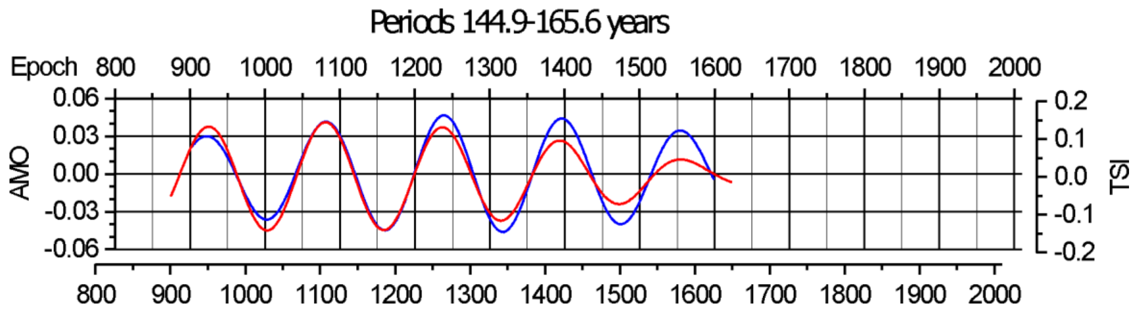

Fig.5. Centennial AMO (blue line) and TSI (red line) cycles with periods 144.9-165.6 years.

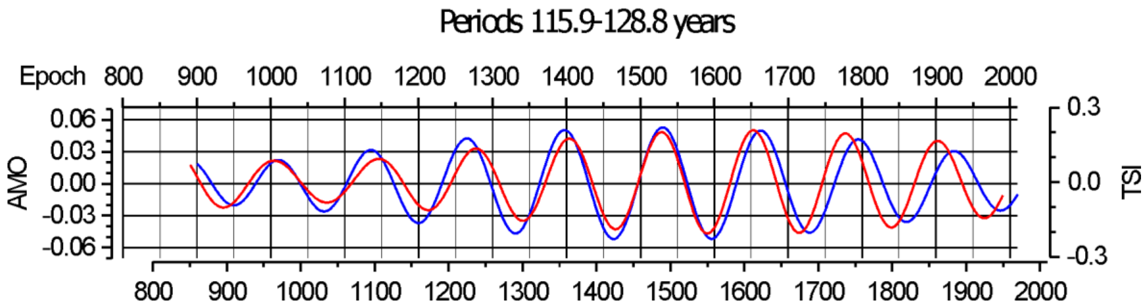

Fig.6. Centennial AMO (blue line) and TSI (red line) cycles with periods 115.9-128.8 years.

c) Solar influence on decadal AMO cycles

The solar influence on decadal AMO oscillations are detected in 4 narrow frequency bands with periodicities 48.3-72.4 years (Figs. 7-10). The decadal TSI and AMO oscillations have excellent agreement and their common cycles may serve as a good base of climate modelling and forecast improvements.

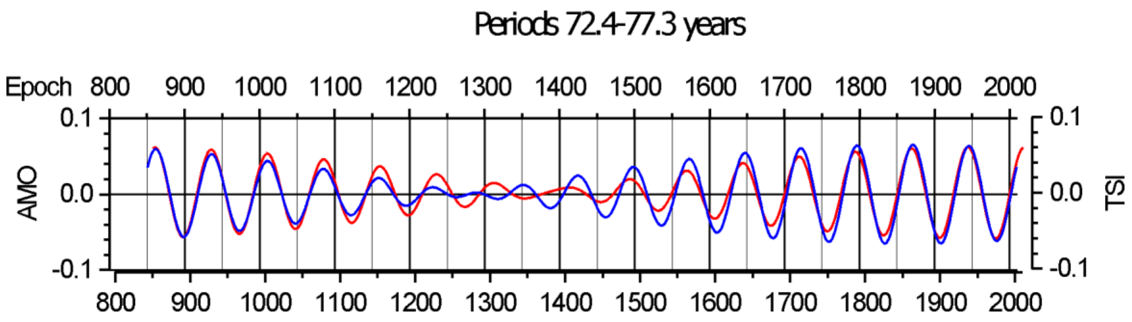

Fig.7. Decadal AMO (blue line) and TSI (red line) cycles with periods 72.4-77.3 years.

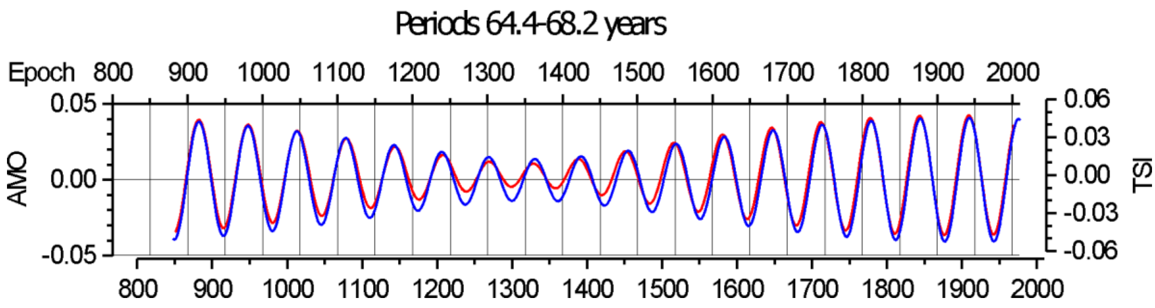

Fig.8. Decadal AMO (blue line) and TSI (red line) cycles with periods 64.4-68.2 years.

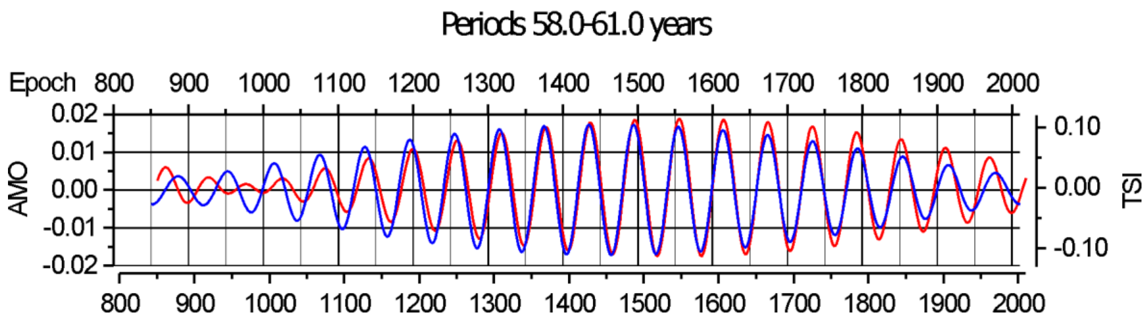

Fig.9. Decadal AMO (blue line) and TSI (red line) cycles with periods 58.0-61.0 years.

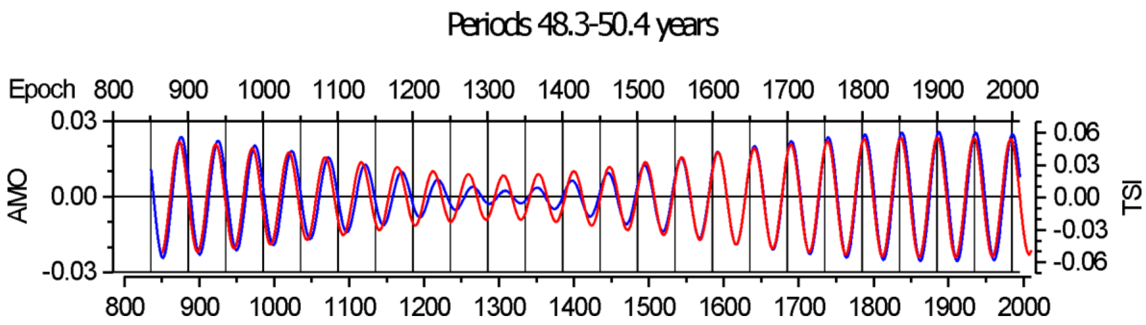

Fig.10. Decadal AMO (blue line) and TSI (red line) cycles with periods 48.3-54.4 years.

Conclusions

The new largest time series of AMO and TSI variations, whose time span cover more than 11 centuries, give good opportunity of better understanding the solar-terrestrial influences in the area of climate variations and climate change. The analyze of AMO and TSI time series by means of the Method of Partial Fourier Approximation determine 3 centennial and 4 decadal narrow frequency bands, where the solar and terrestrial cycles have good agreement. The common TSI and AMO cycles cover periodicities between 48 and 233 years. They may serve as a good instrument of climate modelling and long-term forecasts.

Acknowledgements

The study is supported by the National Science Fund of Bulgaria, Contract KP-06-N34/1 /30-09-2020 "Natural and anthropogenic factors of climate change – analyzes of global and local periodical components and long-term forecasts"

References

Lean, J.L. (2018). Estimating solar irradiance since 850 CE. *Earth Space Sci.* **5**, 133-149. https://doi.org/ 10.1002/2017EA000357

Wang, J., Yang, B., Ljungqvist, F. *et al.* (2017). Internal and external forcing of multidecadal Atlantic climate variability over the past 1,200 years. *Nature Geosci* **10,** 512–517. https://doi.org/10.1038/ngeo2962

Ghosh, Rohit; Müller, Wolfgang A.; Baehr, Johanna; Bader, Jürgen (2016). Impact of observed North Atlantic multidecadal variations to European summer climate: a linear baroclinic response to surface heating. Climate Dynamics. **48** (11–12): 3547.

Zampieri, M.; Toreti, A.; Schindler, A.; Scoccimarro, E.; Gualdi, S. (2017). Atlantic multi-decadal oscillation influence on weather regimes over Europe and the Mediterranean in spring and summer. Global and Planetary Change. **151**: 92–100.

Trenberth, Kevin; Dennis J. Shea (2005). *Atlantic hurricanes and natural variability in 2005*. Geophysical Research Letters. **33** (12): L12704.

Zhang, R.; Delworth, T. L. (2006). "Impact of Atlantic multidecadal oscillations on India/Sahel rainfall and Atlantic hurricanes". Geophys. Res. Lett. **33** (17): L17712.

Solar and Cosmic Rays Influence on Winter Temperature Variations in North Siberia

Chapanov Ya.

Climate, Atmosphere and Water Research Institute, Bulgarian Academy of Sciences
E-mail: yavor.chapanov@gmail.com

Abstract.

The global warming is not uniformly distributed over the Earth surface. Some regions are strongly affected by the global warming. The mean temperature of Siberia is rising stronger during last decades. The anthropogenic factors of this rise cause positive linear trend since 1970, while various natural factors, like solar activity, cosmic rays, geomagnetic field, stratospheric ozone, excite periodic oscillations of the temperature and non-linear trends. The time series of winter temperature of North Siberia (65N-75N; 90E-170E) is analyzed by means of the Method of Partial Fourier Oscillations. The cycles of Siberia winter temperature in narrow frequency bands are compared with corresponding oscillations of Total Solar Irradiance (TSI) and Cosmic Rays (CR) in order to determine the existence of common cycles. The worming trend after 1970 is determine by moving average of time series.

Introduction

The aim of this work is to determine changes of temperature of North Siberia, which is the largest reservoir of natural methane. The global warming is not uniformly distributed over the Earth surface. Some regions are strongly affected by the global warming. The mean temperature of Siberia is rising stronger during last decades. The anthropogenic factors of this rise cause positive linear trend since 1970, while various natural factors, like solar activity, cosmic rays, geomagnetic field, stratospheric ozone, excite periodic oscillations of the temperature and non-linear trends. According National Oceanic and Atmospheric Administration (NOAA), the recent temperature trend during last 30 years is not uniformly spread over Earth surface. The maximal effect of global warming is visible in North Africa and close to the North polar circle (Fig. 1). High temperature rate in polar region is danger about future meltdown of permafrost and large amount of methane release. The permafrost stability is connected with the winter temperature variations and its rising to critical level. The time series of North Siberia winter temperature since 1836 is suitable to study possible climatic disaster after sudden methane release.

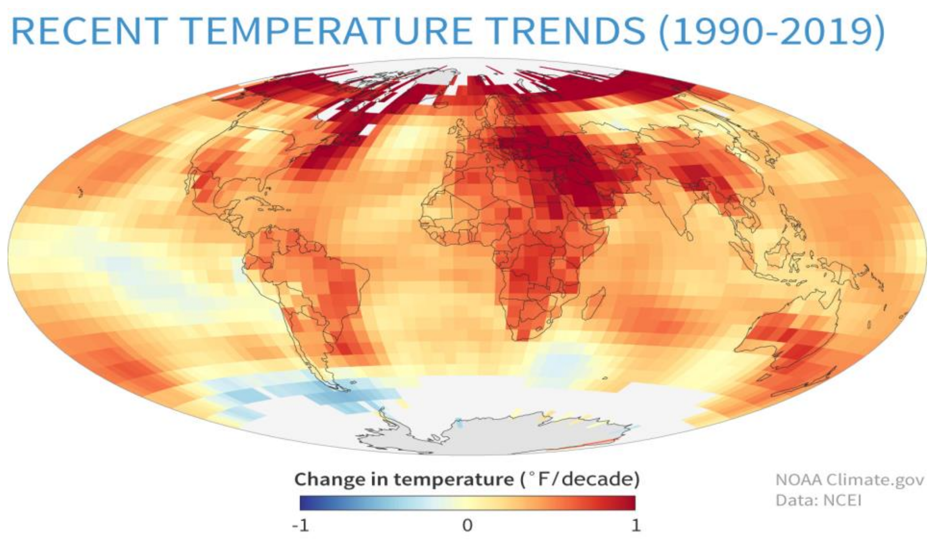

Fig.1. Global temperature trends since 1990 according NOAA.

Data and Methods

a) Cosmic rays and TSI

The TSI and CR data are presented in Fig.2. Solanki et al. (2000, 2002) have reconstructed the open solar magnetic flux for the last 400 years from sunspot data. Using reconstructed magnetic flux as an input to a spherically symmetric quasi-steady state model of the heliosphere, Usoskin at al. (2002, 2005; Alanko-Huotari et al., 2006) calculate the intensity of galactic CR at the Earth’s orbit since 1610.

The daily reconstruction of TSI since 1850 is a composite of SATIRE-T reconstruction from (Krivova et al., 2010) for 1850 to 22 August 1974; and SATIRE-S reconstruction from (Yeo et al., 2014a, 2014b) for 23 August 1974 onwards (Fig. 2, d, yellow color). The monthly values are calculated by the robust Danish Method (Fig.2, d, red color).

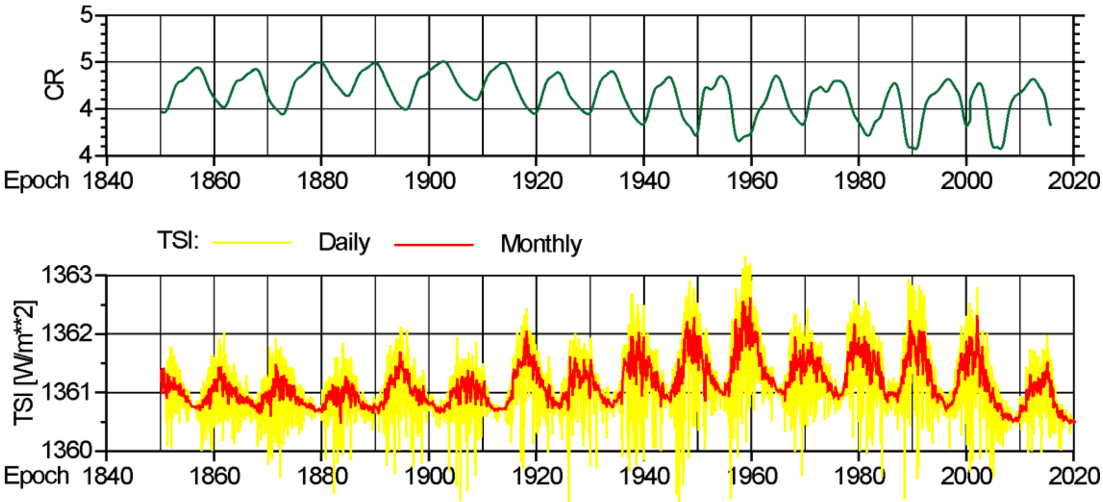

Fig.2. Time series of Cosmic Rays (CR) and TSI. The daily values of TSI are marked by yellow line, their 0.1-year values – by red line.

b) Temperature time series

The North Siberia temperature data are taken from region 65N-75N; 90E-170E (Figs. 3, 4). These data are available from Twentieth Century Reanalysis (20CR) dataset, Version 3.

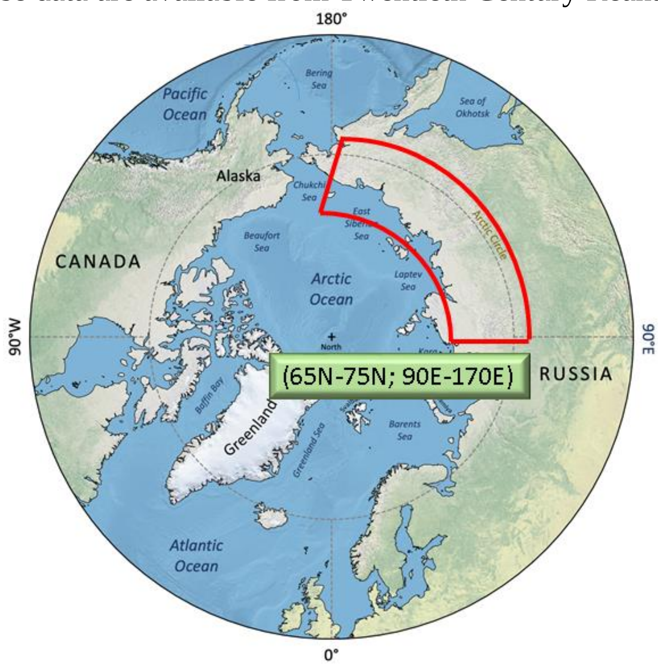

Fig.3. Map of region 65N-75N; 90E-170E of North Siberia.

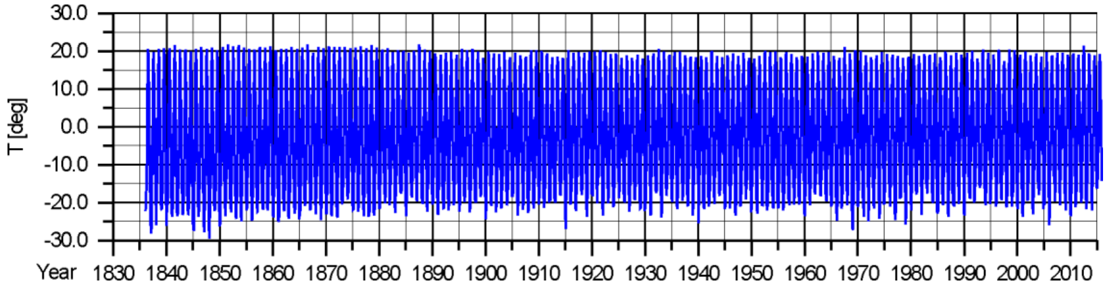

Fig.4. Time series of North Siberia Temperature T for the period 1836-2016.

The time series spectra are calculated by the Fast Fourier Transform (FFT). The time series of oscillations with a given frequency are calculated by the Method of Partial Fourier Approximation (PFA), whose details are described in (Chapanov et al., 2015). The used time series cover 179-year overlapped time interval for CR and T since 1836, and 166-year overlapped time interval for TSI and T since 1850. The PFA performs estimation of 180 harmonics with the accuracy better than 0.0003 for CR, 0.01°C for T, and 5 mW/m^2 for TSI coefficients.

Results

a) FFT spectra

The FFT spectra of the time series (Fig. 5)have some common spectral parts, where the oscillations are with periods around 5, 6, 8, 9, 12, 20-30 and 100 years

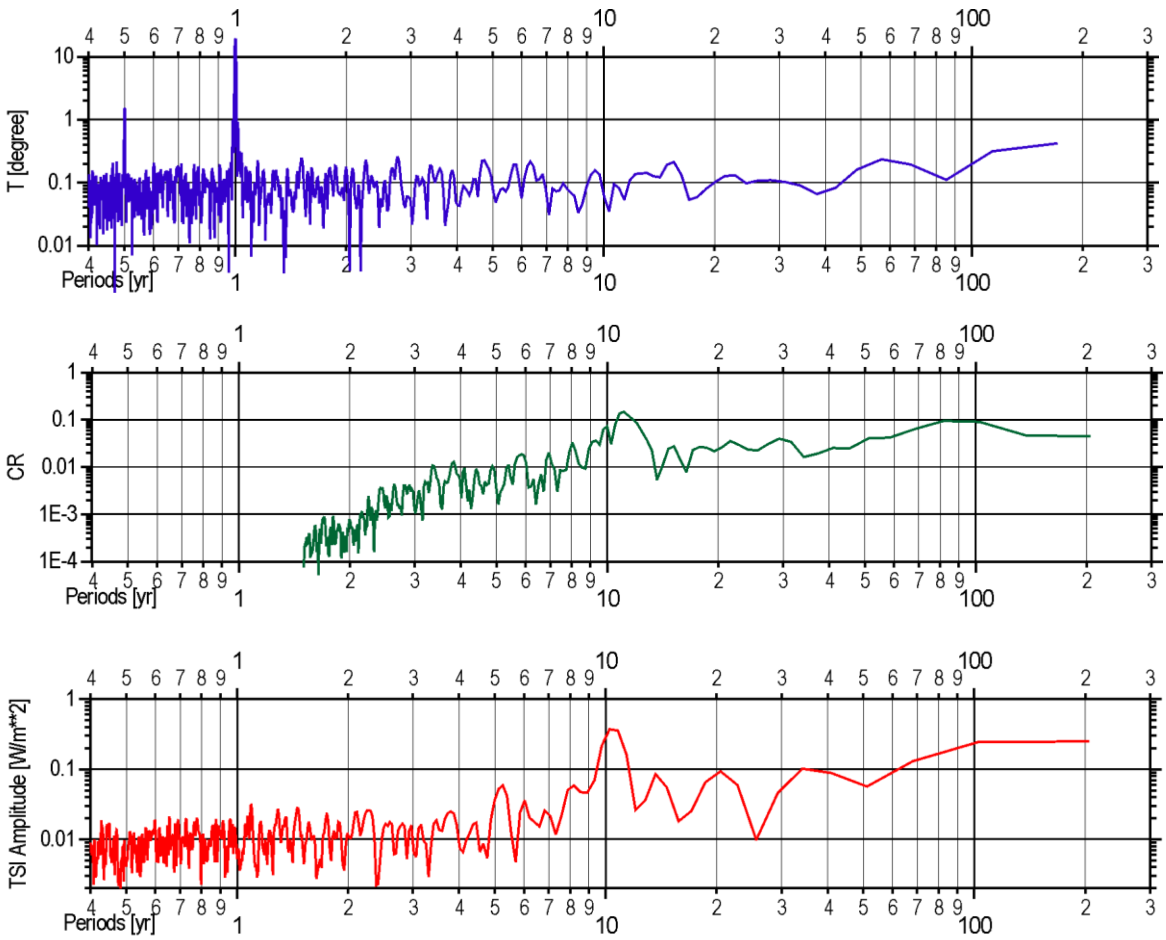

Fig.5. Spectra of CR, TSI and .temperature variations, determined by FFT.

b) TSI influence on winter temperature of North Siberia

The TSI influences on oscillations of winter temperature variations in North Siberia are presented in 5 bands, whose periodicity is 6-10 years and 83---163 years (Fig. 6). The TSI drives long-term variations of winter temperature of North Siberia, where the minimal winter temperature rises by 5°C since 1836 (fig. 8).

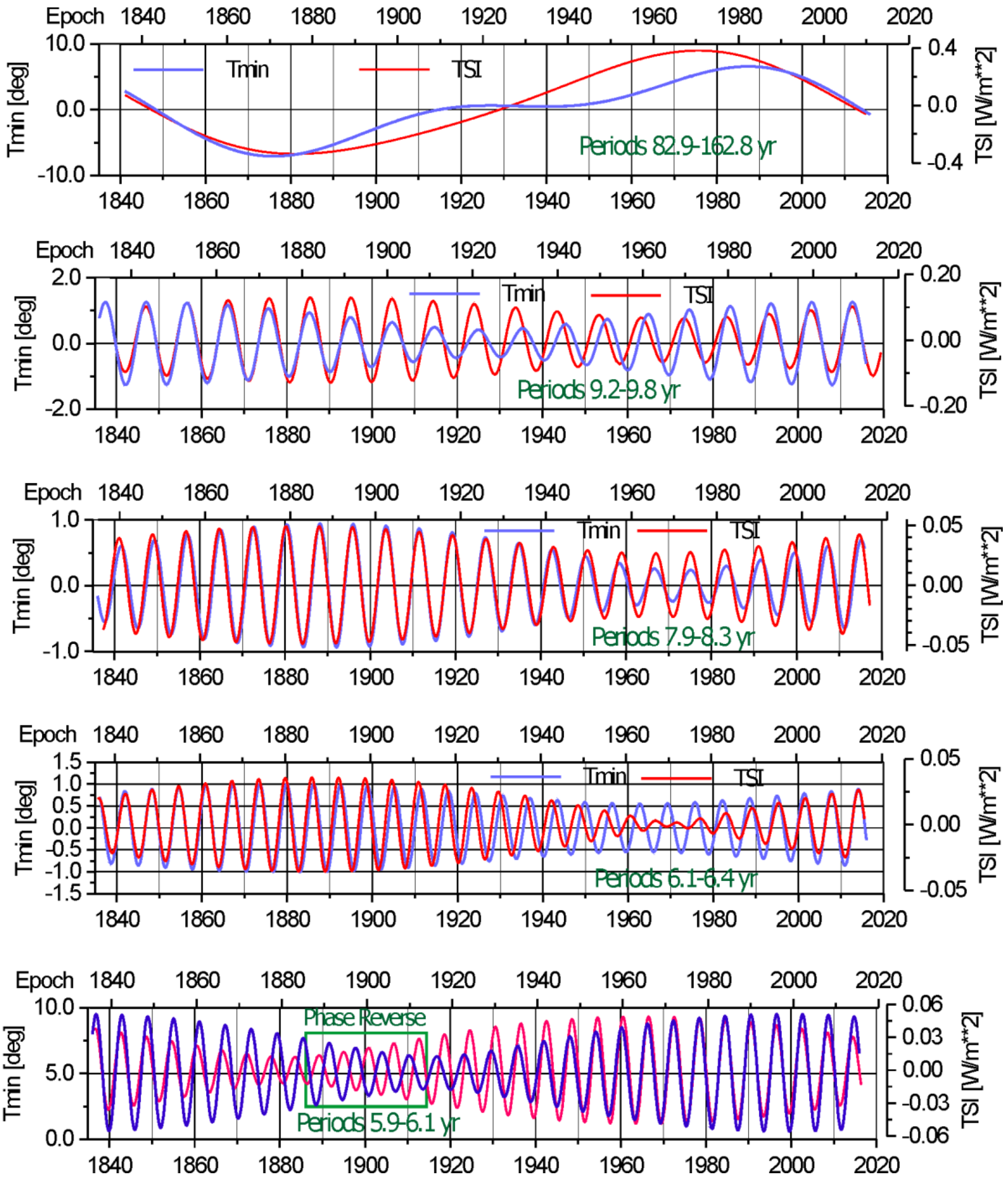

Fig.6. TSI influence on temperature of North Siberia.

c) CR influence on winter temperature of North Siberia

The CR influences on oscillations of winter temperature variations in North Siberia are presented in 5 interannual and decadal bands, whose periodicity is 6-36 years (Fig. 7). The CR and temperature cycles are almost identical for the periodicity below 15 years, while their decadal cycles with periods 30-45 years are partially correlated (Fig. 7).

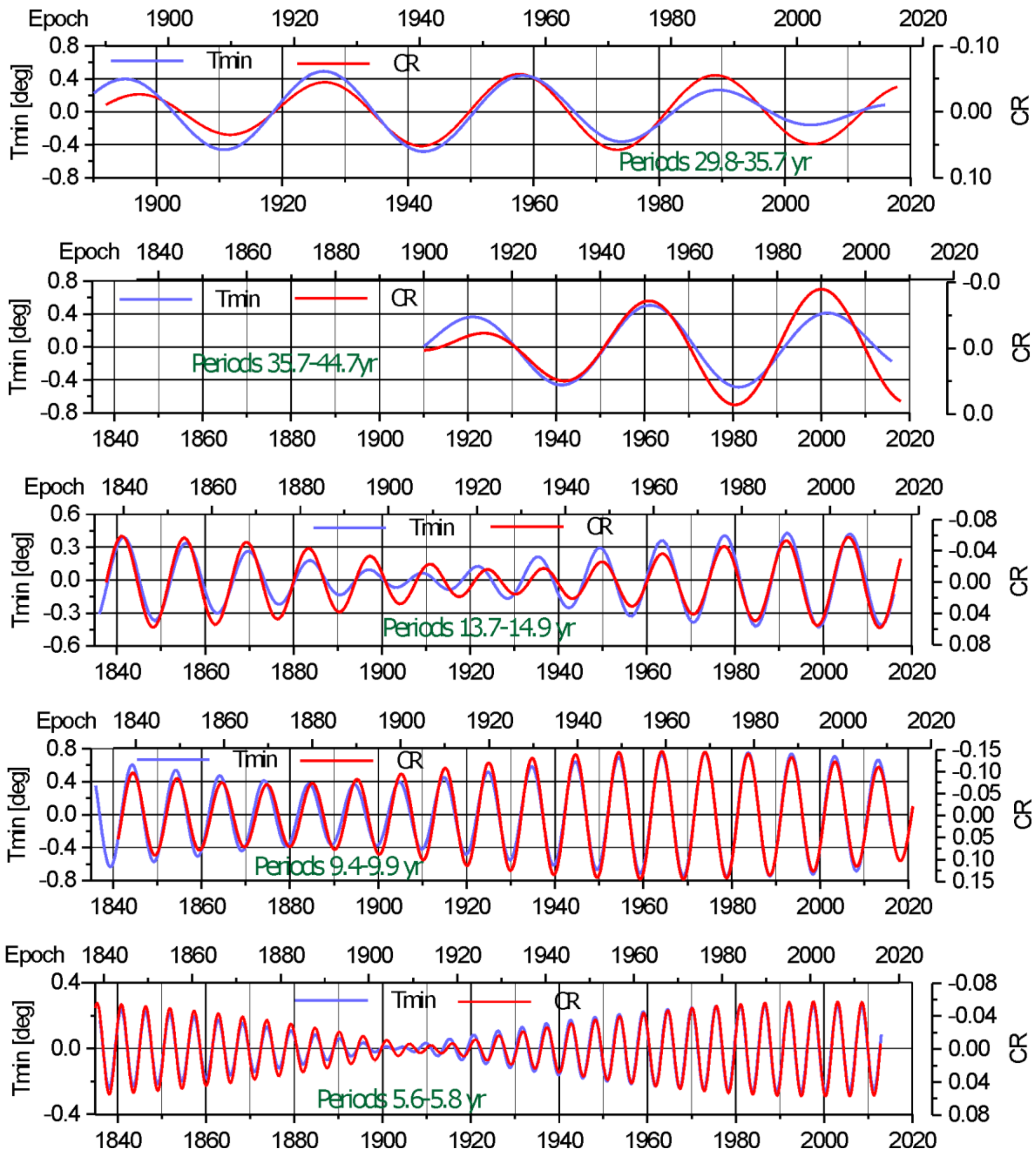

Fig.7. CR influence on temperature of North Siberia.

d) Minimal winter temperature variations and Earth orbit influence

By the definition the TSI represent the total solar energy falling orthogonally to the solar direction over 1 square meter in vacuum, outside the atmosphere in the space near the Earth orbit. The TSI depends on the distance between Earth and Sun, so it varies with annual period, because the Earth distance to the Sun are different at Perihelion and Aphelion. These distances are slowly change in time, due to eccentricity variations of Earth orbit. Laskar et al., (2011) determine that the Earth orbit eccentricity decreased by 0.0004 for the last 1000 years, so it is changed by -7.2×10^{-5} for the period 1836-2016. The Perihelion increased and the aphelion decreased by 0.0072% for this period, and corresponding change of TSI at these points is 0.014%, or 196 mW/m^2. The Earth pass the Perihelion in the beginning of January and Aphelion – in the beginning of July, so, тhe TSI slowly decrease by 0.2 W/m^2 during the Winters since 1836. Nevertheless, the minimal Winter temperature increase by +0.03÷+0.06°C/yr and this rate is not connected with the eccentricity change. The summer temperature is less changed, so the visible decrease of annual amplitude of North Siberia temperature is mostly due to winter temperature rate (fig. 8).

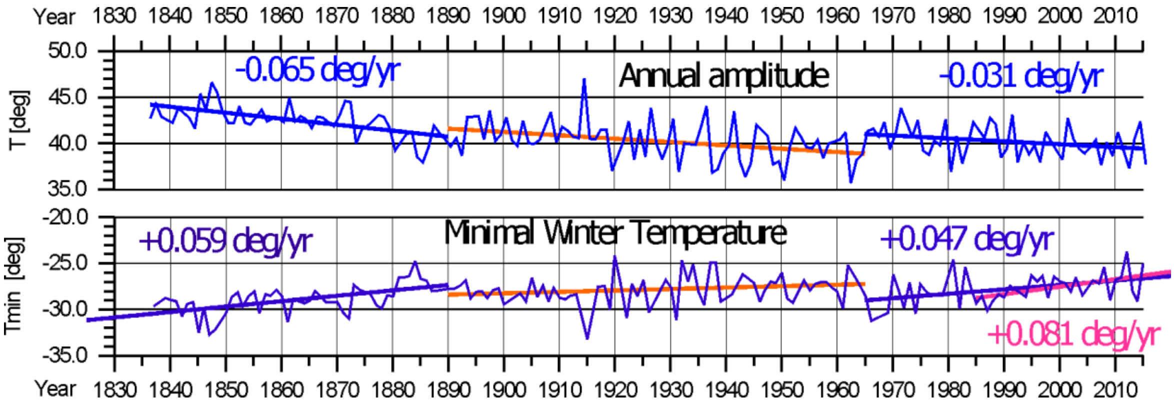

Fig.8. Time series of annual amplitude and minimal winter temperature variations in North Siberia..

Conclusions

The solar activity affects the temperature of North Siberia by means of TSI and cosmic rays variations. The TSI variations affect centennial cycle of Winter Siberia temperature and 4 sbdecadal cycles, while the CR variations affect 4 decadal and 1 subdecadal cycle. The TSI value decreases by 0.2 W/m^2 during the Winters since 1836, due to eccentricity and Perihelion change of Earth orbit, but this value is not essential for the positive trend +0.03 ÷ +0.06°C/yr of winter temperature. This trend, plus additional 0.08°C/yr since 1985 due to anthropogenic global warming, leads to 5°C/yr temperature rise up for the last 180 years without possible direct damage on methane from permafrost for next dacades.

Acknowledgements

The study is supported by the National Science Fund of Bulgaria, Contract KP-06-N34/1 /30-09-2020 "Natural and anthropogenic factors of climate change – analyzes of global and local periodical components and long-term forecasts"

References

Alanko-Huotari, K., I.G. Usoskin, K. Mursula, G.A. Kovaltsov, 2006. Global Heliospheric Parameters and Cosmic-Ray Modulation: An Empirical Relation for the Last Decades, *Solar Physics*, 238, 391-404, doi: 10.1007/s11207-006-0233-z.

Chapanov, Ya., Ron C., Vondrák, J., 2015. Millennial cycles of mean sea level excited by Earth´s orbital variations. *Acta Geodyn. Geomater*., **12**, 3 (179), 259–266.

Krivova N.A., Vieira L.E.A., Solanki S.K. (2010). Reconstruction of solar spectral irradiance since the Maunder minimum. *J. Geoph. Res*. **115** (A12112), 1-11.

Laskar J., A. Fienga, M. Gastineau and H. Manche, 2011, La2010: a new orbital solution for the long-term motion of the Earth, A&A 532, A89, DOI: 10.1051/0004-6361/201116836

Solanki , S. K., Schüssler, M., and Fligge, M., 2000. Evolution of the Sun's large-scale magnetic field since the Maunder minimum, *Nature*, 480, 445–446.

Solanki, S. K., Schüssler, M., and Fligge, M., 2002. Secular variation of the Sun's magnetic flux, *Astronomy and Astrophysics*, 383, 706–712.

Usoskin, I.G., K. Mursula, S.K. Solanki, M. Schuessler, and G.A. Kovaltsov, 2002. A physical reconstruction of cosmic ray intensity since 1610, J. Geophys. Res., 107(A11), 1374, doi:10.1029/2002JA009343.

Usoskin, I., K. Alanko-Huotari, G. Kovaltsov, K. Mursula, 2005. Heliospheric modulation of cosmic rays: Monthly reconstruction for 1951-2004. *J. Geophys. Res.*, 110, A12108, doi:10.1029/2005JA011250JGR.

Yeo K.L., Krivova N.A., Solanki S.K., Glassmeier K.H. (2014a). Reconstruction of total and spectral solar irradiance from 1974 to 2013 based on KPVT, SoHO/MDI and SDO/HMI observations. *Astron. Astrophys*. **570** (A85), 1-18.

Yeo K.L., Krivova N.A., Solanki S.K. (2014b). Solar cycle variation in solar irradiance. Space Sci. Rev. 186, 137-167.

Tropospheric Mesoscale Systems and their Signatures within Ionosphere

Koucka Knizova P., Podolska K., Kouba D., Mosna Z., Potuznikova K., Sindelarova T., Boska J.

Institute of Atmospheric Physics CAS, Prague, Czech Republic
E-mail: pkn@ufa.cas.bg

Abstract.

Ionosphere behavior is predominantly determined by solar and geomagnetic forcing. An important part of its energy budget however, comes from the lower-laying atmospheric regions. The energy transfer between distant regions happens due to atmospheric waves that propagate from their source region up to ionospheric heights. Experimental observations and theoretical studies show the importance of involvement of the troposphere mesoscale systems. With the changing climate severe weather systems occur more often. On the measurements from troposphere up to ionosphere we demonstrate changes within atmospheric parameters up to ionospheric F layer induced by a severe tropospheric frontal system passing above Europe.

Introduction

It is generally accepted now that wave coupling from below is the major source of the observed differences in the ionosphere parameters on the consequent days with stable forcing from above. Ionospheric data cover several solar cycles. On a solar cycle scale, we see that ionospheric parameters well follow the solar variability. Decomposing signal into dominant component that follows solar cycle and irregular part we can see that irregular part form a substantial part of the signal. Decomposition of critical frequency *foF2* for station Juliusruh is demonstrated in Fig. 1.

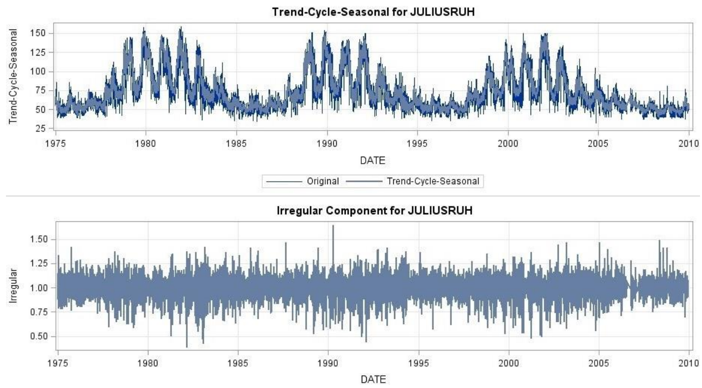

Fig.1. Data from ionospheric station Juliusruh: original data with trend (upper panel) and irregular component (lower panel).

The Earth atmosphere system is not simply vertically coupled. The coupling within the regions must be understood on the multiple space and time scales. The memory of the system cannot be neglected. Distant regions are coupled by dynamical, chemical and electrical processes. The energy transfer between distant atmospheric parts happens due to atmospheric waves that propagate from their source region up to ionospheric heights. Experimental observations show the importance of involvement of the lower atmosphere in ionospheric variability studies in order to accurately capture smaller-scale features of the upper atmosphere [Koucká Knížová et al., 2021].

Coherency between periodic component within solar signals on one side and ionospheric and stratospheric variability on the other side points to the apparent common variability domains. However, they are not stable and vary during solar cycle and/or from one cycle to the following one [Koucká Knížová et al., 2018].

In a recently published paper [Podolská et al., 2021], we analyzed relationship between solar and ionospheric parameters by mean of probabilistic graphical models (CIG). We identified three groups of dependencies. Within them there is no sign of geomagnetic dependence that might lead to splitting into the three groups. But we got three groups that differs in climate regime of the troposphere: East Asia stations (D class – cold), Europe stations (C class – moderate) and North American stations (B class – arid).

It is assumed that the neutral atmosphere effects on the ionosphere have limits in their spatial extent. Evolution of correlation between stations with distance for long time series of foF2 identified "break point" at 10 degrees in longitude and/or Earth's distance of ~1000 km [Koucká Knížová et al., 2015]. Irregular component for close stations is forced by common source. Since the scale of ~1000 km correspond to the typical sizes of mesoscale tropospheric systems, this finding supports connection between the lower atmosphere and the F2 region.

Mesoscale tropospheric systems, especially those that are fast moving, seems to play an important role in the atmospheric vertical coupling, particularly in atmospheric wave generation that are propagate up to the ionospheric heights. Detail analyses of Fabienne storm revealed significant changes associated with rapidly moving cyclone across the Europe [Koucká Knížová et al., 2020]. Following part of this paper focuses on severe cyclone Zyprian and its signatures in the atmosphere up to ionospheric F2 layer.

Mesoscale cyclone Zyprian

Cyclone Zyprian is a recent event from July, 2021. System brought severe weather on the frontal borders and heavy rains followed by floods. Cyclone Zyprian dominated the weather in Germany. Low-pressure area formed in the lee of the Alps. As a result, strong convective storm appeared in a very unstable air mass, including very large hail and wind gusts up to 40 m.s^{-1}. Especially on Thursday 8 July, the cold front brought showers and thunderstorms that were regionally strong. Figure 2 shows synoptic situation above Europe and temperature map at 2 m above the ground zooming on the Czech Republic.

a) Tropospheric situation

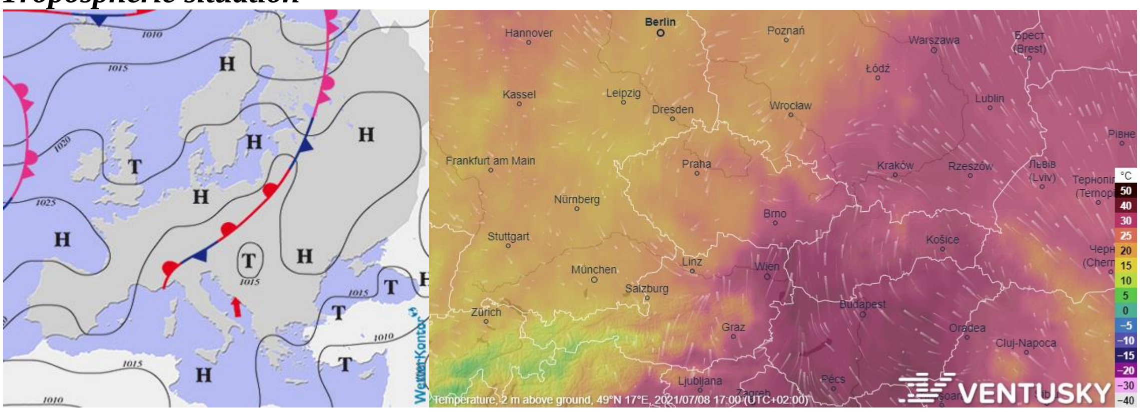

Fig.2. Meteorological situation: Synoptic map (left panel) and temperature radar data (right panel).

Frontal boundary is extending along the Alps through central Poland as seen on Fig.2 on the synoptic map (left panel). This frontal boundary divides hot and well-mixed air masses across the Balkans from moist and cooler air to the west. Along the frontal boundary the strong cyclogenesis occurs. The temperature drop on the frontal border was about 16° C as seen on detail zoom in Fig.2 (right panel) above the Czech Republic. Strong low-level windshear of 20-28 m.s^{-1} (in the 0-6 km layer) was recorded. Showers and thunderstorms on the frontal border were regionally very strong. The ESTOFEX storm space distribution vs. Lightning is shown in Fig.3. on the left map. High lightning activity is seen on the radar helicity index data on the right panel of Fig.3. The helicity index is rather high reaching values of 200 - 300 m^2.s^{-2} in the 0-1 km layer during the late afternoon and evening.

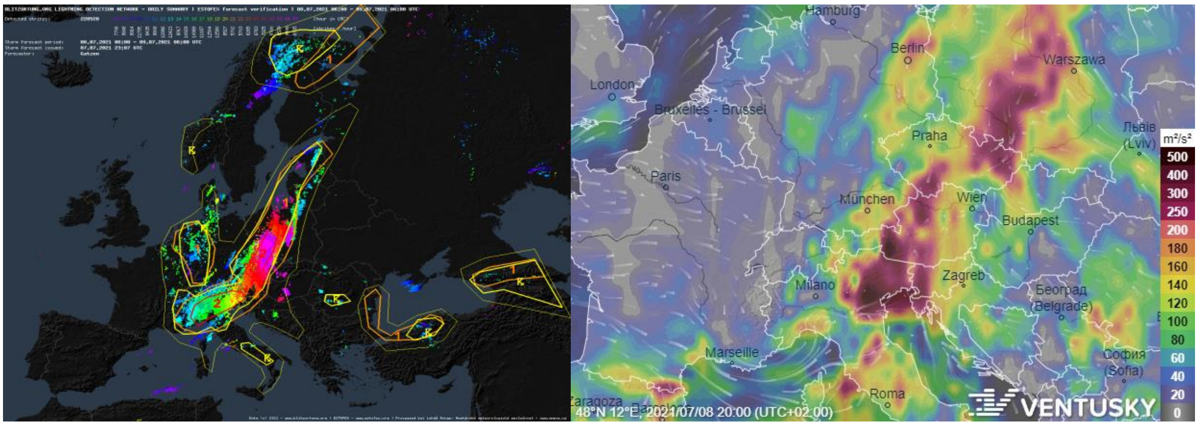

Fig.3. ESTOFEX storm space distribution vs. Strokes Blitzortung measurement 8.7.2021 8 CEST 9.7.2021 8 CEST (left panel) and helicity index radar data (right panel).

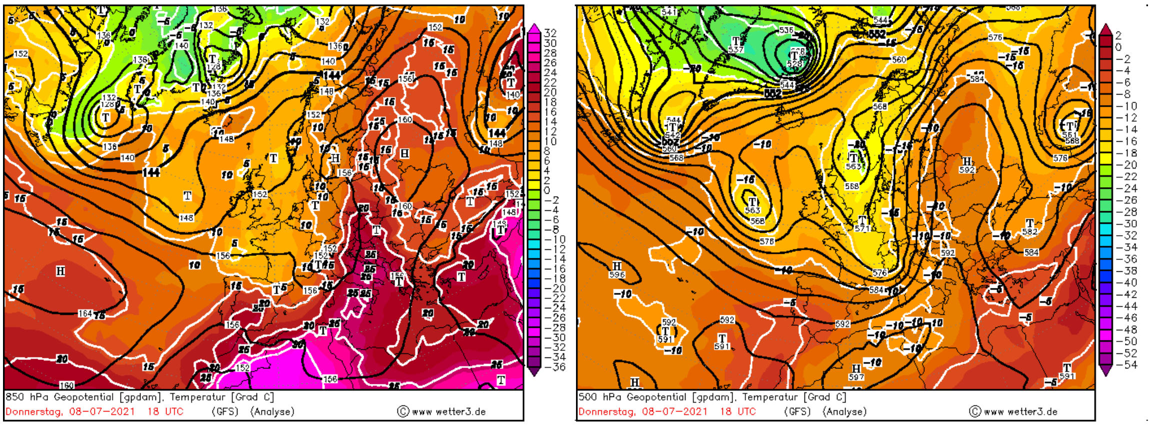

Fig.4. Geopotential temperature at the level of 850hPa (left panel) and 500hPa (right panel).

Fig.4 shows map of geopotential temperature at two levels 850hPa (left panel) and 500hPa (right panel). The division of two air masses with significantly different temperatures is well visible up to the middle troposphere approx. 5.5 km height above the ground.

b) Stratospheric situation

Fig.5 shows three consequent days (7–9 July, 2021) of Aeolus ESA satellite Rayleigh scattering observations of wind profiles (in the middle panels) and the Mie MDS wind velocity profiles (on the right panels). An important feature is seen on the right panels. The position of the polar jet is significantly shifted the after the cyclonal passage.

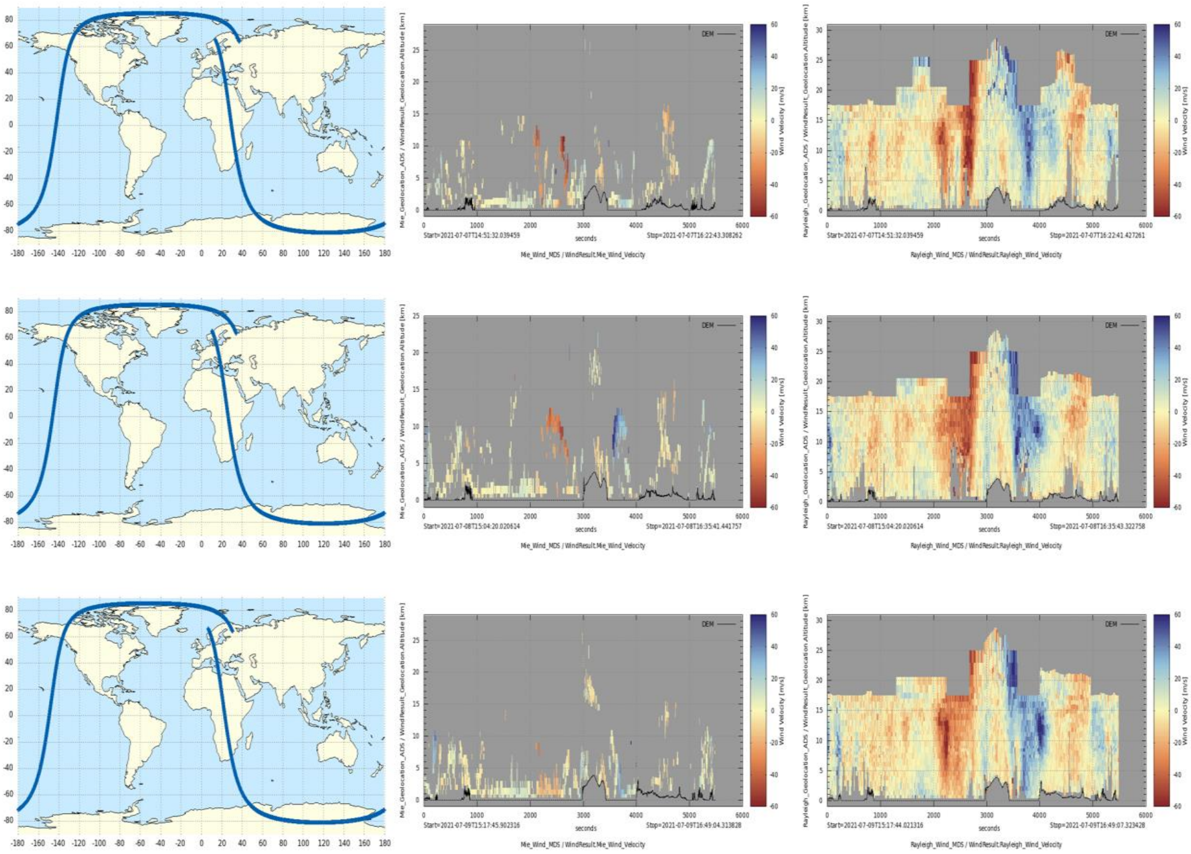

Fig.5. Aeolus satelite measurement for three consequent days, one day before (upper panel), day of cyclone passage (middle panel) and day after (lower panel) the cyclone passage. Visualisation from [http://aeolus-ds.eo.esa.int/socat/L1B_L2_Products.](http://aeolus-ds.eo.esa.int/socat/L1B_L2_Products)

c) Ionospheric situation

Cyclone Zyprian occurred during rather stable solar and geomagnetic situation. The Kp value is less than 3. On the sequence of critical frequency, we see only small decrease. Fig.6 shows three-day sequence of ionograms recorded after 21UT with 15-minute time difference. In the middle panel, there are ionograms with spread F echo, indicating disturbed ionosphere. Ionosphere remains disturbed during following day and then returns to regular stratification. During the day before the cyclone passage, the recorded ionograms indicate well stratified ionosphere without irregularities or undulation caused by propagating waves. From Fig.6 it is evident that critical frequency foF2 does not vary significantly. Fig. 7 represents directogram measurement. The increase in horizontal plasma flow is well visible in the middle part. Change in the color indicate plasma flow shears.

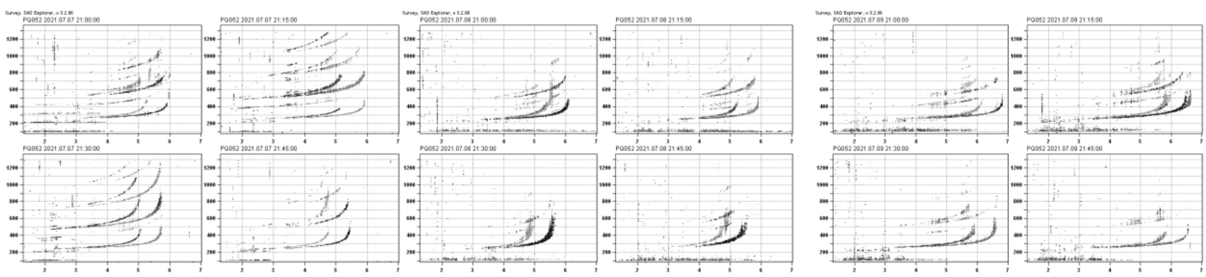

Fig.6. Ionospheric measurement (ionograms) for three consequent days, one day before (upper panel), day of cyclone passage (middle panel) and day after (lower panel) the cyclone passage

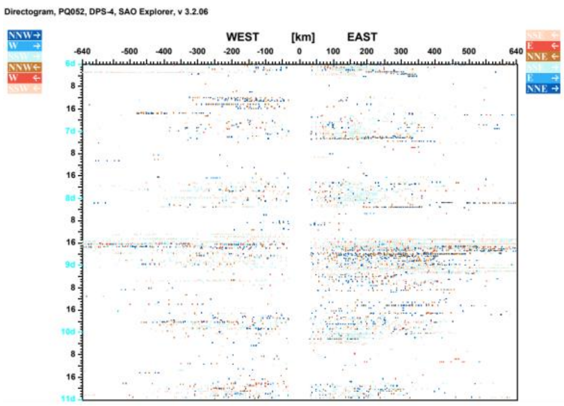

Fig.7. Ionospheric directogram measurement (ionograms) for five consequent days. Significant increase of echo is seen in the central part.

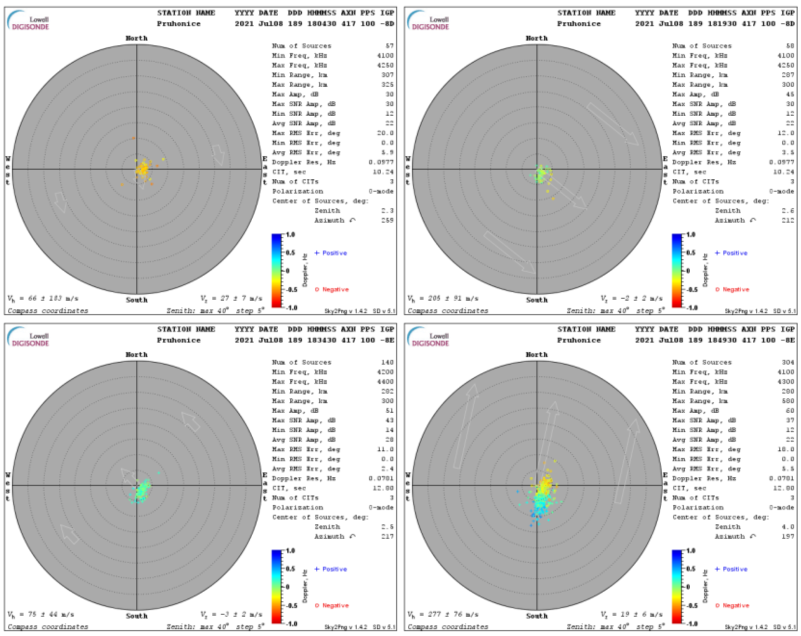

Fig.8. SKYmaps recorded during one hour at 18.04 UT (upper-left panel), 18.19 (upper-right panel), 18.34 (bottom-left panel) and 18.49 UT (bottom-right panel).

Fig. 8 of the sequence of SKYmaps demonstrates how the plasma flow rapidly changes within one hour. There are 15-minute time difference between each measurement. The measurement represents plasma flow at approximately same height below F2 peak. On the top-left panel, plasma flows in South-south East direction, top-right panel 15 minutes later South-East, bottom-left panel North-West and finally bottom-right panel in North North-East. It should be emphasized that geomagnetic activity is low, hence the TIDs of auroral origin are unlikely to be observed. We suppose that there should not be contamination by geomagnetic activity.

Results

Mesoscale systems Zyprian occurred at the beginning of July, 2021. It dominated weather above Western Europe. Large frontal border was characterized by high temperature drop with strong cyclogenesis. Frontal boundary moved rapidly across Europe. High wind gusts were recorded. Heavy rains caused large damages, especially in Germany. Within stratosphere, a shift of polar jet stream was observed. At the ionospheric heights irregular stratification and radio wave reflection planes undulation was observed. Irregularities are attributed to the upward propagating waves launched from frontal boundary as the solar and geomagnetic conditions were low. Strong increase of wave-like activity was detected on ionograms the directograms. On directograms and SKYmaps, strong and rapid changes in the horizontal plasma motion were recorded. However, no prevailing plasma motion direction was identified within F-layer.

Conclusions

Mesoscale systems are effective sources of atmospheric disturbances that can reach ionospheric heights and significantly alter atmospheric and ionospheric conditions. Convective systems like Zyprian and others could affect Earth’s atmosphere on a continental scale and up to F-layer heights. Variability within ionosphere are attributed mainly to Zyprian cyclone as it developed during low geomagnetic activity and stable solar forcing.

References

Koucká Knížová P., Laštovička J., Kouba D., Mošna Z., Podolská K., Potužníková K., Šindelářová T., Chum J. and Rusz J. (2021) Ionosphere Influenced From Lower-Lying Atmospheric Regions. Front. Astron. Space Sci. 8:651445. doi: 10.3389/fspas.2021.651445

Koucká Knížová, P., Podolská, K., Potužníková, K., Kouba, D., Mošna, Z., Boška, J., and Kozubek, M. (2020). Evidence of vertical coupling: meteorological storm Fabienne on 23 September 2018 and its related effects observed up to the ionosphere.Ann. Geophys. 38, 73–93. doi: 10.5194/angeo-38-73-2020

Koucká Knížová, P., Georgieva, K., Mošna, Z., Kozubek, M., Kouba, D., Kirov, B., Potužníková, K., and Boška, J. (2018). Solar signals detected within neutral atmospheric and ionospheric parameters, J. Atmos. Sol.-Terr. Phys., 171, 147–156. doi: 10.1016/j.jastp.2017.12.003

Koucká Knížová, P., Mošna, Z., Kouba, D., Potužníková, K., and Boška, J. (2015). Influence of meteorological systems on the ionosphere over Europe. J. Atmos. Sol.-Terr. Phys. 136, 244-250. doi: 10.1016/j.jastp.2015.07.017

Podolská, K., Koucká Knížová, P., Chum, J., Kozubek, M., Burešová, D. Analysis of Relationship Between Ionospheric and Solar Parameters Using Graphical Models. emJournal of Geophysical Research: Space Physics. /em 2021, 126(5), e2020JA029063. ISSN 2169-9380. E-ISSN 2169-9402

Detecting Common Origin of Atmospheric Electric Responses during SEP

Tonev P.T.

Space Research and Technology Institute BAS, Sofia, Bulgaria, e-mail: ptonev@bas.bg

Abstract.
Experimental investigations of the electric response of atmospheric regions at different latitudes during SEP systematically demonstrate for decades peculiar behavior of electric fields and currents, together with conductivity: these have extremely large and untypical variations. Here four such experiments in mesosphere, in stratosphere, and at surface, at high and low latitudes, are interpreted. These are: *i*) rocket-borne measurements of vertical electric field E_z in middle atmosphere at latitude 58.5°S during the major SEP 19-22 October 1989 accompanied by strong geomagnetic storm which show extremely large E_z~10 V/m in mesosphere; *ii*) balloon-borne measurements in auroral stratosphere (31-33 km) during GLE 69 with unusually large variations and reversals of E_z; *iii*) measurements of E_z at surface, both at: *a*) high, and *b*) low latitudes also demonstrating extremely large variations and change of its sign. It is shown here that results in case (*i*) are related to strong reduction of conductivity, seemingly due to formation and growth of aerosol particles during SEP. The specific behavior of electric fields and currents in the rest cases (*ii*, *iii*) can be considered as result of effective coupling between atmospheric regions at different altitudes and latitudes. The origin of perturbations anywhere is presented by SEP driven processes in mesosphere at high latitudes.

Experiments demonstrating effects of SEP on atmospheric electric characteristics

The aim of this paper is to give hypothetical explanation of the effects of major solar proton events (SPEs) on atmospheric electrical characteristics in different atmospheric regions (in mesosphere, stratosphere, and at ground level) which have been experimentally observed during several decades. We consider four experimental cases demonstrating extremely strong and unusual electric response in these regions at high and auroral latitudes (cases *A*-*C* given below), as well as at surface at low latitudes - case *D*. A short description follows:

Case *A*. During SPE on 19-22 October 1989 the profile of vertical electric field E_z is obtained in a rocket experiment at latitude 58.5°S over Southern Indian Ocean, on 21 October at 19:31 UT (Zadorozhny et al., 1998) when also strong geomagnetic storm takes place with index Kp=8 at the time of flight (during this day Kp reaches 8+). The E_z profile is shown in Fig.1a by thick line 1. E_z reaches extremely high values in mesosphere and upper stratosphere: E_z=+12.2 V/m at altitude z=58 km, and E_z= –9.7 V/m at z=46 km. Another striking fact is the change of sign of the electric field E_z: it points upwards above 50 km, and downwards below that height. There is no satisfying explanation of these features. For comparison, by usual conductivities close to 50 km, 2 - 6 $\times 10^{-11}$ S/m, and fair-weather current -2 pA/m^2 Ez should be about –100 mV/m, i.e. at least two orders of magnitude smaller, and even well below that if accept that conductivity σ enhances due to strong impact ionization during SPE. It should be noted that the electric field peak values E_{zpeak} observed are the biggest ever measured in many tens of similar rocket experiments (Zadorozhny et al, 1998).

Case *B*. Balloon-borne measurements of electric characteristics in Antarctic stratosphere (31-33 km) on 20 January 2005 are in coincidence with SPE of very hard spectrum (GLE 69) (*Kokorowski et al., 2006*). During the day the balloon coordinates changes from (70.9°S, 10.9°W) to (71.4°S, 21.5°W). The geomagnetic conditions during SPE are: *i*) quiet from the SPE onset at t_0=06:51 UT until t_1=14:00 UT; *ii*) geomagnetic activity has an increase from 14:00 UT till the end of day; *iii*) strong geomagnetic substorm took place after t_2=15:54 UT. At times t_1 and t_2 also the protons of energies <5 MeV have sudden increase according to GOES-

10 data for the proton flux (*Kokorowski et al.,* 2006). The observed variations of vertical electric field E_z and of vertical current $J_z=\sigma E_z$ during the day are shown in Fig.2a,b. For the first ~1.5 hours after t_0 E_z is close to zero. Then, until time t_1 $E_z<0$ becomes unusually large, so that the related current J_z exceeds the nominal fair-weather current J_{fw} more than three times. At time t_1 E_z jumps to about zero intensity and remains such until time t_2. At t_2 E_z has another jump to large positive values such that J_z is well above J_{fw}, but now it points upwards until the end of the day. These features remain unexplained.

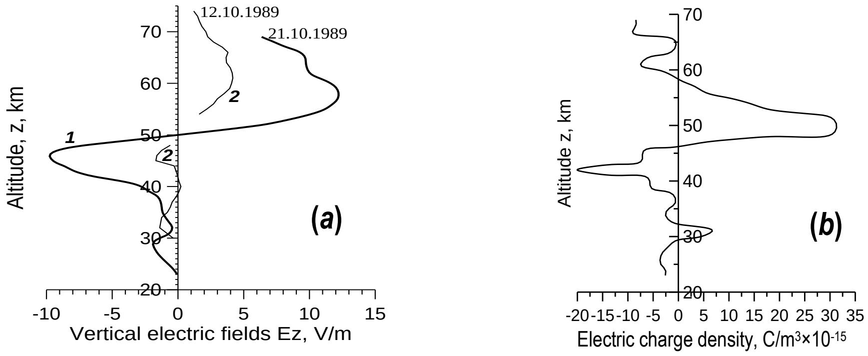

*Fig.1. Profile of vertical electric field E_z from rocket-borne data at latitude 58.5° (Indian Ocean) on 21.10.1989, 19:31 UT during major SPE (GLE 69 event) and strong geomagnetic storm with Kp=8 (Zadorozhny et al., 1998) (**a**). Profile of the electric charge density $\rho(z)$ derived from the profile of Ez by the use of Gauss's law (**b**).*

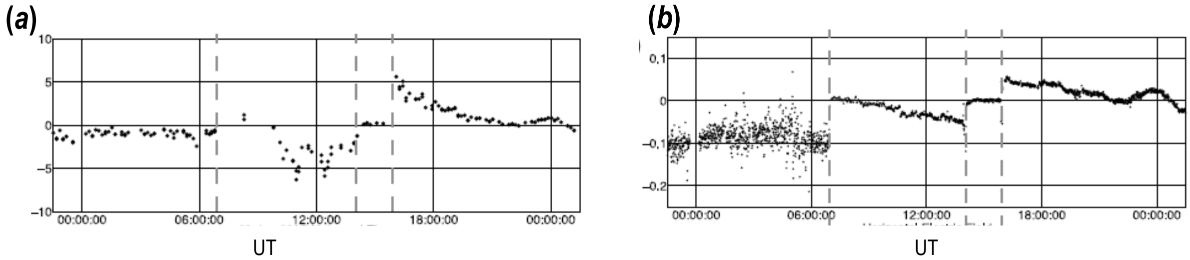

Fig.2. Time variations of the vertical electric field E_z (a) and vertical electric current density J_z (b) at 31-33 km altitude during GLE 69 (Kokorowski et al., 2006). Dashed vertical lines correspond to times: t_0=06:51 of SPE onset, t_1=14:00 UT, and t_2=15:54 UT.

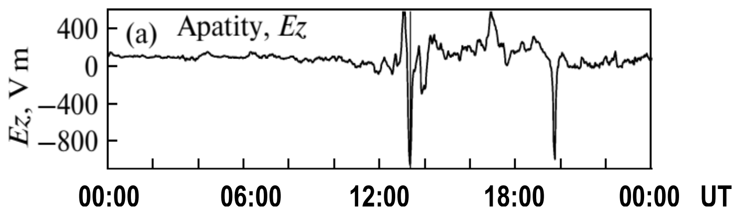

Fig.3. Time variations of the atmospheric electric field E_z at ground level in Apatity during SPE on 14 April 2001 (Shumilov et al., 2015).

Case *C*. The response of the atmospheric electric field at surface (AEF) E_z (here downward direction is accepted to be positive) in Apatity, Russia (67.3°N, 33.2°E) at geomagnetic latitude +63.8° has been examined by *Shumilov et al.* (2015) to three SPE in 2001 of GLE type: on 14.04, 18.04, and 04.11, respectively. Fig.3 shows variations of AEF E_z during SPE on 14 April 2001. The time period from t_1=14:10 UT (at the rise phase of SPE) is considered, since after time t_1 the effect of this last on E_z dominates over other factors which affect AEF E_z before t_1.

AEF E_z reaches its first maximum E_z ~330 V/m at 14:15 UT. Then, variations of E_z are close to 100-150 V/m for about two hours. After 16:40 UT AEF E_z increases to its absolute peak value of almost 600 V/m reached at 17:50 UT. Later E_z varies within limits 0-300 V/m until 19:30 UT, and after that it has a sharp jump to large negative value (more than 1 kV/m) reached at 19:45 UT. After this peak, until the end of the day E_z varies between 0 and 100 V/m most of time, although sometimes E_z becomes negative.

Case *D*. Response of AEF E_z measured at surface at low latitudes to intense SPEs, which have significant proton flux above 100 MeV, is studied in CASLEO, Argentine (31.8°S, 69.3°W) at 2552 m altitude (*Tacza et al.*, 2018). The proton cutoff rigidity at CASLEO is 9.8 GV. Measurements of AEF E_z at surface are conducted during 15 SPEs in the time period from 21 March 2011 until 18 April 2014. Solar proton events are only included in the experiment which satisfy requirements for fair-weather conditions (no lightning activity or strong wind are present) and for low geomagnetic activity (Kp<4). The fluence of these 15 SPEs is within the limits 2.8×10^3 - 3.2×10^5 protons cm^{-2} day^{-1} sr^{-1}. SPE on 17 May 2012 with the highest fluence is marked here as SPE*. Average deviation ΔE_z of AEF E_z from the monthly standard diurnal curve for the AEF is examined with following results:

Time from SPE onset, hours	0 - 3	3 - 6	6 - 9	9 - 12	12 - 15	15 - 18	18 - 21
ΔE_z, V/m	2.0	8.9	6.8	7.5	7.2	5.0	-1.8

E_z has well expressed positive deviation (up to ~15%) during first 18 hours, and only small negative deviation during the succeeding three hours. These deviations are significant. Particularly for SPE* with the largest fluence (on 17 May 2012) the deviation ΔE_z is also significant, however it behaves otherwise in time, as demonstrated in Fig.4. Variations of E_z (shown by black curve) are compared to the monthly standard AEF curve. As opposed to the common case, AEF E_z shows first (for 4.5 hours) a negative deviation (up to ~15%) from the monthly standard curve, and then a positive deviation (up to ~40%) for the next 7 hours.

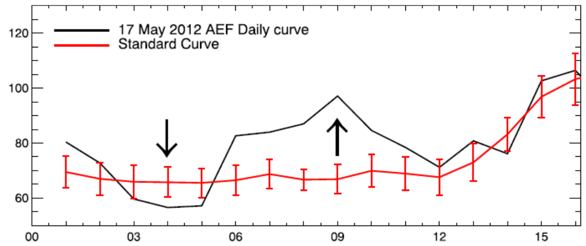

Fig.4. AEF Ez hourly values for the day of SPE (black curve) and the monthly standard curve (red) with respective error bars of one standard deviation (1σ) (Tacza et al., 2018).

Unambiguously, SPEs causes significant deviations of AEF E_z from its average value. Because of the high cutoff rigidity (9.8 GV) these deviations hardly can be explained by a direct effect of energetic protons. Cobb (1967) observes similar AEF response at low latitudes to solar flares (which seemingly have produced SEP events).

Interpretation of experimental results in case *A*

The stopping altitude z_{ps} of energetic protons entering the atmosphere depends by quasi-logarithmic law on their initial energy E_p, as shown below:

E_p, MeV	0.3	1	5	10	30	50	100
z_{ps}, km	100	89	72	63	48	39	30

Any proton which penetrates into the middle atmosphere injects an elementary positive charge $q_e=1.6\times10^{-19}$ C which cannot leave the atmosphere since its carriers have no sufficient energy to enter the magnetosphere. Thus, uncompensated positive spatial charge is being accumulated in the atmosphere during a SPE. This charge would remain uncompensated until a precipitation of electrons of the same quantity which would neutralize the atmosphere. While not neutralized the uncompensated positive charges would redistribute within the atmosphere in order to reach balance. In a case of undisturbed conductivity, these charges would run upwards to the base of the magnetosphere (~150 km) where they would distribute evenly, with no contribution to atmospheric electrical characteristics. However, it is demonstrated here that this is not always the case, because of strong conductivity disturbance in middle atmosphere at high latitudes related to formation and growth of aerosol particles. Enhancement of stratospheric aerosol due to SPEs has been observed (*Shumilov et al*., 1996).

The specific E_z profile in Fig.1a indicates for presence of layers of positive, as well as negative spatial charges of large density ρ. These last are estimated here from the Gauss's law div$\mathbf{E}=\rho/\varepsilon_0$, where $\mathbf{E}$ is the electric field, $\varepsilon_0=8.85\times10^{-12}$ F/m is permittivity. dE_z/dz is the only significant term in div$\mathbf{E}$, hence, the charge density ρ is determined as

$$\rho = \varepsilon_0 dE_z/dz. \tag{1}$$

Fig.1b demonstrates the profile of ρ obtained from the profile of E_z shown in Fig.1a. Further we analyze the main layer L_P of positive charge around 50 km and the columnar positive charge Q_{LP} in it. Layer L_P is hypothetically fed by uncompensated positive charges injected together with energetic protons during SPE. This layer is assumed to be in quasi-steady state at time of the rocket experiment since: i) any precipitations of protons or electrons from the magnetosphere would have no contribution to L_P; *ii*) the decay of proton flux is monotonic and stably slow for many hours before and after the experiment: only ~7% per hour, as follows from energetic proton flux data by GOES-7 (*Marvin and Gorney,* 1992). In quasi-steady state the conductivity in layer L_P satisfies the equation:

$$Q_{LP}/t_R = J_{prot}\ , \tag{2}$$

where $J_{prot}(z) = q_e F_{prot}(z)$ is the source current into L_P formed by the uncompensated positive charges newly injected by stopping protons; $F_{prot}(z)$ is the flux of protons whose stopping altitude is z; $t_R(z)$ is the charge relaxation time at altitude z: $t_R(z) = \varepsilon_0/\sigma(z)$. The source current J_{prot} into the layer is obtained from GOES-7 data for the energetic proton flux (*Marvin and Gorney,* 1992), by assumption of identity between proton flux at the top of atmosphere (~100 km) and that measured at GOES-7 (this assumption is used also by other authors). With account to the results of *Rodger et al.,* (2006) for proton cutoff rigidity as function of Kp index, all protons of energies >1 MeV enter the atmosphere by Kp=8 at the geomagnetic latitude of the rocket experiment, $\Lambda=-62.7°$.

With columnar charge density Q_{LP} in layer L_P, Q_{LP}~10^{-10} Cm^{-2} and source current J_{prot}~10^{-14} Am^{-2} into L_P, the estimation of conductivity σ_{LP} within layer L_P (47-58 km) yields:

$$\sigma_{LP} = J_{prot}\varepsilon_0 / Q_{LP} \sim 10^{-15}\ \text{S/m} \tag{3}$$

This is extremely low conductivity by which fast relaxation of the charge Q_{LP} would be avoid. It could be hypothetically achieved by presence of aerosol particles of needed density and size. For example, extreme reduction of conductivity in a noctilucent cloud in summer mesopause is found by *Holzworth and Goldberg* (2004).

The estimation of columnar resistance r_L of the layer L_P 47-58 km of thickness Δz=11 km yields $r_{LP}= \Delta z/\sigma_{LP}$ ~10^{19} Ωm^2 - more than one order of magnitude larger than the columnar resistance r_0 of region 0 - 20 km which is the total resistance under by undisturbed conditions.

These results demonstrate the following structure of the electrical ionosphere-surface link at high formed until the rocket experiment. The layer L_P of positive spatial charge around the altitude z_B=50 km is formed, where altitude z_B separates regions of upward electric field E_z above z_B and downward E_z below z_B. Layer L_P contains large uncompensated positive spatial electric charge Q_{LP} fed by arriving protons and relaxing through the electric currents J_U above z_B (upward), and J_L below z_B (downward) as shown in Fig.5. Also, altitude z_{PN}=58 km separates layer L_P and an upper layer L_N of negative spatial charge which is induced due to the conductivity gradient. The electric currents J_U and J_D are superimposed to the downward fair-weather current J_{fw} which is ~2 pA.m^{-2} under quiet conditions, but can be strongly diminished during SPE due to reduced conductivity σ_M in middle atmosphere. Respectively, three columnar resistances: *i*) r_{PL} between ~30 km and altitude z_B, *ii*) r_{PU} between z_B and z_{PN}, and *iii*) r_N above z_{PN} gradually increase during SPE together with growth of aerosol particles.

Electric field variations in regions below layer L_P are determined by the vertical current J_z=J_D+J_{fw}, and thus of interplay between group of parameters PARS: the altitudes z_B and z_{PN}, the charge Q_{LP}, and resistances r_{PL}, r_{PU} and r_N. The experiment is conducted long time (54.5 hours) after the onset of SPE when aerosol characteristics determine very large resistances r_{PL} and r_{PU}, and thus, negligible currents J_{fw}, J_D and J_z. In opposite, at earlier phases of SPE the parameters PARS could determine increase of J_z compared to its value before SPE.

Interpretation of experimental results in cases *B* and *C*

We consider first case *B*. From time t_0=06:51 until t_1~08:40 UT resistances r_{PL}, r_{PU} and r_N are too small to affect the vertical electric field E_z; yet, due to highly increased conductivity (up to 20 times), E_z~0. At time period t_1 - t_2 resistances r_{PL} and r_{PU} enlarge moderately; changes of parameters PARS lead to increase of current J_D and decrease of J_{fw}, so that current J_z~J_D increases as result. The jump of E_z from large negative values to ~0 at t_2=14:00 UT is possibly caused by sudden enlargement of resistance r_{PU} + r_N due to change in protons <5 MeV. The second jump at t_3=15:56 UT (the substorm onset) may be caused by strong EEP, eventually leading to change of polarity of layer L_P, and hence, of current J_D.

Variations of AEF E_z in case *C* have similarity with those in case *B*: they both are controlled by electric current J_D.

Interpretation of experimental results in case *D*

The uncompensated positive charge in layer L_P at high latitudes is redistributed to lower latitudes through currents in global atmospheric electrical circuit (GEC) as represented in Fig.5: these currents are J_D (downward, at high latitudes), J_S (through surface), and J_{LT} which is an upward current at lower latitudes and contributes to the positive spatial charge Q_{TC}

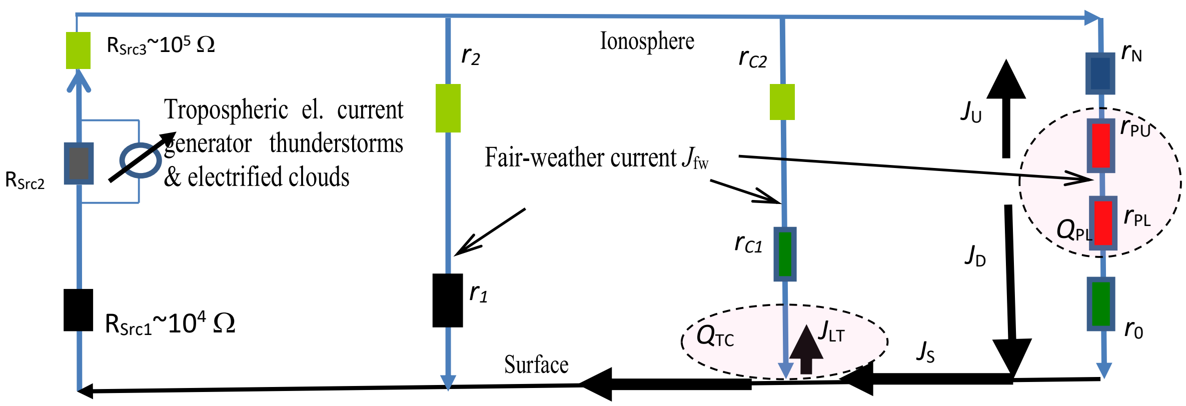

Fig.5. Model scheme of GEC affected by SEP. The four vertical links connecting ionosphere and surface represent currents which flow in regions: i) of tropospheric electric generator; ii) of fair-weather conditions at low and middle latitudes; iii) in particular, of CASLEO location; iv) at high and auroral latitudes where SEP lead to modification of parameters PARS.

induced in the boundary layer. Current J_{LT} is proportional to J_D which is determined by parameters PARS. Each of the 15 SPEs in case *D* has much smaller fluence than that in case *A* in time interval from SPE onset until the experiment. That is why the electric current J_D during these 15 SPEs is not reduced to ~0 (as in case *A* due to extreme r_{PL}+r_{PU}+r_N).

The fair-weather current J_{fw} at low latitudes increases during SPE (changes by ΔJ_{fw}>0) consistently with its decrease at high latitudes. The 14 SPEs whose fluence is less than that of SPE* at their earlier phase (within ~21 hours from their onset) cause relatively smaller increase of resistances r_{PL}, r_{PU} and r_N, and produce smaller positive charge Q_{LP} in layer L_P, compared to SPE*, thus determining relatively smaller currents J_D, respectively J_{LT}. For these SPEs $J_{LT} < \Delta J_{fw}$. This determines positive deviation of AEF E_z at low latitudes, since there J_z=J_{fw}+J_{LT}. The short and small negative deviation of E_z at a latter phase corresponds to restoration of characteristics of high-latitudinal atmosphere taking part before the SPE onset.

The results in Fig.4 related to SPE* correspond to generation of relatively large currents J_D and J_{LT} in an initial phase of SPE*, so that $J_{LT}>\Delta J_{fw}$, and hence the deviation of the current J_z=J_{fw}+J_{LT} is negative in that phase. On the other hand, current J_{LT} causes significant enhancement of the charge Q_{TC}. At a latter phase J_D diminishes, possibly, as result of increase of the resistance r_{PL}+r_{PU}+r_N well above r_0, and current J_{LT} changes its polarity (becomes negative) consistently with decrease of charge Q_{TC} to its initial magnitude. This determines an increase of the total current J_z=J_{fw}+J_{LT} for the time of restoration of parameters of the link corresponding to high latitudes.

Conclusions

1. Large electric fields ~10 V/m measured in mesosphere at auroral latitudes during major SEP are hypothetically considered as result of development of aerosol layers and injection of uncompensated positive electric charge.
2. Processes of aerosol growth in mesosphere and upper stratosphere at high latitudes driven by SEP cause severe decrease of conductivity and control the redistribution of uncompensated positive charge within the atmosphere.
3. Response of atmospheric regions at different latitudes to major SEP is realized through effective coupling between them which is controlled by processes in the mesosphere at high and auroral latitudes.

References

Cobb, W.E. (1967). Evidence of a solar influence on the atmospheric electric elements at Mauna Loa observatory, Monthly weather review, 95, n.12, 1967, 905-911.

Holzworth, R.H. and Goldberg, R.A. (2004). Electric field measurements in noctilucent clouds. J. Geophys. Res. 109: doi: 10.1029/2003JD004468.

Kokorowski, M., Sample, J.G., et al. (2006). Rapid fluctuations of stratospheric electric field following a solar energetic particle event, Geophys. Res. Lett., 33, L20105.

Marvin D.C., D.J. Gorney (1992). Solar Proton Events of **1989:** Effects on Spacecraft Solar Arrays, Aerospace Report No. TR-0091(6945-01)-2.

Rodger, C. J., M. A. Clilverd, P. T. Verronen, T. Ulich, M. J. Jarvis, and E.Turunen (2006), Dynamic geomagnetic rigidity cutoff variations during asolar proton event, J. Geophys. Res., 111, A04222, doi:10.1029/2005JA011395.

Shumilov, O. I., E. A. Kasatkina, K. Henriksen, E. V. Vashenyuk (1996). Enhancement of stratospheric aerosols after solar proton event, Ann. Geophysicae 14, 1119-1123 (1996).

Shumilov O.I., Kasatkina E.A., A. V. Frank-Kamenetsky (2015). Effects of Extraordinary Solar Cosmic Ray Events on Variations in the Atmospheric Electric Field at High Latitudes, Geomag. Aeron., 2015, Vol. 55, No. 5, pp. 666–674 doi: 10.1134/S0016793215050151.

Tacza, J., Raulin, J.-P., Mendonca, R. R. S., Makhmutov, V. S., Marun, A., Fernandez, G. (2018). Solar effects on the atmospheric electric field during 2010–2015 at low latitudes. J. Geophys. Res: Atmospheres, 123 https://doi.org/10.1029/2018JD029121

Zadorozhny, A.M., A.A. Tyutin (1998). Effects of geomagnetic activity on the mesospheric electric fields, Ann. Geophys. 16, 1544–1551, 1998.

Geomagnetic Field's Contribution to the Global Rise of Air Surface Temperature

Velichkova T.P.[1,2], Kilifarska N.A.[2]

[1] National Institute of Geophysics, Geodesy and Geography
Bulgarian Academy of Sciences, Sofia, Bulgaria
[2] Climate, Atmosphere and Water Research Institute,
Bulgarian Academy of Sciences
E-mail: tsvelichkova@geophys.bas.bg, natalya_kilifarska@yahoo.co.uk

Abstract.

CO_2 is recognized as the greatest contributor to the global warming observed since the mid-20th century. Being a long-lived gas, the spatial distribution of CO_2 is largely homogenized by the global atmospheric circulation – particularly near the tropopause, where the effective radiative temperature of all atmospheric gases is very low and their impact in the greenhouse effect is largest. This spatially homogeneous forcing (inserted on the climate system) is not able, however, to explain the regional specificity of temperature evolution, observed during the period under review (1900-2010). Consequently, it is quite probable that the regional variability of the near surface temperature is determined by the action of some unknown additional forcing.

The current investigation demonstrates that the geomagnetic field could be a significant contributor not only to the regional variations but also to the global climatic changes. Analysis of the impact of globally averaged CO_2 density and geomagnetic field intensity into the global surface temperature variability reveals that the latter could be an alternative explanation of the global raise of near surface temperature (typically attributed to the increased anthropogenic forcing) – at least for the analysed 110 years.

Introduction

The global air surface temperature (T_{2m}) has been increasing substantially in the last few decades [IPCC, 2021]. The evidences of such a warming could be found in the field observations [Jones et al., 2012] and the model data [Lacis et al., 2010; Miller, 2014]. Many authors attributed the rise of global temperatures to the accumulation of greenhouse-gas emissions in the atmosphere due to human activity [Hansen et al., 2007; IPCC, 2007].

On other hand, model experiments of Schmidt et al [2010] show that the impact of CO_2 on planetary warming varies between 19 and 24%. In comparison, numerical experiments [Spencer & Braswell, 1997] and satellite measurements [Inamdar et al., 2004] demonstrate that about 90% of the greenhouse effect of the whole atmospheric water vapour is due to the upper tropospheric humidity. Moreover, the reduction of the positive trend in surface temperature, since the beginning of 21^{-th} century, does not correspond to the continuously increasing CO_2 density. For this reason, the search for alternative explanatory factors of global warming still continues.

The idea about geomagnetic influence on climate appears in the second half of 20-th century [Elsasser, 1956]. Furthermore, comparison of paleomagnetic and paleoclimatic records leads some authors to the conclusion that strengthening of geomagnetic field is accompanied by climate cooling [Valet & Meynadier, 1993; Worm, 1997; Courtillot et al., 2007; Knudsen & Riisager, 2009; Kitaba et al., 2013]. Despite some discrepancy with the results of other researches, stating just the opposite [Wollin et al., 1971; Nurgaliev, 1991; Butchvarova & Kovacheva, 1993; Gallet et al., 2005;], we decided to analyse the contemporary observational records of geomagnetic field and air surface temperature.

Data and methods

We have used average annual values of carbon dioxide from the Mauna Loa Observatory in Hawaii – since 1958. For the first half of 20-th century have been used historical records acquired from the Law Dome DE08, DE08-2, and DSS ice cores. For geomagnetic field we have taken the annual data from the International Geomagnetic Reference Field model. The gridded monthly data for the temperature at 2 m above the Earth's surface, for the period 1900-2010, is taken from ERA 20 century reanalysis (ERA20C).

The method used for data analyses is a nonlinear regression technic, adopting non-linear functional dependences between studied variables. The nonlinear regression coefficients (R) are calculated as the square root of the difference between the total variability of the dependent variable and the error of the regression model, normalized to the total variability. The square of the regression coefficient (R^2), multiplied by 100, illustrates the percentage of variability of the dependent variable, which the non-linear regression model is able to describe. The accuracy of the models is based on a number of criteria, which we will describe in the next paragraphs.

Results

We have examined the relationships of carbon dioxide density (CO_2) and geomagnetic field intensity (F) with the globally averaged near surface temperature T_{2m}, during the period 1900-2010. For the T_{2m} dependence on CO_2 is suggested a second order polynomial (Eq. 1), while the T_{2m} relation to F is modeled by a third order expression (Eq. 2):

$$\boldsymbol{T_2\,m = a_0 + a_1 * CO_2 + a_2 * (CO_2)^2} \qquad (\mathbf{1})$$

$$\boldsymbol{T_2 m = a_0 + a_1 * F + a_2 * \ (F)^2 + a_3 * (F)^3} \qquad (\mathbf{2})$$

where coefficients $\boldsymbol{a_i}$ are regression coefficients, determined by minimisation of the model's error, applying the least square criterion and the *Levenberg-Marquardt* algorithm.

The first formal criterion for model's goodness shows that both regression coefficients are identical, having the value R=0.87. This means that each regression model explain 76% of the total temperature variability (i.e. R_2*100). This result implies that the geomagnetic field could be an alternative explanation of the observed warming trend in the surface temperature (since the beginning of 20-th century).

The scatter plots of T_{2m} with the CO_2 density and the geomagnetic field (blue dots), together with modelled functional dependencies (red curves) are shown in in Fig. 1 and Fig. 2. The figures illustrate fairly well the non-stationarity of the near surface air temperature relation with average CO_2 density and geomagnetic field intensity – especially well illustrated in Fig. 2. Moreover, the Fig. 2 reveals that strengthening of geomagnetic intensity is accompanied by cooling of the surface temperature. This result is in a good correspondence with the previous findings of [Valet and Meynadier, 1993; Worm, 1997; Knudsen and Riisager, 2009; Kitaba et al., 2013], based on the analyses of paleomagnetic and paleoclimatic data records.

Another diagnostic of model's goodness is the normal distribution of errors (residuals, i.e. measured – modelled values). There are different ways to estimate normality of errors' distribution. One of them is examination of histogram of model's residuals. In Fig. 3 and Fig.4 are presented normal probability plots of models' errors. On the x-axis are plotted observed model's residuals (i.e. the differences between the measured and modelled values of T_{2m}) while on the y-axis are plotted standardized values of the expected normally distributed errors. The proposed model is good when all values follow a straight line. If the model's errors are not normally distributed, then they will form an S shape pattern. Consequently, the Figs. 3 and 4 illustrate the fulfilment of the second requirement for model's goodness – i.e. normally distributed errors.

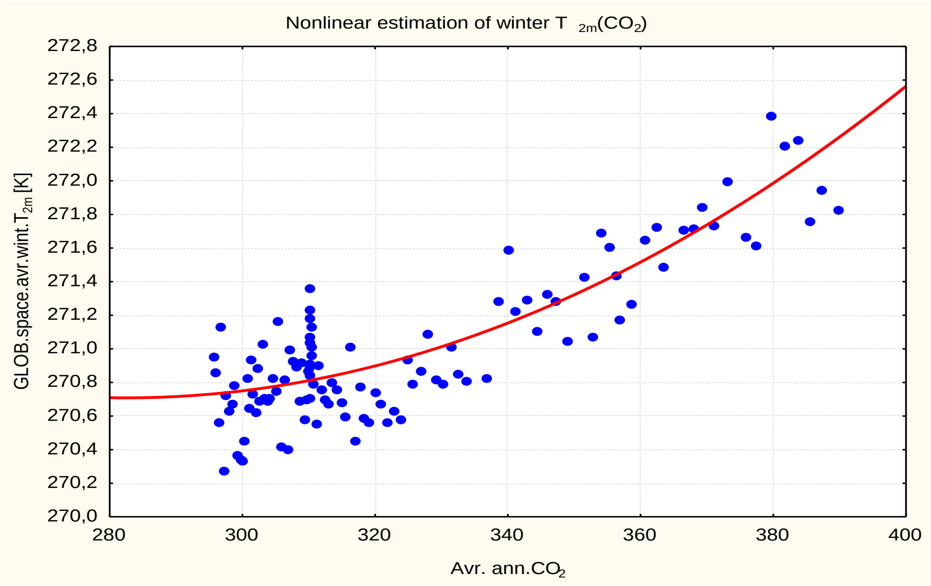

Fig.1. Scatterplot of CO_2 density and the global air surface temperature T_{2m} (spatially averaged) within the period 1900-2010. The functional dependency described by Eq.1 is presented by the red curve.

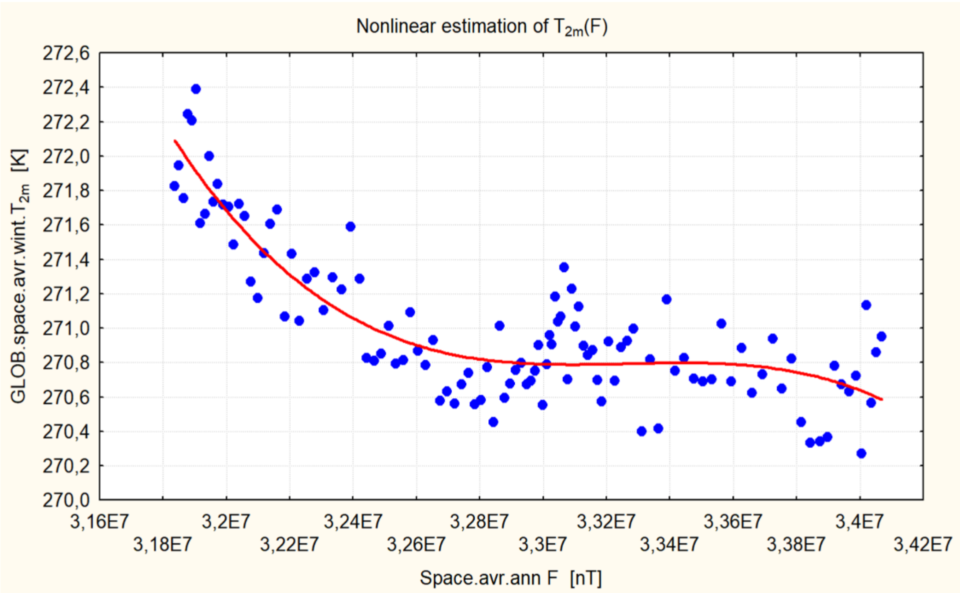

Fig.2. Scatterplot of geomagnetic field intensity and the global surface temperature T_{2m} (spatially averaged) within time interval 1900-2010 (blue dots). The functional dependency described by Eq.2 (red curve) matches fairly well the relationship between the two variables.

A third criterion for model's accuracy requires a randomness of the model's errors. The fulfilment of this criterion could be estimated by the analysis of the autocorrelation function of model's residuals. Fig.5 and Fig.6 illustrate that model's errors of each functional dependency do not auto-correlate. There are a lot of diagnostics, provided by the standard statistical packages (like STATISTICA), confirming the accuracy of our models, which have not been included in this paper. All of them, however, increase our confidence that temporal variations of geomagnetic field intensity could be an alternative explanation of detected raise of near surface temperature during 20-th and 21-st centuries.

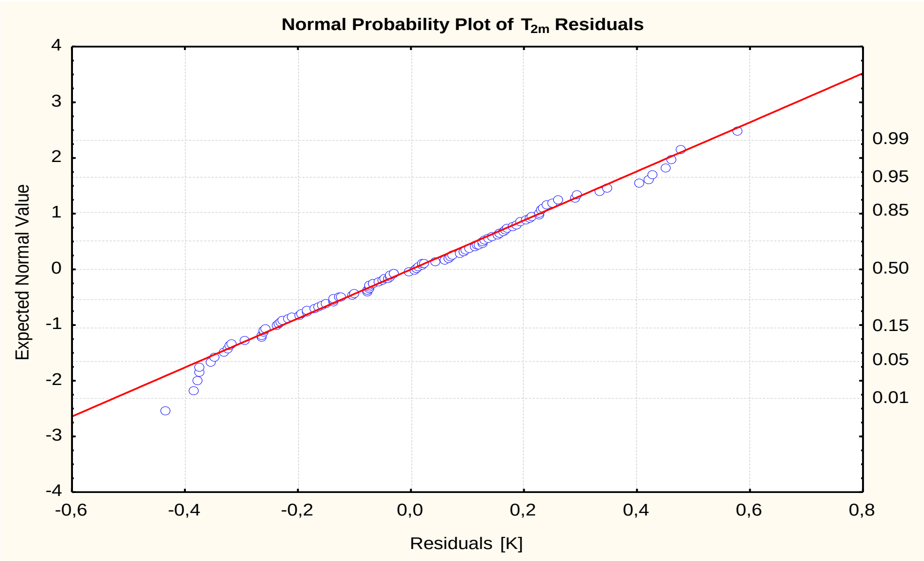

Fig.3. The normal probability plot of T_{2m} residuals for CO_2 model.

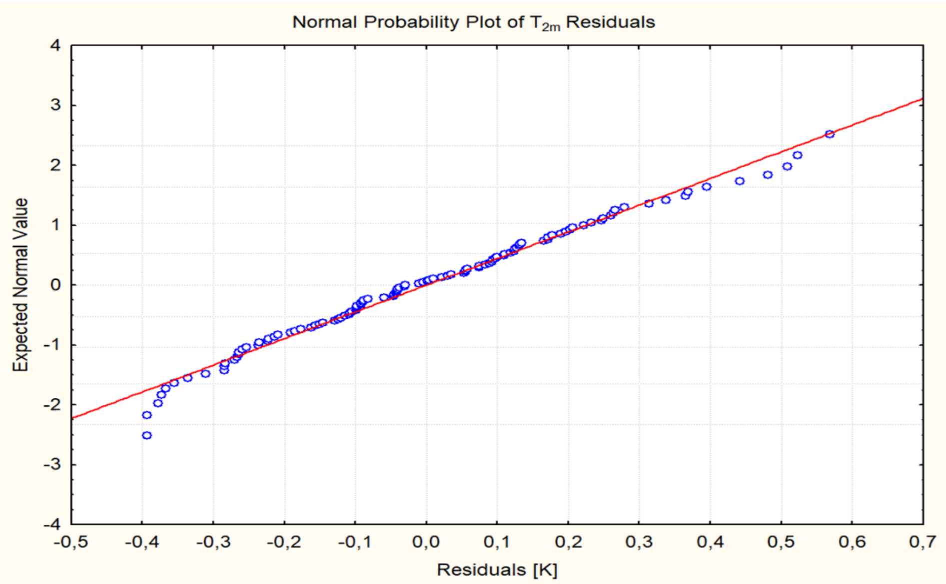

Fig.4. The normal probability plot of T_{2m} residuals for geomagnetic field model.

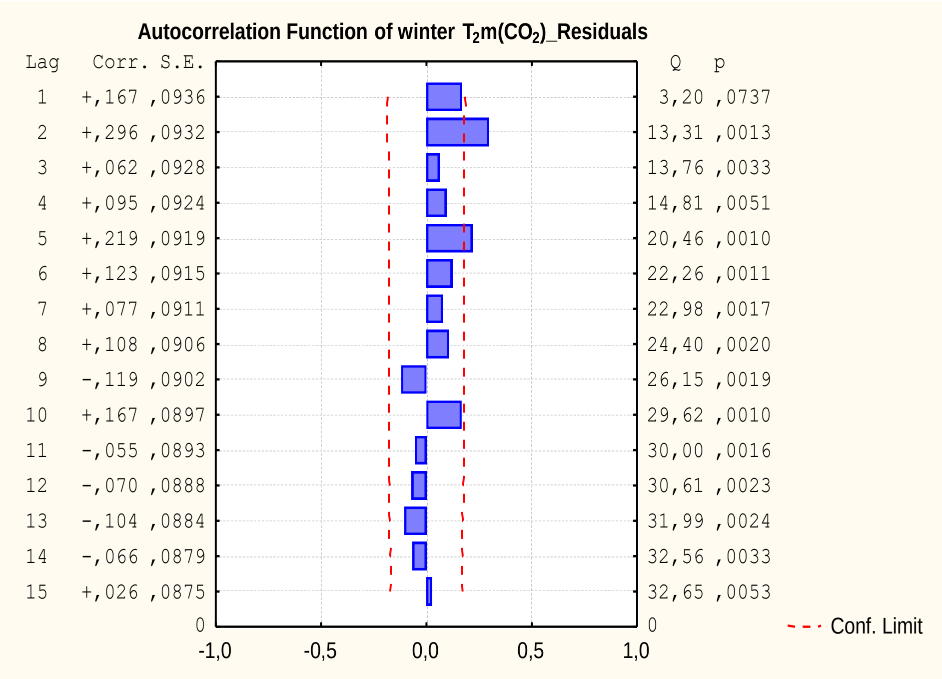

Fig.5. Autocorrelation of the model residuals $T_{2m} = f\,(CO_2)$. Model's errors do not correlate with each other, i.e. they are randomly distributed.

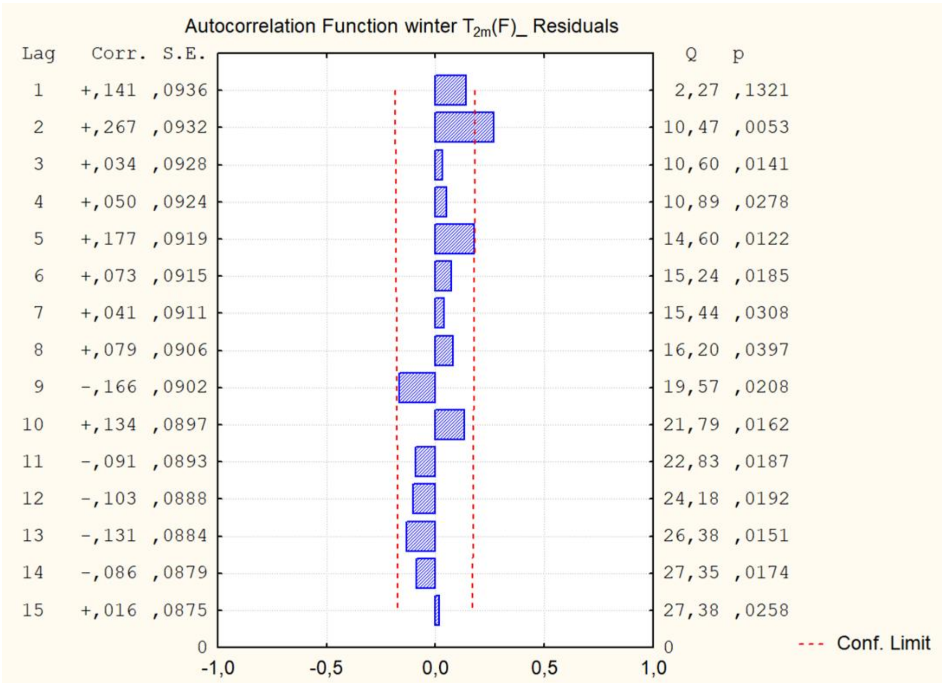

Fig.6. Autocorrelation of the model residuals $T_{2m} = f\,(F)$. Model's errors do not correlate with each other, i.e. they are randomly distributed.

Without a mechanism for geomagnetic influence on temperature, however, this statistical relation will remain only a curious result. Fortunately, recently has been proposed a mechanism of such an influence [Kilifarska et al., 2020a, b]. The hypothesis goes through the geomagnetic modulation of the intensity and depth of galactic cosmic rays (GCR) penetration in Earth's atmosphere. The heterogeneously distributed geomagnetic field acts as a lens – focusing GCR in some regions over the globe and defocusing them in others – creating in such a way a heterogeneous ionization layer in the lower stratosphere (known as Regener-Pfotzer maximum). This secondary ionization alters the lower stratospheric ozone density through activation of various ion-molecular reactions [Kilifarska, 2013]. The ozone variability at these levels impacts the near tropopause temperature and humidity, which alter the strength of greenhouse warming and near surface temperature [Kilifarska, 2012; Velichkova and Kilifarska, 2019; Velichkova and Kilifarska, 2020].

Conclusions

The non-linear analysis of the global air surface temperature (T_{2m}), CO_2 density and geomagnetic field intensity during the period 1900-2010 reveals an alternative explanation of the recent global warming. We found that CO_2 and geomagnetic field statistical models describes equivalent part of the total T_{2m} variability (namely 76%). The mechanism of geomagnetic influence is described by a consecutive chain of relations between: (i) heterogeneous geomagnetic field intensity, (ii) secondary ionisation in the lower stratosphere, which alters the ozone density there, (iii) the near tropopause temperature and humidity, which are projected on the surface through modulation of the greenhouse effect.

This result indicates that the factors and mechanisms of the observed raise of global temperature need more careful examination, especially in the context of the regionality of climate changes.

Acknowledgements

This work is partially supported by the Bulgarian FNI, contract DN 14/1 from 11.12.2017; Contract KP-06-N34/1 /30-09-2020 "Natural and anthropogenic factors of climate change – analyses of global and local periodical components and long-term forecasts"; and Bulgarian Ministry of Education and Science under the National Research Programme "Young scientists and postdoctoral students" approved by DCM # 577 / 17.08.2018.

References

Butchvarova V., Kovacheva M.,1993. European changes in the paleotemperature and Bulgarian rchaeomagnetic data, Bulg. Geophys. J. 19, 19 – 23.

Courtillot V, Gallet Y, Le Mouël J-L, Fluteau F, Genevey A., 2007, Are there connections between the Earth's magnetic field and climate? Earth Planet. Sci. Lett.; 253: 328–339.

Elsasser W., Ney E.P. and Winckler J.R., 1956. Cosmicray intensity and geomagnetism. Nature, 178, 1226, https: // doi.org / 10.1038 / 1781226a0

Gallet Y, Genevet A, Fluteau F., 2005, Does Earth's magnetic field secular variation control centennial climate change? Earth Planet. Sci. Lett.; 236: 339–347.

Hansen, J., Sato, M., Ruedy, R., Kharecha, P., Lacis, A. et al., 2007, Dangerous human-made interference with climate: a GISS modelE study, Atmos. Chem. Phys., 7, 2287–2312, https://doi.org/10.5194/acp-7-2287-2007, 2007.

Jones, P. D., Lister, D. H., Osborn, T. J., Harpham, C., Salmon, M., and Morice, C. P., 2012, Hemispheric and large-scale land-surface air temperature variations: An extensive revision and an update to 2010, *J. Geophys. Res.*, 117, D05127, doi:10.1029/2011JD017139.

Inamdar, A.K., Ramanathan, V., Loeb, N.G., 2004, Satellite observations of the water vapour greenhouse effect and column longwave cooling rates: Relative roles of the continuum and vibration-rotation to pure rotation bands, *J.Geophys.Res., 10, D06104, doi:10.1029/2003JD003980.*

IPCC, 2007, (Intergovernmental Panel on Climate Change), Climate Change 2007: The Physical Science Basis, edited by Solomon, S., et al., Cambridge Univ. Press, New York. 996 pp.

IPCC, 2021: Climate Change 2021: The Physical Science Basis. Contribution of Working Group I to the Sixth Assessment Report of the Intergovernmental Panel on Climate Change [Masson-Delmotte, V., P. Zhai, A. Pirani, S.L. Connors, C. Péan, S. Berger, N. Caud, Y. Chen, L. Goldfarb, M.I. Gomis, M. Huang, K. Leitzell, E. Lonnoy, J.B.R. Matthews, T.K. Maycock, T. Waterfield, O. Yelekçi, R. Yu, and B. Zhou (eds.)]. Cambridge University Press. In Press

Kilifarska, N. A., 2012, Mechanism of lower stratospheric ozone influence on climate, Int. Rev. Phys., 6, 3, 279–290.

Kilifarska, N. A., 2013, An autocatalytic cycle for ozone production in the lower stratosphere initiated by Galactic Cosmic rays, C. R. Acad. Bulg. Sci., 66, 2, 243–252.

Kilifarska, N. A., Bakhmutov, V. G. And Melnyk, G. V., 2020a, The hidden link between Earth's magnetic field and climate, Elsevier, p. 215, ISBN: 978-0-12-819346-4.

Kilifarska N.A., Bakhmutov V.G., Melnyk G.V., 2020b, Geomagnetic field's imprint on the 20-th century climate variability, Geological Society of London Spatial Publications 497, GSLSpecPub2019-38R4, https://doi.org/10.1144/SP497-2019-38.

Kitaba I., M. Hyodo, S. Katoh, D.L. Dettman, H. Sato, 2013, Midlatitude cooling caused by geomagnetic field minimum during polarity reversal, PNAS, 110, 1215–1220, https://doi.org/10.1073/pnas.1213389110.

Knudsen M.F. and P. Riisager, 2009, Is there a link between Earth's magnetic field and low-latitude precipitation?, Geology 37, 71–74. https://doi.org/10.1130/G25238A.1.

Lacis, A. A., Schmidt, G. A., Rind, R. & Ruedy, R. A., 2010, Atmospheric CO2: Principal Knob Governing Earth's Temperature. Science 330, 356–359.

Miller, R. L., et al., 2014, CMIP5 historical simulations (1850–2012) with GISS ModelE2, *J. Adv. Model. Earth Syst.*, 6, 441– 478, doi:10.1002/2013MS000266.

Nurgaliev, D.K., 1991. Solar activity, geomagnetic variations, and climate changes. Geomagnetism and Aeronomy 31, 14–18.

Schmidt, G.A., Ruedy, R.A., Miller, R.L., Lacis, A.A., 2010, Attribution of the present-day total greenhouse effect, *J. Geophys. Res., 115, D20106, doi:10.1029/2010JD014287*.

Spencer, R.W., Braswell, W.D., 1997, How Dry is the Tropical Free Troposphere? Implications for Global Warming Theory, *Bull. Amer. Meteor. Soc.* 78(6), 1097-1106.

Valet, J., Meynadier, L., 1993, Geomagnetic field intensity and reversals during the past four million years, Nature, 366, 234. https://doi.org/10.1038/366234a0.

Velichkova, Ts., Kilifarska, N., 2019. Lower stratospheric ozone's influence on the NAO climatic mode, Comptes rendus de l'Acade'mie bulgare des Sciences, Vol 72, No2, pp.219-225, DOI: 10.7546/CRABS.2019.02.11.

Velichkova, Tsvetelina & Kilifarska, Natalya, 2020, Inter-decadal Variations of the ENSO Climatic Mode and Lower Stratospheric Ozone. Comptes rendus de l'Acade'mie bulgare des Sciences, Vol 73, No4, pp.539-546, DOI: 10.7546/CRABS.2020.04.13.

Wollin G, Ericson DB, Ryan WBF, 1971, Magnetism of the Earth and climatic changes. Earth Planet. Sci. Lett. 1971; 12: 175–183.

Worm H.-U., 1997, A link between geomagnetic reversals and events and glaciations, Earth and Planetary Science Letters, 147, 55–67, https://doi.org/10.1016/S0012-821X(97)00008-3.

Influence of Solar Proton Events of January 2005 on the Middle Atmosphere Circulation: Southern Hemisphere

Veretenenko S.

Ioffe Institute RAS, St. Petersburg, Russia
E-mail: s.veretenenko@mail.ioffe.ru

Abstract.
Influence of Solar Proton Events (SPEs) of January 2005 on the middle atmosphere circulation in the Southern hemisphere was studied. It was found that circulation disturbances associated with these events reveal a strong dependence both on height and latitude. In the upper stratosphere (30-10 hPa), where eastern transport of air masses dominates in the whole hemisphere in summer months (December-February), a weakening of zonal eastern winds was detected at middle and high latitudes (>40ºS), whereas at lower latitudes these winds were found to strengthen. Unlike the upper stratosphere, circulation of the undisturbed lower stratosphere (100-50 hPa) in summer is characterized by eastern winds at polar and low latitudes, as well as a strong western zonal flow at middle latitudes (30-55ºS). In the course of the studied events a weakening of eastern winds was found at polar latitudes (>60ºS), with a maximum of zonal western winds being shifted about 10 degrees to the south. The detected circulation disturbances seem to be caused by changes in the radiation-thermal balance of the polar middle atmosphere which, in turn, may be associated with changes in its chemical composition due to ionization increase during solar proton intrusions.

Introduction

Solar Proton Events (SPEs) are abrupt enhancements of solar cosmic rays (mostly protons) occurring sporadically in the near-Earth space. Due to a steep energy spectrum and geomagnetic cutoff, intrusions of solar protons into the Earth’s atmosphere are usually limited by polar latitudes. However, their fluxes may be huge compared with those of galactic cosmic rays, which results in considerable increases of atmospheric ionization. Ionization changes associated with solar proton intrusions produce a large number of geophysical effects, such as variations of chemical composition of the atmosphere (ozone depletion caused by enhanced production of nitrogen and hydrogen oxides participating in catalytic cycles of ozone destruction), perturbations in the global electric circuit, changes in atmospheric transparency and cloudiness [*Miroshnichenko*, 2008]. This suggests an important part of solar cosmic rays in Sun-weather relationships. Indeed, a noticeable intensification of extratropical cyclones in the North Atlantic was detected in the course of SPEs, with energies of particles exceeding 90 MeV [*Veretenenko and Thejll*, 2004, 2005].

In the work [*Veretenenko*, 2021] an impact of strong Solar Proton Events in January 2005 on the middle atmosphere circulation was investigated. It was found that in the Northern hemisphere the studied events were accompanied by a pronounced enhancement of western winds in the latitudinal belt 50-80ºN at all the stratospheric levels. This indicated a strong intensification of the stratospheric polar vortex, which is a characteristic feature of stratosphere circulation in winter. So, the aim of this study is to investigate an impact of Solar Proton Events of January 2005 on stratospheric circulation in the Southern (summer) hemisphere.

Solar Proton Events of January 2005

A series of strong Solar Proton Events, associated with an increase of flare activity on the Sun occurred in January 2005, i.e., at the deep descending phase of the 23rd solar cycle. Integral fluxes of solar protons with energies >5, >50 and >100 MeV are shown in Fig.1a according to the GOES-11 satellite data. One can see pronounced increases of proton fluxes, with particle energies >100 MeV, on 15, 16, 17 and 20 January. The estimates according to $E = a \cdot r^{b}$, where E is proton energy in MeV, r is the path length in $g \cdot cm^{-2}$, a = 29.4, b = 0.57 [*Bazilevskaya et al.*, 2003], show that particles with energies $E \sim 100$ MeV reach stratospheric levels ~10 hPa (~30 km) losing their energy to ionization. The strongest event occurred on 20 January and was accompanied by a growth of solar proton fluxes with energies >500 MeV. Particles with such energies reach altitudes of the lower stratosphere (~15 km) and participate in nuclear interactions producing secondary particles (neutrons), which can be registered by ground-based neutron monitor (so called Ground Level Enhancement, GLE). The GLE on 20 January 2005 was the strongest event after the GLE observed on 23 February 1956.

Solar proton intrusions in January 2005 resulted in a considerable increase of ionization rate in the high-latitudinal atmosphere at altitudes above 20 km. Daily mean ionization rates at geomagnetic latitudes 60-90º are shown in Fig.1b according to the data by the international working group SOLARIS-HEPPA (https://solarisheppa.geomar.de/). One can see that the greatest ionization rates (up to ~1000 $cm^{-3} \cdot s^{-1}$) took place on 17 and 20 January in the mesosphere (~50–70 km) and the upper stratosphere (~35–40 km), respectively.

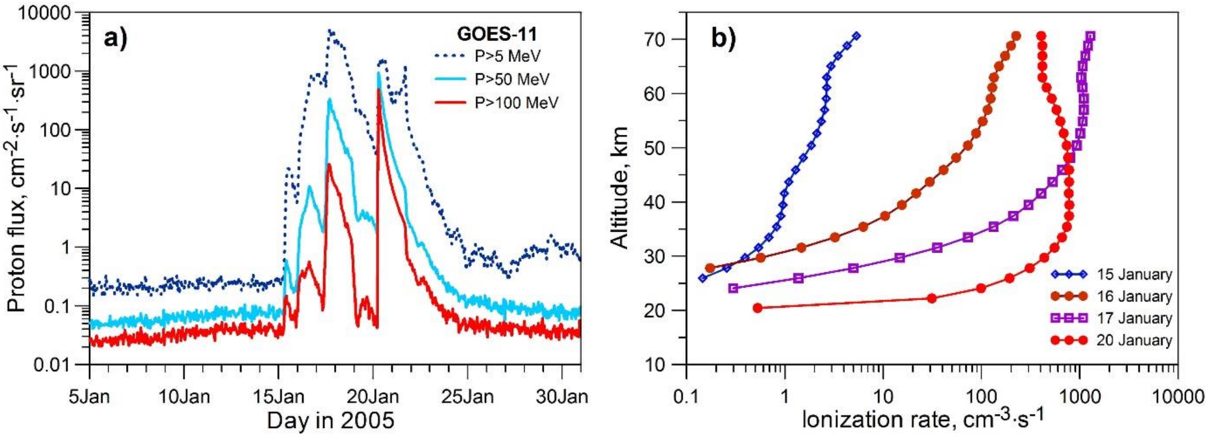

Fig.1. a) Solar proton fluxes with energies > 5, > 50 and > 100 MeV according to the GOES-11 data (https://www.swpc.noaa.gov/products/goes-proton-flux/); b) daily mean ionization rates at geomagnetic latitudes 60-90º on the days of Solar Proton Events in January2005 . (https://solarisheppa.geomar.de/solarprotonfluxes).

Peculiarities of stratospheric circulation in the Southern hemisphere in summer period

Unlike the Northern hemisphere in winter, where the polar vortex is observed in the whole stratosphere, stratospheric circulation in the Southern hemisphere in summer reveals strong altitudinal dependence. The data in Fig.2 show distributions of monthly mean values of the U-component of wind velocity (the positive direction is from west to east) at the levels 50 hPa (the lower stratosphere) and 10 hPa (the upper stratosphere) in January 2005. One can see that in the upper stratosphere strong eastern transport of air mass dominates in the whole hemisphere. This is caused by meridional temperature gradients in the summer stratosphere directed from the pole to the equator (in winter the direction of these temperature gradients is opposite, so strong western winds arise forming the stratospheric polar vortex). In the lower stratosphere, however, we can see eastern winds only at polar and low latitudes, whereas a rather strong western zonal flow takes place at middle latitudes 30-55ºS. This flow seems to arise due to persistent temperature contrasts between the icy surface of the Antarctic and the warmer ocean surface at middle latitudes, which creates temperature gradients directed to high latitudes both in winter and summer periods and influencing circulation not only in the troposphere, but apparently in the lower stratosphere too.

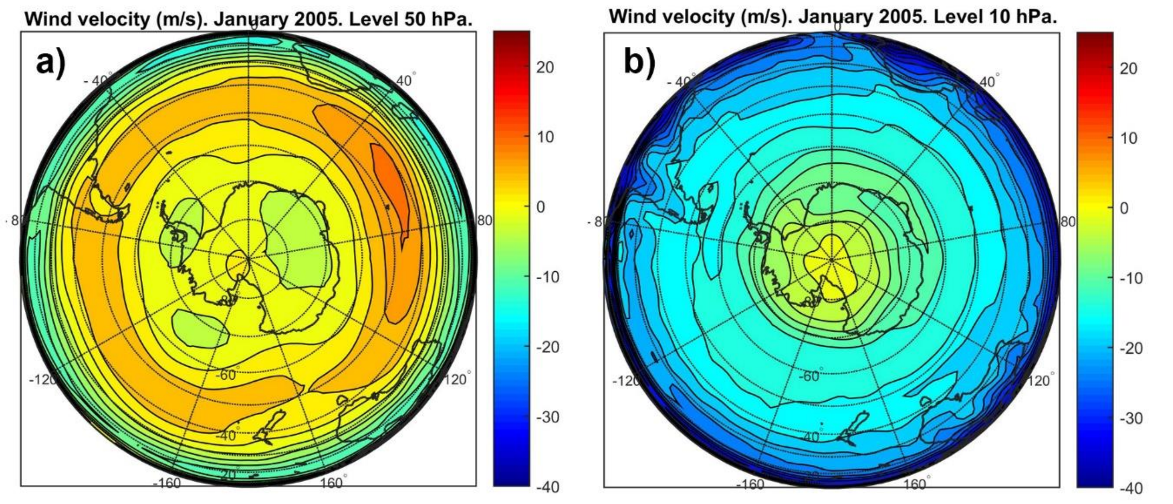

Fig.2. Monthly mean values of the U-component of wind velocity (in m·s^{-1}) in the lower stratosphere (50 hPa) and the upper stratosphere (10 hPa) in January 2005.

Effects of Solar Proton Events of January 2005 on wind velocity

Let us consider circulation changes in the course of the SPEs under study. As experimental data for the analysis, daily values of the *U*-component of wind velocity at different stratospheric levels (100, 70, 50, 30, 20 and 10 hPa) taken from the NCEP-DOE reanalysis-2 archive [*Kanamitsu et al.*, 2002] were used. Fig.3 demonstrates the charts of the *U*-component of wind velocity before the onset of the SPE series (13 January) and on the 4th day after the onset (18 January) in the upper stratosphere (the level 10 hPa). One can see a noticeable intensification of eastern winds (winds with negative *U*-values) at latitudes below 40ºS on the days of the studied SPE series (the area of wind velocities $U < -20$ m·s^{-1} (dark blue) increased markedly). At the same time, at middle and high latitudes (40-70ºS) a pronounced weakening of eastern winds took place (the area covered by winds with velocities $-20 < U < -15$ m·s^{-1} (light blue) reduced, whereas the area of wind velocities $-15 < U < -10$ m·s^{-1} (green) increased and stretched to lower latitudes).

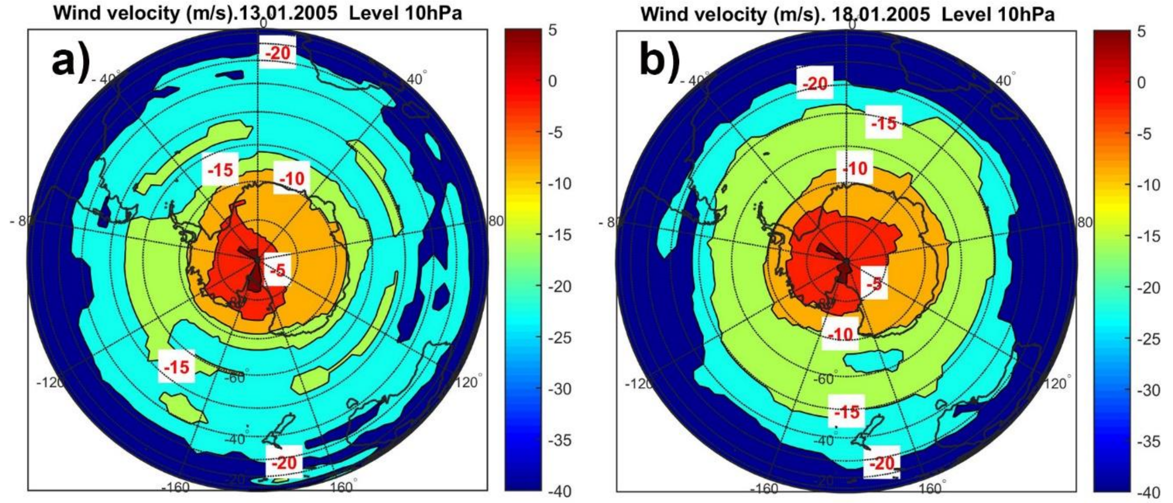

Fig.3. Charts of daily mean values of the U-component of wind velocity (in m·s^{-1}) in the upper stratosphere (10 hPa): a) before the onset of the SPE series (13 January 2005); b) after the onset of the SPE series (18 January 2005).

Charts of wind velocity before and after the onset of the SPE series in the lower stratosphere (the level 50 hPa) are shown in Fig.4. One can see that in the course of the SPEs under study a weakening of eastern winds took place only at polar latitudes >60ºS (the area of negative values of the *U*-component of wind velocity (light blue) reduced noticeably, so did the area of $U < -5$ m·s^{-1}). This results in a shift of western flow (enlargement of the area of positive *U*-values) to higher latitudes.

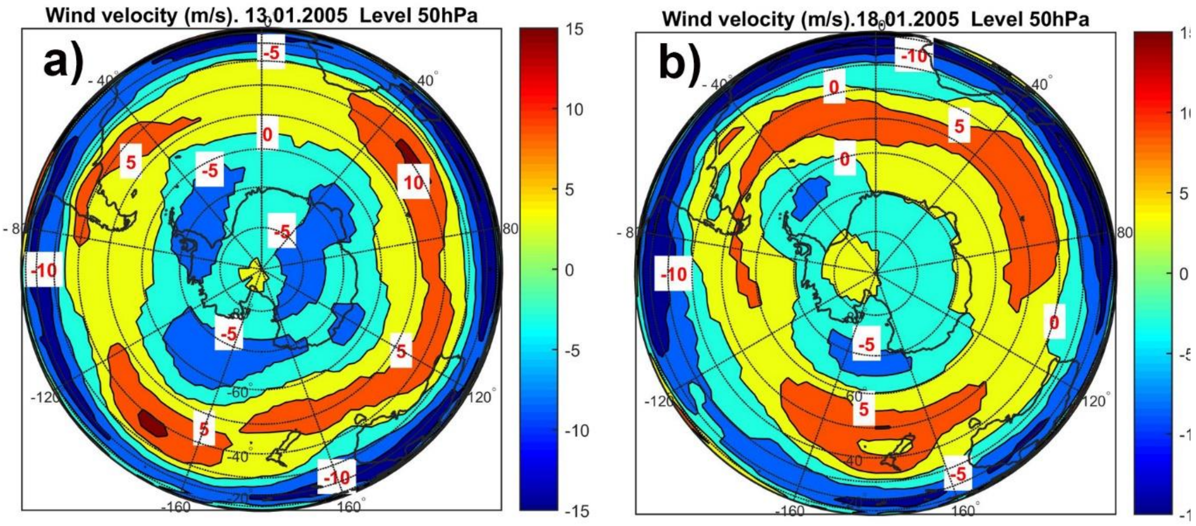

Fig.4. The same as in Fig.3, but for the lower stratosphere (50 hPa).

Fig.5 demonstrates zonal values of wind velocity on 13 and 18 January in the upper (10 hPa) and lower (50 hPa) stratosphere. The presented data confirm that a weakening of eastern winds did really take place at middle and high latitudes (>40ºS) in the upper stratosphere, whereas in the lower stratosphere this effect was limited by the polar area (>60ºS). It is seen (Fig.5b) that western zonal flow is displaced to higher latitudes, with a maximum of this flow having a ~10-degree shift to the south (from ~40ºS to ~50ºS).

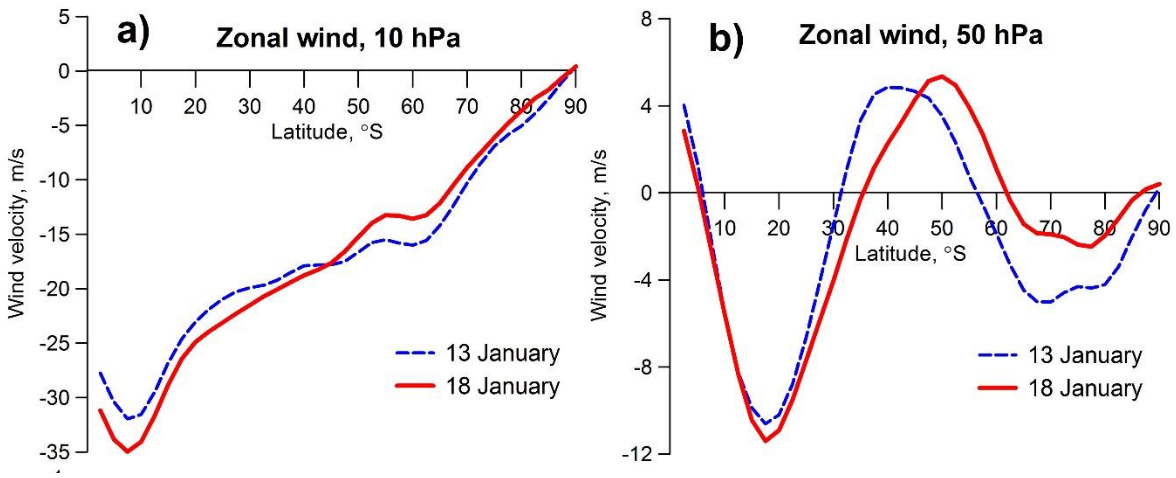

Fig.5. Zonal wind velocity before (13 January) and after (18 January) the onset of the SPEs series in the upper (a) and lower (b) stratosphere.

A possible mechanism of SPE effects on stratospheric circulation in summer period

The data presented above indicate that the SPEs of January 2005 were accompanied by noticeable disturbances of stratospheric circulation not only in the Northern (winter) hemisphere, as it was shown earlier, but also in the Southern (summer) hemisphere. In the Northern hemisphere, where the stratospheric polar vortex is formed in the cold half of the year, the events under study contributed to a pronounced intensification of the vortex (enhancement of western winds at all stratospheric levels) [*Veretenenko,* 2021]. In the Southern hemisphere the regime of stratospheric circulation in summer is quite different, with eastern winds dominating at all latitudes in the upper stratosphere. In the lower stratosphere eastern winds are observed only at polar and low latitudes, with a rather intensive western flow taking place at middle ones. So, the SPEs effects in the Southern (summer) hemisphere revealed a strong dependence both on altitude and latitude. Weakening of eastern winds was detected at middle and high latitudes in the upper stratosphere, whereas in the lower stratosphere this effect was observed only at polar latitudes, being accompanied by a shift of zonal western flow to the south.

Weakening of eastern winds observed in the Southern hemisphere during January 2005 SPEs provides evidence of a decrease of meridional gradients of temperature which are directed to the equator in summer stratosphere. This is possibly due to changes of the temperature regime of the polar stratosphere caused by changes of its chemical composition associated with SPEs (ozone depletion). As it was shown in a number of studies (e.g., [*Verronen et al*., 2006; *Damiani et al*., 2008]), increases of ionization rate during solar proton intrusions contribute to more intensive production of nitrogen (*NOx*) and hydrogen (*HOx*) oxides participating in catalytic cycles of ozone destruction. Ozone is known to be a radiatively active gas significantly influencing radiation fluxes both in shortwave and longwave ranges [*Brasseur and Solomon,* 2005]. Under summer (sunlight) conditions ozone absorbs solar UV radiation contributing to the stratosphere warming. So, ozone depletion associated with SPEs in summer may result in a cooling of the polar stratosphere and a reduction of meridional temperature gradients. Weakening of eastern winds in the Northern (summer) hemisphere associated with the SPE on 14 July 2000 was revealed by model simulations [*Krivolutsky et al.,* 2006]. Thus, a sequence of processes resulting in the detected weakening of eastern winds may be as shown in Fig.6. Reasons for the enhancement of eastern winds at low latitudes are not clear at the moment and need further investigations.

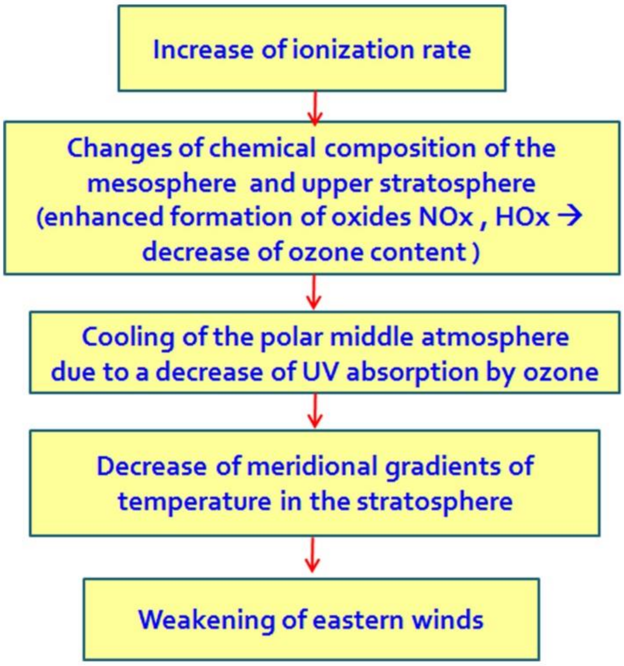

Fig.6. A possible scheme of SPE influence on stratospheric circulation in summer period.

Conclusions

1. Solar Proton Events of January 2005 were accompanied by noticeable disturbances of stratospheric circulation both in the Northern (winter) and Southern (summer) hemispheres, with the SPE effects in the winter and summer stratosphere differing significantly.
2. SPE effects on stratospheric circulation in the Southern hemisphere in summer revealed a strong dependence on altitude and latitude.
3. In the upper stratosphere a pronounced weakening of eastern winds associated with the studied SPEs was detected at middle and high latitudes (>40ºS). At lower latitudes eastern winds were found to enhance.
4. In the lower stratosphere weakening of eastern winds was limited by the polar area (>60ºS). Zonal western flow of middle latitudes was found to displace ~10 degrees to the south.
5. A possible mechanism of the detected effects seems to involve changes in the radiation-thermal balance of the polar middle atmosphere caused by changes in its chemical composition associated with ionization increase during SPEs.

References

Bazilevskaya, G.A., Krainev, M.B., et al. (2003). Solar proton events observed in the FIAN stratospheric experiment. Geomagn. Aeron. 43, no 4, 412-421.

Brasseur, G.P., Solomon, S. (2005). Aeronomy of the middle atmosphere. Springer, The Netherlands.

Damiani, A., Storini, M., et al. (2008). Solar particle effects on minor components of the Polar atmosphere. Ann. Geophys. 26, no 2, 361-370.

Kanamitsu, M., Ebisuzaki, W., et al. (2002). NCEP-DOE AMIP-II Reanalysis (R-2). Bull. Amer. Meteorol. Soc. 83, no 11, 1631-1644.

Krivolutsky, A.A., Klyuchnikova, A.V., et al. (2006). Dynamical response of the middle atmosphere to solar proton event of July 2000: Three-dimensional model simulations. Adv. Space Res. 37, no 8, 1602-1613.

Miroshnichenko, L.I. (2008). Solar cosmic rays in the system of solar-terrestrial relations. J. Atmos. Sol.-Terr. Phys. 70, 450-466.

Veretenenko S. (2021). Effects of Solar Proton Events of January 2005 on the middle atmosphere dynamics in the Northern hemisphere. Adv. Space Res. 68, no 4, 1814-1824.

Veretenenko, S., Thejll, P. (2004). Effects of energetic Solar Proton Events on the cyclone development in the North Atlantic. J. Atmos. Sol.-Terr. Phys. 66, no 5, 393-405.

Veretenenko, S.V., Thejll, P. (2005). Cyclone regeneration in the North Atlantic intensified by energetic solar proton events. Adv. Space Res. 25, no 3, 470-475.

Verronen, P.T., Seppälä, A., et al. (2006). Production of odd hydrogen in the mesosphere during the January 2005 solar proton event. Geophys. Res. Lett. 33, L24811.

Criteria for identification of geoeffective solar events

Georgieva K., Asenovski S., Kirov B.

SRTI-BAS; kgeorgieva@space.bas.bg

1. Abstract

"Space weather" is defined as conditions in the interplanetary and near-Earth space that can affect the performance and reliability of space-borne and ground-based technology, as well as human life and physiological conditions. It is well known that the drivers of space weather are geoeffective solar transients propagating from the Sun to the Earth. These drivers have different characteristics and different effects on the Earth. Various authors have proposed different criteria to identify these solar activity drivers. After a brief overview of the proposed so far criteria, we formulate our own criteria to be used for identifying geoeffective solar drivers and their effects on space weather.

Keywords: space weather, geoeffective solar agents, criteria

2. Introduction

There are basically three types of solar wind in which the Earth is immersed: slow solar wind (SSW) from the streamer belt, high speed solar wind streams (HSS) from solar coronal holes, and coronal mass ejections (CMEs).

The physical mechanism for the coupling of the interplanetary magnetic field (IMF) with the Earth's magnetic field is magnetic reconnection which is possible when the IMF vertical component Bz is negative – southward (Dungey, …). The energy transfer from the solar wind to the magnetosphere is different for CMEs and HSS (Tsurutani and Gonzalez, 1997) and, consequently, the geomagnetic disturbances which they cause are also different.

If a CME is faster than the ambient solar wind, it drives a shock/sheath ahead of it and the storm has an initial phase caused by the increase in the plasma ram pressure associated with the increase in density and speed in the sheath at the interface between the CME and the Earth's magnetosphere. The storm's main phase is due to the southward IMFs in the ejecta itself. If the fields are southward in both of the sheath and the ejecta, a two-step main phase storm can result. The storm recovery phase begins when the IMF turns less southward, and lasts for about 10 hours (Tsurutani and Gonzalez, 1997).

Corotating Interaction Regions (CIRs) are created when fast HSS emanating from the solar coronal holes interact with the high density, low-speed solar wind associated with the heliospheric current sheet. As the Bz component in CIRs is typically highly fluctuating, the main phases of the resultant magnetic storms typically have highly irregular profiles and are weaker than the ones caused by CMEs. On the other hand, the CIR-related storm recovery phases can last from many days to weeks (Tsurutani and Gonzalez, 1997). Therefore, though the most intense geomagnetic storms (defined by Kp) at both solar minimum and solar maximum are almost all generated by CMEs, the long-term (> solar rotation) averages of the geomagnetic activity indices closely follow the magnetic field variations in CIRs and slow solar wind (Richardson et al., 2002).

3. Identification schemes

3.1. Previous classifications

The **coronal mass ejections** originate from active regions of closed field lines, so their number and intensity are related to the number and surface area of sunspots which are also associated with regions of closed field lines. When enough energy is accumulated so that the such an active region loses stability, it ejects coronal matter with embedded magnetic fields. CMEs are characterized by unusually low proton temperature or low plasma beta (ratio of plasma pressure to magnetic pressure), composition anomalies, bidirectional suprathermal electron strahls indicating looped magnetic field lines rooted at both ends on the Sun. Fast CME’s drive shocks with enhanced plasma speed, density and temperature. An Earth-directed CME is observed as a halo around the Sun. A subclass of CME's are magnetic clouds (MC's) distinguished by enhanced magnetic field with smooth rotation inside the structure.

Various methodologies have been developed to identify and separate CMEs and magnetic clouds. The earlier ones mainly focused on anomalously low proton temperatures (Gosling et al., 1973; Elliott et al., 2005). Gosling et al. (1987) and Skoug et al. (2000) looked for the presence of a bidirectional electron strahl indicating that both ends of the magnetic field tube are attached to the solar surface. Cane and Richardson (2003) and Richardson and Cane (2010) provided a list of CMEs in the near-Earth space based on the combination of proton temperature, O7+/O6+ density ratio, electron strahl, magnetic field structure, and energetic particle measurements. An important parameter is the ration between the observed and expected proton velocity Tp/Texp, where Texp is the expected temperature for the observed solar wind speed Vsw:

$T_{ex}= 3(0.0106V_{sw} – 0.287)$ if $V_{sw} < 500$ km/s and

$T_{ex} = (0.77V_{sw} – 265)$ if $V_{sw} > 500$ km/s

In this list, Cane and Richardson 2003) included all CMEs, both magnetic cloud and mon-magnetic cloud ones. On the other hand, Lepping et al. (2005), Wu et al. (2011) compiled lists of only magnetic clouds. To this end, they developed a computer program to automatically detect MCs and MC-like structures, based on requirements for 1) enhanced magnetic field strength, 2) a smooth change in field direction as observed by a spacecraft passing through the MC, and 3) low proton temperature (and low proton plasma beta) compared to the ambient plasma. Jian et al. (2006) produced a catalog of ICMEs at Earth based on the total pressure, the proton temperature, the alpha-to-proton density ratio, the magnetic field structure, and the presence of bidirectional electron streaming.

We are here concentrating on criteria which can be calculated from data included in OMNI and OMNI2 database because they cover the longest period of in situ measurements.

Yermolaev et al. (2009) formulated 9 solar wind types, and used a preliminary identification program with preset threshold criteria for the plasma types to identify them based on parameters calculated from data compiled in the original OMNI database (for more details, see their Table 1):

1) Heliospheric current sheet: $N<7$ cm^{-3}; $V<500$ km/s; $\beta>0.7$
2) Slow solar wind: $N>3$ cm^{-3}; $V<450$ km/s; $\beta<1$
3) Fast solar wind: $N<20$ cm^{-3}; $V\geq450$ km/s; $\beta<1$
4) Corotation interaction region: $N>3$ cm^{-3}; $B>5$ nT; $T/T_{exp}>1$; thermal pressure $NkT >0.007$; $\beta<1$
5) Ejecta (CMEs): $N<10$; $T/Texp<0.5$; $NkT<0.01$; $\beta<0.5$
6) Magnetic clouds: $N<10$; $B>10$; $T/Texp<0.5$; $NkT<0.01$; $\beta<0.5$
7) Rarefaction regions: $N \leq1$; $V <500$; $T/Texp<1$; $NkT<0.01$.

We are not dealing here with the IS - forward interplanetary shock, and ISa - reverse interplanetary shock, as these events are very short, of the order of a minute.

Xu and Borovsky (2014) defined 4 categories of geoeffective solar transients, further separating the slow solar wind into streamer belt solar wind plasma and sector-reversal-region plasma. The authors used the Lepping et al. (2005) list of MCs, with the continuation by Wu et al. (2011). They conducted a detailed study of the separation of the 4 categories, and presented criteria for separating MCs from the other geoeffective drivers. Fig.1, upper left, demonstrates that MCs are easily distinguishable from other solar wind transients in terms of plasma beta. MCs (ejecta) have much lower plasma beta than HSS-related ("coronal hole") and slow solar wind ("streamer belt" and "sector reversal region" plasma). This is confirmed by Fig.1, upper right, illustrating the ratio between the expected and the observed proton temperature in the different solar wind structures. This ratio is much higher in CME ("ejecta") type plasma than in all other transients. Another indicative parameter is the Alfven speed which in the case of CMEs is lower than the other categories (Fig.1, bottom right). Finally, Fig.1, bottom left demonstrates that the magnetic field fluctuations in a MC (and in a CME in general) are much lower than in other solar wind times.

Based on these statistical results, Xu and Borovsky (2014) developed an algebraic scheme to categorize the solar wind plasma into the above four types. The scheme uses three solar wind parameters: (1) the proton-specific entropy $S_p = T_p/n_p^{2/3}$, (2) the proton Alfvén speed $V_A = B/(4\pi m_p n_p)^{1/2}$, and (3) the ratio of the measured proton temperature T_p compared with the velocity-dependent expected temperature for the solar wind speed $T_{exp}= (V_{sw}/258)^{3.113}$. To calculate those three parameters, four solar wind quantities are used: the proton number density n_p, the proton temperature T_p, the magnetic field strength B, and the solar wind speed V_{sw}.

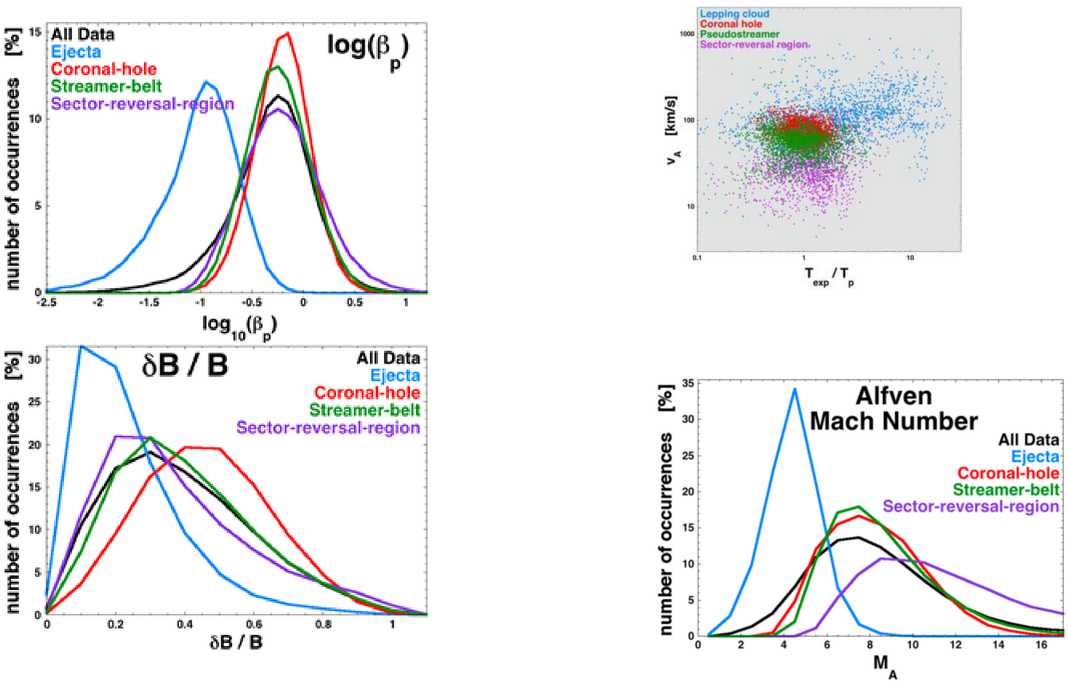

Figure1. Comparison of MC, HSS, streamer belt and sector reversal region plasma (see the text). From Xu and Borovsky (2014).

Veselovsky et al. (2018) produced a binary classification of solar wind types according to three main hydrodynamic parameters—the proton speed, the proton temperature, and the proton density, and therefore 9 types of solar wind types which arise at different frequencies and originate from different sorts of solar activity:

(1) fast–hot–dense, (2) fast–hot–rarefied, (3) fast–cold–dense, (4) fast–cold–rarefied,
(5) slow–hot–dense, (6) slow–hot–rarefied, (7) slow–cold–dense, (8) slow–cold–rarefied.
They assumed that a solar wind is:

fast if V >450 km/s and slow if V <400 km/s; hot if $T > 10^5$ K and cold if $T < 7.5 \times 10^4$ K,
dense if $n > 6$ cm^{-3} and rarefied if $n < 5$ cm^{-3}.

If at least one parameter turns to be within the excluded interval, the respective wind is categorized as (9) – "zero type" which is found to cover about 32.5% of time. The second most frequent type of solar wind (25.2%) is ***fhr*** which originates from long-term flows from coronal holes, and the third one is ***scd*** which is formed by flows from coronal streamers and pseudostreamers, as well as by heliospheric plasma layers near magnetic sectors.

Feldman et al. (1976) studied the high-speed solar wind flow parameters at 1 AU, and accepted a stream for study only if the maximum speed exceeded 650 km/s. According to Bame et al. (1976), an HSS is an observed variation of solar wind speed, with an increase of at least 150 km/s within a five-day interval during which the speed stays above $(V_0 + V_m)/2$ where V_0 is the base speed out of which the stream rises, and V_m is the maximum speed attained within the stream.

Broussard et al. (1978) defined it as a period in which the solar wind speed is faster than 500 km/s averaged over a day.

Venkatesan et al. (1982) defined the starting day of a high speed stream by a substantial increase ($\Delta V \gtrsim 200$ km/s) in the solar wind speed to values of $\gtrsim 550$ km/s and which persists at such high values for an interval of at least three days.

Lindblad and Lundstedt (1981) provided a **catalogue** of high speed solar wind streams during 1964-75. In this period, 346 streams were detected, defined as periods in which the velocity difference between the lowest 3-h velocity value and the highest 3-h value of the following day is greater than 100 km/s, and it lasts for at least two days. Two continuations of this catalogue were published: for the period 1975-78 (Lindblad and Lundstedt, 1983), and for the period 1978-82 (Lindblad et al., 1989).

Mavromichalaki et al. (1988) and Mavromichalaki and Vassilaki (1998) updated the catalogues of Lindblad and Lundstedt, using the same criteria as Lindblad and Lundstedt (1981). Additionally, Mavromichalaki et al. (1988) divided the high speed solar wind streams into two groups: ones originating from coronal holes ("Corotating Streams"), and others related to active regions ("Flare Generated Streams"). The authors showed that the magnetic field magnitude and polarity, bulk speed, proton density, and temperature of the solar wind are different for the two types of streams. Maris and Maris (2005) further extended and derailed this group of catalogs, adding the parameter "importance" I and "sum importance" ΣI of the stream $I = \Delta V_{max} * d$ where $\Delta V_{max} = (V_{max} - V_0)$, d is the duration of the high speed stream, V_{max} is its maximum daily mean velocity, and V_0 is the mean velocity.

3.2. Our classification

3.2.1. CMEs

Comparing the various catalogs, it can be noted that they do not always coincide.
As an example, we look at the most powerful CME of 2011, Dst=-147 (Fig.1).

- Cane and Richardson have determined that the CME started at 22:00 on October 24 and ended at 16:00 on October 25;
- In Xu and Borovsky's list the CME started at 23:00 on October 24 and ended at 21:00 on October 25;
- In Yermolaev et al's list this CME has been identified as a magnetic cloud lasting from 12:00 on October 23 to 12:00 on October 24.

One of the reasons for the discrepancies lies in the different definitions of the expected proton temperature based on the solar wind velocity (see above). We have performed visual inspection of the CMEs included in the various catalogs, and have formulated the following criteria for identifying a CME:

-Proton temperature $Tp < 0.5T\text{exp}$, where $T\text{exp} = 3(0.0106V\text{sw} – 0.287)$ if $V\text{sw} < 500$ km/s and $T\text{exp} = (0.77V\text{sw} – 265)$ if $V\text{sw} > 500$ km/s

-Magnetic field magnitude $B \geq 10$ nT

-Plasma Beta ≤ 0.8 for at least 5 hours.

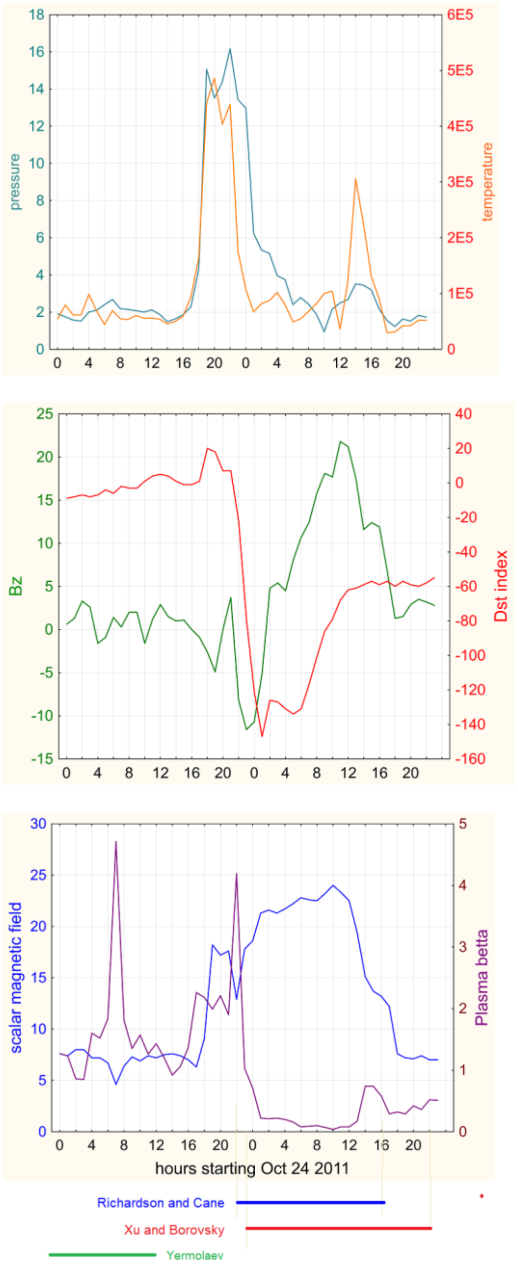

Fig.2 (left). Parameters of a CME observed in October 2011 (first 3 panels) together with its duration determined in the catalogs of Richardson and Cane (blue horizontal line), Xu and Borovsky (red horizontal line) and of Yermolaev (green horizontal line)

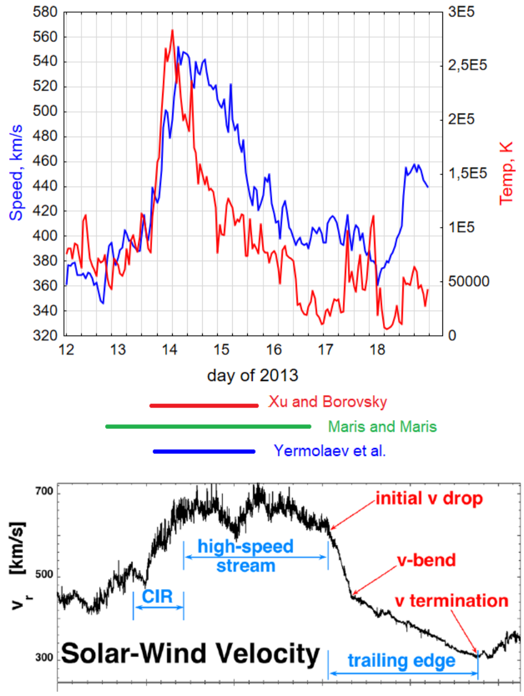

Fig.3 (upper panel) A HSS in January 2013 with its duration determined in the catalogs of Xu and Borovsky (red horizontal line) Maris and Maris (green horizontal line)and of Yermolaev (blue horizontal line); Bottom panel: the definition of the phases of a HSS by Borovsky and Denton (2016).

3.2.2. HSS

Fig.3 presents a HSS in January 2013. In Xu and Borovsky’s list this HSS starts at 21:00 on January 13 and ends on 13:00 on January 15. In the catalog of Maris and Maris it starts between 15:00 and 19:00 on January 12 and ends between 19:00 and 21:00 on January 16. In Yermolaev’s catalog the fast wind starts at 18:00 on January 13 and lasts until 12:00 on January 15.

The main difference is the determination of the end of the HSS. We have adopted the definition of Borovsky and Denton (2016) presented in the bottom panel of Fig.3. According to it, a HSS starts with a corotating interaction region (CIR) characterized by a sharp jump in the plasma speed, density and temperature, followed by the body co high speed stream with persisting high plasma flow speed, then by a two-step decrease of the speed, and ends with the beginning of the velocity rise.

Our criteria for a HSS include an increase of the solar wind velocity by at least 100 km/s in no more than one day to at least 500 km/s for at least 5 hours, accompanied by high temperature ($T_p>T_{exp}$) and low density, and lasts until V increase for at least 5 hours.

Acknowledgements

This research has been supported by the National Science Fund grant KP-06-N44/2.

References

Bame, S.J., Asbridg,e J.R., Feldman, W.C., Gosling, J. (1976) Solar cycle evolution of high-speed solar wind streams. Astrophysical Journal 207, Aug. 1, 1976, pt. 1, p. 977-980, doi:10.1086/154566

Borovsky, J.E., Denton, M.H. (2016) The trailing edges of high-speed streams at 1 AU. JGR Space Physics 121 (7), 107-6140, https://doi.org/10.1002/2016JA022863

Broussard, R.M., Sheeley, N.R. Jr., Tousey, R., Underwood, J. H., (1978) A survey of coronal holes and their solar wind associations throughout sunspot cycle 20. Solar Physics 56 (1), 161-183, DOI:10.1007/BF00152641,

Cane H.V., and I. G. Richardson (2003), Interplanetary coronal mass ejections in the near-Earth solar wind during 1996–2002, J. Geophys. Res., 108, 1156, doi:10.1029/2002JA009817.

Elliott, H.A., D.J. McComas, N.A. Schwadron, J. T. Gosling, R.M. Skoug, G. Gloeckler, and T. H. Zurbuchen (2005), An improved expected temperature formula for identifying ICMEs, J. Geophys. Res., 110, A04103, doi:10.1029/2004JA010794.

Farrell, W.M., Desch, M.D. (2002). Solar proton events and the fair weather electric field at ground, Geophys. Res. Lett., Vol 29, No 9, pp. 1323- 1326, DOI: 10.1029/2001GL013908.

Feldman W.C., Asbridge J.R., Bame S.J. Gosling J.T. (1076) High-speed solar wind flow parameters at 1 AU. Journal of Geophysical Research, Volume 81, Issue A28, p. 5054-5061, DOI:10.1029/JA081i028p05054.

Gosling, J. T., V. Pizzo, and S. J. Bame (1973), Anomalously low proton temperatures in the solar wind following interplanetary shock waves—Evidence for magnetic bottles, J. Geophys. Res., 78, 2001–2009.

Gosling, J. T., D. N. Baker, S. J. Bame, W. C. Feldman, R. D. Zwickl, and E. J. Smith (1987), Bidirectional solar wind electron heat flux events, J. Geophys. Res., 92, 8519–8535.

Hozworth, R.H. Norville, K.W., Williamson, P.R. (1987). Solar flare perturbations in stratospheric current systems, Geophys. Res. Lett. 14 (8), 52-855.

Lepping, R. P., C.-C. Wu, and D. B. Berdichevsky (2005), Automatic identification of magnetic cloud-like regions at 1 AU: Occurrence rate and other properties, Ann. Geophys., 23, 2687-2704. SRef-ID: 1432-0576/ag/2005-23-2687

Maris O., Maris G (2005) Specific features of the high-speed plasma stream cycles. Advances in Space Research 35 (12), 2129-2140, doi:10.1016/j.asr.2005.02.068

Mavromichalaki, H., Vassilaki, A., Marmatsouri, E. (1988) A catalogue of high-speed solar-wind streams: Further evidence of their relationship to Ap-index. Solar Physics, Volume 115, Issue 2, pp.345-365, DOI:10.1007/BF00148733,

Mavromichalaki, H., Vassilaki, A. (1998) Fast Plasma Streams Recorded Near the Earth During 1985–1996. Solar Physics 183, 181–200. https://doi.org/10.1023/A:1005004328071

Richardson, I.G., Cane, H.V., Cliver, E.W. (2002) Sources of geomagnetic activity during nearly three solar cycles (1972-2000). JGR Space Physic 107 (A8), CiteID 1187, DOI 10.1029/2001JA000504,

Richardson, I. G., and H. V. Cane (2010), Near-Earth interplanetary coronal mass ejections during solar cycle 23 (1996–2009): Catalog and summary of properties, Sol. Phys., 264, 189.

Skoug, R. M., W. C. Feldman, J. T. Gosling, D. J. McComas, and C. W. Smith (2000), Solar wind electron characteristics inside and outside coronal mass ejections, J. Geophys. Res., 105, 23,069–23,084.

Tsurutani B.T.; Gonzalez, W. D. (1997), The Interplanetary causes of magnetic storms: A review. In: Magnetic Storms., Geophys. Monogr. Ser., vol. 98, edited by B. T. Tsurutani et al., pp. 77-89, AGU, Washington, D. C.

Venkatesan D., Shukla A.K., Agrawal S.P., (1982) Cosmic-Ray Intensity Variations and Two Types of High-Speed Solar Streams, Solar Physics 81 (2), 375-381,

Yermolaev, Y.I., Nikolaeva, N.S., Lodkina, I.G. et al. (2009). Catalog of large-scale solar wind phenomena during 1976–2000. Cosmic Res 47, 81–94, https://doi.org/10.1134/S0010952509020014

Xu F., Borovsky J.E. (2014) A new four-plasma categorization scheme for the solar wind, JGR Space Physics 120 (1) 70-100, https://doi.org/10.1002/2014JA020412